Springer Geography

Assefa M. Melesse
Mekdelawit M. Deribe
Ethiopia B. Zeleke *Editors*

Land and Water Degradation in Ethiopia

Climate and Land Use Change Implications

Springer

Springer Geography

The Springer Geography series seeks to publish a broad portfolio of scientific books, aiming at researchers, students, and everyone interested in geographical research.

The series includes peer-reviewed monographs, edited volumes, textbooks, and conference proceedings. It covers the major topics in geography and geographical sciences including, but not limited to; Economic Geography, Landscape and Urban Planning, Urban Geography, Physical Geography and Environmental Geography.

Springer Geography—now indexed in Scopus

Assefa M. Melesse · Mekdelawit M. Deribe ·
Ethiopia B. Zeleke
Editors

Land and Water Degradation in Ethiopia

Climate and Land Use Change Implications

Springer

Editors
Assefa M. Melesse
Department of Earth and Environment
Institute of Environment
Florida International University
Miami, FL, USA

Mekdelawit M. Deribe
Department of Earth and Environment
Institute of Environment
Florida International University
Miami, FL, USA

Ethiopia B. Zeleke
Department of Earth and Environment
Institute of Environment
Florida International University
Miami, FL, USA

ISSN 2194-315X ISSN 2194-3168 (electronic)
Springer Geography
ISBN 978-3-031-60250-4 ISBN 978-3-031-60251-1 (eBook)
https://doi.org/10.1007/978-3-031-60251-1

Preface

Land degradation issues in Ethiopia include soil erosion, nutrient depletion, deforestation, and loss of vegetation cover. In addition to the human-induced land cover changes that have led to severe land degradation, climate change is exacerbating land degradation through increased warming, shifting rainfall patterns, vegetation desiccation, and more frequent extreme weather events such as droughts and floods. All of these factors result in poor agricultural yield and hence food shortages. As the second most populous country in Africa, Ethiopia has experienced rapid population growth resulting in land and water resource overuse, land encroachment, overgrazing, and unsustainable land management practices. Overuse and poor land and water management have been the major factors in the decline of agricultural productivity. This book aims to shed light on the critical issue of land and water degradation in Ethiopia brought about by the complex interplay of climate change and land use dynamics.

Drought, unsustainable resource use, poor land and water management practices, and climate change have contributed to environmental degradation in Ethiopia. Over the last few decades, deforestation, soil erosion, and land degradation have increased due to prolonged dry periods and erratic rainfall. This, in turn, exacerbates the vulnerability of the agricultural sector and threatens the country's biodiversity and its ability to produce enough food for its citizens and develop its economy. As the climate change impact is getting severe in Ethiopia, its ability to avoid consequences and reduce vulnerability is low and hence grappling with the far-reaching consequences of these changes. Simultaneously, rapid land use changes driven by population growth, urbanization, and expanding agricultural practices have intensified the pressure on Ethiopia's fragile ecosystems.

This book covers various topics related to land and water degradation in Ethiopia. It explores the intertwined relationship between climate change, land use changes, water quality, soil erosion, land degradation, drought, floods, groundwater, water pollution, and land management.

The book has 20 chapters divided into four thematic areas: Land cover dynamics, soil and land management, climate change and water management, and water supply and quality. Chapters on land cover dynamics explore mapping and prediction of

land use/cover and their implications for future water availability. Factors influencing land use changes and their implications for the environment and water resources are examined. The impact of climate change on future water availability and risk, factors affecting channel stability, such as sedimentation and bank erosion, and the proposal of appropriate engineering techniques for river stabilization, factors influencing water consumption patterns, and exploration of the potential for water demand management and conservation strategies in urban areas are included. Climate variability and agricultural drought and their implications for rainfed agriculture are also presented.

The book will provide some insight into the issues of land degradation for meaningful action to improve land and water resources in the face of climate change and land use dynamics. The book will be beneficial for researchers, water resources and environmental managers, students, policymakers, and others.

Miami, USA

Assefa M. Melesse
Mekdelawit M. Deribe
Ethiopia B. Zeleke

Contents

Chapter 1
Introduction

Ethiopia B. Zeleke, Mekdelawit M. Deribe, and Assefa M. Melesse

Abstract The world is facing an unprecedented level of land and water degradation, the two most important resources for human survival and proper functioning of the environment. As the population grows, the need for land and water has increased dramatically, leading to deterioration of water quality and loss of land fertility, impacting human health and agricultural productivity. These impacts are pronounced in developing countries where watershed management and farming practices are traditional and poor. These effects are also highly compounded by the impact of climate change increasing the vulnerability of communities to droughts and floods. This book aims to shed light on the complex interplay between climate change and land use change and their implications for land and water degradation in Ethiopia.

Keywords Land degradation · Water degradation · Climate change · Agricultural productivity · Vulnerability

Overview

The degradation of land and water resources has far-reaching implications for food security, livelihoods, and the environment. Land and water degradation in Ethiopia, a country heavily reliant on agriculture and natural resources, poses significant challenges to the country's sustainable development and population well-being. This book aims to shed light on the complex interplay between climate change and land use change and their implications for land and water degradation in Ethiopia. It presents the multidimensional dynamics of landcover change, the impact of soil degradation, the challenges posed by climate change and the importance of water management, to provide a comprehensive understanding of the issues at hand. The book highlights four major themes: landcover dynamics, soil and land management, climate change and water management, and water supply.

E. B. Zeleke (✉) · M. M. Deribe · A. M. Melesse
Department of Earth and Environment, Florida International University, Modesto A. Maidique Campus, Miami, FL 33199, USA
e-mail: ebisratz@fiu.edu

A. M. Melesse et al. (eds.), *Land and Water Degradation in Ethiopia*, Springer Geography, https://doi.org/10.1007/978-3-031-60251-1_1

Landcover Dynamics, Soil and Land Management

Land system dynamics refers to the process and patterns of land use (anthropogenic use) and landcover (biophysical conditions) change. Over the past decades, the increased magnitude and rate at which the Earth's land surface has been altered has been noted by several studies (Lambin et al., 2001; Rindfuss et al., 2004; Newbold et al., 2015). Humans, as primary contributors and significant drivers of change, contribute to land use change through deforestation, rangeland modification, urbanization, and agricultural expansion and intensification (Gurtner et al. 2011). These changes directly impact global biodiversity, contribute to changing weather patterns at local and regional scales, and increase the susceptibility of soil to erosion.

Landcover dynamics in Ethiopia have undergone changes over the years, driven by population growth, urbanization, and agricultural expansion (Muke 2019). Among the implications associated with such changes is poor land management and the loss of fertile soil, which reduces agricultural productivity and hampers food security. Understanding trends in landcover change and highlighting the drivers, spatial extent, and consequences of land degradation are essential to formulating effective land management strategies. Land management approaches that address land degradation require a comprehensive understanding of the drivers and impacts of change to select suitable mitigation measures. This involves quantifying the impacts of land degradation and environmental change, assessing the suitability of different practices, and designing policies that promote sustainable land management.

Climate Change and Water Management

Climate change poses significant risks to water resources in Ethiopia (Conway and Schipper 2011), with shifting rainfall patterns and rising temperatures threatening water resource availability and increasing uncertainty in the timing and intensity of associated floods and droughts (Funk 2012; Nicholson 2015). Projected rainfall patterns do not show a clear direction of change at short temporal resolutions, which poses limitations in understanding and responding to risks posed by climate change. This lack of clarity makes it challenging to anticipate the future availability and distribution of water resources, hindering effective planning and management efforts. Therefore, to understand the implication of and risks posed by climate change on water availability (timing and quantity) and quality, modeling climate patterns, analyzing recent trends of rainfall variability, understanding the interaction between climate components and anthropogenic factors, and prioritizing vulnerability reduction approaches need to be pursued. With such approaches, it is possible to better navigate climate change impacts and associated uncertainties and enhance resilience to future challenges.

Water Supply, Quality, and Distribution

The dynamic rise in anthropogenic water demand has resulted in increased pressure on water resources, contributing to water scarcity. In Ethiopia, rapid urbanization, particularly in Addis Ababa, further compounds the pressure on water resources, leading to a projected deficiency in water supply (Arsiso et al., 2017). Competition for water across sectors including urban, agricultural, and environmental needs has intensified. Additionally, access to good-quality water is declining due to overexploitation and pollution of available sources. The rising capital and operational costs of water treatment, transportation, and distribution have further compounded the challenge of providing regular access to clean drinking water for the growing population (Sharma and Vairavamoorthy, 2009).

However, the supply side is also not static and is driven by climate variability. Climate change can magnify and/or alter the impacts of water scarcity, especially in already stressed systems and vulnerable social groups. Therefore, it is crucial to recognize the dynamic nature of water supply and its interconnectedness with human activities and climate patterns.

Managing water resources ranges from improving societal resilience to short-term variability of water resources to adaptation to long-term climate-induced changes. Adaptive water management approaches that acknowledge that water availability is influenced by complex interactions of natural and manmade processes with intrinsic uncertainties offer the most effective ways to assess and mitigate the impacts of water scarcity. They involve proactive measures such as improving water use efficiency, implementing demand management techniques, promoting water conservation practices, and diversifying water sources.

In conclusion, this book provides an analysis of the complex relationship between climate change, land use change and water management in Ethiopia and explores heir impact on the degradation of land and water resources. The interconnected themes of landcover dynamics, soil and land management, climate change and water management highlight the multidimensional challenges facing the country's sustainable future.

The theme of landcover dynamics explores the historical and current trends of landcover changes, highlighting the drivers and consequences of land degradation. It goes into impacts of landcover changes on watershed processes and presents current approaches to simulate and forecast landcover change. The soil theme focuses on understanding the properties, qualities, and management of soil resources. Chapters within this theme examine various aspects of soil, including composition, structure, fertility, and vulnerability to erosion. These chapters also highlight the importance of soil conservation measures and sustainable agricultural practices to maintain soil health, prevent erosion, enhance nutrient management, and improve overall land productivity. The theme of climate change and water management investigates the interaction between climate variability, water resources and agricultural systems. These chapters examine the impacts of climate variability on rainfed agriculture, drought management, and water resource planning. Adaptation strategies and policies

to enhance water management practices, improve water use efficiency, and promote sustainable agricultural practices are also highlighted. Assessment and management of water resources for domestic and agricultural purposes are presented in the water supply and irrigation theme. Chapters within this theme assess the performance of water supply distribution networks, evaluate alternative supply sources and their feasibility in meeting the growing water demand. Irrigation practices that optimize water use in agriculture while maintaining crop productivity are also presented.

Researchers, policy makers, and stakeholders can gain insight into the underlying causes of various environmental challenges in Ethiopia and potential options for intervention that are backed by sound policies.

References

Arsiso BK, Tsidu GM, Stoffberg GH, Tadesse T (2017) Climate change and population growth impacts on surface water supply and demand of Addis Ababa, Ethiopia. Clim Risk Manag 18:21–33

Gurtner M, Liniger H, Studer RM, Hauert C (2011) Sustainable land management in practice: guidelines and best practices for Sub-Saharan Africa

Lambin EF, Turner BL, Geist HJ, Agbola SB, Angelsen A, Bruce JW, Coomes OT, Dirzo R, Fischer G, Folke C, George P (2001) The causes of land-use and land-cover change: moving beyond the myths. Glob Environ Chang 11(4):261–269

Muke M (2019) Reported driving factors of land-use/cover changes and its mounting consequences in Ethiopia: a review. Afr J Environ Sci Technol 13(7):273–280

Newbold T, Hudson LN, Hill SL, Contu S, Lysenko I, Senior RA, Börger L, Bennett DJ, Choimes A, Collen B, Day J (2015) Global effects of land use on local terrestrial biodiversity. Nature 520(7545):45–50

Rindfuss RR, Walsh SJ, Turner BL, Fox J, Mishra V (2004) Developing a science of land change: challenges and methodological issues. Proc Natl Acad Sci 101(39):13976–13981

Sharma SK, Vairavamoorthy K (2009) Urban water demand management: prospects and challenges for the developing countries. Water Environ J 23(3):210–218

Declan, Conway E. Lisa F., Schipper (2011) Adaptation to climate change in Africa: Challenges and opportunities identified from Ethiopia Global Environmental Change 21(1) 227-237 10.1016/j.gloenvcha.2010.07.013

Nicholson, S.E. (2015) The Predictability of Rainfall over the Greater Horn of Africa. Part II: Prediction of Monthly Rainfall during the Long Rains Abstract Journal of Hydrometeorology 16(5) 2001-2012 10.1175/JHM-D-14-0138.1

Funk, C.C. (2012) Explaining Extreme Events of 2011 from a Climate Perspective Bulletin of the American Meteorological Society 93(7) 1041-1067 10.1175/BAMS-D-12-00021.1

Chapter 2
Understanding the Effect of Land Use Land Cover (LULC) Dynamics on the Streamflow of Gelda Watershed, Abay Basin, Ethiopia

Mulugeta A. Tegegne and Temesgen Enku

Abstract Globally, land cover has drastically changed over the last five decades, especially in tropical regions like the Nile basin. Changes in land use and land cover (LULC) have affected the streamflow in the highlands of Ethiopia. Remote sensing data and Geographical Information System (GIS) were used to understand the effect of LULC change dynamics on the streamflow of the Gelda watershed that drains into Lake Tana of the Abay Basin. The Landsat images from 1984, 2000, and 2016 were extracted and analyzed using ENVI and ArcGIS software. Land cover maps were classified using Maximum Likelihood Algorithm classification technique in ENVI 5.3 platform. In the Gelda watershed five major LULC classes (grazing land, agricultural land, forest land, bush land, and built-up area) were found. The streamflow of the watershed was evaluated using SWAT (Soil and Water Assessment Tool) model. During the study period, it was found that 32.8% of the bush land, forest, and grazing land was changed to agricultural land. This has resulted in streamflow change over the years. The monthly stream flow modeling showed a very good agreement between measured and simulated flows. The results show an increase in the peak flow during the wet months and a decrease in low flows during the dry months. The model results showed that the streamflow characteristics were changed due to the LULC changes during the study period (1984–2016).

Keywords Land use land cover · Streamflow · Abay Basin · Lake Tana · Ethiopia

M. A. Tegegne
Department of Water Technology, Bahir Dar Polytechnic College, Bahir Dar, Ethiopia

M. A. Tegegne · T. Enku (✉)
Faculty of Civil and Water Resources Engineering, Bahir Dar Institute of Technology, Bahir Dar University, Bahir Dar, Ethiopia
e-mail: temesgene@bdu.edu.et

A. M. Melesse et al. (eds.), *Land and Water Degradation in Ethiopia*, Springer Geography, https://doi.org/10.1007/978-3-031-60251-1_2

Introduction

Land use and land cover (LULC) change is a major challenge of global environment (Prakasam 2010). Land use change is the alteration of land use due to human intervention for various purposes, such as agriculture, settlement, transportation, infrastructure, manufacturing, parking, recreational uses, mining, and fishery. Land cover change refers to the conversion of land cover from one category to another and/or the modifications of conditions within a category (Meyer and Turner 1992). Various studies used land cover mapping tools and methods to understand land use changes, inventory of forest and natural resources as well as understand the changes in the hydrologic behavior of watersheds (Getachew and Melesse 2012; Mango et al. 2011a, b; Wondie et al. 2011, 2012; Melesse and Jordan 2002; Bekele et al. 2017; Mohammed et al. 2013). LULC is directly linked to human activities. LULC dynamics modify the availability of different resources including vegetation, soil, and water (Ahmadizadeh 2014).

Land use dynamics and land degradation are major environmental challenges in Ethiopia. Land degradation includes all processes that diminish the capacity of land resources to perform essential functions and ecosystem services, which are caused by two interlocking complex systems: the natural ecosystem and the human social system (Hurni et al. 2010). The major causes of land degradation in Ethiopia are rapid population increase, severe soil loss, deforestation, low vegetative cover and unbalanced crop and livestock production (Girma 2001). LULC changes and land degradation are interrelated because LULC changes are associated with deforestation, biodiversity loss, and land degradation (Messay 2011). Studies conducted in various parts of the country reported a significant decrease in vegetation cover due to the expansion of cultivated land for more food production (Abate 2011). Tilahun et al. (2001) and Belay (2002) stated that majority of the LULC changes were toward cultivated land which also aggravated soil erosion in the region. Evaluating existing LULC and its periodic change and land degradation is useful for natural resource managers and policy makers (Tahir et al. 2013).

Remote Sensing (RS) data has been used to understand the spatial and temporal variations in a watershed over time and the interaction of the hydrological components of a watershed (Ashraf 2013). Landsat images have served a great deal in the classification of different landscape components at larger scales (Ozesmi and Bauer 2002). A variety of supervised classification methods have been applied extensively for land use change analysis throughout the world, with results up to 95% accuracy (Butt et al. 2015). Boori et al. (2015) analyzed the LULC disturbance caused by tourism using a few remote sensing and GIS-based techniques including supervised classification. Changes in LULC alter both runoff behavior and the balance that exists between evapotranspiration, groundwater recharge and stream discharge in specific areas and in entire watersheds, with considerable consequence for all water users. The LULC changes in the past three decades are mostly linked to agricultural development attributed to population pressure and environmental changes (Akpoti et al. 2016). Current trends in land use land cover must be studied and improved

for appropriate natural resources management and knowledge-based decision. Such studies should be done in teamwork with the participation of all stakeholders for effective natural resources management and sustainable development (Asres et al. 2016).

This study aims to understand the effects of LULC dynamics on the hydrology of Gelda watershed. This paper attempts to quantify the major LULC changes and assess the effect of LULC change on the hydrology of Gelda watershed over the past three decades from 1984 to 2016.

Materials and Methods

Study Area Description

This study was carried out in the Gelda watershed. The watershed is located between latitudes of 357,196.65 and 348,512.32° N, and longitudes of 1,287,075.46 and 1,294,859.33° E (Fig. 2.1). The watershed flows from east to west and finally drains to Lake Tana in the southeast portion of the lake.

The Gelda watershed covers an area of 4479 ha and the elevation of this watershed ranges from 2017 to 2480 m above mean sea level. The average annual minimum and maximum temperatures are 7.8 °C and 29.8 °C, respectively. The average annual rainfall ranges from 1200 to 1500 mm. The altitude of this watershed ranges from 2017 to 2480 m. According to local climate classification system based on altitude and temperature, Gelda watershed is characterized as Woynadega (partially warm at 1500–2500 m altitude) agro-ecological zone. The Gelda watershed has three major soil types, namely Nitosols (7.5%), Luvisols (25.5%), and Vertisols (67%). The upstream of Gelda watershed is characterized by steep valley slopes while downstream areas have gentle slopes. The watershed contains two main perennial ungagged rivers called Memoshita and Wushit, which form the main Gelda River. The observed stream flow from 1984 to 2018 showed peak steam flows occur in July and August while minimum flow occurs at the end of dry period, usually in May.

Image Preprocessing and Classification

Cloud-free Landsat images were selected for LULC classification. Different satellite images were used in different years. Landsat-5 TM, Landsat-7 ETM+, and Landsat-8 OL/TIRS images were used for 1984, 2000, and 2016, respectively. Radiometric calibration and Atmospheric corrections were done to avoid radiometric errors and avoid absorption and scattering of solar radiation from objects. Supervised LULC classification using Maximum Likelihood classification approach was applied in ENVI 5.3 and Arc GIS 10.4.1.

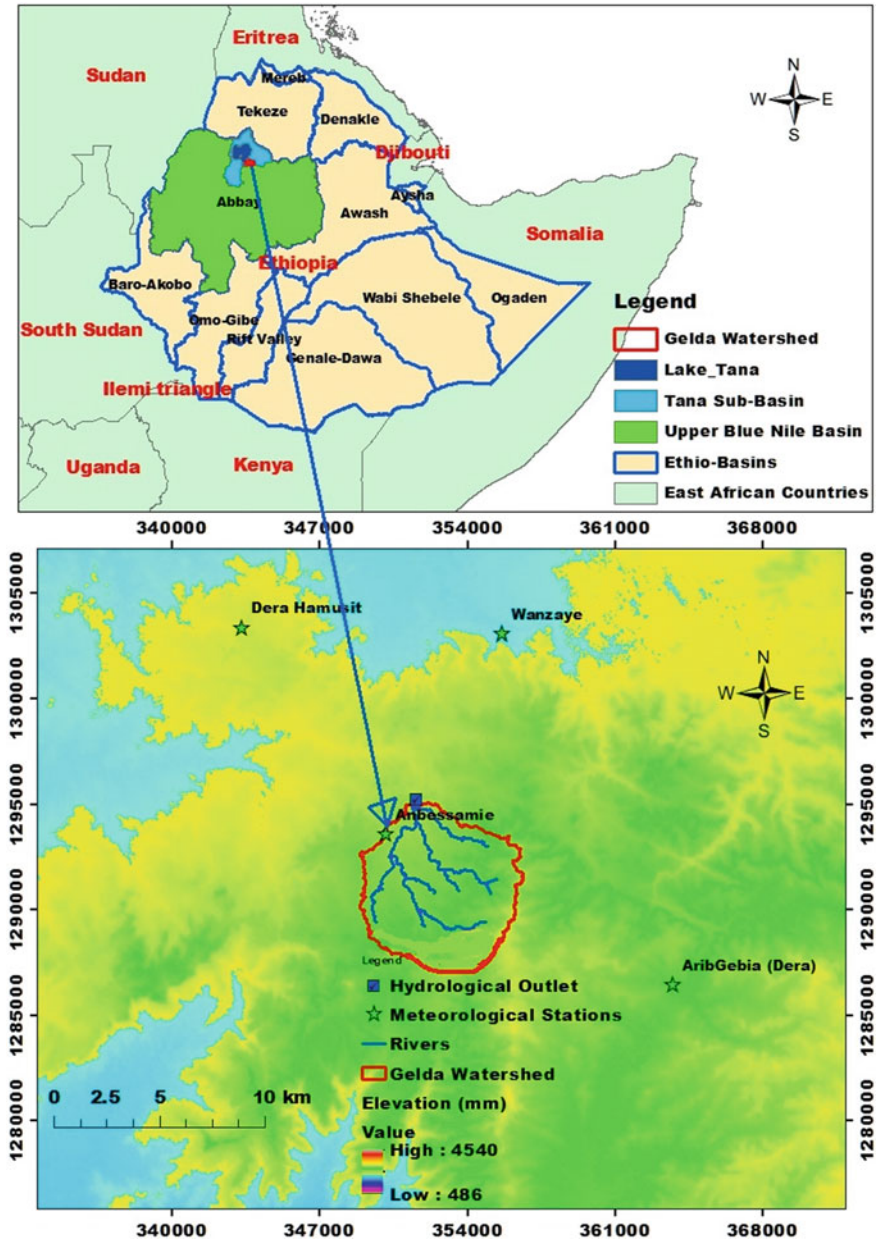

Fig. 2.1 Location map of the Gelda watershed

Images Classification Accuracy Assessment

The objective of Accuracy Assessment for Classified images is to determine quantitatively how pixels were grouped successfully into the correct feature classes (Manandhar et al. 2009). To assess classification accuracy, confusion matrix was used including ground control points to validate the classified image for each image and checked by Google earth. From this error matrix, overall accuracy, user's accuracy, and producer's accuracy were determined (Valiquette et al. 1994). In addition, the kappa statistic is used for the accuracy assessment. The Kappa statistic incorporates the diagonal elements of the error matrices (i.e., classification errors) and represents agreement obtained after removing the proportion of agreement that could be expected to occur by chance. Kappa value lies between − 1 and 1, where − 1 represents no agreement at all, and 1 indicates perfect agreement. The equation used Kappa statistic is:

$$K = P_{\mathrm{o}} - P_{\mathrm{e}}/1 - P_{\mathrm{e}} \tag{2.1}$$

where P_{o} is proportion of correct agreements and P_{e} is proportion of expected agreement.

Change Detection Analysis

Post-classification, change detection statistics were computed by comparing values of area of one data set with the corresponding value of the second data set in each period. The method used for LULC change detection in this study is the comparison statistics. The percentage area for each land cover class was derived from the classified images for each year (1984, 2000, and 2016) separately using ENVI 5.3. Then change detection between 1984 and 2016 images were done. This extended period gives significant dynamic changes over 33 years.

Climate Forecast System Reanalysis (CFSR) Data

Correctly representing weather data is critical in hydrological modeling. Poor-quality observations often compromise model accuracy (Zhang et al. 2012). CFSR data sets help to address this basic challenge by providing continuous global records. However, the use of CFSR data for hydrological modeling in tropical and semi-tropical basins has not been adequately evaluated (Fuka et al. 2014). In this study area, there is lack of complete long-term climate data. Before using the CFSR data in the watershed, the following steps were implemented:

- Adding both local and CFSR data on the GIS interface using their longitude, latitude, and elevation. In this step, CFSR rainfall stations are near and far from the study area are identified.
- Making a linear relationship between each local station with respect to coefficient of determination (R^2) between CFSR and observed Meta data.
- Developing correlation equations for each station $Y = \alpha X \pm b$ where Y is observed Meta data, α is coefficient of CFSR Meta data, X is CFSR data and b is the intercept.
- Converting the CFSR data into observed data by using the developed correlation equation.
- Using the Thiessen polygon method in GIS to select the most dominant rainfall stations to the watershed.
- Measuring the aerial distances starting from the mean center of the watershed.
- Taking the selected nearest stations depending on their distance from the mean center and topographic conditions of the watershed.
- Making long-term annual mean rainfall for the selected stations based on observed and CFSR Rainfall data and then developing conversion factor (c).

$$C = \mathrm{OD}/\mathrm{CD} \tag{2.2}$$

where C is conversion factor, OD is Observed data and CD is the CFSR data.

- To characterize the selected watershed in rainfall, an average value of the nearest stations must be calculated if their conversion factors are close to each other.
- Preparing the average daily rain fall data for SWAT model as an input in the form of database (dbf).
- Run the model (simulation) using this converted CFSR rainfall data followed by calibration and validation on SWAT and SWAT-CUP models, respectively.

Data quality check must be performed before using for SWAT model using double Mass Curve (DMC) method and Homogeneity test at 90, 95, and 99% probability using RAINBOW software.

Soil and Water Assessment Tool (SWAT) Model

In the SWAT model, there are two options for Hydrologic Response Unit (HRU) definition: assign a single HRU to each sub watershed or assign multiple HRUs to each sub watershed based on a certain threshold value. The SWAT user manual by Winchell et al. (2007) suggests a 20% land use threshold, 10% soil threshold and 20% slope threshold are adequate for most modeling applications. These threshold values indicate that land uses and slopes which form at least 20% of the sub watershed area and soils which form at least 10% of the area within each of the selected land uses were considered in HRUs. For this study, HRU definition with multiple options was used. SWAT requires daily precipitation, air temperature, solar radiation, wind speed,

and relative humidity. These data will be generated when measured data is missing (Rajawatta et al. 2014). In this study, the daily values of all climatic variables from CFSR data were used instead of measured data obtained from https://swat.tamu.edu/data/cfsr for the stations around Gelda watershed.

Sensitivity Analysis, Calibration, and Validation in the SWAT-CUP Model

Sensitivity analysis is used to determine the most sensitive parameters in the basin for the calibration and validation process and helps to understand the model's behavior and the predominant processes (Narsimlu et al. 2015). The calibration was performed to get a good agreement between the simulated and observed catchment runoff volume, shape of the hydrograph, peak and low flows with respect to timing, rate, and volume. To fulfill these objectives, the Sequential Uncertainty Fitting (SUFI-2) model for optimization and uncertainties analysis was used in the SWAT-CUP for calibration and validation.

Model Performance Evaluation

Calibration and validation results indicate that SWAT model is an effective watershed management tool that can be run with available data. For this study, three objective functions have been used to measure the overall fit between the observed and predicted stream flow by SWAT model:

Per cent of Bias (PBIAS): As a general rule given by Moriasi et al. (2007), a PBIAS of 10% or less was considered "very good", between ± 10 and ± 15% is "good", and between ± 15 and ± 25% is "satisfactory" whereas values greater than 25% indicate an "unsatisfactory" model simulation. The optimal value of PBIAS is zero. A positive PBIAS value indicates the model is under-predicting whereas negative values indicate over-predicting.

Coefficient of Determination (R^2): R^2 ranges from 0 (indicating poor model prediction) to 1 (good model prediction), with higher values indicating smaller error in variance, and values greater than 0.6 considered acceptable (Bonumá et al. 2015).

Nash–Sutcliffe Efficiency (NSE): The value of NSE ranges from negative infinity to 1, $(-\infty, 1]$. NSE value < 0.5 indicates the mean observed value is better predictor than the simulated value, which indicates unacceptable performance, while NSE values greater than 0.5, the simulated value is better predictor than mean measured value and viewed as acceptable performance. The NSE indicates that how well the plots of observed versus simulated data fits the 1:1 function.

Evaluation of Stream Flow Changes Due to LULC Change

Simulation of the impacts of LULC change on Gelda stream flow was one of the most significant parts of this study. Expansion of cultivated lands at the expense of forest, bush, and grazing lands was observed during the study period. To evaluate the variability of stream flow due to LULC change from 1984 to 2016, three independent simulation runs were conducted on a yearly basis using all LULC maps for each period keeping other input parameters unchanged.

Seasonal stream flow variability of 1984, 2000, and 2016 due to LULC changes was assessed, and comparisons were made on stream flow contributions based on observed stream flow data, and surface runoff and ground water flow contributions to stream flow based on the simulation outputs using SWAT viewer.

Results and Discussion

Accuracy Assessment Using Confusion Matrixes

A classification is not complete until its accuracy is assessed using the known Kappa statistics (Forkuor and Cofie 2011). To assess the classification accuracy, confusion matrix was used including overall user's and producer's accuracies. In this study, the confusion matrix was used depending on ground control points to validate the classified images in each period in addition to unchanged ground control points from 1984 to 2016.

In this study, the overall accuracies (Table 2.1) in 1984, 2000, and 2016 were, 81.3%, 83.2%, and 90.4%, with Kappa statistics of 73.0%, 76.1%, and 87.2% and User's and producer's accuracies of individual classes were ranging from 66.7% to 96.4% and 75% to 96%, respectively.

Table 2.1 Accuracy assessments from 1984 to 2016

Year	Overall accuracy (%)	User's accuracy (%)	Producer's accuracy (%)	Kappa coefficient (%)
1984	81.3	66.7–92.9	75–92.9	73.0
2000	83.2	76.5–95.5	76.5–88.9	76.1
2016	90.4	83.3–96.4	84.2–96	87.2

Land Use and Land Cover Maps

Based on the information from field surveys, forest land, bush land, grazing (grass) land, agricultural land and built-up areas were the major LULC classes of Gelda watershed (Fig. 2.2). Land cover conversions are measured as a shift from one land cover category to another, notable in the case of agricultural expansion, deforestation, or change in urban extent. After relevant bands were selected, false color composite was considered for layer stacking. Red, Green, and Blue (bands 3, 2, 1 for 1984 and 2000 images and bands 4, 3, 2 for 2016 images) were combined to make natural color composite images before any classification was done for each year.

The results show there has been a notable change in LULC in the watershed. Agricultural land increased from 36.63 to 68.86%, and built-up area increased from 0.33 to 1.62% while forest cover decreased from 16.49 to 8.40%, bush land decreased from 22.78 to 12.25% and grazing land decreased from 23.77 to 8.87% in 33 years from 1984 to 2016 (Table 2.2). The rise in agricultural and built-up areas at the expense of forest, bush land and grazing areas could be attributed to the increase in population driving the demand for agriculture and built-up spaces. This LULC change may have effect on the hydrology of the catchment.

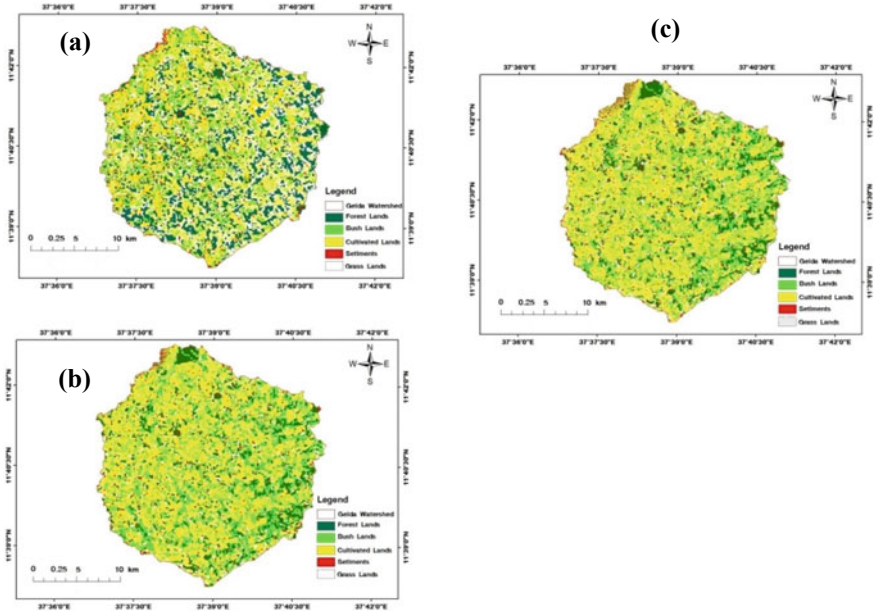

Fig. 2.2 LULC classification map of Gelda watershed: **a** 1984, **b** 2000, **c** 2016

Table 2.2 Summaries of land cover classes from 1984 to 2016

LU classes	1984		2000		2016	
	Area (ha)	Area (%)	Area (ha)	Area (%)	Area (ha)	Area (%)
Forest land	738.83	16.49	612.32	13.67	376.16	8.40
Bush/shrub land	1020.42	22.78	693.78	15.49	548.64	12.25
Grazing land	1064.62	23.77	752.64	16.80	397.42	8.87
Agricultural land	1640.84	36.63	2384.43	53.23	3084.49	68.86
Built-up area	14.72	0.33	36.26	0.81	72.72	1.62
Total	4479.43	100.00	4479.43	100.00	4479.43	100.00

Table 2.3 Summary of LULC class rates from their original size

LULC type	Rate (1984–2000)		Rate (2000–2016)		Rate (1984–2016)	
	Area	%	Area	%	Area	%
Forest land	− 126.51	− 17.12	− 236.16	− 38.57	− 362.67	− 49.09
Bush/shrub land	− 326.64	− 32.01	− 145.14	− 20.92	− 471.78	− 46.23
Grazing land	− 311.98	− 29.30	− 355.22	− 47.20	− 667.20	− 62.67
Agricultural land	743.59	31.19	700.06	22.70	1443.65	46.80
Built-up area	21.54	59.40	36.46	50.14	58.00	79.76

Rate of LULC Change

The magnitude of change is the degree of expansion or reduction in the LULC changes over time. A negative value represents a decreasing LULC sizes/values while a positive value indicates an increasing LULC sizes/values (Mahmud and Achide 2012). The percentage change between 1984 to 2000, 2000 to 2016, and 1984 to 2016 from their initial (original) value and final value were calculated and described in Table 2.3 using the following equation:

$$R = (\mathrm{FV} - \mathrm{IV}) * 100/\mathrm{FV} \tag{2.3}$$

where

R is the percentage rate (change) value between two years,
IV is the initial (referenced) year value, and
FV is the final year value.

Change Detection Analysis

Change detection based on remote sensing images is applied in research for LULC change, natural resource management and environment monitoring and protection

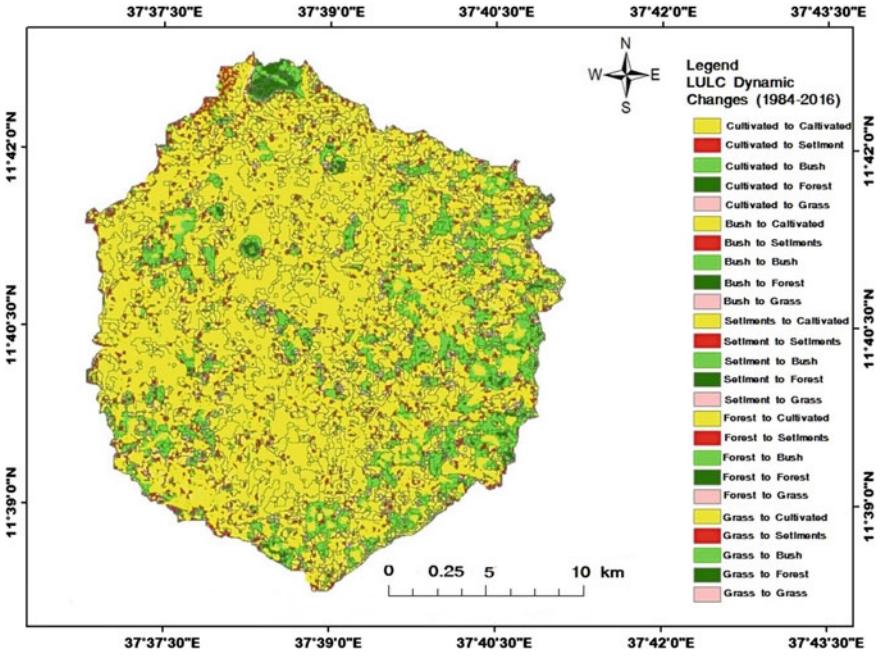

Fig. 2.3 Change detection analyses map of Gelda watershed between 1984 and 2016

(Zhang et al. 2014). In this study, the LULC change detection statistics was done using ENVI 5.3 software. To show notable change, the period between 1984 and 2016 was used (Fig. 2.3 and Table 2.4).

In the period between 1984 and 2016, forest land (7.74%), bush land (10.71%), and grazing land (14.32%) were changed to agricultural land while forest land (0.11%), bush land (0.42%), and grazing land (0.61%) were changed to built-up area by due to increase in population size and expansion of their demands on relevant infrastructures. Minimal changes of built-up areas to forest land (0.01%), bush land (0.03%), grazing land (0.01%), and agricultural land (0.06%) was also observed, due to dynamic human activities like shifting of settlement area. This change of LULC may affect the hydrology of the catchment.

Sensitivity Analysis

Sensitivity analysis was needed to determine the most sensitive parameters in the watershed for the calibration process using simultaneous analysis method, varying, and adjusting all parameter minimum and maximum values at the same time before running. After 50–1000 iterations were done, ten most sensitive parameters were

Table 2.4 Change detection analyses between 1984 and 2016

LULC shifts (1984–2016)		Area		LULC shifts (1984–2016)		Area	
1984	2016	(ha)	(%)	1984	2016	(ha)	(%)
Agriculture	Agriculture	1613.84	36.03	Built-up	Forest	0.64	0.01
Agriculture	Built-up	11.81	0.26	Built-up	Grazing	0.62	0.01
Agriculture	Bush	4.63	0.10	Forest	Agriculture	346.59	7.74
Agriculture	Forest	3.58	0.08	Forest	Built-up	4.85	0.11
Agriculture	Grazing	5.72	0.13	Forest	Bush	18.86	0.42
Bush	Agriculture	479.76	10.71	Forest	Forest	359.67	8.03
Bush	Built-up	18.92	0.42	Forest	Grazing	7.66	0.17
Bush	Bush	510.78	11.40	Grazing	Agriculture	641.67	14.32
Bush	Forest	7.84	0.18	Grazing	Built-up	27.42	0.61
Bush	Grazing	3.84	0.09	Grazing	Bush	13.46	0.30
Built-up	Agriculture	2.62	0.06	Grazing	Forest	4.52	0.10
Built-up	Built-up	9.72	0.22	Grazing	Grazing	379.20	8.47
Built-up	Bush	1.17	0.03				
				Total		4479.43	100.00

selected and used during the calibration and validation process including parameter sensitivity ranks (Table 2.5).

Table 2.5 gives the summary of the most sensitive parameters; their final range given by the last iteration in SUFI-2, the fitted values, and the sensitivity rank. Parameter ranking is based on the *t*-stat and the *p*-value in the SUFI-2 program. *T*-test is a measure of sensitivity, the larger the *t*-stat in absolute value, the more sensitive the parameter is. The *p*-value determines the significance of the sensitivity, the smaller the *p*-value, the more sensitive the parameter is (Abbaspour 2013).

Calibration and Validation

Following the sensitivity analysis, model calibration was done by adjusting minimum and maximum values of each parameter, more iteration was done to fit good simulation. Calibration covers two-thirds of the total sampled data. In this study, there were 33 stream flow sample data (1984–2016), the calibration covers 20 years starting from the year 1987 to 2006. Validation was done without adjusting the minimum and maximum value of each parameter and covers one-third of the total sample data. In this study, the validation covers 10 years from the year 2007 to 2016.

Table 2.5 Final parameter sensitivity analyses and their rank

Parameter name	*t*-stat	*p*-value	Fitted value	Minimum value	Maximum value	Sensitivity rank
R__CN2.mgt	− 5.35	0.00	0.05	− 0.20	0.20	1
V__GW_DELAY.gw	− 1.89	0.06	158.10	30.00	450.00	2
R__SOL_AWC(1).sol	1.88	0.07	− 0.54	− 1.00	1.00	3
V__ALPHA_BF.gw	− 1.80	0.07	0.11	0.00	1.00	4
V__ESCO.hru	1.09	0.28	58.29	− 1.00	100.00	5
V__REVAPMN.gw	0.93	0.35	4545.00	0.00	5000.00	6
V__RCHRG_DP.gw	− 0.82	0.41	76.33	10.00	100.00	7
V__GWQMN.gw	− 0.70	0.49	0.66	0.00	2.00	8
V__GW_REVAP.gw	− 0.63	0.53	82.09	10.00	100.00	9
V__CH_K2.rte	− 0.25	0.80	8.32	1.00	20.00	10

Average Monthly Calibration

The average monthly calibration (Fig. 2.4) showed that the percentage bias is 0.08, the objective function which is the Nash–Sutcliffe coefficient (NSE) is 0.81 and the goodness of fit between the measured and the simulated coefficient of determination (R^2) is also 0.88. The result of calibration for monthly stream flow showed that there is a good agreement between the measured and simulated average monthly flows.

Average Monthly Validation

The average monthly validation (Fig. 2.5) showed that the percentage bias is 0.11, the Nash–Sutcliffe coefficient (NSE) is 0.78 while the goodness of fit between the measured and the simulated coefficient of determination (R^2) is also 0.86. The result showed the good agreement of simulated and observed average monthly flow.

The hydrographs (Figs. 2.4 and 2.5) showed under prediction of the model (because observed stream flow values are greater than simulated one) and the difference between observed (Table 2.6). This could be due to the technique used for filling missing data, nearby station method on flow data type.

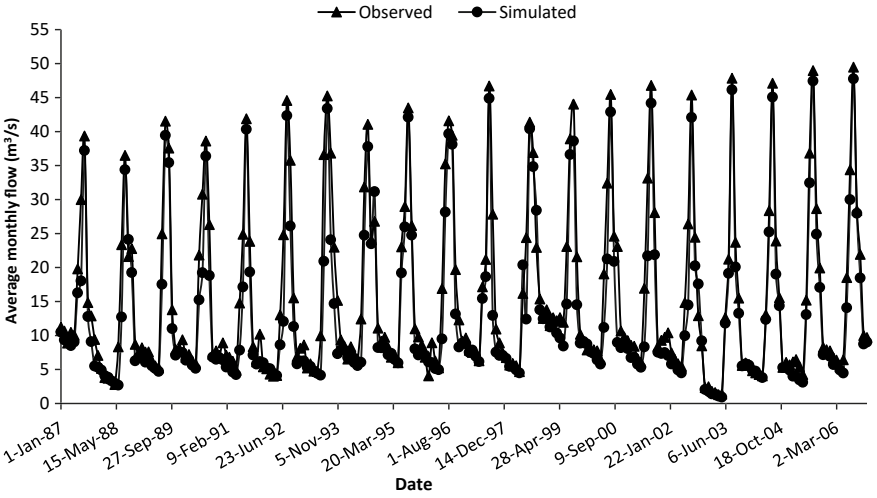

Fig. 2.4 Result of calibration for average monthly stream flows

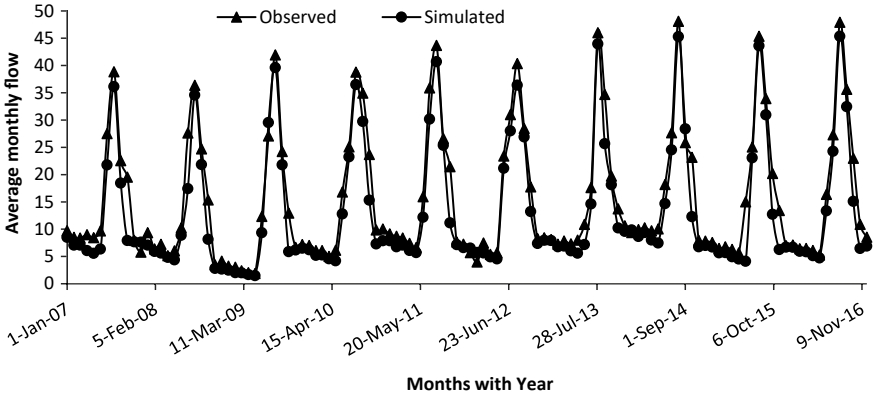

Fig. 2.5 Average monthly validations for stream flows

Table 2.6 Summary of calibrated and validated values

Model evaluator	Calibration		Validation	
	Daily (%)	Monthly (%)	Daily (%)	Monthly (%)
PBIAS	12	8	14	11
NSE	75	81	72	78
R^2	79	88	76	86

Table 2.7 Mean seasonal wet and dry stream flow and their variability

Different years of LU	Mean seasonal flow (m^3/s)		Changes (m^3/s)			
	Wet months	Dry months	Wet	Percent (%)	Dry	Percent (%)
	(Jun–Sept)	(Jan–Apr)				
LULC map of 1984	64.36	3.18	–	–	–	–
LULC map of 2000	92.42	2.23	28.06	43.6	− 0.95	− 29.87
LULC map of 2016	128.68	1.07	36.26	39.23	− 1.16	− 52.02

The negative (−) sign indicates the decreased values

Evaluation of Stream Flow Due to LULC Change Dynamics (1984–2016)

After calibration and validation of the model, evaluation of stream flow was done to quantify the variability of stream flow due to the change of LULC. There was a high expansion of cultivated land at the expense of forest, bush, and grazing lands during the study period. The evaluation was done on the impact of LULC changes on the seasonal stream flow and variations on the major components of stream flow including surface runoff and groundwater flow from 1984 to 2016. LULC change has a major influence on the rainfall-runoff process; reduction in forest and bush land covers results in reduction of infiltration and percolation and increase in runoff.

To evaluate the variability of stream flow due to LULC change, three independent simulation runs were conducted keeping the most sensitive input parameters unchanged. Seasonal stream flow variability of 1984, 2000, and 2016 due to LULC change was assessed and comparison made based on observed data. Both surface runoff and ground water flow contributions to stream flow were based on SWAT output data after simulation using SWAT viewer. Changes in stream flow during the wettest months (June–September) and the driest months (January–April) were calculated and used as indicators to estimate the effect of LULC change on Gelda stream flow. This evaluation was done on seasonal stream flow, annual surface runoff (SURQ), and annual ground water flow (GWQ) independently as indicated in Tables 2.7 and 2.8, respectively.

Change Evaluation in Seasonal Stream Flow

Based on the observed data, the mean seasonal stream flow for wet months increased from 64.36 to 92.42 m^3/s by 43.6% from 1984 to 2000 and from 92.42 to 128.68 m^3/s by 39.2% from 2000 to 2016. This is due to reduction of forest and bush covers on the watershed, which allows high runoff in wet season. The mean seasonal stream flow for dry season decreased from 3.18 to 2.23 m^3/s by 29.9% from 1984 to 2000 and 2.23 to 1.07 m^3/s by 52.0% from 2000 to 2016. This is due to increase in temperature

Table 2.8 Annual SURQ and GWQ of the stream from simulated values

D/t years of LU	SURQ (mm)	GWQ (mm)	Change			
			SURQ	Percent (%)	GWQ	Percent (%)
LULC map of 1984	241.54	68.47	–	–	–	–
LULC map of 2000	318.12	51.21	76.58	24.10	− 17.26	− 25.2
LULC map of 2016	436.89	30.58	118.77	27.20	− 21.63	− 40.3

The negative (−) sign indicates the decreased values

and evapotranspiration related to forest and bush cover reduction in and around the watershed. This may have adversely resulted on stream flow reduction in dry months.

The overall rate of stream flow increased by 64.3 m^3/s (50%) during the wet season from 1984 to 2016 while the rate of stream flow decreased by 2.11 m^3/s (66.4%) during the dry season in the same period.

Change Evaluation in Annual Surface Runoff and Ground Water Flow

Change evaluation analysis was made on the surface runoff (SURQ) and ground water flow (GWQ). Table 2.8 describes the SURQ and GWQ of the stream simulated using 1984, 2000, and 2016 LULC maps for each period. These values were calculated from the SWAT outputs (simulations) using SWAT Viewer software on annual basis for the selected years 1984, 2000, and 2016, respectively.

The SWAT output shows that the contribution of surface runoff has increased from 241.54 to 318.12 mm (24.1%) from 1984 to 2000, and from 318.12 to 436.89 mm (27.2%) from 2000 to 2016 due to deforestation, expansion of built-up area, and increase in soil compactness. Ground water flow decreased from 68.47 to 51.21 mm (25.2%) from 1984 to 2000 and from 51.21 to 30.58 mm (40.3%) from 2000 to 2016 due to decrease in infiltration followed by percolation, increase in surface runoff, increase in legal/illegal abstraction of ground water. The rate of groundwater flow decreased by 37.89 mm (55.3%), whereas the surface runoff has increased by 195.4mm (44.7%) between 1984 and 2016.

The hydrological investigation with respect to the LULC changes within Gelda watershed showed that the flow characteristics have changed significantly, with increase in surface flow (during wet season) and reduction of base flow (in dry season) during the study period from 1984 to 2016.

Conclusion

This study addressed the impact of LULC change on Gelda watershed over 33 years. The classification of LULC and stream flow calibration and validation were performed. This study showed that LULC changes in Gelda watershed in the period from 1984 to 2016 were identified using satellite images. The LULC maps of each year were prepared, and the accuracy assessments of these maps were checked using the confusion matrix. Sensitivity analysis, calibration, validation, and evaluation of SWAT model performance were also performed.

From the LULC change analysis, the LULC of the watershed for the period between 1984 and 2016 showed significant changes. Agricultural land increased from 36.6 to 68.9% (1984–2016). The expansions of agricultural land and small town have an impact on the reductions of forest and bush lands. Forest land cover decreased from 16.5 to 8.4% (1984–2016). Cultivated and built-up areas increased from 36.6 to 68.9% and 0.33 to 1.62% (1984–2016) respectively. In the change detection analysis showed forest, bush, and grazing lands were significantly changed to agricultural land, whereas forest, bush, and grazing lands were changed slightly to built-up area due to increase in population size and expansion of their demands on relevant infrastructures. These changes in LULC influence the hydrology of the Gelda catchment.

Sensitivity analysis using SWAT-CUP model identified ten most sensitive parameters that control the stream flow of the studied watershed. Monthly model performance for both calibration and validation were done with objective functions of PBIAS, NSE, and the coefficient determination of R^2 values of 0.08, 0.81, and 0.88 for calibration periods, and 0.11, 0.78, and 0.86 for validation periods, respectively. LULC changes have major impacts on stream flow, surface runoff, and groundwater flow. The result of the model for all LULCs (1984, 2000, and 2016) indicated that the mean seasonal stream flow increased by 50% in wet seasons and decreased by 66% in the dry season between 1984 and 2016. The annual surface runoff increased by 44.6%, whereas the annual groundwater flow was decreased by 55% from during the same period. The study results highlight the need for conservation of natural resources and watershed management to ensure sustainable development in the Gelda watershed.

References

Abate S (2011) Evaluating the land use and land cover dynamics in Borena Woreda of South Wollo highlands, Ethiopia. J Sustain Dev Africa 13(1):87–105

Abbaspour KC (2013) SWAT-CUP 2012: SWAT calibration and uncertainty programs—a user manual. Eawag, Dübendorf, p 103

Ahmadizadeh S (2014) Land use change detection using remote sensing and artificial neural network: application to Birjand, Iran. Comput Ecol Softw 4:276

Akpoti K, Antwi EO, Kabo-Bah AT (2016) Impacts of rainfall variability, land use and land cover change on stream flow of the black Volta Basin, West Africa. Hydrology 3:26

Ashraf A (2013) Changing hydrology of the Himalayan watershed. In: Current perspectives in contaminant hydrology and water resources sustainability. Intech, Islamabad

Asres RS, Tilahun SA, Ayele GT, Melesse AM (2016) Analyses of land use/land cover change dynamics in the upland watersheds of Upper Blue Nile Basin. In: Landscape dynamics, soils and hydrological processes in varied climates. Springer

Bekele B, Alamirew T, Kebede A, Zeleke G, Melesse AM (2017) Analysis of rainfall trend and variability for agricultural water management in Awash River Basin, Ethiopia. J Water Clim Change 8(1):127–141

Belay T (2002) Land-cover/land-use changes in the Derekolli catchment of the South Welo Zone of Amhara Region, Ethiopia. Michigan State Univ Press 18(1):1–20

Bonumá NB, Reichert JM, Rodrigues MF, Monteiro JAF, Arnold JG, Srinivasan R (2015) Modeling surface hydrology, soil erosion, nutrient transport, and future scenarios with the ecohydrological SWAT model in Brazilian watersheds and river basins. Tóp Ci Solo 9:241–290

Boori MS, Voženílek V, Choudhary K (2015) Land use/cover disturbance due to tourism in Jeseníky Mountain, Czech Republic: a remote sensing and GIS based approach. Egypt J Remote Sens Space Sci 18(1):17–26. https://doi.org/10.1016/j.ejrs.2014.12.002

Butt A, Shabbir R, Ahmad SS, Aziz N, Nawaz M, Shah MTA (2015) Land cover classification and change detection analysis of Rawal watershed using remote sensing data. J Biol Environ Sci 6(1):236–248

Forkuor G, Cofie O (2011) Dynamics of land-use and land-cover change in Freetown, Sierra Leone, and its effects on urban and peri-urban agriculture—a remote sensing approach. Int J Remote Sens 32:1017–1037

Fuka DR, Walter MT, Macalister C, Degaetano AT, Steenhuis TS, Easton ZM (2014) Using the climate forecast system reanalysis as weather input data for watershed models. Hydrol Process 28:5613–5623

Getachew HE, Melesse AM (2012) Impact of land use/land cover change on the hydrology of Angereb Watershed, Ethiopia. Int J Water Sci 1(4):1–7. https://doi.org/10.5772/56266

Girma T (2001) Land degradation: a challenge to Ethiopia. International Livestock Research Institute, Addis Ababa, Ethiopia, pp 815–823

Hurni H, Solomon A, Amare B, Berhanu D, Ludi E, Portner B, Birru Y, Gete Z (2010) Land degradation and sustainable land management in the highlands of Ethiopia. In: Hurni H, Wiesmann U (eds) with an international group of co-editors. Global change and sustainable development: a synthesis of regional experiences from research partnerships. Geogr Bernensia 5:187–201

Mahmud A, Achide AS (2012) Analysis of land use/land cover changes to monitor urban sprawl in Keffi-Nigeria. Environ Res J 6:129–134

Manandhar R, Odeh IO, Ancev T (2009) Improving the accuracy of land use and land cover classification of Landsat data using post-classification enhancement. Remote Sens 1:330–344

Mango L, Melesse AM, McClain ME, Gann D, Setegn SG (2011a) Land use and climate change impacts on the hydrology of the upper Mara River Basin, Kenya: results of a modeling study to support better resource management. Special issue: climate, weather and hydrology of East African Highlands. Hydrol Earth Syst Sci 15:2245–2258. https://doi.org/10.5194/hess-15-2245-2011

Mango L, Melesse AM, McClain ME, Gann D, Setegn SG (2011b) Hydro-meteorology and water budget of Mara River basin, Kenya: a land use change scenarios analysis, chap 2. In: Melesse A (ed) Nile river basin: hydrology, climate and water use. Springer Science Publisher, pp 39–68. https://doi.org/10.1007/978-94-007-0689-7_2

Melesse AM, Jordan JD (2002) A comparison of fuzzy vs. augmented-ISODATA classification algorithm for cloud and cloud-shadow discrimination in Landsat imagery. Photogramm Eng Remote Sens 68(9):905–911

Melesse A, Weng Q, Thenkabail P, Senay G (2007) Remote sensing sensors and applications in environmental resources mapping and modeling. Special issue: remote sensing of natural resources and the environment. Sensors 7:3209–3241

Messay M (2011) Land-use/land-cover dynamics in Nonno district, Central Ethiopia. J Sustain Dev Afr 13(1):123–139

Meyer W, Turner IIB (1992) Human population growth and global land-use/cover change. Annu Rev Ecol Syst 23:39–57

Mohammed H, Alamirew A, Assen M, Melesse A (2013) Spatiotemporal mapping of land cover in Lake Hardibo Drainage Basin, Northeast Ethiopia: 1957–2007. In: Water conservation: practices, challenges and future implications. Nova Publishers, pp 147–164

Moriasi DN, Arnold JG, Van Liew MW, Bingner RL, Harmel RD, Veith TL (2007) Model evaluation guidelines for systematic quantification of accuracy in watershed simulations. Trans ASABE 50:885–900

Narsimlu B, Gosain AK, Chahar BR, Singh SK, Srivastava PK (2015) SWAT model calibration and uncertainty analysis for streamflow prediction in the Kunwari River Basin, India, using sequential uncertainty fitting. Environ Process 2:79–95

Ozesmi SL, Bauer ME (2002) Satellite remote sensing of wetlands. Wetlands Ecol Manage 10:381–402

Prakasam C (2010) Land use and land cover change detection through remote sensing approach: a case study of Kodaikanal taluk, Tamil Nadu. Int J Geomat Geosci 1(2):150–158

Rajawatta K, He D, Mkdk P (2014) CMWSim: development and evaluation of probability-based weather generating software for crop growth simulation. Ital J Agrometeorol-Riv Ital Agrometeorol 19:5–14

Tahir M, Imam E, Hussain T (2013) Evaluation of land use/land cover changes in Mekelle City, Ethiopia using remote sensing and GIS. Comput Ecol Softw 3(1):9–16

Tilahun A, Takele B, Endrias G (2001) Reversing the degradation of arable land in the Ethiopian Highlands. Managing Africa's Soils No. 23. International Center for Research in Agro Forestry

Valiquette CA, Lesage AD, Cyr M, Toupin J (1994) Computing Cohen's kappa coefficients using SPSS MATRIX. Behav Res Methods Instrum Comput 26:60–61

Winchell M, Srinivasan R, Di Luzio M, Arnold J (2007) ArcSWAT interface for SWAT 2005. In: User's guide. Blackland Research Center, Texas Agricultural Experiment Station, Temple

Wondie M, Schneider W, Melesse AM, Teketay D (2011) Spatial and temporal land cover changes in the Simen Mountains National Park, a World Heritage Site in Northwestern Ethiopia. Remote Sens 3:752–766. https://doi.org/10.3390/rs3040752

Wondie M, Teketay D, Melesse AM, Schneider W (2012) Relationship between topographic variables and land cover in the Simen Mountains National Park, a World Heritage Site in northern Ethiopia. Int J Remote Sens Appl 2(2):36–43

Zhang L, Kumar A, Wang W (2012) Influence of changes in observations on precipitation: a case study for the Climate Forecast System Reanalysis (CFSR). J Geophys Res Atmos 117

Zhang T, Zhang X, Xia D, Liu Y (2014) An analysis of land use change dynamics and its impacts on hydrological processes in the Jialing River Basin. Water 6:3758–3782

Chapter 3
Dynamics and Predictability of Land Use/Land Cover Change using Artificial Neural Network-Based Cellular Automata (ANN-CA): The Case of the Upper Awash River Basin, Ethiopia

Gebreyohannes Abrha Meresa, Addisalem Bitew Mitiku, and Abel Tadesse Weldemichael

Abstract Changes in land use and land cover (LULC) modify the hydrological and hydraulic processes of watersheds and can increase surface runoff and streamflow, which results in flooding. Increasing flood events have been observed globally and in Ethiopia, particularly in the Awash River Basin. It has been a chronic problem resulting in loss of human lives and economic damage. The upper Awash River Basin is an area that is highly susceptible to seasonal flooding. Taking a wider view of the interactions between land and water environments within a river basin and the broader socioeconomic and environmental implications of floods, the integrated flood management (IFM) approach provides a sound, conceptual basis to bring about a convergence between land use planning and flood management. Therefore, to implement sustainable IFM plans and mitigate flooding consequences, it is vital to have information and understand the dynamics of the current and future land use and land cover changes in the study area, thus helping to model, quantify and predict the impact of LULC change on flooding. This study assessed the LULC change dynamics of the upper Awash River Basin over the past 20 years (1998–2018) and predicted future land use and land cover change scenarios for 2038 and 2058 using an artificial neural network-based cellular automata (ANN-CA) model. The land use-land cover changes in the upper Awash River Basin were modeled and validated using historical data. Spatial variables such as elevation, population density, distance to rivers and distance to the road network were considered in predicting the land use and land cover for years 2038 and 2058. The historical analysis showed that there was an increase in forest, wetland, and settlement/urban areas by 0.82%, 0.002% and 1.77%, respectively, while there was a decrease in agricultural land, shrub land, grassland, bare land, and water bodies by 2.17%, 0.34%, 0.11%, 0.02%, and 0.15%, respectively.

G. A. Meresa (✉) · A. B. Mitiku · A. T. Weldemichael
Surveying, Geospatial, and Civil Informatics Center-Ethiopian Construction Design and Supervision Works Corporation, Addis Ababa, Ethiopia
e-mail: gebrushewit@gmail.com

A. M. Melesse et al. (eds.), *Land and Water Degradation in Ethiopia*, Springer Geography, https://doi.org/10.1007/978-3-031-60251-1_3

On the other hand, analysis of the predicted LULC change for the coming 20 years (i.e., for 2038) revealed that there will be an increase in settlement/urban areas by 0.24%. However, it also resulted in a decrease in the LULC types of agriculture, forest, shrub land, grassland, wetland, bare land, and water bodies by 0.19%, 0.02%, 0.052%, 0.002%, 0.0008%, 0.0002%, and 0.003%, respectively.

Keywords LULC dynamics · Upper Awash River Basin · Cellular Automata

Introduction

The assessment of land use and land cover (LULC) changes in hydrology is essential for the development of sustainable water resource strategies. Specifically, understanding how the change in each LULC class influences hydrological components will greatly improve the predictability of hydrological consequences to LULC changes and thus can help stakeholders make better decisions. Changes in land use/land cover can have negative impacts on the hydrological and hydraulic processes in river basins and watersheds, such as an increase in surface runoff and peak flows, which poses a greater risk and increases vulnerability to flooding.

Increasing flood hazard events have been observed globally and in Ethiopia, particularly in the Awash River Basin (ECDSWC, 2021), where flood hazard events have been a chronic problem that results in significant losses and economic damages. The Upper Awash Basin is a highly flood-prone area, and annually, there is a high risk of flooding; consequently, there is damage to property and life. As such, the Awash Basin Authority (ECDSWC, 2021) is planning to implement an integrated flood management (IFM) approach to sustainably minimize the human, economic and ecological losses from floods while simultaneously maximizing the social, economic, and ecological benefits in the vicinity.

Taking a wider view of the interactions between land and water environments within a river basin and the broader socioeconomic and environmental implications of floods, the IFM approach provides a sound conceptual basis to bring about a convergence between land use planning and flood management. To implement sustainable IFM plans and mitigate flooding consequences, it is vital to assess and understand LULC change dynamics and predict future LULC change scenarios, which can contribute to sustainable land use planning and management and, in turn, contribute to sustainable IFM approaches in minimizing flood vulnerability.

As Roy et al. (2015) stated, geographic information system (GIS) and remote sensing (RS) have long been used and widely accepted as very powerful techniques in the change analysis and simulation of LULC. It is also stated that combined GIS and RS approaches are capable of critical analysis and decision support in Earth's surface changes within a short period of time and with reasonable accuracy. RS is applied to retrieve information from the analysis of earth observatory multitemporal and multispectral satellite images of different spatial resolutions. These images offer tremendous opportunity in LULC monitoring (Loveland et al., 1995), including

historical trends and future simulations, which are undoubtedly necessary in sustainable land use, planning and policy making for both governmental and nongovernmental levels. Information obtained from remotely sensed data is further used in GIS to perform modeling and simulation of LULC (Lu et al., 2011).

There are basically two categories of LULC models, of which one is spatial, and the other is aspatial (Seto and Kaufmann, 2003). Spatial models are used to quantify predicted LULC in a particular region and associated driving forces (Seto and Kaufmann, 2003), whereas empirical-statistical models and rule-based models included in the spatial category are mainly used in the analysis of LULC change patterns and the spatial location of existing and future potential changes.

According to Pontius and Chen (2006), modeling of land use and land cover is a scientific field that is growing rapidly because of its importance in identifying the effects of humans on the environment. In view of this importance, scientists have constituted an international organization named the Land use and Cover Change (LUCC) organization that is connected with the International Geosphere Biosphere Program and the International Human Dimensions of Global Change Program. Land use changes are highly related human and climate induced activities strongly impacting moisture availability and fluxes of water and energy (Getachew and Melesse 2012; Mango et al. 2011a; 2011b; Wondie et al. 2011, 2012; Melesse and Jordan 2002, 2003; Melesse et al. 2007; Mohamed et al. 2013).

Dijst and veldkamp (2004) stated that land use modeling currently plays a pivotal role in many natural resource management and decision-making processes. It is also stated that these models are effective tools to analyze the causes and consequences of land use-land cover change and create an enhanced understanding of the land use system in an area. Researchers around the globe have been devising and utilizing a wide variety of land use models, all of which are diverse in their formulations, objectives, and capabilities. There are whole landscape models, distributional landscape models and spatial landscape models (Baker, 1989; Singh, 2003). Since spatial details, including natural and human processes, have greater impacts on land use change, spatial modeling has taken over other modeling methods in many studies. Progress in remote sensing and GIS research has made significant contributions to these spatial landscape modeling methods (Singh, 2003).

Spatial land use modeling research has employed various approaches, among which models use machine learning to process changes based on historical events and factors that provide the input for change. One of the models is an artificial neural network-based cellular automata (ANN-CA), which was developed to simulate multiple land use changes and complex land use systems (Li and Yeh, 2002). This approach can be used to determine LULC changes by considering the possible factors that may influence the changes. Therefore, in this study, ANN-CA is used to evaluate the dynamics and predictability of land use and land cover change in the Upper Awash Basin.

Artificial Neural Network Models

According to Voženílek (2009), an artificial neural network is a computer program designed to model the human brain and its ability to learn tasks through the use of mathematical models. The neural network consists of a series of processing units that are collectively connected, such as synapses in the human brain. In artificial neural networks, the knowledge stored as the strength of the interconnection weights (a numeric parameter) is modified through a process called learning using a learning algorithm (Hassoun, 1995). This algorithmic function, in conjunction with a learning rule (i.e., back-propagation), is used to modify the weights in the network in an orderly fashion (Kavzoglu and Mather, 2003). ANNs are also used frequently to make predictions in numerous areas, including remote sensing (Benediktsson et al., 1990). ANN serves as a machine learning tool that is capable of quantifying and forecasting complex behaviors and patterns of LULC change (Pijanowski et al., 2002). ANN imitates the interconnected neural system in the human brain. The basic element or nodes, called neurons, are connected in layers and perform the processing in an ANN model. The neuron's output is derived from multiplying the input signal by specific weights, which are determined by using training algorithms, of which back propagation is the most popular approach (Pijanowski et al., 2005). ANN is used to identify the pattern of land use change, and hence, the transition from one land use type to another can be predicted.

Cellular Automata Model

Cellular automata (CA) is a cell-based framework that includes cell states, transition rules, infinite discrete cells, and neighborhoods. CA-based models are effective in addressing LULC change. The CA estimates the time taken in transition that can generate complex spatial patterns from a simple set of rules and predicts future LULC changes (Singh, 2003). CA can be incorporated with a spatial component and address the dynamics of change with simple rules that increase computational efficiency, making it one of the most preferred models of LULC change (Singh, 2003).

Artificial Neural Network-Based Cellular Automaton Model

Based on the research performed by Saputra and Lee (2019), ANN can be used to determine the transition probability of LULC using multiple output neurons for simulating multiple LULC changes within the structure of ANN-CA. CA is used to model the LULC changes by applying the transition probabilities from the ANN learning process. The overall analytic procedure is described in Fig. 3.1. The output

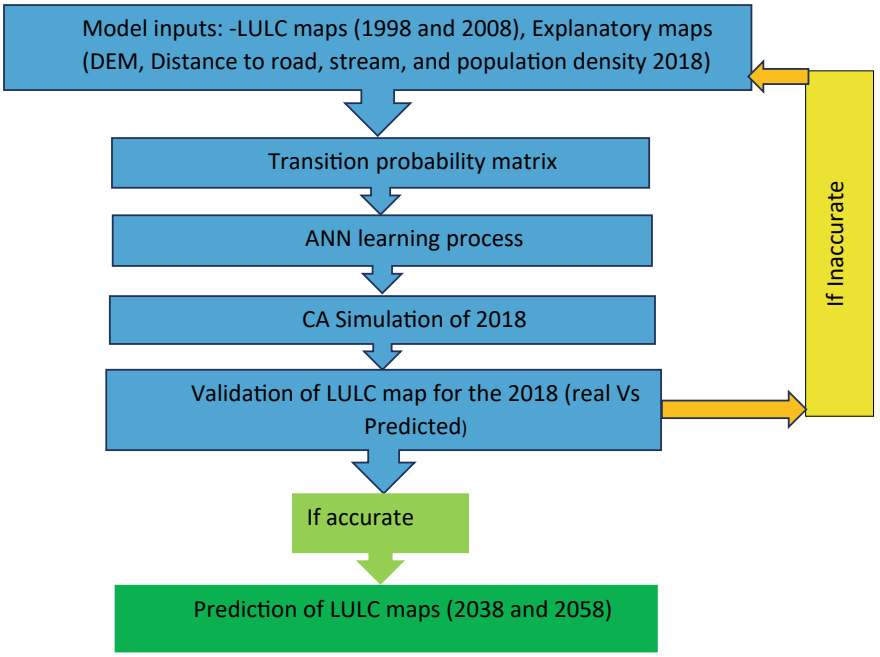

Fig. 3.1 Procedure for land use change analysis using CA-ANN

layer of the network determines the transition probabilities of multiple land uses by using multiple output neurons, while the parameters are automatically determined by a training procedure of neural networks. No explicit transition rules are required in the ANN-CA model. The only task is to train the neural network to obtain parameter values based on empirical data. Consequently, this ANN-CA model has been applied in this study to estimate the probable LULC type of the basin in the future.

Simulating Land Use and Land Cover Change

Existing Land Use and Land Cover Map and Distribution

The existing land cover map for the given three periods (1998, 2008, and 2018) of the Upper Awash Basin was obtained from the ESA (European Space Agency) website through the CCI (Climate Change Initiative) land cover project. For change detection purposes, the Global 22 land cover classification system land classes (LCCS) obtained from the CCI land project are grouped into 6 IPCC (Intergovernmental Panel on Climate Change) land categories with the consideration of subcategories shrub land, spares vegetation, bare area and water (forming "Others").

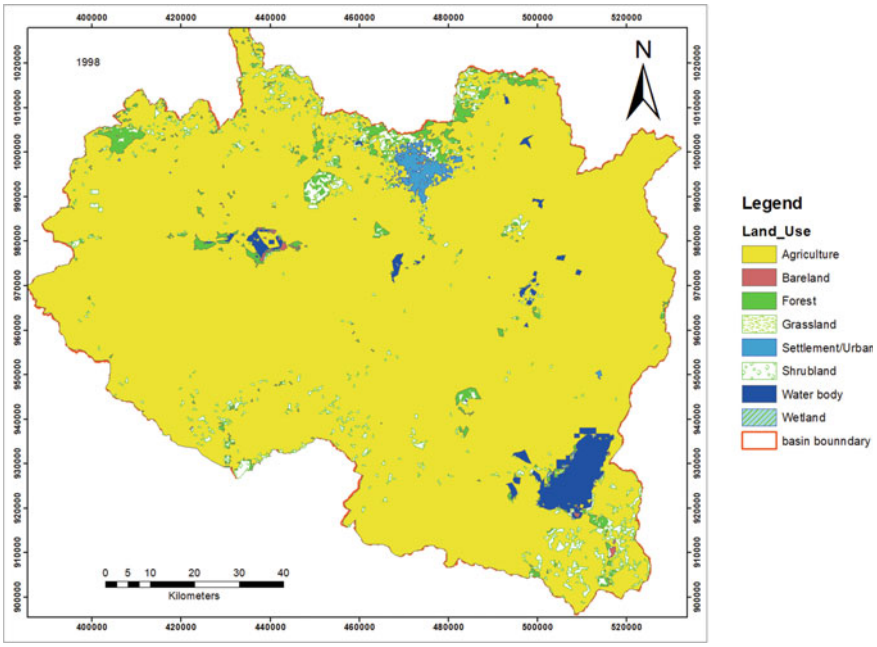

Fig. 3.2 LULC map of the upper Awash basin in 1998

For this particular study, the 6 IPCC LCCS main land categories and three of the subcategories (shrub land, bare area and water) are considered the main land covers. Accordingly, the thematic maps, area, and percentage distribution of Upper Awash land use and land cover for the given three periods (1998, 2008, and 2018) are given in Figs. 3.2, 3.3 and 3.4 and Table 3.1, respectively.

In 1998, urban land, grass land, bare land, and wetland occupied the fewest classes, with just 7796.58 ha (0.65%), 1944.19 ha (0.16%), 1129.22 ha (0.09%), 286.22 ha (0.02%), respectively, of the total classes. On the other hand, agriculture, shrub land, forest, and water bodies occupy the largest proportions, with 1078268.4 ha (92.32%), 31770.26 ha (2.58%), 23693.25 ha (2.03%) and 23040.35 ha (1.97%), respectively, of the total classes.

In 2008, agriculture, shrub land, forest and water bodies occupied the highest classes, with 1071710.87 ha (91.76%), 30231.09 ha (2.45%), 26546.54 ha (2.1%), and 21822.32 ha (1.83%), respectively. Wetland, grass land, and bare land, with area coverages of 317.29 ha (0.03%), 1227.07 ha (0.09%) and 1387.14 ha (0.12%), respectively, accounted for the lowest percentages of the total classes.

In 2018, agriculture, forest, urban land, shrub land, and water bodies occupied the highest classes, with 1052892.08 ha (90.15%), 34668.57 ha (2.70%), 29469.24 ha (2.42%), 27881.26 ha (2.23%), and 21209.79 ha (1.78), respectively. On the other hand, bare land, grassland, and wetland, with area coverages of 923.94 ha (0.08%),

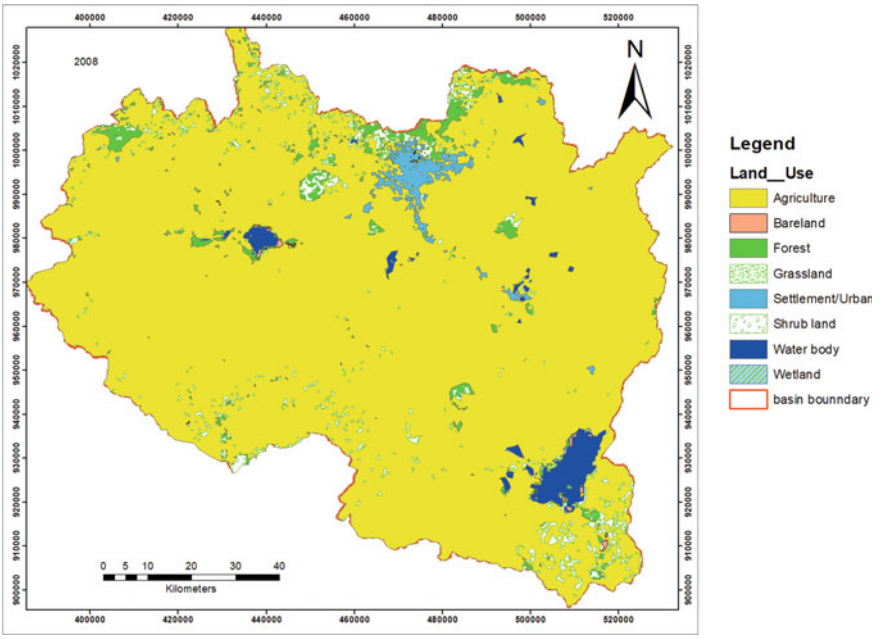

Fig. 3.3 LULC map of the upper Awash basin in 2008

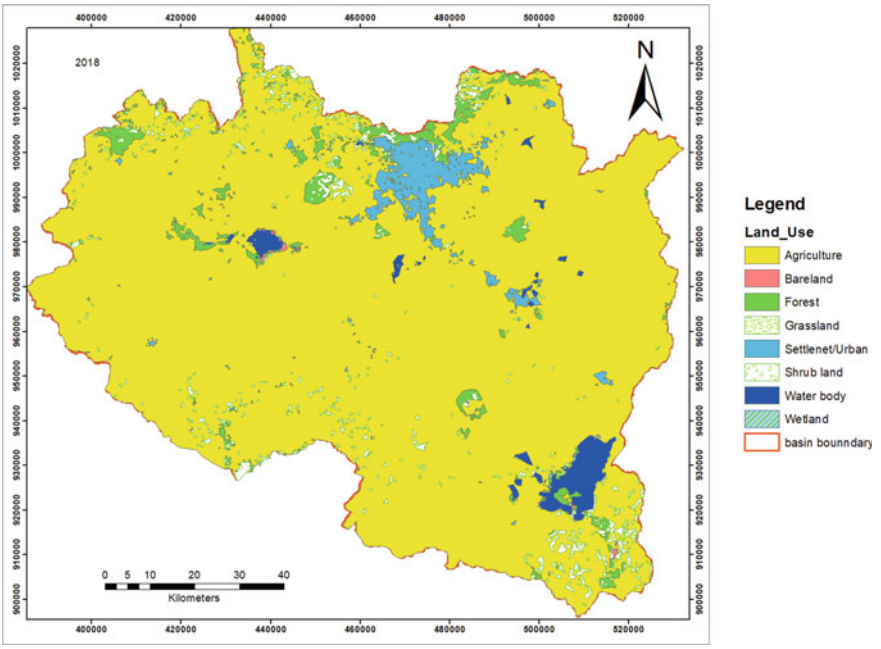

Fig. 3.4 LULC map of the upper Awash basin in 2018

Table 3.1 LULC distribution for 1998, 2008, and 2018

Land use	Area coverage (ha) of each LULC in 1998	Percentage distribution of each LULC class in 1998	Area coverage (ha) of each LULC in 2008	Percentage distribution of each LULC class in 2008	Area coverage (ha) of each LULC in 2018	Percentage distribution of each LULC class in 2018
Agriculture	1,078,268.14	92.32	1,071,710.87	91.76	1,052,892.08	90.15
Forest	23,693.25	2.03	26,546.54	2.1	34,668.57	2.70
Grassland	1944.19	0.16	1227.07	0.09	555.09	0.04
Shrub land	31,770.26	2.58	30,231.09	2.45	27,881.26	2.23
Wetland	286.22	0.02	317.29	0.03	317.29	0.03
Settlement/ Urban	7796.58	0.65	14,683.67	1.22	29,469.24	2.42
Bare land	1129.22	0.09	1387.14	0.12	923.94	0.08
Water body	23,040.35	1.97	21,822.32	1.83	21,209.79	1.78

555.09 ha (0.04%), and 317.29 ha (0.03%), respectively, accounted for the lowest percentage of the total classes.

Predicted LULC Simulation

To predict future scenarios of the land use/land cover distribution for the coming 20 years and 40 years from the reference map of 2018, this study used the artificial neural network-based cellular automata method, found in the MOLUSCE (Modules for the Land use/land cover Change Evaluation) plugin of QGIS. Previous studies such as Alam et al. (2021), Aneesha Satya et al. (2020), Mzava et al. (2019), Muhammad et al. (2022), Perović et al. (2018), and Satya et al. (2020) also showed that the MOLUSCE module is a more advanced model and able to accurately reflect nonlinear spatially probabilistic land use transformation. LULC changes are generally governed by a combination of geographical, environmental, and socioeconomic factors. In this regard, economic development and related population growth and urbanization as well as topographical characteristics such as elevation, distance from roads, and distance from streams or rivers highly affect the evolution of LULC (Alam et al., 2021; Muhammad et al., 2022; Hassan et al., 2016). Consequently, LULC maps from 1998, 2008, and 2018 and additional spatial variables that are widely used for LULC change analysis and provide effective information about the effect of people on LULC, such as population density, elevation, distance from road, and distance from streams or rivers, were used as input data sets in this study.

First, to predict the LULC for 2018, the classified LULC map of 1998 (as the initial year) and LULC map of 2008 (as the final year) were used as input variables. In addition to the classified maps, some of the variables that are widely used for

LULC change and provide effective information about the effect of people on LULC, such as distance to road networks, DEM and population density, were also used as explanatory spatial variables. These variables were first resampled, normalized, and geometrically matched with the LULC raster classes of 1998 (initial year) and 2008 (final year) to predict the land use/land cover of 2018. Once the real reference map of 2018 and predicted map of 2018 were validated using the validation algorithm of the plugin. These explanatory variables were also used as spatial variable inputs to consequently predict the land use/land cover of 2038 and 2038 by considering the trend of these spatial variables.

As many studies have been conducted on LULC change dynamics and predictions, especially using ANN-CA modeling of the MOLUSCE plugin, model validation is performed by statistically validating using the real/reference map with the predicted map of the same year and calculating Kappa values using the validation algorithm. Therefore, based on the indicated initial and final year inputs and spatial variables to validate the modeling performance, the predicted and classified images of 2018 were compared using the validation algorithm in the plugins. As a result, the model was able to predict the future correctly with a correctness of prediction of 97.8%, and almost all kappa values were above 0.88.

In addition, to indicate the certainty of the model prediction, it is possible to compare the area coverage of the real map of 2018 and the predicted map of 2018. Table 3.2 and Fig. 3.5 indicate the comparison between the real map and the predicted map.

Second, future LULC scenarios of the coming 20 years (i.e., 2038) and 40 years (i.e., 2058) from the reference period 2018 were predicted using the classified images of 2008 and 2018 and normalized spatial variables as an input to the ANN-CA model.

Finally, the future LULC maps of the Upper Awash Basin for the coming 20 years and 40 years (i.e., 2038 and 2058) were produced. Based on the modeling output,

Table 3.2 Comparison of changes between the predicted and real maps in 2018

Classification	Real/ reference map 2018	Predicted map 2018	Δ	Real/ reference map 2018%	Predicted map 2018%	Δ %
Agriculture	994,000.7	1,010,925.68	16,924.98	90.90	92.44	1.5477
Forest	31,985.03	28,967.4	− 3017.63	2.92	2.65	− 0.2759
Shrub land	21,854.41	21,854.41	0	2.00	2.00	0.0000
Grassland	431.09	665.38	234.29	0.04	0.06	0.0214
Wetland	346.75	234.29	− 112.46	0.03	0.02	− 0.0103
Settlement/ Urban	29,604.66	13,841.75	− 15,762.91	2.71	1.27	− 1.4414
Bare land	749.72	787.21	37.49	0.07	0.07	0.0034
Water body	14,591.47	16,287.72	1696.25	1.33	1.49	0.1551

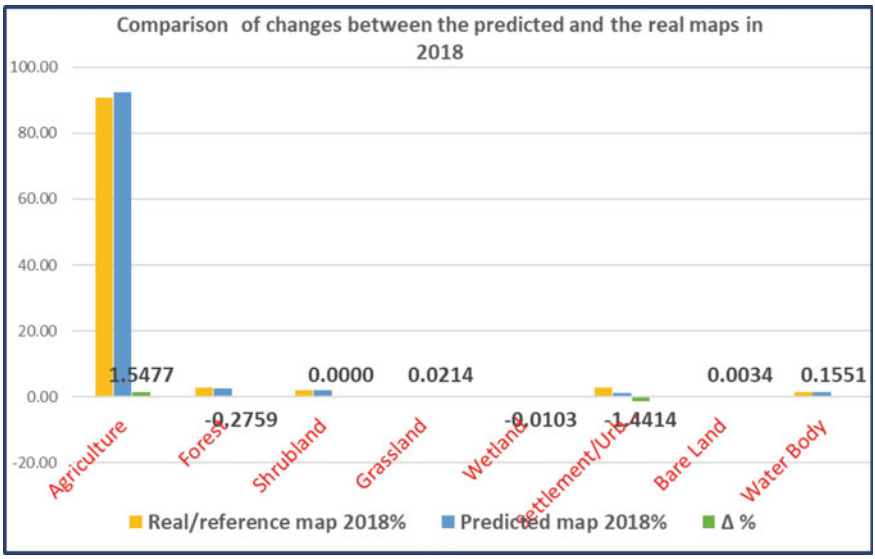

Fig. 3.5 Comparison of the observed versus simulated map of 2018

the future thematic maps and LULC distribution are given in Figs. 3.6 and 3.7 and Table 3.3, respectively.

Change in Land Use and Land Cover: Trend and Magnitude

Land cover change analysis of the historical LULC scenarios for 1998, 2008, and 2018 and future land use and land cover scenarios predicted for 2038 and 2058 are presented in this section. The magnitude and percentage distribution change of the historical and predicted future LULC between a given subperiod (1998–2008, 2008–2018, 1998–2018) and (2018–2038 and 2038–2058) are summarized in Tables 3.4 and 3.5, respectively.

The magnitude of historical land cover change analysis for the subperiods (1998–2008) in Table 3.3 revealed a negative change (i.e., a reduction) in the LULC categories of agriculture, shrub land, water body and grass land by 6557.28 ha, 1539.17 ha, 1218.03 ha, 717.11 ha, respectively. The LULC categories of settlement/urban, forest, and wetland increased by 6887.09 ha, 2853.29 ha, and 31.07 ha, respectively.

The period between 2008 and 2018 witnessed a drop in the agriculture, shrub land, grass land, water body, and bare land LULC by 18,818.79 ha, 2349.84 ha, 671.99 ha, 612.53 ha, and 463.2 ha, respectively. On the other hand, the LULC categories of settlement/urban and forest increased by 14,785.57 ha and 8122.02 ha, respectively.

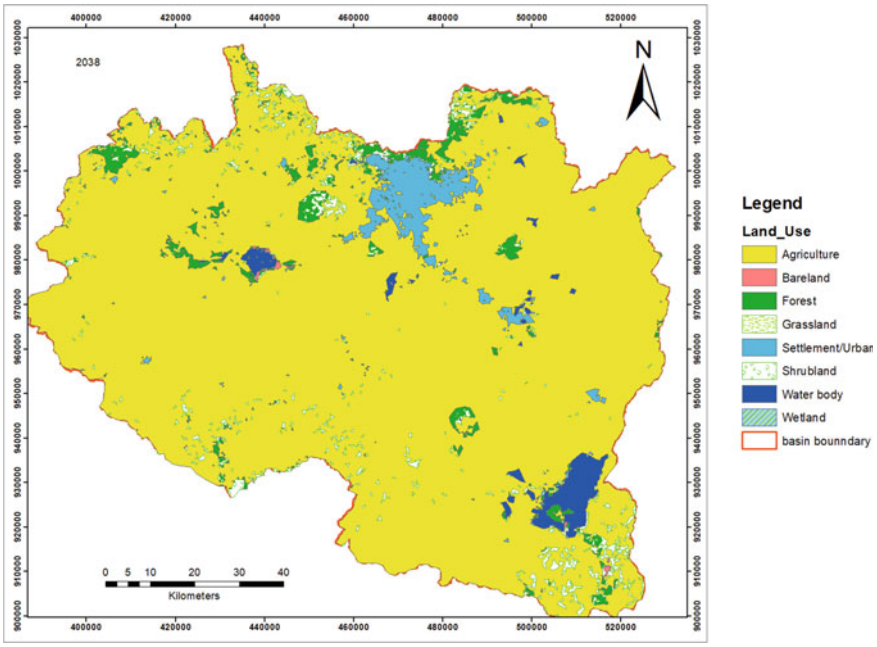

Fig. 3.6 Predicted LULC map for 2038

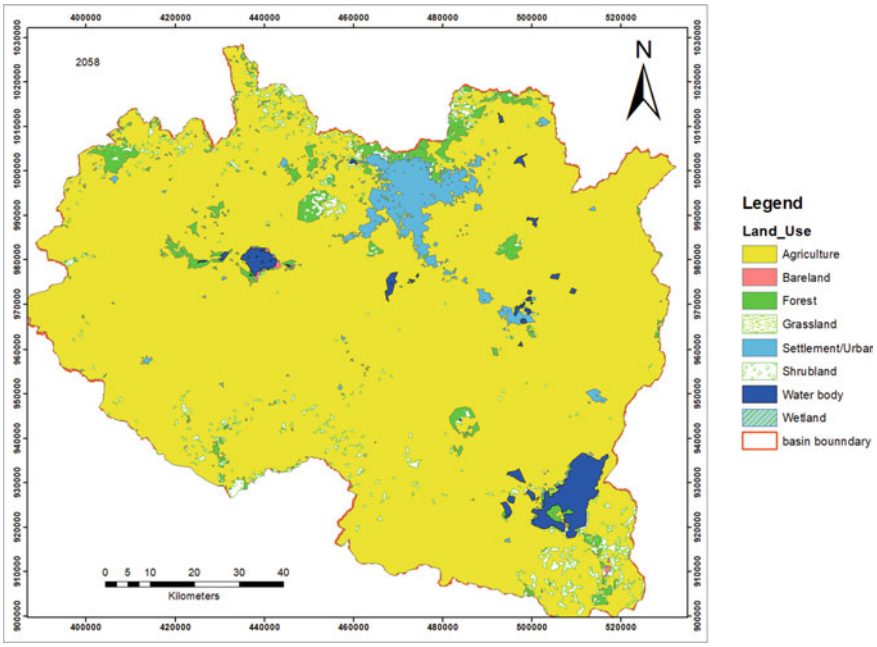

Fig. 3.7 Predicted LULC map for 2058

Table 3.3 Predicted LULC distribution for 2038 and 2058

Land use	Area coverage (ha) of each LULC in 2038	Percentage of area covered under each LULC class in 2038	Area coverage (ha) of each LULC in 2058	Percentage of area covered under each LULC class in 2058
Agriculture	1,050,698.28	89.97	1,050,219.68	89.92
Forest	34,496.26	2.68	34,478.43	2.68
Grassland	533.48	0.04	533.48	0.04
Shrub land	27,286.61	2.18	27,274.14	2.18
Wetland	307.92	0.03	298.54	0.02
Settlement/Urban	32,496.53	2.66	33,078.45	2.7
Bare land	921.07	0.08	921.07	0.08
Water body	21,177.11	1.78	21,113.46	1.78

Table 3.4 LULC distribution change between 1998–2008, 2008–2018, and 1998–2018

LULC Type	Area change (ha) between 1998 and 2008	Percentage change between 1998 and 2008 (%)	Area change (ha) between 2008 and 2018	Percentage change between 2008 and 2018 (%)	Area change (ha) between 1998 and 2018	Percentage change between 1998 and 2018 (%)
Agriculture	− 6557.28	− 0.56	− 18,818.79	− 1.61	− 25,376.06	− 2.17
Forest	2853.29	0.22	8122.02	0.60	10,975.32	0.82
Grassland	− 717.11	− 0.06	− 671.99	− 0.06	− 1389.1	− 0.11
Shrub land	− 1539.17	− 0.13	− 2349.84	− 0.21	− 3889	− 0.34
Wetland	31.07	0.002	0	− 0.0003	31.07	0.002
Settlement/ Urban	6887.09	0.57	14,785.57	1.20	21,672.66	1.77
Bare land	257.92	0.022	− 463.2	− 0.04	− 205.28	− 0.02
Water body	− 1218.03	− 0.10039	− 612.53	− 0.05	− 1830.56	− 0.15095

From the predicted LULC distribution change analysis in Table 3.5 and Fig. 3.8 between 2018 and 2038, it can be inferred that settlement/urban land will increase by almost 0.24%, and the remaining LULC categories will decrease. Nevertheless, the LULC change analysis results between 2038 and 2058 revealed that settlement/urban LULC will increase by almost 0.05%, the remaining LULC categories of agriculture, forest, shrub land, wetland and water body will decrease, and grass land and bare land will remain unchanged in this given period.

LULC analysis and change detection have been used as primary information in different decision support mechanisms, such as in land management processes, water resource management, monitoring afforestation/deforestation, and in general, achieving sustainable developments. Studies have also revealed that LULC evolution

Table 3.5 Predicted LULC distribution change between 2018–2038 and 2038–2058

LULC type	Area change (ha) between 2018 and 2038	Percentage between 2018 and 2038 (%)	Area change (ha) between 2038 and 2058	Percentage change between 2038 and 2058 (%)
Agriculture	− 2193.8	− 0.19	− 478.6	− 0.04
Forest	− 172.31	− 0.02	− 17.83	− 0.0024
Grassland	− 21.61	− 0.002	0	0.00002
Shrub land	− 594.65	− 0.052	− 12.47	− 0.002
Wetland	− 9.37	− 0.001	− 9.37	− 0.001
Settlement/Urban	3027.29	0.24	581.92	0.047
Bare land	− 2.87	− 0.00024	0	0.00
Water body	− 32.68	− 0.003	− 63.65	− 0.01

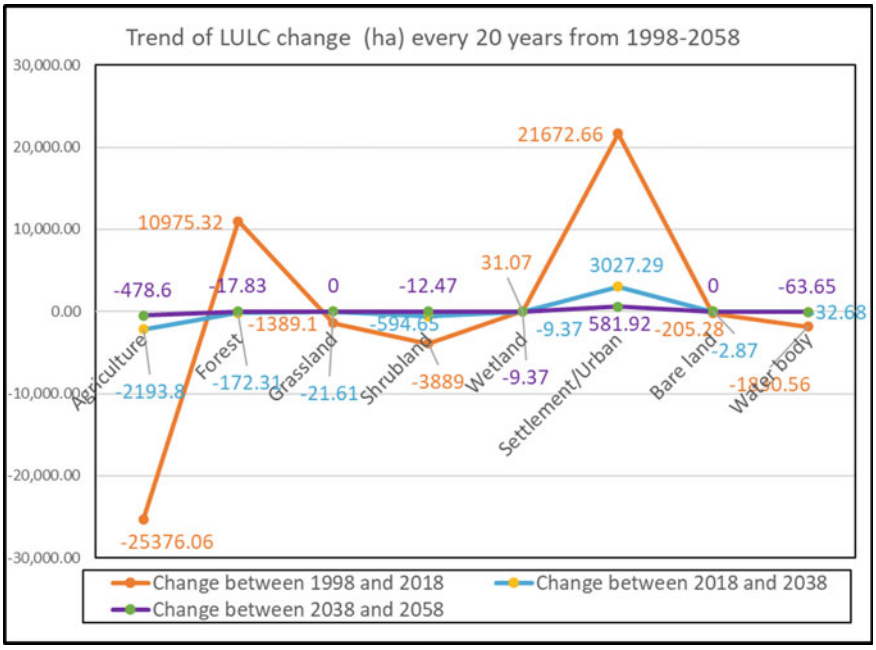

Fig. 3.8 Graph showing the trend of LULC change in ha from 1998–2058

highly influences overland flow and thus stream discharge (Belihu et al., 2020; Boru et al., 2019; Huyen et al., 2017; Neupane and Kumar, 2015; Sriwongsitanon and Taesombat 2011; Sulamo et al. 2021). Consequently, the LULC change analysis performed in this study was used to examine its impact on the hydrological responses of the upper Awash River basin (Mitiku et al., 2022). According to Mitiku et al. (2022), the influence of LULC change on river flow has an almost one-digit percentile

change (for instance, 2.64% and 1.43%) in the upstream and downstream parts of the basin where more settlements are located. However, the LULC changes had a tenth-digit percentile change in river flow in the middle of the basin, where the basin has a lower population density.

Conclusions

This study assessed the LULC change dynamics of the upper Awash River Basin over the past 20 years (i.e., between 1998 and 2018) and predicted future land use/land cover change scenarios for 2038 and 2058 (i.e., for the coming 20-year and 40-year periods) using an artificial neural network-based cellular automata (ANN-CA) model using MOLUSCE (modules for land cover evaluation) in the QGIS environment.

The land use and land cover changes in the upper Awash River Basin were modeled and validated using historical data. Additional spatial variables such as elevation, population density, distance to rivers and distance to the road network were also considered to predict the land use and land cover for 2038 and 2058. The historical analysis showed that there was an increase in forest, wetland, and settlement/urban areas by 0.82%, 0.002% and 1.77%, respectively, while there was a decrease in agricultural land, shrub land, grassland, bare land, and water bodies by 2.17%, 0.34%, 0.11%, 0.02%, and 0.15%, respectively.

On the other hand, analysis of the predicted LULC change for the coming 20 years (i.e., for 2038) revealed that there will be an increase in settlement/urban areas by 0.24% and decreases in agriculture, forest, shrub land, grassland, wetland, bare land, and water bodies by 0.19%, 0.02%, 0.052%, 0.002%, 0.0008%, 0.0002%, and 0.003%, respectively.

Generally, from historical and predicted LULC change scenarios every 20 years from 1998 to 2058, the trend of LULC change between 1998 and 2018 reveals that agriculture, shrub land, grassland water bodies, and bare land have a decreasing trend and settlement/urban, forest and wetland have an increasing trend. The trend of the predicted LULC change between 2018 and 2038 indicates that settlement/urban land cover will increase, and the remaining LULC will decrease. The trend of LULC change between 2038 and 2058 also reveals that settlement/urban land cover will increase and agriculture, water body, forest, shrub land and wetland LULC will decrease, but grass land and bare land will remain unchanged.

Acknowledgements The researchers would like to acknowledge Ethiopian Construction Design and Supervision Works Corporation for providing research facilities and a good working environment. The researchers would also like to extend their acknowledgments to environment and society conference organizers to open the door for this research to be published as a book chapter entitled “Land and Water Degradation in Ethiopia: Climate and Land Use Change Implications".

References

Alam N, Saha S, Gupta S, Chakraborty S (2021) Prediction modeling of riverine landscape dynamics in the context of sustainable management of floodplain: a geospatial approach. Ann GIS 27(3):299–314. https://doi.org/10.1080/19475683.2020.1870558

Aneesha Satya B, Shashi M, Deva P (2020) Future land uses land cover scenario simulation using open source GIS for the city of Warangal, Telangana, India. Appl Geomatics 12:281–681. https://doi.org/10.1007/s12518-020-00298-4

Baker WL (1989) A review of models of landscape change. Landscape Ecol 2(2):111–133

Belihu M, Tekleab S, Abate B, Bewket W (2020) Hydrologic response to land use land cover change in the Upper Gidabo Watershed, Rift Valley Lakes Basin, Ethiopia. Hydro Res 3:85–94. https://doi.org/10.1016/j.hydres.2020.07.001

Benediktsson JA, Swain PH, Ersoy OK (1990) Neural network approaches versus statistical methods in classification of multisource remote sensing data. IEEE Trans Geosci Remote Sens 28(4):540–551

Boru GF, Gonfa ZB, Diga GM (2019) Impacts of climate change on streamflow and water availability in Anger subbasin, Nile Basin of Ethiopia. Sustain Water Resour Manag 5(4):1755–1764. https://doi.org/10.1007/s40899-019-00327-0

Dijst PMJ, Veldkamp A (2004) Land use modeling: current practice and research priorities. Geojournal 61:309–324

ECDSWC (2021) Feasibility and detailed design of Upper Awash Integrated Flood Management project, study report

Getachew HE, Melesse AM (2012) Impact of land use /Land cover change on the hydrology of angereb watershed. Ethiop Int J Water Sci. https://doi.org/10.5772/56266,Vol.1,4:1-7

Hassan Z, Shabbir R, Ahmad SS, Malik AH, Aziz N, Butt A, Erum S (2016) Dynamics of land use and land cover change (LULCC) using geospatial techniques: a case study of Islamabad Pakistan. SpringerPlus 5. https://doi.org/10.1186/s40064-016-2414-z

Hassoun MH (1995) Fundamentals of artificial neural network. Massachusetts Institute of Technology (MIT) Press, Cambridge

Huyen NT, Tram VNQ, Minh DN, Liem ND, Loi NK (2017) Assessing the impacts of climate change on water resources in the Srepok watershed, central Highland of Vietnam. J Water Clim Change 8(3):524–534. https://doi.org/10.2166/wcc.2017.135

Kavzoglu, Mather P (2003) The use of backpropagating artificial neural networks in land cover classification. Int J Remote Sens 24(23):4907–1938

Li X, Yeh AG-O (2002) Neural-network-based cellular automata for simulating multiple land use changes using GIS. Int J Geogr Inf Sci 16:323–343

Loveland T, Zhu Z, Ohlen D, Brown J, Reed B, Yang L (1995) An analysis of IGBP global land-cover characterization process. Photogramm Eng Remote Sens 65(9):1021–1032

Lu D, Moran E, Hetrick S, Li G (2011) Land-use and land-cover change detection. In: Weng Q (ed) Advances in environmental remote sensing: sensors, algorithms and applications. CRC Press, Boca Raton, pp 273–291

Mango L, Melesse AM, McClain ME, Gann D, Setegn SG (2011a) Land use and climate change impacts on the hydrology of the upper Mara River Basin, Kenya: Results of a modeling study to support better resource management, Special Issue: Climate, weather and hydrology of East African Highlands. Hydrol Earth Syst Sci 15:2245–2258. https://doi.org/10.5194/hess-15-2245-2011

Mango L, Melesse AM, McClain ME, Gann D, Setegn SG (2011b) Hydro-meteorology and water budget of Mara River basin, Kenya: A land use change scenarios analysis. In: Melesse, A (ed) Nile river basin: hydrology, climate and water use. Springer Science Publisher, Chapter 2, 39–68, DOI: https://doi.org/10.1007/978-94-007-0689-7_2

Melesse A, Weng Q, Thenkabail P, Senay G (2007) Remote Sensing sensors and applications in environmental resources mapping and modeling. Special Issue Remote Sens Nat Resour Environ Sens 7:3209–3241

Melesse AM, Jordan JD (2002) A comparison of fuzzy vs. augmented-ISODATA classification algorithm for cloud and cloud-shadow discrimination in landsat imagery. Photogramm Eng Remote Sens 68(9):905–911

Melesse AM, Jordan JD (2003) Spatially Distributed watershed mapping and modeling: land cover and microclimate mapping using landsat imagery Part 1, J. of Spatial Hydrol (e-J), 3(2)

Mitiku AB, Abrha G, Mulu T, Woldemichael TA (2022) Environmental variability and climate change impacts on stream flow for the case of Awash River basin, Ethiopia. Hydro Res 6:16–28. https://doi.org/10.1016/j.hydres.2022.12.002

Mohammed H, Alamirew A, Assen M, Melesse A (2013) Spatiotemporal mapping of land cover in Lake Hardibo Drainage Basin, Northeast Ethiopia: 1957–2007. Water conservation: practices. Nova Publishers, Challenges and Future Implications, pp 147–164

Muhammad R, Zhang W, Abbas Z, Guo F, Gwiazdzinski L (2022) Spatiotemporal change analysis and prediction of future land use and land cover changes using QGIS MOLUSCE plugin and remote sensing big data: a case study of Linyi. China Land 11(3):419. https://doi.org/10.3390/land11030419

Mzava P, Nobert J, Valimba P (2019) Land cover change detection in the urban catchments of dares salaam, Tanzania using remote sensing and GIS technique ,Tanzani. J Sci 45:315–329

Neupane R, Kumar S (2015) Estimating the effects of potential climate and land use changes on hydrologic processes of a large agriculture dominated watershed. J Hydrol 529:418–429. https://doi.org/10.1016/j.jhydrol.2015.07.050

Perović V, Jakšić D, Jaramaz D, Koković N, Čakmak D, Mitrović M, Pavlović P (2018) Spatiotemporal analysis of land use/land cover change and its effects on soil erosion (Case study in the Oplenac wine-producing area, Serbia). Environ Monit Assess 190:1–18. https://doi.org/10.1007/s10661-018-7025-4

Pijanowski BC, Brown DG, Shellito BA, Manik GA (2002) Using neural networks and GIS to forecast land use changes: a land transformation model. Comput Environ Urban Syst 26(6):553–575

Pijanowski B, Pithadia S, Shellito B (2005) Calibrating a neural network-based urban change model for two metropolitan areas of the Upper Midwest of the United States. Int J Geogr Inf 19(2):197–215

Pontius GR, Chen H (2006) GEOMOD modeling: land use and cover change modeling tutorial. Clark University

Prestele R, Alexander P, Rounsevell MDA, Arneth A, Calvin K, Doelman J, Eitelberg DA, Engstrom K, Fujimori S, Hasegawa T et al (2016) Hotspots of uncertainty in land-use and land-cover change projections: a global-scale model comparison. Glob Change Biol 22:3967–3983

Roy S, Farzana K, Papia M, Hasan M (2015) Monitoring and prediction of land use/land cover change using the integration of the markov chain model and cellular automation in the southeastern tertiary hilly area of Bangladesh. Int J Sci Basic Appl Res (IJSBAR)

Saputra MH, Lee HS (2019) Prediction of land use and land cover changes for North Sumatra, Indonesia, Using an Artificial-Neural-Network-Based Cellular Automaton

Satya BA, Shashi M, Deva P (2020) Future land use land cover scenario simulation using open source GIS for the city of Warangal, Telangana, India. Appl Geomatics 12:281–290. https://doi.org/10.1007/s12518-020-00298-4

Seto K, Kaufmann R (2003) Modeling the drivers of urban land use change in the pearl river Delta, China: integrating remote sensing with socioeconomic data. Land Econ 79(1):106–121

Singh AK (2003) Modeling land use land cover changes using cellular automata in a geo-spatial environment. Unpublished thesis. ITC, Enschede, The Netherlands

Sohl TL, Claggett PR (2013) Clarity versus complexity: land-use modeling as a practical tool for decision-makers. J Environ Manag 129:235–243

Srishti G, Rajendra S (2023) Comprehensive review on land use/land cover (LULC) change modeling for urban development: current status and future prospects. Sustainability 15:903. https://doi.org/10.3390/su15020903

Sriwongsitanon N, Taesombat W (2011) Effects of land cover on runoff coefficient. J Hydrol 410:226–238. https://doi.org/10.1016/j.jhydrol.2011.09.021

Sulamo MA, Kassa AK, Roba NT (2021) Evaluation of the impacts of land use/cover changes on water balance of Bilate watershed, Rift valley basin, Ethiopia. Water Pract Technol 16(4):1108–1127. https://doi.org/10.2166/wpt.2021.063

Voženílek V (2009) Artificial intelligence and GIS: mutual meeting and passing. In: International conference on intelligent networking and collaborative systems (INCOS 2009), pp 279–284. ISBN 978-1-4244-5165-4

Wondie M, Teketay D, Melesse AM, Schneider W (2012) Relationship between topographic variables and land cover in the Simen Mountains National Park, a World Heritage Site in northern Ethiopia. Int J Remote Sens Appl 2(2):36–43

Wondie M, Schneider W, Melesse AM, Teketay D (2011) Spatial and temporal land cover changes in the simen mountains national park, a world heritage site in Northwestern Ethiopia. Remote Sens 2011, 3:752–766; https://doi.org/10.3390/rs3040752

Chapter 4
The Contribution of Microbial Endophytes Associated with Climate-Smart Brachiaria Grass Species to Sustainable Agriculture and Environment

Goshu Misganaw and Collins Mutai

Abstract Brachiaria grass species is widely grown in African savannahs and grasslands. It is native to Africa. It is a perennial grass species that is a source of green herbage for livestock during drought seasons. Grass possesses useful agronomic traits, including drought tolerance, resistance to insect pests and phytopathogens, the ability to grow in acidic and low-fertility soils, high nitrogen use efficiency, the capacity to sequester atmospheric carbon, the ability to form an extensive root system useful for water and nutrient acquisition, and the ability to form high biomass useful for organic matter addition, which would in turn improve soil fertility properties. Studies show that grass species adapted to adverse environments and climatic conditions usually form mutualistic microbes that enhance the fitness and productivity of host partners under stress conditions. These are one group of microorganisms called endophytes that support the growth and development of host plants through the production of phytohormones, inhibition of phytopathogens, increased uptake and availability of essential nutrients, production of siderophores, and production of plant growth-regulating compounds and enzymes (ACC deaminase), thereby reducing and alleviating plant stress conditions. The aim of this chapter is to dissect and explore endophytes associated with Brachiaria grass species that are useful for sustainable agriculture and the environment.

Keywords Brachiaria · Brachiaria endophytes · Agricultural biologics sustainable environment and agriculture

G. Misganaw (✉)
Department of Biotechnology, College of Natural and Computational Sciences, Hawassa University, Hawassa, Ethiopia
e-mail: goshumis@hu.edu.et

G. Misganaw · C. Mutai
Biosciences for Eastern and Central Africa-International Livestock Research Institute (BecA-LRI Hub), Nairobi, Kenya
e-mail: c.mutai@cgiar.org

A. M. Melesse et al. (eds.), *Land and Water Degradation in Ethiopia*, Springer Geography, https://doi.org/10.1007/978-3-031-60251-1_4

Introduction

Brachiaria (syn. *Urochloa*) species have been extensively useful for increasing livestock productivity in tropical and subtropical regions of the world (Njarui et al. 2021) It is native to eastern and central Africa. Brachiaria grasses of African savannahs have supported millions of African herbivores over thousands of years. Although Brachiaria is native to the region, its role in fodder production and green herbage provision during drought periods, climate change mitigation, environmental protection and biodiversity conservation, and soil–water conservation in degraded and impoverished sites remains to be fully realized. It has important agronomic traits and performance with high biomass production potential, is adapted to semiarid environments, and has proven to be a climate-smart grass species that can provide quality herbage for livestock in drought-affected regions of the tropics with economic viability for smallholder farmers (Kelemu et al. 2002; Maass et al. 2018).

Brachiaria grass is climate-smart because it has a C_4 photosynthetic pathway, high nitrogen use efficiency, deep root system enabling the acquisition of water and nutrients from soils, ability to sequester atmospheric carbon dioxide into soils and extensive root system contributing to high amounts of organic carbon that can in turn improve soil fertility (Igiehon and Babalola 2018;Maass et al. 2018; Romero and Pieckenstain 2014; Shen et al., 2019; Njarui et al. 2021).

Grass species are usually reported to have symbiotic associations with beneficial microorganisms that enhance plant hosts to survive and reproduce under adverse environmental and climatic conditions (Mohanty et al. 2016). These are one group of microorganisms called endophytes that live inside plant tissues but do not cause apparent harm and disease symptoms on the host plant.

Endophyte-based bioproducts (biofertilizers, biopesticides, bioweedicides, bionematicides, biofungicides) are commercialized, which are suitable for the environment, biodiversity, and human health and are promising alternatives to replace agrochemicals that are extensively applied in conventional agriculture, often with negative impacts on the environment and biodiversity.

Therefore, the objective of this study was to investigate the role of microbial endophytes associated with Brachiaria grass species (collected in Ethiopia) and explore possible plant growth promotion properties that could be scaled up for agricultural and environmental applications.

Background

Sustainability has been the center of discourse in different scholars for the last 40 years. Scholars have argued about the malicious development concepts of the nineteenth century and the finite nature of natural resources. The seventeenth century industrial revolution brought a dramatic change in human civilization changing the standard of living of human beings through the transportation system, agricultural

production system and productivity, contributing to human population productivity. Despite the industrial revolution contribution to the development of human civilization, it also brought a drastic disaster to the environment and biodiversity loss (e.g., the UK lost 50% of its biodiversity since the industrial revolution) (UN Environment 2020).

This has happened because of linear economic development policy, which is a concept of development that does not consider the real connection between ecological degradation, biodiversity, and economic development and its consequences in the long run. Since ecological and biodiversity-related problems in the end become economic problems, linear economic development was seriously condemned, and the issue of sustainability became the central agenda in the twenty-first century. As a result, another concept of economic development was designed: the circular economy agenda (Ng et al. 2019), which considers environmental sustainability and biodiversity conservation for sustained development.

Among the industrial revolution outputs were the emergence of agrochemical-producing factories that are useful to increase and improve crop production through insect pest protection with the use of synthetic fertilizers and chemical pesticides that affect soil health (environment), cause serious negative effects on biodiversity, and risks related to human health and side effects on nontarget organisms. As a result, environmentalists and other pressure groups have raised concerns about environmental degradation, air pollution, loss of biodiversity, and human security under such agricultural traditions (modern agriculture). They have cautioned that human development will be hampered unless proactive conservation and protection measures are taken to replace the current agricultural practices.

The concept of the circular economy was designed to alleviate the problems related to land and water degradation and biodiversity loss, focused on relieving strategies to avert current harmful practices, and designed and envisioned to create jobs for youth through sound production and processing technologies (biotechnology-based approach) that do not harm the environment and biodiversity (WWF and ILO 2020).

Brachiaria grass species are considered climate-smart in that they possess climate-resilient features such as C_4 photosynthetic pathways, adaptation to a wider range of ecological conditions, lower irrigational requirements, better growth and productivity in low nutrient input conditions, less reliance on synthetic fertilizers, and minimum vulnerability to environmental stressors and climate change (Midega et al. 2018). These important attributes make Brachiaria one of the climate-compliant grass species useful for the concept and implementation of the sustainability development of the 2050 agenda.

In addition, Brachiaria harbors useful microbial endophytes that contribute to climate smart agriculture (endophytes as agricultural biologics), which could be applied in agriculture to increase and improve crop productivity. The contribution of Brachiaria to environmental sustainability and rehabilitation is immensely important. It could rehabilitate degraded and impoverished ecological regions in semiarid regions of the tropics (including Ethiopia).

Ethiopia possesses genetically and morphologically diversified Brachiaria grass species that are grown in different ecological regions of the country, which could

be remedial for degraded land rehabilitation and conservation of soil–water loss in regions prone to sedimentation, runoff and flood.

Among the Ethiopian regions that require conservation and protection with plants (grasses) is the region around the Great Ethiopian Renaissance Dam of Ethiopia (GERD). Rehabilitation and mitigation work and programs are important for the sustainable use of dams. The upper catchment of the Abbay River (the Blue Nile) is prone to erosion and sedimentation problems that affect the long-term use and sustainability of the dam. Conservation and protection of the upper catchment through the use of Brachiaria grass species is a good alternative for mitigation and remediation of regions affected by runoff and floods. Brachiaria is useful for the conservation and protection of soil–water loss, which subsequently reduces and mitigates sedimentation problems in the GERD (Abdallah 2021).

Promotion and dissemination of Brachiaria forage development is needed by the government and NGOs that would have multiple benefits to rural and smallholder farmers. Since the grass is proven to be a perennial grass species with green forage provision capacity during drought periods, the local communities would benefit from Brachiaria forage development while protecting the environments from flood and runoff.

The GERD is now the heart of Ethiopia and significant financial, energy, and time investments have been made by the people of Ethiopia. However, land degradation (deforestation, soil and water erosion) and sedimentation would be a threat to the long-term use of GERD. Hence, the selection and promotion of planting and sowing targeted mixed grass species is important to efficiently conserve soil–water resources in the upper catchment (Soldatov et al. 2020).

Among the grass species, Brachiaria has been proven to have a role in the rehabilitation of degraded lands with added value (fodder production and provision) for local communities. Ethiopia is the center of origin and center of diversity for Brachiaria grass species. The use of Brachiaria grasses could tackle (check) sedimentation problems that would occur around GERD.

In general, Brachiaria could contribute to soil–water conservation and biodiversity conservation, enrich ecosystem services, inhibit nitrification processes, combat climate change and enhance mitigation processes, and improve smallholder farmers' livelihoods through forage and fodder supply, which would be done through direct sowing and planting (mixed grass seeds and roots) around the Abbay basin (GERD site), thereby reducing runoff and flooding with a period of three months.

Climate and Environment Mitigation Role of Brachiaria

Biological Nitrification Inhibition (BNI)

The global nitrogen cycle is influenced by microbial activities that generate nitrates through the nitrification process (Venkata et al. 2015). This process determines the form of nitrogen present, and therefore how nitrogen is absorbed, utilized, or

dispersed into the environment (Sun et al. 2016). This would in turn affect plant productivity and environmental quality. During the nitrification process, the relatively immobile $NH4^+$ is converted to the highly mobile NO_3^- (Taylor et al. 2007). This process strongly influences N utilization by plants because the NO_3^- formed is highly susceptible to loss from the root zone by leaching and/or denitrification (Subbarao et al. 2009).

Plants' ability to produce and release nitrification inhibitors from roots and suppress/slow soil-nitrifier activity is termed "biological nitrification inhibition" (BNI) (Subbarao et al. 2017). Regulating nitrification could be a key strategy in improving N recovery and agronomic *N*-use efficiency in situations where the loss of N following nitrification is significant (Subabarao et al. 2017). To date, there has been no conclusive evidence suggesting that tropical grass ecosystems have a significant role in reducing the nitrification process in soils. A study conducted by (Subbarao et al. 2009) on Brachiaria grass pasture BNI (*Brachiaria humidicola*) showed that Brachiaria roots release chemical compounds that inhibit the nitrification process in soil microbes (*Nitrosomonas* sp.) resulting in improved soil health and environmental quality. Therefore, Brachiaria has potential biological nitrification inhibition (BNI) capacity that is useful for increasing nitrogen use efficiency (NUE) in agronomical practices. It is widely known that most nitrogen fertilizers are synthesized in the form of NH_4^+ (ammonium), which can be converted into nitrate by soil bacteria and lost to land and water in the form of nitrate (NO_3^-) through nitrification and denitrification processes, causing major environmental pollution and nitrogen loss from croplands (Subbarao et al. 2012). It is ironic that nearly 70% of N fertilizers applied to agricultural soils are lost and returned to the atmosphere as oxides of N and N_2 (by microbial nitrification and denitrification processes) before the crops can absorb and assimilate them into plant protein with no net benefits to humans (Venkata et al. 2015).

Nearly 80% of global emissions of nitrous oxide (N_2O), a greenhouse gas 300 times more potent than CO_2, comes from the production and utilization of N fertilizers in agriculture (Subbarao et al. 2017). Hence, designing and exploring regulatory mechanisms to reduce nitrogen loss through nitrate (NO_3^-) formation from ammonium (NH_4^+) in agricultural practices is immensely important to increase agricultural productivity. Among the mechanisms useful to control nitrogen loss is to apply nature-based approaches (plant-mediated nitrification inhibition), which have been found to be effective in increasing the nitrogen use efficiency of plants and reducing nitrous oxide (N_2O) formation from the oxidation of ammonium (NH_4^+) by soil bacteria, which is friendly to the environment and contributes to sustainable agriculture and food security.

The typical chemical compounds secreted and involved in *B. humidicola* roots are named Brachialactones, which have shown 60–90% inhibition of soil nitrifying bacteria (*Nitrosomonas* and *Nitrobacter* spp.) (Subbarao et al. 2009). Studies have been conducted on the BNI capacity of several agronomic crops, and promising results have been recorded in *Sorghum bicolor*, wild wheat grass, and rice (Sun et al. 2016; Subbarao et al. 2021).

In conclusion, a suite of genetic, soil and environmental factors regulate BNI activity in plants, and BNI function can be genetically exploited to improve the BNI capacity of major food and feed crops to develop next-generation production systems with reduced nitrification and N_2O emission rates to benefit both agriculture and the environment.

In this case, climate-smart Brachiaria could play a key role in enhancing and establishing a low nitrification process used for crop productivity with low nitrate production and N_2O emission reduction, which is a nature-friendly mechanism to mitigate GHG emissions.

Role of Brachiaria in Push–Pull Technology Systems

Push–pull technology is a technique that emerged as an integrated insect pest management (IPM) strategy 60 years ago in California, USA. During that time, entomologists observed that the sole use of chemical pesticides could not be the solution to insect pest problems (Abdel Farag El-Shafie 2020), as there were insects that showed resistance to applied insecticides. In addition, the emergence of pesticide-resistant pests, the concerns of biodiversity loss, and the severe economic effects of pesticide application (approx. $46B per annum) and economic affordability by smallholder farmers were fundamental to considering that chemical pesticides would not be a permanent solution for managing insect pests in agriculture. This has prompted the need to explore alternative methods of pest control mechanisms that are effective in managing insects in agriculture and the environment (Andrew and Hill 2017; Abdel Farag El-Shafie 2020).

To prevent significant economic losses from insect pests in agricultural production, it is crucial to develop and implement new methods and strategies, such as utilizing natural and ecologically sound principles. The IPM principle is a widely accepted method for controlling pests globally, and it prioritizes environmentally friendly techniques to minimize economic loss and harmful impacts on the environment. This approach combines cultural, chemical, and biological methods to control harmful insect pests while preserving beneficial insects. It also involves the use of a combination of physical, social, and biochemical control strategies to control pests and reduce insect infestation of crops under changing climate conditions (Andrew and Hill 2017).

Among the techniques used by IPM strategies as sustainable insect pest management and control mechanisms is the climate-adapted push–pull technology or stimulo-deterrent diversionary strategy developed for the control of cereal stem borers in drier agro-ecologies (Khan et al. 2011). Additionally, it has been proven to be an effective tool in managing the fall armyworm (*Spodoptera frugiperda*), which caused huge maize yield losses and damage to other crops in native central America as well as in Africa and Asia in the recent past (Midega et al. 2018). The protection of fall armyworms comprises intercropping maize with drought-tolerant silver leaf or green leaf Desmodium and planting Napier grass and/or hybrid Brachiaria cv. Mulato II as a border crop around this intercrop. Protection to maize is provided by

semiochemicals (signal chemicals) that are emitted by the intercrop that repel (push) stem borer moths, while those released by the border crop attract (pull) them away from the main crop (Midega et al. 2018). Insect pests are attracted toward chemical compounds produced by one plant species (pull) which is carefully selected for this function (Brachiaria or Napier grass), and repelled by chemical compounds produced by another plant (push), Desmodium green leaf, which reduces the number of eggs and larvae laid on maize crops in the intercropping system compared to the maize crop under monoculture (Khan et al. 2016). Push–pull technology (PPT) not only controls insect pests through a false attract principle but also improves soil fertility and reduces weeds of Striga through its parasitoid properties, which include suicidal germination and killing other parasites.

Currently, adoption of this technology is expanding, and thousands of smallholder farmers are involved in this novel IPM strategy in Kenya, Tanzania, Ethiopia, and Uganda which improves and expands their income sources with less energy, time and minimum inputs to protect staple cereal crops (including sorghum, maize, beans, finger millet, etc.).

Microbial Endophytes - Agricultural Biologics

Endophytes are microorganisms (including bacteria and fungi) that associate within healthy plant tissues but do not cause or elicit signs of disease symptoms on the host plant (Petrini 1991; Hallmann et al. 1997). The term endophyte was originally defined by De Bary (1866) as "Any organism occurring within plant tissues".

Previous studies on plants adapted to adverse climatic and environmental conditions have focused on their genetic makeup, physiology, metabolism, phenology, and molecular nature to understand the mechanism of plant survival under harsh environmental conditions (Hallmann et al. 1997). Recent research has shown that the survival, reproductive success and fitness of plants growing in arid and marginalized environments are governed by communities of microorganisms that live inside the tissues of host plants. These microorganisms support their host partner to cope with and withstand biotic and abiotic stressors (Rodriguez et al. 2003; Kiani et al. 2015). Currently, the exploration and characterization of microorganisms associated with plants (in various habitats) adapted to harsh environments are centers of research interest because these microbes have been confirmed to have potential applications in agriculture, the environment, industry, and biotechnology.

The application of nature-based (endophyte-based) approaches to agriculture is receiving considerable attention from agronomists and microbiologists due to the suitability of the approach to the environment, biodiversity, human health and economic viability to smallholder farmers (Verma et al. 2021). Development, mass production and formulation of endophytes (in the form of biological products) for biofertilizers, biopesticides, biofungicides, bionematicides, and bio yield enhancement agents used to improve and increase crop productivity are preferred compared to

synthetic chemicals that harm soil health, affect biodiversity with a phenomenon that yield is decreasing year after although extensive application of these agrochemicals.

Agricultural biologics (including biofertilizers, biopesticides, and biostimulants) are animal, plant, and microbial in origin and are useful for improving and increasing crop yield in sound with the environment. The global bio-insecticide-biological market share reached $4 billion in 2019.

Endophyte-based products are developed from endophytes of plant origin and are reliable to control insect pests and phytopathogens, sound with environment, biodiversity conservation, economically viable, and safe to human health.

Endophytes have been isolated from different species of cereals and plants with economic relevance, such as wheat, maize, rice, sugarcane, banana, enset, cotton, coffee, soybeans, sorghum, Brachiaria, and finger millet (Misaghi and Donndelinger 1990; Backman and Sikora 2008; Vega et al. 2008; Puri et al. 2016; Singh et al. 2016; Ribeiro et al. 2018; Misganaw et al. 2019; Sinno et al. 2020).

Endophytes can greatly improve the growth and development of host plants through various mechanisms, including direct and indirect contributions to plant physiology and biochemistry (Hallmann et al. 1997; Harman 2011; Gundel et al. 2017). The direct contribution of endophytes to host plants occurs through improvement of nutrient uptake and availability, nitrogen fixation, production of phytohormones, production of antifungal and antibacterial compounds, production of siderophores, and production of growth regulating and modulation compounds (ACC-deaminase production controls the level of ethylene production in plants) (Andrews et al. 2003; Doty 2011; Zhang et al. 2011; Ali et al. 2014). The indirect contributions include competition with pathogens for food and niches and triggering induced systemic resistance (ISR) of host plants before they are attacked by fungal or bacterial pathogens (Ramamoorthy et al. 2001; Gao et al. 2010). Studies have also shown that plants that associate with mutualistic endophytes have better survival and fitness under stressful environmental conditions than plants that lack associative mutualistic microbial endophytes within their tissues (Hardoim et al. 2012; Pande et al. 2016).

Bioprospection of Endophytes

There are diverse species of plants on earth (approximately 300,000 species of plants), and endophytes colonize intercellular and intracellular spaces of plant tissues, where one plant species is reported to harbor one or more endophytic microbes (i.e., plant tissues are not free of endophytes) (Alam et al. 2021). Nearly one-tenth of plant species are not studied for their endophyte assemblages, limiting their exploitation for agricultural, environmental, medicinal and health, industrial, and biotechnological applications. Fungal endophyte diversity is estimated to be more than 1 million based on the vascular plant to fungal endophyte ratio (1:4 or 1:5), where less than 1% of the diversity of endophytes has been studied and investigated for the benefit of humankind (Sun and Guo 2012). Endophyte-based agriculture is sought to replace the

current conventional agriculture that is dependent on agrochemicals that are harmful to the environment.

The Role of Metagenomics in Endophyte Discovery

The new era of omics has opened a new opportunity to study and explore microbial genetics and functional diversity associated with plants. The technique enables the study of the full profile and picture of associated and endophytic microbes living with plant species (deciphering both cultivable and uncultivable microbes). The technology is accelerating the identification and characterization of microbiomes (at the cellular and molecular levels with biotic and abiotic interactions), which simplifies the further understanding, development, and use of microbial genetic resources in agriculture, biotechnology, industry, the environment, medicine, and health (Kaul et al. 2016). The approach has resolved the limitations of culture-dependent approaches and unraveled the study and investigation of all types of microbes associated with plant tissues and their functional role. The technique (microbial ecology and metagenomics) involves plant sample maceration, microbial DNA extraction, PCR amplification, next-generation sequencing, and chromatographic data analysis. This specifically allowed us to study and unravel problems associated with *obligate* endophytes (microbes that require host tissue to multiply and to do its job) that are not recovered and investigated with the use of artificial growth media, which support screening (max. 0.05%) of the total microbial population found inside plant tissues or soil samples that are left unstudied and uncovered under normal culture media. Characterization and exploitation of a wider range of endophytes associated with different plant species found in different habitats and mechanisms study them, and scale-up and further application in agriculture, industry, and the environment is possible through metagenomics, functional and structural genomics, metabolomics and proteomics (Kaul et al. 2016).

The approach not only unravels the genetic and functional diversity of microbes found inside tissues (any habitat) but also provides detailed information on the properties and mechanisms to develop and use the cells to meet different human needs (Qadri et al. 2020). It has revolutionized the study of plant–endophyte interactions, innovations and the development of endophyte-based products that are applied in agriculture and are safe for the environment and biodiversity conservation (Poosakkannu et al. 2015; Bonatelli et al. 2021).

The introduction of beneficial microbial endophytes with drought- and disease-resistant traits, through cross-inoculation, to nonhost plants contributed to organic agriculture that eliminated the need for agrochemicals in conventional agricultural production systems (Kumar and Verma 2018). This in turn contributes to creating a sustainable and climate-resilient environment in the twenty-first century (Bonatelli et al. 2021; Mishra and Sharma 2022). Endophytic bacteria are a promising tool in the development of sustainable agriculture. They fix atmospheric nitrogen, solubilize phosphate, produce phytohormones, inhibit plant pathogens and insect pests and promote plant growth with no need for the application of chemical fertilizers and

chemical pesticides that seriously affect the environment and biodiversity (Lourenço et al. 2021).

The panorama of technological development and the demand for endophyte-based products is increasing, and the commercialization of products is approved in the USA and other countries (Lugtenberg et al. 2016). For example, the application of endophytes to three important agricultural crops, i.e., corn, soybean, and sugarcane, was studied and confirmed to improve the yield and productivity of these important crops (Data et al. 2013). In the last two decades, there has been increasing interest in studying endophytic fungi for potential application in bioremediation (phytoremediation) capacity, biocontrol of herbivores and pathogens, abiotic stress tolerance and plant growth promotion (Ortega and Torres-mendoza 2020).

As a result, patent rights and intellectual property rights application and publication have increased in the last two decades. There were 88 patent applications related to plant stress tolerance and growth promotion, 90 patent applications related to biological control of plant pathogens and herbivores, and 7 patent applications related to bioremediation and phytoremediation using endophytic fungi for 1988–2020 (Ortega and Torres-mendoza 2020).

Contribution of Endophytes to Sustainable Agriculture

Plant Growth Promotion and Development Properties

Plant beneficial microbes, such as plant growth-promoting bacteria, rhizobia, arbuscular mycorrhizal fungi, and trichoderma, can reduce the use of agrochemicals and increase plant yield, nutrition, and tolerance to biotic and abiotic stresses (Newitt et al. 2019). The use of biobased formulations and products, such as those derived from endophytes, mycorrhizae, and Trichoderma, has been shown to improve the performance, productivity, and yield of agricultural crops. These natural alternatives (nature-based approaches) have been sought to replace synthetic chemicals that are harmful to the environment, biodiversity, and human health (Vassilev et al. 2015; Singh et al. 2016; Timmusk et al. 2017).

Recent studies have shown that the use of fungal strains as inoculants for cereal crops such as maize can lead to an increase in fresh biomass at the end of the growing season. In comparison, non-inoculated maize cereal crops show stunted growth and less green biomass than those treated with beneficial endophytic fungi (e.g., Trichoderma fungal species) (Harman 2011).

Increasing Fitness and Drought Tolerance of Plants

Endophytes with drought tolerance traits have the potential to improve plant fitness against drought and moisture stress through inoculation of seeds and seedlings of crops of agricultural importance. An investigation of tomato seedlings inoculated with *Trichoderma harzianum* fungal species confirmed the beneficial role of endophytes in tolerating drought and moisture stress compared to non-Trichoderma-treated tomato seedlings (Harman 2011) when exposed to moisture stress for several weeks. Trichoderma fungal species not only act as biocontrol agents but also offer multiple benefits to plants that host them (Harman 2011; Tucci et al. 2011).

Insect Pathogenic Properties of Endophytes

Phytopathogens cause serious damage and reduction in crop yield and product quality, accounting for 40% of global crop production (Bahadur 2018). Insect pests alone are considered a major threat, responsible for an estimated 10.80% of agricultural losses worldwide in the post green revolution era (Deka et al. 2021). Recent findings have shown that insect pests have caused a reduction in agricultural outputs (18–26% per annum), which are worth $470 billion (Mantzoukas and Eliopoulos 2020). Insecticides are used to reduce these losses and, as a result, have become an essential method for controlling insect pest infestations and have been applied to protect crops against important insect pests. However, the concentrated application of chemicals has led to the development of resistance in more than 500 insect species, with as many as 80% of cases showing resistance to one or more classes of insecticides (Sharma and Sharma 2021). As a result, entomopathogens, which include fungi, viruses, protozoa, and bacteria, are seen as regulatory operators of pest infestations.

Biological control methods that use bacteria, fungi, viruses, and nematodes, which cause fatal disease and kill insect pests, are termed entomopathogens (insect pathogens). Bacterial and viral entomopathogens could cause death in specific species of insect pests, whereas entomopathogenic fungi cause disease in a wider range of insect pest species (Deka et al. 2021).

Recent studies have shown that plants host a diverse group of entomopathogenic endophytes (fungi and bacteria), which could be isolated from plant tissues and characterized for insect pathogenicity properties to control insect pests of agricultural importance. These products are friendly to the environment, biodiversity, and human health (Caruso et al. 2022). Fungal and bacterial endophytes that have entomopathogenic properties (parasitism and pathogenicity) have been mass-produced and formulated for use in controlling pest populations in a manner analogous to chemical pesticides applied on crops (Singh et al. 2016). These endophytes can effectively manage pest populations without causing their complete elimination or causing negative effects beyond what is economically acceptable (Lacey et al. 2015).

To date, crops such as wheat, maize, rice, sorghum, Soya beans, grapevines, peppers, strawberry, cotton, faba beans, tomatoes, and coffee berries have been protected against insect infestations with the use of entomopathogenic endophytes, which are commercialized and applied in agriculture (Litwin et al. 2020).

Investigation of the Mechanisms of Fungal Insect Pathogens to Control Insect Pests in Agriculture

Fungi that kill arthropods (insect pests) contribute to crop protection and crop yield improvements. Micro fungi that associate with plant hosts have been studied and investigated for their potential to limit insect pest populations in agriculture (Vega et al. 2008; Jaber and Enkerli 2017). These are called entomopathogenic fungi sourced from plant origins (fungal endophytes), which are confirmed to have inhibitory effects against insect pests, nematodes, and phytopathogens (Lacey et al. 2015). Recent studies have shown that using fungal endophytes as a defense mechanism in plants is a new and effective mechanism to control insect pests in agriculture (Sinno et al. 2020). For example, fungal pathogens of insect pests of the coffee berry borer, the most destructive coffee pest worldwide, are controlled with the use of fungal entomopathogens of *Beauveria bassiana,* which has been commercialized by 11 companies found in the U.S. with 16 products used to control insect pests of tomato, potato, beans, cabbages, and corn (Vega et al. 2008). The approach is friendly to the environment, promotes biodiversity, is economically viable for smallholders and is safe for human health (plant origin). Endophytes that were isolated from coffee berries were identified as *Acremonium*, *Beauveria*, *Cladosporium*, *Clonostachys*, and *Paecilomyces*, from which two of these, *B. bassiana* and *Clonostachys rosea*, were tested against the coffee berry borer and were shown to possess the property of insect pathogenicity against coffee berry disease (Vega et al. 2008).

Mode of Action of Fungal Endophytes on Insect Pests

Entomopathogenic fungi typically cause fatal diseases in insects when spores come in contact with the insect (arthropod) host. Under ideal conditions of moderate temperatures and high relative humidity, fungal spores germinate and breach the insect cuticle through enzymatic degradation and mechanical pressure to gain entry into the insect body (Sandhu et al. 2012). Once inside the insect body, the fungi multiply, invade the insect tissues, emerge from dead insects, and produce more spores, resulting in the fatal death (24 h) of the insect pest.

Fugal endophyte-based bioinoculants are insect specific, environmentally safe, suitable for biodiversity, cost-effective, and safe for human health. In addition, the application of live fungal cells and their byproducts (bioactive compounds) could cause death to target insect pests but did not cause side effects on nontarget organisms (Litwin et al. 2020; Sharma and Sharma 2021).

Investigation of Mechanisms of Entomopathogenic Bacteria to Control Insect Pests in Agriculture

The use of insect pathogenic bacteria (entomopathogenic bacteria) to protect crops from insect pests is an emerging and suitable technology that is cost-effective, acceptable, viable and economically affordable for smallholder farmers. Regarding the environment and biodiversity conservation, it has become one of the best biological innovations for sustainable development. Protection of crops based on entomopathogenic bacteria, fungi, nematodes, and viruses is termed a microbial control approach in modern times (Uiu et al. 2013).

Recent studies indicate that bacterial endophytes (live cells) can colonize and parasitize insect pests or kill insect pests through the production of bioactive compounds that are easily degraded in the environment (Mishra and Sharma 2022). Both live cells and microbial compounds produced could be applied as biopesticides to inhibit insect larvae and reduce insect pest populations, which would damage crops of agricultural importance. Due to their eco-friendly properties, the use of biopesticides is increasing, which is important to decrease the pressure on the environment and biodiversity (Jaber and Enkerli 2017; Mantzoukas and Eliopoulos 2020).

Mode of Action of Insect Pathogenic Bacteria

The mechanism of entry of insect pathogenic bacteria starts through ingestion of the bacteria by a susceptible insect host (Loulou et al. 2023). Then, bacteria enter the insect body and continue to multiply. Most entomopathogenic bacteria belong to the Bacillus species, which form spores inside insect bodies. These include *Bacillus* spp., *Paenibacillus* spp., *Clostridium* spp., and nonspore-forming bacteria that belong to the genera *Pseudomonas*, *Serratia*, *Yersinia*, *Photorhabdus*, and *Xenorhabdus* (Glare et al. 2017). Several species of soil-borne bacteria, Bacillus and Paenibacillus, are pathogenic to coleopteran, dipteran, and lepidopteran insects. *Bacillus thuringiensis*, which is isolated from soils, is effectively used for controlling different groups of target insects.

When an insect pathogenic bacterium is ingested, alkaline conditions in the insect gut (pH 8–11) activate the toxin protein (delta-endotoxin) that attaches to the receptor sites in the midgut and creates pores in midgut cells. This leads to the loss of osmoregulation, midgut paralysis, and cell lysis. Contents of the gut leak into the insect's body cavity (hemocoel), and blood (hemolymph) leaks into the gut, disrupting the pH balance. Bacteria that enter the body cavity cause septicemia and eventual death of the host insect (Glare et al. 2017).

In conclusion, the emerging entomopathogenic technology (use of fungi, bacteria, viruses, and nematodes as bioinsecticides) to control insect pests is increasing by 15.6% annual growth on the market. Insect pathology is a new requirement of an IPM strategy that is vital toward developing biopesticides that have better efficacy, specificity, and biodegradability.

Endophytes Associated with Brachiaria Grass Species

Brachiaria grass species, as mentioned in the previous sections, have multiple functional traits that contribute to establishing a sustainable environment and agriculture. One of its key benefits is that it is a perennial grass species that provides green forage (a substitute fodder) for livestock during drought seasons. It has the capacity to grow in acidic and low-fertility soils and contribute to soil–water conservation through its dense and deep root system, which is useful for soil organic carbon addition and soil fertility improvements (Njarui et al. 2021). In addition, Brachiaria forms a symbiotic relationship (mutualism) with diversified fungal and bacterial endophytes, which are vital for the adaptation and productivity of grass under moisture stress and harsh climatic conditions. There is limited information on the potential application of endosymbiotic microbes associated with Brachiaria grass species (African savannahs), which have been documented to enhance the survival and fitness of the plant in adverse environmental and climatic conditions (unlike temperate regions) (Odokonyero et al. 2017). This has limited the exploitation of endophyte use in agriculture, the environment, biotechnology, industry, medicine, and health.

Isolation of Grass-Associated Microbial Endophytes

The first step in endophytes study is isolation of the strains from surface-sterilized plant tissues. To eliminate surface-associated microorganisms (contaminants) while retaining microbes living inside the tissues of plants, different levels and stringencies of surface sterilization protocols are employed. The surface sterility of the plant samples was confirmed with a negative control sample (by plating from the final rinse water). Any growth of microorganisms on agar plates from the final rinse indicates that the surface sterilization process is not perfect and suggests that the experiment should be discarded. Reagents that are frequently used in plant tissue surface sterilization include 70% ethanol, NaOCl, and H_2O_2.

Brachiaria samples were collected from various locations in Ethiopia. Brachiaria aboveground and belowground plant parts were taken from both natural ecotypes and gene bank collections during the months May and June of 2014. Isolation and characterization of endophytes from these samples was conducted to identify potential endophytes useful for plant growth promotion and development. The study began with the surface sterilization and cultivation of endophytes on suitable media, with endophytes being defined as microbes that are grown and emerge from surface-sterilized healthy plant tissues (Hallmann et al. 1997). Surface sterilization of plant tissues to remove surface contaminants (epiphytes) is vital to recover endogenous microbes, which will be considered for functional studies and evaluation. However, it is crucial to ensure that the sterilization process does not harm or inhibit the growth of microbes that are naturally present within plant tissues (Barraquio et al. 1997; Cao et al. 2004). The surface sterilization protocol and endophyte population vary with

plant tissue type, season of isolation, habitat where the host plant was grown, and the genetic variation of host plants (Ghimire et al. 2011; Harrison and Griffin 2019).

Brachiaria leaf, root, stem, and seed samples were processed, and surface disinfected according to established protocols (Taghavi et al. 2009; Poosakkannu et al. 2015). Samples were thoroughly washed in running tap water and then cut into 3–4 cm pieces, surface disinfected in 70% ethanol for 1 min, and subsequently in 1.2% sodium hypochlorite (NaOCl), amended with two drops of Tween-20 per 100 ml solution, for 10 min for leaf and stems, 20 min for root and seed samples. The samples were rinsed three times in sterile distilled water and blot dried in between with sterile paper towels.

For each sample, 1 g surface-disinfected plant tissue was cut into 3–4 mm pieces and macerated in 9 ml of 10 mM/L magnesium sulfate (MgSO4) solution using a sterile mortar and pestle, and the suspension was diluted serially. Then, a total volume of 100 µl samples from serial dilutions were plated on nutrient agar and 869 media in 90 mm petri dishes and incubated at 28 °C for up to 3 days, and the emergent colonies were picked and purified through repeated streaking to obtain a single-colony bacterial subculture.

A total of 215 cultivable bacterial endophyte strains were recovered from seeds ($n = 26$), leaves ($n = 77$), leaf sheaths ($n = 35$), stems ($n = 46$), and roots ($n = 31$) and were tested for plant beneficial properties. Analysis of endophytes isolated from different plant parts (Brachiaria) showed the presence of diversified bacterial endophytes associated with the tissues collected from six different sites of Ethiopia. The number of bacteria isolated from different locations and corresponding plant parts are presented below (see Table 4.1).

Sequence-Based Identification of Endophytes

The hypervariant 16S rRNA gene is used to identify and evaluate the diversity of microbes associated with a plant sample. Genomic DNA extraction, 16S rRNA partial gene amplification with PCR, gel electrophoresis, DNA quantitation and concentration measurement, and DNA sequencing were performed (Sanger). Raw DNA sequences were trimmed (cleaned) and assembled using clcbiomain workbench v7.1 (http://www.clcgenomics) software, and the sequences were converted to FASTA sequence format. Sequence-based identification of endophytes is an important aspect of endophyte study, which is vital to investigate the genetic diversity of strains at the DNA level and study their taxonomy based on their sequence alignment and similarity analysis in addition to morphological and biochemical studies (Upholt 1977).

NCBI database (Gene bank) retrieval was performed to explore the closely related species for the query sequence, where the BLAST tool on the NCBI database (http://www.ncbi.nlm.nih.gov/blast) was used to identify the closest matches of the endophytes by comparing query sequences where a query coverage of 99–100% and sequence similarity match of 99% or higher were considered. As a result, endophytic

Table 4.1 Site, host plant species, and number of bacterial isolates obtained

Sites	Brachiaria host	Plant part(s)	# of bacterial isolates
Wondo Genet College of Forestry	Ecotype	Seed, leaf, stem, and root	31
Wondo Genet Centre, Ethiopian Institute of Agricultural Research	*B. decumbens*	Seed, leaf, stem, and root	21
Awassa Previous Airport	*B. mutica*	Seed, leaf, stem, and root	47
Awassa Saint Gebrel Church Compound	Ecotype	Seed, leaf, stem, and root	16
Awassa University College of Agriculture	Ecotype	Leaf, stem, and root	24
Ziway forage seed gene bank site, International Livestock Research Institute	*B. jubata*	Leaf, leaf sheath, and stem	76
	B. brizantha	Leaf, leaf sheath, and stem	
	B. decumbens	Leaf, leaf sheath, and stem	
	B. humidicola	Leaf, leaf sheath, and stem	
	B. lachnantha	Leaf, leaf sheath, and stem	
	B. bovonei	Leaf, leaf sheath, and stem	
		Total	215

strains were classified into various taxa levels (phyla, classes, orders, families, and genera), with the most frequently isolated and associated phyla being Proteobacteria. Other major bacterial phyla were discovered, with lineages of Proteobacteria, Actinobacteria, Firmicutes, and Bacteroidetes identified with variable frequencies. The 215 strains were grouped into 36 taxa, where the genera *Pseudomonas* and *Pantoea* were the most dominant groups of endophytic bacteria isolated from Brachiaria grass tissues. Among the useful bacterial isolates obtained from Brachiaria grass hosts with potential agricultural and biotechnological applications include *Pseudomonas fluorescens*, *Agrobacterium* sp., *Bacillus* species, *Bacillus simplex*, *Flavobacterium* sp., *Rahnella* sp., and *Brevibacterium* sp., which showed positive results for bioassays focused on traits important for plant growth promotion and development. The

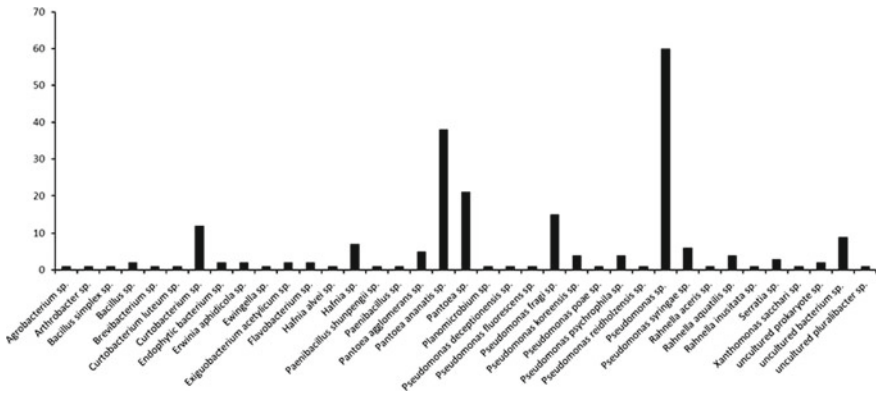

Fig. 4.1 Frequency of endophytic bacterial strains isolated from Brachiaria grass species from Ethiopia

frequency of endophytes associated with Brachiaria grass samples is shown (see Fig. 4.1).

Phylogenetic Tree Reconstruction

A phylogenetic tree of endophytes was constructed by importing the FASTA sequences into MEGA software v 7.1 (Kumar et al. 2016). Nucleotide multiple sequence alignments (MSA) were performed with an out-group Archeae species (*Archeaoglobus fulgidus* strain DSM 4304), MSA was edited and cleaned, and the data were converted into MEGA file format. Then, phylogenetic tree reconstruction was performed using the maximum composite likelihood statistical method of analysis using the Junks–Cantor model with bootstrap values of 1000 replications. Evolutionary relationships were inferred from the branches corresponding to partitions reproduced in less than 50% bootstrap replicates that were collapsed. This analysis involved 159 informative nucleotide sequences. The percentage of replicate trees in which the associated taxa clustered together in the bootstrap test are shown next to the branches (see Fig. 4.2).

Biochemical Assay of Bacterial Endophytes

Endophyte characterization based on bioassay approaches has been useful for identifying putative beneficial traits of endophytes for plant growth promotion and development. In vitro tests of endophytes for plant growth promotion traits such as IAA production, ACC deaminase production, siderophore production, antifungal activity,

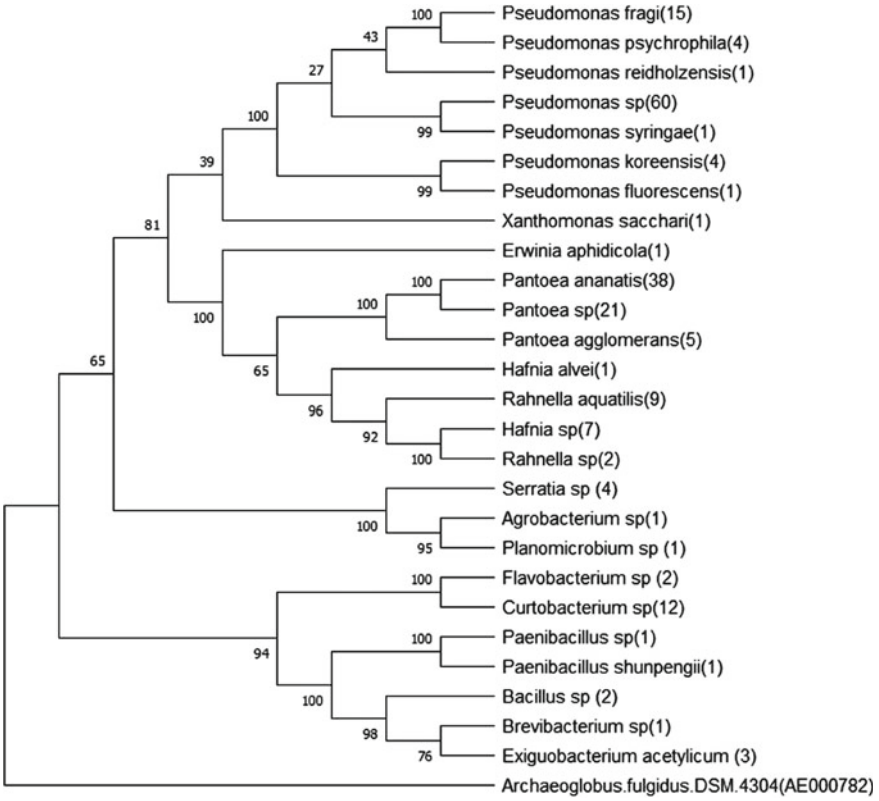

Fig. 4.2 Phylogenetic tree reconstruction with maximum likelihood statistical analysis with Junks Cantor model with 1000 bootstrap values (replications). Numbers in parenthesis indicate the frequency of the isolates obtained from Brachiaria tissues

nitrogen fixation, phosphate solubilization, disease suppression, drought tolerance, and flood tolerance properties of plants with endophytes and without endophytes have been employed to identify efficient endophytes for agricultural applications. Useful fungi and bacterial endophytes were investigated from the tissues of Brachiaria grass species and were studied for their ability to promote plant growth and development under in vitro and in vivo conditions. For example, *Acremonium implicatum* and other bacterial endophytes were considered (isolated from Brachiaria tissues) and were reconsidered for beneficial properties to enhance plant tolerance to moisture stress and increase nitrogen use efficiency, which will have a concomitant effect on plant biomass and performance compared with host plants that lack associative endophytes (Abello et al. 2008; Odokonyero et al. 2017).

The bacterial and fungal symbionts of Brachiaria studied to date have shown useful properties to enhance plant growth and development under stress conditions, increase seed germination and development, increase root and shoot biomass, suppress phytopathogens of the host plants, and increase the uptake and availability

of essential nutrients and minerals when there is competition or limitation of the vital nutrients in the system, which are necessary for the growth and development of the plant in adverse climatic conditions.

Endophytes could be added to modern agriculture to improve and increase crop yield and productivity. Limited research has been conducted related to Brachiaria (Ethiopian context where high genetic and morphological diversity exist in the country) endophyte diversity and their potential application to agriculture.

For example, *Acremonium implicatum* fugal species were isolated from the tissues of Brachiaria grass species and tested for plant protection properties (Abello et al. 2008).

The examination of the 215 strains of endophytic bacteria for various functional properties revealed variations in their ability to solubilize inorganic phosphate, produce indole-3-acetic acid, synthesize siderophores, synthesize 1-aminocylopropane-1-carboxylic acid deaminase (ACC-Deaminase) activities, and inhibit the growth of phytopathogens (*Aspergillus flavus* strain 006 and *Aspergillus flavus* strain 023). Endophytes with positive and negative responses for the bioassays performed are indicated below (see Table 4.2).

Plant growth-promoting bacteria have been isolated from Brachiaria tissues and the rhizosphere of Brachiaria grass cultivated land and were characterized for their ability to boost plant growth and development through cross-inoculation of nonhost plants (Kelemu et al. 2002).

Endophyte-inoculated Brachiaria genotypes showed better plant biomass with long root and shoot formation compared to their counterpart parts, which did not take the endophytes for plant growth promotion and development (Mutai et al. 2017). Endophytes possess useful properties, such as the ability to inhibit phytopathogens through siderophore production (iron molecule collecting and chelating ligands), which makes iron unavailable for phytopathogens, thereby leading to the subsequent death of plant pathogens as a result of scarcity of essential nutrients from the environment. This makes endophytes ideal biocontrol agents in plant protection and disease suppression (Zhao et al. 2015) through siderophore production (Table 4.2). In addition, endophytes can enhance plant growth promotion and development by

Table 4.2 Biochemical assays performed on endophytes associated with Brachiaria

Biochemical assay	Number of strains	Positive strains	Negative strains
IAA test	215	121 (56%)	94 (44%)
Siderophores test	215	77 (36%)	138 (64%)
Phosphate test	215	82 (38%)	133 (62%)
ACC-deaminase test	215	72 (33%)	143 (67%)
Antifungal activity test			
A. flavus strain 023 *A.flavus* strain 006	215 215	70 (32%) 96 (45%)	145 (68%) 119 (55%)
Plant growth promotion test	#55 strains were selected	Tested on commercial wheat	Data under record

producing plant growth promotion hormones (IAA), increase the uptake of essential nutrients and minerals (nitrogen fixation, phosphate solubilization) (Puri et al. 2016; Rosenblueth et al. 2018), enable drought and disease resistance (Mona et al. 2017; Ullah et al. 2021), and increase the water and nitrogen use efficiency of cereals grown in moisture-limited environments (Kandel et al. 2015; Odokonyero et al. 2017). Endophytes also play a role in ACC-deaminase production, which aids in regulating and modulating the level of ethylene production in plants (Jha et al. 2012) as well as controlling invasive weed propagation through the release of stimulant and abortive compounds, thereby accelerating early germination of seed propagules of invasive weeds such as *Striga hermonthica* and resulting in improved crop growth and development (Mounde et al. 2020).

Different studies have indicated that endophytic bacteria isolated from Brachiaria tissues have potential applications in agriculture, as reviewed in the literature. This indicates that these microbes could be developed for potential use in promoting plant growth and development, protecting against fungal phytopathogens, increasing and improving crop productivity through nitrogen fixation and phosphate solubilization, and protecting against insect pests through insecticide properties (see Table 4.3).

The nature-based approach (biobased agriculture) formulated from endophytes is immensely important to increase and improve crop production, which contributes to environmental and agricultural sustainability while reducing the application of artificial chemicals to promote plant growth promotion and development at the expense of the environment, biodiversity loss, and human health risks.

Conclusion

Brachiaria grass species are vital grass species adapted to semiarid regions of the tropics (Savannah's). It is native to Ethiopia. It grows in different geographic locations of the country (both cultivated and wild habitats). It is useful forage for livestock and wildlife. Brachiaria possess useful properties, such as high water and nitrogen use efficiency, the capacity to grow in acidic and low-fertility soils, deep and extensive root systems useful for soil fertility and water retention, and the ability to tolerate drought stress conditions in semiarid regions, which provide green manure for animals during dry seasons, which is important for smallholder farmer livelihood improvement. Endophytes associated with plant hosts are vital for the adaptation of plants grown under harsh environmental and climatic conditions. The adaptation of Brachiaria grass species to adverse environmental conditions might be ascribed to the presence of beneficial endophytes (bacteria and fungi) inside the tissues of the plants. Endophytes isolated from Brachiaria grass tissues that were collected from field gene banks (accessions) and wild habitats (ecotypes) in Ethiopia showed genetic and functional diversity.

The results of characterization of the endophytic strains (isolated from Brachiaria) for their ability to produce indole-acetic acid and ACC deaminase, solubilize inorganic phosphate, produce siderophores, and exhibit antifungal activity suggest that

Table 4.3 Endophytes with potential application to agriculture

Genera/taxa	Isolated from	Application	Citations
Agrobacterium sp.	Rice	Tested in rice, and lettuce growth promotion	Barazani and Friedman, (1999), Shrivastava (2015)
Arthrobacter sp.	Grapevine organs; rice seeds	Antifungal activity	Compant et al. (2011), Cottyn et al. (2000)
Bacillus sp.	Commercial seeds	Antifungal activity	Díaz et al. (2016), Pleban et al. (1995)
Curtobacterium sp.	Mustard seeds	PGP	Truyens et al. (2014)
Exiguobacterium sp.	Tomato leaves	Biocontrol of plant disease	Romero and Pieckenstain (2014), Singh (2016)
Hafnia sp.	maize seeds	Produces acetoin	Johnston-monje and Raizada (2011), Truyens et al. (2014)
Paenibacillus sp.	Sorghum	Act against pathogens	Budi et al. (2000)
Pantoea sp.	Deep-water rice wet resistance	produces ACC	Verma et al. (2004), Zhang et al. (2011)
Pseudomonas sp.	Sweet sorghum	Bio control agent	Mareque et al. (2018)
Rhanella sp.	Maize	Fixes nitrogen	Rodríguez et al. (2012)
Serratia sp.	Rice (root, stem)	Biocontrol and PGP	Amaresan et al. (2014), Gyaneshwar et al. (2001)
Xanthomonas sp.	Rice seeds; grapevine	Antifungal activity	(Compant et al., 2011; Cottyn et al., 2000)

most of the strains possessed multiple functional properties, indicating that the strains would have potential contributions to the growth and development of the host plant. Therefore, the development and scale-up of Brachiaria and the associated endophytes could be for possible agricultural and environmental applications.

Acknowledgements I am thankful for the African Biosciences Challenge Fund-2014 program of the BecA-ILRI Hub capacity building and research development fellowships program for supporting the research work on climate-smart Brachiaria grass species and their associated microorganism roles in sustainable agriculture.

We thank Dr. Sita Ghimire for his excellent and unreserved supervision during the entire research fellowship on bacterial and fungal endophytes associated with Brachiaria grass species at BecA-ILRI Hub.

I would like to thank the Environment and Society Conference (Land and Water Degradation in Ethiopia: Climate and Land Use Change Implications) for funding for the publication and for reviewing the manuscript under this book chapter contribution and making the work reach the public.

References

Abdallah L (2021) Environmental impacts of the grand ethiopian renaissance dam (GERD) on environmental impacts of the Grand Ethiopian Renaissance Dam (GERD) on Egypt Lamiaa Abdallah

Abdel Farag El-Shafie H (2020) Integrated insect pest management. Pests Control Acarol. https://doi.org/10.5772/intechopen.81827

Abello J, Kelemu S, García C (2008) Agrobacterium-mediated transformation of the endophytic fungus *Acremonium implicatum* associated with Brachiaria grasses. Mycol Res 112:407–413. https://doi.org/10.1016/j.mycres.2007.10.008

Alam B, Lǐ J, Gě Q et al (2021) Endophytic fungi: from symbiosis to secondary metabolite communications or vice versa? Front Plant Sci 12:1–24. https://doi.org/10.3389/fpls.2021.791033

Ali S, Charles TC, Glick BR (2014) Amelioration of high salinity stress damage by plant growth-promoting bacterial endophytes that contain ACC deaminase. Plant Physiol Biochem 80:160–167. https://doi.org/10.1016/j.plaphy.2014.04.003

Amaresan N, Jayakumar V, Thajuddin N (2014) Isolation and characterization of endophytic bacteria associated with chilli (*Capsicum annuum*) grown in coastal agricultural ecosystem. 13:247–255

Andrew NR, Hill SJ (2017) Effect of climate change on insect pest management. Environ Pest Manag 195–223. https://doi.org/10.1002/9781119255574.ch9

Andrews M, James EK, Cummings SP et al (2003) Review article use of nitrogen fixing bacteria inoculants as a substitute for nitrogen fertilizer for dryland graminaceous crops: progress made. Mech Action Fut Potent 34:1–21

Backman PA, Sikora RA (2008) Endophytes : an emerging tool for biological control reference : to appear in : Received Date : Accepted Date : Introduction and commentary to a special issue of biological control endophytes : an emerging tool for biological control. https://doi.org/10.1016/j.biocontrol.2008.03.009

Bahadur AB (2018) Entomopathogens : role of insect pest management in crops. Trends Hortic 1:1–9. https://doi.org/10.24294/th.v1i4.833

Barazani O, Friedman J (1999) Is IAA the major root growth factor secreted from plant-growth-mediating bacteria? J Chem Ecol 25:2397–2406. https://doi.org/10.1023/A:1020890311499

Barraquio WL, Revilla L, Ladha JK (1997) Isolation of endophytic diazotrophic bacteria from wetland rice. Plant Soil 194:15–24. https://doi.org/10.1007/978-94-011-5744-5_3

Bonatelli ML, Lacerda-júnior GV, Bueno F, et al (2021) Beneficial plant-associated microorganisms from semiarid regions and seasonally dry environments : a review. 11:1–16. https://doi.org/10.3389/fmicb.2020.553223

Budi SW, Tuinen D Van, Arnould C, Gianinazzi S (2000) Hydrolytic enzyme activity of Paenibacillus sp . strain B2 and effects of the antagonistic bacterium on cell integrity of two soil-borne pathogenic fungi. 15:191–199

Cao L, Qiu Z, You J et al (2004) Isolation and characterization of endophytic Streptomyces strains from surface-sterilized tomato (*Lycopersicon esculentum*) roots. Lett Appl Microbiol 39:425–430. https://doi.org/10.1111/j.1472-765X.2004.01606.x

Caruso DJ, Palombo EA, Molton SE, Zaferanloo B (2022) Exploring the promise of endophytic fungi: a review of novel antimicrobial compounds. Microorganisms 10. https://doi.org/10.3390/microorganisms10101990

Compant S, Mitter B, Colli-mull JG, et al (2011) Endophytes of grapevine flowers , berries , and seeds : identification of cultivable bacteria , comparison with other plant parts , and visualization of niches of colonization. 188–197. https://doi.org/10.1007/s00248-011-9883-y

Cottyn B, Regalado E, Lanoot B et al (2000) Bacterial populations associated with rice seed in the tropical environment, pp 282–292

Data RUSA, Koepke M, Segovia S (2013) (12) Patent Application Publication (10) Pub . No. US 2013/0217096 A1.1

Deka B, Baruah C, Babu A (2021) Entomopathogenic microorganisms: their role in insect pest management. Egypt J Biol Pest Control 31. https://doi.org/10.1186/s41938-021-00466-7

De Bary A (1866) Morphologie und Physiologie der Pilze, Flechten, und Myxomyceten. In: Hofmeister's handbook of physiological botany. Vol II, Engelmannm, Leipzig, Germany

Díaz S, Grossi C, Zawoznik M, Daniela M (2016) Wheat seeds harbor bacterial endophytes with potential as plant growth promoters and biocontrol agents of *Fusarium graminearum* microbiological research wheat seeds harbor bacterial endophytes with potential as plant growth promoters and biocontrol agent. Microbiol Res 186–187:37–43. https://doi.org/10.1016/j.micres.2016.03.002

Doty SL (2011) Nitrogen-fixing endophytic bacteria for improved plant growth. 183–199. https://doi.org/10.1007/978-3-642-20332-9

Gao F, Dai C, Liu X (2010) Mechanisms of fungal endophytes in plant protection against pathogens. **4**:1346–1351

Ghimire SR, Charlton ND, Bell JD et al (2011) Biodiversity of fungal endophyte communities inhabiting switchgrass (*Panicum virgatum* L.) growing in the native tallgrass prairie of northern Oklahoma. Fungal Divers 47:19–27. https://doi.org/10.1007/s13225-010-0085-6

Glare TR, Jurat-Fuentes JL, O'Callaghan M (2017) Basic and applied research: entomopathogenic bacteria. Elsevier, Amsterdam

Gundel PE, Rudgers JA, Whitney KD (2017) Vertically transmitted symbionts as mechanisms of transgenerational effects. Am J Bot 104:787–792. https://doi.org/10.3732/ajb.1700036

Gyaneshwar P, James EK, Mathan N et al (2001) Endophytic colonization of rice by a diazotrophic strain of *Serratia marcescens*. 183:2634–2645. https://doi.org/10.1128/JB.183.8.2634

Hallmann J, Quadt-Hallmann A, Mahaffee WF, Kloepper JW (1997) Bacterial endophytes in agricultural crops. Can J Microbiol 43:895–914. https://doi.org/10.1139/m97-131

Hardoim PR, Hardoim CCP, van Overbeek LS, van Elsas JD (2012) Dynamics of seed-borne rice endophytes on early plant growth stages. PLoS One 7. https://doi.org/10.1371/journal.pone.0030438

Harman GE (2011) Trichoderma—not just for biocontrol anymore, pp 103–108. https://doi.org/10.1007/s12600-011-0151-y

Harrison JG, Griffin EA (2019) and host tissues—how far have we come and where do we go from here ? The diversity and distribution of endophytes across biomes, plant phylogeny , and host tissues—how far have we come and where do we go from here ? https://doi.org/10.1101/793471

Igiehon NO, Babalola OO (2018) Below-ground-above-ground plant-microbial interactions: focusing on Soybean, Rhizobacteria and Mycorrhizal Fungi. Open Microbiol J 12:261–279. https://doi.org/10.2174/1874285801812010261

Jaber LR, Enkerli J (2017) Fungal entomopathogens as endophytes: can they promote plant growth? Biocontrol Sci Technol 27:28–41. https://doi.org/10.1080/09583157.2016.1243227

Jha B, Gontia I, Hartmann A (2012) The roots of the halophyte *Salicornia brachiata* are a source of new halotolerant diazotrophic bacteria with plant growth-promoting potential. Plant Soil 356:265–277. https://doi.org/10.1007/s11104-011-0877-9

Johnston-monje D, Raizada MN (2011) Conservation and diversity of seed associated endophytes in Zea across boundaries of evolution. Ethnogr Ecol 6. https://doi.org/10.1371/journal.pone.0020396

Kandel SL, Herschberger N, Kim SH, Doty SL (2015) Diazotrophic endophytes of poplar and willow for growth promotion of rice plants in nitrogen-limited conditions. Crop Sci 55. https://doi.org/10.2135/cropsci2014.08.0570

Kaul S, Sharma T, Dhar MK (2016) "Omics" tools for better understanding the plant—Endophyte Interact 7:1–9. https://doi.org/10.3389/fpls.2016.00955

Kelemu S, Fory P, Zuleta C et al (2002) Detecting bacterial endophytes in tropical grasses of the *Brachiaria* genus and determining their role in improving plant growth. Afr J Biotechnol 10:965–976. https://doi.org/10.5897/AJB10.1305

Khan Z, Midega C, Pittchar J, et al (2011) Push–pull technology : a conservation agriculture pests , weeds and soil health in Africa Push–pull technology : a conservation agriculture approach

for integrated management of insect pests , weeds and soil health in Africa UK government ' s Foresigh. 5903. https://doi.org/10.3763/ijas.2010.0558
Khan Z, Midega CAO, Hooper A, Pickett J (2016) Push-pull : chemical ecology-based integrated pest management technology
Kiani MZ, Ali A, Sultan T et al (2015) Plant growth promoting rhizobacteria having 1-aminocyclopropane-1-carboxylic acid deaminase to induce salt tolerance in sunflower (*Helianthus annus* L.). Nat Resour 06:391–397. https://doi.org/10.4236/nr.2015.66037
Kumar A, Verma JP (2018) Does plant—microbe interaction confer stress tolerance in plants: a review? Microbiol Res 207:41–52. https://doi.org/10.1016/j.micres.2017.11.004
Kumar S, Stecher G, Tamura K (2016) MEGA7: molecular evolutionary genetics analysis Version 7.0 for bigger datasets. Mol Biol Evol 33:1870–1874. https://doi.org/10.1093/molbev/msw054
Lacey LA, Grzywacz D, Shapiro-Ilan DI et al (2015) Insect pathogens as biological control agents: back to the future. J Invertebr Pathol 132:1–41. https://doi.org/10.1016/j.jip.2015.07.009
Litwin A, Nowak M, Ro S (2020) Entomopathogenic fungi : unconventional applications. 1:23–42. https://doi.org/10.1007/s11157-020-09525-1
Loulou A, Mastore M, Caramella S et al (2023) Entomopathogenic potential of bacteria associated with soil-borne nematodes and insect immune responses to their infection. PLoS ONE 18:e0280675. https://doi.org/10.1371/journal.pone.0280675
Lourenço M, Ribeiro A, Grace S, Ricardo C (2021) Endophytic bacteria : a possible path toward a sustainable agriculture. 5
Lugtenberg BJJ, Caradus JR, Johnson LJ (2016) Fungal endophytes for sustainable crop production 1–17. https://doi.org/10.1093/femsec/fiw194
Maass BL, Midega CAO, Mutimura M et al (2018) Homecoming of brachiaria: improved hybrids prove useful for african animal agriculture. East Afr Agric for J 81:71–78. https://doi.org/10.1080/00128325.2015.1041263
Mantzoukas S, Eliopoulos PA (2020) Applied sciences endophytic entomopathogenic fungi : a valuable biological control tool against plant pests
Mareque C, Freitas T, Vollú RE et al (2018) the endophytic bacterial microbiota associated with sweet sorghum (*Sorghum bicolor*) is modulated by the application of chemical N fertilizer to the field
Midega CAO, Pittchar JO, Pickett JA et al (2018) A climate-adapted push-pull system effectively controls fall armyworm, *Spodoptera frugiperda* (J E Smith), in maize in East Africa. Crop Prot 105:10–15. https://doi.org/10.1016/j.cropro.2017.11.003
Misaghi IJ, Donndelinger CR (1990) Endophytic bacteria in symptom-free cotton plants, pp 808–811
Misganaw G, Simachew A, Gessesse A (2019) Endophytes of finger millet (*Eleusine coracana*) seeds. Symbiosis. https://doi.org/10.1007/s13199-019-00607-5
Mishra S, Sharma S (2022) Metabolomic insights into endophyte-derived bioactive compounds. 13. https://doi.org/10.3389/fmicb.2022.835931
Mohanty SR, Dubey G, Kollah B (2016) Endophytes of *Jatropha curcas* promote growth of maize. Rhizosphere 3. https://doi.org/10.1016/j.rhisph.2016.11.001
Mona SA, Hashem A, Abd Allah EF et al (2017) Increased resistance of drought by *Trichoderma harzianum* fungal treatment correlates with increased secondary metabolites and proline content. J Integr Agric 16:1751–1757. https://doi.org/10.1016/S2095-3119(17)61695-2
Mounde LG, Anteyi WO, Rasche F, et al (2020) Tripartite interaction between *Striga* spp., cereals , and plant root-associated microorganisms : a review. https://doi.org/10.1079/PAVSNNR202015005
Mutai C, Njuguna J, Ghimire S (2017) Brachiaria Grasses (*Brachiaria* spp.) harbor a diverse bacterial community with multiple attributes beneficial to plant growth and development. Microbiologyopen 6:1–11. https://doi.org/10.1002/mbo3.497
Newitt JT, Prudence SMM, Hutchings MI, Worsley SF (2019) Biocontrol of cereal crop diseases using streptomycetes. Pathogens 8. https://doi.org/10.3390/pathogens8020078

Ng KS, Yang A, Yakovleva N (2019) Sustainable waste management through synergistic utilization of commercial and domestic organic waste for efficient resource recovery and valorization in the UK. J Clean Prod 227:248–262. https://doi.org/10.1016/j.jclepro.2019.04.136

Njarui DMG, Gatheru M, Ghimire SR (2021a) Brachiaria grass for climate resilient and sustainable livestock production in Kenya. African Handb Clim Chang Adapt 755–776. https://doi.org/10.1007/978-3-030-45106-6_146

Odokonyero K, Acuna TB, Cardoso JA et al (2017) Effect of endophyte association with brachiaria species on shoot and root morpho-physiological responses under drought stress. J Plant Biochem Physiol 05:1–10. https://doi.org/10.4172/2329-9029.1000190

Ortega HE, Torres-mendoza D (2020) Patents on endophytic fungi for agriculture and bio and phytoremediation applications. 1–26

Pande A, Dutta S, Haider ZA (2016) Endophytes of finger millet (*Eleusine coracana* Gaertn. L.). Indian J Ecol 43:665–674

Petrini O (1991) Tree leaves. Microb Ecol Leaves 179–180

Pleban S, Ingel F, Chet I (1995) Control of *Rhizoctonia solani* and *Sclerotium rolfsii* in the greenhouse using endophytic Bacillus spp. 1991–1992

Poosakkannu A, Nissinen R, Kytöviita MM (2015) Culturable endophytic microbial communities in the circumpolar grass, *Deschampsia flexuosa* in a sub-Arctic inland primary succession are habitat and growth stage specific. Environ Microbiol Rep 7:111–122. https://doi.org/10.1111/1758-2229.12195

Puri A, Padda KP, Chanway CP (2016) Seedling growth promotion and nitrogen fixation by a bacterial endophyte *Paenibacillus polymyxa* P2b–2R and its GFP derivative in corn in a long-term trial. Symbiosis 69:123–129. https://doi.org/10.1007/s13199-016-0385-z

Qadri M, Short S, Gast K et al (2020) Microbiome innovation in agriculture: development of microbial based tools for insect pest management. Front Sustain Food Syst 4:1–20. https://doi.org/10.3389/fsufs.2020.547751

Ramamoorthy V, Viswanathan R, Raguchander T et al (2001) Induction of systemic resistance by plant growth promoting rhizobacteria in crop plants against pests and diseases. 20

Ribeiro VP, Marriel IE, de Sousa SM et al (2018) Endophytic Bacillus strains enhance pearl millet growth and nutrient uptake under low-P. Brazilian J Microbiol 49:40–46. https://doi.org/10.1016/j.bjm.2018.06.005

Rodríguez A, Barlocco C, Beracochea M et al (2012) Characterization of cultivable putative endophytic plant growth promoting bacteria associated with maize cultivars (*Zea mays* L .) and their inoculation effects in vitro. 58:21–28. https://doi.org/10.1016/j.apsoil.2012.02.009

Rodriguez RJ, Redman RS, Henson JM (2003) Plants to high stress environments, pp 261–272

Romero FM, Pieckenstain FL (2014) The communities of tomato (*Solanum lycopersicum* L.) leaf endophytic bacteria, analyzed by 16S-ribosomal RNA gene pyrosequencing. 351:187–194. https://doi.org/10.1111/1574-6968.12377

Rosenblueth M, Ormeño-Orrillo E, López-López A et al (2018) Nitrogen fixation in cereals. Front Microbiol 9:1–13. https://doi.org/10.3389/fmicb.2018.01794

Sandhu SS, Sharma AK, Beniwal V et al (2012) Myco-biocontrol of insect pests: factors involved, mechanism, and regulation. J Pathog 2012:1–10. https://doi.org/10.1155/2012/126819

Sharma R, Sharma P (2021) Fungal entomopathogens: a systematic review. Egypt J Biol Pest Control 31. https://doi.org/10.1186/s41938-021-00404-7

Shen FT, Yen JH, Liao C Sen et al (2019) Screening of rice endophytic biofertilizers with fungicide tolerance and plant growth-promoting characteristics. Sustain 11. https://doi.org/10.3390/su11041133

Shrivastava UP (2015) Plant growth promotion assessment in rice plant enhanced by inoculation of rhizobacteria. Acad Voices A Multidiscip J 4:73–84. https://doi.org/10.3126/av.v4i0.12362

Singh DP, Singh HB, Prabha R (2016) Microbial inoculants in sustainable agricultural productivity: vol 1: Research perspectives. Microb inoculants Sustain Agric Product Vol 1: research perspect, pp 1–343. https://doi.org/10.1007/978-81-322-2647-5

Singh V (2016) Plant pathology and microbiology potential of bacterial endophytes as plant growth promoting factors. 7. https://doi.org/10.4172/2157-7471.1000376
Sinno M, Ranesi M, Gioia L et al (2020) Endophytic fungi of tomato and their potential applications for crop improvement. Agriculture 10:1–22. https://doi.org/10.3390/agriculture10120587
Soldatov E, Dzhibilov S, Soldatova I, Guluyeva L (2020) Restoration of degraded mountain pastures of the central caucasus by targeted sowing of seeds of perennial grasses. E3S Web Conf 175:0–7. https://doi.org/10.1051/e3sconf/202017509013
Subbarao GV, Arango J, Masahiro K et al (2017) Plant science genetic mitigation strategies to tackle agricultural GHG emissions : the case for biological nitri fi cation inhibition technology. Plant Sci 0–1. https://doi.org/10.1016/j.plantsci.2017.05.004
Subbarao GV, Kishii M, Bozal-leorri A, et al (2021) Enlisting wild grass genes to combat nitrification in wheat farming : a nature-based solution. 1–9. https://doi.org/10.1073/pnas.2106595118/-/DCSupplemental.Published
Subbarao GV, Nakahara K, Hurtado MP et al (2009) Evidence for biological nitrification inhibition in Brachiaria pastures
Subbarao GV, Sahrawat KL, Nakahara K et al (2012) Biological nitrification inhibition—a novel strategy to regulate nitrification in agricultural systems, 1st edn. Elsevier, Amsterdam
Sun L, Lu Y, Yu F et al (2016) Biological nitrification inhibition by rice root exudates and its relationship with nitrogen-use efficiency. https://doi.org/10.1111/nph.14057
Sun X, Guo LD (2012) Endophytic fungal diversity: review of traditional and molecular techniques. Mycology 3:65–76. https://doi.org/10.1080/21501203.2012.656724
Taghavi S, Garafola C, Monchy S et al (2009) Genome survey and characterization of endophytic bacteria exhibiting a beneficial effect on growth and development of poplar trees. Appl Environ Microbiol 75:748–757. https://doi.org/10.1128/AEM.02239-08
Taylor P, Subbarao G V, Ito O et al (2007) Critical reviews in plant sciences scope and strategies for regulation of nitrification in agricultural systems—challenges and opportunities scope and strategies for regulation of nitrification in agricultural systems—challenges and opportunities. 37–41. https://doi.org/10.1080/07352680600794232
Timmusk S, Behers L, Muthoni J, Muraya A (2017) Perspectives and challenges of microbial application for crop improvement. 8:1–10. https://doi.org/10.3389/fpls.2017.00049
Truyens S, Weyens N, Cuypers A, Vangronsveld J (2014) Minireview bacterial seed endophytes: genera , vertical transmission and interaction with plants. https://doi.org/10.1111/1758-2229.12181
Tucci M, Ruocco M, Masi LDE, et al (2011) The beneficial effect of *Trichoderma* spp. on tomato is modulated by the plant genotype. 12:341–354. https://doi.org/10.1111/J.1364-3703.2010.00674.X
Uiu LR, Atta AS, Loris IF (2013) Emerging entomopathogenic bacteria for insect pest management
Ullah U, Abu M, Saddique B, Ali Z (2021) Fungal and bacterial endophytes for rice improvement with special reference to drought stress
UN Environment (2020) A new deal for Nature. 3
Upholt WB (1977) Nucleic acids research. 4:1257–1265
Vassilev N, Vassileva M, Lopez A, et al (2015) Unexploited potential of some biotechnological techniques for biofertilizer production and formulation, pp 4983–4996. https://doi.org/10.1007/s00253-015-6656-4
Vega FE, Posada F, Aime MC et al (2008) Entomopathogenic fungal endophytes. 46:72–82. https://doi.org/10.1016/j.biocontrol.2008.01.008
Venkata G, Yoshihashi T, Worthington M et al (2015) Plant science suppression of soil nitrification by plants. Plant Sci 233:155–164. https://doi.org/10.1016/j.plantsci.2015.01.012
Verma H, Kumar D, Kumar V et al (2021) The potential application of endophytes in management of stress from drought and salinity in crop plants. Microorganisms 9:1–19. https://doi.org/10.3390/microorganisms9081729

Verma SC, Singh A, Chowdhury SP, Tripathi AK (2004) Endophytic colonization ability of two deep-water rice endophytes, *Pantoea* sp. and *Ochrobactrum* sp. using green fluorescent protein reporter, pp 425–429

WWF, ILO (2020) Nature hires: how nature-based solutions can power a green jobs recovery

Zhang YF, He LY, Chen ZJ et al (2011) Characterization of ACC deaminase-producing endophytic bacteria isolated from copper-tolerant plants and their potential in promoting the growth and copper accumulation of *Brassica napus*. Chemosphere 83:57–62. https://doi.org/10.1016/j.chemosphere.2011.01.041

Zhao L, Xu Y, Lai XH et al (2015) Screening and characterization of endophytic bacillus and paenibacillus strains from medicinal plant *Lonicera japonica* for use as potential plant growth promoters. Brazilian J Microbiol 46:977–989. https://doi.org/10.1590/S1517-838246420140024

Chapter 5
Land Suitability Mapping for Surface Irrigation Using GIS-Based Multicriteria Evaluation Techniques in the Andassa Watershed, Abay Basin, Ethiopia

Workie A. Tiruneh and Anwar A. Adem

Abstract Irrigation agriculture plays a valuable role in upholding sustainable food security by enhancing agricultural production. Uneven distribution and shortage of rainfall has resulted in unsustainable food production, leading to food insecurity in Ethiopia. The establishment of irrigation development strategies may have a significant role in reducing the risk posed by uneven distribution of rainfall. This study aims to map suitable land for surface irrigation development in the Abay Basin of the Andassa watershed, Ethiopia, based on a GIS-based multicriteria evaluation (MCE) technique. Biophysical factors (land use and land cover, soil, slope, and river proximity) that significantly affect surface irrigation suitability were considered. Each of these was processed and analyzed for its potential contribution to surface irrigation suitability on a pixel-by-pixel basis. The factors were weighted using a pairwise comparison matrix, and weights were combined using weighted overlay analysis. The analysis results indicated that approximately 60% of the watershed land was highly (9%) and moderately (51%) suitable for surface irrigation. Slope and river proximity were the major limiting factors during the suitability assessment. Of the 60% of suitable land, 70% could be irrigated with the water resource potential of the Andassa River. The remaining 30% of the area needs other means of water harvesting techniques. Future works need to consider soil chemical properties as a determining factor for surface irrigation suitability since this study did not consider these properties as a factor in the overlay analysis.

Keywords Pairwise overlay · Crop water requirement · Irrigable land · Water availability

W. A. Tiruneh
East Gojjam Zone, Bibugn Woreda, Digua Tsion, Amhara, Ethiopia

A. A. Adem (✉)
Department of Natural Resources Management, Bahir Dar University, Bahir Dar, Ethiopia
e-mail: anwarasefa@gmail.com

Blue Nile Water Institute, Bahir Dar University, Bahir Dar, Ethiopia

A. M. Melesse et al. (eds.), *Land and Water Degradation in Ethiopia*, Springer Geography, https://doi.org/10.1007/978-3-031-60251-1_5

Introduction

Rainfed agriculture plays a vital role in global food production, as 80% of cultivation is rainfed and subsidizes approximately 58% of the global food basket (Wani et al. 2009). As reported by Wani et al. (2009), rainfed areas are also hot spots of poverty, malnourishment, water shortage, severe land degradation, and underprivileged physical and financial infrastructure. Although rainfed agriculture is the world's most important source of food and contributes 70 to 85% of global food production (Rosegrant et al. 2002), rainfed agriculture is diminishing globally because of the uneven distribution of rainfall productivity (Bandyopadhyay et al. 2009). Irrigated agriculture is more efficient and effective than rain-fed agriculture, which yields low productivity (Kedir et al. 2022). Irrigation is the world's backbone of agriculture (Teshome and Halefom 2020). In irrigated agriculture, water resources are utilized to overcome the effects of rainfall variability and unreliability by providing supplementary and full-season irrigation (Binyam and Desale 2015).

The rural economy of sub-Saharan Africa (SSA) accounts for 30–40% of the country's gross domestic product (GDP), generating over 60% of their yearly income (Rockström et al. 2002). It has been reported that approximately 95% of agriculture in SSA is rainfed agriculture (Rockström et al. 2002). SSA countries plow only a fraction of their potential cultivable land and use only a fraction of their renewable water resources (Abou Zaki et al. 2018). This results in low productivity, falling further behind the rest of the world, and famine, especially during the dry season when there is little or no rainfall (Bjornlund et al. 2020). Irrigation agriculture is a crucial component for raising a country's agricultural productivity and it plays a vital role in fulfilling the Malabo Articulation commitment to ending starvation in Africa (Xie et al. 2021). SSA irrigation has largely focused on surface water irrigation frameworks, without exploring ground-water irrigation's advancement potential (Warner et al. 2019).

A country in the sub-Saharan region, Ethiopia, is largely characterized by rain-fed mixed farming with traditional technologies (Baye 2017). The people of Ethiopia have been dominantly agricultural societies with subsistence ways of living under rainfed husbandry. They are exposed to climate variability and change because considerable parts of the population are poor and depend on agrarian income, which is much more sensitive to rainfall variability (Bishaw et al. 2013). Due to this variability, crop collapses and food instability are frequent in the country (Awulachew 2019; Gebremedhin 2015). As a result, a comprehensive irrigation development that may help people in rural areas have better lives and overcome the consequences of rainfall unpredictability could be the answer to ending food insecurity (Weldeabzgi et al. 2021).

Although Ethiopia is blessed with abundant water resources, including 2.65 billion m^3 of untapped groundwater potential and 12 river basins with annual runoff quantities of 122 billion m^3 (Awulachew et al. 2007), the economic impact of irrigated agriculture is negligible when compared to rain-fed agriculture. This is because a significant portion of the country's land that is suitable for irrigation

has not been fully utilized, with only a small percentage (4–5%) of the total potential area (30–70 million hectares) being utilized for irrigation purposes (Awulachew and Merrey 2007). This problem can be solved through optimal surface irrigation development starting with identifying suitable land for irrigation agriculture. Land suitability identification for irrigation is a prerequisite for better utilization of human resources, infrastructures, biophysical resources, and all other social and economic resources (Akpoti et al. 2019). Before design and implementation, irrigation development works need sufficient information about the available land and water resources (Berhe et al. 2022). Making the best choices when choosing suitable land for irrigation agriculture development may involve the identification of acceptable land for surface irrigation utilizing a GIS-based multicriteria evaluation (MCE) technique.

There is considerable interest in using GIS capabilities in conjunction with multicriteria decision-making procedures to identify places that may benefit from surface irrigation (Chen 2014). GIS is unique in its ability to integrate and perform spatial analysis on multisource datasets, including information on land use, population, topography, hydrology, climate, vegetation, transportation networks, and public infrastructure (Malczewski 2006). It can also be used to automatically create maps. Important data on the environmental compatibility of irrigation projects is provided by GIS-based MCE analysis (Xie et al. 2021). The data are altered and evaluated, as stated by Malczewski (2006), to produce information suitable for a specific application, such as a land suitability study. The goal of GIS is to facilitate the process of making spatial decisions (Tercan and Dereli 2020). GIS aids in decision-making and assists in determining which places are most and least suitable for a certain purpose in the context of land suitability study (Dožić 2019).

Globally as well as in Ethiopia, research has been conducted on the identification of suitable areas for surface irrigation by using GIS-based MCE techniques and the analytical hierarchy process (AHP) model for weighted overlay analysis (Adem et al. 2022; Danbara and Zewdie 2022; Mandal et al. 2018; Paul et al. 2020; Worqlul et al. 2019). Despite the substantial contribution of the previous studies, studies that identify suitable lands for surface irrigation are still inadequate in Ethiopia due to several influencing factors and spatiotemporal variability. Therefore, the objective of this study was to identify suitable land for surface irrigation in the Andassa watershed using a GIS-based MCE technique. Attribute and spatial inputs such as slope, soil, land use, and river proximity were used to identify suitable land for surface irrigation. This research output will be important for planners and practitioners for irrigation practices to improve crop productivity and food security.

Materials and Methods

Study Area

The Andassa River is a primary source in the studied watershed, which is also among the tributaries that feed the Abbay River, covering an area of approximately 58,761 ha. It originates from the highland spring of Adama Mountain in northwestern Ethiopia. The main river flows northeast to the Abbay River. Geographically, the Andassa watershed is the headwater of the Abbay basin within geographic coordinates of 37°16′00” to 37°33′00” easting and 11°08′00″ to 11°32′00″ northing (Fig. 5.1). The elevation of the watershed ranges from 1710 to 3216 m above mean sea level. The highest elevation of the study area is located in the southern part of the watershed. The topography of the watershed is hilly, and the outlet is situated in the northern part, which is near a confluence point of the Abbay River (Fig. 5.1). Approximately 30% of the watershed has a slope greater than 8%, which is not suitable for surface irrigation.

The watershed has an agroclimatic zone that is humid and subhumid, with mean annual rainfall of 1314 mm (Abebe et al. 2022). The study area is characterized by a unimodal rainfall regime. From June through September, during the primary rainy season known as Kiremt, rain-fed agriculture production takes place. The average

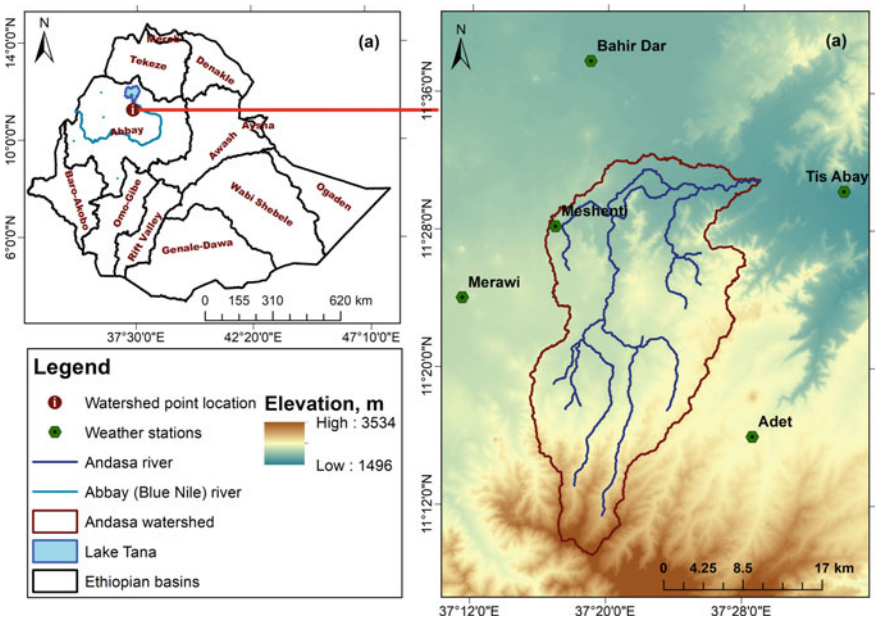

Fig. 5.1 Location of the study area: **a** Ethiopian basins and **b** Andassa watershed and weather stations used for this study

monthly precipitation varies from 4.1 mm in January to 361 mm in July. Alisols and Leptosols are the dominant soil types of the watershed that cover 47 and 24% of the watershed area, respectively. Vertisols, Nitosols, and Luvisols also constitute 29% of the Andassa watershed. Texturally, clay and clay loam soils are dominant. More than half of the watershed is covered by cultivated land. Forest, bush, and shrub lands take second place in terms of land use. In the watershed, annual irrigation takes place during the dry season from December to May. Onion, cabbage, pepper, tomato, and sugarcane are the primary irrigation agriculture crops.

Dataset

Hydrometeorological, spatial, crop, and topographic data were collected from different institutions (Table 5.1). The United States Geological Survey (USGS) provided a 30-m resolution Global Shuttle Radar Topography Mission (SRTM) Digital Elevation Model (DEM), which was used to define the watershed, create streamlines, and determine the slope of the watershed pixel-by-pixel. Rainfall data for the Bahir Dar, Adet, Merawi, Meshenti, and Tis Abay weather stations between 1996 and 2020 were collected from the National Meteorological Agency (NMA) of Ethiopia. The rainfall data was used to compute an effective rainfall deficit map. A 30 by 30 m resolution soil and land use data were collected from the Bureau of Amhara Rural Land Administration (BoARLA) to compute soil and land use suitability maps. A historical streamflow record was used to compute the irrigable land based on surface water availability. Crop data and information were collected from the Bahir Dar Zuria Woreda Agricultural Office (BDZAO) and Food and Agricultural Organization (FAO) guidelines to calculate crop and irrigation water requirements. According to BDZAO, the dominant vegetables that have been grown in the study areas are onion (*Allium cepa L.*), cabbage (*Brassica oleracea*), pepper (*Capsicum*), tomato (*Solanum lycopersicum*), and sugarcane (*Saccharum officinarum L*).

Analysis

Preprocessing

The first step to prepare the analysis inputs on a defined boundary was the watershed delineation of the study region. The terrain processing tool of the ArcHydro toolset was used to fill the input DEM and to compute flow direction, flow accumulation, and stream generation during the watershed delineation process. Treating missed rainfall data was the other preprocessing activity of the analysis. The selected stations with missing rainfall data were filled using the arithmetic mean method since the percentage of missed days was less than 10%.

Table 5.1 Data types, resolutions, and sources used in this study. The derived factors or parameters from each data are also included

Data type	Spatial Resolution	Source	Derived factor/ parameter
Soil	30 × 30 m	Bureau of Amhara Rural Land Administration (BoARLA)	Soil suitability
Land use	30 × 30 m	Bureau of Amhara Rural Land Administration (BoARLA)	Land use suitability
Rainfall	Point	National Meteorology Agency (NMA)	Effective rainfall, Rainfall deficit
Elevation	30 × 30 m	United States Geological Survey (USGS)	Slope, river proximity
Crop data	Kebele based	Bahir Dar Zuria Woreda Agricultural Office and FAO guidelines	Crop water requirement
Stream flow	Point	Ministry of Water and Energy (MoWE)	Irrigable land

Factor Analysis and Suitability Mapping

Data regarding the land, soil, climate, and vegetation are analyzed as part of the land appraisal process to identify practical options for further exploitation. With the aid of GIS-based MCE methodologies that were taken from earlier research, the appropriateness of the land for surface irrigation was evaluated in this study by considering the slope, soil (texture, type, depth, and drainage), land use, and the distance from rivers (Adem et al. 2022; Danbara and Zewdie 2022; Mandal et al. 2018; Paul et al. 2020; Worqlul et al. 2019). Based on the FAO's (1976) rules for evaluating land, each component was categorized as highly appropriate (S1), moderately suitable (S2), marginally suitable (S3), and not suitable (N1). Weighting overlay analysis methods were used to locate the last piece of potentially irrigable land.

I. Slope

When determining suitable sites for surface irrigation, the slope is the most crucial topographic feature. The slope was calculated from the DEM using ArcGIS's spatial analysis tool. A classification of the slope was done, and the class rating was taken from FAO (1976) recommendations. The watershed was categorized into four groups based on the quality of the land and the features of the slope for surface irrigation (Table 5.2).

II. Soil suitability analysis

Important determining elements in evaluating whether a piece of land is suitable for surface irrigation are the characteristics of the soil to the spatial extent of the study area (Hagos et al. 2022). The most relevant soil characteristics utilized in the earlier

Table 5.2 Slope type, range, and suitability class based on the FAO (1976) guideline

Slope type	Slope range, %	Suitability class
Horizontal	0–2	Highly suitable, S1
Very flat	2–5	Moderately suitable, S2
Flat	5–8	Marginally suitable, S3
Steep	> 8	Not suitable, N1

land suitability evaluation for surface irrigation, which was also employed in this study, were soil depth, soil texture, soil type, and soil drainage.

A. Soil texture

One of the physical features of soil that impacts the rate of infiltration, water-holding capacity, and transportation of water through the soil is soil texture, which is the relative amount of sand, silt, and clay in the soil (Guo et al. 2022). While soil with a coarse texture has a low water-holding capacity and a high infiltration rate, soil with a fine texture has a high water-holding capacity and a low infiltration rate. The infiltration rate may have an impact on crop choice, irrigation method, run length, field area, and irrigation development expenses. The textural and appropriateness grades for the Andassa watershed are displayed in Table 5.3.

B. Soil depth

The possible rooting depth of plants and any soil limitations that can prevent rooting depth are determined by the depth of the soil. Any soil discontinuities caused by sand, gravel, or even bedrock layers might physically restrict root irrigation. In this study, the soil depth of the study area was divided into suitability classes to select surface irrigation potential by adopting the recommended classes from FAO (1976) guidelines (Table 5.3).

Table 5.3 Soil texture and suitability classes of the Andassa watershed adopted from FAO (1976) guidelines

Texture class	Soil depth, cm	Soil drainage	Soil type	Suitability class
Clay, silty clay	> 100	Well drained	Chromic Luvisols, Haplic Luvisols	Highly suitable, S1
Silt clay, clay loam	50–100	Moderately	Eutric Vertisols	Moderately suitable, S2
Sandy loam, Sandy clay loam	25–50	Imperfectly	Haplic Alisols	Marginally suitable, S3
Coarse sand	< 25	Poorly drained	Eutric Leptosols, Lithic Leptosols	Not suitable, N1

C. Soil drainage

Normal plant growth is enabled by soil drainage, so considering this requirement is essential when choosing a site for irrigation. To guarantee ongoing output and enable efficiency in farming operations, adequate soil drainage is crucial. According to FAO (1976), there are five different categories of soil drainage: well-drained, moderately well-drained, imperfectly drained, poorly drained, and very poorly drained (Table 5.3).

D. Soil type

There are seven soil types in the Andassa watershed: Chromic Luvisols, Haplic luvisols, Haplic Nitosols, Eutric Vertisols, Haplic Alisols, Eutric Leptosols, and Lithic Leptosols. Based on the FAO's (1976) soil classification and characterization guide for agricultural suitability and the findings of various researchers, the soil types were classed into suitability classes (Table 5.3).

For further weighted overlay analysis, the physical characteristics of the soil were produced in raster format. Based on FAO (1976) recommendations and other pieces of literature, the suitability rating classes for each soil factor were established. Each aspect received a relative weight based on its importance and the opinions of experts. Based on pairwise comparison criteria, each factor was given a value (1 to 5 and their reciprocal). The final weight of each element was determined using the pairwise comparison approach. The consistency ratio, which was determined using the ratio between the consistency and the random indices, was used to evaluate the consistency of the pairwise matrix. The reclassified map was overlaid using the weighted overlay tool in ArcGIS to acquire the cumulative influence of all factors based on the components' final weights.

III. Land use suitability analysis

The use of the land was another consideration when determining whether a plot was suitable for surface irrigation. Finding the regions that are most suited for surface irrigation requires evaluating the quality of the soil for various applications. This makes it possible for surface irrigation to operate at its best and ensures that water is distributed to regions with the greatest potential for agricultural production. The primary FAO (1976) principles were used to categorize the land use types into suitability classes (Table 5.4).

Table 5.4 Land use types of Andassa watersheds and suitability classes

Land use and land cover type	Suitability class
Annual cropland, open grassland	Highly suitable, S1
Sparse forest, open shrubland, closed grassland	Moderately suitable, S2
Moderate forest, closed shrubland, bare Soil	Marginally suitable, S3
Dense forest, water body, settlement, woodland, and bare land	Not suitable, N1

Table 5.5 River proximity (Euclidean distance) suitability ranges of the study areas for surface irrigation

Distance from rivers, m	Suitability class	Symbol
0–1342.6	Highly suitable	S_1
1342.6–2685.2	Moderately suitable	S_2
2685.2–4027.8	Marginally suitable	S_3
4027.8–5370.3	Not suitable	S_4

IV. River proximity

By computing the Euclidean distance between each river for the corresponding irrigable terrain, river closeness was calculated. The analysis made use of first- and second-order perennial stream networks (Adem et al. 2022). In order to categorize river proximity into appropriate classifications, the equal interval method was applied (Table 5.5).

Overall Irrigation Suitability Analysis

The parameters are graded according to their relative importance and given weights based on their relative effects on irrigation suitability (Adem et al. 2022; Teshome and Halefom 2020; Worqlul et al. 2017). Based on pairwise comparison criteria, a value (1 to 4 and their reciprocal) was assigned to each factor. The pairwise comparison matrix, which was used to balance the components, describes the process of evaluating factors in pairs to determine which one is preferred (Assefa et al. 2018). Slope, soil, land use, and river proximity were the four main characteristics that were evaluated one to one and graded on a scale. The weights for the criteria maps are determined using the analytical hierarchy process (AHP). It is a structured approach for decomposing difficult choices into pairwise, two-at-a-time possibilities (Saaty 1990). The analytical hierarchy approach determines comparable weights for each criterion layer using the pairwise comparison matrix. Additionally, during pairwise criteria comparisons, it generates a consistency ratio that measures the logical consistency of expert (user) assessments.

$$\mathrm{CR} = \frac{\mathrm{CI}}{\mathrm{RI}} \tag{5.1}$$

where RI represents the random index and CI represents the consistency index, which is calculated by the formula:

$$\mathrm{CI} = \frac{\lambda\,\mathrm{max} - n}{n - 1} \tag{5.2}$$

where λmax is the largest principal eigenvalue of a positive reciprocal pairwise comparison matrix of size n.

Saaty (1990) asserts that the judgments made during pairwise comparison are reliable if the CR value is less than 0.1 since they are not too near for randomness. Potentially irrigable land was obtained by creating an irrigation suitability analysis using the ArcGIS-based weighting overlay of values from all datasets, including soil, slope, land use, and the separation of irrigation land from a water source, after ensuring the consistency of the factor's weights.

Irrigation Water Requirement

The amount of water needed for irrigation was determined using the CROPWAT model (Dawit et al. 2020). The FAO developed the model, a decision-support tool that uses rainfall, soil, crop, and climate data to determine reference evapotranspiration (ET_o), crop water requirement (CWR), irrigation schedule, and irrigation water requirement (Allen 2005). The climatic stations inside and outside the research region were utilized to estimate the irrigation water needs of a few chosen crops. The CropWat 8.0 model was first fitted with data for monthly maximum and lowest temperatures, relative humidity, solar radiation, and wind speed. Crop evapotranspiration (ET_c) values were the model output and were calculated by multiplying ET_o by a crop coefficient (K_c). The ETo was calculated with the Penman–Monteith method. The method is the only one that is widely used, and it works well in Ethiopia's highlands (Adem et al. 2017). The crop coefficient during the early, middle and late stages of development is known as K_c. Varying crops will require different amounts of water due to their different crop coefficients. The FAO's recommendations and literature were used to determine the K_c of the chosen crops.

$$ET_c = ET_o * K_c \tag{5.3}$$

The amount of water needed for net irrigation depends on the agricultural pattern and environment. The net irrigation requirements for primary irrigation crops in the study area were determined using the mean monthly rainfall data and the ETc. When irrigation water is applied and transported, a variety of losses occur, including runoff, seepage, evaporation, and percolation. Certain amounts of water are needed for processes including leaching, transplantation, and land preparation. Therefore, CWR accounts for ET and losses incurred during the application of water for these uses (Al-Muaini et al. 2019).

$$NIR = ET_c - P_{eff} \tag{5.4}$$

where ET_c stands for crop evapotranspiration, P_{eff} is for effective rainfall, and NIR stands for the net irrigation requirement of crops. Effective rainfall is the amount of rain that falls during the crop's growing season that is available to provide the crop's evapotranspiration needs or consumptive water needs. After losses from surface runoff and deep infiltration, it is a portion of the rainfall that is efficiently used by the crop. Using CROPWAT and the average rainfall data for each month, effective rainfall was computed.

Based on efficiency from the source to the specified command area, the gross irrigation water requirements of the crops at the identified possible irrigable locations were estimated. Then, using the following formula, the gross irrigation water need was determined:

$$\text{GIWR} = \frac{\text{NIR}}{E_{ff}} \tag{5.5}$$

where E_{ff} is the overall irrigation efficiency expressed as a percentage and GIWR is the gross irrigation water requirement. The amount of water used effectively for crop development in the field is expressed as a percentage of the amount of water taken in from the water source. Most E_{ff} accounts for 40% to 60% of surface irrigation systems in the Ethiopian standard (Brouwer and Heibloem 1986). For estimating the gross irrigation needs in this study, E_{ff} was set at 45% for surface irrigation.

Irrigation Potential by Water Availability

Surface, sprinkler, and drip irrigation efficiency and water requirements for special applications such as land preparation and leaching are assumed to be 60%, 75%, and 90%, respectively (Brouwer et al. 1988). The irrigation potential of the rivers was calculated as the quotient of the 80% monthly averaged discharge exceedance probability and the total depth irrigation (IR) of the dominant crops in the area for the growing season.

$$\text{Area} = \frac{Q(80)}{\text{IR}} * E_{ff} \tag{5.6}$$

where Q (80) is the runoff at the gauge location with an 80% chance of exceeding the threshold in million m^3, IR is the irrigation requirement, and E_{ff} is the irrigation efficiency.

Results and Discussion

Factor Suitability

Slope Suitability

The slope suitability class reveals that 30% (17,486 ha) of the area was unsuitable for surface irrigation due to a slope range greater than 8% (Table 5.6 and Fig. 5.2). About 70% of the total land area is classified as highly suitable to marginally suitable for surface irrigation (Table 5.6 and Fig. 5.2). About 13% were highly suitable,

while 37% were moderately suitable. The highly and moderately suitable areas were distributed throughout the watershed's central and downstream sections (Fig. 5.2).

Table 5.6 Slope classes, suitability classes, and the areal coverage of each class

Slope class, %	Area, ha	Area, %	Suitability
0–2	7498	13	Highly suitable, S1
2–5	22,007	37	Moderately suitable, S2
5–8	11,770	20	Marginally suitable, S3
> 8	17,486	30	Not suitable, N1

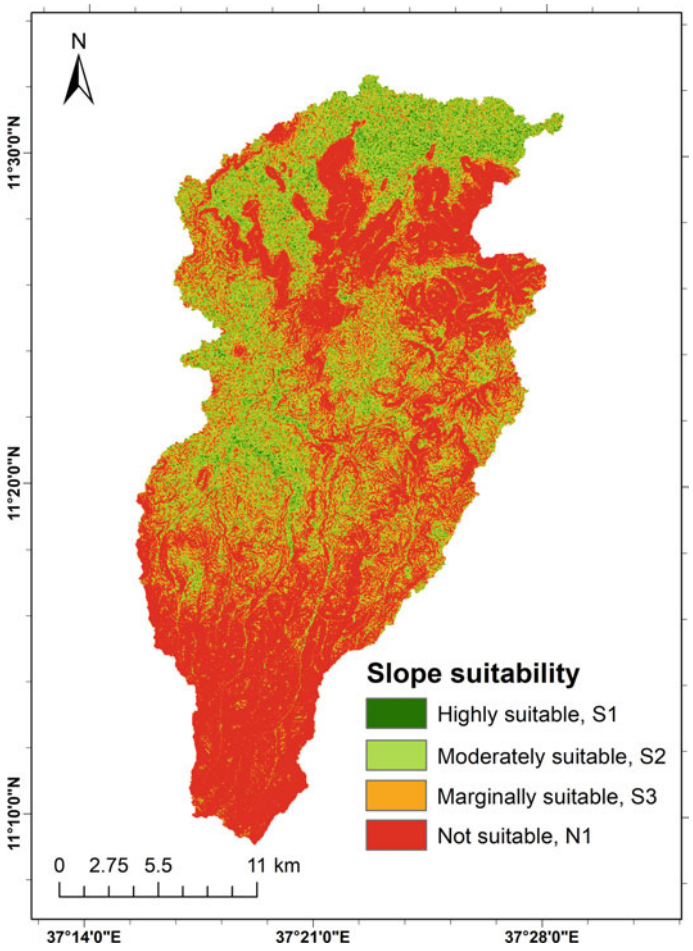

Fig. 5.2 Slope suitability map for surface irrigation in the Andassa watershed

Soil Suitability

A. Soil parameter suitability

Table 5.7 and Fig. 5.3 show the suitability classes of factors derived from soil properties. The texture class analysis results show that the area is dominated by fine-textured soil that is suitable for surface irrigation. More than 59% of the watershed area is highly and moderately suitable for surface irrigation, according to the textural class of the soils (Table 5.7 and Fig. 5.3a). Because the watershed has textured soil throughout, there were no unsuitable classes for surface irrigation development. Soil depth suitability revealed that 44,375 ha (75%) of the total area was highly suitable for surface irrigation, while 13,920 ha (24%) was marginally suitable (Table 5.7 and Fig. 5.3b). In the case of soil texture and soil depth, the upper and lower parts of the watershed are highly suitable for surface irrigation (Fig. 5.3a and b).

The drainage suitability class results showed that more than half (68.8%) of the watershed area was classified as highly suitable, while 23.5% of the watershed was classified as unsuitable for surface irrigation (Table 5.7 and Fig. 5.3c). The presence of areas with poorly drained soils in the watershed contributes to the large unsuitable area for surface irrigation in terms of drainage. About 47% of the study areas were classified as marginally suitable based on soil types. The watershed area was divided into two classes: highly suitable and unsuitable (Table 5.7 and Fig. 5.3d). Luvisols and Nitosols were discovered to be excellent choices for surface irrigation. These soils are distinguished by their depth and well-drained nature. Vertisols are soils that are moderately suitable for surface irrigation and are extremely hard when dry, very sticky when wet, and plastic when wet, indicating their poor workability (Birhanu et al. 2019). Alisols, the watershed's dominant soils, are highly acidic soils with a subsurface accumulation of high-activity clays (Deressa et al. 2018). Surface irrigation is not appropriate for leptosols, which are shallow in depth and well-drained soils (Birhanu et al. 2019).

B. Overall soil suitability

The weights of each factor were calculated using a pairwise matrix based on each soil parameter's importance for surface irrigation (Table 5.8). According to the calculated result, a high weight was given to soil depth (53%). The next largest weight was given to soil texture and soil type since the factors influencing surface irrigation are accordingly different. This was done based on a review of similar literature

Table 5.7 Soil parameter suitability classes and the areal coverage in hectares (percent) for the Andassa watershed

Suitability class	Soil texture	Soil depth	Soil drainage	Soil type
Highly suitable, S1	21,005 (35.8)	44,375 (75)	40,446 (68.8)	12,397 (21.5)
Moderately suitable, S2	13,920 (23.7)	113 (0.2)	171 (0.3)	4,315 (7.2)
Marginally suitable, S3	23,837 (40.5)	13,920 (24)	4,352 (7.4)	27,776 (47)
Not suitable, N1	–	354 (0.8)	13,792 (23.5)	14,273 (24.3)

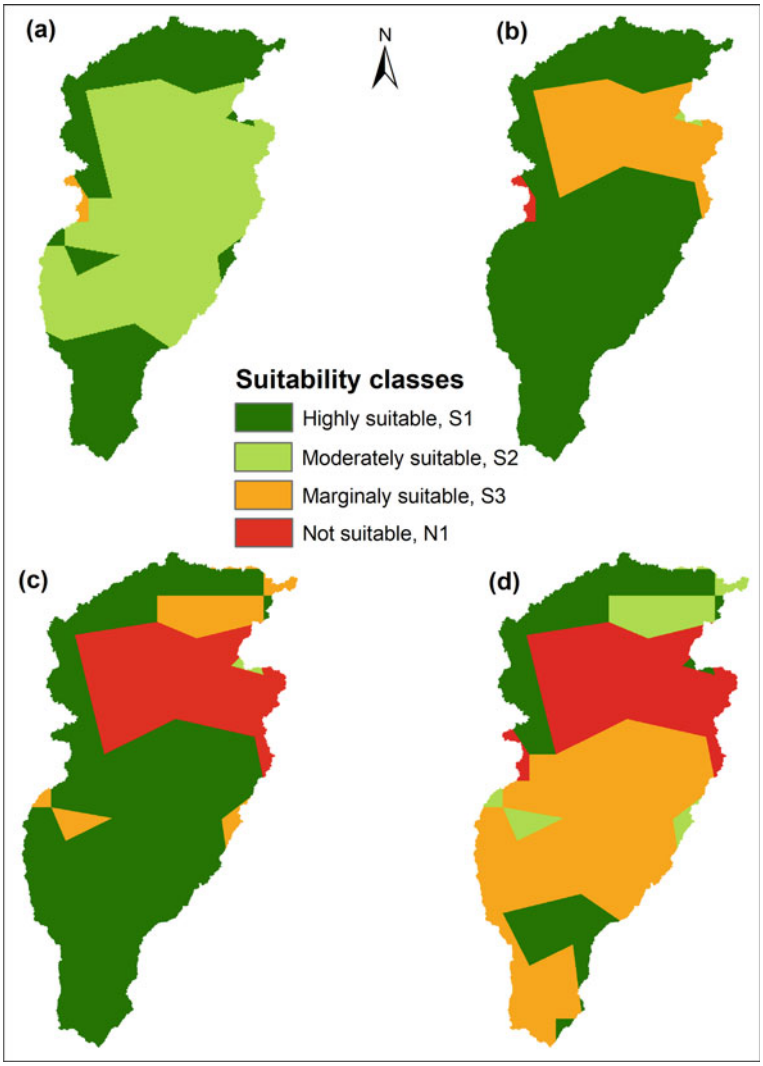

Fig. 5.3 Soil parameter suitability for surface irrigation: **a** soil texture, **b** soil depth, **c** soil drainage, and **d** soil type

(Hussien et al. 2019), field observation, and expert judgment. The weighted overlay was performed using the weight of the factors to map the overall suitability of soil for surface irrigation.

The results obtained from the weighted overlay of the four soil physical parameters (depth, drainage, type, and texture) showed that 35.6, 40, 23.7 and 0.7% of the watershed was highly, moderately, marginally, and not suitable for surface irrigation, respectively (Table 5.9 and Fig. 5.4). Generally, approximately 75% of the soil of

Table 5.8 Pairwise comparison matrix and the weight of each soil parameter for overall soil suitability

Factor	Soil depth	Soil drainage	Soil texture	Soil type	Criteria weight, %	Consistency
Soil depth	1	5	4	3	53	4.34
Soil drainage	0.2	1	0.33	0.33	8	4.14
Soil texture	0.25	3	1	2	22	4.25
Soil type	0.33	3	0.5	1	17	4.09
Total	1.78	12	5.83	6.33	λmax	4.21
					CI	0.07
					RI	0.9
					CR	0.08

Table 5.9 Overall soil suitability classes and the areal coverage in the Andassa watershed

Suitability class	Area, ha	Area, %
Highly suitable, S1	20,892	35.6
Moderately suitable, S2	23,596	40
Marginally suitable, S3	13,920	23.7
Not suitable, N1	354	0.7

the Andassa watershed was classified as highly to moderately suitable (Table 5.9 and Fig. 5.4). Similar to this study, Mengie (2017) reported that 75% of the soil of the Andassa watershed was classified as highly to marginally suitable. In this study, the highly suitable areas were located upslope and downslope of the watershed (Fig. 5.4).

Land Use Suitability

More than half of the watershed area (57%) was highly suitable for land use, while the remaining 20% was moderately suitable (Table 5.10 and Fig. 5.5). Approximately 22% of the area was marginally suitable, while the rest was unsuitable. Annual cropland and open grassland were deemed highly suitable for surface irrigation with few restrictions, while sparse forest, open shrub, and closed grassland were deemed moderately suitable. Land cover classes such as moderate forest and closed shrub, on the other hand, were marginally suitable, while the remainder of bare land, dense forest, water body, settlement, and woodland were classified as unsuitable for surface irrigation development. In the case of land use suitability, highly suitable lands were distributed throughout the watershed since agriculture is practiced in most of the study area (Fig. 5.5).

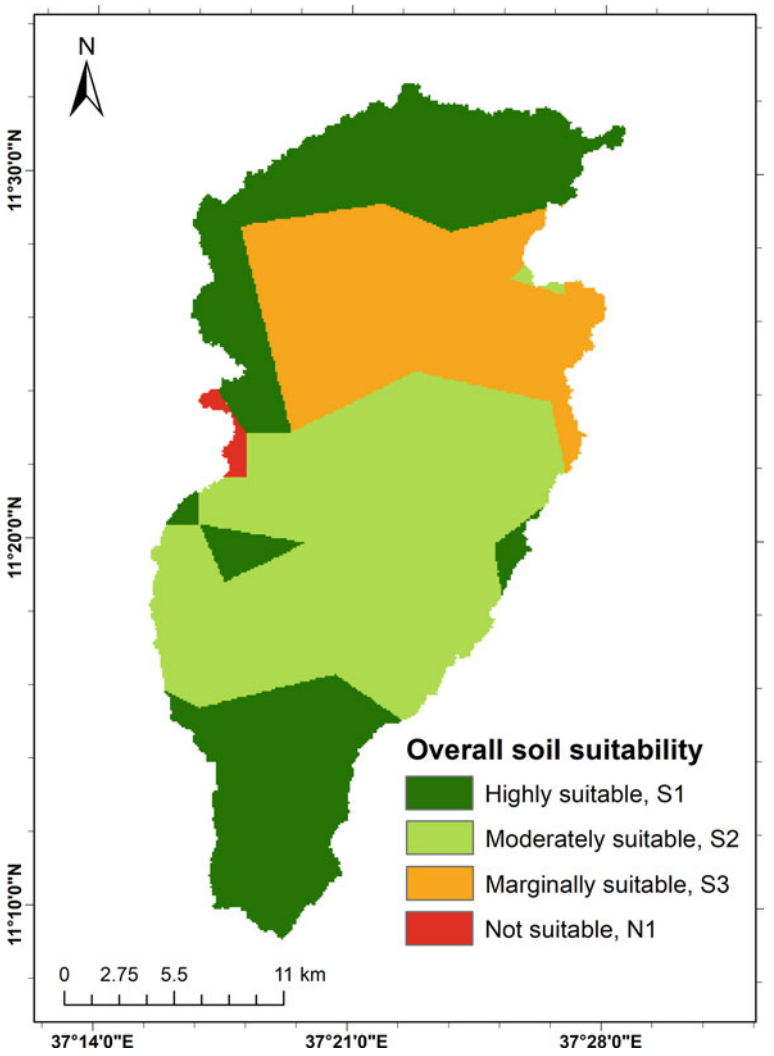

Fig. 5.4 Overall soil suitability map of the Andassa watershed

Table 5.10 Land use suitability classes and the areal coverage in the Andassa watershed

Suitability class	Area, ha	Area, %
Highly suitable, S1	33,494	57
Moderately suitable, S2	11,752	20
Marginally suitable, S3	12,928	22
Not suitable, N1	588	1

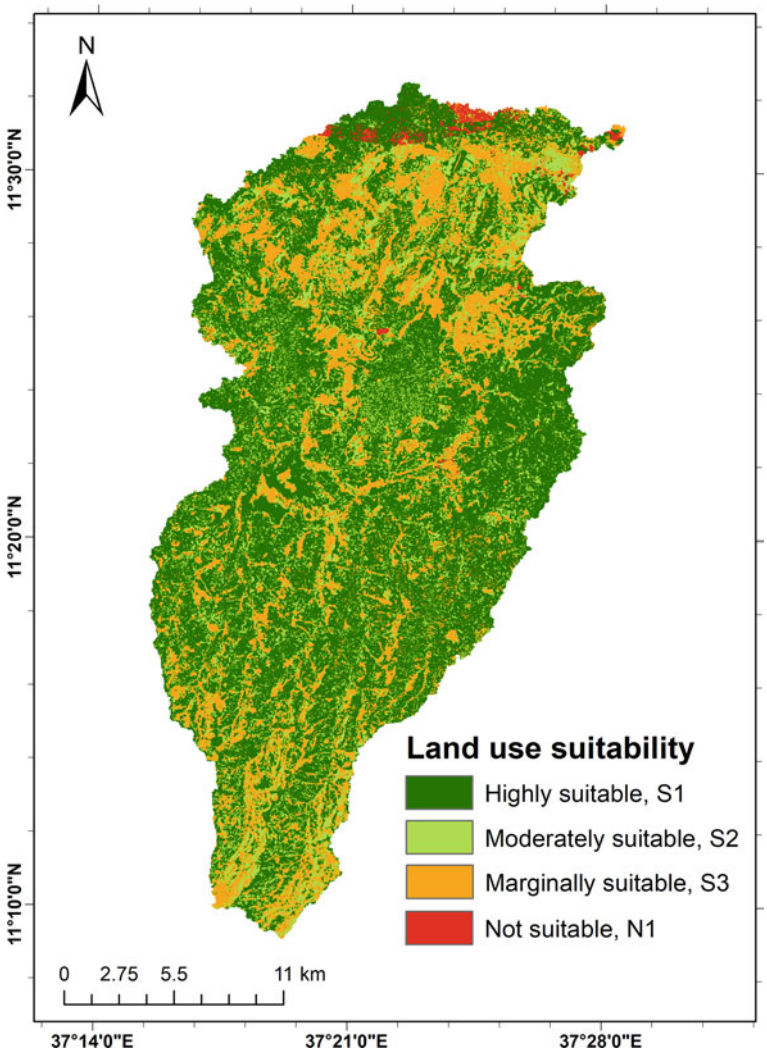

Fig. 5.5 Land use suitability map of the Andassa watershed

River Proximity

The proximity to surface irrigation water sources revealed that 61% and 29% of the watershed area were highly and moderately suitable for surface irrigation, respectively. The remaining watershed area is classified as marginally and unsuitable (Table 5.11 and Fig. 5.6). As a result, lands near rivers will have a high chance of suitability. Surface irrigation is only marginally feasible in the areas surrounding the ridges (watershed boundary) (Fig. 5.6).

Table 5.11 Areal coverage of suitable areas in the case of river proximity

Suitability class	Area, ha	Area, %
Highly suitable, S1	36,126	61
Moderately suitable, S2	17,184	29
Marginally suitable, S3	4548	8
Not suitable, N1	903	2

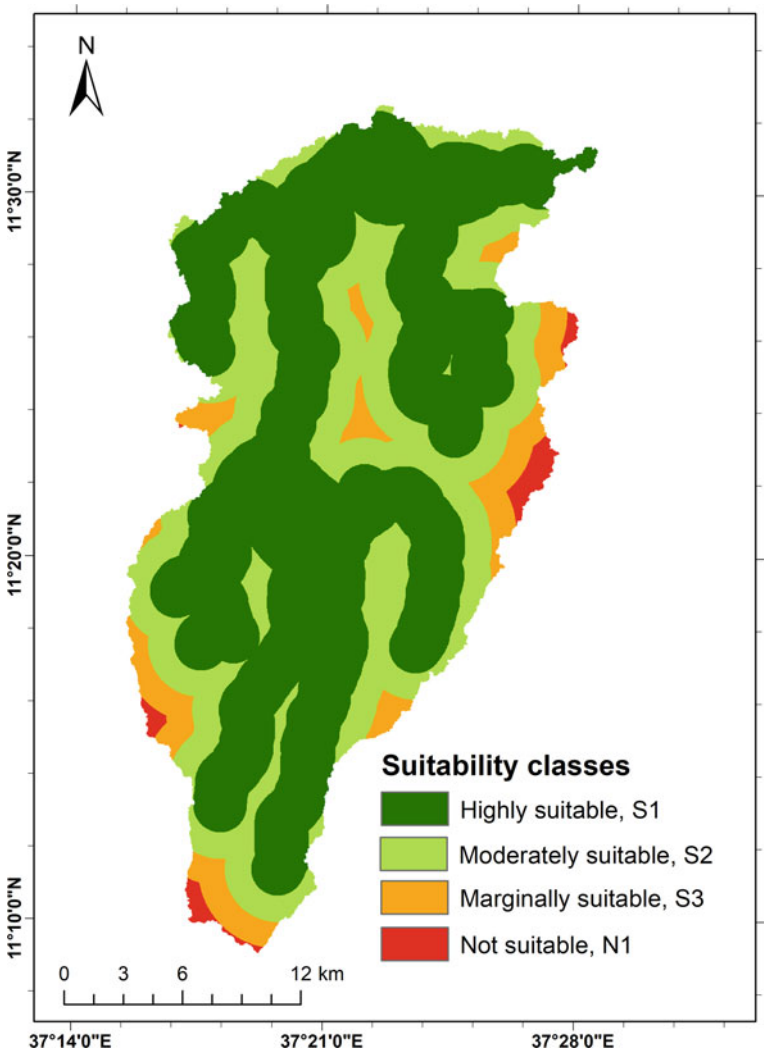

Fig. 5.6 Suitability map as a function of river proximity

Overall Suitability for Surface Irrigation

The weights of each factor (slope, soil, land use, and river proximity) were calculated using a pairwise matrix based on each soil parameter's importance for surface irrigation (Table 4). According to the calculated result, weights of 45, 32, 13, and 10% influence were given for slope, river, soil, and land use, respectively. As indicated in Table 5.12, the consistency ratio (CR) of the pairwise matrix was 0.05. As reported by Saaty (1990), the CR value is acceptable and consistent when it is less than 0.1%. Therefore, each factor of land evaluation was given a weight based on its importance, and weighted overlay analysis was conducted.

According to the weighted overlay result, only 9% of the watershed was highly suitable for surface irrigation (Table 5.13 and Fig. 5.7). The majority of the watershed area (51%) was suitable for moderate surface irrigation. Around 39% of the watershed area was designated as marginally suitable. 1% of the watershed area is unsuitable. Surface irrigation is highly and moderately suitable in the watershed's western, central, and northern parts (Fig. 5.7). In most previous similar studies, less than 10% of the study watersheds were highly suitable for surface irrigation implementation (Admas et al. 2022; Balew et al. 2021; Danbara and Zewdie 2022). This is due to the limiting factors of slope and river proximity for gravity-fed surface irrigation.

Table 5.12 Pairwise matrix for the main factors used for the identification of land for surface irrigation

Factors	River proximity	Slope	Soil	Land use	Criteria weight, %	Consistency
River proximity	1	0.5	3	4	32	4.18
Slope	2	1	4	3	45	4.22
Soil	0.33	0.25	1	2	13	4.12
Land use	0.25	0.33	0.5	1	10	4.05
Total	3.58	2.08	8.5	10	λmax	4.14
					CI	0.05
					RI	0.90
					CR	0.05

Table 5.13 Overall suitability of lands for surface irrigation in the Andassa watershed

Suitability class	Area, ha	Area, %
Highly suitable, S1	5119	9
Moderately suitable, S2	30,028	51
Marginally suitable, S3	22,968	39
Not suitable, N1	645	1

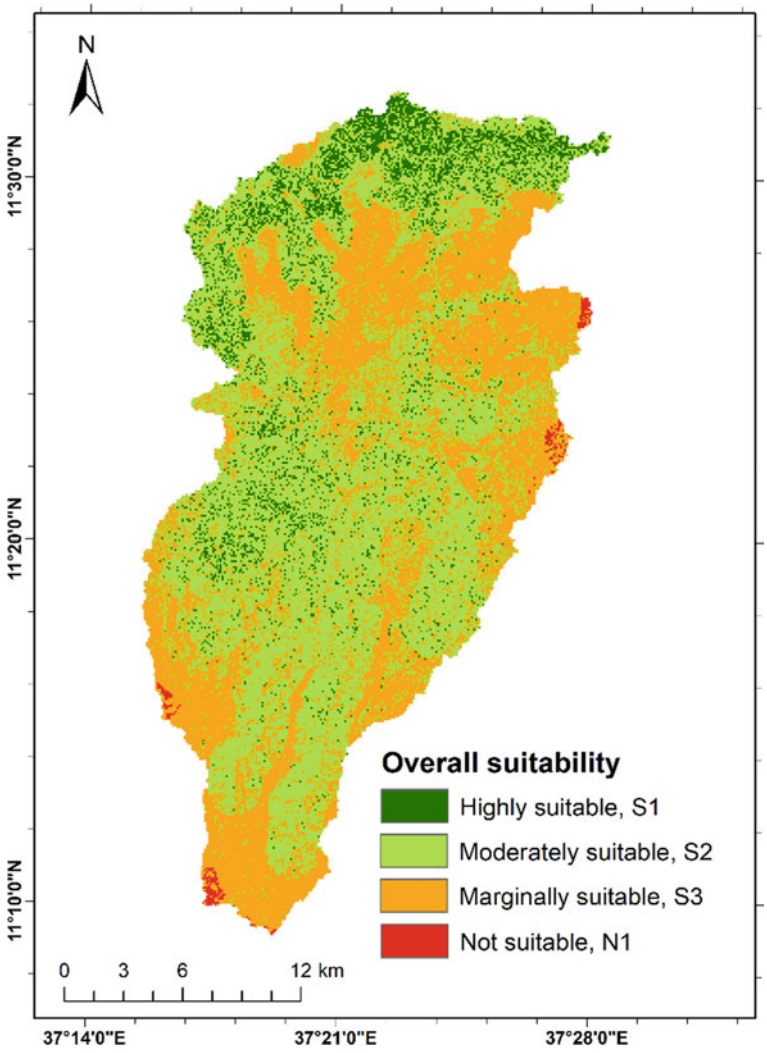

Fig. 5.7 Overall suitability map of lands for surface irrigation in the Andassa watershed

Assessment of Crop and Irrigation Water Requirements

The rainfall deficit result indicated that rainfall was greater than crop evapotranspiration during the wet season (June to August). As a result, we exclude the three months from the crop water requirement estimation (Table 5.14). Rainfed crops planted during the wet season are expected to be harvested between September and December. Irrigated crops were planted during the dry season, which lasted from September to May. Table 5.14 shows that the water requirements of onion, cabbage,

pepper, and tomato were zero in various months. This is due to the crops' sowing dates and the length of their growing seasons.

Within the study area, different crops have different crop water requirements each month. From all selected crops, the water needed by the crop was higher in sugarcane, which was 1758.3 mm throughout the growing period. The minimum water needed by the crop is for cabbage, which is 312.4 mm throughout the growing period (Table 5.14). The maximum water required by all crops was observed in March (507 mm). Other similar research throughout the world showed that the crop water requirement of sugarcane was the highest compared to other crop types (Qin et al. 2023).

Gross irrigation water requirements for the selected crops were calculated by 45% application efficiency and 90% conveyance efficiency for surface irrigation. The net and gross irrigation water requirements for all crops considered in this study were 2891 and 6424 mm throughout the growing period, respectively (Table 5.15). Fifty-three percent of the total net and gross irrigation water requirements were shared by sugarcane. This is because the growing period of sugarcane is 620 days. The average net and gross irrigation water requirements of the selected crops were 587 and 1285 mm, respectively (Table 5.15). Similar findings were reported by Bayush (2020); Mengie (2017). The Andassa watershed has the potential to produce crops all year. Growers of onions, cabbage, peppers, tomatoes, and sugarcane have traditionally used the most traditional surface irrigation system, the furrow irrigation system, which is characterized by low irrigation efficiency. Crop productivity can be increased with furrow irrigation by applying the appropriate amount at the appropriate time. As a result, it is recommended that crops receive light and frequent irrigation to avoid water stress.

Table 5.14 Crop water requirements (millimeters) of primary and selected crops of the Andassa watershed

Crop type	Sugarcane	Onion	Cabbage	Pepper	Tomato	Total
January	211.6	97.4	0.0	0.0	21.4	330.4
February	194.2	78.4	0.0	59.0	61.2	392.8
March	214.2	0.0	88.5	92.7	111.7	507.1
April	118.8	0.0	101.7	116.7	129.2	466.4
May	33.2	0.0	122.2	120.1	129.2	404.7
September	271.2	0.0	0.0	0.0	0.0	271.2
October	269.9	86.9	0.0	0.0	0.0	356.8
November	239.6	103.4	0.0	0.0	0.0	343.0
December	205.6	90.5	0.0	0.0	0.0	296.1
Total	1758.3	456.6	312.4	388.5	452.7	

Table 5.15 Crop evapotranspiration, effective rainfall (Peff), net irrigation requirement (NIR), and gross irrigation requirement of selected crops in the Andassa watershed

Crop type	Growing period, days	ETc, mm	Peff, mm	NIR, mm	GIWR, mm
Onion	150	457	108	348	774
Cabbage	165	540	138	402	893
Pepper	125	405	142	263	584
Tomato	145	498	146	351	780
Sugarcane	620	2298	771	1527	3393
Total		4197	1307	2891	6424

Surface Irrigation Potential by Water Availability

The average annual river flow of the Andassa watershed at 80% exceedance in the 9 water-scarce months of the year is 148.3 million m^3. The irrigable land at 80% exceedance probability of the annual river flow was 24,626 ha, which could irrigate 70% of the highly and moderately suitable land (35,148 ha) identified for surface irrigation with 60% application efficiency. This indicated that the surface water resource potential of the Andassa watershed is not sufficient to develop surface irrigation throughout the identified suitable areas (highly and moderately suitable) for surface irrigation methods. This means that an alternative water harvesting mechanism is mandatory for further surface irrigation developments.

Conclusions

This study was carried out in the Andassa watershed to identify suitable lands for surface irrigation using GIS-based multicriteria evaluation (MCE). The slope, soil, land use, and river proximity were the primary irrigation suitability factors investigated during the study. The overall analysis of the suitability evaluation revealed that approximately 60% of the Andassa watershed was highly (9%) and moderately (51%). Five primary irrigation crops were chosen for the study area, and their net and gross irrigation water requirements were calculated, which will be used for irrigation development. Accordingly, sugarcane is a crop that takes a long period of growing time. As a result, the crop requires large amounts of water for irrigation. In addition to sugarcane, onion and tomato are the third and fourth crops that require a large amount of water for irrigation, respectively. The available water in the Andassa River can only irrigate 70% of the highly and moderately suitable lands. An alternative water harvesting mechanism will be required to irrigate all suitable lands to increase crop production. In addition to the factors used in this study, future studies need to consider additional factors that determine lands suitable for surface irrigation, including soil chemical properties.

References

Abebe BK, Zimale FA, Gelaye KK, Gashaw T, Dagnaw EG, Adem AA (2022) Application of hydrological and sediment modeling with limited data in the abbay (Upper blue nile) Basin, Ethiopia. Hydrology 9(10):167. https://doi.org/10.3390/hydrology9100167

Abou Zaki N, Torabi Haghighi A, Rossi PM, Xenarios S, Kløve B (2018) An index-based approach to assess the water availability for irrigated agriculture in Sub-Saharan Africa. Water 10(7). https://doi.org/10.3390/w10070896

Adem AA, Aynalem DW, Tilahun SA, Steenhuis TS (2017) Predicting reference evaporation for the Ethiopian highlands. J Water Resour Prot 9:1244–1269. https://doi.org/10.4236/jwarp.2017.911081

Adem AA, Yibeltal M, Mhiret DA, Tilahun SA, Zimale FA, Worqlul AW, Enku T, Teferi ET (2022) Identification of suitable land for supplemental surface irrigation in semi-arid areas of Northwestern Ethiopia. Remote Sens Appl Soc Environ 100899. https://doi.org/10.1016/j.rsase.2022.100899

Admas BF, Gashaw T, Adem AA, Worqlul AW, Dile, YT Molla E (2022) Identification of soil erosion hot-spot areas for prioritization of conservation measures using the SWAT model in Ribb watershed, Ethiopia. Resour Environ Sustain 100059. https://doi.org/10.1016/j.resenv.2022.100059

Akpoti K, Kabo-bah AT, Zwart SJ (2019) Review—Agricultural land suitability analysis: state-of-the-art and outlooks for integration of climate change analysis. Agric Syst 173:172–208. https://doi.org/10.1016/j.agsy.2019.02.013

Allen RG (2005) FAO-56 dual crop coefficient method for estimating evaporation from soil and application extensions. J Irrig Drain Eng 131(1):2. https://doi.org/10.1061/(ASCE)0733-9437(2005)131:1(2)

Al-Muaini A, Green S, Dakheel A, Abdullah A-H, Sallam O, Abou Dahr WA, Dixon S, Kemp P, Clothier B (2019) Water requirements for irrigation with saline groundwater of three date-palm cultivars with different salt-tolerances in the hyper-arid United Arab Emirates. Agric Water Manag 222:213–220. https://doi.org/10.1016/j.agwat.2019.05.022

Assefa T, Jha M, Reyes M, Srinivasan R, Worqlul AW (2018) Assessment of suitable areas for home gardens for irrigation potential, water availability, and water-lifting technologies. Water 10(4):495. https://doi.org/10.3390/w10040495

Awulachew SB, Merrey DJ (2007) Assessment of small scale irrigation and water harvesting in Ethiopian agricultural development. Inter Water Manage Inst (IWMI), 11. https://www.academia.edu/download/32299286/IWMI-Seleshi___Merrey-Assessment_of_Small_Scale_Irrigation_and_WH_in_Ethiopia.pdf

Awulachew SB, Yilma AD, Loulseged M, Loiskandl W, Ayana M, Alamirew T (2007) Water resources and irrigation development in Ethiopia. International Water Management Institute, Colombo, Sri Lanka

Awulachew SB (2019) Irrigation potential in Ethiopia: constraints and opportunities for enhancing the system. Gates Open Res 3(22). https://doi.org/10.21955/gatesopenres.1114943.1

Balew A, Nega W, Legese B, Semaw F (2021) Suitable potential land evaluation for surface water irrigation using remote sensing and GIS–MCE in the case of Rib-Gumara Watershed, Ethiopia. J Indian Soc Remote Sens 49(9):2273–2290. https://doi.org/10.1007/s12524-021-01383-w

Bandyopadhyay S, Jaiswal RK, Hegde VS, Jayaraman V (2009) Assessment of land suitability potentials for agriculture using a remote sensing and GIS based approach. Int J Remote Sens 30(4):879–895. https://doi.org/10.1080/01431160802395235

Baye TG (2017) Poverty, peasantry and agriculture in Ethiopia. Ann Agrarian Sci 15(3):420–430. https://doi.org/10.1016/j.aasci.2017.04.002

Bayush M (2020) Assessment of surface irrigation potential and optimization of cropping pattern: case study of danse Watershed, Oromia Region ASTU]

Berhe GT, Baartman JEM, Veldwisch GJ, Grum B, Ritsema CJ (2022) Irrigation development and management practices in Ethiopia: a systematic review on existing problems, sustainability

issues and future directions. Agric Water Manag 274:107959. https://doi.org/10.1016/j.agwat.2022.107959
Binyam AY, Desale KA (2015) Rainwater harvesting: An option for dry land agriculture in arid and semi-arid Ethiopia. Int J Water Resour Environ Eng 7(2):17–28. https://doi.org/10.5897/IJWREE2014.0539
Birhanu A, Murlidhar Pingale S, Soundharajan B-S, Singh P (2019) GIS-based surface irrigation potential assessment for Ethiopian river basin. Irrig Drain 68(4):607–616. https://doi.org/10.1002/ird.2346
Bishaw B, Neufeldt H, Mowo J, Abdelkadir A, Muriuki J, Dalle G, Assefa T, Guillozet K, Kassa H, Dawson IK, Luedeling E, Mbow C (2013) Farmers' strategies for adapting to and mitigating climate variability and change through agroforestry in Ethiopia and Kenya [Book]. Forestry Communications Group, Oregon State University. https://ir.library.oregonstate.edu/concern/defaults/5999n3901
Bjornlund V, Bjornlund H, Van Rooyen AF (2020) Why agricultural production in sub-Saharan Africa remains low compared to the rest of the world—A historical perspective. Int J Water Resour Dev 36(sup1):S20–S53. https://doi.org/10.1080/07900627.2020.1739512
Brouwer C, Heibloem M (1986) Irrigation water management: irrigation water needs. Training Manual, Food and Agriculture Organization of the United Nations, Rome, Italy, p 3
Brouwer C, Prins K, Kay M, Heibloem M (1988) Irrigation water management: irrigation methods. Training Manual, FAO 9(5):5–7. https://www.wec.edu.ye/wp-content/uploads/2015/11/Manual5.pdf
Chen J (2014) GIS-based multi-criteria analysis for land use suitability assessment in City of Regina. Environ Syst Res 3(1):13. https://doi.org/10.1186/2193-2697-3-13
Danbara TT, Zewdie M (2022) Assessment of suitable land for surface irrigation using spatial information systems: case of Bilate River Basin in the Rift Valley Lakes Basin, Ethiopia. Comput Electron Agric 202:107402. https://doi.org/10.1016/j.compag.2022.107402
Dawit M, Dinka MO, Leta OT (2020) Implications of adopting drip irrigation system on crop yield and gender-sensitive issues: the case of Haramaya District, Ethiopia. J Open Innov Technol Mark Complexity 6(4)
Deressa A, Yli-Halla M, Mohamed M, Wogi L (2018) Soil classification of humid Western Ethiopia: a transect study along a toposequence in Didessa watershed. CATENA 163:184–195. https://doi.org/10.1016/j.catena.2017.12.020
Dožić S (2019) Multi-criteria decision making methods: application in the aviation industry. J Air Transp Manag 79:101683. https://doi.org/10.1016/j.jairtraman.2019.101683
FAO (1976) A framework for land evaluation, vol. 32. Bernan Press (PA)
Gebremedhin GH (2015) Irrigation in Ethiopia, a review. J Environ Earth Sci 5(15):141–147. http://www.iiste.org/.../25796
Guo Z, Li P, Yang X, Wang Z, Lu B, Chen W, Wu Y, Li G, Zhao Z, Liu G, Ritsema C, Geissen V, Xue S (2022) Soil texture is an important factor determining how microplastics affect soil hydraulic characteristics. Environ Int 165:107293. https://doi.org/10.1016/j.envint.2022.107293
Hagos YG, Mengie MA, Andualem TG, Yibeltal M, Linh NTT, Tenagashaw DY, Hewa G (2022) Land suitability assessment for surface irrigation development at Ethiopian highlands using geospatial technology. Appl Water Sci 12(5):98. https://doi.org/10.1007/s13201-022-01618-2
Hussien K, Woldu G, Birhanu S (2019) A GIS-based multi-criteria land suitability analysis for surface irrigation along the Erer Watershed, Eastern Hararghe Zone, Ethiopia. East Afr J Sci 13(2):169–184
Kedir Y, Berhanu B, Alamirew T (2022) Analysis of water–energy–crop nexus indicators in irrigated sugarcane of Awash Basin, Ethiopia. Environ Syst Res 11(1):17. https://doi.org/10.1186/s40068-022-00263-7
Malczewski J (2006) GIS-based multicriteria decision analysis: a survey of the literature. Int J Geogr Inf Sci 20(7):703–726. https://doi.org/10.1080/13658810600661508

Mandal B, Dolui G, Satpathy S (2018) Land suitability assessment for potential surface irrigation of river catchment for irrigation development in Kansai watershed, Purulia, West Bengal, India. Sustain Water Resour Manage 4(4):699–714. https://doi.org/10.1007/s40899-017-0155-y

Mengie BT (2017) GIS supported investigation of irrigable land and surface water resources: the case of Andassa Watershed, Ethiopia. https://nadre.ethernet.edu.et/record/2933/files/BayeTilahunFinalThesisprinted.pdf

Paul M, Negahban-Azar M, Shirmohammadi A, Montas H (2020) Assessment of agricultural land suitability for irrigation with reclaimed water using geospatial multi-criteria decision analysis. Agric Water Manag 231:105987. https://doi.org/10.1016/j.agwat.2019.105987

Qin N, Lu Q, Fu G, Wang J, Fei K, Gao L (2023) Assessing the drought impact on sugarcane yield based on crop water requirements and standardized precipitation evapotranspiration index. Agric Water Manag 275:108037. https://doi.org/10.1016/j.agwat.2022.108037

Rockström J, Barron J, Fox P (2002) Rainwater management for increased productivity among small-holder farmers in drought prone environments. Physics Chem Earth Parts a/b/c 27(11):949–959. https://doi.org/10.1016/S1474-7065(02)00098-0

Rosegrant MW, Cai X, Cline SA, Nakagawa N (2002) The role of rainfed agriculture in the future of global food production. I. F. P. R. Institute

Saaty TL (1990) How to make a decision: the analytic hierarchy process. Eur J Oper Res 48(1):9–26. https://doi.org/10.1016/0377-2217(90)90057-I

Tercan E, Dereli MA (2020) Development of a land suitability model for citrus cultivation using GIS and multi-criteria assessment techniques in Antalya province of Turkey. Ecol Ind 117:106549. https://doi.org/10.1016/j.ecolind.2020.106549

Teshome A, Halefom A (2020) Potential land suitability identification for surface irrigation: in case of Gumara watershed, Blue Nile basin, Ethiopia. Model Earth Syst Environ 6(2):929–942. https://doi.org/10.1007/s40808-020-00729-6

Wani SP, Sreedevi T, Rockström J, Ramakrishna Y (2009) Rainfed agriculture–past trends and future prospects. In: Rainfed agriculture: unlocking the potential, vol 7, pp 1–33. http://oar.icrisat.org/2428/1/Rainfed_agriculture_-_past_trends_and_future_prospects.pdf

Warner K, Zommers Z, Wreford A, Hurlbert M, Viner D, Scantlan J, Halsey K, Halsey K, Tamang C (2019) Characteristics of transformational adaptation in climate-land-society interactions. Sustainability 11(2)

Weldeabzgi GG, Ketema T, Gashu G, Deressa S (2021) Land suitability evaluation for surface irrigation development using parametric evaluation approach: The case of Gudina Wacho watershed, Western Ethiopia. Int J Agric Sci Food Technol 7(3):302–309. https://doi.org/10.17352/2455-815X.000124

Worqlul AW, Jeong J, Dile YT, Osorio J, Schmitter P, Gerik T, Srinivasan R, Clark N (2017) Assessing potential land suitable for surface irrigation using groundwater in Ethiopia. Appl Geogr 85:1–13. https://doi.org/10.1016/j.apgeog.2017.05.010

Worqlul AW, Dile YT, Jeong J, Adimassu Z, Lefore N, Gerik T, Srinivasan R, Clarke N (2019) Effect of climate change on land suitability for surface irrigation and irrigation potential of the shallow groundwater in Ghana. Comput Electron Agric 157:110–125. https://doi.org/10.1016/j.compag.2018.12.040

Xie H, You L, Dile YT, Worqlul AW, Bizimana J-C, Srinivasan R, Richardson JW, Gerik T, Clark N (2021) Mapping development potential of dry-season small-scale irrigation in Sub-Saharan African countries under joint biophysical and economic constraints—An agent-based modeling approach with an application to Ethiopia. Agric Syst 186:102987. https://doi.org/10.1016/j.agsy.2020.102987

Chapter 6
Exploring Soil Properties from Spectrometry for Better Management in the Abay River Basin

Gizachew Ayalew Tiruneh, Derege Tsegaye Meshesha, Enyew Adgo, Atsushi Tsunekawa, Nigussie Haregeweyn, Ayele Almaw Fenta, Tiringo Yilak Alemayehu, Genetu Fekadu, Temesgen Mulualem, Simeneh Demissie, Kefyialew Tilahun, and José Miguel Reichert

Abstract The objective of this study is to evaluate how soil bunds affect important soil characteristics based on soil reflectance in Kecha, a midland in the Ethiopian Abay River Basin. Soil samples were taken from 48 plots at 0–30 cm depth and were analyzed for soil texture, pH, organic carbon (OC), total nitrogen (TN), available phosphorus (av. P), and potassium (av. K). The reflectance of air-dried, pulverized, and sieved soils was evaluated using a spectroradiometer. Regression modeling was used to locate and forecast changes in soil parameters. Soil properties were identified and predicted using the models, which were evaluated using the coefficient of determination (R^2), root mean square error (RMSE), and Nash–Sutcliffe efficiency (NSE). The model results showed that soils from bunded plots had less

G. A. Tiruneh (✉)
Department of Natural Resource Management, Debre Tabor University, P.O. Box 272, Debre Tabor, Ethiopia
e-mail: tiruneh1972@gmail.com

D. T. Meshesha · E. Adgo · G. Fekadu · T. Mulualem · S. Demissie · K. Tilahun
Department of Natural Resource Management, Bahir Dar University, P.O. Box 1289, Bahir Dar, Ethiopia

A. Tsunekawa
Arid Land Research Center, Tottori University, 1390 Hamasaka, Tottori 680-0001, Japan
e-mail: tsunekawa@tottori-u.ac.jp

N. Haregeweyn · A. A. Fenta
International Platform for Dryland Research and Education, Tottori University, 1390 Hamasaka, Tottori 680-0001, Japan

T. Y. Alemayehu
Department of Plant Sciences, Debre Tabor University, P.O. Box 272, Debre Tabor, Ethiopia

J. M. Reichert
Soils Department, Universidade Federal de Santa Maria (UFSM), Av. Roraima 1000, Santa Maria, RS 97105-900, Brazil
e-mail: reichert@ufsm.br

A. M. Melesse et al. (eds.), *Land and Water Degradation in Ethiopia*, Springer Geography, https://doi.org/10.1007/978-3-031-60251-1_6

reflection, and the coefficient of determination (R^2) was excellent (0.96) and (0.93) for the soil brightness index and reflectance using polynomial and linear models for soil OC and clay contents, respectively. Spectroradiometry could therefore complement conventional soil analysis, but more studies are needed to enhance its prediction performance.

Keywords Reflectance spectroscopy · Soil property · Soil management

Introduction

Soil qualities are widely distributed in Ethiopia (Kassawmar et al. 2018). Sustainable land management (SLM) techniques, such as soil bunding, can change essential soil properties and thereby affect soil functions (Berihun et al. 2020). SLM practices can improve soil quality and increase crop yields (Reichert et al. 2022).

Characterizing and evaluating geographic variation in soil parameters is necessary to understand soil quality (De Marins et al. 2018). Details on soil fertility are required for location-based soil and crop management (Rosemary et al. 2017). To quantify soil fertility, people frequently rely on crop yield and production, plant indicators, and the texture and color of the soil (Karltun et al. 2013).

Laboratory and soil spectrometry in the visible, near-infrared, and shortwave infrared (Vis-NIR-SWIR, 350–2500 nm) ranges can be supplements to physical and chemical soil research (Gholizadeh et al. 2013). The contents of soil organic carbon (OC) (Vašát et al. 2017), clay (Tümsavaş et al. 2018), total nitrogen (TN) (Morellos et al. 2016), and soil texture (Vasava et al. 2019) could be predicted from reflectance. SLM practices, such as soil bunds, are crucial to ensure environmental sustainability (Bastos Lima 2021). Bunds increase soil fertility by minimizing runoff and soil erosion (Nyssen et al. 2006; Amare et al. 2013).

Low agricultural yield is a serious problem in the Kecha catchment due to soil erosion and diminished soil productivity. Therefore, it would be beneficial to change conventional laboratory soil analysis. According to Amare et al. (2013), spectroradiometry was effective at quantifying soil carbon in Ethiopia's various agro-ecologies and soil types. However, there are no conclusions about the effects of soil bunding on soil properties in the catchment, in Ethiopia or Africa. Therefore, the aim of this study was to establish how soil bunding affected soil texture, pH, OC, TN, available phosphorus (av. P), and potassium (av. K) based on spectroradiometric data.

Description of the Study Area

The experiment was performed in the Kecha catchment, which is situated in the midland region of the Abbay River basin in Ethiopia (Fig. 6.1b). This location is designated as a midland area by Peel et al. (2007) and lies at an elevation of 1900–2000 m above sea level. The research site receives an average annual rainfall of 1076 to 1953 mm and experiences a maximum monthly temperature of 27.0 °C and a minimum monthly temperature of 12.6 °C, as per the data collected from nearby meteorological stations between 1994 and 2021 (Fig. 6.2). The rainy season lasts from June to August (NMSA 2004).

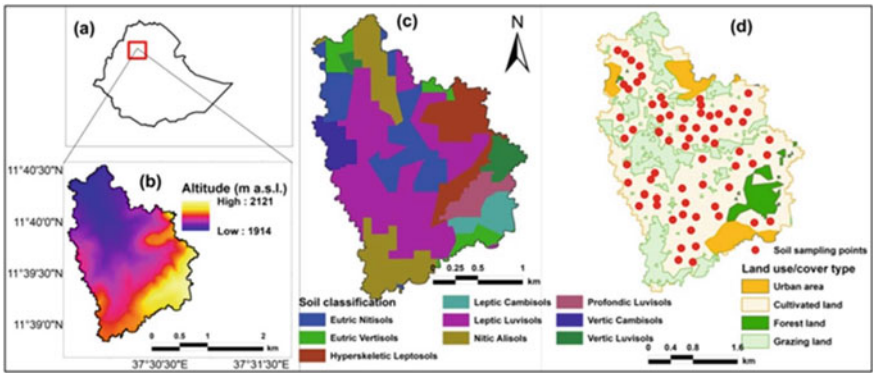

Fig. 6.1 Setting of the research site and soil plots: **a** Ethiopia, **b** elevation model of the Kecha catchment, **c** soil classification map of the Kecha catchment, and **d** soil sampling points in cultivated lands in the Kecha catchment

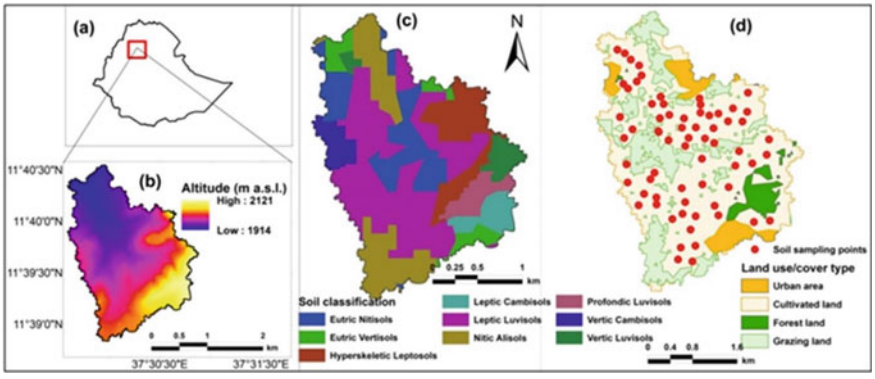

Fig. 6.2 Monthly rainfall and temperature in the Kecha catchment

Data and Methods

Soil Sample Collection

Cultivated soils were sampled from Sentinel-2 image-based land-use/cover data (https://sentinels.Copernicus.eu/) on March 12/2019 (Fig. 6.1d). The site, spanning over 425 ha, was divided into three topographic classes based on a digital elevation model with a resolution of 0.5 m: gentle (2–5%), moderate (5–10%), and steep (10–15%). Two land management scenarios were tested, with 24 plots featuring no soil bunding (WB) and 24 plots with soil bunds (SB) that were constructed five years ago and are 0.8 m wide and 0.5 m high. The selected plots had soil bunds in some plots and not in others (Fig. 6.1d), and five soil samples were collected from each plot at a depth of 0–30 cm using an Edelman auger.

Laboratory Procedures

Soil samples ($n = 48$) were crushed, sieved to 2 mm, and air-dried. Later, they were examined at Amhara Design and Supervision Works Enterprise for soil texture, pH, OC, TN, av. P, and av. K. The hydrometer method was used to determine the soil's texture (sand, silt, and clay) following the breakdown of organic matter (OM) and soil dispersion (Bouyoucos 1962). The proportion of sand was computed as the difference between the amounts of silt and clay, which were measured using a hydrometer. Finally, we determined soil textural classes using the USDA system's textural triangle (USDA 1996; Rowell 1997).

A digital pH meter was used to potentiometrically measure the pH of the soil in a 1:2.5 (soil: water) supernatant suspension (Peech 2016). The wet digestion method was used to measure soil OC levels (Walkley and Black 1934), and the Kjeldahl method was used to estimate TN. The Bray II method as reported by (Bray and Kurtz 1945) was used to measure available P. Then, a spectrophotometer was used to measure the av. P. (Murphy and Riley 1962). The amount of av. K was determined by using Morgan's solution to extract a soil sample and a flame photometer to measure the amount of available K (Morgan 1941).

Collecting and Preprocessing Soil Spectra

A spectroradiometer was used to measure the soil reflectance in the visible, near-infrared, and shortwave infrared (350–2500 nm) spectra (Brown et al. 2006) using direct sunlight to assess reflection between 10:30 A.M. and 11:00 A.M. The instrument was calibrated using a white Spectralon reference standard. The reflectance data were analyzed using Remote Sensing 3 v. 6.4 and View Spec Pro v. 6.2 software.

Table 6.1 Spectral color indices of soils in the study area

Index	Formula	Index property
Brightness index (BI)	$\frac{\sqrt{R^2+G^2+B^2}}{\sqrt{3}}$	Average soil reflectance magnitude
Hue index (HI)	$\frac{2*R-G-B}{G-B}$	Dominant wavelength, primary colors
Redness index (RI)	$\frac{R^2}{B*G^3}$	Hematite content

Source Mathieu and Pouget (1998), Escadafal et al. (1994)

Data Analysis

We used SAS 9.4 to analyze variance and regression. For calibration (31 soil samples) and validation, we computed the coefficient of determination (R^2; Moriasi et al. 2007), root mean square error (RMSE), and Nash–Sutcliffe efficiency (NSE; Nash and Sutcliffe 1970) as follows:

$$R^2 = 1 - \frac{\sum_{i=1}^{n}(y_i - \hat{y}_i)^2}{\sum_{i=1}^{n}(y_i - \hat{y}_i)^2} \tag{6.1}$$

$$\text{RMSE} = \sqrt{\frac{\sum_{i=1}^{n}(\hat{y}_i - y_i)^2}{n}} \tag{6.2}$$

$$\text{NSE} = 1 - \frac{\sum_{i=1}^{n}(y_i - \hat{y}_i)^2}{\sum_{i=1}^{n}(y_i - \overline{y}_i)^2} \tag{6.3}$$

where n is the number of samples, $\hat{y}$ is the predicted value, $\overline{y}$ is the mean measured value, and y is the observed value. The color indices of the soils were also calculated, as shown in Table 6.1.

Results and Discussion

Effects of Soil Bunding on Modifications to Soil Properties

Significant differences were observed in soil texture, OC, and av. P concentrations between bunded and non-bunded plots across the three slope categories (Table 6.2). The soil pH in the Kecha catchment ranges from severely acidic to moderately acidic (EthioSIS 2014). The higher soil pH in bunded plots might be due to the presence of clay and organic matter (OM), which hold basic cations. On the other hand, the lower pH values in non-bunded plots could be due to improper use of ammonium-based fertilizers and increased leaching of basic cations (Osman et al. 2013; Tellen and

Yerima 2018). These findings suggest that soil acidity may pose a threat to the soil in the study area.

Soil texture in the Kecha catchment ranges from clayey to sandy loam (USDA 1996). The predominance of silt and clay particles in bunded plots in all three slope classes (S1B, S2B, and S3B see Table 6.3) may be attributed to the effectiveness of bunding in reducing soil erosion. On the other hand, sand can predominate in non-bunded plots on steep slopes (S2W and S3W) due to the selective erosion of smaller soil particles (Reichert and Norton 2013). Similarly, higher silt and clay and lower sand contents were observed in bunded soils (Guadie et al. 2020). Values of OC (except S1B), av. P, and av. K were smaller than those mentioned in the catchment (Ebabu et al. 2020) and the Uwite Catchment, Ethiopia (Hadaro et al. 2021).

Table 6.2 Influence of bunds on soil parameters in the Kecha catchment

Treatments		Soil parameters						
		pH	Sand (%)	Silt (%)	Clay (%)	OC (%)	Av.P (ppm)	Av. K (mg kg^{-1})
Bunded plots ($n = 24$)	S1B	5.62^{a}	18.75^{c}	20.25^{c}	61.00^{b}	2.30^{b}	13.72^{b}	116.55^{a}
	S2B	5.72^{a}	22.38^{ac}	31.00^{ab}	46.63^{ab}	1.51^{ab}	10.23^{a}	97.35^{a}
	S3B	5.60^{a}	18.88^{c}	25.75^{ac}	55.38^{b}	1.57^{ab}	11.03^{b}	106.71^{a}
Non-bunded plots ($n = 24$)	S1W	5.54^{a}	33.25^{ab}	31.25^{ab}	35.50^{ac}	1.22^{ac}	10.41^{b}	106.73^{a}
	S2W	5.63^{a}	35.50^{b}	33.25^{b}	31.25^{c}	1.54^{ab}	13.03^{b}	101.30^{a}
	S3W	5.52^{a}	36.75^{b}	27.50^{ab}	35.75^{ac}	0.90^{c}	6.37^{a}	94.61^{a}
Mean		5.61	27.58	28.17	44.25	1.45	10.5	103.88
Significance		ns	**	***	***	***	*	ns

$^{a, b, c}$Different letters indicate significant differences in the table

OC Soil organic carbon; *av. P* Available phosphorus; *av. K* Available potassium. *S1* 2–5%; *S2* 5–10%; *S3* 10–15%; *B* soil bund; *W* without soil bund; values followed by the same letter are not significantly different at a probability level of 0.01; *ns* Not significant; * significance level; $n = 48$

Table 6.3 Relationship between soil color indices and soil parameters

Soil parameter	Model	RMSE (calibration)	RMSE (validation)
Clay	$y = 4.98 * HI + 39.76$	17.04	8.34
	$y = 39.50 * RI + 21.62$	16.98	7.54
Sand	$y = -376.39 * BI + 38.90$	13.57	7.96
	$y = -21.88 * RI + 43.12$	13.56	8.46
	$y = -2.01 * HI + 29.87$	13.71	8.89
OC	$y = 1.97 * RI + 0.49$	0.75	1.23
	$y = 24.27 * BI + 0.89$	0.75	1.23
	$y = 0.19 * HI + 1.43$	0.76	1.30

OC Soil organic carbon; *RMSE* Root mean square error; *RI* Redness index; *BI* Brightness index; *HI* Hue index

To explain the decreasing soil fertility in the Kecha catchment, Iticha and Takele (2019) suggested that inappropriate cultivation practices, clearance of crop residue and animal dung, leaching, and increased rates of erosion may be the cause of low levels of OC and av. K (Iticha and Takele 2019). However, bunding appears to have improved soil quality in mild slope classes (S1B) by enhancing the build-up of fine soil particles and readily available nutrients, resulting in the highest amounts of clay (61%), OC (2.30%), av. P (13.72 ppm), and av. K (116.55 mg/kg) values (Table 6.3).

These findings are consistent with claims that bundling can improve soil fertility (Ebabu et al. 2019). Nonetheless, pH, OC, av. P, and av. K values in the catchment are still below threshold levels, indicating a need to increase soil OM values via the use of sustainable land management (SLM) techniques (Reichert et al. 2021) to improve the soil quality in Ethiopia.

Modeling Soil Properties

To explore the association between soil parameters and soil reflectance, we conducted a regression analysis using spectral color indices as variables. To predict soil attributes based on soil color, it is typical to calibrate reflectance indices using models (Bachofer et al. 2015). Soil color is affected by soil humus and soil water content (Schulze et al. 1993). However, soil OC, clay, and sand contents were related weekly with color indices (Table 6.3).

This study utilized regression analysis to examine the association between soil parameters and soil reflectance-based indices such as the brightness index (BI), redness index (RI), and hue index (HI) as independent variables. The results showed that BI (Fig. 6.3a), RI (Fig. 6.3b), and HI (Fig. 6.3c) had an excellent coefficient of determination ($R^2 > 0.84$) for soil OC content. However, sand (Fig. 6.4a–c) and clay (Fig. 6.5a–b) contents showed low association ($R^2 < 0.57$) for all color indices. Regression models were created from reflectance and soil parameters to calibrate spectral indices for forecasting soil properties from soil color (Schulze et al. 1993; Bachofer et al. 2015).

The model was utilized to validate the performance of predicting soil parameters based on soil reflectance. There was a high coefficient of determination (R^2) for both calibration and validation of clay (0.93 and 0.96, respectively, with RMSE values of 4.51 and 3.97; Fig. 6.6). These results were better than those reported by similar studies in the sampling approaches and parameters evaluated, including Camargo et al. (2015); 0.70, Zhang et al. (2017); 0.64, and Silva et al. (2021); 0.66, and $R^2 =$ 0.73 and RMSE = 5.40 (Vasava et al. 2019), $R^2 = 0.83$ and RMSE = 0.34 (Yang et al. 2020), $R^2 = 0.62$ and RMSE = 2.06 (Haghi et al. 2021), and $R^2 = 0.71$–84 (Zhao et al. 2021).

For sand, we obtained $R^2 = 0.83$ and RMSE = 5.36 for calibration and $R^2 = 0.83$ and RMSE = 6.23 for validation (Fig. 6.6). Our findings are similar to those reported by (Vasava et al. 2019; $R^2 = 0.80$ with RMSE = 3.28) (Tümsavaş et al. 2018; R^2 = 0.81 with RMSE = 3.84), (Haghi et al. 2021; $R^2 = 0.90$, RMSE = 11.66) (Zhao

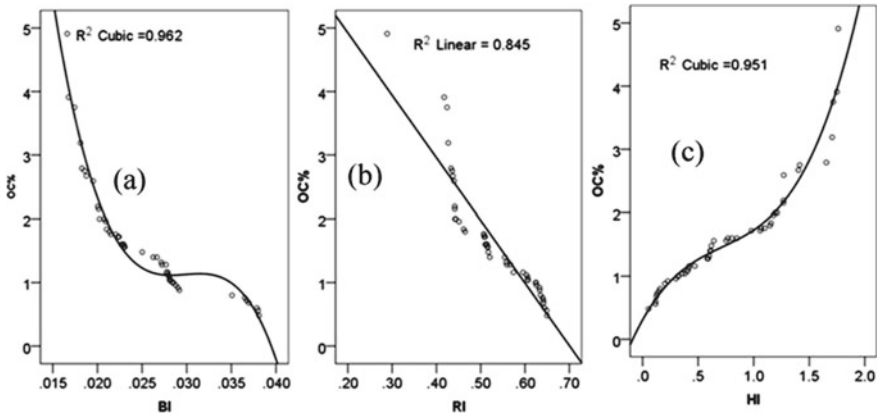

Fig. 6.3 Association between soil organic carbon (OC) content (%) and soil color indices. *OC* Soil organic carbon; R^2 Coefficient of determination; *RI* Redness index; *BI* Brightness index; *HI* Hue index

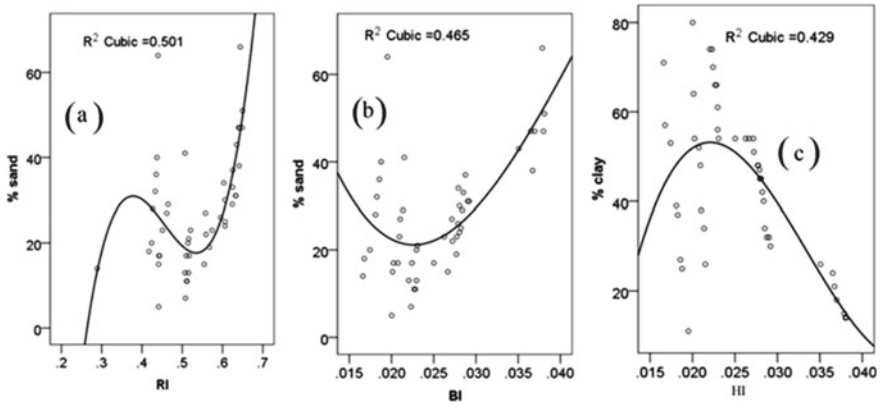

Fig. 6.4 Association between sand content (%) and soil color indices. R^2 Coefficient of determination of cubic regression; *RI* Redness index; *BI* brightness index; *HI* Hue index

et al. 2021; $R^2 = 0.56$ to 0.71) but more precise than those reported by (Yang et al. (2020); $R^2 = 0.76$ and RMSE = 0.92) and (Rodríguez-Pérez et al. 2021; $R^2 = 0.77$).

For soil OC, we obtained $R^2 = 0.82$ and 0.83 for calibration and validation, respectively, with RMSE values of 0.29 and 0.35 (Fig. 6.6). These values were excellent according to the R^2 threshold values of Saeys et al. (2005) and were consistent with those reported in earlier research, including (Leone et al. 2012; $R^2 = 0.84$–0.93), (Kuang and Mouazen 2012; $R^2 = 0.63$–0.90 and RMSE = 6.40–0.78), (Yang et al. 2012; $R^2 = 0.91$), (Amin et al. 2020; $R^2 = 0.85$ and RMSE = 3.77), (Gomez et al. 2013; $R^2 = 0.57$–0.7), (Gras et al. 2014; Wijevardane et al. 2016; $R^2 = 0.77$–0.83), and (Feyziyev et al. 2016; $R^2 = 0.764$ and RMSE = 0.344).

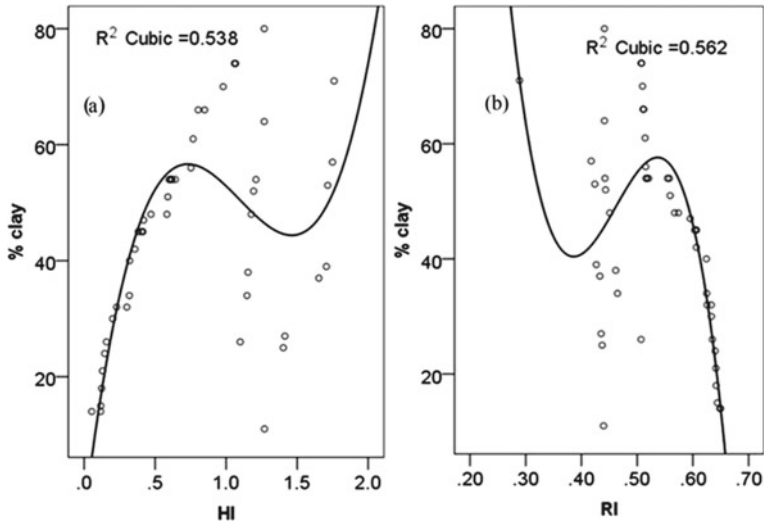

Fig. 6.5 Association between clay content (%) and HI and RI. R^2 coefficient of determination; *HI* Hue index

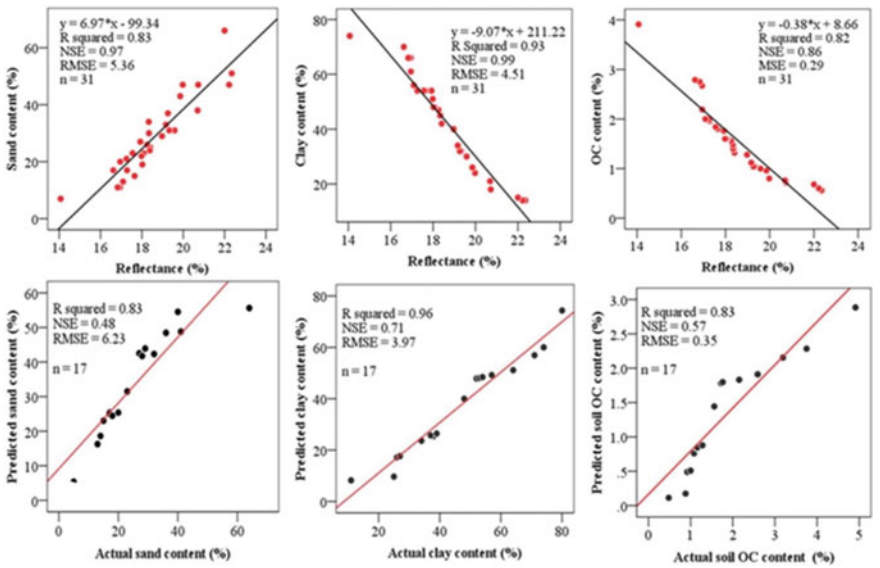

Fig. 6.6 Upper plots show scatter plots between sand, clay, and soil organic carbon (OC) content versus reflectance % (red dots) and best fitted model (black line). Bottom plots show scatter plots between predicted and actual sand, clay, and OC contents (%) along with performance metrics for each. The estimates are strongly correlated with the observed reflectance and OC, sand, and clay contents

Conclusions

In the Kecha catchment, soil bunds were found to have a beneficial effect on soil texture and organic carbon (OC) values. The differences in soil texture and OC between bunded and non-bunded plots on various slopes were substantial. It was observed that soils on lower slopes had higher pH values and higher concentrations of texture and OC than soils on higher slopes. These findings suggest that for sustainable soil management in the research area, it is essential to have site-specific data that can guide soil management interventions such as soil bundling. The study also revealed that bunded plot soils with lower reflectance showed increased soil quality. While soil organic carbon, clay, and sand content were poorly explained with reflectance indices, empirical equations were developed to accurately predict the texture and OC contents.

The study underscores the prospects of spectroscopy as a rapid, nondestructive technique for soil characterization and evaluation. It also has implications for spatial soil property monitoring. The establishment of improved and location-specific soil management methods using spectroradiometrically based soil prediction models would benefit landowners and governments. However, extra studies are needed to recognize which parts of the spectrum could enhance the projecting capabilities of spectroscopy, aid soil management improvements, and investigate their influences on more soil metrics.

Acknowledgements The Japan Science and Technology Research Partnership for Sustainable Development (JPMJSA1601) sponsored the work. We appreciate the help with our fieldwork and laboratory work that Anteneh Wubet, Agerselam Gualie, and Melkamu Wudu provided. We also appreciate the Kecha catchment farmers who allowed us to use their land. Finally, we acknowledge the anonymous reviewers and editors of the journal for their valuable comments on this paper.

References

Amare T, Terefe A, Selassie YG, Yitaferu B, Wolfgramm B, Hurni H (2013) Soil properties and crop yields along the terraces and toposequece of Anjeni Catchment, Central Highlands of Ethiopia. J Agric Sci 5(2):134. https://doi.org/10.5539/jas.v5n2p134

Amin I, Fikrat F, Mammadov E, Babayev M (2020) Soil organic carbon prediction by Vis-NIR spectroscopy: case study the Kur-Aras Plain, Azerbaijan. Commun Soil Sci Plant Anal 51(6):726–734. https://doi.org/10.1080/00103624.2020.1729367

Bachofer F, Quénéhervé G, Hochschild V, Maerker M (2015) Multisensoral topsoil mapping in the semiarid Lake Manyara region, Northern Tanzania. Remote Sens 7(8):9563–9586. https://doi.org/10.3390/rs70809563

Bastos Lima MG (2021) The contested sustainability of biofuels in a north–south context. In: The politics of bioeconomy and sustainability. Springer, Cham, pp 23–47. https://doi.org/10.1007/978-3-030-66838-92

Berihun ML, Tsunekawa A, Haregeweyn N, Dile YT, Tsubo M, Fenta AA et al (2020) Evaluating runoff and sediment responses to soil and water conservation practices by employing alternative

modeling approaches. Sci Total Environ 747:141118. https://doi.org/10.1016/j.scitotenv.2020.141118

Bouyoucos GJ (1962) Hydrometer method improved for making particle size analyses of soils. Agron J 54:464–465. https://doi.org/10.2134/agronj1962.00021962005400050028x

Bray RH, Kurtz LT (1945) Determination of total, organic, and available forms of phosphorus in soils. Soil Sci 59(1):39–46. https://doi.org/10.1097/00010694-194501000-00006

Brown DJ, Shepherd KD, Walsh MG, Dewayne Mays M, Reinsch TG (2006) Global soil characterization with VNIR diffuse reflectance spectroscopy. Geoderma 132:273–290. https://doi.org/10.1016/j.geoderma.2005.04.025

Camargo LA, Júnior JM, Barrón V, Alleoni LRF, Barbosa RS, Pereira GT (2015) Mapping of clay, iron oxide and adsorbed phosphate in Oxisols using diffuse reflectance spectroscopy. Geoderma 251:124–132. https://doi.org/10.1016/j.geoderma.2015.03.03.027

Ebabu K, Tsunekawa A, Haregeweyn N, Adgo E, Meshesha DT, Aklog D et al (2019) Effects of land-use and sustainable land management practices on runoff and soil loss in the Upper Blue Nile Basin, Ethiopia. Sci Total Environ 648:1462–1475. https://doi.org/10.1016/j.scitotenv.2018.08.273

Ebabu K, Tsunekawa A, Haregeweyn N, Adgo E, Meshesha DT, Aklog D et al (2020) Exploring the variability of soil properties as influenced by land-use and management practices: a case study in the Upper Blue Nile Basin, Ethiopia. Soil Tillage Res. 200:104614. https://doi.org/10.1016/j.still.2020.104614

Escadafal R, Belghit A, Ben-Moussa A (1994) Indices spectraux pour la télédétection de la dégradation des milieux naturels en Tunisie aride. In: Proceedings of the 6th international symposium on physical measurements and signatures in remote sensing, pp 17–21

EthioSIS (Ethiopia Soil Information System) (2014) Soil fertility status and fertilizer recommendation atlas for Tigray regional state, Ethiopia. July 2014, Addis Ababa, Ethiopia

Feyziyev F, Babayev M, Priori S, L'Abate G (2016) Using visible-near-infrared spectroscopy to predict soil properties of Mugan Plain, Azerbaijan. Open J Soil Sci 6(03):52–58. https://doi.org/10.4236/ojss.2016.63006

Gholizadeh A, Borůvka L, Saberioon M, Vašát R (2013) Visible, near-infrared, and mid-infrared spectroscopy applications for soil assessment with emphasis on soil organic matter content and quality: state-of-the-art and key issues. Appl Spectrosc 67(12):1349–1362. https://doi.org/10.1366/13-07288

Gomez C, Le Bissonnais Y, Annabi M, Bahri H, Raclot D (2013) Laboratory Vis–NIR spectroscopy as an alternative method for estimating the soil aggregate stability indices of Mediterranean soils. Geoderma 209:86–97. https://doi.org/10.1016/j.geoderma.013.06.002

Gras JP, Barthès BG, Mahaut B, Trupin S (2014) Best practices for obtaining and processing field visible and near-infrared (VNIR) spectra of topsoils. Geoderma 214:126–134. https://doi.org/10.1016/j.geoderma.2013.09.021

Guadie M, Molla E, Mekonnen M, Cerda A (2020) Effects of soil bund and stone-faced soil bund on soil physicochemical properties and crop yield under rain-fed conditions of Northwest Ethiopia. Land 9(1):13 (2020). https://doi.org/10.3390/land9010013

Hadaro M, Ayele T, Parshotam Datt S, Teshome R (2021) Soil properties as affected by soil conservation practices and soil depths in Uwite Catchment, Hadero Tunto District, Southern Ethiopia. Appl Environ Soil Sci, 1–13. https://doi.org/10.1155/2021/5542326

Haghi RK, Pérez-Fernández E, Robertson AHJ (2021) Prediction of various soil properties for a national spatial dataset of Scottish soils based on four different chemometric approaches: a comparison of near-infrared and mid-infrared spectroscopy. Geoderma 396:115071. https://doi.org/10.1016/j.geoderma.2021.115071

Iticha B, Takele C (2019) Digital soil mapping for site-specific management of soils. Geoderma 351:85–91. https://doi.org/10.1016/j.geoderma.2019.05.026

Karltun E, Lemenih M, Tolera M (2013) Comparing farmers' perception of soil fertility change with soil properties and crop performance in Beseku, Ethiopia. Land Degrad Dev 24(3):228–235. https://doi.org/10.1002/ldr.1118

Kassawmar T, Zeleke G, Bantider A, Gessesse GD, Abraha L (2018) A synoptic land change assessment of Ethiopia's rain-fed agricultural area for evidence-based agricultural ecosystem management. Heliyon 4(11):e00914. https://doi.org/10.1016/j.heliyon.2018.e00914

Kuang B, Mouazen AM (2012) Influence of the number of samples on prediction error of visible and near-infrared spectroscopy of selected soil properties at the farm scale. Eur J Soil Sci 63(3):421–429. https://doi.org/10.1111/j.1365-2389.2012.01456.X

Leone APA, Viscarra-Rossel R, Amenta P, Buondonno A (2012) Prediction of soil properties with PLSR and Vis-NIR spectroscopy: application to Mediterranean soils from Southern Italy. Curr Anal Chem 8(2):283–299

De Marins AC, Reichert JM, Secco D, Rosa HA, Veloso G (2018) Crambe grain yield and oil content affected by spatial variability in soil physical properties. Renew Sustain Energy Rev. https://doi.org/10.1016/j.rser.2017.08.003

Mathieu R, Pouget M (1998) Relationships between satellite-based radiometric indices simulated using laboratory reflectance data and typic soil color of an arid environment. Remote Sens Environ 66:17–28. https://doi.org/10.1016/s0034-4257(98)00030-3

Morellos A, Pantazi XE, Moshou D, Alexandridis T, Whetton R, Tziotzios G et al (2016) Machine learning based prediction of soil total nitrogen, organic carbon, and moisture content by using Vis-NIR spectroscopy. Biosyst Eng 152:104–116. https://doi.org/10.1016/j.biosystemseng.2016.04.018

Morgan GH (1941) Chemical diagnosis by the Universal Soil Testing System. Conn. Agr. Exp. Sta. (New Haven), Bull 450. USA, pp 573–628

Moriasi DN, Arnold JG, Van Liew MW, Bingner RL, Harmel RD, Veith TL (2007) Model evaluation guidelines for systematic quantification of accuracy in catchment simulations. Trans ASABE 50(3):885–900

Murphy J, Riley JP (1962) A modified single-solution method for the determination of phosphorus in natural waters. Anal Chim Acta 27:31–36. https://doi.org/10.1016/S0003-2670(00)88444-5

Nash JE, Sutcliffe JV (1970) River flow forecasting through conceptual models part I—a discussion of principles. J Hydrol 10:282–290. https://doi.org/10.1016/0022-1694(70)90255-6

NMSA (National Meteorological Survey Agency) (2004) Ethiopia. http://www.Ethiomet.gov.et/

Nyssen J, Poesen J, Gebremichael D, Vancampenhout K, D'aes M, Yihdego GM et al (2006) Assessment of mined soils in erosion-degraded farmlands in southeastern Nigeria. Estudos de Biologia 28(65)

Osman EAM, El-Masry AA, Khatab KA (2013) Effect of nitrogen fertilizer sources and foliar spray of humic and/or fulvic acids on yield and quality of rice plants. Adv Appl Sci Res 4(4):174–183

Peech M (2016) Hydrogen-ion activity. Amer Soc Agron Madison, Wisconsin 9:914–926

Peel MC, Finlayson BL, McMahon TA (2007) Updated world map of the Köppen-Geiger climate classification. Hydrol Earth Sys Sci Discussions 4:439–473

Reichert JM, Corcini AL, Awe GO, Reinert DJ, Albuquerque JA, Gallarreta CCG et al (2022) Onion-forage cropping systems on a Vertic Argiudoll in Uruguay: onion yield and soil organic matter, aggregation, porosity and permeability. Soil Tillage Res. 216:105229. https://doi.org/10.1016/j.still.2021.105229

Reichert JM, Norton LD (2013) Rill and interrill erodibility and sediment characteristics of clayey Australian Vertosols and a Ferrosol. Soil Res 51(1):1–9. https://doi.org/10.1071/SR12243

Reichert JM, Fontanela E, Awe GO, Fasinmirin JT (2021a) Is cassava yield affected by inverting tillage, chiseling or additional compaction of no-till sandy-loam soil? Revista Brasileira de Ciência do Solo 45:e0200134. https://doi.org/10.36783/18069657rbcs20200134

Rodríguez-Pérez JR, Marcelo V, Pereira-Obaya D, García-Fernández M, Sanz-Ablanedo E (2021) Estimating soil properties and nutrients by visible and infrared diffuse reflectance spectroscopy to characterize vineyards. Agronomy 11(10):1895. https://doi.org/10.3390/agronomy11101895

Rosemary F, Indraratne SP, Weerasooriya R, Mishra U (2017) Exploring the spatial variability of soil properties in an Alfisol soil catena. CATENA 150:53–61. https://doi.org/10.1016/j.catena.2016.10.017

Rowell DL (1997) Soil science: methods and applications. Longman Singapore Publishers Ltd., Singapore, 350 p

Saeys W, Mouazen AM, Ramon H (2005) Potential for onsite and online analysis of pig manure using visible and near-infrared reflectance spectroscopy. Biosyst Eng 91(4):393–402

Schulze DG, Nagel JL, Van Scoyoc GE, Henderson TL, Baumgardner MF, Stott DE (1993) Significance of organic matter in determining soil colors. Soil Color 31:71–90. https://doi.org/10.2136/sssaspecpub31.c5

Silva IM, Romero DJ, Guimarães CCB, Alves MR, Osco LP, Souza ABE et al (2021) Readily dispersible clay in soils from different Brazilian regions by visible, near, and mid-infrared spectral data. Int J Remote Sens 42(18):6943–6960. https://doi.org/10.1080/01431161.2021.1948625

Tellen VA, Yerima BP (2018) Effects of land-use change on soil physicochemical properties in selected areas in the North West region of Cameroon. Environ Syst Res 7:3. https://doi.org/10.1186/s40068-018-0106-0

Tümsavaş Z, Tekin Y, Ulusoy Y, Mouazen AM (2018) Prediction and mapping of soil clay and sand contents using visible and near-infrared spectroscopy. Biosyst Eng, 1–11. https://doi.org/10.1016/j.biosystemseng.2018.06.008

USDA (United States Department of Agriculture) (1996) Soil survey laboratory methods manual. Soil Survey investigations Rep. 42, Ver.3.0. National Soil Survey Center, Lincoln, NE

Vašát R, Kodešová R, Borůvka L, Jakšík O, Klement A, Brodský L (2017) Combining reflectance spectroscopy and the digital elevation model for soil oxidizable carbon estimation. Geoderma 303:133–142. https://doi.org/10.1016/j.geoderma.2017.05.018

Vasava HB, Gupta A, Arora R, Das BS (2019) Assessment of soil texture from spectral reflectance data of bulk soil samples and their dry-sieved aggregate size fractions. Geoderma 337:914–926. https://doi.org/10.1016/j.geoderma.2018.11.004

Walkley A, Black CA (1934) An examination of the Degtijareff method for determining soil organic matter and a proposed modification of the chromic acid filtration method. Soil Sci 37:93–101. https://doi.org/10.1097/00010694-193401000-00003

Wijevardane N, Ge Y, Wills S, Loecke T (2016) Prediction of soil carbon in the conterminous United States: visible and near-infrared reflectance spectroscopy analysis of the rapid carbon assessment project. Soil Sci Soc Am J 80(4):973–982. https://doi.org/10.2136/sssaj2016.02.0052

Yang H, Kuang B, Mouazen AM (2012) Quantitative analysis of soil nitrogen and carbon at a farm scale using visible and near-infrared spectroscopy coupled with wavelength reduction. Eur J Soil Sci 63(3):410–420. https://doi.org/10.1111/j.1365-2389.2012.01443.x

Yang M, Mouazen A, Zhao X, Guo X (2020) Assessment of a soil fertility index using visible and near-infrared spectroscopy in the rice paddy region of Southern China. Eur J Soil Sci 71(4):615–626. https://doi.org/10.1111/ejss.12907

Zhang C, Jiang H, Liu F, He Y (2017) Application of near-infrared hyperspectral imaging with variable selection methods to determine and visualize caffeine content of coffee beans. Food Bioprocess Technol 10:213–221. https://doi.org/10.1007/s11947-016-809-8

Zhao D, Arshad M, Li N, Triantafilis J (2021) Predicting soil physical and chemical properties using Vis-NIR in Australian cotton areas. CATENA 196:104938. https://doi.org/10.1016/j.catena.2020.104938

Chapter 7
Identifying Soil Erosion Hotspot Areas Using GIS and MCDA Techniques: Case Study of the Dengora and Meno Watersheds in Belesa Woredas, Amhara Region

Kefale Munye, Gashaw Sintayehu, Alemshet Belayneh, Mamaru Ayalew, and Melaku Wendachew

Abstract In Ethiopia, accelerated soil erosion and land degradation have become key issues because of the country's rugged terrain and steep slope topography. The main objective of this study was to identify soil erosion hotspot areas in the Dengora and Meno watersheds using the Revised Universal Soil Loss Equation (RUSLE) and multicriteria decision analysis (MCDA) techniques. To achieve this objective, the RUSLE model was used to estimate potential soil losses by utilizing information on soil, land use/cover, topography, and climate data. The MCDA technique considered land use, soil type, topographic wetness index, stream power index, and potential location of gullies. The factors were weighted using a pairwise comparison matrix, and weights were combined using weighted overlay. Based on the RUSLE model, the average annual soil loss of the Dengora and Meno watersheds reached 223.97 and 256.09 tons ha^{-1} yr^{-1}, respectively. In the Dengora watershed, 70.4%, 18.7%, 10.74%, and 0.14% of the total watershed area were slightly, moderately, highly, and very highly sensitive to soil erosion, respectively, while in the Meno watershed, 76%, 16.54%, 7.3%, and 0.14% were the corresponding values. The GIS-based MCDA technique revealed that in the Dengora watershed, 9.7%, 64.5%, 18%, and 7.8% of the total watershed area were highly, moderately, slightly, and currently not sensitive to soil erosion, respectively. The corresponding values for the Meno watershed were

K. Munye (✉) · G. Sintayehu · A. Belayneh
Department of Water Resources and Irrigation Engineering, Institute of Technology, Woldia University, P.O. Box 400, Woldia, Ethiopia
e-mail: kefalemunye1921@gmail.com

M. Ayalew
Department of Hydraulic and Water Resources Engineering, Institute of Technology, Bahir Dar University, P.O. Box 76, Bahir Dar, Ethiopia

M. Wendachew
Department of Water Resources and Irrigation Engineering, Institute of Technology, Woldia University, P.O. Box 400, Woldia, Ethiopia

A. M. Melesse et al. (eds.), *Land and Water Degradation in Ethiopia*, Springer Geography, https://doi.org/10.1007/978-3-031-60251-1_7

6.1%, 71.3%, 23.23%, and 0.375%, respectively. Based on validation and field-level observations, the MCDA model prediction was more accurate than that of the RUSLE model. Both watersheds were at moderate risk. The bottomlands of the watersheds were highly sensitive to erosion. Therefore, immediate attention should be given to soil and water conservation practices.

Keywords Dengora watershed · Erosion hotspot · GIS · Meno watershed · MCDA · RUSLE

Introduction

In Ethiopia, accelerated soil erosion and land degradation have become key issues because of the country's rugged terrain and steep slope topography. Poor land use practices, particularly inadequate soil and water conservation practices and cultivation of steep slopes, significantly contribute to soil erosion and land degradation (Onyando et al. 2005). Soil erosion is worsening due to deforestation, overgrazing, poor farming practices, and cultivation of marginal lands (Valentin et al. 2005). It has on-site and off-site impacts; the on-site impacts include loss of agricultural land leading to reduction in food production, while off-site effects include siltation of rivers and reservoirs leading to water quality deterioration (Asquith et al. 2005). Soil erosion and sediment transport studies have shown that areas of land degradation correspond to poor watershed management and severed deforestation (Aga et al. 2018, 2019; Defersha and Melesse 2012a, b; Defersha et al. 2010, 2012; Defersha et al. 2011; Maalim and Melesse 2013; Maalim et al. 2013; Setegn et al. 2010; Melesse et al. 2011; Msagahaa et al. 2014; Wang et al. 2008; Mekonnen and Melesse 2011; Setegn et al. 2009; Mohammed et al. 2015).

According to the Ethiopian highland reclamation study (Yilma and Awulachew 2009), in the mid-1980s, 27 million hectares or almost 50% of the highland area was significantly eroded, 14 million hectares was seriously eroded, and over 2 million hectares was beyond reclamation. Efforts have been made to manage this loss. However, a number of previous studies have noted that such arrangements were unsatisfactory and incompatible due to ineffective community participation in the planning stage, improper intervention selection, poor management after construction, lack of integration with biological conservation measures, and other factors among smallholder farmers (Hurni 1989). Immediate action is required to estimate the soil erosion rate and identify high erosion source areas in watersheds.

The highlands of Ethiopia, in which the Dengora and Meno watersheds are located, are facing severe problems arising from excessive erosion resulting in decreasing agricultural productivity, decreasing reservoir storage capacity, and increasing environmental degradation. Due to decreasing crop production, communities living in both watersheds have been categorized as food-insecure areas since 1999 by the regional government. In most watersheds, gully formation and sheet erosion with exposure of rock and stones on previously cultivated steep upper slopes are the

most visible evidence showing erosion problems in this area (Birru 2007). Excessive soil erosion from the Dengora watershed has reduced the storage capacity of the Atilkanay artificial reservoir located at the outlet of the Dengora watershed. Soil and water conservation measures have been implemented in the watershed in recent decades. However, these were not successful due to a lack of targeted recommendation measures.

The purpose of this study is to identify the soil erosion source areas in the Dengora and Meno watersheds for conservation priority. The RUSLE model was used to estimate soil loss, and GIS-based multicriteria decision analysis (MCDA) was used to identify erosion hotspot source areas from watersheds. This helps to identify different soil and water conservation measures required in the watershed.

Materials and Methods

Description of the Study Area

The study areas, the Dengora and Meno watersheds, are located in the Tekeze basin of Amhara National Regional State in East and West Belesa Woredas, respectively (Fig. 7.1). The geographical coordinates of the Dengora watershed range from 38°2′35″ E to 38°3′15″ E and 12°23′0″ N to 12°23′30″ N, and the Meno watershed ranges from 37°46′2″ E to 37°46′45″ E and 12°26′50″ E to 12°27′25″ N. Both watersheds are characterized by highly rugged and undulating topography on the upper part and gently flat valley bottom land. The elevation ranges in the Dengora and Meno watersheds are between 1898 and 2172 m and 1888 and 2091 m above mean sea level, respectively. The climate of both watersheds can be characterized as semiarid, with mean annual rainfalls of 949.5 and 841.85 mm/year and average temperatures of 31.5 °C and 30 °C for the Dengora and Meno watersheds, respectively. Most of the rainfall occurs between July and August during the main rainy season.

Data and Methods

The RUSLE model and GIS-based MCDA technique require spatial data input. The required data include rainfall, gully location, land use, digital elevation model (DEM), and soil type. The necessary data were collected from both primary and secondary sources (Table 7.1).

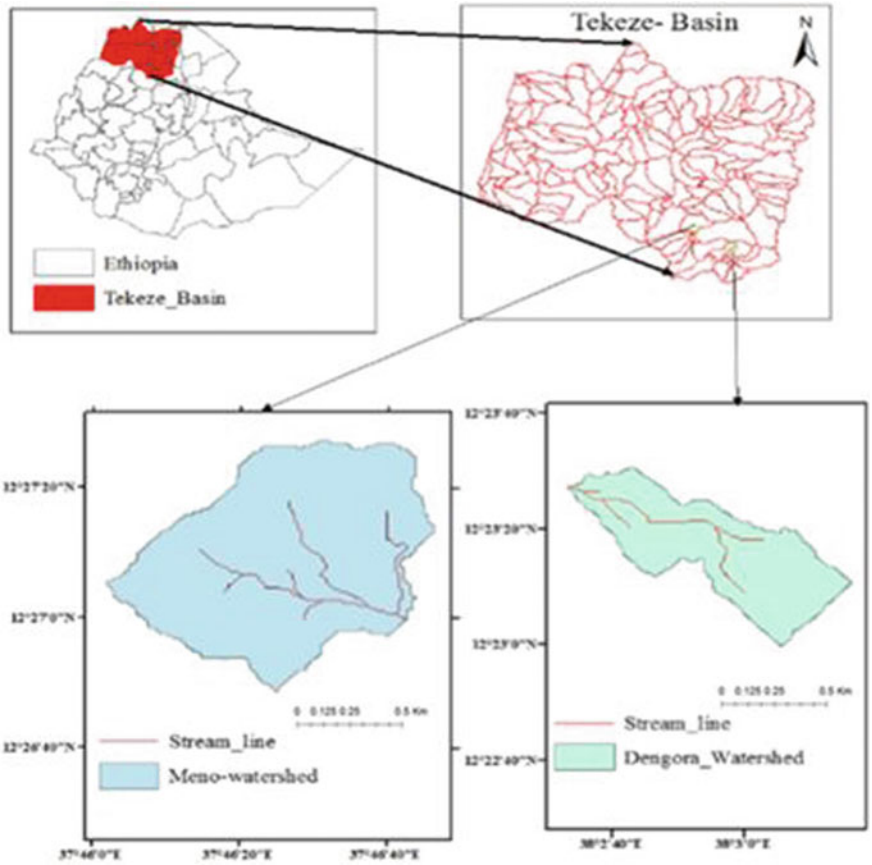

Fig. 7.1 Location of the study area

Table 7.1 Type, purpose, and sources of data/material

S. No.	Data type	Purposes	Sources
1	Digital elevation model (DEM)	To delineate watershed and generate slope	Website: http://gdex.cr.usgs.gov/gdex/
2	Landsat 8 images	To generate land use land cover map (LULC)	Website: http://landsat.usgs.gov/landsat8.php
3	Soil type	To produce soil map	Ministry of Water, Irrigation and Energy (MoWIE), Addis Ababa
4	Rainfall	To generate rainfall map	National Meteorological Agency (NMA), Arbay and Guala metrological branch
5	Global positioning systems (GPS)	For ground control points (LULC and gully location)	–

Group Discussion and Participatory Transect Walk

Focus group discussion is a qualitative research method and data collection technique in which a selected group of people discuss a given topic in depth, facilitated by a professional, external moderator (Twinn 1998). For this study, a total of four focus group discussions were conducted independently in both watersheds. A total of 8 women and 10 men participated in the focus group discussions. Additionally, in-depth interviews with Kebele-level development agents were conducted in each watershed. A total of four development agents were interviewed, two development agents per watershed. After discussing the community and the development agents and understanding soil erosion risk and resource status (vegetation density, soil, and water), factors contributing to soil erosion in the watersheds were identified. After focus group discussion, members also participated in transect walks across the watersheds. During the transect walk, land use/land cover types, slope gradient, highly erodible areas/gully locations, slope length, soil color, and drainage patterns were documented. The transect walk was also used for validation of hotspot areas.

Data Analysis

After collecting the required data, spatial analysis was performed to prepare the MCDA criteria map and RUSLE factors for the source area investigation and soil loss estimation, respectively. Landsat 8 images together with intensive field point data collection were used to perform supervised land use classification in the ArcGIS environment. The output map is validated and used to produce a land use criteria map based on land use suitability classes. A soil map from the Ministry of Water, Irrigation and Energy (MoWIE) was directly used to produce a soil criteria map based on soil type suitability classes. A digital elevation model (DEM) with a 30 m resolution was used to produce three criteria maps: topographic wetness index, stream power index, and potential location of gullies. The topographic wetness index and stream power index of the catchment were predicted based on the flow accumulation and slope of individual pixels.

The potential locations of gullies were predicted based on the threshold concept of two criteria: the topographic wetness index and stream power index. The parameters were identified and classified into subclasses to obtain the relative weights using the pairwise comparison method, and the soil erosion factors were weighted and overlaid to produce final soil erosion source areas in terms of spatial representation in the watershed.

RUSLE Model Description

Modeling of soil erosion and estimation of soil loss were performed using the Revised Universal Soil Loss Equation (RUSLE). The Revised Universal Soil Loss Equation (RUSLE) by Renard et al. (1991) is the most widely used soil erosion model (Salehi et al. 1991; Mhiret et al. 2019). The RUSLE model predicts long-term average annual soil erosion for a range of sites where the mineral soil has been exposed to raindrop impacts and surface runoff. The RUSLE model is computer-based and replaces tables, monographs, and calculations with keyboard entries (Dube et al. 2014; Mhiret et al. 2019; Desmet and Govers 1996).

This method was developed based on the Universal Soil Loss Equation (USLE) (Renard et al. 1991; Mhiret et al. 2019). RUSLE uses the same formula as USLE but has several improvements. Hurni (1985) modified the USLE to fit Ethiopian conditions. The RUSLE model parameters, such as the potential ability of rain to cause erosion, are a function of the physical characteristics of rainfall, represented by rainfall erosivity (R), and the resistance of soil to detachment from parent material and transport from its original position, represented by the soil erodibility factor (K). The effect of soil erosion on topography on soil erosion is accounted for by the slope steepness length factor (LS). The cover (C) factor represents the ratio of soil loss under a given cover to that of bare soil, and conservation practice (P), reflecting the positive impacts of management through the control of runoff, was estimated and used for quantifying the mean annual soil erosion loss rate in the Dengora and Meno watersheds.

Multicriteria Decision Analysis (MCDA)

Multicriteria decision analysis (MCDA) is an instrument that helps users improve their decision-making processes. It helps to explore a range of alternatives considering multiple criteria and goals (Voogd 1983). Multicriteria decision analysis compares different alternatives based on specific criteria. These criteria are often translations of the study objectives. Numerous researchers have studied the use of MCDA techniques in particular areas to conserve natural resources management (Tecle 1990; Malczewski 1996). In this study, the GIS-based MCDA technique helps to delineate the most erosion-prone area within the study areas. It is used to compare various alternatives with the help of certain criteria to identify erosion hotspot areas. MCDA helps in prioritizing high-risk watersheds for soil conservation practices. The outcomes are often in the form of selection, classification, or ranking of alternatives.

To perform MCDA for hotspot area identification using GIS, land use/cover, soil type, topographic wetness index, stream power index (SPI), and potential gully location were used as input factors. GIS-aided analysis was then performed to obtain a map for each criterion. For the multicriteria evaluation of factor generation, three main types of data inputs were used: land cover, DEM, and soil type. These are then

used to generate soil erosion factor maps such as land use/land cover maps, soil maps, slopes, and potential gully location maps of the Dengora and Meno watersheds. This study used a pairwise comparison technique to assign the weights of the decision factors since it has less bias than other techniques, such as the ranking technique. In the pairwise comparison technique, each factor is matched head-to-head (one-to-one) with each other, and a comparison matrix was prepared to express the relative importance.

Identification of Potential Gully Location

For the prediction of potential gully locations, the wetness of the catchment or topographic wetness index (TWI) and stream power index (SPI) were predicted based on the flow accumulation and slope of individual pixels on the Dengora and Meno watershed boundaries to derive gully locations. The potential locations of gullies were predicted to be where two thresholds were satisfied, i.e., the stream power index (SPI) was greater than 16.8 and the topographic wetness index (TWI) was greater than 6.8 (Lulseged and Vlek 2005). The SPI indicates locations where gullies might be more likely to form on the landscape. A higher value of SPI indicates a possible source of soil erosion due to concentrated runoff. The TWI predicts zones of saturation encountered along drainage paths and in zones of water concentration in landscapes. Gullies occur where surface water flow has become trapped in a small, concentrated stream and begins to erode channels in the ground surface. Therefore, we consider the effect of the SPI in combination with the TWI to identify gully prone areas, which are included in the pairwise matrix named "gully". TWI and SPI maps were overlaid to generate a combined map of potential gully locations (Fig. 7.2).

Results and Discussions

Soil Loss Factors

Rainfall Erosivity Factor

The erosion contribution of precipitation is represented by the rainfall erosivity factor R. R was originally estimated from both rainfall and rainfall intensity. However, these data are usually unavailable in developing countries unless there are standard meteorological stations. A common solution is to use correlations between the R factor and annual rainfall to estimate the erosivity factor as derived by (Hurni 1985) for Ethiopian conditions. With mean annual rainfall of 949.5 and 841.85 mm/year for the Dengora and Meno watersheds, respectively, the corresponding erosivity factors are 804.84 and 712.67 mm, respectively.

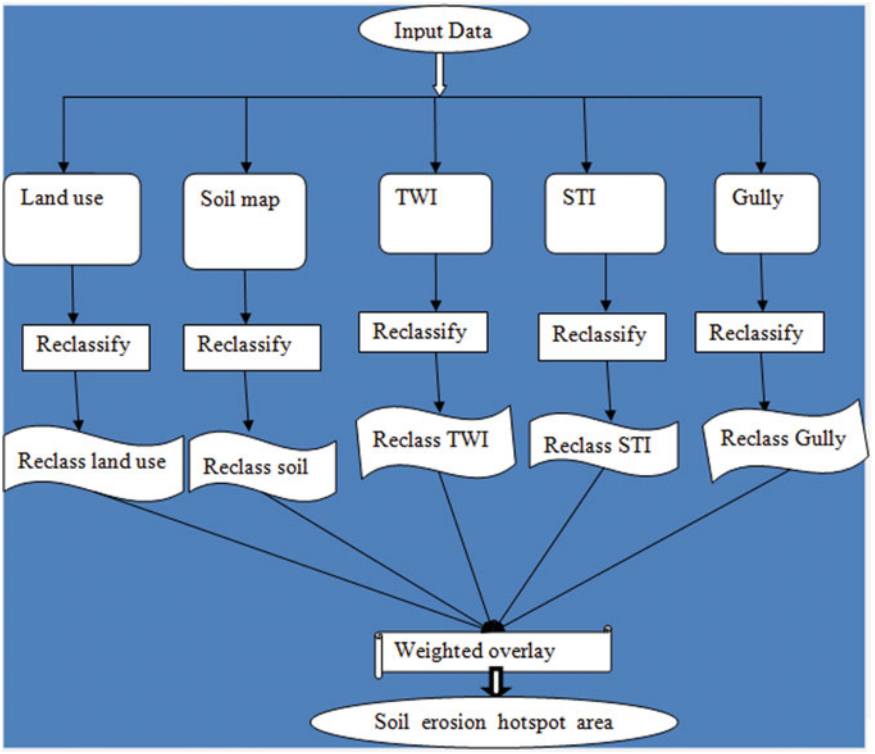

Fig. 7.2 Workflow charts of the criteria weighting using MCDA in Arc GIS 10.1

Soil Erodibility Factor (*K*)

Soil erodibility represents the effect of soil properties on soil erosion. A high *k* factor value indicates a higher vulnerability of soil to erosion, and a smaller value shows a lower vulnerability to soil erosion. In this study, the FAO standard classification of soil type was obtained from the Ministry of Water, Irrigation and Electricity (MoWIE) (Fig. 7.3).

Based on the soil erodibility map, Leptic Luvisols, Heplic Luvisols, and Hyperskeletic Leptosols had higher *K* values (0.2), indicating that they were more sensitive to soil erosion. The other two soil types (Eutric Leptosols and Eutric Leptosols) had medium *k* values (0.15), and Lithic Leptosols had small *k* values (0.1). Exposed rock constrained soil erosion. Based on soil erodibility capacity (*K*) values, the upper and lower parts of the Dengora watershed and the lower part of the Meno watershed were relatively highly sensitive to soil erosion. Soil physical properties such as soil wetness, water holding capacity, and infiltration rate have a great influence on the erodibility of soil.

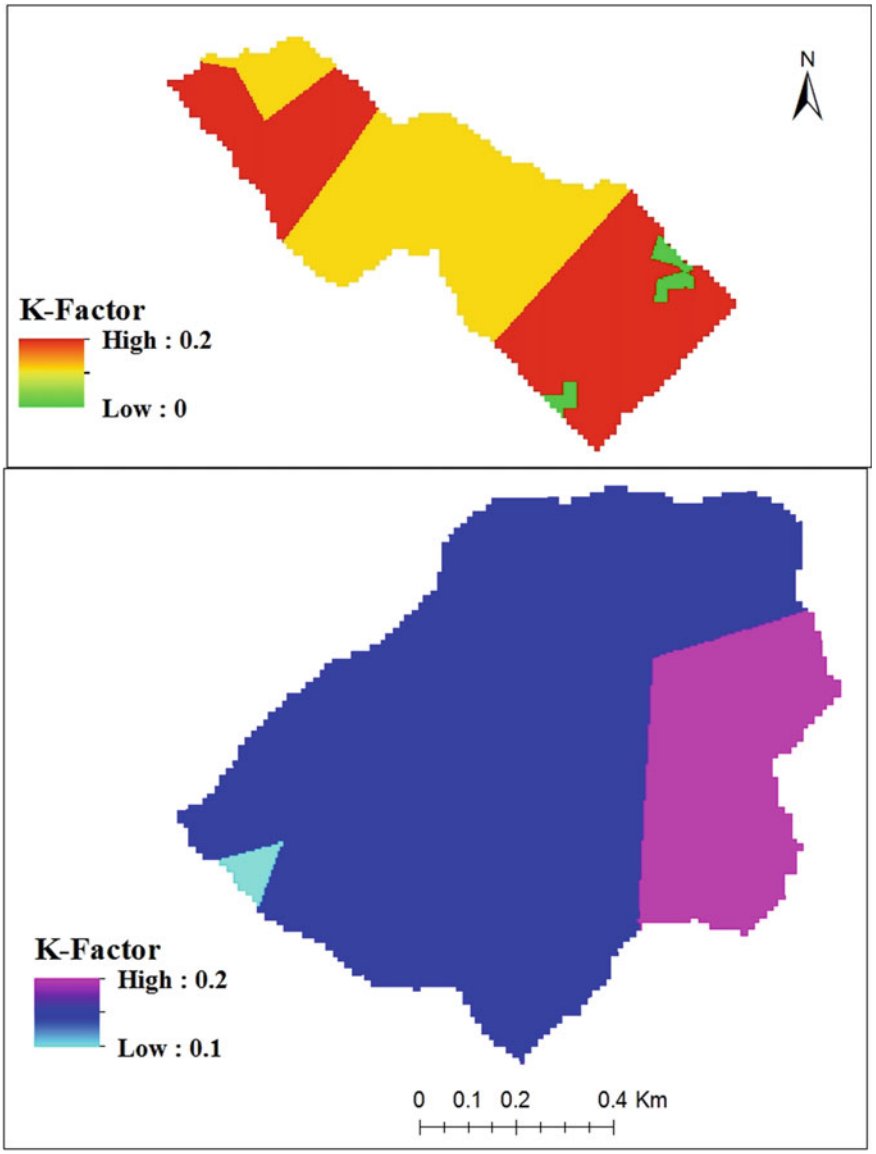

Fig. 7.3 *K* factor map of Dengora (top) and Meno (bottom) watersheds

Topographic Factors (LS)

Topographic factors (LS) were one of the major contributors to the soil erosion rate. The values of the LS factor range from 0 to 41.19 and 0 to 46.69 for the Dengora and Meno watersheds, respectively, as indicated in Fig. 7.4.

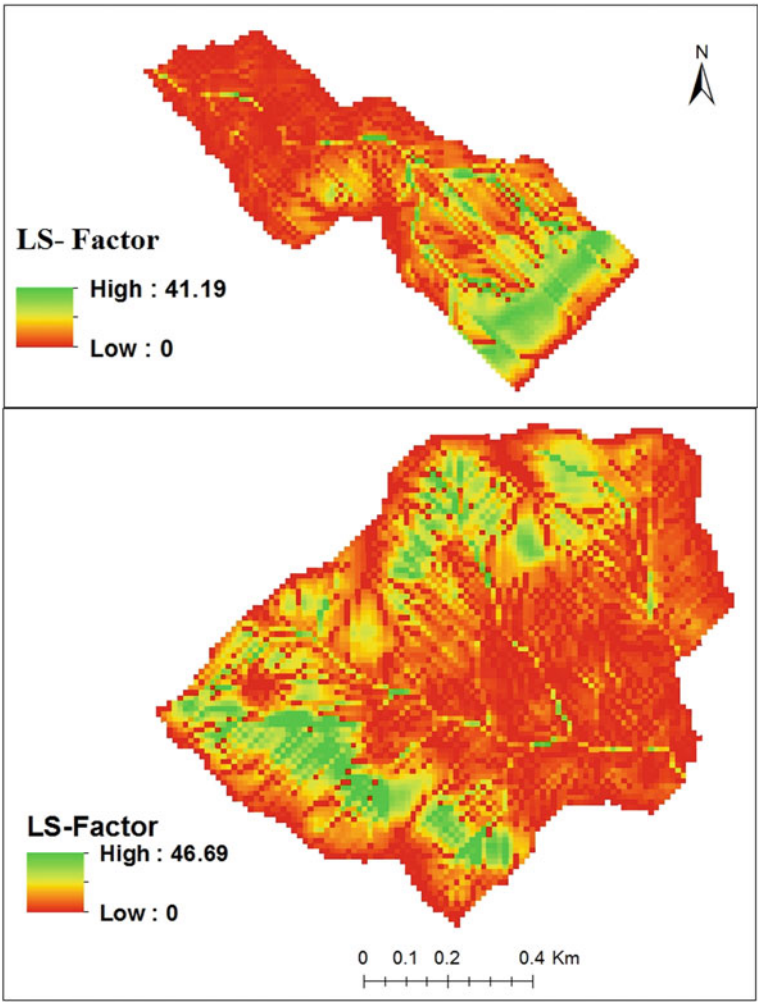

Fig. 7.4 Topographic (LS) factor of Dengora (top) and Meno (bottom) watersheds

Land Cover Factor (*C*)

A land use and land cover map of the study area was prepared from Landsat 8 satellite images acquired in 2019. The maximum likelihood supervised land use/land cover classification type was employed using ArcGIS software. In addition, ground truthing data were used as a vital reference for supervised classification, accuracy assessment, and validation of the results. In the supervised image classification technique, land use and land cover types were classified to use the classified images as inputs for generating the crop management (*C*) factor and support practice (*P*) factor. Based on

the land cover classification map, a corresponding *C* value was suggested by Hurni (1985). The land cover factor map is presented in Fig. 7.5.

Land Management Practice Factor (*P*)

The *P* factor was assessed using major land cover and slope interactions adopted by Wischmeier and Smith (1978) for Ethiopia. The data related to the management practices of the study watershed were collected during field work. Therefore, values

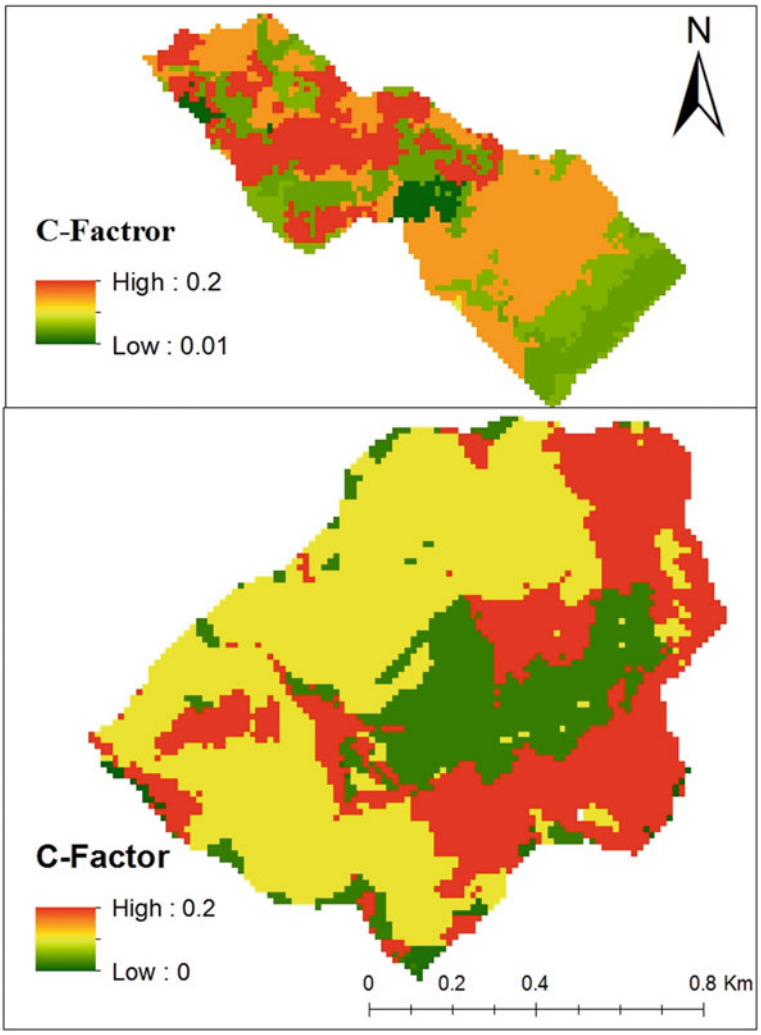

Fig. 7.5 Land cover (*C*) factor map for the Dengora (top) and Meno (bottom) watersheds

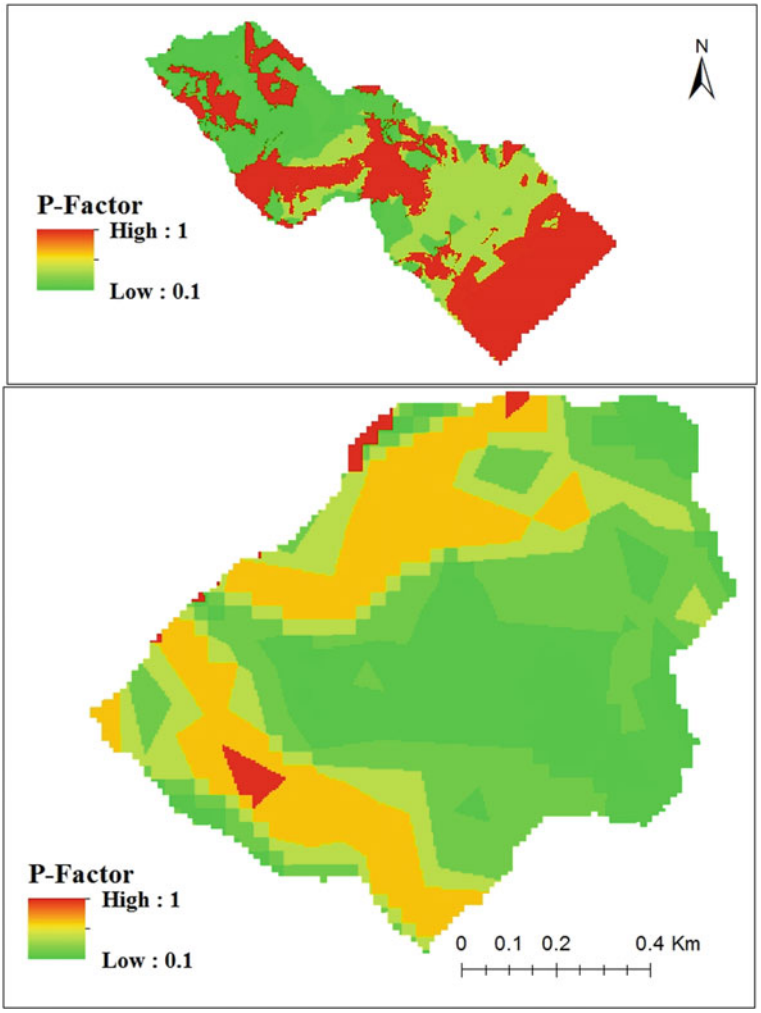

Fig. 7.6 Land management (*P*) factor Dengora (top) and Meno (bottom) watersheds

for this factor were assigned considering local management practices based on slope ranges and taking the weighed value for similar land use types. The conservation practice (*P*) factor value ranges from 0.1 to 0.33 for cultivated land and 1 for other land uses since there is no influence on soil erosion. Based on conservation practice (*P*) values, a *P* factor map was developed in GIS by intersecting the land use/land cover type and slope for both watersheds (Fig. 7.6).

Soil erosion control measures are predominantly practiced in sloping and cultivated areas. The lower the *P* value, the more effective the conservation practice is supposed to be at reducing soil erosion.

Soil Loss Estimation

The annual soil loss rate was computed spatially by multiplying the RUSLE factors over the watersheds using the raster calculator in ArcGIS. Based on the analysis, the estimated annual soil losses for the Dengora and Meno watersheds were 0–223.97 and 0–256.09 tons ha^{-1} $year^{-1}$, respectively, while their mean annual soil losses were 16.34 and 23.26 tons ha^{-1} $year^{-1}$, respectively. The estimated soil loss in both watersheds is within the range of soil loss estimated for the Ethiopian highlands by the Soil Conservation Research Program (SCRP), which was in the range of 0–300 tons ha^{-1} yr^{-1} (Hurni 1985). In the highlands of Ethiopia and Eritrea, soil losses are extremely high, with an estimated average of 20 metric tons ha^{-1} $year^{-1}$ (Hurni 1985). The results for the soil loss rate and the spatial patterns of this study conform well to what is observed in the literature. Therefore, this model gives a good estimate of soil loss in the Dengora and Meno watersheds, as they are parts of the Ethiopian highlands.

RUSLE model prediction has the limitation of not considering gully erosion, which is the main contributor to soil loss in the Ethiopian highlands. A recent study by Tamene et al. (2017) in Tigray indicated that the RUSLE model predicted higher soil loss rates at steep slopes and middle slope positions as well as along gullies. The predicted soil loss in the Dengora and Meno watersheds was relatively smaller at lower slope positions. This is because the slope of the watershed is the dominant factor for the model. However, in the bottom land of the watersheds, several active gully erosions, gully heads, bank collapses, and more cultivated practices were found. This observation is in line with what has been reported by Tebebu et al. (2010) and Zegeye et al. (2016), in which the rise of the perched groundwater table in the saturated bottomland areas of the Debre Mawi watershed resulted in the formation and expansion of gullies. Gullies have been found in the bottomlands of the study watersheds. This study identified erosion hotspot areas in the watersheds considering gully susceptible areas.

Based on the results of this study (Fig. 7.7), all parts of the watershed are at slight to moderate risk of soil erosion. According to Hurni (1983) and Morgan (2005), tolerable soil loss is the maximum soil loss that occurs from land without resulting in land degradation (11 ton ha^{-1} yr^{-1}). Analysis of the results showed that 70.4% and 72.6% of the Dengora and Meno watersheds, respectively, had soil loss rates within the range of the tolerable soil loss rate, and most of the upland parts of both watersheds exceeded the tolerable soil loss rate.

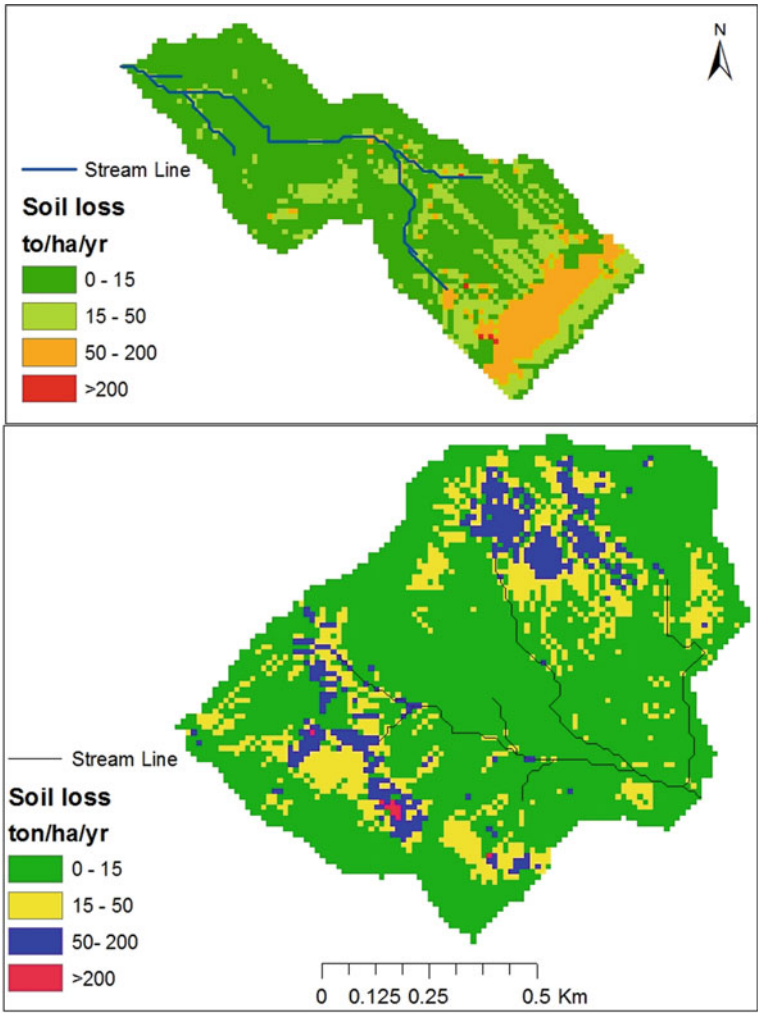

Fig. 7.7 Estimated annual soil loss for the Dengora (top) and Meno (bottom) watersheds

Multicriteria Decision Analysis (MCDA)

Land Use/Land Cover Map

Different land use/land cover types were identified in the Dengora and Meno watersheds. Image classification accuracy was conducted on classified images to determine how well the classification process was accomplished using an error matrix. The overall accuracies for the Dengora and Meno watershed land use/land cover maps were 83.33% and 90%, respectively. The kappa coefficients were 82% and

86%, respectively, which were within acceptable limits according to (Anderson et al. 1976). Land use/land cover maps of the watersheds were weighted based on an analytical hierarchy process (AHP) comparison to evaluate the effects on soil erosion (Fig. 7.8).

Accuracy assessment is necessary for validation of the image classification process by evaluating how well pixels were correctly grouped. The error matrix is the basis for accuracy assessment. The matrix gives a cross-tabulation of the class label predicted against the ground truth GPS data. The error matrixes provide important information on image classification for both map users and producer communities.

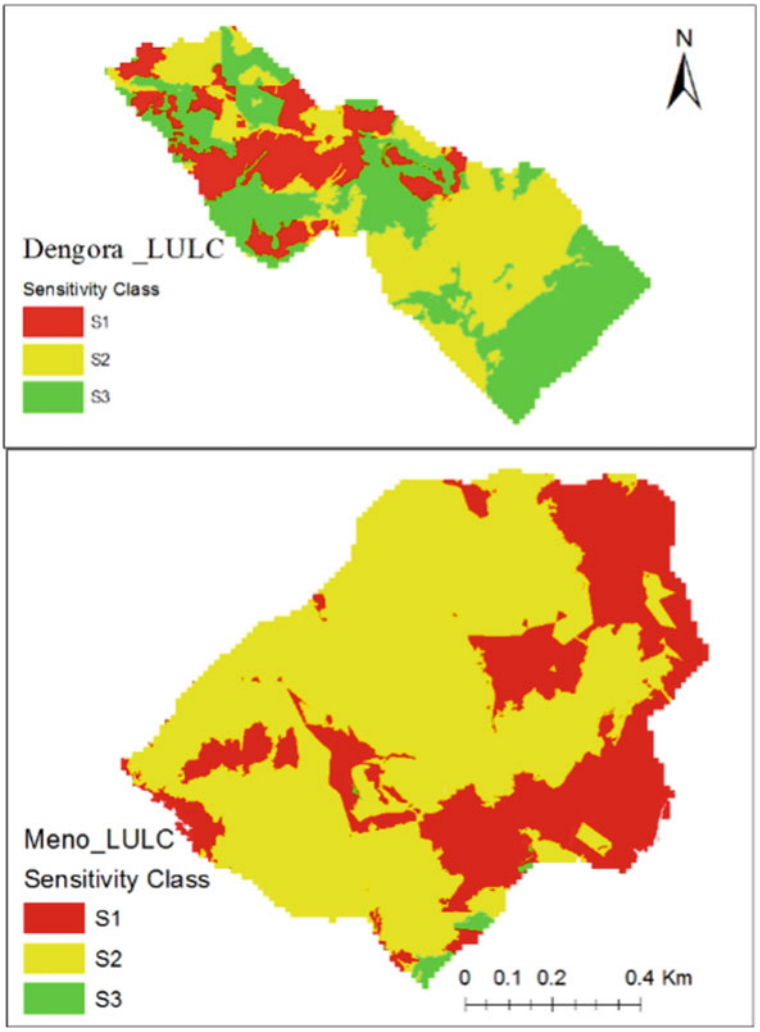

Fig. 7.8 LULC sensitivity map

Table 7.2 Land use/land cover accuracy assessment of the study area

Land use/ Dengora watershed	Producer accuracy (%)	Omission error (%)	User accuracy (%)	Commission error (%)	Overall accuracy (%)	Kappa coefficient (%)
Forest area	1	0	0.67	0.33	0.83	0.82
Cultivated land	0.72	0.28	0.83	0.17		
Cultivated terrace	0.72	0.29	0.83	0.17		
Bush land	0.86		1	0		
Shrub land	0.83	0.27	0.83	0.17		
Land use/ Meno watershed	Producer accuracy (%)	Omission error (%)	User accuracy (%)	Commission error (%)	Overall accuracy (%)	Kappa coefficient (%)
Forest area	0.8	0.2	0.67	0.33	0.9	0.86
Cultivated land	0.83	0.17	0.83	0.17		
Grazing land	0.67	0.33	0.67	0.33		
Bush land	0.72	0.28	0.83	0.17		
Shrub land	0.67	0.33	0.67	0.33		
Road	1	0	1	0		

Kappa is used to measure the accuracy between the remote sensing-derived classification map and the reference data indicated by the major diagonals and the chance agreement, which is indicated by the row and column totals (Janssen and Rietveld 1990).

The overall accuracy (Table 7.2) is often the only accuracy statistic reported with predictive landscape models (Congalton 1991), but the error matrix provides a means to calculate numerous additional metrics describing model performance.

$$\text{Overall accuracy} = (\text{Number of pixels correctly classified})/(\text{total number of pixels})$$

Soil Map

The other criterion in MCDA to estimate the potential soil erosion risk area is erodibility, which is the vulnerability of the soil to erosion. Soil with low K factor values is less susceptible to erosion agents, and soil with high K factor values is more susceptible. The major soil types that were obtained in both watersheds were reclassified and weighted based on their sensitivity to soil erosion using the pairwise comparison

method. Leptic Luvisols, Heplic Luvisols, and Hyperskeletic Leptosols were highly sensitive (S1), Eutric Leptosols had the dominant soil in the watershed, which was moderately sensitive (S2), and Lithic Leptosols were slightly sensitive (S3) to soil erosion based on soil erodibility, and exposed rock was constrained in soil erosion due to the properties of each soil (Fig. 7.9).

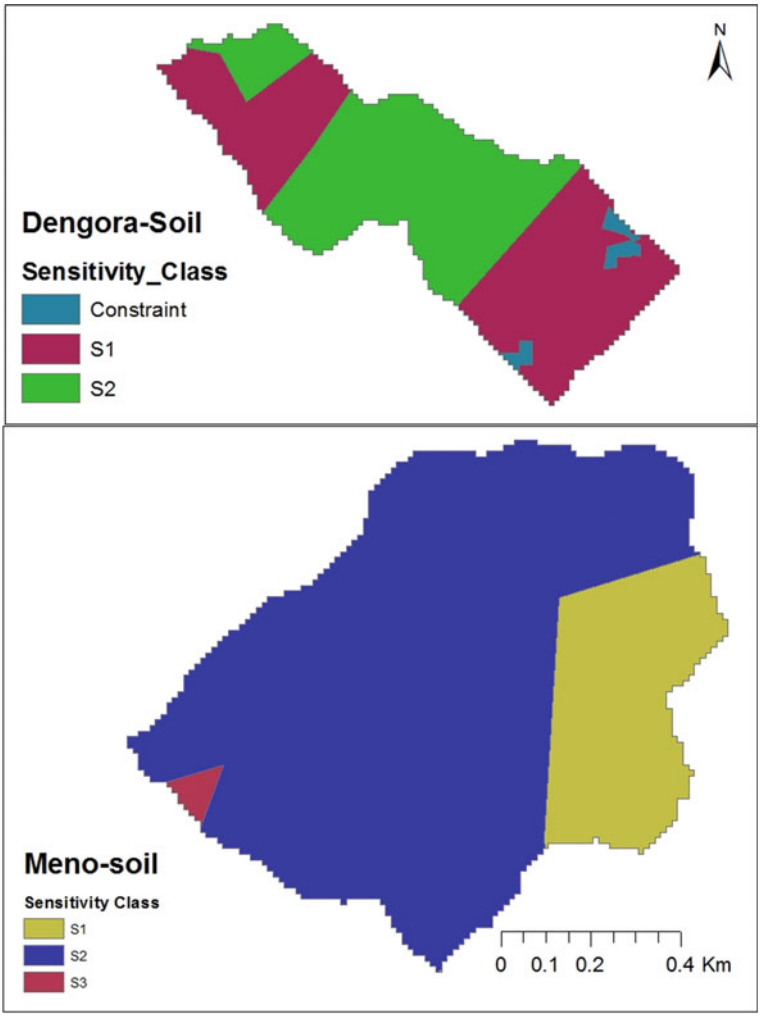

Fig. 7.9 Soil type sensitivity maps

Topographic Wetness Index (TWI) Factor

Another important factor for the identification of erosion hotspot areas was TWI. It is used to quantitatively simulate the upslope areas contributing to soil erosion and soil moisture conditions in a watershed. It is used as an indicator of static soil moisture content. It is also useful for distributed hydrological modeling to describe the effect of topography, mapping drainage, soil type, soil infiltration, and crop or vegetation distribution on soil erosion. In this study, the TWI was extracted from a digital elevation model (DEM). Determining the saturated excess runoff generation over the land represented with the topographic wetness index. The reclassified TWI map is shown in Fig. 7.10. Higher elevation areas have low TWI values, whereas the lowest elevation areas have high TWI values. Hill slopes in the watershed were characterized by low TWI values, indicating dry areas, whereas TWI values increased in the lower reaches of the watershed, i.e., in the piedmont and flood plains, indicating possible source areas for saturated overland flow.

Stream Power Index (SPI) Factor

The stream power index (SPI) is a measure of the erosive power of flowing water. The SPI is calculated based on slope and contributing area. The SPI approximates locations where gullies might be more likely to form on the landscape. The SPI factor was found to be the major factor contributing to soil erosion in the study areas. It is the rate of the energy of flowing water expended on the bed and banks of a streamline. The reclassified SPI map is shown in Fig. 7.11. Higher SPI values were also observed along both sides of streams in the watershed, indicating a possible source of soil erosion due to the concentrated flow of runoff.

Gully Potential Location Map

In this study, gully locations were found where water flow was concentrated as small streams and around waterway sides of the ground surfaces (stream routes). The potential locations of gullies in both watersheds were identified based on SPI and TWI threshold values by overlaying their maps with the "AND" Boolean operation in the ArcGIS raster calculator. The expression SPI > 12 and TWI > 6.8 was used to obtain the locations of gullies in the watershed. The resulting map (Fig. 7.12) shows areas with no gullies and with gully formation.

Gully formation follows the streamlines of the watersheds, and the map clearly shows that small gullies (plot level) were not captured by the threshold used. Gully locations were highly sensitive (S1), while no gully location was less sensitive (S3). The sensitivity classes were used to reclassify the gully map (Fig. 7.12).

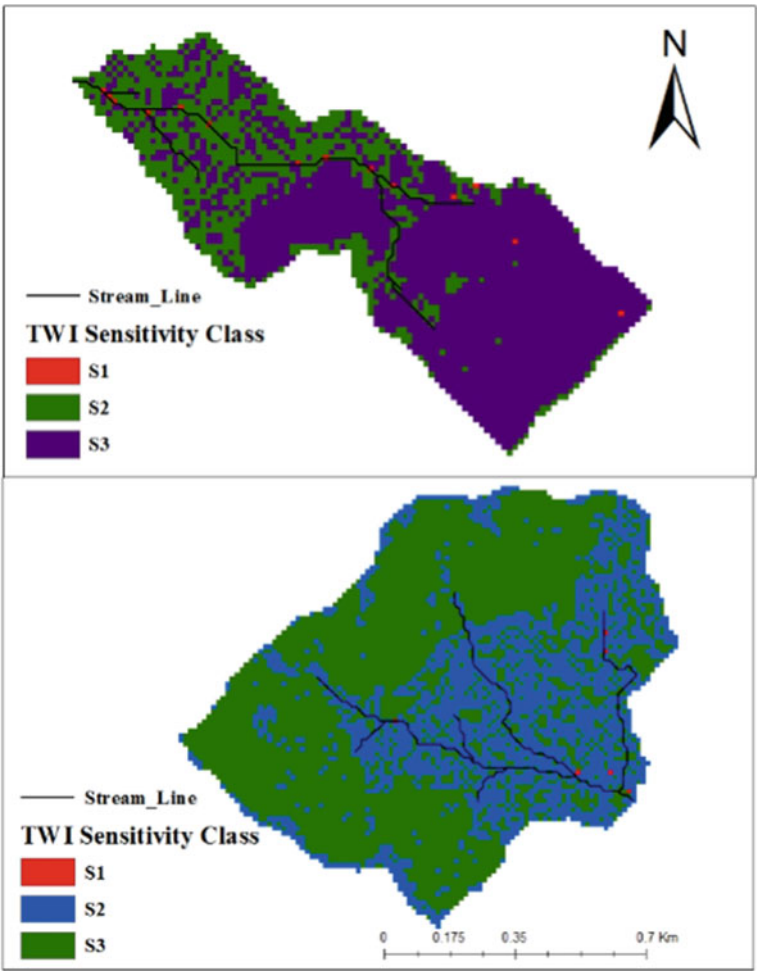

Fig. 7.10 TWI sensitivity class

Validation of Potential Gully Location

Gully sites and density were identified from the stream power index (SPI) within the range of 12–16.47 and a topographic wetness index of 6.8–15.38 for the Dengora watershed, and stream power index values of 12–16.84 and a topographic wetness index of 6.8–17.92 for the Meno watershed were overlaid to obtain potential gully locations. The results of the stream power index analysis for the Dengora and Meno watersheds indicated ranges of 0.72–16.48 and 2.88–16.84, respectively. According to Lulseged and Vlek (2005), areas in a watershed with a stream power index greater than 18 are susceptible to gully formation. However, the watershed gully location indicated a stream power index value of 12, which can be taken as a threshold

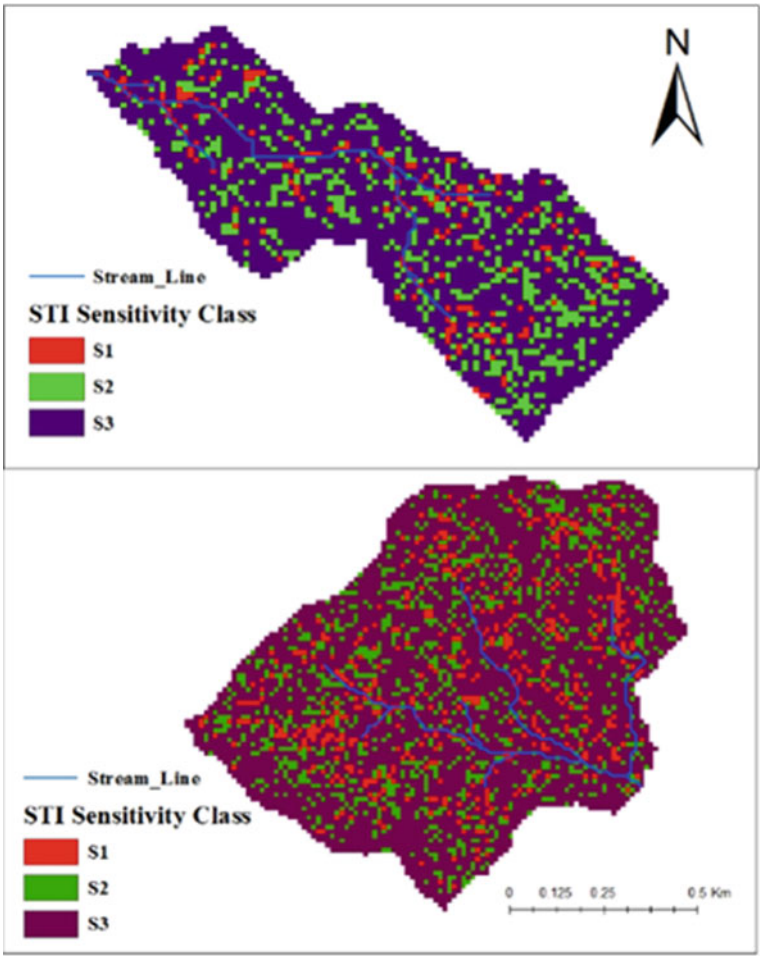

Fig. 7.11 SPI sensitivity class

value of gully prone areas in the study watershed. Similarly, the topographic wetness index of the watershed can be used as the threshold value of 6.8 and greater for susceptibility to gully erosion risk (Lulseged and Vlek 2005). This result can be taken as a good indicator of threshold variability for gully susceptible area identification in the watershed. The overlaid map of the topographic wetness index and stream power index (Fig. 7.11) indicated that gullies were found. Based on the results, gullies were found along the natural streamlines within the higher stream power index (SPI) of both watersheds. This was validated during the transect walk, and gullies were observed along the route of the stream of the two watersheds, as shown in Fig. 7.13.

Validation was performed to cross-check potential gully sites by overlaying on the watershed boundary. Randomly sampled gullies were digitalized, and their locations

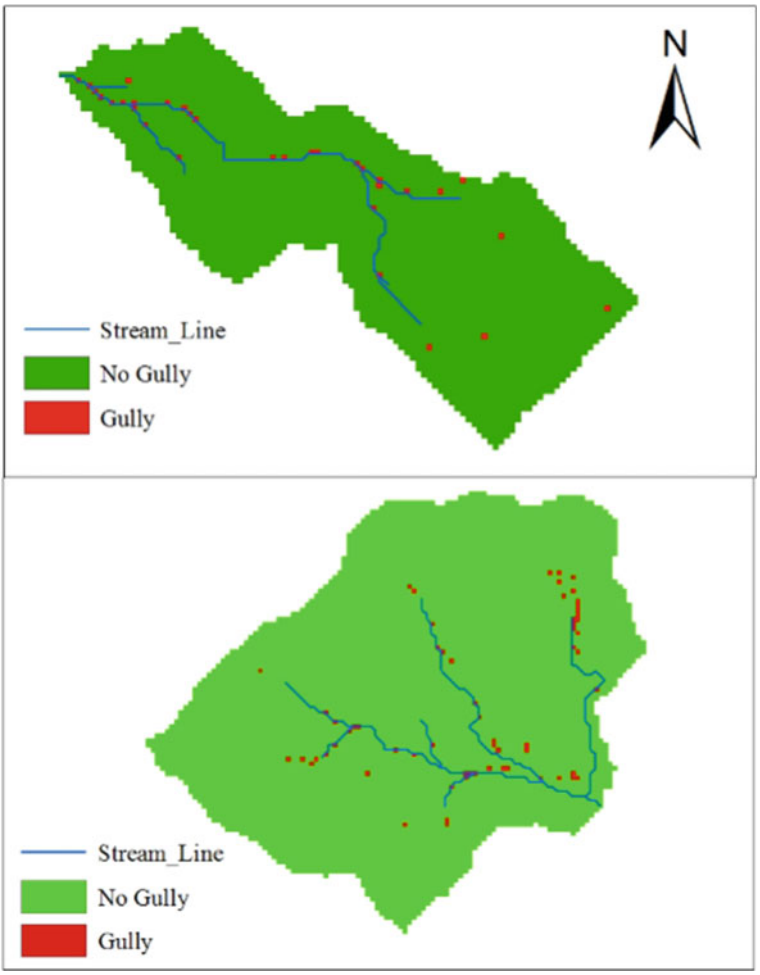

Fig. 7.12 Potential locations of gullies

were collected by GPS and cross-tabulated with gully locations. The validation results were 78.6% and 86.7% for the Dengora and Meno watersheds, respectively.

Pairwise Comparison for Parameters

For assigning weights in this study, the pairwise comparison method was used to reduce the complexity of decision-making since two components are considered at a time. The highest value indicates absolute importance, and the reciprocal kept in the transpose position indicates absolute insignificance. The weights of the factors were

Fig. 7.13 Photograph of the sample gully in the Meno watershed

computed after normalizing the eigenvector by its cumulative value and multiplying by 100%. The reliability of the weights was checked by computing the consistency of the comparison matrix, which was 9.03% and 4.6% for the Dengora and Meno watersheds, respectively, both of which are under the accepted consistency ratio (< 10%). Accordingly, the pairwise weights were accepted and consistent, so the process was continued. Finally, the MCDA erosion intensity map of the area was produced by multiplying the four criterion layers by their weight derived from pairwise comparison and then summing the results by the weighted linear combination (WLC) equation in the raster calculator operation of ArcGIS (Fig. 7.14).

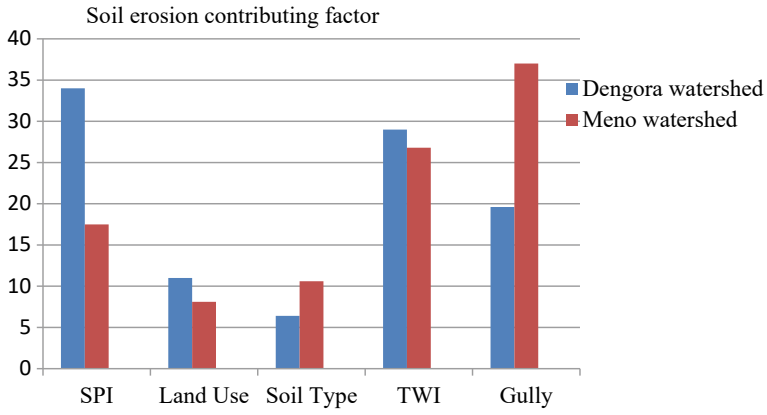

Fig. 7.14 Overall contributions of parameters to soil erosion

Identification of Soil Erosion Hotspot Areas

Based on the methodology designed for the identification of soil erosion hotspot areas, all selected factors were overlaid to identify the area sensitive to erosion as highly, moderately, slightly, and currently not sensitive (constraint). The sensitivity map (Fig. 7.15) shows the relative ranking of the erosion potential sites generated by weighted overlay mapping. According to the weight of the concerned criteria, the most sensitive areas to erosion under the multicriteria evaluation (S1) spatially coincided with the actual gully locations. Therefore, the MCDA technique is more accurate than RUSLE prediction because the RUSLE model is more sensitive to slope and does not consider gullies, but MCDA considers pairwise comparisons of all factors that affect soil erosion. This is consistent with the findings reported by Zegeye et al. (2016) and Poesen et al. (2003) in that gullies are critical sediment sources in the Ethiopian highlands, and accurate soil erosion prediction should properly address estimating gully erosion. The weighted overlay of all factors was important for soil erosion source area assessments to obtain the most severe sites in the Dengora and Meno watersheds.

The results showed that for the Dengora watershed, 9.7% of the total watershed area was highly sensitive, 64.5% was moderately sensitive, 18% was slightly sensitive, and 7.8% was currently not sensitive (exposed rocky areas). For the Meno watershed, 6.1% of the total watershed area was highly sensitive, 71.3% was moderately sensitive, 23.23% was slightly sensitive, and 0.375% of the total area was currently not sensitive to soil erosion based on the combined effect of the annual soil loss class and the MCDA technique of soil erosion hotspot area identification in the watershed. The results indicated that the Dengora and Meno watersheds were at moderate risk. Moreover, the MCDA revealed that the upper parts of the watersheds are slightly sensitive (S3) to soil erosion, which could be explained by the fact that there were no gullies in the upland areas.

Conclusion and Recommendations

Conclusion

In this study, the RUSLE model and MCDA technique were used to identify erosion hotspot areas in the Dengora and Meno watersheds. The RUSLE model prediction indicated that the upslope portion of the watersheds is highly sensitive to erosion. The multicriteria decision analysis (MCDA) technique indicated that the bottom slope or the saturated bottomland is highly sensitive to erosion. The topographic wetness index (TWI) and stream power index (SPI) were powerful predictors of potential gully formation, which coincided with our field gully mapping. The results from model prediction in combination with gully validation indicated that areas in the Dengora and Meno watersheds with TWI $\geq$ 6.8 and SPI $\geq$ 12 were sensitive to

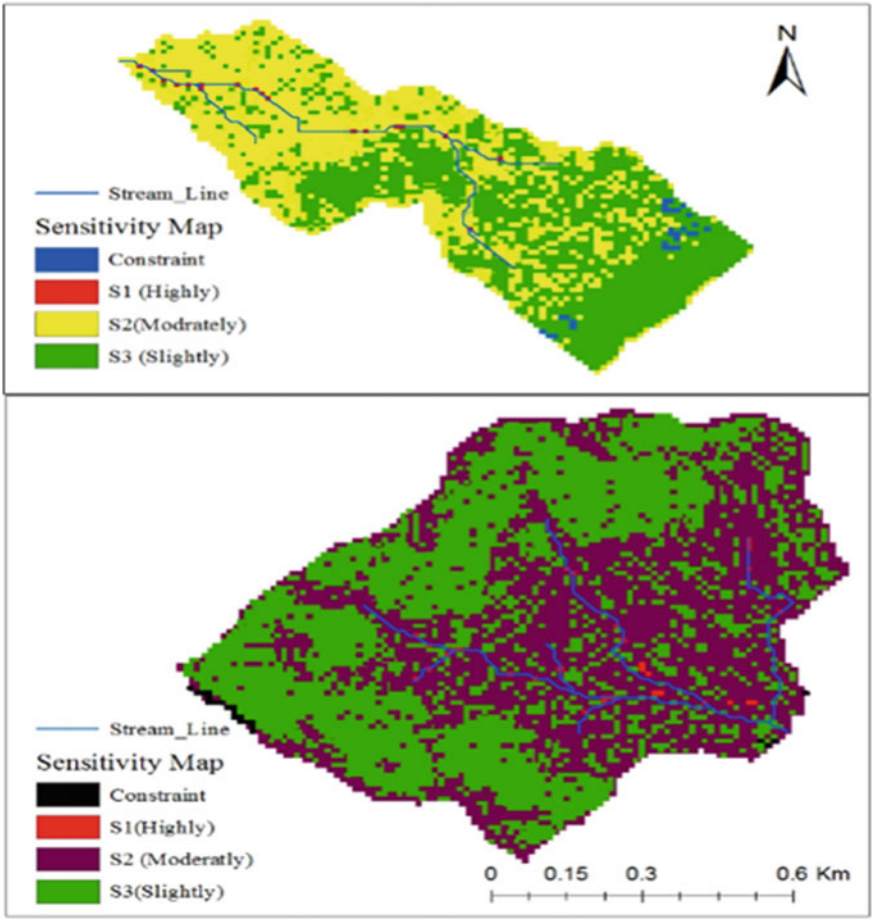

Fig. 7.15 Overall soil erosion risk map

gully erosion. The overall result of this study was that the bottomlands were the most important erosion-prone areas of the watersheds. Thus, these areas should be given priority in the intervention of integrated watershed management practices focused on gully erosion areas.

The overall study indicated that most erosion hotspot areas were found in the valley bottomlands (gullies) of the watersheds, and it was extremely important to consider valley bottoms as priority intervention areas in the planning of watershed interventions. The identification of erosion-prone areas is useful information in decision-making and the implementation of interventions in areas with limited resources and manpower. From the validation of the results, the MCDA technique was observed to be more powerful than RUSEL for planning and targeting intervention areas.

Recommendations

This study provides detailed information for planners, decision-makers, and other concerned stakeholders to implement effective soil and water conservation practices to reduce soil loss by improving the water holding capacity of the watershed. The study is also vital in reducing soil erosion from the lower part of the Dengora and Meno watersheds to the artificial reservoirs of the Atikayina dam and Meno gravity dam. Based on the present research outlook, it is recommended that valley bottomlands of watersheds characterized by high soil erosion-prone areas need immediate attention to soil and water conservation practices. Local people should also be made aware of soil loss and encouraged to apply effective intervention mechanisms to tackle the problem. In planning watershed development programs, identifying the target areas and technology options is very important. This study also showed that models that used comprehensive watershed characteristics such as MCDA performed better than the RUSLE model.

References

Aga AO, Chane B, Melesse AM (2018) Soil erosion modelling and risk assessment in data scarce Rift Valley Lake Regions, Ethiopia. Water 10:1684. https://doi.org/10.3390/w10111684

Aga AO, Melesse AM, Chane B (2019) Estimating the sediment flux and budget for a data limited Rift Valley Lake in Ethiopia. Hydrology 6(1). https://doi.org/10.3390/hydrology6010001

Anderson JR, Hardey EE, Roach JT, Witmer RE (1976) A land use and land cover classification system for use with remote sensor data. U.S. Geological Survey professional paper 964, USGS, Reston, VA

Asquith P, Pathak PA, Ritter JR (2005) Short interest, institutional ownership, and stock returns. J Financ Econ 78:243–276

Birru Y (2007) Land degradation and options for sustainable land management in the Lake Tana Basin (LTB), Amhara Region, Ethiopia. Ph.D. Thesis, Centre for Development and Environment (CDE), Geographic Institute, University Bern, Bern, Switzerland. Solid Earth Discussions

Congalton RG (1991) A review assessing the accuracy of classifications of remotely sensed data. Remote Sens Environ 37:35–46

Defersha MB, Melesse AM (2012a) Effect of rainfall intensity, slope and antecedent moisture content on sediment concentration and sediment enrichment ratio. CATENA 90:47–52

Defersha MB, Melesse AM (2012b) Field-scale investigation of the effect of land use on sediment yield and surface runoff using runoff plot data and models in the Mara River basin, Kenya. CATENA 89:54–64

Defersha MB, Quraishi S, Melesse AM (2010) Interrill erosion, runoff and sediment size distribution as affected by slope steepness and antecedent moisture content. Hydrol Earth Syst Sci Discuss 7:6447–6489

Defersha MB, Quraishi S, Melesse AM (2011) The effect of slope steepness and antecedent moisture content on interrill erosion, runoff and sediment size distribution in the highlands of Ethiopia. Hydrol Earth Syst Sci 15:2367–2375. https://doi.org/10.5194/hess-15-2367-2011

Defersha MB, Melesse AM, McClain M (2012) Watershed scale application of WEPP and EROSION 3D models for assessment of potential sediment source areas and runoff flux in the Mara River Basin, Kenya. CATENA 95:63–72

Mhiret DA, Dagnew DC, Assefa TT, Tilahun SA, Zaitchik BF, Steenhuis TS (2019) Erosion hotspot identification in the subhumid Ethiopian highlands. Ecohydrol Hydrobiol, 146–154
Desmet P, Govers G (1996) A GIS procedure for automatically calculating the USLE LS factor on topographically complex landscape units. J Soil Water Conserv 51:427–433
Dube F, Nhapi I, Murwira A, Gumindoga W, Goldin J, Mashauri D (2014) Potential of weight of evidence modeling for gully erosion hazard assessment in Mbire District-Zimbabwe. Phys Chem Earth Parts a/b/c 67:145–152
Hurni H (1983) Soil erosion and soil formation in agricultural ecosystems: Ethiopia and Northern Thailand. Mountain Res Dev, 131–142
Hurni H (1985) Erosion-productivity-conservation systems in Ethiopia
Hurni H (1989) Degradation and conservation of the resources in the Ethiopian highlands. Mountain Res Dev 8(2/3):123−130
Janssen R, Rietveld P (1990) Multicriteria analysis and geographical information systems: an application to agricultural land use in the Netherlands. In: Geographical information systems for urban and regional planning. Springer
Lulseged T, Vlek P (2005) GIS-based landscape characterization to assess soil erosion and its delivery potential in the highlands of northern Ethiopia. In: Proceedings of the 1st international conference on remote sensing and geoinformation processing in the assessment and monitoring of land degradation and desertification (ICRS '05), pp 7–9
Maalim FK, Melesse AM (2013) Modeling the impacts of subsurface drainage systems on runoff and sediment yield in the Le Sueur Watershed, Minnesota. Hydrol Sci J 58(3):1–17
Maalim FK, Melesse AM, Belmont P, Gran K (2013) Modeling the impact of land use changes on runoff and sediment yield in the Le Sueur Watershed, Minnesota using GeoWEPP. Catena 107:35–45
Malczewski J (1996) GIS-based approach to multiple criteria group decision-making. Int J Geogr Inf Sci 10(8); Water Resour Res, 321–339
Mekonnen M, Melesse A (2011) Soil erosion mapping and hotspot area identification using GIS and remote sensing in northwest Ethiopian highlands, near Lake Tana. In: Melesse A (ed) Nile River Basin: hydrology, climate and water use, Springer Science Publisher Chapter 10, pp 207–224. https://doi.org/10.1007/978-94-007-0689-7_10
Melesse AM, Ahmad S, McClain M, Wang X, Lim H (2011) Sediment load prediction in large rivers: ann approach. Agr Water Manage 98:855–866
Mohammed H, Alamirew T, Assen M, Melesse AM (2015) Modeling of sediment yield in Maybar gauged watershed using SWAT, Northeast Ethiopia. CATENA 127:191–205
Morgan RPC (2005) Soil erosion and conservation, 3rd edn. Blackwell Publishing, New York, USA
Msaghaa JJ, Melesse AM, Ndomba PM (2014) Modeling sediment dynamics: effect of land use, topography and land management. In: Melesse AM, Abtew W, Setegn S (eds) Nile River Basin: ecohydrological challenges, climate change and hydropolitics, pp 165–192
Onyando J, Kisoyan P, Chemelil M (2005) Estimation of potential soil erosion for river Perkerra Catchment in Kenya. Water Resour Manage 19:133–143
Poesen J, Nachtergaele J, Verstraeten G, Valentin C (2003) Gully erosion and environmental change: importance and research needs. CATENA 50:91–133
Renard KG, Foster GR, Weesies GA, Porter JP (1991) RUSLE: revised universal soil loss equation. J Soil Water Conserv 46:30–33
Salehi F, Pesant A, Lagace R (1991) Validation of the universal soil loss equation for three cropping systems under natural rainfall in Southeastern Quebec. Can Agric Eng 33:11–16
Setegn SG, Srinivasan R, Dargahi B, Melesse AM (2009) Spatial delineation of soil erosion prone areas: application of SWAT and MCE approaches in the Lake Tana Basin, Ethiopia. Hydrol Processes, Special Issue: Nile Hydrol 23(26):3738–3750
Setegn SG, Bijan Dargahi B, Srinivasan R, Melesse AM (2010) Modelling of sediment yield from Anjeni Gauged Watershed, Ethiopia using SWAT. JAWRA 46(3):514–526

Tamene L, Adimassu Z, Ellison J, Yaekob T, Woldearegay K, Mekonnen K, Thorne P, Le QB (2017) Mapping soil erosion hotspots and assessing the potential impacts of land management practices in the highlands of Ethiopia. Geomorphology 292:153–163

Tebebu T, Abiy A, Zegeye A, Dahlke H, Easton Z, Tilahun S, Collick A, Kidnau S, Moges S, Dadgari F (2010) Surface and subsurface flow effect on permanent gully formation and upland erosion near Lake Tana in the northern highlands of Ethiopia. Hydrol Earth Syst Sci 14:2207–2217

Tecle AYM (1990) Preference ranking of alternative irrigation technologies via a multi criterion decision making procedure. Trans ASAE 3(5):1509–1517

Twinn DS (1998) An analysis of the effectiveness of focus groups as a method of qualitative data collection with Chinese populations in nursing research. J Adv Nurs 28:654–661

Valentin C, Poesen J, Li Y (2005) Gully erosion: impacts, factors and control. CATENA 63:132–153

Voogd H (1983) Multi-criteria evaluation for urban and regional planning. Pion Ltd., London

Wang X, Garza J, Whitney M, Melesse AM, Yang W (2008) Prediction of sediment source areas within watersheds as affected by soil data resolution. In: Findley PN (ed) Environmental modelling: new research), chap 7. Nova Science Publishers, Inc., Hauppauge, pp 151–185. ISBN 978-1-60692-034-3

Wischmeier WH, Smith DD (1978) Predicting rainfall erosion losses-a guide to conservation planning. In: Predicting rainfall erosion losses-a guide to conservation planning

Yilma AD, Awulachew SB (2009) Blue Nile Basin characterization and geospatial atlas. In: Improved water and land management in the Ethiopian Highlands: its impact on downstream stakeholders dependent on the Blue Nile**,** 6

Zegeye AD, Langendoen EJ, Stoof CR, Tilahun SA, Dagnew DC, Zimale FA, Guzman CD, Yitaferu B, Steenhuis TS (2016) Morphological dynamics of gully systems in the subhumid Ethiopian Highlands: the Debre Mawi watershed. Soil 2:443–458

Chapter 8
Soil Erosion Risk Assessment—A Key to Conservation Planning in the Ethiopian Highland in East Hararghe

Gezahegn Weldu Woldemariam, Berhan Gessesse Awoke, and Kalid Hassen Yasin

Abstract Spatial modeling and detailed erosion risk analysis provide robust insights into what must be done and where to improve ecosystems. This chapter presents a comprehensive soil erosion estimate using an empirical modeling approach incorporating remote sensing and GIS techniques in the East Hararghe Zone in Ethiopia. First, we present soil loss rates and dynamics of soil erosion risk during the past three decades (1990–2020). Second, we explore conventional conservation practices that could reduce soil loss in croplands. Annual soil loss was estimated to be 9.16 Mt yr^{-1} in 1990, 14.02 Mt yr^{-1} in 2000, 12.20 Mt yr^{-1} in 2010, and 10.84 Mt yr^{-1} in 2020, with respective average rates (t ha^{-1} yr^{-1}) of 32.94, 50.42, 43.84, and 38.99, showing an 18.37% increase from 1990 to 2020. The results show that over two-thirds of the study area is susceptible to low erosion risk, accounting for a smaller share of the annual soil loss rates. Districts with elevated erosion risk, contributing to more than 80% of soil loss, are situated in mountainous landscapes in the northwest, necessitating priority for soil and water conservation (SWC) practices. Based on standard conservation practices for cropland fields, our key findings show that terracing, strip cropping and contouring could reduce the average erosion rate by 87.05%, 64.66%, and 29.32%, respectively. The research showcases the effectiveness of sustainable land management (SLM) and emphasizes the importance of conducting a comprehensive cost-benefit analysis to develop and execute optimal conservation measures.

Keywords Soil erosion · Remote sensing · GIS · RUSLE · SWC planning

G. W. Woldemariam (✉) · B. G. Awoke · K. H. Yasin
Department of Remote Sensing and Application Research and Development, Space Science and Geospatial Institute, Entoto Observatory and Research Center, P.O. Box 33679, Addis Ababa, Ethiopia
e-mail: gezahegnw3@gmail.com

G. W. Woldemariam · K. H. Yasin
Geo-Information Science Program, School of Geography and Environmental Studies, Haramaya University, P.O. Box138, 3220 Dire Dawa, Ethiopia

A. M. Melesse et al. (eds.), *Land and Water Degradation in Ethiopia*, Springer Geography, https://doi.org/10.1007/978-3-031-60251-1_8

Introduction

Soil erosion caused by water has become a pressing global concern. Scientific evidence has revealed that activities related to humans are accelerating soil loss rates at various scales (Borrelli et al. 2020; Eekhout and Vente 2022; Kumar et al. 2022). Topsoil displacement caused by erosion, particularly in upland ecosystems, exacerbates land degradation, leading to lower soil fertility, reduced agricultural productivity, and increased production costs (Kumar et al. 2019; Nambajimana et al. 2020; Wagari and Tamiru 2021). A number of studies used laboratory, field scales and modeling studies to understand soil erosion and sediment dynamics in various regions (Aga et al. 2018, 2019; Defersha and Melesse 2012a, b; Defersha et al. 2010, 2012; Maalim and Melesse 2013; Maalim et al. 2013; Setegn et al. 2010; Melesse et al. 2011; Msagahaa et al. 2014; Wang et al. 2008; Mekonnen and Melesse 2011; Setegn et al. 2009; Mohamed et al. 2015).

Research findings have also linked the consequences of soil erosion, such as flooding, sedimentation, reduced nutrient and water storage, soil structure degradation, pollution, and freshwater scarcity, with severe environmental and socioeconomic issues (Kogo et al. 2020; Tessema et al. 2020; Woldemariam and Harka 2020). Estimates indicate that soil erosion rates are increasing, and climate and land use changes may exacerbate soil loss, particularly in Africa, which is currently at significant risk (Borrelli et al. 2020).

However, the magnitude of soil erosion and its adverse impacts vary across global regions, as noted by various studies (Gil et al. 2021; Polovina et al. 2021; Watene et al. 2021). Developing countries in tropical regions experience the most extensive soil erosion risk (Karamage et al. 2017; Kogo et al. 2020). High population growth, elevated rainfall, agricultural intensification and expansion, overgrazing, high soil erodibility, and poor soil and water conservation (SWC) practices explain why tropical countries are susceptible to severe erosion (Fenta et al. 2021; Watene et al. 2021). Recent studies indicate that this situation is no different but is more pronounced in most East African countries, including Ethiopia (Eniyew et al. 2021; Kogo et al. 2020; Nambajimana et al. 2020; Watene et al. 2021; Woldemariam et al. 2018).

In Ethiopia, researchers have increasingly focused on soil erosion due to the growing need for detailed knowledge of erosion risk to support appropriate conservation planning (Endalamaw et al. 2021; Eniyew et al. 2021; Fenta et al. 2021; Girma and Gebre 2020; Sinshaw et al. 2021; Tsegaye and Bharti 2021). These researchers concluded that water erosion is a major cause of widespread land degradation, threatening biodiversity and ecosystem sustainability. In addition, it has been increasingly linked to the country's agricultural sector (FDRE 2015; Woldemariam et al. 2018).

Since a significant segment of Ethiopia's population relies on subsistence production systems and is prone to recurring dry spells and rainfall fluctuations, the detrimental impacts of soil erosion and resulting land degradation have severe consequences for their livelihoods, food security, and economic growth (Nyssen et al. 2015; Woldemariam et al. 2018; Moges et al. 2020). Consequently, urgent proactive measures are needed to counteract the degradation caused by water erosion and

improve agricultural production and productivity (Ebabu et al. 2019; Fenta et al. 2021; Haregeweyn et al. 2017; Tesfaye et al. 2021).

The East Hararghe Zone (EHZ) in eastern Ethiopia is known for its extensively degraded landscape (FAO 1986). Unfortunately, the zone continues to face high risks of soil erosion, resulting in severe environmental and socioeconomic issues (Woldemariam et al. 2018). The growing population has further exacerbated soil erosion and degradation by necessitating more land for settlement areas and agriculture over time (Haile and Fetene 2012; Woldemariam and Harka 2020). As in other regions of the country, large-scale erosion in the EHZ can be attributed to climate change, land-use and land-cover (LULC), and unsustainable human activities (Girma and Gebre 2020; Moges et al. 2020; Moisa et al. 2021).

Over the past few decades, numerous research studies have evaluated rates of soil loss at the catchment level (Daba 2003; Muleta et al. 2006; Samuel 2014; Senti et al. 2014) and assessed erosion risk at the scale of watersheds/subbasins for soil and water conservation (SWC) planning (Woldemariam et al. 2018; Woldemariam and Harka 2020). Nevertheless, none of these studies have addressed the long-term assessment of soil erosion in the whole landscape at the zonal scale. This chapter provides the first comprehensive estimate of soil erosion caused by water and its evolution under changing land-use/land-cover (LULC), rainfall, and topography during the last three decades (1990–2020). Additionally, we examine the implications of soil and water conservation (SWC) practices, which have enormous potential to reduce soil loss rates in cropland areas in Ethiopia's EHZ. The study's temporally and spatially explicit soil erosion database can serve as a foundation for adopting effective land management strategies, minimizing ecological degradation and its repercussions on the local communities in the landscape under investigation.

Study Area

This study was conducted in EHZ of Oromia Regional State, which covers an area of 25,039.74 km^2 and covers eighteen woredas (Fig. 8.1). These woredas are distinguished by their complex topography, with characteristic deep gorges, plateaus, and chains of rugged mountains in the northern part, as well as a variety of land uses and geomorphological features. In contrast, the southern part is flat plains. The spatial extent of the study area is approximately 186 km from east to west, and the north–south reaches up to 218 km. Within this range, the altitudinal variation is from 471 m in Meyu Muleke in the southernmost part to more than 3388 m at the peak of Gara Muleta in the northern part, with an average altitude of 1505 m above sea level. The maximum annual rainfall in the area is 2416 mm yr^{-1}, with 60% falling between June and August. The average minimum and maximum temperatures are 10 °C and 25 °C, respectively (Nurgi et al. 2021).

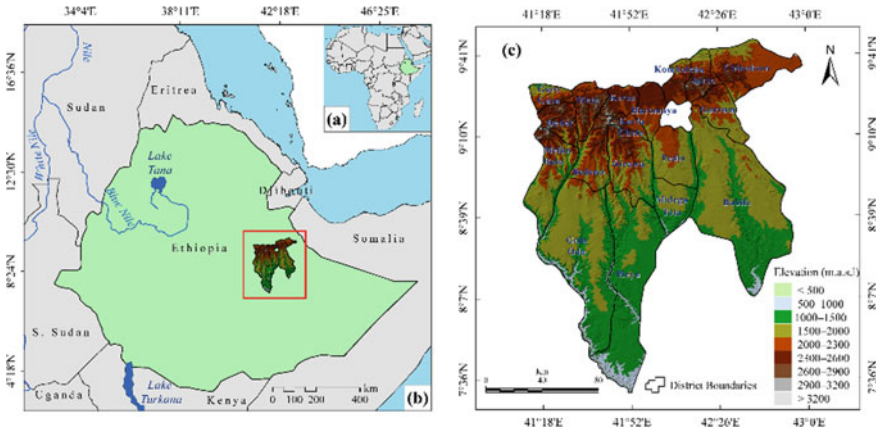

Fig. 8.1 Location of the study area

Data

Datasets from various sources were used to generate model variables for the Revised Universal Soil Loss Equation (RUSLE). The datasets used and their corresponding sources are provided in Table 8.1.

Table 8.1 The geospatial datasets used for this study

Datasets	Data specification and source
DEM[a]	SRTM-DEM[b] (30 × 30 m): https://dwtkns.com.gov/srtm/
Satellite imagery	Landsat 5 TM[c] (1990, 2000, 2010) and OLI/TIRS[d] (2020) (Level 2, surface reflectance (SR); 30 × 30 m): https://earthexplorer.usgs.gov/
Rainfall	Monthly rainfall produced by CHIRPS[e] (0.05° × 0.05°): https://data.chc.ucsb.edu/products/CHIRPS-2.0/africa_monthly/tiffs/
Soil map	FAO-UNESCO[f] Digital Soil Map of the World (1:5,000,000 scale): www.fao.org/geonetwork/srv/en/metadata.show?id=14116&currTab=distribution
Sample[g]	Google-Earth Pro (Google Inc., Amphitheatre Parkway, Mountain View, CA, USA)

[a] DEM—Digital Elevation Model; [b] SRTM—Shuttle Radar Topographic Mission; [c] TM—Thematic Mapper; [d] OLI/TIRS—Operational Land Imager/Thermal Infrared Sensor; [e] CHIRPS—Climate Hazards Group InfraRed Precipitation with Stations; [f] FAO–UNESCO-Food and Agriculture Organization, the United Nations Educational, Scientific, and Cultural Organization; [g] Sample—The sample points for LULC classification were collected from high-spatial-resolution Google-Earth Pro images, with 70% of the points picked based on the stratified random sampling method used to train and run the support vector machine (SVM) algorithm. The remaining 30% of the sample was the validation points for each year's accuracy calculation for the classified LULC maps

Methodology

Land-Use and Land-Cover (LULC) Classification

The LULC maps were prepared using classification procedures that involved initial training to mark spectral signatures for LULC classes from composite Landsat images and actual classification based on the spatial position of predefined references from Google Earth. We utilized a support vector machine (SVM), a supervised image classification algorithm that classifies remote sensing images based on the classifier definition described in Woldemariam et al. (2021). We classified seven LULC categories (bare land, built-up areas, farmland, forestland, grassland, shrubland, and water bodies) for four time periods (1990, 2000, 2010, and 2020), as outlined in Table 8.2. The spatial distributions of the LULC classes are shown in Fig. 8.2.

We used statistical measurements commonly used for confirming the quality of LULC maps, which included overall accuracy (OA), user's accuracy (UA), producer's accuracy (PA), and Kappa (K) coefficients. These were applied to validation samples and their corresponding sites in the classified images. The OA validation classification resulted in accuracies of 92.86% for 1990, 94.52% for 2000, 94.52% for 2010, and 95% for 2020, with corresponding K values of 0.91, 0.93, 0.93, and 0.94, respectively (see Table 8.3). The LULC classification of 1990 had higher omission errors (OE) and commission errors (CE), which may be attributed to the unavailability of reference data that matched the image acquisition date.

Table 8.2 The area share and the rate of change in the land-use and land-cover classes

Year	Area	LULC class						
		Bare land	Built-up	Cropland	Forest	Grassland	Shrubland	Waterbody
1990	km^2	2,147.59	28.7	12,240.32	2517.66	111.17	7985.88	8.4
	%	8.58	0.11	48.88	10.05	0.44	31.89	0.03
2000	km^2	2,376.78	54.44	17,018.70	2,531.89	29.8	3018.09	10.04
	%	9.49	0.22	67.97	10.11	0.12	12.05	0.04
2010	km^2	2,534.40	54.78	15,307.94	1,879.08	42.91	5217.37	3.26
	%	10.12	0.22	61.13	7.5	0.17	20.84	0.01
2020	km^2	1,473.80	139.14	12,518.10	2086.09	101.25	8705.00	16.35
	%	5.89	0.56	49.99	8.33	0.4	34.76	0.07
		Rate of change						
1990–2000	km^2	229.19	25.74	4778.38	14.23	– 81.37	– 4967.79	1.64
	%	10.67	89.69	39.04	0.57	– 73.19	– 62.21	19.52
2000–2010	km^2	157.62	0.34	– 1710.76	–652.81	13.11	2199.28	–6.78
	%	6.63	0.62	– 10.05	–25.78	43.99	72.87	–67.53
2010–2020	km^2	– 1060.6	84.36	– 2789.84	207.01	58.34	3487.63	13.09
	%	– 41.85	154.00	– 18.22	11.02	135.96	66.85	401.53

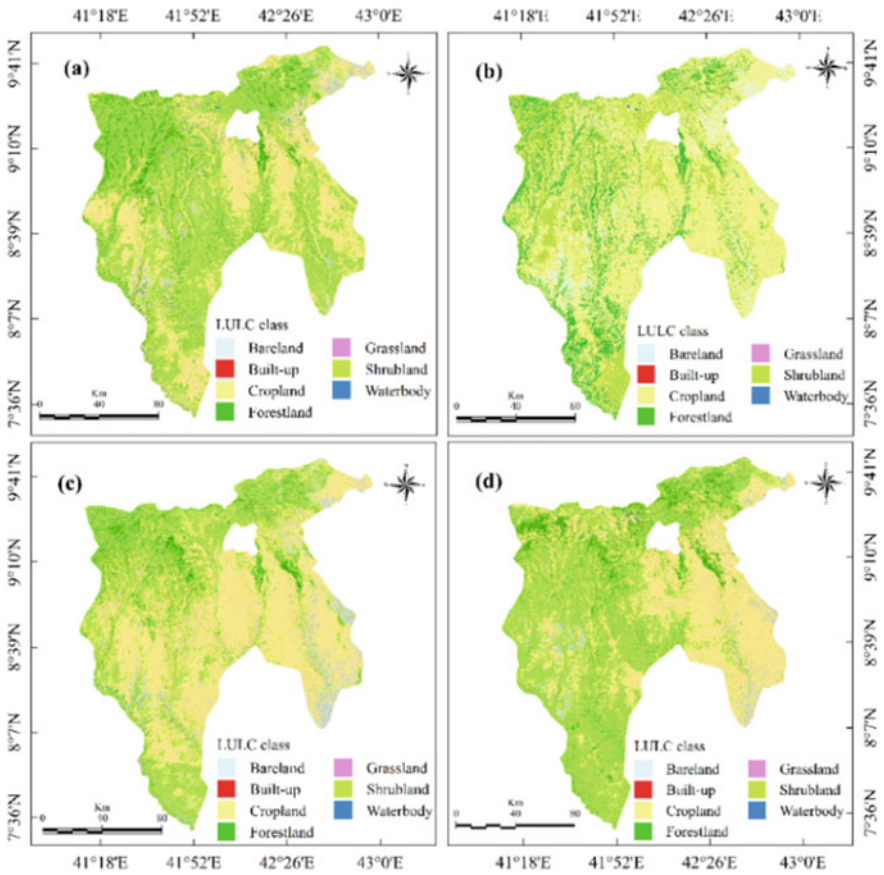

Fig. 8.2 The land-use and land-cover classes: **a** 1990, **b** 2000, **c** 2010, and **d** 2020

However, there was less confusion between reference points and classified images for 2000, 2010, and 2020, indicating insignificant classification errors (Table 8.2). The classification accuracy for the four reference periods exceeded the recommended minimum overall accuracy (OA) of 85% and 70% for each class, which suggests that the classified images were suitable for postclassification comparison and corresponded well with the reference data.

RUSLE Model Factors

Five factors were required to estimate the soil loss rate using the RUSLE model. These factors included rainfall erosivity (R), soil erodibility (K), slope length and steepness (LS), cover management (C), and support practice (P) (Renard et al. 1997). The

Table 8.3 Percentages of LULC classification accuracy for 1990, 2000, 2010, and 2020

LULC Class	1990		2000		2010		2020	
	PA	UA	PA	UA	PA	UA	PA	UA
Bare land	90.77	84.29	93.85	91.04	100.00	98.48	92.31	98.36
Built-up	82.00	95.35	86.00	97.73	88.00	100.00	94.00	95.92
Cropland	94.44	94.44	94.44	91.40	97.78	94.62	97.78	95.65
Forestland	94.29	97.06	95.71	95.71	97.14	89.47	94.29	95.65
Grassland	86.67	96.30	96.67	100.00	90.00	100.00	93.33	96.55
Shrubland	97.65	90.22	96.47	94.25	89.41	89.41	94.12	88.89
Waterbody	100	100.00	100.00	100.00	96.67	100.00	100.00	100.00
	1990		2000		2010		2020	
Overall accuracy (%)	92.86		94.52		94.52		95.00	
Kappa (K^) statistics	0.914		0.934		0.931		0.940	

spatial analyst toolset presented in ArcGIS Desktop software version 10.8 (Environmental Systems Research Institute (Esri), Inc., Redlands, CA, USA) was utilized for deriving these parameters. Each input variable was transformed into a raster format to form the model and then reprojected to a standard spatial reference based on the World Geodetic System 1984 spheroid, along with the Universal Transverse Mercator (UTM) and Adindan Zone 37 N. Subsequently, each input layer was synchronized to a ground resolution of 30 m × 30 m. Equation 8.1 was then applied by multiplying each input layer of the factors contributing to soil erosion.

$$A = R \times K \times \mathrm{LS} \times C \times P \tag{8.1}$$

where A is the average annual soil loss (t ha^{-1} yr^{-1}); R is the rainfall-runoff erosivity factor (MJ mm ha^{-1} h^{-1} y^{-1}); K is a soil erodibility factor (t ha h ha^{-1} MJ^{-1} mm^{-1}); LS is a slope length-steepness factor (dimensionless); C is a cover management factor (dimensionless); and P is a conservation support practice factor (dimensionless).

Rainfall Erosivity (*R*) Factor

The R factor represents the intensity of soil erosion caused by rainfall runoff, in which soil materials are detached and transported due to the combined forces of rainfall volume, kinetic energy, duration, and potential in a particular area (Polovina et al. 2021; Tsegaye et al. 2020). In this study, the Climate Hazards Group InfraRed Precipitation with Station data (CHIRPS dataset) was used to create an annual time series based on mean monthly rainfall data in four time frames, namely, 1981–1990, 1991–2000, 2001–2010, and 2011–2020, from which the R factor was calculated for

1990, 2000, 2010, and 2020. We followed the computation method proposed by Lo et al. (1985) to determine the R factor.

$$R = 38.46 + 3.48 \times P \tag{8.2}$$

R is the rainfall erosivity (MJ mm ha^{-1} h^{-1} y^{-1}), and P is the average annual rainfall.

Soil Erodibility (K) Factor

The K factor value for each soil class was obtained using the erosivity-productivity effect calculator by Williams (1995), which identifies a particle's resistance to deterioration and rainwater movement, according to Watene et al. (2021). In addition, Renard et al. (1997) and Woldemariam et al. (2018) indicated that the average soil loss determined for a rainfall erosion index unit at a typical plot, apart from human effects, also depends on the soil profile and its qualities, such as texture, organic matter, structure, and permeability. The erosivity-productivity impact calculator (EPIC) tool estimates the K factor value for soil classes (Williams 1995) as follows:

$$K_{\mathrm{USLE}} = F_{\mathrm{csand}} \times F_{\mathrm{cl\,-\,si}} \times F_{\mathrm{orgC}} \times F_{\mathrm{hisand}} \tag{8.3}$$

where:

$$F_{\mathrm{csand}} = \left\{0.2 + 0.3\exp\left[-0.0256\mathrm{SAN}\left(1 - \frac{\mathrm{SIL}}{100}\right)\right]\right\} \tag{8.3a}$$

$$F_{\mathrm{cl\,-\,si}} = \left[\frac{\mathrm{SIL}}{\mathrm{CLA} + \mathrm{SIL}}\right]^{0.3} \tag{8.3b}$$

$$F_{\mathrm{orgc}} = \left[1.0 - \frac{0.0256C}{C + \exp(3.72 - 2.95C)}\right] \tag{8.3c}$$

$$F_{\mathrm{hisand}} = \left[1.0 - \frac{0.70\mathrm{SN1}}{\mathrm{SN1} + \exp(-5.51 + 22.9\mathrm{SN1})}\right] \tag{8.3d}$$

SAN, SIL, and CLA denote the percent sand, silt, and clay contents, respectively; C is the proportion of organic carbon content of each soil; and SN1 is the sand content subtracted from 1 and divided by 100 (Karamage et al. 2017).

Slope Length and Steepness (LS) Factor

The LS factor displays the percentage of soil loss at a specific site, considering a slope length (L) of 22.13 m and slope steepness (S) of 9%, as well as clear vegetation and left-in seedbed conditions. The ArcHydro extension and raster calculator (a

geoprocessing tool) were employed in ArcGIS Desktop software to calculate the LS factor using the SRTM-DEM of the study area (Eq. 8.4–8.8). Moreover, *L* and *S* are two separate subfactors of the LS factor that consider how topography affects erosion (Girma and Gebre 2020; Watene et al. 2021; Woldemariam and Harka 2020).

$$L = \left(\frac{\lambda}{22.1}\right)^{m} \tag{8.4}$$

where *L* is the slope length, λ is the field slope length in meters, and m is the variable slope length exponent related to the value of the slope gradient: 0.5 for a slope gradient of 4.5% or more, 0.4 for slopes 3–4.5%, 0.3 for slopes 1–3%, and 0.2 for slopes ≤ 1% (Uddin et al. 2018).

$$L_{i,j} = \frac{\left(A_{i,j-in} + D^2\right)^{m+1} - A_{i,j-in}^{m+1}}{D^{m+1} \cdot x_{i,j}^{m} \cdot 22.13^{m}} \tag{8.5}$$

$$m = \left(\frac{\beta}{1+\beta}\right) \tag{8.6}$$

$$\beta = \frac{\mathrm{Sin}\theta/0.0896}{3(\mathrm{Sin}\theta)^{0.8} + 0.56} \tag{8.7}$$

$$S_{i\cdot j} = \begin{cases} 10.8 \sin\theta_{i.j} + 0.03, & \tan\theta_{i.j} < 9\% \\ 16.8 \sin\theta_{i.j} - 0.50, & \tan\theta_{i.j} \geq 9\% \end{cases} \tag{8.8}$$

where $A_{i,j-\mathrm{in}}$ is the contributing area at the grid cell inlet (i, j) in m^2; D is the grid cell size; $x_{\mathrm{i,j}}$ is $\sin a_{i,j} + \cos_{i,j}$; $a_{i,j}$ is the aspect direction of the grid cell (i, j); m is a variable slope length exponent related to the ratio of β of rill erosion produced by flow and interrill erosion caused by raindrop impacts; and θ is the slope angle (gradient).

Cover Management (*C*) Factor

The *C*-factor is a dimensionless indicator of how land management methods, including soil cover, surface roughness, and moisture conditions, affect soil loss (Eniyew et al. 2021; Watene et al. 2021). The magnitude of soil loss increases with extensive tillage, which leaves a smooth surface that creates much rainfall runoff and soil erosion (Woldemariam et al. 2018). Table 8.4 provides the C coefficients for the LULC classes.

Table 8.4 The *C*-factor values adopted from published literature for LULC classes

LULC class	*C*-factor	Sources
Bare land	0.05	Haile and Fetene (2012), Belayneh et al. (2019)
Built-up	0.004	Kayet et al. (2018), Gashaw et al.(2019)
Cropland	0.15	Girma and Gebre (2020), Gashaw et al.(2020), Watene et al. (2021)
Forest	0.001	Yang et al. (2003), Zerihun et al. (2018), Moisa et al. (2021)
Grassland	0.01	Moges and Bhat (2018)
Shrubland	0.014	Gelagay and Minale (2016), Moges and Bhat (2018), Belayneh et al. (2019)
Waterbody	0.00	Gelagay and Minale (2016), Moges and Bhat (2018)

Support Practice (P) Factor

The support practice component for estimating soil loss rates represents the conservation measures implemented to prevent soil deterioration in a specific location (Renard et al. 1997). It is characterized by factor *P*, whose value ranges from zero to one. A value of one indicates areas with little or no conservation practices, while zero indicates fields with effective conservation practices (Moges et al. 2020). However, due to the lack of data on conservation practices, we resorted to setting the P-factor value based on a slope classification for cropland and noncropland classes, following the reference (Wischmeier and Smith 1978). This enabled us to account for the contributing conservation practices aimed at reducing soil erosion. Additionally, the soil loss rate in cropland areas for 2020 was estimated, considering contouring, strip cropping, and terracing based on slope classes and the recommended P values by Shin (1999), as outlined in Table 8.5.

Table 8.5 The slope classes with the P-factor for erosion control practices

Slope (%)	Area (%)	Conservation support practice (*P*) factors		
		Contouring	Strip cropping	Terracing
0–7.0	44.41	0.55	0.27	0.10
7.0–11.3	12.71	0.60	0.30	0.12
11.3–17.6	12.40	0.80	0.40	0.16
17.6–26.8	11.94	0.90	0.45	0.18
> 26.8	18.54	1.00	0.50	0.20

Estimated Rate of Soil Erosion

The estimated total soil loss rates in the EHZ were 9.16 Mt yr^{-1} (1990), 14.02 Mt yr^{-1} (2000), 12.20 Mt yr^{-1} (2010), and 10.84 Mt yr^{-1} (2020), showing an overall increase of 18.37% from 1990 to 2020. The resulting spatial patterns of soil erosion risk are shown in Fig. 8.3. The average soil erosion rates were estimated at 32.94 t ha^{-1} yr^{-1}, 50.42 t ha^{-1} yr^{-1}, 43.84 t ha^{-1} yr^{-1}, and 38.99 t ha^{-1} yr^{-1} for 1990, 2000, 2010, and 2020, respectively, with values ranging from 0 to 1502.17 t ha^{-1} yr^{-1}, 0 to 1,015.34 t ha^{-1} yr^{-1}, 0 to 1,289.87 t ha^{-1} yr^{-1}, and 0 to 1,150.78 t ha^{-1} yr^{-1}, respectively. The results revealed that 81.27%, 80.31%, 79.65%, and 82.03% of the area had a sustainable loss (< 10 t ha^{-1} yr^{-1}; (Fenta et al. 2021) in 1990, 2000, 2010, and 2020, respectively. High erosion risk-prone areas were found across mountainous terrains in the northern parts. In contrast, southern areas were less susceptible to soil loss throughout the study period.

Our district wise analysis showed that none of the eighteen EHZ districts had very high (80–120 t ha^{-1} yr^{-1}) or extremely high (> 120 t ha^{-1} yr^{-1}) soil erosion risks in 1990 (Table 8.7). During the first study period, most districts were prone to high-medium to very-high risk, with an average erosion rate ranging from 40 to 80 t ha^{-1} yr^{-1}. Among them, nine districts (average erosion rates ranged from 22.22 to 38.45 t ha^{-1} yr^{-1}) accounted for 36.09% of the area, namely, Kombolcha (22.22 t ha^{-1} yr^{-1}), Jarso (22.91 t ha^{-1} yr^{-1}), Haro Maya (22.95 t ha^{-1} yr^{-1}), Meyu Muleke (26.39 t ha^{-1} yr^{-1}), Bedeno (32.36 t ha^{-1} yr^{-1}), Girawa (32.36 t ha^{-1} yr^{-1}), Kersa (35.84 t ha^{-1} yr^{-1}), Deder (36.10 t ha^{-1} yr^{-1}), and Kurfa Chele (38.45 t ha^{-1} yr^{-1}), which contributed 32.22% of the annual soil loss. At the zonal level, four districts had average erosion rates in the range of 40–80 t ha^{-1} yr^{-1}, characterized by medium–high (40–60 t ha^{-1} yr^{-1}) and high (60–80 t ha^{-1} yr^{-1}) erosion risks: Melka Balo lost 69.82 t ha^{-1} yr^{-1}, Golo Oda lost 59.97 t ha^{-1} yr^{-1}, Meta lost 58.81 t ha^{-1} yr^{-1}, and Goro Gutu lost 56.44 t ha^{-1} yr^{-1}, accounting for 49% of annual soil erosion by water. Meanwhile, Fedis, Gursum, Chinaksen, and Midega Tola, with low rainfall rates (a mean value ranging from 598.09 to 678.50 mm yr^{-1}; mean slope ranging from 6.69 to 14.17%), had an average soil loss range of 10–20 t ha^{-1} yr^{-1}, and they were categorized as districts with low-medium erosion risk (Fig. 8.4).

The results confirmed an increase in the soil erosion rate between 1990 and 2000, with the highest increase estimated in Meta (8.21×10^5 t), followed by Melka Balo (7.58×10^5 t), Deder (7.32×10^5 t), Bedeno (6.32×10^5 t), Babile (6.07×10^5 t), and Girawa (4.96×10^5 t), which occupied 41.22% of the study area and contributed 54.90% of the soil loss in 2000. However, Golo Oda and Meyu Muleke showed the highest reduction in the estimated soil erosion rate, with total soil losses of 3.7×10^5 t and 5.03×10^5 t, respectively. During the same period, Meta, Deder, and Melka Balo were all exposed to extremely high erosion risk (> 120 t ha^{-1} yr^{-1}), with average rates of 171.58 t ha^{-1} yr^{-1}, 145.72 t ha^{-1} yr^{-1}, and 119.56 t ha^{-1} yr^{-1}, respectively.

Our estimate further indicated that between 2000 and 2010, soil loss was reduced in fourteen districts that occupied 61.17%, with Deder having the most significant reduction (5.52×10^5 t or 82.64 t ha^{-1} yr^{-1}), Meta having 3.94 × 105 t (54.15 t

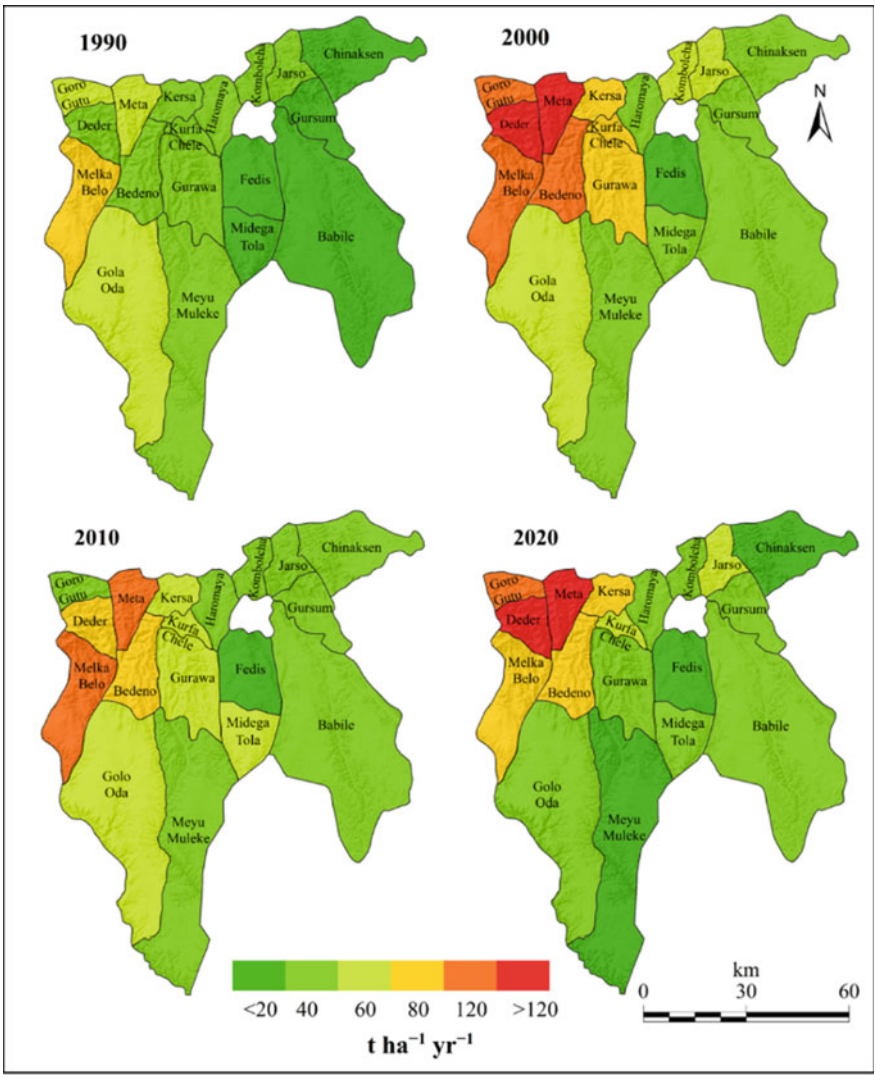

Fig. 8.3 Spatial patterns of mean soil loss rates: **a** 1990; **b** 2000; **c** 2010; and **d** 2020

ha^{-1} yr^{-1}), Goro Gutu having 2.75 $\times$ 10^5 t (61.19 t ha^{-1} yr^{-1}), Bedeno having 2.57 $\times$ 10^5 t (23.71 t ha^{-1} yr^{-1}), and Girawa having 1.96 $\times$ 10^5 t (12.06 t ha^{-1} yr^{-1}). In contrast, it is worth revealing that soil loss rates increased in Golo Oda: 3.4 $\times$ 10^5 t (7.57 t ha^{-1} yr^{-1}; the average slope is 13.47%); Meyu Muleke: 1.36 $\times$ 10^5 t (3.31 t ha^{-1} yr^{-1}; 12.10%); and Midega Tola: 3.18 $\times$ 10^4 t (3.48 t ha^{-1} yr^{-1}; 11.39%), which are situated in the south and the southwestern parts; and Fedis: 2.04 $\times$ 10^4 t (1.59 t ha^{-1} yr^{-1}; the average slope is 6.69%) in the southeastern part.

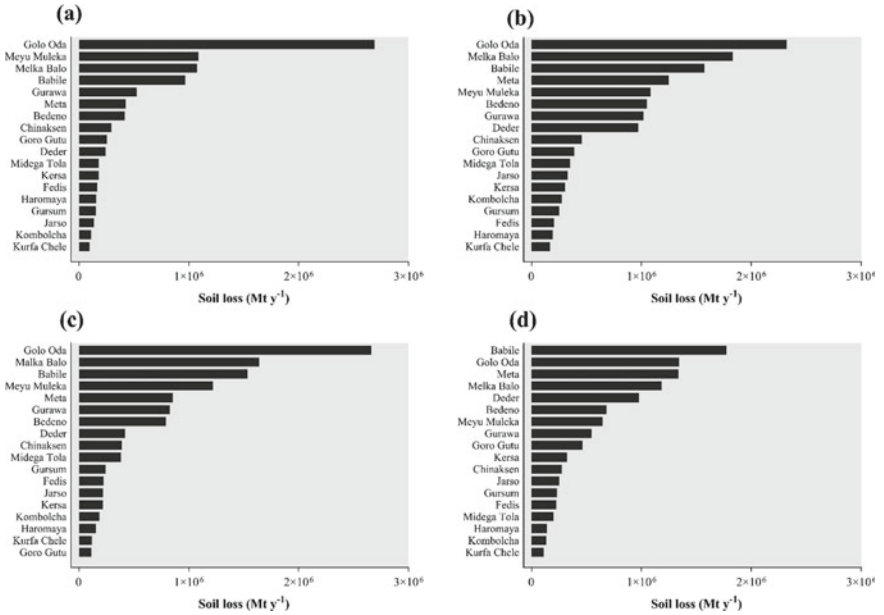

Fig. 8.4 Estimated total soil loss per district in the EHZ, Ethiopia: **a** 1990; **b** 2000; **c** 2010; and **d** 2020

From 2010 to 2020, Deder observed the most remarkable increase in the soil loss estimate of 5.56×10^5 t, followed by Meta (4.83×10^5 t), Goro Gutu (3.49×10^5 t), Babile (2.42×10^5 t), Kersa (1.05×105 t), Jarso (3.16×10^4 t), and Fedis (6.53×10^2 t), while a more considerable reduction appeared in Golo Oda (1.32×10^6 t), Meyu Muleke (5.73×10^5 t), Melka Balo (4.56×10^5 t), and Girawa (2.82×10^5 t). In 2020, the estimated annual soil erosion was found to be up to 1.77×10^6 t (30.43 t ha^{-1} yr^{-1}) in Babile, 1.34×10^6 t in Meta (183.72 t ha^{-1} yr^{-1}), 1.18×10^6 t in Golo Oda (29.91 t ha^{-1} yr^{-1}), and 1.18×10^6 t (77.05 t ha^{-1} yr^{-1}) in Melka Balo, which are the top priority districts for comprehensive SWC practices. These districts (accounting for 45.23% of the area and contributing 52.02% of the annual soil loss) have a higher erosion risk attributable to the combined effects of increased rainfall intensity (average rainfall reaches 962.69 mm yr^{-1}), steep slopes, deforestation, and overgrazing. The average slope in these districts ranged from 9.17% in Babile, located in the southwestern part, to 29.93% in Meta, in the northwestern part. Deder (9.78×10^5 t), Bedeno (6.82×10^5 t), Meyu Muleke (6.47×10^5 t), Girawa (5.44×10^5 t), and Goro Gutu (4.63×105 t) were identified as second priorities, with average soil loss rates of 146.31 t ha^{-1} yr^{-1}, 62.97 t ha^{-1} yr^{-1}, 15.68 t ha^{-1} yr^{-1}, and 102.96 t ha^{-1} yr^{-1}, respectively. Furthermore, the remaining districts (i.e., accounting for 26.21% of the area and 17.42% of the annual soil erosion), such as Jarso, Kersa, Chinaksen, Gursum, Fedis, Midega Tola, Haro Maya, Kombolcha, and Kurfa Chele, have soil loss ranging from 1.10×10^5 to 3.22×10^5 t and are

identified as the third priority, which can be considered for appropriate intervention in SWC measures. The average erosion rates (in 2020; t ha^{-1} yr^{-1}) for the third priority districts were estimated at 41.57, 64.52, 16.33, 26.22, 17.52, 21.91, 20.57, 27.38, and 42.23, respectively.

Erosion Risk Along Slope Gradients

This subsection presents the estimated erosion rates for different gradients, showing that the soil loss levels increased linearly with rising slope gradients and rainfall (Table 8.8). This might be attributable to the eruptive power of precipitation that strikes the soil surface per unit time, shortening infiltration time, and aggravating runoff and soil erosion (Karamage et al. 2017; Shojaei et al. 2020; Watene et al. 2021). Moreover, the results showed that cropland soil loss increased with increasing slope. For example, croplands with high-intensity rainfall ranges of 693 to 767 mm yr^{-1} had steeper slopes ($\beta > 26.8\%$) and high average soil loss values of 259.4 t ha^{-1} yr^{-1} in 1990, 236 t ha^{-1} yr^{-1} in 2000, 242.9 t ha^{-1} yr^{-1} in 2010, and 257.6 t ha^{-1} yr^{-1} in 2020.

Long-term changes in LULC could potentially lead to a decrease in land productivity, which could have contributed to the expansion of croplands in upslope areas. However, despite the expansion of croplands, inadequate vegetation cover, and unsustainable land use and management practices in these regions, the heightened vulnerability increased the likelihood of higher soil erosion rates during the period under study. This observation aligns with the findings of Fenta et al. (2021), which suggest that human activities significantly increase the risk of erosion over time. As the population grows and food demands rise, more land is being cleared for agriculture, extending into unsuitable areas such as steep slopes and closed regions, resulting in higher soil erosion rates in sloping landscapes. This, in turn, reduces land productivity and has been highlighted by previous studies (Haile et al. 2006; Nijimbere and Lizana 2019; Tesfaye et al. 2021).

Table 8.8 shows the temporal variability in erosion rates along slope gradients within the four reference periods. The comparative analysis of the estimated soil erosion flanked by different slope classes showed that the soil loss rates increased considerably in the 1990–2000 period and decreased slightly in the following 10-year period (2000–2010) and the latter decade (2010–2020). For example, the risk of soil erosion in the lower slope grade ($\beta < 7\%$) decreased by 4.42% between 1990 and 2000, while the increase in the average soil loss of this slope class (5.93%) in the 2000–2010 period decreased significantly (16.8%) in the 2010–2020 period. Moreover, the present study found that landscapes with very steep slopes (> 26%) and high average rainfall intensity (693.06–767.32 mm yr^{-1}) accounted for 48.60% of soil loss in 1990, 51.95% in 2000, 49.96% in 2010, and 50.39% in 2020. In contrast, the lower slope gradient of the study area had a low average soil erosion rate with a relatively moderate rise ($\beta < 7\%$); 11.3 t ha^{-1} yr^{-1}, 11.8 t ha^{-1} yr^{-1}, 12.5 t ha^{-1} yr^{-1}, and 10.4 t ha^{-1} yr^{-1}, respectively. During each period, the lowest soil

loss in the flat terrain is relatively attributable to the low-intensity average rainfall for the slope class: 549–634 mm yr^{-1}, accounting for 15.30%, 10.38%, 12.72%, and 11.91% of the annual soil loss.

Our result resonates with the findings of Watene et al. (2021) for the Kenyan Great Rift Valley Region. They reported that the average annual soil loss (14.99 t ha^{-1} yr^{-1} in 1990) for areas with steep slopes ($\beta = 17.6–26.8\%$) showed the most significant soil erosion net change in 2015, with a rate of 18.53 t ha^{-1} yr^{-1}. Yesuph and Dagnew (2019) also reported a direct link between the highest soil loss rates and steeper slopes, showing that the soil loss ranges from 91 t ha^{-1} yr^{-1} to 935 t ha^{-1} yr^{-1} in areas with a slope higher than 60% in the Beshillo Catchment, Blue Nile Basin, Ethiopia. Olorunfemi et al. (2020) reported a similar observation in Ekiti State, Nigeria, which estimated the highest erosion rate of 15.07 t ha^{-1} yr^{-1} for landscapes under very steep slopes. In comparison, the lower soil erosion rate of 0.39 t ha^{-1} yr^{-1} on gentle slopes (Olorunfemi et al. 2020) was corroborated by our results. Rodrigo-Comino et al. (2017) also concluded that sloping Mediterranean agriculture fields under bare soils with limited protective vegetation resulted in the highest runoff and soil loss rates. Supporting these findings, Karamage et al. (2016) and Nambajimana et al. (2020) highlighted that the growth of widespread agriculture and unsustainable practices, such as deforestation on steep slope areas, significantly increases water erosion. Woldemariam et al. (2018) established that the priority areas with higher soil loss rates and increasing erosion risks were confined to steep slopes ranging from 30 to 50% and above, demanding intensive conservation measures. Endalamaw et al. (2021) reported that the Gilgel Beles watershed in the Upper Abay River basin, Ethiopia, also shows severe soil loss on steep slopes with intensive farming, while lower soil loss in saturated downstream areas is susceptible to gully formation. Our results further resonate with the findings of studies in many regions elsewhere, in which high soil erosion rates accompanied steep slopes, while the lowest erosion was associated with flat and gentle gradients (Belayneh et al. 2019; Karamage et al. 2017; Kayet et al. 2018; Mohammed et al. 2020; Molla and Sisheber 2017; Shojaei et al. 2020; Uddin et al. 2018; Zerihun et al. 2018).

Effect of LULC Change on Soil Erosion

LULCs are bound to undergo nonlinear changes due to interconnected natural and human-induced factors. These changes are frequently associated with soil erosion. (Kogo et al. 2020; Tesfaye et al. 2021; Woldemariam and Harka 2020). According to Eekhout and Vente (2022), alterations in LULC can result in soil loss through agricultural expansion and deforestation or decrease soil erosion attributable to agricultural abandonment and reforestation. Figure 8.5 shows the estimated soil loss rates for LULC classes in 1990, 2000, 2010, and 2020, while Table 8.6 provides information on the change between classes and their contribution to changes (increasing or decreasing) in the soil erosion estimate during the periods 1990–2000, 2000–2010, and 2010–2020. The LULC map of the study area (Sect. 8.4.1; Fig. 8.2a–d) revealed

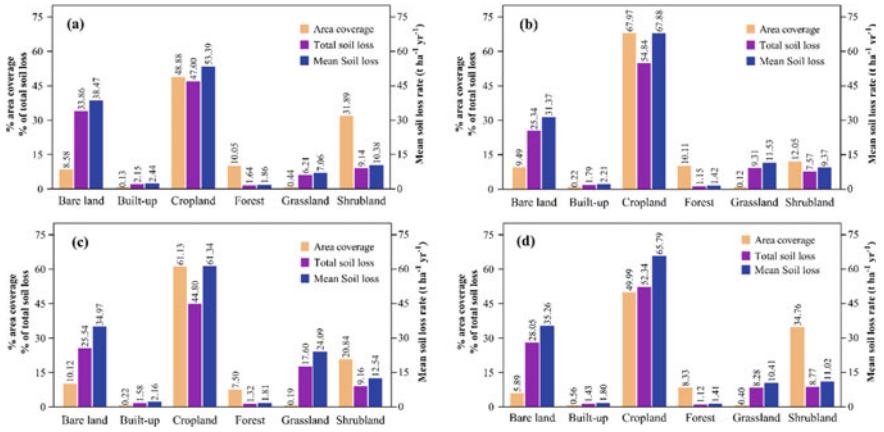

Fig. 8.5 Area coverage, mean soil erosion, and the corresponding proportion of total annual soil loss per LULC class in Ethiopia's East Hararghe Zone; **a** 1990, **b** 2000, **c** 2010, and **d** 2020

that cropland was the dominant category, accounting for 48.88%, 67.97%, 61.13%, and 49.99% in 1990, 2000, 2010, and 2020, respectively.

The estimated average soil erosion rates corresponding to different LULC categories in 1990 revealed that cropland's average soil loss was 53.39 t ha^{-1} yr^{-1}, much higher than the moderate soil loss rates on bare land, 38.47 t ha^{-1} yr^{-1}, grassland, 7.06 t ha^{-1} yr^{-1}, and shrubland, 10.38 t ha^{-1} yr^{-1}. In contrast, forestland had the lowest average soil loss of 1.86 t ha^{-1} yr^{-1}, followed by built-up area (2.44 t ha^{-1} yr^{-1}), which was resistant to soil loss by water erosion. Congruently, several studies have been carried out in East African countries (Karamage et al. 2017; Kogo et al. 2020; Watene et al. 2021; Woldemariam and Harka 2020) and elsewhere in the world (Koirala et al. 2019; Uddin et al. 2018) and have estimated relatively lower average soil loss in forestlands, which regulate soil erosion (Olorunfemi et al. 2020; Rajbanshi and Bhattacharya 2020), compared to other LULC types, which is most likely attributable to a lower C-factor value in vegetated areas (Fenta et al. 2021).

Between 1990 and 2000, the average soil loss rate for LULC classes under cropland and grassland areas increased by 27.14% (+ 14.49 t ha^{-1} yr^{-1}) and 63.31% (+ 4.47 t ha^{-1} yr^{-1}), respectively. In contrast, the average soil loss rate decreased by 18.46% (− 7.1 t ha^{-1} yr^{-1}), 9.43% (− 0.23 t ha^{-1} yr^{-1}), 23.66% (− 0.44 t ha^{-1} yr^{-1}), and 9.73% (− 1.01 t ha^{-1} yr^{-1}) for the bare land, built-up, forest, and shrubland LULC classes, respectively. During this period, the landscape that experienced LULC change accounted for 49.33% (12,347.98 km^2) of the total, of which 17.24% showed an increase in the average soil erosion of 79.74 t ha^{-1} yr^{-1}. The remaining landscapes (3820.7 km^2 or 15.27%) under LULC change showed a reduction in average soil loss of 79.20 t ha^{-1} yr^{-1}. The highest increase in average soil loss rates was found in areas where land once protected by the forest was turned into cropland (+ 16.61 t ha^{-1} yr^{-1}), followed by grassland to cropland (+ 6.36 t ha^{-1} yr^{-1}). This finding agreed with a study that estimated the highest soil losses in croplands

Table 8.6 LULC changes and associated soil erosion (t ha − 1 yr − 1) in Ethiopia's East Hararghe Zone

		Bare land	Built-up	Cropland	Forest	Grassland	Shrubland
2000–2010	Bare land	0.60	− 3.03	5.04	− 2.89	− 2.68	− 3.82
	Built-up	1.35	0.01	4.37	− 0.47	0.43	0.89
	Cropland	− 5.98	− 7.90	0.61	− 18.97	− 9.31	− 7.85
	Forest	5.37	0.23	16.61	− 0.02	0.39	1.11
	Grassland	2.65	− 1.00	6.36	− 1.36	0.03	0.77
	Shrubland	3.69	− 0.53	4.05	− 2.06	− 0.25	0.10
2000–2010	Bare land	− 0.37	− 1.67	5.39	− 3.86	− 2.94	− 3.11
	Built-up	2.06	− 0.01	6.40	− 0.30	0.07	0.62
	Cropland	− 5.17	− 6.24	− 0.46	− 16.42	− 11.17	− 4.93
	Forest	4.83	0.22	16.30	− 0.02	0.62	1.60
	Grassland	9.94	− 2.59	32.32	− 0.72	− 0.14	0.72
	Shrubland	3.22	− 0.77	10.00	− 1.35	− 0.76	− 0.11
2010–2020	Bare land	− 0.11	− 2.20	4.61	− 1.31	− 10.57	− 2.96
	Built-up	1.36	0.00	4.12	− 0.35	0.32	0.71
	Cropland	− 5.00	− 6.59	− 0.09	− 20.74	− 29.67	− 11.71
	Forestland	2.12	0.21	11.28	0.00	1.17	1.13
	Grassland	3.14	− 0.92	7.94	− 0.84	− 0.02	0.72
	Shrubland	3.39	− 0.74	7.76	− 2.24	− 1.01	− 0.02

established at the expense of forest clearance compared to areas exchanged simultaneously from cropland into forestland (Woldemariam and Harka 2020), suggesting that the conversion of noncropland regions to croplands increased the amount of soil loss by water erosion (Borrelli et al. 2017; Fenta et al. 2021; Moisa et al. 2021).

Moreover, the findings of Kogo et al. (2020) for the Sio, Yala, and Upper Nzoia subbasins in Kenya confirmed our results, showing that the highest soil erosion was observed in the transformation of forest and grassland/shrub areas into farmland. Similarly, Raiesi and Beheshti (2022) demonstrated a distinctive phenomenon of how deforestation, along with the change of natural forests to cropland areas, has caused the degradation of soil quality in the Hyrcanian forests of Northern Iran. Therefore, restriction of deforestation practices, improved agricultural management methods, and proper policy measures are required for restoring degraded forests and mitigating detrimental environmental impacts (Raiesi and Beheshti 2022). The conversion of areas covered by cropland to a built-up area (0.07%), forest (3.38%), shrubland (23.04%), and grassland (0.20%) reduced the average soil erosion by 87.14% (7.9 t ha^{-1} yr^{-1}), 80.02% (18.97 t ha^{-1} yr^{-1}), 32.23% (7.85 t ha^{-1} yr^{-1}), and 10.63% (9.31 t ha^{-1} yr^{-1}), respectively. Similarly, Liu et al. (2022) reported that shade-tolerant herb species reduced runoff volume and could effectively moderate

Table 8.7 Estimated total and mean actual soil loss per district in the East Hararghe Zone

District name	Area (%)	1990		2000		2010		2020		Net Change 1990–2020
		Total Mt y^{-1}	Mean t ha^{-1} y^{-1}	Total Mt y^{-1}	Mean t ha^{-1} y^{-1}	Total Mt y^{-1}	Mean t ha^{-1} y^{-1}	Total Mt y^{-1}	Mean t ha^{-1} y^{-1}	
Jarso	2.18	0.14	22.91	0.33	54.42	0.22	36.35	0.25	41.57	18.66
Kombolcha	1.77	0.11	22.22	0.27	55.5	0.19	37.87	0.14	27.38	5.16
Meta	2.62	0.43	58.81	1.25	171.58	0.86	117.42	1.34	183.72	124.91
Haramaya	2.47	0.16	22.95	0.19	27.99	0.15	22.22	0.14	20.57	–2.38
Goro Gutu	1.62	0.25	56.44	0.39	86.59	0.11	25.41	0.46	102.96	46.52
Gursum	3.18	0.15	17.37	0.25	28.52	0.24	27.39	0.23	26.22	8.85
Kersa	1.79	0.18	35.84	0.30	61.03	0.22	43.51	0.32	64.52	28.68
Deder	2.4	0.24	36.1	0.97	145.72	0.42	63.07	0.98	146.31	110.21
Babile	20.95	0.97	16.61	1.57	27.02	1.53	26.29	1.77	30.43	13.82
Kurfa Chele	0.93	0.10	37.1	0.17	64.9	0.12	45.11	0.11	42.23	5.13
Bedeno	3.89	0.42	38.45	1.05	96.84	0.79	73.13	0.68	62.97	24.52
Gurawa	5.83	0.52	32.36	1.02	62.96	0.83	50.9	0.54	33.54	1.18
Melka Balo	5.53	1.07	69.82	1.83	119.56	1.64	106.73	1.18	77.05	7.23
Golo Oda	16.13	2.69	59.97	2.32	51.71	2.66	59.27	1.34	29.91	–30.06
Fedis	4.6	0.17	12.93	0.20	15.87	0.22	17.46	0.22	17.52	4.59
Midega Tola	3.28	0.18	19.74	0.35	38.39	0.38	41.88	0.20	21.91	2.17
Meyu Muleka	14.83	1.09	26.39	1.08	26.27	1.22	29.58	0.65	15.68	–10.71
Chinaksen	6.01	0.30	17.66	0.46	27.27	0.39	23.45	0.27	16.33	–1.33
Total	100	9.16	32.94	14.02	50.42	12.20	43.84	10.84	38.99	6.05

Table 8.8 Estimated soil erosion per slope class and the contribution to annual soil loss, the proportion of the total cropland areas with average soil loss rates, and mean annual rainfall in 1990, 2000, 2010, and 2020

Slope (%)	Mean soil loss in the class (t ha^{-1} yr^{-1})	% of annual soil loss	% of cropland in the class	Soil loss in cropland (t ha^{-1} yr^{-1})	Mean rainfall (mm y^{-1})
1990					
< 7.0	11.3	15.30	61.54	15.1	634.66
7.0–11.3	22.3	8.62	12.17	39.5	685.19
11.3–17.6	31.1	11.73	9.31	66.9	714.20
17.6–26.8	43.3	15.76	7.48	109.7	736.05
> 26.8	86	48.60	9.51	259.4	763.60
Total	16.47	100.00	100.00	5.34	686.89
2000					
< 7.0	11.8	10.38	48.79	14.6	549.36
7.0–11.3	30.3	7.65	13.05	39.6	612.49
11.3–17.6	49.2	12.13	12.20	67.1	644.03
17.6–26.8	75.4	17.89	11.10	109.8	667.38
> 26.8	140.9	51.95	14.86	236	693.06
Total	32.93	100.00	100.00	6.79	609.73
2010					
< 7.0	12.5	12.72	55.34	15.2	607.95
7.0–11.3	28.3	8.22	12.46	41.8	676.68
11.3–17.6	42.7	12.11	10.76	70.3	709.40
17.6–26.8	62.3	17.00	9.27	112.9	733.24
> 26.8	117.8	49.96	12.17	242.9	759.26
Total	24.99	100.00	100.00	6.13	672.14
2020					
< 7.0	10.4	11.91	55.16	15.1	622.58
7.0–11.3	23.5	7.68	12.10	42.8	685.79
11.3–17.6	37.6	11.98	10.64	75.6	717.83
17.6–26.8	58.8	18.04	9.65	125.6	740.67
> 26.8	105.7	50.39	12.45	257.6	767.32
Total	23.31	100.00	100.00	65.79	659.81

soil erosion in a forest-grassland complex ecosystem in the Loess Plateau Yangling, Shaanxi Province, China.

The estimated average erosion rates for LULC classes in 2010 were as follows: cropland (61.34 t ha^{-1} yr^{-1}), bare land (34.97 t ha^{-1} yr^{-1}), grassland (24.09 t ha^{-1} yr^{-1}), shrubland (12.54 t ha^{-1} yr^{-1}), and built-up areas (2.16 t ha^{-1} yr^{-1}) (Figs. 8.2c and 8.5c). Additionally, based on the 2020 LULC categories, cropland

had the highest average soil erosion rate (65.79 t ha^{-1} yr^{-1}), followed by bare land (35.26 t ha^{-1} yr^{-1}), shrubland (11.02 t ha^{-1} yr^{-1}), grassland (10.41 t ha^{-1} yr^{-1}), and built-up areas (1.80 t ha^{-1} yr^{-1}) (Figs. 8.2d and 8.5d). In contrast, forestland areas accounted for approximately 7.50% and 8.33% in 2010 and 2020, respectively (Fig. 8.2c, d), with average values of 1.81 t ha^{-1} yr^{-1} in 2010 and 1.41 t ha^{-1} yr^{-1} in 2020, which significantly mitigated soil loss due to water erosion. Our results demonstrated an increase in the average soil loss rates of cropland (+ 7.25%) and bare land (+ 0.83%) but a reduction in the average soil loss rates of grassland (− 56.79%), forestland (− 22.10%), built-up (− 16.67%), and shrublands (− 12.12%) from 2010 to 2020.

We found a reduction in the spatial extent of LULC changes within the second and third periods. This might be the main factor in reducing soil loss by 13.04% and 13.06%, respectively. Likewise, we estimated a reduction in the average erosion for landscapes that experienced LULC change in the second period (4280.48 km^2) with 17.09 t ha^{-1} yr^{-1} and the third period (3870.68 km^2) with 15.46 t ha^{-1} yr^{-1}. In contrast, an increase in average soil loss of 113.75 t ha^{-1} yr^{-1} and 56.17 t ha^{-1} yr^{-1} occurred in the remaining landscape that experienced changes in the second (5655 km^2) and third (7454.34 km^2) periods, attributed primarily to cropland extension at the expense of other LULC categories. While Nambajimana et al. (2020) reported the highest average soil loss rate of 91.6 t ha^{-1} yr^{-1} in landscape areas changed from grassland to forestland, which is, however, not valid in the case of the current study's result, we conversely estimated a reduction in the average soil loss rate of 0.72 t ha^{-1} yr^{-1} and 0.84 t ha^{-1} yr^{-1} in 200–2010 and 2010–2020, respectively, for those changes that have occurred in landscape areas under the same LULC category (Table 8.6).

Contrasting Conservation Strategies

Topsoil loss due to water erosion represents the most severe environmental issue in Ethiopia's EHZ. This problem endangers soil and water resources (Daba 2003; Woldemariam and Harka 2020). During the last few decades, the government, development partners, and local communities at various levels have become heavily involved in SWC programs. These programs seek to enhance agricultural productivity potential and restore degraded lands. One example of such involvement is through multiple free labor mobilization events (Woldemariam et al. 2018). Gashaw (2015) and Gadisa (2021) reviewed erosion risks, SWC implementation challenges, and positive contributions to various regions in the country. However, despite established management efforts and considerable SWC investments, their effectiveness in reducing soil erosion has rarely been researched. This prompts a comprehensive assessment to determine effective measures to minimize the removal of nutrient-rich, fertile topsoil and ensure long-term sustainability for ecosystems and their services.

On the other hand, bridging the research gap and developing efficient anti-exposure and SWC measures to combat land degradation will require performing

local studies. These studies identify erosion-prone areas to prioritize the best management methods for intervention (Dibaba et al. 2021; Woldemariam et al. 2018). In this study, we investigated the potential of conventional support practices in reducing soil erosion rates in cropland areas of Ethiopia's EHZ. To achieve this goal, we determined the P-factors, a management index related to overall crop performance, based on topography (slope gradient). We assigned them to well-established conservation practices assumed to be implemented in cropland areas, namely, contouring, strip cropping, and terracing.

According to the recommendations by Wischmeier and Smith (1978), the P-factor was established for the 2020 LULC classes. Modeled soil erosion for baseline land management revealed that the EHZ's cropland covered 49.99% (Table 8.2; Fig. 8.2d) and that the average soil loss was estimated at 65.79 t ha^{-1} yr^{-1} (Fig. 8.6a), accounting for 52.34% of the annual soil loss. The soil loss estimates for a baseline scenario are much higher than the Ethiopian Highland Reclamation Study (FAO 1986), which estimated the average soil erosion on cropland fields in Ethiopia at 42 t ha^{-1} yr^{-1}. Our estimate is also approximately twice the national average soil erosion rate (36.5 t ha^{-1} yr^{-1}) for croplands, 26 × 10^6 ha (Fenta et al. 2021). Previous investigators in the EHZ (Woldemariam & Harka 2020), other regions of the country (Endalamaw et al. 2021; Yesuph & Dagnew 2019), and elsewhere in the world (Borrelli et al. 2017; Karamage et al. 2017; Watene et al. 2021) also predicted higher soil loss rates in croplands than in other LULC classes. Our baseline soil loss value shows that all croplands (12,518.10 km^2) are at high erosion risk, with 25.07% of them experiencing unsustainable soil loss rates (> 1 t ha^{-1} yr^{-1}) (Karamage et al. 2017; Watene et al. 2021). In contrast, the estimated soil loss rate of 14.10% of the cropland area exceeds the soil loss tolerance of 10 t ha^{-1} yr^{-1} (Fenta et al. 2020). They were found on steep slopes (β = 22%–44%) with a high rainfall intensity of 741–1227 mm yr^{-1} (Table 8.8).

Our analysis of the potential contribution of conservation practices allowed us to examine the implications of assumed support practices in reducing average soil erosion rates in cropland areas. Overall, the estimated soil erosion was much lower in all three support practices than in the baseline. The conducted comparison showed

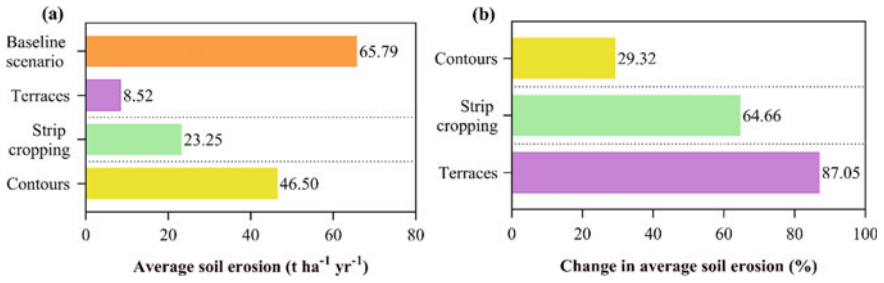

Fig. 8.6 The soil erosion rate under the baseline conservation practices (**a**) and the reduced average soil erosion compared to the baseline scenario (**b**)

that the reductions in the baseline soil loss rate varied depending on the conservation scenarios considered in the model. According to our estimates, terraces could reduce average soil loss rates in cropland areas of the studied landscape by 87.05%, or from baseline to 8.52 t ha^{-1} yr^{-1}. In comparison, strip cropping decreased the average soil loss rates by 64.66%, from baseline to 23.25 t ha^{-1} yr^{-1}. Furthermore, cropland management based on contouring could reduce the average rate of soil loss by approximately 29.32% compared to the baseline scenario, given that the corresponding soil loss rate might become 46.50 t ha^{-1} yr^{-1}. Hence, the contour-based estimated average soil erosion was 19.29 t ha^{-1} yr^{-1} lower than the baseline average soil loss but higher than the terracing- and strip-cropping-estimated rates by 81.68% (37.98 t ha^{-1} yr^{-1}) and 50% (23.25 t ha^{-1} yr^{-1}), respectively.

We compared the current study's results to previous studies' findings that have explored similar practices to confirm the robustness of each measure in croplands in tropical Africa. For example, our results agreed well with the more recent work by Watene et al. (2021), which stated a reduction in the average soil loss rate compared to the baseline scenario of 84.4%, or from 18.0 t ha^{-1} yr^{-1} to 2.8 t ha^{-1} yr^{-1}, 60%, or from 18.0 t ha^{-1} yr^{-1} to 7.2 t ha^{-1} yr^{-1}, and 24.44%, or from 18.0 t ha − 1 yr^{-1} to 14.4 t ha^{-1} yr^{-1}, for terraces, strip cropping, and contouring, respectively. Karamage et al. (2016) conducted a similar study in the Nyabarongo River catchment, Rwanda. They found that implementing terracing, strip cropping, and contouring in cropland areas might reduce the average annual soil loss by 7 t ha^{-1} yr^{-1}, 18 t ha^{-1} yr^{-1}, and 35 t ha^{-1} yr^{-1}, respectively, from the baseline estimate (Karamage et al., 2016). A study from the same county found that terracing, over other land management practices such as strip cropping and contouring, could reduce the average soil loss rate in cropland areas by up to 19.86%, or 11.7 t ha^{-1} yr^{-1}, compared to the baseline value of 14.6 t ha^{-1} yr^{-1}, demonstrating that spatially explicit conservation measures can significantly contribute to a reduction in soil erosion by water at a national scale (Nambajimana et al. 2020). At the same time, a large proportion of the country's cropland areas (45.2%; average slopes, 28.5–85%) may continue to experience higher soil loss rates, estimated to be more than 10 t ha^{-1} yr^{-1}. Strip cropping and contouring, according to the authors, would intensify soil loss rates by two to four times, exceeding the estimated mean soil loss compared to the baseline state, and were not recommended in the context of their study area (Nambajimana et al. 2020), where they could, in our case, considerably reduce soil loss in cropland areas (Fig. 8.6b). A companion RUSLE model-based investigation on Uganda's cropland areas also confirmed our analysis, showing that compared to the baseline scenario, well-planned terraces and strip cropping would reduce the predicted soil loss by 80% (from 1.5 to 0.3 t ha^{-1} yr^{-1}) and 47% (from 1.5 to 0.8 t ha^{-1} yr^{-1}), respectively, which is lower than the sustainable soil loss tolerance value, 1 t ha^{-1} yr^{-1}, for SWC (Karamage et al. 2017). According to Karamage et al., with a moderate average soil loss estimate of 1.6 t ha^{-1} yr^{-1}, cropland with contour-based conservation practices has been found to have approximately the same average rate of soil loss as that of the baseline condition, in which the average soil loss was estimated at 1.5 t ha^{-1} yr^{-1} (2017).

Summary

The study applied remote sensing data and GIS-based modeling approaches to estimate soil loss, evaluated the spatial and temporal changes in erosion risk, and examined the potential of support practices to reduce erosion rates in cropland areas in Ethiopia's EHZ. We used the RUSLE to estimate the soil loss rate and detect districts at high erosion risk for operational SWC planning. The average annual soil loss rates (in t ha^{-1} yr^{-1}) were calculated to be 32.94, 50.42, 43.84, and 38.99 for 1990, 2000, 2010, and 2020, respectively, suggesting an overall increase of 18.34% during the last three decades (1990–2020). Our analysis revealed that over two-thirds of the area was susceptible to very low erosion risk, with a small share of annual soil erosion. In contrast, an extremely high erosion risk significantly contributes to more than 80% of the soil loss during each period. Changes from noncropland to cropland areas considerably increased soil loss rates by 36.43 t ha^{-1} yr^{-1} on average from 1990 to 2000, 70.41 t ha^{-1} yr^{-1} from 2000 to 2010, and 35.71 t ha^{-1} yr^{-1} from 2010 to 2020. These results highlight the need for appropriate intervention measures to reduce the most fertile topsoil loss by SWC and integrated land-use planning to curtail detrimental impacts. The erosion risk assessment along different slopes showed that areas with the highest exposure to excessive erosion were found in the northwest, southwest, and southeast; hotspot districts with higher erosion risks were prioritized for SWC planning: Babile, Meta, Golo Oda, and Melka Balo were the most prominent priority districts for soil management and conservation practices.

Our findings suggest that well-planned conservation practices, such as terracing, strip cropping, and contours, can reduce cropland baseline erosion by 87.05%, 64.66%, and 29.32%, respectively. The assessment of erosion risk severity presented in this chapter can help minimize the detrimental effects of soil erosion by informing policy and decision-makers on implementing SWC and improving land-use planning to protect natural resources. After detailed validation, the model developed to estimate erosion rates and prioritize districts most prone to soil loss can be replicated in other areas under similar settings. As the RUSLE has limitations in identifying gully prone areas, we only modeled rill-and-interrill erosion. Thus, based on the results of this study and operational models, it is recommended that future research studies concentrate on modeling gully erosion, which is the most common form of erosion responsible for nutrient losses and sedimentation and a significant contributor to land degradation.

Appendix

See Tables 8.7 and 8.8.

References

Aga AO, Chane B, Melesse AM (2018) Soil erosion modelling and risk assessment in data scarce rift valley lake regions, Ethiopia. Water 10:1684. https://doi.org/10.3390/w10111684

Aga AO, Melesse AM, Chane B (2019) Estimating the sediment flux and budget for a data limited rift valley lake in Ethiopia. Hydrology 6(1). https://doi.org/10.3390/hydrology6010001

Belayneh M, Yirgu T, Tsegaye D (2019) Potential soil erosion estimation and area prioritization for better conservation planning in Gumara watershed using RUSLE and GIS techniques. Environ Syst Res 8. https://doi.org/10.1186/s40068-019-0149-x

Borrelli P, Robinson DA, Fleischer LR, Lugato E, Ballabio C, Alewell C, Meusburger K, Modugno S, Schütt B, Ferro V, Bagarello V, Van Oost K, Montanarella L, Panagos P (2017) An assessment of the global impact of 21st century land use change on soil erosion. Nat Commun 8. https://doi.org/10.1038/s41467-017-02142-7

Borrelli P, Robinson DA, Panagos P, Lugato E, Yang JE, Alewell C, Wuepper D, Montanarella L, Ballabio C (2020) Land use and climate change impacts on global soil erosion by water (2015–2070). PNAS Latest Artic, 1–8. https://doi.org/10.1073/pnas.2001403117

Daba S (2003) An investigation of the physical and socioeconomic determinants of soil erosion in the Hararghe highlands, Eastern Ethiopia. L Degrad Dev 14:69–81. https://doi.org/10.1002/ldr.520

Defersha MB, Melesse AM (2012a) Effect of rainfall intensity, slope and antecedent moisture content on sediment concentration and sediment enrichment ratio. CATENA 90:47–52

Defersha MB, Melesse AM (2012b) Field-scale investigation of the effect of land use on sediment yield and surface runoff using runoff plot data and models in the Mara River basin, Kenya. CATENA 89:54–64

Defersha MB, Quraishi S, Melesse AM (2010) Interrill erosion, runoff and sediment size distribution as affected by slope steepness and antecedent moisture content. Hydrol Earth Syst Sci Discuss 7:6447–6489

Defersha MB, Quraishi S, Melesse AM (2011) The effect of slope steepness and antecedent moisture content on interrill erosion, runoff and sediment size distribution in the highlands of Ethiopia. Hydrol Earth Syst Sci 15:2367–2375. https://doi.org/10.5194/hess-15-2367-2011

Defersha MB, Melesse AM, McClain M (2012) Watershed scale application of WEPP and EROSION 3D models for assessment of potential sediment source areas and runoff flux in the Mara River Basin, Kenya. CATENA 95:63–72

Dibaba WT, Demissie TA, Miegel K (2021) Evaluation of best management practices in Highland Ethiopia, Finchaa Catchment. Land 10. https://doi.org/10.3390/land10060650

Ebabu K, Tsunekawa A, Haregeweyn N, Adgo E, Meshesha DT, Aklog D, Masunaga T, Tsubo M, Sultan D, Sultan D, Yibeltal M (2019) Effects of land use and sustainable land management practices on runoff and soil loss in the Upper Blue Nile basin, Ethiopia. Sci Total Environ 648:1462–1475. https://doi.org/10.1016/j.scitotenv.2018.08.273

Eekhout JPC, De Vente J (2022) Global impact of climate change on soil erosion and potential for adaptation through soil conservation. Earth-Sci Rev 226:103921. https://doi.org/10.1016/j.earscirev.2022.103921

Endalamaw NT, Moges MA, Kebede YS, Alehegn BM, Sinshaw BG (2021) Potential soil loss estimation for conservation planning, Upper Blue Nile. Environ Challenges 5:100224. https://doi.org/10.1016/j.envc.2021.100224

Eniyew S, Teshome M, Sisay E, Bezabih T (2021) Integrating RUSLE model with remote sensing and GIS for evaluation soil erosion in Telkwonz Watershed, Northwestern Ethiopia. Remote Sens Appl Soc Environ 24:100623. https://doi.org/10.1016/j.rsase.2021.100623

FAO (1986) Ethiopian Highland Reclamation Study (EHRS); Final Report. Rome, Italy

FDRE (2015) Ethiopia-Land Degradation Neutrality National Report (ELDNR). Addis Ababa

Fenta AA, Tsunekawa A, Haregeweyn N, Poesen J, Tsubo M, Borrelli P, Panagos P, Vanmaercke M, Broeckx J, Yasuda H, Kawai T, Kurosaki Y (2020) Land susceptibility to water and wind

erosion risks in the East Africa region. Sci Total Environ 703:135016. https://doi.org/10.1016/j.scitotenv.2019.135016

Fenta AA, Tsunekawa A, Haregeweyn N, Tsubo M, Yasuda H, Kawai T, Ebabu K, Berihun ML, Belay AS, Sultan D (2021) Agroecology-based soil erosion assessment for better conservation planning in Ethiopian river basins. Environ Res 195:110786. https://doi.org/10.1016/j.envres.2021.110786

Gadisa N (2021) Soil and water conservation measures in Ethiopia: importance and adoption challenges. World J Agric Soil Sci 6. https://doi.org/10.33552/wjass.2021.06.000636

Gashaw T (2015) Soil erosion in Ethiopia: extent, conservation efforts and issues of sustainability. Palgo J Agric 2:38–48

Gashaw T, Tulu T, Argaw M, Worqlul AW (2019) Modeling the impacts of land use—land cover changes on soil erosion and sediment yield in the Andassa watershed, upper Blue Nile basin. Environ Earth Sci 78:1–22. https://doi.org/10.1007/s12665-019-8726-x

Gashaw T, Worqlul AW, Dile YT, Addisu S, Bantider A, Zeleke G (2020) Evaluating potential impacts of land management practices on soil erosion in the Gilgel Abay watershed, upper Blue Nile basin. Heliyon 6:e04777. https://doi.org/10.1016/j.heliyon.2020.e04777

Gelagay HS, Minale AS (2016) Soil loss estimation using GIS and remote sensing techniques: a case of Koga Watershed, Northwestern Ethiopia. Int Soil Water Conserv Res 4:126–136. https://doi.org/10.1016/j.iswcr.2016.01.002

Gil E, Kijowska-Strugała M, Demczuk P (2021) Soil erosion dynamics on a cultivated slope in the Western Polish Carpathians based on over 30 years of plot studies. CATENA 207. https://doi.org/10.1016/j.catena.2021.105682

Girma R, Gebre E (2020) Spatial modeling of erosion hotspots using GIS-RUSLE interface in Omo-Gibe river basin, Southern Ethiopia: implication for soil and water conservation planning. Environ Syst Res 9. https://doi.org/10.1186/s40068-020-00180-7

Haile M, Herweg K, Stillhardt B (2006) Sustainable land management: a new approach to soil and water conservation in Ethiopia. Mekelle University, Mekelle, Ethiopia; Centre for Development and Environment (CDE) and NCCR North–South, University of Bern, Switzerland

Haile GW, Fetene M (2012) Assessment of soil erosion hazard in Kilie catchment, East Shoa, Ethiopia. L Degrad Dev 23:293–306

Haregeweyn N, Tsunekawa A, Poesen J, Tsubo M, Meshesha DT, Fenta AA, Nyssen J, Adgo E (2017) Comprehensive assessment of soil erosion risk for better land use planning in river basins: case study of the Upper Blue Nile River. Sci Total Environ 574:95–108. https://doi.org/10.1016/j.scitotenv.2016.09.019

Karamage F, Shao H, Chen X, Ndayisaba F, Nahayo L, Kayiranga A, Omifolaji JK, Liu T, Zhang C (2016) Deforestation effects on soil erosion in the Lake Kivu Basin, D.R. Congo-Rwanda. Forests 7:1–17. https://doi.org/10.3390/f7110281

Karamage F, Zhang C, Liu T, Maganda A, Isabwe A (2017) Soil erosion risk assessment in Uganda. Forests 8. https://doi.org/10.3390/f8020052

Kayet N, Pathak K, Chakrabarty A, Sahoo S (2018) Evaluation of soil loss estimation using the RUSLE model and SCS-CN method in hill slope mining areas. Int Soil Water Conserv Res 6:31–42

Kogo BK, Kumar L, Koech R (2020) Impact of land use/cover changes on soil erosion in western Kenya. Sustainability 12:1–17. https://doi.org/10.3390/su12229740

Koirala P, Thakuri S, Joshi S, Chauhan R (2019) Estimation of soil erosion in Nepal Using a RUSLE modeling and geospatial tool. Geosciences 9. https://doi.org/10.3390/geosciences9040147

Kumar M, Sahu AP, Sahoo N, Sandeep S (2022) Global-scale application of the RUSLE model: a comprehensive review. Hydrol Sci J. https://doi.org/10.1080/02626667.2021.2020277

Kumar T, Jhariya DC, Pandey HK (2019) Comparative study of different models for soil erosion and sediment yield in Pairi watershed, Chhattisgarh, India. Geocarto Int, 1–22. https://doi.org/10.1080/10106049.2019.1576779

Liu Y-f, Huang Z, Meng L, Li S, Wang Y, Liu Y (2022) Understory shading exacerbated grassland soil erosion by changing community composition. CATENA 208. https://doi.org/10.1016/j.catena.2021.105771

Lo A, El-Swaify SA, Dangler EW, Shinshiro L (1985) Effectiveness of El30 as an erosivity index in Hawaii (Eds: E1-Swaify SA, Moldenhauer WC, Lo A). Soil Conservation Society of America, Ankeny, IA, USA

Maalim FK, Melesse AM (2013) Modeling the impacts of subsurface drainage systems on runoff and sediment yield in the Le Sueur watershed, Minnesota. Hydrol Sci J 58(3):1–17

Maalim FK, Melesse AM, Belmont P, Gran K (2013) Modeling the impact of land use changes on runoff and sediment yield in the Le Sueur watershed, Minnesota using GeoWEPP. CATENA 107:35–45

Mekonnen M, Melesse A (2011) Soil erosion mapping and hotspot area identification using GIS and remote sensing in Northwest Ethiopian highlands, near Lake Tana. In: Melesse A (ed) Nile River Basin: hydrology, climate and water use, chap 10. Springer, pp 207–224. https://doi.org/10.1007/978-94-007-0689-7_10

Melesse AM, Ahmad S, McClain M, Wang X, Lim H (2011) Sediment load prediction in large rivers: ANN approach. Agric Water Manag 98:855–866

Moges DM, Kmoch A, Bhat HG, Uuemaa E (2020) Future soil loss in highland Ethiopia under changing climate and land use. Reg Environ Chang 20:1–14. https://doi.org/10.1007/s10113-020-01617-6

Moges DM, Bhat H (2018) An insight into land use/cover changes and their impacts in Rib watershed, Northwestern highland Ethiopia. Land Degrad Dev 29. https://doi.org/10.1002/ldr.3091

Mohammed H, Alamirew T, Assen M, Melesse AM (2015) Modeling of sediment yield in Maybar gauged watershed using SWAT, northeast Ethiopia. CATENA 127:191–205

Mohammed S, Alsafadi K, Talukdar S, Kiwan S, Hennawi S, Alshihabi O, Sharaf M, Harsanyie E (2020) Estimation of soil erosion risk in southern part of Syria by using RUSLE integrating geo informatics approach. Remote Sens Appl Soc Environ 20:100375. https://doi.org/10.1016/j.rsase.2020.100375

Moisa MB, Negash DA, Merga BB, Gemeda DO (2021) Impact of land-use and land-cover change on soil erosion using the RUSLE model and the geographic information system: a case of Temeji watershed , Western Ethiopia. J Water Clim Chang, 1–17. https://doi.org/10.2166/wcc.2021.131

Molla T, Sisheber B (2017) Estimating soil erosion risk and evaluating erosion control measures for soil conservation planning at Koga watershed in the highlands of Ethiopia. Solid Earth 8:13–25. https://doi.org/10.5194/se-8-13-2017

Msagahaa J, Ndomba, Melesse AM (2014) Modeling Sediment dynamics: effect of land use, topography and land management. In: Melesse AM, Abtew W, Setegn S (eds) Nile river basin: ecohydrological challenges, climate change and hydropolitics, pp 165–192.

Muleta S, Yohannes F, Rashid SM (2006) Soil erosion assessment of Lake Alemaya catchment, Ethiopia. L Degrad Dev 17:333–341

Nambajimana JDD, He X, Zhou J, Justine MF, Li J, Khurram D, Mind R, Nsabimana G (2020) Land use change impacts on water erosion in Rwanda. Sustainability 12. https://doi.org/10.3390/su12010050

Nijimbere G, Lizana CR (2019) Assessment of soil erosion of Burundi using remote sensing and GIS by RUSLE model. Rudn J Ecol Life Saf 27:17–28. https://doi.org/10.22363/2313-2310-2019-27-1-17-28

Nurgi N, Tana T, Dechassa N, Alemayehu Y, Tesso B (2021) On-farm diversity of faba bean (*Vicia faba* L .) farmers' varieties in Eastern Hararghe Zone. Res Sq, 1–32. https://doi.org/10.21203/rs.3.rs-1098405/v1

Nyssen J, Frankl A, Zenebe A, Deckers J, Poesen J (2015) Land management in the Northern Ethiopian highlands: local and global perspectives; past, present and future. L Degrad Dev 764:759–764

Olorunfemi IE, Komolafe AA, Fasinmirin JT, Olufayo AA, Akande SO (2020) A GIS-based assessment of the potential soil erosion and flood hazard zones in Ekiti State, Southwestern Nigeria using integrated RUSLE and HAND models. CATENA 194:104725. https://doi.org/10.1016/j.catena.2020.104725

Polovina S, Radi B, Risti R, Jovan K, Milcanovi V, Živanovic N (2021) Soil erosion assessment and prediction in urban landscapes: a new G2 model approach. Appl Sci 11:1–20

Raiesi F, Beheshti A (2022) Evaluating forest soil quality after deforestation and loss of ecosystem services using network analysis and factor analysis techniques. CATENA 208:105778. https://doi.org/10.1016/j.catena.2021.105778

Rajbanshi J, Bhattacharya S (2020) Assessment of soil erosion, sediment yield and basin specific controlling factors using RUSLE-SDR and PLSR approach in Konar river basin, India. J Hydrol 587:124935. https://doi.org/10.1016/j.jhydrol.2020.124935

Renard K, Foster G, Weesies GA, McCool DK, Yoder DC (1997) Predicting soil erosion by water: a guide to conservation planning with the revised universal soil loss equation (RUSLE); Agriculture Handbook. USDA, Washington, DC, USA

Rodrigo-Comino J, Martínez-Hernández C, Iserloh T, Cerdà A (2017) The contrasted impact of land abandonment on soil erosion in mediterranean agriculture fields. Pedosphere 0160. https://doi.org/10.1016/S1002-0160(17)60441-7

Samuel LM (2014) Prediction of runoff and sediment yield using AnnAGNPS model: case of Erer-Guda Catchment, East Hararghe, Ethiopia. ARPN J Sci Technol, 575–595

Senti ET, Tufa BW, Gebrehiwot KA (2014) Soil erosion, sediment yield and conservation practices assessment on Lake Haramaya Catchment. World J Agric Sci 2:186–193

Setegn SG, Srinivasan R, Dargahi B, Melesse AM, (2009) Spatial delineation of soil erosion prone areas: application of SWAT and MCE approaches in the Lake Tana Basin, Ethiopia. Hydrol Processes, Special Issue: Nile Hydrol 23(26):3738–3750

Setegn SG, Bijan Dargahi B, Srinivasan R, Melesse AM (2010) Modelling of sediment yield from Anjeni Gauged Watershed, Ethiopia using SWAT. JAWRA 46(3):514–526

Shin J (1999) The analysis of soil erosion in watershed using GIS. Gang-Won National University, Chuncheon

Shojaei S, Kalantari Z, Rodrigo-Comino J (2020) Prediction of factors affecting activation of soil erosion by mathematical modeling at pedon scale under laboratory conditions. Sci Rep 10:1–12. https://doi.org/10.1038/s41598-020-76926-1

Sinshaw BG, Belete AM, Mekeonen BM, Wubetu TG, Lakew T, Dessie W, Atinkut HB, Adugna A, Bilkew T, Tefera AK, Dessie AB, Fenta HM, Beyene AM, Bizuneh BB, Alem HT, Eshete DG, Atanaw SB, Tebkew M, Mossie M (2021) Watershed-based soil erosion and sediment yield modeling in the Rib watershed of the Upper Blue Nile Basin, Ethiopia. Energy Nexus, 100023. https://doi.org/10.1016/j.nexus.2021.100023

Tesfaye B, Lengoiboni M, Zevenbergen J, Simane B (2021) Mapping land use land cover changes and their determinants in the context of a massive free labor mobilization campaign: evidence from South Wollo, Ethiopia. Remote Sens 13. https://doi.org/10.3390/rs13245078

Tessema YM, Nska JJ, Yadeta LT, Switoniak M, Puchałka R, Gebregeorgis EG (2020) Soil loss estimation for conservation planning in the welmel watershed of the Genale Dawa Basin. Agronomy 10(777):1–19. https://doi.org/10.3390/agronomy10060777

Tsegaye L, Bharti R (2021) Soil erosion and sediment yield assessment using RUSLE and GIS-based approach in Anjeb watershed, Northwest Ethiopia. SN Appl Sci 3:1–19. https://doi.org/10.1007/s42452-021-04564-x

Tsegaye K, Addis HK, Hassen EE (2020) Soil Erosion impact assessment using USLE/GIS approaches to identify high erosion risk areas in the lowland agricultural watershed of Blue Nile Basin, Ethiopia. Int Ann Sci 8:120–129

Uddin K, Matin MA, Maharjan S (2018) Assessment of land cover change and its impact on changes in soil erosion risk in Nepal. Sustainability 10:4715. https://doi.org/10.3390/su10124715

Wagari M, Tamiru H (2021) RUSLE model based annual soil loss quantification for soil erosion protection: a case of Fincha Catchment, Ethiopia. Air, Soil Water Res 14:1–12. https://doi.org/10.1177/11786221211046234

Wang X, Garza J, Whitney M, Melesse AM, Yang W (2008) Prediction of sediment source areas within watersheds as affected by soil data resolution. In: Findley PN (ed) Environmental modelling: new research, chap 7, pp 151–185. Nova Science Publishers, Inc., Hauppauge. ISBN 978-1-60692-034-3

Watene G, Yu L, Nie Y, Zhu J, Ngigi T, Nambajimana JDD, Kenduiywo B (2021) Water erosion risk assessment in the Kenya great rift valley region. Sustainability 13

Williams JR (1995) The EPIC model. In: Computer models of watershed hydrology. Water Resources Publications, Highlands Ranch. CO, USA

Wischmeier WH, Smith DD (1978) Predicting rainfall erosion losses—a guide to conservation planning; Agriculture Handbook No. 537. US Department of Agriculture Science and Education Administration, Washington, DC, USA

Woldemariam GW, Harka AE (2020) Effect of land use and land cover change on soil erosion in Erer Sub-Basin, Northeast Wabi Shebelle Basin, Ethiopia. Land 9:111. https://doi.org/10.3390/land9040111

Woldemariam G, Iguala A, Tekalign S, Reddy R (2018) Spatial modeling of soil erosion risk and its implication for conservation planning: the case of the Gobele Watershed, East Hararghe Zone, Ethiopia. Land 7:25. https://doi.org/10.3390/land7010025

Woldemariam GW, Tibebe D, Mengesha TE, Gelete TB (2021) Machine-learning algorithms for land use dynamics in Lake Haramaya Watershed, Ethiopia. Model Earth Syst Environ. https://doi.org/10.1007/s40808-021-01296-0

Yang D, Kanae S, Oki T, Koike T, Musiake K, Yang DW, Shinjiro K, Taikan O, Toshio K, Katumi M (2003) Global potential soil erosion with reference to land use and climate changes. Hydrol Process 17:2913–2928

Yesuph AY, Dagnew AB (2019) Soil erosion mapping and severity analysis based on RUSLE model and local perception in the Beshillo Catchment of the Blue Nile Basin. Environ Syst Res, 1–21. https://doi.org/10.1186/s40068-019-0145-1

Zerihun M, Mohammedyasin MS, Sewnet D, Adem AA, Lakew L (2018) Assessment of soil erosion using RUSLE, GIS and remote sensing in NW Ethiopia. Geoderma Reg 12:83–90

Chapter 9
Channel Stability Assessment and Stabilization Measure of Mersa River, Ethiopia

Getanew Sewnetu

Abstract The objective of this study is to evaluate channel stability and recommend appropriate mitigation measures for the Mersa River, in Awash River Basin, Ethiopia. The HEC-RAS5.0.7 model was used to evaluate the Mersa riverbed and bank stability, quantify the depth or mass sediment erosion amount, and identify flood-prone areas. To achieve this objective, both field investigations, such as river cross-section data collection and soil sample collection, and experimental tasks, such as sieve analysis and triaxial compression tests, were carried out. The HEC-RAS model simulation with the Yang sediment transport formula is the best fit for the study compared to the Meyer, Peter, and Muller sediment transport methods. For the entire simulation period, the average aggradation was 1.24 m and 0.98 m in the upstream and downstream reaches, respectively, whereas the average degradation in both the upstream and downstream reaches was 1.25 m. The average sediment erosion generated by the Mersa River was 22.47 kt/yr. Both aggradation and degradation were observed in the study reach, but the Mersa River reach was more affected by erosion than deposition. Mersa riverbank stability and toe erosion assessed by BSTEM of HEC-RAS were safe, and the bank toe neither aggraded nor degraded in response to the flow. Additionally, the water surface of the Mersa River was computed using steady flow analysis, showing that floods over the top above the bank and adjacent area (Mersa town) were affected by floods, and the reality was also true. It was shown that there was farmland loss and property damage due to floods. Finally, this investigation showed that the channel bed was unstable while the bank was stable. Different stabilization measures, such as the Gabion bank, check dam, and drop structure, were recommended to prevent flood-prone areas from experiencing floods and to control channel bed instability.

Keywords Sieve analysis · Triaxial compression test · Channel bed and bank stability · HEC-RAS model · BSTEM · Aggradation and degradation · Stabilization measure

G. Sewnetu (✉)
Department of Hydraulic and Water Resources Engineering, Woldia University, Woldia, Ethiopia
e-mail: getanew.s@wldu.edu.et

A. M. Melesse et al. (eds.), *Land and Water Degradation in Ethiopia*, Springer Geography, https://doi.org/10.1007/978-3-031-60251-1_9

Study Area Description

Location

The Mersa River is found in the western highlands of the Awash Terminal, the subbasins of the A wash basin (Fig. 9.1). The Mersa River originates from mountains and drains to the downstream passes in Mersa town. Mersa town is found in North Wollo, Amhara region, Ethiopia, 495 km from Addis Ababa and is geographically located at 11° 40′ N latitude and 39° 39.5′ E longitude and 1600 m elevation mean above sea level. Mersa is situated along country (Ethiopian) Highway 2, and the highway passes in the Mersa River.

The watershed is delineated using HEC-GeoHMS, which is an extension of ArcGIS (for this thesis, ArcGIS 10.4 was used) with a 30 m resolution digital elevation model (DEM).

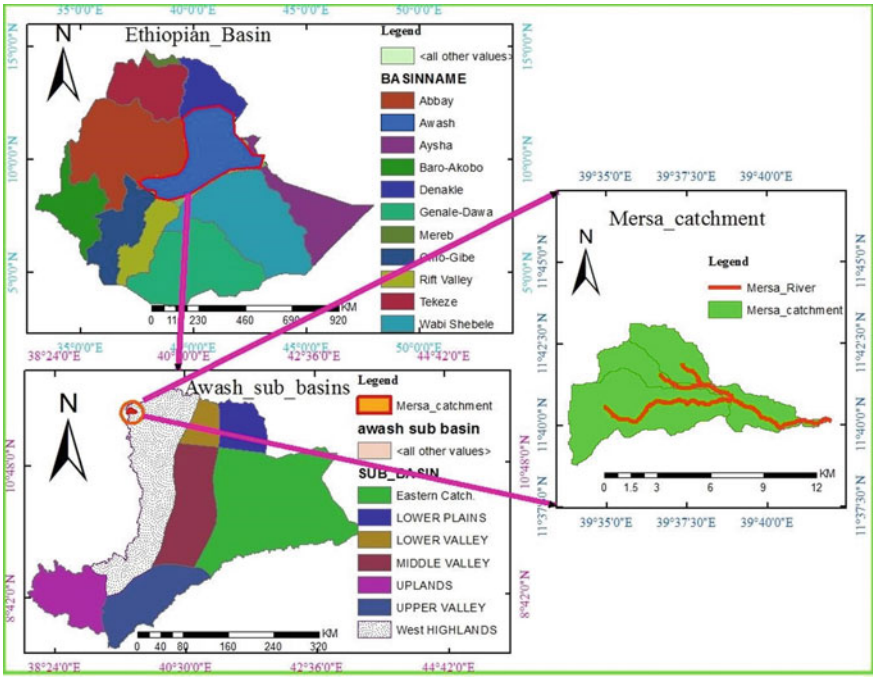

Fig. 9.1 Location of the Mersa catchment

Soil

The earth material (soil) in the Mersa catchment is grounded on soil type criteria eutric cambisols, eutric regosols, leptosols, and vetric cambisols, while according to texture, sandy loam and gravel have the greatest coverage in the watershed of Mersa. Figure 9.2 shows a soil map of the watershed.

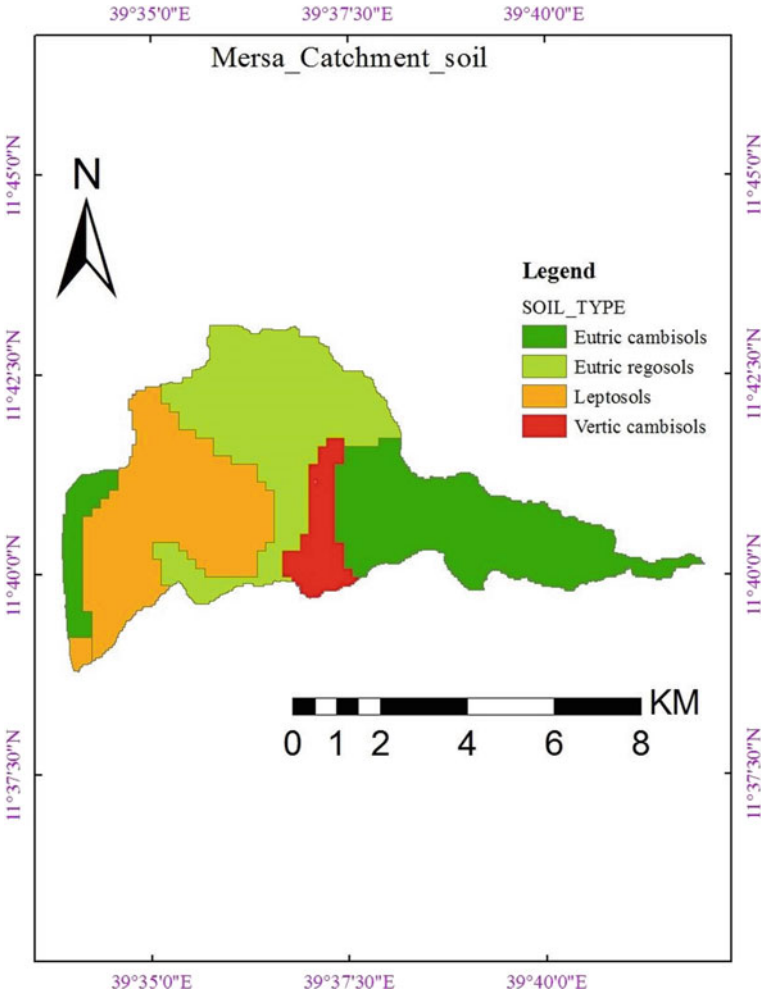

Fig. 9.2 Soil map of the Mersa catchment

Table 9.1 Geological formation of the Mersa catchment

No.	Symbol	Stratigraphy	Age	Lithology	Description
1	P2a	Cenozoic volcano	Eocene	ASHANGI Formation	Deeply weathered alkaline and transitional basalt flows with rare intercalations of tuff, often tilted (includes Akobo Basalts of SW Ethiopia)
2	P3a	Cenozoic volcano	MIDDLE–LATE OLIGOCENE	AIBA Basalts	Flood basalts with rare basic tuff
3	PNa	Cenozoic volcano	OLIGOCENE–MIOCENE	ALAGE formation	Transitional and subalkaline basalts with less rhyolite with trachyte eruptive

Geology

The geological situation is the basis and cornerstone of river stability investigations. Any stratigraphic classification of water-bearing formations should begin from lithological classifications by accounting for geological arrangements such as faults, joints, folds, and other tectonic features with hydrological importance.[1]

According to age, the geological formation in the study watershed includes EOCENE, MIDDLE–LATE OLIGOCENE, and OLIGOCENE–MIOCENE[2,3]. The general description of the geological state of the study catchment is compiled in Table 9.1.

Land Use and Land Cover

The land usage and coverage of the Mersa catchment (Fig. 9.3) was prepared under ArcGIS 10.4. First, a Landsat 8 image from the USGS earth explorer (http://earthexplorer.usgs) was created to account for any area desired for the latest or updated image

[1] Ethiopia Health Infrastructure Program, Health Centres Groundwater Investigation Final Report February 2016.

[2] www.ethiogrio.com/files//Ethiopia_Map_251592290.pdf

[3] Identification and Engineering Geological Studies of Small Hydropower Sites in Muger, Jemma and Waleka Sub-Basins (Central Ethiopia) By Nehemia Solomon.

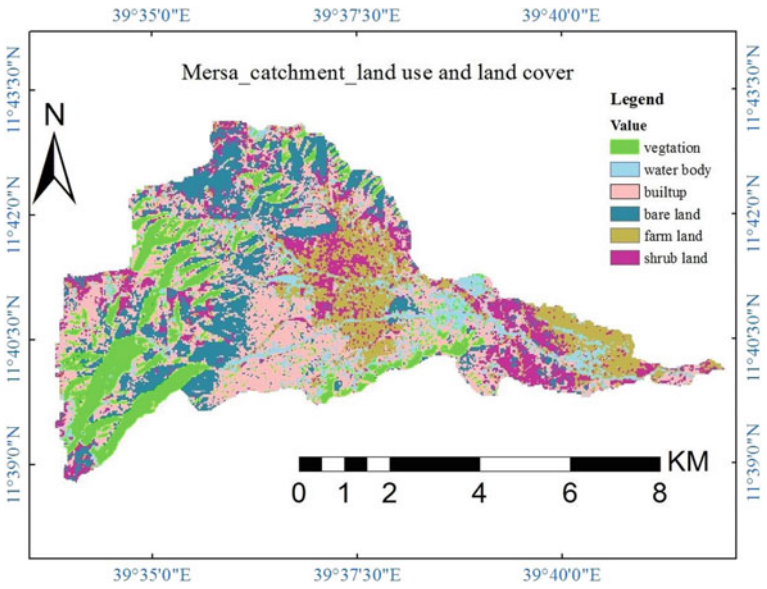

Fig. 9.3 Land use and land cover of the Mersa catchment

for this investigation. The image released on February 27, 2019, was downloaded and used to composite the 11 downloaded bands, and the image classification method was unsupervised classification. Finally, by relating the composite to the real image at Google Earth, the land use and land cover were prepared.

Climate

The minimum and maximum temperatures in the catchment are 10 °C and 34 °C, respectively. The district receives average yearly rainfall ranging from 350–835 mm. The main rainy season is from June to the end of September. The mean annual wind speed, relative humidity and solar radiation in the catchment are 2.5 m/sec, 0.506, and 26 MJ/m^2, respectively.

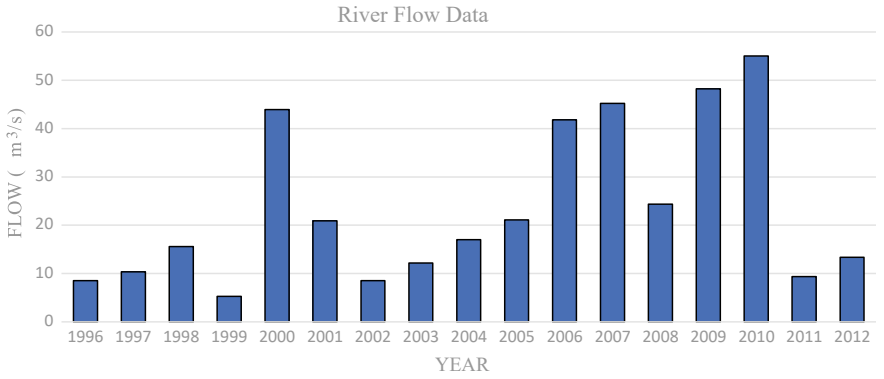

Fig. 9.4 Annual maximum mean daily river flow data of the Mersa River

Data Collection

Hydrology

The recorded flow data were collected from the Minster of Water, Irrigation, and Electricity for the Mersa River between 1996 and 2012, and the annual maximum mean daily instantaneous flow data (Fig. 9.4) were used to estimate the dominant and bank full discharge of the river.

Soil Sample for Gradation and Triaxial Compression Test

The possible representative soil sample is taken from the riverbed, left side, and right side bank for gradation analysis at six different places to obtain the possible accurate data regarding the soil characteristics of the selected 2.6 km channel reach so at left, right, and riverbed for each taken at two different places, while the triaxial compression experiment sample is taken from the riverbank at three different places.

Geometric Data

River Cross-Section Data

Channel cross-section data are essential inputs in the HEC-RAS model, so for this study, 42 reach sections were taken along a 2.6 km interval from 50 to 100 m depending on river meandering and straightness conditions.

The cross-section data contain the station number, y distance of the point from a reference point and z elevation. The downstream reach length is calculated from the difference between two successive coordinates y or the distance of the points.

Generally, the river of Mersa in the first two reaches is narrow, while beginning from the 3rd station to station 26, it becomes very wide, and between stations 26 and 27, there is a Multi Span RC Deck Girder Bridge structure with a span length of 42.8 m, bridge opening length of 22.5 m and bridge width of 8 m.

Manning Roughness Coefficient

The Manning roughness coefficient is another basic input for the HEC-RAS model setup, but the challenge is earning the exact value for the stream because the roughness coefficient depends on the channel grade of irregularity, variations in the channel cross-section, relative to effective obstructions, vegetation, and meandering degree. According to Chow (1959), the surface roughness coefficient value can be calculated by considering the existing channel physical characteristics, such as surface roughness, vegetation, obstruction, channel alignment and channel bank, and bed materials. Considering various primary variables affecting the roughness coefficient, Manning's n value can be calculated using

$$n = (n_0 + n_1 + n_2 + n_3 + n_4)m_5 \tag{9.1}$$

where $n_0 =$ is a basic n value for a straight, uniform, smooth channel in the natural materials involved (Chow 1959) and $n_1 =$ is a value added to n_o to correct for the effect of surface irregularities (Chow 1959).

n_2 is a value for variations in the shape and size of the channel cross-section, (Chow 1959) n_3 is a value for obstructions, (Chow 1959) n_4 is a value for vegetation and flow conditions, (Chow 1959) and m_5 is a correction factor for meandering of the channel (Chow 1959).

The basic n_0 is calculated in the empirical formula developed from the channel bank and bed soil material that is done at sieve analysis, whereas starting from n_1 to m_5 estimated from Table 9.2.

According to French (1986), the basic n_0 is calculated by the following empirical equation. $n_0 = 0.038 * {d_{90}}^{1/6}$ d in metermetres Meyer Peter and Muller (1948) $n_0 = 0.039 * {d_{50}}^{1/6}$ d in feet Garde and Ranga Raju (1978) $n_0 = 0.047 * {d_{50}}^{1/6}$ d in meters,

where d_i is the grain soil size, in which i is the percentage of material by weight finer than d.

For illustration, Manning's roughness n of the Mersa River upstream of the channel bed at station 42.

The other values are carefully chosen from Table 9.3: $n_1 = 0.005$, moderate degree of irregularity $n_2 = 0.013$, channel cross-section varies occasionally $n_3 = 0.02$, obstruction is negligible except at the bridges, which will be considered separately $n_4 = 0.007$, vegetation effect $m = 1.00$, and degree of meandering is minor.

Table 9.2 Gradation result at cross-section 42

Sieve size	Soil laboratory gradation result
D90 (mm)	8.4015
D90 (m)	0.00840
D50 (mm)	3.1664
D50 (ft)	0.0104
D50 (m)	0.0032
Garde and Raju	0.0182
Subramanya	0.0180
Meyer Peter and Muller	0.0171
Average n_0	0.018

Table 9.3 Contraction and expansion for various channel conditions

Channel condition	Coefficient	
	Expansion	Contraction
Gradual change	0.3	0–0.1
Abrupt change	0.5	0.5

Then, $n = (0.018 + 0.005 + 0.013 + 0.02 + 0.007) \times 1.00 = 0.065$. For the remaining channel reach, Manning's roughness values were estimated in a similar fashion as above.

Coefficients of Contraction and Expansion

According to Chow (1959), the recommended contraction and expansion coefficients for different channel conditions are presented in Table 9.3 (Fig. 9.5).

Data Analysis

Analysis of data is essential for the future to process in model application, and it simply examines the data quality, sufficiency, quantity, etc. According to Hawi (2018), data analysis assesses data by means of analytical logical reasoning to examine each component of the data provided. Data analysis is the first and essential of several steps that must be carried out when conducting a research experiment. Data from several sources are collected, reviewed, and analyzed to form some findings or conclusions. For the 17-year sample stream flow data of the Mersa River analyzed in this study, there were no high outliers or low outliers.

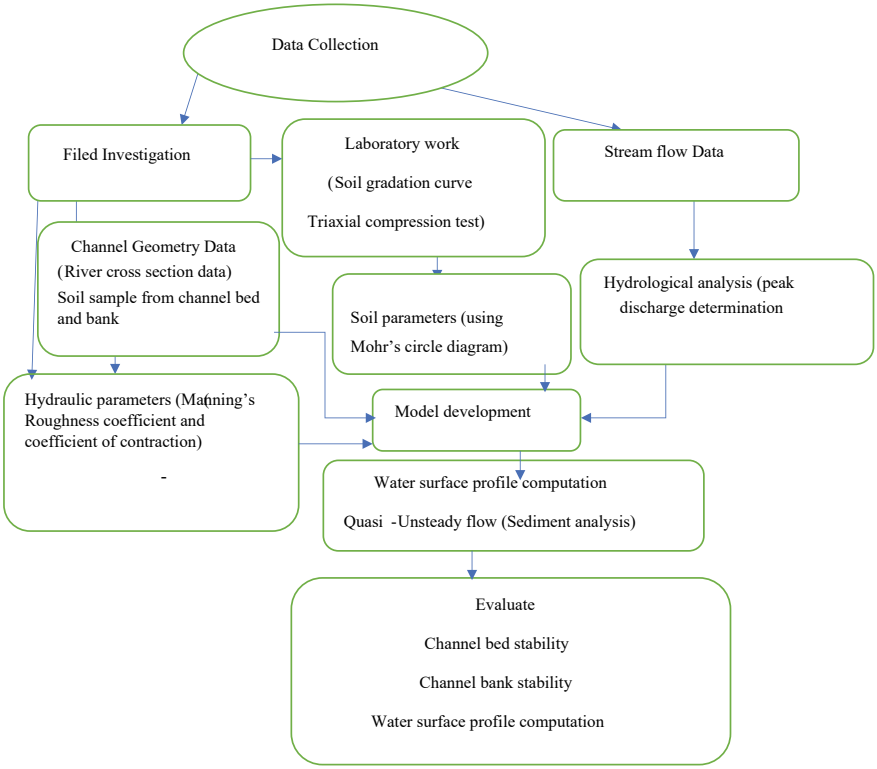

Fig. 9.5 Conceptual framework

Hydrologic Analysis

The maximum design flood is the river peak discharge that corresponds to a certain recurrence interval, which is important in the practical design of all irrigation and hydraulic structures (Subramanya 2008).

Frequency Analysis of Floods

It is one method to estimate the extreme flood of the channel that is utilized to design any hydraulic structure (Brunner 2016). Flow in the watershed is dependent on the characteristics of the watershed, rainfall and antecedent humidity condition individually, and these factors in turn bank on a list of constituent variables. This makes the estimation of the flood peak a very complex problem, leading to different approaches. The empirical formula and unit hydrograph method have been described in the previous chapter. Another approach to the prediction of flood flow is frequency analysis, which must consider all catchment factors. In frequency analysis approaches, the common problem is to forecast extreme flood events. Toward the extreme, specific extreme value distributions are supposed, the desired statistical

parameters are estimated from available data, and the flood magnitude for the specific return period is estimated. The 17 successive year stream gauged data are analyzed for the outlier test next, and the peak flood for different return periods would be computed as follows, but before this, to which method of frequency flood analysis the recorded is fitted must be carried out primarily using the l-moment ratio diagram.

L-Moment Ratio Diagram

It is a diagram based on the coefficient of skewness (Cs) versus the coefficient of kurtosis to identify appropriate distributions. L-moment ratio diagram plotted for a given regional sample size. The identification of a parent dispersion can be achieved much more easily by using an L-moment ratio diagram, especially for skewed distributions. Some useful relationships for constructing diagrams of the L-moment ratio for some common distributions are given by Hosking (1990, 1991).

From the L-moment ratio diagram analysis shown below, the collected stream gauged data best fit the general extreme value (Gumbel's method) (Fig. 9.6).

Soil Laboratory Analysis

Generally, the laboratory analysis category in to two for this research, i.e., the soil gradation (particle size distribution) and triaxial compression test. Both gradation curve and triaxial compression tests were carried out at Woldia University, Civil Engineering Department, Soil Laboratory.

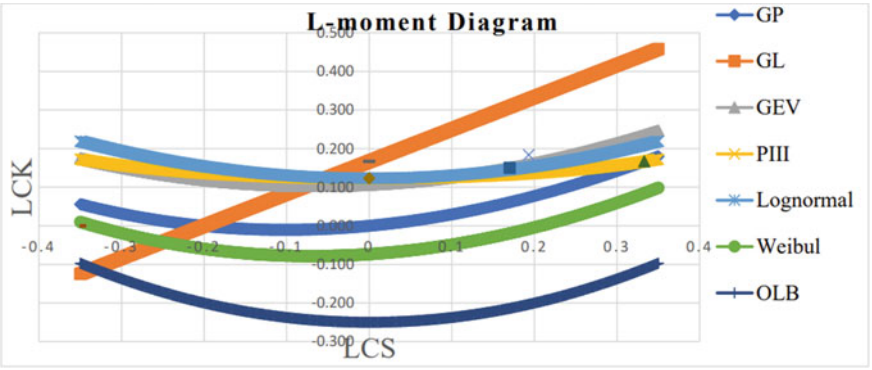

Fig. 9.6 L-moment ratio diagram

Soil Gradation Analysis

A soil gradation curve is performed to estimate the percentage of different grain sizes contained within the soil. As discussed above for the bed river, the left bank and right channel bank of the Mersa River sample were taken at 2 different places for each, and finally, a total sample was taken at six places.

For this research, the cone dimeter used started from pan, 0.075–9.5 mm according to Arora (2008) coarse-grained soils (size > 4.75 mm) and sand fraction (75 μm < size < 4.75 mm), so the soil retained above sieve diameter 4.75 mm was considered gravel, the soil retained in between sieve diameter 0.106–4.75 mm was considered sand, and the soil retained at sieve diameter 0.075 mm and at the pan was considered fine soil.

The laboratory results of sieve analysis were grouped into two broad classes: riverbank and riverbed material. Gradation curve of soil for six representative soil samples taken from different places to determine the proportion of gravel, sand, and fine parts of the soil material. The study channel reach has two parts: the upper reach and lower reach, so samples were taken from the upper three parts of the left riverbank, right riverbank and riverbed soil, and samples were also taken in the same way from the lower channel reach.

1. Riverbed material composition

The gradation curve analysis result of the bed material composition characterized by coarse grains, including sand and gravel, shows that the bed material above 95% of the total sample was coarser with particle grain sizes greater than 0.075 mm.

As shown in Table 9.4 and Fig. 9.7, for the soil particles in the upper reach of the Mersa riverbed soil material, the percentages of gravel, sand and fine soil material are 43.23 with particle sizes larger than 4.75 mm, 54.39 with particle grain sizes in the range between 0.075 mm and 4.75 mm, and 2.38 with particle sizes less than 0.075 mm, respectively, showing that more than 95% of the bed material is gravel and sand. D84, D50, and D16 indicate particle sizes of 7.74, 3.16, and 0.32, respectively, at which 84%, 50%, and 16% of the soil materials are finer than this size. In the same method, the gradation curve result for the bed sediment composition of the lower channel reach showed that the coarse-grained soil was dominated by sand (fine sand to very coarse sand) and gravel (from very fine gravel to medium gravel). The uniformity coefficients (D60/D10) for both the upstream and lower reaches were 23 and 14, respectively, for sand and gravel, which had uniformity coefficients greater than 6 for sand and 4 for gravel, showing well-graded coarse-grained soil.

Triaxial Compression Test Analysis

The triaxial compression test is used to determine the shear parameters in soils under various drainage conditions. A triaxial compression test is necessary to determine the soil parameters that affect the soil shear strength. Shear strength is the primary engineering property that controls soil mass stability under loading (Arora 2008). According to (Murthy 2002), the shear strength parameter c is cohesion, and ϕ is the angle of shearing resistance of soils either in the undisturbed or remolded states.

Table 9.4 Upper reach riverbed material particle size curve analysis

Sieve No.	Sieve diameter	Mass of empty sieve (g)	Mass of sieve + soil retained (g)	Soil retained (g)	Mass cumulative retained (g)	Percent retained (%)
	9.5	495.8	495.8	0	0	0
4	4.75	460.5	698.5	238	238	43.24
10	2	402.6	467.2	64.6	302.6	54.99
20	0.84	386.5	445.3	58.8	361.4	65.66
40	0.425	391.6	455.6	64	425.4	77.29
60	0.25	384.1	447.7	63.6	489	88.84
140	0.106	363.5	398.2	34.7	523.7	95.15
200	0.075	357.5	371.1	13.6	537.3	97.62
pan		352.6	365.7	13.1	550.4	100
Total		3242.1	3779.4	537.3	2877.4	522.79

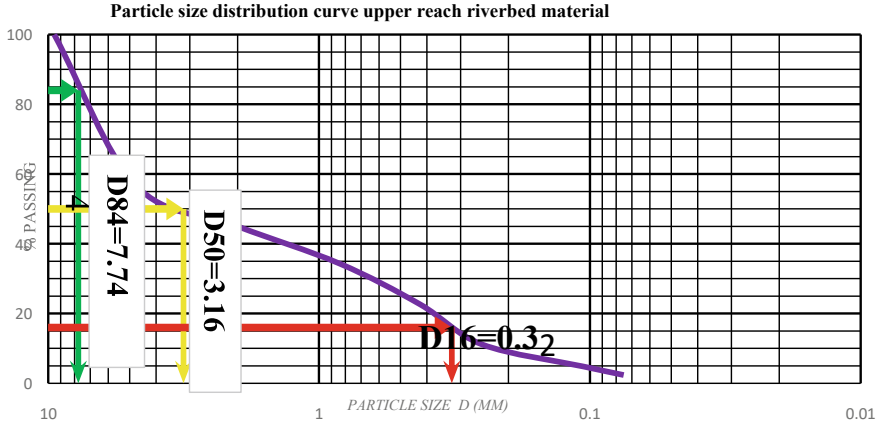

Fig. 9.7 Grain size distribution curve of the upper reach riverbed material

For this research, disturbed soil was taken from the Mersa reach and remolded in the laboratory. The soil sample was taken at 3 different places from the riverbank for the triaxial compression test.

Soil parameter cohesion c and angle of internal friction ϕ are essential inputs for the BSTEM model that should be determined in the laboratory. As defined earlier, the triaxial compression test is used to determine the soil parameter or variables (c and ϕ). Specifically, for this study, triaxial compression tests were performed on riverbank soil samples under 50, 100, and 200 kN load conditions. Although the experiment (triaxial compression test) was not adequate to determine the soil strength parameter, it requires Mohr's circle analysis with these experimental results. According to Arora (2008), Mohr's circle is a diagram or graphical technique for the estimation of stresses

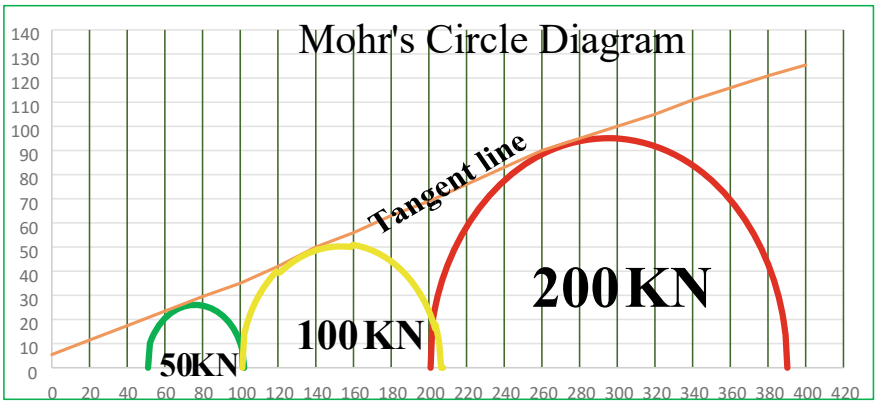

Fig. 9.8 Mohr's circle diagram for different axial loads (50, 100 and 200 kN)

on a plane inclined to the principal planes. By drawing the Mohr's circle, the three-test result in a single graph as presented below soil shear strength variables or parameter become cohesion, $C = 5.46$ kPa and shearing resistance angle, $\phi = 14°$ (Fig. 9.8)

HEC-RAS Model Development

As discussed in the previous chapter, HEC-RAS allows users to perform one-dimensional steady flow to water flow surface profile computations, unsteady flow simulations, quasiunsteady sediment transport/mobile boundary computations, and water quality analyses (Brunner 2016). For this study, a 1D HEC-RAS model is developed to compute sediment transport capacity, to predict riverbed changes by using sediment balance equations and to assess the water surface profile.

Steady Flow Analysis and Flood Inundation Map

Steady Flow Simulation

The energy equation is used to compute the water flow surface profile. This is solved by an iterative procedure, which is called the direct standard step method from one cross-section to the other (Brunner 2016). The model also uses the Manning equation to compute water discharge (Brunner 2016).

The surveyed cross-section collected data were used to establish a 1D steady flow model for different discharge scenarios to analyze the water level in all reaches. The discharge computed by GEV is used for the upstream boundary and the downstream boundary condition of the normal depth, which is determined from the longitudinal

Table 9.5 Steady flow upstream boundary conditions

Return period (year)	Discharge (m^3/s)
Upstream boundary condition	
2	41
10	68
50	91
100	101

slope of the river reach. The discharge used in the steady flow analysis is shown in Table 9.5 with a return period of 2–100 years.

The water surface profile for 2-, 10-, 50-, and 100-year return periods of peak discharge was computed in the model using Manning's formula by considering gradually varied flow (direct step iteration method). The scenarios for maximum discharge of 2-year, 10-year, 50-year, and 100-year return periods are discussed below.

The water surface profile for 2-, 10-, 50-, and 100-year return periods of peak discharge was computed in the model using Manning's formula by considering gradually varied flow (direct step iteration method). The scenarios for maximum discharge of 2-year, 10-year, 50-year, and 100-year return periods are discussed below.

A. 2-year and 10-year return period design discharge scenarios

From the results shown in the model, the 2-year and 10-year design discharges were nearly accommodated within a floodplain limit in all reaches of the Mersa station except for some reaches that had small riverbanks under one or both banks.

Generally, the problem was more frequently observed in the upper reach because of bank height differences and in the downstream reach because both had small bank heights on both sides compared to the preceding river reach in addition to the bank height differences. However, there are reaches that would accommodate the design discharge of all recurrence intervals within the floodplain limit.

Flood Plain Delineation

A flood inundation map is prepared using both HEC-RAS and HEC-GeoRAS (ArcGIS extension), and the following sequential step is followed to obtain a flood plain map.

A flood inundation map was generated after postprocessing in HEC-GeoRAS with input water surface elevations TIN and cross-section (XS) cut lines within the limits of the bounding polygon. Floodplain mapping was completed after water surface generation and flood plain delineation using a raster.

Sediment Transport Computations

To simulate the sediment analysis or riverbed change in the channel, quasiunsteady flow is used. Its capabilities are unique to sediment transport analysis and simulate the flow series by assuming an approximate continuous hydrograph (histograms) with a sequence of steady flow computations in corresponding flow durations (Brunner 2016). From 17-year recorded flow data, the 7-year daily flow events that start from January 01, 2006 to December 31, 2012 are used for this study to model the simulation of sediment. The annual hydrograph selected is discretized to a series of daily flows. Daily discretized flow records and daily temperature are required in quasiunsteady sediment transport analysis for this study, and 7-year daily flow events out of 17-year recorded flow data, and 7-year average daily temperature of Mersa are used for analysis starting from January 01, 2006 to December 31, 2012. Additionally, hydrograph data of both daily discharge and average daily temperature are presented as follows.

Bank Stability and Toe Erosion Model (BSTEM) Analysis

Riverbank failure clearly led to life and property losses. According to Arora (2008), it is essential to check channel stability through a recent soil testing method and stability analysis. In this study, as discussed earlier, a soil sample was taken from the bank for the triaxial compression test to determine the soil parameters, and BSTEM was used for stability analysis. Bank stability and toe erosion models are bank failure analyses that depend on fundamental force stability, with a toe scour model that allows response between the hydraulic hydrodynamics on the bank toe, which could exacerbate the failure risk during toe scour or decrease failure risk during toe protection (CEIWR-HEC 2015). The aims of HEC-RAS with BSTEM are to construct a model that simulates the responses between riverbanks and bed processes. BESTEM input data are all the data that were used in the sediment analysis, and additionally, the right and left edge and toe station, selection of the corresponding bank failure method and ground water method and BESTEM layer parameters or soil parameter (c and ϕ) are needed. In this thesis, the method of bank failure is the slice method because it is more conventional geotechnical to planer failure and ensures that the force and momentum balance calculated for individual segments of the failure plane is closer to comparable geotechnical analysis and computes a more realistic distribution along the failure plane (CEIWR-HEC 2015). The ground water elevation for BSTEM is taken as 200 m below the ground surface, and these data are obtained from the AWWDS, which is the average ground water elevation in the study area.

Channel Stability Evaluation

Channel stability can be evaluated by assessing the channel bed change, channel bank variation and water surface profile for different recurrence intervals to check its effect over the neighboring area. Thus, the evaluation system is described in detail in the next section.

Channel Bed Stability Analysis

Different methods have been used to simulate sediment transport. This selection was based on the soil composition of the study watershed or catchment. In this study, Meyer Peter Muller and Yang used a sediment transport simulation model with 7 years of daily flow and temperature data. In the HECRAS manual for sand and gravel soil material, the Yang and Meyer Peter Muller transport function is recommended. The simulation results show that aggradation and degradation were observed together along the Mersa River reach. Channel bed change in the Mersa River was checked in two ways: one evaluating the vertical bed change and the other assessing the quantity of sediment entry with sediment leaving.

Vertical Channel Bed Change

The vertical channel bed change simply indicates the amount of erosion or deposition at depth. According to the Yang sediment transport formula, the aggradation and degradation simulated results for the 7-year daily discharge of the Mersa River reach are tabulated and plotted as follows. A maximum deposition of 2.23 m at station 28 and an extreme degradation of 2 m at station 7 were observed. An average degradation of 1.31 m and an average aggradation of 1.09 m were recorded, so the outcomes show that the degradation pattern is somewhat greater than the aggradation in the Mersa River reach.

As presented in Table 9.6, even if aggradation and degradation were observed, some cross-sections also neither aggraded nor degraded at stations 27, 29, 33… can be mentioned by the Yang sediment transport method.

Generally, Yang's transport method result could be grouped under category one: There was no aggradation or degradation from both banks, but deposition or erosion was observed in the channel bed. Second, no aggradation or degradation at the left and right banks, including the channel bed, was observed, and the remaining aggradation or degradation was observed at the right and left banks in addition to the channel bed.

It was found that there was no aggradation and degradation or erosion in the riverbank, whereas degradation was observed at the channel bed only.

Table 9.6 Channel bed elevation change according to Yang

No.	River	Reach	RS	Elevation (m) @Jan 1, 2006	Elevation (m) @Dec 31, 2012	Difference (m)
1	Mersa	All reach	42	1776.981	1775.675	− 1.31
2	Mersa	All reach	41	1775.755	1773.759	− 2.00
3	Mersa	All reach	40	1774.207	1772.916	− 1.29
4	Mersa	All reach	39	1772.954	1772.444	− 0.51
5	Mersa	All reach	38	1771.871	1769.874	− 2.00
6	Mersa	All reach	37	1770.617	1770.581	− 0.04
7	Mersa	All reach	36	1768.513	1766.514	− 2.00
8	Mersa	All reach	35	1767.059	1767.059	0.00
9	Mersa	All reach	34	1765.785	1765.785	0.00
10	Mersa	All reach	33	1764.21	1764.21	0.00
11	Mersa	All reach	32	1762.539	1762.539	0.00
12	Mersa	All reach	31	1761.182	1761.182	0.00
13	Mersa	All reach	30	1759.98	1759.146	− 0.83
14	Mersa	All reach	29	1758.247	1757.622	− 0.62
15	Mersa	All reach	28	1756.402	1758.631	2.23
16	Mersa	All reach	27	1755.367	1755.377	0.01
17	Mersa	All reach	26	1751.532	1752.479	0.95
18	Mersa	All reach	25	1752.921	1750.922	− 2.00
19	Mersa	All reach	24	1751.589	1751.097	− 0.49
20	Mersa	All reach	23	1750.289	1748.29	− 2.00
21	Mersa	All reach	22	1748.751	1747.794	− 0.96
22	Mersa	All reach	21	1747.705	1747.705	0.00
23	Mersa	All reach	20	1745.997	1743.999	− 2.00
24	Mersa	All reach	19	1744.521	1743.486	− 1.04
25	Mersa	All reach	18	1743.531	1743.531	0.00
26	Mersa	All reach	17	1741.037	1741.285	0.25
27	Mersa	All reach	16	1738.831	1738.831	0.00
28	Mersa	All reach	15	1736.616	1735.484	− 1.13
29	Mersa	All reach	14	1736.084	1736.084	0.00
30	Mersa	All reach	13	1733.537	1732.767	− 0.77
31	Mersa	All reach	12	1731.328	1733.126	1.80
32	Mersa	All reach	11	1730.245	1728.246	− 2.00
33	Mersa	All reach	10	1728.954	1728.954	0.00
34	Mersa	All reach	9	1720.103	1722.112	2.01
35	Mersa	All reach	8	1718.622	1719.835	1.21
36	Mersa	All reach	7	1716.877	1714.877	− 2.00

(continued)

Table 9.6 (continued)

No.	River	Reach	RS	Elevation (m) @Jan 1, 2006	Elevation (m) @Dec 31, 2012	Difference (m)
37	Mersa	All reach	6	1714.803	1715.432	0.63
38	Mersa	All reach	5	1712.324	1713.181	0.86
39	Mersa	All reach	4	1709.991	1710.383	0.39
40	Mersa	All reach	3	1707.437	1709.068	1.63
41	Mersa	All reach	2	1705.965	1705.965	0.00
42	Mersa	All reach	1	1703.185	1703.027	− 0.16

Another method that was used in this investigation, Meyer Peter and Muller, gave an acceptable result in aggradation compared to field observations, and for the same fashion as the Yang sediment transport formula, the simulation for 7-year daily discharge in the study reach was performed, and deposition or degradation was observed in various reaches of the Mersa River. Accordingly, Meyer Peter and Muller reported a maximum aggradation or deposition of 3.33 m at station 26 and degradation of 2 m at stations 5, 7, 11, 25, 31, 36, and 41, as shown in Table 9.7. Additionally, the average aggradation was 1.12 m, and the degradation was also 1.52 m, thus showing that the Mersa reach was more disposed of by erosion.

When we compare the simulation results of both transport functions (Yang's and Meyer Peter Muller's methods), nearly half of the river reaches had similar or the same channel bed changes, especially on channel reaches that were neither aggraded nor degraded, and some reaches had the same degradation.

For station 30, deposition was observed near the left riverbank, at channel degradation and on the right riverbank aggradation. Additionally, the trend of aggradation and degradation for the complete 7-year daily discharge simulation, as shown in the figure below, shows that only for the first year to half of a year was the trend not uniform after half of 2006 to the end of 2012. At station 29 near both banks, large aggradation was observed, while in the middle of the reach, small aggradation and degradation were observed.

According to the above two scenarios (Yang transport method and Meyer Peter and Muller transport method), the results could be grouped into three conditions as follows. The initial condition near 49% of the Mersa River reach had equivalent results on both transport methods, the second condition near 46% of the Mersa River reach also had similar results, and the remaining 5% of the Mersa River reach had the opposite mean on one method of deposition on the other degradation. Finally, which works better or is acceptable for the reach of the channel must be determined to help recommend appropriate mitigation measures to change the channel bed. To differentiate the appropriate method for studying rivers, reach field observations and sample cross-sections surveyed one year later in January 2020 (the same benchmark as before) were compared with the one-year model results from both methods. The aggradation or degradation data were surveyed in 2019, and later 2020 is shown in Table 9.8 below for selected river reaches upstream and downstream.

Table 9.7 Channel bed elevation according to MPM

River	Reach	RS	Elevation (m) @Jan 1, 2006	Elevation (m) @Dec 31, 2012	Difference (m)
Mersa	All reach	42	1776.981	1775.391	− 1.59
Mersa	All reach	41	1775.755	1773.756	− 2.00
Mersa	All reach	40	1774.207	1772.908	− 1.30
Mersa	All reach	39	1772.954	1771.409	− 1.54
Mersa	All reach	38	1771.871	1769.882	− 1.99
Mersa	All reach	37	1770.617	1770.894	0.28
Mersa	All reach	36	1768.513	1766.514	− 2.00
Mersa	All reach	35	1767.059	1767.059	0.00
Mersa	All reach	34	1765.785	1765.785	0.00
Mersa	All reach	33	1764.21	1764.21	0.00
Mersa	All reach	32	1762.539	1762.539	0.00
Mersa	All reach	31	1761.182	1759.182	− 2.00
Mersa	All reach	30	1759.98	1759.819	− 0.16
Mersa	All reach	29	1758.247	1758.062	− 0.19
Mersa	All reach	28	1756.402	1757.478	1.08
Mersa	All reach	27	1755.367	1753.367	− 2.00
Mersa	All reach	26	1751.532	1754.864	3.33
Mersa	All reach	25	1752.921	1750.922	− 2.00
Mersa	All reach	24	1751.589	1751.74	0.15
Mersa	All reach	23	1750.289	1748.462	− 1.83
Mersa	All reach	22	1748.751	1747.479	− 1.27
Mersa	All reach	21	1747.705	1747.705	0.00
Mersa	All reach	20	1745.997	1744.553	− 1.44
Mersa	All reach	19	1744.521	1743.691	− 0.83
Mersa	All reach	18	1743.531	1743.531	0.00
Mersa	All reach	17	1741.037	1741.221	0.18
Mersa	All reach	16	1738.831	1738.831	0.00
Mersa	All reach	15	1736.616	1735.5	− 1.12
Mersa	All reach	14	1736.084	1736.084	0.00
Mersa	All reach	13	1733.537	1731.953	− 1.58
Mersa	All reach	12	1731.328	1731.842	0.51
Mersa	All reach	11	1730.245	1728.246	− 2.00
Mersa	all reach	10	1728.954	1728.954	0.00
Mersa	All reach	9	1720.103	1718.157	− 1.95
Mersa	All reach	8	1718.622	1717.941	− 0.68
Mersa	All reach	7	1716.877	1714.877	− 2.00

(continued)

Table 9.7 (continued)

River	Reach	RS	Elevation (m) @Jan 1, 2006	Elevation (m) @Dec 31, 2012	Difference (m)
Mersa	All reach	6	1714.803	1714.83	0.03
Mersa	All reach	5	1712.324	1710.325	− 2.00
Mersa	All reach	4	1709.991	1711.2	1.21
Mersa	All reach	3	1707.437	1710.733	3.30
Mersa	All reach	2	1705.965	1705.965	0.00
Mersa	All reach	1	1703.185	1701.585	− 1.60

Table 9.8 One-year simulation result and field survey collected data comparison

Channel bed change	River reach	Sediment transport formula		Field surveyed cross-section
		1 year simulation result (m/year)		1 year later collected (m/year)
		Yang	Meyer Peter and muller	
Aggradation	Upstream reach	1.12	1.08	1.07
	Downstream reach	0.22	1.21	0.21
Degradation (negative)	Upstream reach	1.18	2	1.16
	Downstream reach	2	1.83	1.94

A comparison between the simulation result and the reality in the field is shown in Table 9.8. The result of upstream reach aggradation or deposition according to Meyer Peter and Muller (MPM) and Yang compared to the field observations Yang overestimated, but MPM best fit, the aggradation of the upstream river reach. Downstream reach aggradation compared to site aggradation was fitted to Yang rather than MPM because it overestimates deposition. Degradation in both the upstream and downstream reaches was fitted with the Yang sediment transport formula rather than the MPM transport function. According to the MPM results, degradation upstream overestimates the realistic situation, while in the downstream reach, it underestimates the field observations. In conclusion, Yang gives a more realistic vertical change than MPM; therefore, the Yang sediment formula was the best representative transport function for our Mersa River reach.

Sediment Quantity Change

As discussed above, there was a vertical change or that the channel was obviously not stable. In addition to these vertical changes, the quantity of sediment entry (mass entry) and sediment leave (mass leave) in the channel must be explained. Therefore,

the mass input to the Mersa River and mass leave in each year from the Mersa River are presented in Table 9.9.

Table 9.9 shows the amount of sediment mass change in the channel, and the negative sign and positive sign indicate erosion and deposition, respectively; the cumulative mass in and out from the channel is shown in Appendix D. Finally, the Mersa River was affected by erosion rather than deposition, with an average cumulative sediment eroded from the channel of 22,470 tons per year. The delineated Mersa catchment was under the subbasin Awash Terminal, and according to ARBA (2017), the total erosion generated from this subbasin or Awash Terminal was 38.2 Mt/yr. The result obtained from the Mersa River was 22.47, which is acceptable.

Channel Bank Stability Analysis

As mentioned in the previous chapter, the bank stability and toe erosion model simulation was performed with a static ground water table for the ground water method, and the bank failure method was performed with the slice method. The BSTEM analysis results show that all Mersa River reach factors of safety were greater than unity except at reaches 33 and 26, where the safety factor was 0 for the right bank and left bank, respectively. Both the right and left banks were stable (no bank failure), and there was also no toe erosion. The stability conditions at both the bank and toe stations were stable against severe erosion. Table 9.10 and Fig. 9.9 show the shear stress produced by flow for the entire simulation period (from 2006 to 2012). The maximum or extreme shear stress was 152 Pa at river reach 23 in 2008, and the average shear stress was 10.6 pa.

Summary

Channels dynamically change in response to variations in flow and sediment transport. This change may cause the destruction of infrastructure, farmland, and property losses. Therefore, channel stability should be assessed, and appropriate stabilization measures should be provided to prevent such damage. This study tried to cover hydrological and hydraulic analyses to investigate the Mersa riverbed and bank stability. An L-moment diagram was used to identify the best fit distribution for gauged data, and out of 12 equations plotted in the diagram, the recorded data were fitted to the general extreme value method (Gumbel's method). Peak floods were estimated using the general extreme value frequency analysis method based on 17 years of stream flow data, and peak discharges for return periods of 2 years, 10 years, 50 years, and 100 years were 41 m^3/s, 68 m^3/s, 91 m^3/s, and 101 m^3/s, respectively.

Sieve analysis and triaxial compression tests were performed to determine the particle size gradation curve and BSTEM parameters, respectively. A gradation curve was used to determine the channel bank and bed material composition and in sediment

Table 9.9 Sediment mass in and out difference (tones)

RS	Station (m)	Year						
		2006	2007	2008	2009	2010	2011	2012
42	0.0	− 165.0	14.9	149.5	181.5	181.5	183.2	184.6
41	67.3	− 110.3	66.7	240.0	285.3	289.5	292.6	305.8
40	106.0	684.9	1018.0	1202.8	1355.2	1369.1	1428.4	1457.7
39	182.0	1104.6	1375.0	1658.9	1683.4	1686.7	1732.9	1756.2
38	249.1	1434.5	2029.9	2332.1	2469.2	2486.4	2501.4	2539.1
37	282.7	1884.8	2231.3	2571.0	2608.5	2609.7	2610.4	2625.4
36	363.0	214.8	15.9	122.9	− 36.9	− 36.9	− 36.9	− 27.9
35	444.7	1158.1	1702.2	2159.6	2211.0	2211.7	2212.0	2233.2
34	518.7	4321.3	4096.5	1956.1	1800.2	1805.9	1808.5	1858.8
33	600.9	− 367.6	62.1	66.9	66.9	66.9	66.9	80.6
32	641.7	677.4	654.3	654.4	654.4	654.4	654.4	528.1
31	714.7	2580.6	3085.7	3091.3	3091.3	3091.3	3091.4	3114.7
30	776.6	1728.1	706.2	− 508.9	− 988.6	− 1183.2	− 1362.8	-647.8
29	866.8	-4733.3	-4451.3	− 4451.3	− 4451.3	− 4451.3	− 4451.3	− 4451.3
28	932.2	− 4676.8	− 4772.8	− 4765.1	− 4746.6	− 4734.1	− 4717.5	− 4707.5
27	1022.6	− 1531.3	− 1357.7	− 1357.7	− 1357.1	− 1357.1	− 1357.1	− 1355.6
26	1100.3	2177.0	− 1494.2	− 1494.2	− 1465.7	− 1459.7	− 1459.6	− 1387.4
25	1164.0	− 713.6	− 711.5	− 711.5	− 711.4	− 711.4	− 711.4	− 711.3
24	1230.8	− 2012.1	− 1966.9	− 1858.0	− 1826.5	− 1764.2	− 1709.9	− 1651.7
23	1298.4	− 2330.2	− 2330.2	− 2330.2	− 2330.2	− 2330.2	− 2330.2	− 2335.4
22	1351.2	281.0	282.0	282.0	282.1	282.2	282.2	286.9
21	1394.2	− 672.3	− 631.4	− 620.4	− 605.0	− 598.7	− 598.3	− 589.6
20	1437.9	− 463.5	− 463.5	− 463.5	− 463.5	− 463.5	− 463.5	− 463.5
19	1513.5	− 493.4	− 163.8	56.0	276.1	374.5	446.0	812.4
18	1595.6	− 1477.7	− 1480.0	− 1407.3	− 1480.9	− 1458.0	− 1439.8	− 1573.7
17	1673.3	2726.1	2758.3	2637.7	2841.9	2851.9	2987.2	1372.0
16	1718.3	2422.8	4368.5	8311.5	9405.9	9567.4	9442.3	9377.0
15	1767.7	8494.5	10,442.2	7791.3	7373.7	7336.0	7375.9	7381.5
14	1814.2	4675.7	5525.4	4422.8	3489.8	2881.4	2352.3	2350.8
13	1865.5	91.0	− 3272.1	− 4531.5	− 5957.0	− 6674.4	− 7682.1	− 8623.3
12	1948.0	− 5018.1	− 7389.9	− 7389.9	− 7389.9	− 7389.9	− 7389.9	− 7389.9
11	2004.8	− 6025.0	− 6025.0	− 6025.0	− 6025.0	− 6025.0	− 6025.0	− 6025.0
10	2088.2	− 9560.6	− 9560.6	− 9560.6	− 9560.6	− 9560.6	− 9560.6	− 9560.6
9	2140.5	− 4652.4	− 4652.4	− 4652.4	− 4652.4	− 4652.4	− 4652.4	− 4652.4
8	2197.4	− 939.7	− 938.5	− 937.0	− 937.0	− 937.0	− 937.0	− 937.0
7	2240.0	− 760.4	− 757.0	− 757.0	− 757.0	− 757.0	− 757.0	− 757.0

(continued)

Table 9.9 (continued)

RS	Station (m)	Year						
		2006	2007	2008	2009	2010	2011	2012
6	2297.6	− 762.0	− 757.4	− 757.2	− 757.2	− 757.2	− 757.2	− 757.2
5	2338.3	− 830.8	− 864.4	− 864.4	− 864.4	− 864.4	− 864.4	− 864.4
4	2419.5	− 317.8	− 272.7	− 260.6	− 260.6	− 260.6	− 260.6	− 260.6
3	2485.5	− 1467.3	− 2453.4	− 2768.6	− 2768.6	− 2768.6	− 2768.6	− 2768.6
2	2555.9	− 1875.7	− 1875.7	− 1875.7	− 1875.7	− 1875.7	− 1875.7	− 1875.7
1	2618.4	− 973.7	− 973.7	− 973.7	− 973.7	− 973.7	− 973.7	− 973.7

transport analysis to assess the channel bed change. Triaxial compression tests were performed at 50 kN, 100 kN, and 200 kN loads in the laboratory, and the BSTEM parameters cohesion, C = 5.46 kPa, and angle of shearing resistance, $\phi = 140$, were determined from Mohr's circle after the results obtained from the triaxial compression test were drawn.

The HEC-RAS model was developed with the above inputs, such as the design flood for steady flow analysis for water surface profile computation using the direct step standard method. The result shows that there is overtopping on the bank edge, and adjacent areas were affected due to floods.

Sediment transport simulation and BSTEM analysis were simulated to assess channel bed stability and investigate channel bank conditions. The Mersa River reach exhibits both aggradation and degradation. In the upper reach, the maximum aggradation is 1.08 m at reach 28 over the entire simulation period, while the lower reach reaches 2.01 m at reach 9. The maximum degradation, both at the upper reach and lower reach, is 2 m at different reaches for the entire simulation period. The amount of sediment erosion generated from the study channel is on average cumulative at 22.47 kt/yr. However, both aggradation and degradation observed in the Mersa River channel bed are affected by erosion or degradation more dominantly than aggradation, and the total Mersa River channel bed is unstable.

The BSTEM model analysis results show that there was no erosion on the bank toe, and the safety factor was greater than one except at reaches 33 and 26. It can be concluded that the channel bank of the Mersa River reach is stable. Generally, from the Mersa River investigation, the channel bed is unstable, the bank is stable, and the area adjacent to the river is adversely affected by floods, as analyzed in the water surface profile. To minimize flood impact and stabilize the channel bed, appropriate stabilization measures are recommended. Vertical gabion bank for controlling flood in prone area, check dam and drop structure for stabilizing channel bed based on reach degradation.

Table 9.10 Mersa River reach shear stress

River	RS	Shear Stress (pa)						
		2006	2007	2008	2009	2010	2011	2012
Mersa	42	6.00	0.80	5.13	0.48	0.48	0.09	0.43
Mersa	41	0.95	6.31	18.07	3.39	3.39	0.80	3.76
Mersa	40	0.84	0.26	1.09	0.14	0.14	0.03	0.13
Mersa	39	8.81	5.48	12.99	4.40	4.40	4.70	4.34
Mersa	38	0.06	0.01	0.80	0.00	0.00	0.00	0.00
Mersa	37	1.43	0.70	4.15	0.45	0.45	0.08	0.41
Mersa	36	0.06	0.01	0.64	0.00	0.00	0.00	0.00
Mersa	35	2.57	0.99	14.14	0.65	0.65	0.33	0.63
Mersa	34	1.77	1.04	2.61	0.52	0.52	0.07	0.47
Mersa	33	1.09	0.63	4.60	0.34	0.34	0.13	0.34
Mersa	32	1.15	0.54	1.02	0.37	0.37	0.03	0.31
Mersa	31	0.37	0.30	4.28	0.16	0.17	0.08	0.17
Mersa	30	2.30	1.04	0.86	1.59	1.59	0.11	1.56
Mersa	29	2.16	0.56	1.86	0.14	0.01	0.00	0.00
Mersa	28	30.69	16.66	45.06	12.59	12.61	10.25	11.97
Mersa	27	2.03	0.43	2.87	0.15	0.15	0.10	0.15
Mersa	26	8.00	4.48	16.66	2.76	2.69	0.64	2.22
Mersa	25	1.31	0.33	1.96	0.06	0.04	0.01	0.01
Mersa	24	1.55	0.94	3.46	0.67	0.68	0.18	0.69
Mersa	23	87.37	49.74	152.27	31.34	31.34	5.99	29.94
Mersa	22	0.24	0.12	1.14	0.09	0.10	0.05	0.12
Mersa	21	4.05	1.72	9.37	0.94	0.94	0.17	0.89
Mersa	20	2.62	1.25	2.39	0.77	0.77	0.19	0.74
Mersa	19	0.11	0.04	0.64	0.02	0.02	0.00	0.03
Mersa	18	5.37	3.23	9.65	2.00	2.00	0.53	1.92
Mersa	17	1.95	0.98	5.24	0.61	0.61	0.12	0.59
Mersa	16	4.55	2.19	7.72	1.37	1.37	0.42	1.30
Mersa	15	0.07	0.03	1.15	0.01	0.01	0.00	0.01
Mersa	14	3.50	3.09	5.20	2.26	2.26	0.81	2.59
Mersa	13	0.53	0.13	0.23	0.00	0.00	0.00	0.00
Mersa	12	3.25	3.11	5.99	2.26	2.26	0.41	2.58
Mersa	11	0.32	0.05	2.87	0.01	0.01	0.00	0.01
Mersa	10	4.07	2.50	8.72	1.60	1.60	0.54	1.33
Mersa	9	1.46	0.74	4.16	0.49	0.49	0.11	0.44
Mersa	8	8.58	4.71	11.92	2.79	2.79	1.31	3.10
Mersa	7	2.90	0.87	4.53	0.36	0.40	0.03	0.34

(continued)

Table 9.10 (continued)

River	RS	Shear Stress (pa)						
		2006	2007	2008	2009	2010	2011	2012
Mersa	6	3.81	2.03	13.27	3.66	1.32	0.40	3.97
Mersa	5	7.79	3.80	11.77	0.90	2.35	0.47	0.84
Mersa	4	0.66	0.25	1.83	0.64	0.13	0.03	0.61
Mersa	3	5.88	2.99	14.72	2.03	2.04	0.81	1.99
Mersa	2	8.45	4.76	16.33	3.46	3.46	2.16	3.41
Mersa	1	4.45	3.06	7.95	1.86	1.86	0.48	1.80

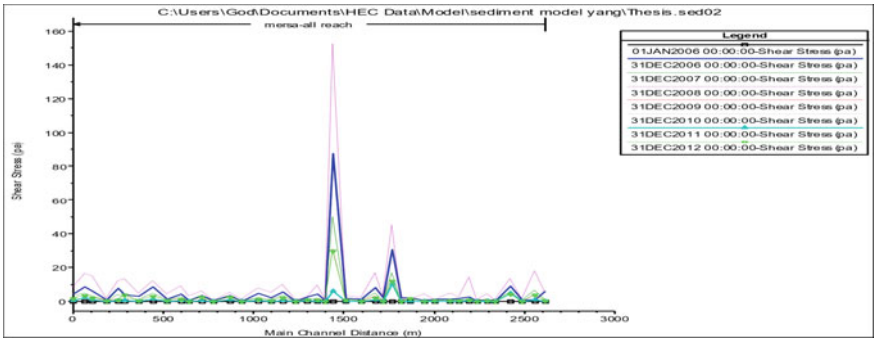

Fig. 9.9 Mersa River shear stress for the simulation period from 2006 to 2012

References

Arora KR (2008) Soil mechanics and foundation engineering (geotechnical engineering): In SI units. Standard publishers

Awash River Basin Authority (2017) Executive summary of strategic river basin plan for Awash Basin

Brunner GW (2016) HEC-RAS river analysis system: hydraulic reference manual, version 5.0. US Army Corps of Engineers–Hydrologic Engineering Center, 547

CEIWR-HEC (2015) HEC-RAS USDA-ARS bank stability & toe erosion model (BSTEM), Technical Reference & User's Manual

Chow VT, Maidment DR, Mays LW (1988) Applied hydrology. McGrawHill, New York

Chow VT (1959) Open channel hydraulics. Caldwell. The Blackburn Press, New Jersey

French RH (1986) Open channel hydraulics. McGraw-Hill New York

Garde RJ, Ranga Raju KG (1978) Mechanics of sediment transportation and alluvial stream problems. Wiley Eastern Ltd, New Delhi

Hawi A (2018) Investigating the effect of scouring on hydraulic performance of cross drainage structure (case study of Ginchi Awash Bridge). Thesis, Addis Ababa University

Hosking JRM (1990) L-moments: analysis and estimation of distributions using linear combinations of order statistics. J Royal Stat Soc

Hosking JRM (1991) Approximations for use in constructing L-moments ratio diagrams, vol 3. Res Report, RC-16635. IBM Res Division, New York

Meyer-Peter E, Müller R (1948) Formulas for bed-load transport. Proc., 2nd Meeting. IAHR, Stockholm, Sweden
Murthy VNS (2002) Geotechnical engineering: principles and practices of soil mechanics and foundation engineering. CRC Press, Boca Raton
Subramanya K (2008) Engineering hydrology. McGraw-Hill, New York

Chapter 10
Effects of Climate Variability on Crop Diversity Over the Agroecological Zones of Gumara Watershed, Northwest Ethiopia

Belay M. Tegegne, Mintesinot A. Taye, Sileshie M. Leyew, and Assefa M. Melesse

Abstract This study demonstrated the trend of climate and the decadal dynamics of the crop diversity in the Gumara watershed, Ethiopia. The Gridded Satellite and observed historical climate data from the period of 1987–2016 and the crop-climate history were the data sources. The Mann–Kendall test and Sen's slopes estimator were used for trend analysis. Ratings from the Food and Agriculture Organization (FAO) crop-climate requirements were used for crop diversity dynamics. The results indicated a nonsignificant increase in decadal Kiremit rainfall of 27 mm at Weyna Dega and 43 mm at Dega agroecological zones. The Kiremit season temperature variables exhibit statistically significant increasing trends in all zones. In general, decadal increments of 0.4 °C for minimum and maximum temperatures and 0.5 °C for mean temperature were recorded in the watershed. The recent period of decadal increment in maximum temperature negatively affected most selected indigenous crops at the lower elevation and helped to move the crops forward to the higher elevation. The study revealed that improved crop varieties should be introduced according to the watershed agroecological zones. The traditional agroecological zone classification system of Ethiopia must be systematically updated. In addition, to detect detailed information on crop-climate associations and the effects of climate variability on crop

B. M. Tegegne (✉)
Nature and Biodiversity Conservation Union (NABU), Bahir Dar, Ethiopia
e-mail: belaymulu2013@gmail.com

M. A. Taye
Bahir Dar University, Bahir Dar, Ethiopia
e-mail: Mintesinot.Azene@bdu.edu.et

S. M. Leyew
Amhara Design and Supervision Works Enterprise, Bahir Dar, Ethiopia

A. M. Melesse
Department of Earth and Environment, Institute of Environment, Florida International University Miami, Miami, USA
e-mail: melessea@fiu.edu

A. M. Melesse et al. (eds.), *Land and Water Degradation in Ethiopia*, Springer Geography, https://doi.org/10.1007/978-3-031-60251-1_10

diversity, yearly analysis rather than decadal analysis is suggested for governments and future research.

Keywords Climate variability · Indigenous crop · Crop diversity · Agroecological zones

Introduction

Climate is the most important factor that governs food production and can cause variability in socioeconomic and environmental systems related to the availability of water resources in its changing state (Pachauri et al. 2014; Koudahe et al. 2018). Altered frequencies and intensities of extreme weather are expected to have mostly adverse effects on natural and human systems. Agricultural production, including access to food, in many African countries is projected to be severely compromised. This would further adversely affect food security and exacerbate malnutrition (Pachauri et al. 2014). On the other hand, according to FAO and World Bank reports, agriculture does not only feed the entire human race but also produces fiber for clothing, feed for livestock and bioenergy. In the developing world, agriculture contributes significantly to the gross domestic product, leads the way in reducing poverty and accounts for a large share of employment opportunities (Agbossou et al. 2012).

Africa is highly vulnerable to future climate change and variability, and Ethiopia is often cited as one of the most extreme examples (Alemayehu 2016). Ethiopia's agriculture is primarily rain-fed and hence it is sensitive to the fluctuations in rainfall; thus, the economy is highly exposed to climate variability and extremes (UNDP 2011; Sadoff 2019; Taye et al. 2013). Current climate variability also has a significant influence on crop production in the area and any unfavorable change in the local climate in the future will have serious implications for household-level food security in the country (Alemayehu 2016).

Various analysts have reasoned that the persistence of the subsistence nature of Ethiopian agriculture is partly due to the lack of proper understanding of the agroclimatic resources of the country. The agroclimatic zone is a land unit, in terms of major climate and growing period that is climatically suitable for a certain range of crops and cultivars. Agroclimatic zonation schemes are standard tools for prioritizing agricultural research because they offer relevant available information about the target environments (Ganaie et al. 2014).

Of the climatic factors, the two limiting climatic elements, i.e., the number of days in which adequate moisture is available for growth and development of plants and conducive temperature for adaptation of a certain (botanical) community of plants and animals are given high priority and due considerations (Hurni 1998). Owing to its large altitudinal variation, Ethiopia is a home to several food crop varieties suited to the dry and high temperature conditions of the lowlands and the wet and cooler temperature conditions of the highlands (Di Falco et al. 2010). Based on

their agroclimatic suitable zone, many crops are grown in a diversified manner in Ethiopia, including cereals, pulses, oilseeds, vegetables, roots, tubers, fruits, fibers, and sugarcane (Benin et al. 2003; Gorfu 2012).

Crop biodiversity is the foundation of food production and supply (Di Falco et al. 2010). However, due to the variability of climate from time to time the climatic zones that control species distribution will move to higher elevations; consequently, the species diversity will shift with the climate zone, and then the local diversity shift will be faced with diversity degradation, and new species will also emerge (IPCC 1990). To challenge the complex climatic effects on crop production, farmers and breeders are practically using biodiversity to adapt crops to different and changing production environments (Di Falco et al. 2010).

Species movements and their diverse societal and environmental impacts and awareness of 'species on the move' should be incorporated into local, regional, and global assessments as standard practice (Pecl et al. 2017). The differential effects of climate change on farms in various agroecological zones have not yet been quantified (Seo 2011). Farms in different agroecological zones clearly face different conditions for farming. To solve this problem, small-scale projects and case studies need to be scaled up and multiplied to encourage the direction of large-scale funding toward local solutions (Swiderska 2008).

Further analysis is needed to identify priority species and areas to target for climate adaptation strategies, particularly for improved climate change tolerant varieties (Lane and Jarvis 2007). Additionally, they indicated that rich species and genetic diversity that exists in landraces should be exploited and used to guide crop variety selection.

The Gumara watershed is rich in agroecological zones (elevated from 1784 to 3800 m.a.s.l) and crop diversity in a small square kilometer (Melke 2015). However, these indigenous crop diversity situations have been observed to be unstable and degraded in their original places within the watershed agroecological zones, and crops diversification has not been found.

To date, however, studies on the potential effects of climate variability on crop diversity at the watershed level are still very limited. This chapter investigates the effect of climate variability on crop diversity over the agroecological zones of the Gumara watershed, in the northwest highlands of Ethiopia. Then, the trends of climate variability and decadal crop diversity dynamics were analyzed. In addition, which climate factors are more impactful on crops and which crop species are more sensitive to this climate variability were also analyzed.

Area Description

The Gumara watershed (Fig. 10.1) is located into the east direction of Lake Tana and drained by the Gumara Rivers in south Gondar zone of the Amhara National Regional State. It is located between latitudes of 11° 35' and 11° 55' N and longitudes of 37° 40' and 38° 10' E, at 624 km north of Addis Ababa (Melke 2015; Chakilu and

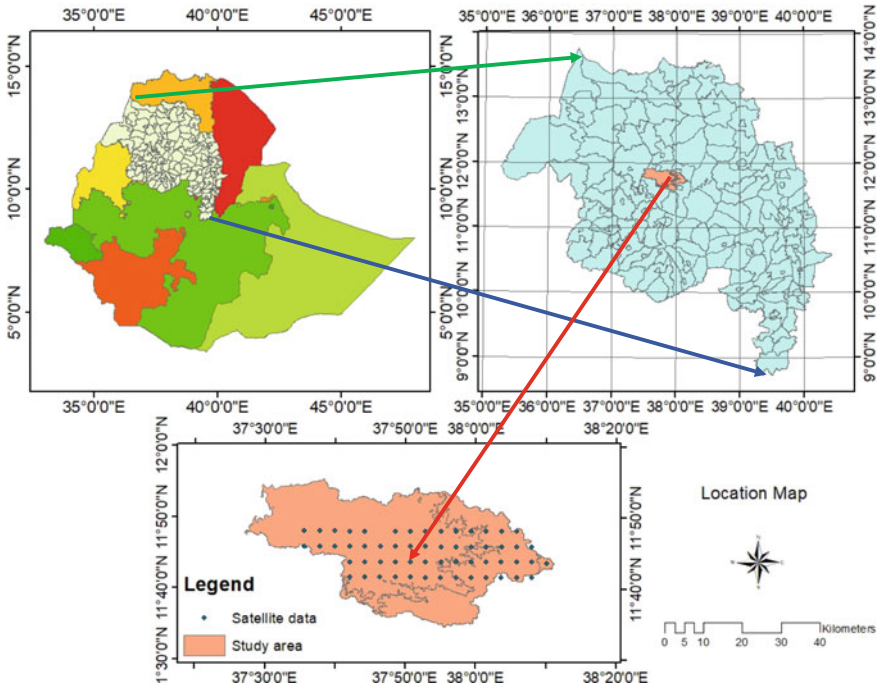

Fig. 10.1 Map of study area. *Source* Extracted from Amhara region shape file (2019)

Moges 2017). The watershed elevation ranges from 1784 m.a.s.l. at the lake to 3800 m.a.s.l. in the highlands, with slopes ranging from 0 to 70%. The stream length from its origin is approximately 132.5 km before the edge of Lake Tana. The total area of the watershed covers about 1639 km^2. It is part of the Lake Tana subbasin and contributes significant inflows to the lake. It drains *Dera, Farta, Fogera,* and some parts of *Estie Woredas* (Chakilu and Moges 2017).

Climate Condition

Bahir Dar, Debre Tabor, Amedber, Woreta, Amde Genet, Nifas Mewucha, Wanzaye, and Gassay are some meteorological stations within the study area which are monitored by the Ethiopian Meteorological Agency. Among these Bahir Dar, Debire Tabor, and Nefas Mewucha stations of relative humidity, sunshine hour and wind speed data were used to calculate the potential evapotranspiration conditions of the watershed agroecological zones. The annual climate may be divided into two seasons: rainy and dry. The four rainy months (Kiremit) cover 84% of the total annual rainfall. The remaining months, being from October to May, have a total rainfall of approximately 16% of the mean annual rainfall. Melke (2015) reported

Table 10.1 Traditional agroecological zones and physical characteristics

Zone	Altitude (m.a.s.l.)	Rainfall (mm/year)	Average annual temperature (°C)	Length of growing period (days)
Wurch (upper highlands)	> 3200	900–2200	< 11.5	211–365
Dega (highland)	2,300–3,200	900–1,200	17.5/16–11.5	121–210
Weyna Dega (midland)	1,500–2,300	800–1,200	20.0–17.5/16	91–120
Kola (lowland)	500–1,500	200–800	27.5–20	46–90
Bereha (desert)	< 500	< 200	> 27.5	0–45

Source Hurni (1998)

85% of the annual rainfall in the watershed comes in *Kiremit*, the main rainy season, and 15% in other months. Referring to the Ethiopian Meteorological Service Agency (EMSA), the climatic type is generally humid, with the mean annual temperature of 20.5 °C and an average total annual rainfall of 1300 mm (Wubie et al. 2016). Wetland areas commonly exist at the lower banks of the river near Lake Tana (Melke 2015). Table 10.1 shows the agroecological zones of Ethiopia.

Socioeconomic Conditions

The total population of the watershed is 487,576 (Wubie et al. 2016). Agriculture is the main livelihood activity in the watershed. The Central Statistical Agency (CSA) report in 2001 notes 91% of the total cultivated area was cropped during the *meher* or *Kiremit* in the 2000/2001 cropping year. The major cereal crops grown in the watershed are Tef, Maize, Barley, Wheat, and Finger Millet as well as oil seeds such as Linseed (*Telba*/and Niger Seed (*Noug*/(Woldeamlak 2009).

Data Collection Methods and Sources

To identify any changes in the climate, it was necessary to compare the climate statistical parameters (precipitation and temperature) for the three different climate periods from the 30 years of data (Asai 2017). Based on the annual average climate data, the decadal climate dynamics of the study area were determined (Taye et al. 2013; Asai 2017). The 30 year (1987–2016) CHIRPS-sourced (4 km * 4 km) gridded satellite climate data (daily rainfall and temperature) were collected at National Meteorological Services Agency (NMSA). The gridded climate data are reconstructed data based on records of gauge stations and meteorological satellite observations. The

gridded data set is very useful in view of the fact that weather stations are limited in number, unevenly distributed and have a missing data problem and a short period of observations (Asfaw et al. 2018). Among other satellite data sources, the CHIRPS satellite data source was evaluated and preferred by different previous scholars for East Africa (Gebrechorkos et al. 2018) and the Ethiopia Tekeze-Atbara basin by (Gebremicael et al. 2017). This is also true in the nearby study area of the Upper Blue Nile River Basin evaluated by Bayissa et al. (2017).

According to the Food and Agriculture Organization, a major challenge to calculate the evapotranspiration of the zones was to find other climate variables such as relative humidity, sunshine hour, and wind speed data in the area where the rainfall and temperature data are collected. Although the solution was suggested by FAO (1996) itself, we can collect those data from neighboring stations through interpolation (linear regression) mechanisms and used by Surendran et al. (2015).

Then, we collected these data from the Nefas Mewcha, Debre Tabor, and Bahir Dar stations for the Wurch (Upper highland), Dega (Highland), and Weyna Dega (Midland) agroecological zones, respectively, for the purpose of length of growing period calculation. The agroecologically neighboring observed meteorological data for the purpose of comparison with gridded satellite data were used by Esayas et al. (2018).

Sampling Techniques

Crop Type Sampling

Dominantly growing indigenous crop types (Table 10.2) in the past 15–20 years in the watershed were identified from the previous literature (Woldeamlak 2009), and the administration of South Gonder Zone agricultural sector experts (2019). Thus, based on the crop types abstained, their botanical/scientific names were identified in FAO (1989) and used for crop-climate relationship analysis.

Table 10.2 Indigenous crop types in the watershed

No.	Name crop type	Botanical/scientific name
1	Maize	Zea mays
2	Tef	Eragrostis abyssinica
3	Barley	Hordeum vulgare
4	Wheat	Triticum aestivum
5	Finger Millet	Eleusine coracana
6	Linseed (flax for oil seed)	Linum usitatissimum
7	Niger seed	Guizotia abyssinica

Source FAO (1989)

The Climate Data Sampling Technique

According to Hurni (1998), the traditional elevational coverage of the watershed ranges from the Weyna Dega zone (1784–2300 m.a.s.l), Dega zone (2301–3200), and Wurch zone (3201–3800 m.a.s.l). Based on the area coverage of each agroecological zone within the total area of 1639 km^2 of watershed, each agroecological zone covers 1103.6, 357.4, and 178 km^2 in the Weyna Dega, Dega, and Wurch zones, respectively.

Based on the Ethiopian traditional agroecological classification system, the Gumara watershed was classified into agroecological zones. In each agroecological zone, the *Weyna Dega, Dega,* and *Wurch* zones, had 39, 18, and 1 gridded data share, respectively.

Data Set and Quality Control

Outlier Detection

The Tukey fence was used to screen outliers greater than a threshold value that can affect the detection of inhomogeneity (Ngongondo et al. 2011).

The data range is represented as:

$$[\mathrm{Q1} - 1:5 \times \mathrm{IQR},\ \mathrm{Q3} + 1:5 \times \mathrm{IQR}] \tag{10.1}$$

where Q1 and Q3 are the lower and upper quartile points, respectively, and IQR is the interquartile range. Values outside the Tukey fence are considered outliers. In this paper, such outliers were set to a limit value corresponding to 1.5 × IQR. Values below the lower limit and above the upper limit were considered outliers and rejected.

Methods of Data Analysis

Length of Growing Period (LGP) Calculation

We examined the main crop growing season (June–September) for the crop-climate relationships. We followed the crop-moisture availability conditions of the area related to crop-moisture requirements during their growing season based on the (FAO 1989) specifications.

Although the United Nation Development Program Food and Agricultural Organization (FAO 1989) suggested that the LGP analysis could be assessed by two alternative methods, such as calculation from rainfall and PET data and from the growing

period zone map of Ethiopia, we followed and used the LGP calculation method from rainfall PET data due to its potentially accuracy compared to reading from the LGP map. Thus, to calculate the LGP the PET were calculated through Penman Monteith (CROPWAT8.0 Software) using the minimum and maximum temperature, relative humidity, sunshine hours, and wind speed as input data (FAO 1998). According to the United Nation Food and Agriculture (FAO) specification, we determined the LGP through the area precipitation data that are greater than half of the potential evapotranspiration (FAO 1989).

The FAO Penman–Monteith method is recommended as the sole ETo method for determining potential evapotranspiration. CROPWAT.8 software was used to compute ETo as follows:

$$\mathrm{ETo} = 0.408 * \Delta = \left((\mathrm{Rn} - G) + y * \frac{\frac{900}{T+273} * \mathrm{U2}(\mathrm{es} - \mathrm{ea})}{(\Delta + y * (1 + 0.34 * \mathrm{u2}))} \right) \tag{10.2}$$

where ETo: reference Evapotranspiration (mm/day), Rn: Net radiation at the crop surface ($\mathrm{MJm}^{-2}\ \mathrm{day}^{-1}$), T: Mean daily temperature at 2 m height (°C), Es: saturation vapor pressure (kPa), Ea: actual vapor pressure (kPa), Es-Ea; saturation vapor pressure deficit (kPa), Δ: slope vapor pressure curve (kPa °C), G: soil heat flux density ($\mathrm{MJm}^{-2}\ \mathrm{day}^{-1}$), y: Psychometric constant (kPa), and U2: wind speed at 2 m height (ms^{-1}).

Climate Trend Analysis

The Mann–Kendall Test and Sen's Slope Estimator

The Mann–Kendall test was used to detect the trend of climate variables (rainfall, temperature, and length of growing periods) and the magnitude was analyzed by Sen's slope estimator. Mann–Kendall's test is a nonparametric method that is less sensitive to outliers and tests for a trend in a time series without specifying whether the trend is linear or nonlinear (Yue et al. 2002; Partal and Kahya 2006; Bekele et al. 2016; Asfaw et al. 2018). The initial value of the Z test statistic (S) is assumed to be zero, implying no trend. If a data value from a later time period is found to be greater than the data value from an earlier time period, then S is increased by one. On the other hand, if the data value from the later time period is lower than that of the earlier period, the Z test statistic S is reduced by one. The overall result of all increments and decrements provides the final S value, which lies between −1 and + 1. The null hypothesis of the Z test is that no change has occurred during the time (no trend). However, the alternative hypothesis of the Z test is that a significant change has occurred over time. Mann–Kendall and Sen Slope tests are widely known and used by different authors to detect trends in meteorological variables (Seleshi and Zanke 2004; Degefu and Bewket 2014; Kiros et al. 2016; Asfaw et al. 2018; Bekele et al. 2016).

The Mann–Kendall test statistics are given as follows (Salmi et al. 2002; Longobardi and Villani 2010; Bekele et al. 2016).

$$S = \sum_{i=1}^{n-1} \sum_{j=i+1}^{n} \text{sgn}(xj - xi) \tag{10.3}$$

The application of the trend test is performed on a time series xi that is ranked from $i = 1, 2 \ldots n-1$ and xj, which is ranked from $j = i + 1, 2 \ldots n$. Each of the data points xi is taken as a reference point, which is compared with the rest of the data point's xj. Then,

$$\text{sgn} = (xj - xi) = \begin{cases} +1 \text{ if } (xj - xi) > 0 \\ 0 \text{ if } (xj - xi) = 0 \\ -1 \text{ if } (xj - xi) < 0 \end{cases} \tag{10.4}$$

where xj and xi are the annual values in years j and i ($j >$ i), respectively.

It has been documented that when the number of observations is more than 10($n \geq 10$), the statistic 's' is normally distributed with a mean value of zero, and the variance is calculated using Equation

$$\text{Var}(S) = \frac{n(n-1)(2n-5) - (x+a)^n = \sum_{t=1}^{m} (ti(ti-1)(2ti-5)}{18} \tag{10.5}$$

where n is the number of observations and ti is the sample time series. The test statistic Z is as follows:

$$Z = \begin{cases} \frac{S-1}{\sigma} \text{ if } S > 0 \\ 0 \text{ if } s = 0 \\ \frac{S+1}{\sigma} \text{ if } S < 0 \end{cases} \tag{10.6}$$

The decision to either reject or accept the null hypothesis is then made by comparing the calculated Z with the critical value at a chosen level of significance.

Sen's slope estimator is also a nonparametric test by which the true slope (change per year) of a trend is estimated (Salmi et al. 2002; Bekele et al. 2016). Sen's test is used when the trend is assumed to be linear, i.e.,

$$f(t) = \delta t + B \tag{10.7}$$

where $f(t)$ is an increasing or decreasing function of time, i.e., the trend δ is the slope and B is the intercept (constant). The slope of each data pair δi is calculated as:

$$\delta i = \frac{Xj - xk}{j - k} \tag{10.8}$$

where $j > k$ and, if there is n number of xj in the time series, we obtain as many as $N \frac{n(n-1)}{2}$ slope estimates of δi.

Then, the values of Qi are ranked from small to large, the median of which is Sen's slope (δ):

$$\delta = \begin{cases} \delta\left[\frac{N+1}{2}\right] \text{ if } N \text{ is odd} \\ (\delta\left[\frac{1}{2}\right]\delta\left[\frac{(N+2)}{2}\right] \text{ if } N \text{ is even} \end{cases} \tag{10.9}$$

Analysis of Coefficient of Variability (CV)

The coefficient of variability (CV) is a unit-less normalized measure of dispersion of a probability distribution. It expresses the standard deviation as a fraction of the mean and is useful when interest is in the size of variation relative to the size of the observation. It is expressed as the ratio of the standard deviation to the mean (Araya et al. 2011; Bekele et al. 2016).

$$\text{CV} = \left[\frac{S}{X}\right] * 100. \tag{10.10}$$

where CV is the coefficient of variation; X is the average long-term rainfall, and S is the standard deviation of rainfall. The CV was used to compare the long-term variation in wet season rainfall to that of individual years. The result of the coefficient of variability (CV) was expressed as a percentage, and the degree of variability of rainfall events was classified based on (Hare 2003) as follows: CV < 20% = less/slightly variable, CV from 20 to 30% = moderately variable, and CV > 30% = highly variable.

Analysis of Decadal Crop Diversity Dynamics

All climate variables do not equally support and affect crops at the same time and place. Thus, to analyze the decadal effects of climate variability on crop diversity within the identified AEZs, three decadal periods were bounded as [(1987–1996), (1997–2006), and (2007–2016)] in each zone. Finally, the number of suitably growing indigenous crops was identified, counted, and numbered on a decadal basis in each agroecological zone.

The minimum and maximum temperature and moisture requirements of crops were used to discuss which climate variabilities had the greatest effect. The crop-temperature suitability analyses with each variable (minimum and maximum temperature) may provide a proper insight rather than the analysis with mean value alone.

Rating Method

FAO (1989) specified the crop-climate suitability conditions. In this chapter, we used the specification ranges to analyze the decadal crop diversity dynamics by rating the decadal climate data to the crop suitability ranges in the study area agroecological zones. Thus, based on the decadal number of suitably growing selected crops, the decadal dynamics in the agroecological zones were analyzed.

The following tables (Tables 10.3 and 10.5) present the main climate variables, such as moisture and temperature, which determine the distribution and occurrences of crops in an area specified by FAO (1989). We used these tables for all zones in the decadal crop diversity dynamics analysis. The suitability rating with the selected crops (Table 10.6) in each agroecological zone was made in the decadal bases in the period of 1987–2016 through calculated moisture availability (length of growing period) and temperature. The calculated decadal LGP in the AEZ zones are shown in Table 10.4.

Results and Discussion

Results of Data Set and Quality Controls

The Tukey fence properly detected outliers greater than (Q3) and less than (Q1) the threshold value that can affect the detection of inhomogeneity. Values outside the Tukey fence were considered outliers/anomalies and removed from the data before the aggregation of the daily gridded satellite data into monthly and yearly data.

Climate Trends in the Study Area

Table 10.7 indicates the climate trends in the watershed. A positive trend with a p-value greater than the alpha value was noticed in all annual temperature variables. The calculated P-value of the temperature was statistically significant at the 5% level. A positive Sen's slope was found, and it established a rising trend in temperature year-by-year.

Table 10.3 The FAO crop-moisture suitability ranges in the agroecological zones (AEZs)

Crop types ↓	Mean moisture requirement (days) at the mean elevation of the zones			Minimum LGP requirement			Maximum LGP requirement		
	Weyna Dega (2000 masl)	Dega (2500 masl)	Wurch (3000 masl)	Weyna Dega (2000 masl)	Dega (2500 masl)	Wurch (3000 masl)	Weyna Dega (2000 masl)	Dega (2500 masl)	Wurch (3000 masl)
Suitability ranges →	S1	S1	S1	S2	S2	S2	S2	S2	S2
Maize	140–255	245–360	> 285	120–140	255–245	NS	255–300	310–360	350–360
Tef	95–230	145–280	180–315	80–95	130–145	165–180	230–255	260–285	280–305
Barley	105–240	155–290	190–325	90–105	140–155	175–190	240–260	240–260	140–260
Wheat	115–240	165–290	200–325	100–115	150–165	185–200	240–265	240–265	240–265
Niger Seed	120–155	120–155	120–155	110–120	110–120	110–120	150–210	150–210	150–210
Linseed	130–240	160–270	180–290	110–130	140–160	160–180	240–270	240–270	240–270
Finger Millet	90–120	160–280	NS	75–90	145–160	NS	NS	NS	NS

Source FAO (1989)

Table 10.4 The calculated decadal LGP in the AEZ zones

Decadal periods	Agroecological zones LGP		
	Weyna Dega	Dega	Wurch
1987–1996	150	190	168
1997–2006	156	165	165
2007–2016	156	180	180

Source Our calculation from Penman–Monteith (CROPWAT. Software)

Table 10.5 The FAO crop-temperature suitability range of selected crops

Minimum temperature requirement					Crop types	Maximum temperature requirement					Mean temperature requirement
Ns	S4	S3	S2	S1		S1	S2	S3	S4	Ns	Mean
< 12	12–14	14–15	15–16	16–26	Maize	16–26	26–30	30–34	34–38	> 38	16–26
< 11	11–12	12–14	14–15	15–21	Tef	15–21	21–22	22–23	23–25	> 25	15–21
< 5	5–7	7–9	9–11	11–24	Barley	11–24	24–27	27–28	28–30	> 30	11–24
< 10	10–11	11–12	12–14	14–24	Wheat	14–24	24–27	27–28	28–30	> 30	14–24
< 12	12–13	13–15	15–17	17–23	Nigger seed	17–23	23–24	24–26	26–29	> 29	17–23
< 10	10–12	12–14	14–16	16–24	Linseed	16–24	24–26	26–28	28–30	> 30	16–24
< 14	14–15	15–16	16–17	17–30	Finger millet	17–30	30–35	35–38	38–40	> 40	17–30

Source FAO (1989)
Where S1 = First Suitable/best suitable/no effect/, S2 = Second Suitable/some effect/, S3 and S4 are with high effect, and NS = Not Suitable

Table 10.6 Spatial and temporal crop growing season temperature values in the AEZs

Decadal periods	W/Dega temperatures			Dega temperatures			Wurch temperatures		
	T min	T max	T mean	T min	T max	T mean	T min	T max	T mean
1987–1996	11.3	23.3	17.5	9.7	20.7	15.2	8.9	20.2	14.5
1997–2006	11.9	24.1	18.2	10.1	21.3	15.6	9.2	20.7	15.3
2007–2016	12.8	24.1	18.7	10.5	21.7	16.0	9.8	21.3	16.4

Source Spatially and temporally recorded climate data (2019)

The increment of rainfall was insignificant at the same significance level. However, based on our analysis in the agroclimatic zones by dense gridded climate data, there were the fluctuations in the results for each variable, especially rainfall at different grid points. The result variation among grid points was presented by (Wagesho et al. 2013). In addition, the trend of the length of the growing period (moisture availability conditions in the crop growing season /*Kiremit*/) of the watershed follows the

Table 10.7 Annual climate variability trends in the watershed

Variables		Trend determinants		
No.	Climate variables	Kendall's tau	P-value	Sen's slope:
1	T min	0.5	< 0.0001	0.044
2	T max	0.4	0.0004	0.04
3	T mean	0.6	< 0.0001	0.05
4	Rainfall	0.2	0.19	5.13
5	LGP	0.02	4	LGP

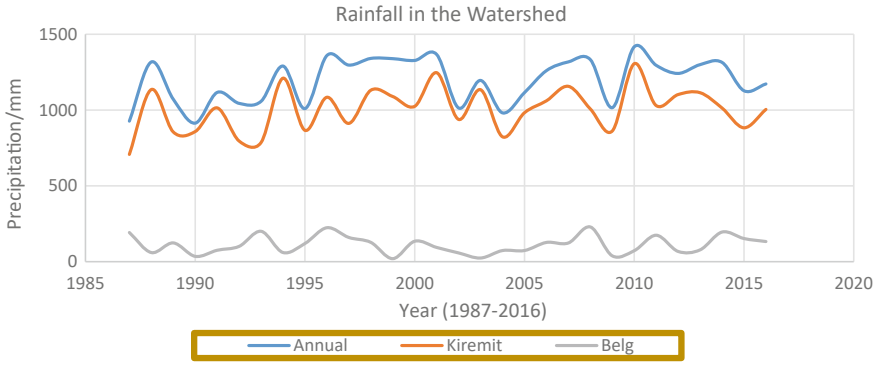

Fig. 10.2 Rainfall trends and variability in the agroecological zones

significantly increasing trends of temperature and insignificantly increasing trends of rainfall (Fig. 10.2).

*Annual and Crop Growing Season (***Kiremit***) Rainfall Trends in the AEZs*

Table 10.8 presents the mean value of the rainfall trend in the agroecological zones. Except for the Wurch zone annual rainfall, both the annual and Kiremit season rainfall showed insignificant increasing trends in the Weyna Dega and Dega agroecological zones with decadal increments of 30.6 mm and 27 mm with 3.069 mm and 2.781 mm/year rates and 40.21 mm and 40.33 mm with 4.21 and 4.33 yearly increments, respectively (Figs. 10.3 and 10.4).

Woldeamlak (2007) reported that there were intra-annual and intraregional differences in the amount and variability of rainfall in the Amhara region. However, there was no systematic pattern of change across the region regarding trends in annual and seasonal rainfall. This is true in our study area agroecological zone rainfall trends.

Table 10.8 Annual and Kiremit season rainfall trends and variability in the AEZs

AEZs	Season	Mean Rainfall	Contribution %	Trend		
				MK(Z)	P-value	Slope (δ)
Weyna Dega	Annual	1200.0	100.0	0.122	0.357	3.069
	Kiremit	1029.2	85.8	0.108	0.416	2.781
Dega	Annual	1200.0	100.0	0.122	0.357	4.206
	Kiremit	1001.2	83.4	0.154	0.242	4.331
Wurch	Annual	1188.1	100.0	0.310	0.016	7.833
	Kiremit	983.1	82.7	0.228	0.081	7.533

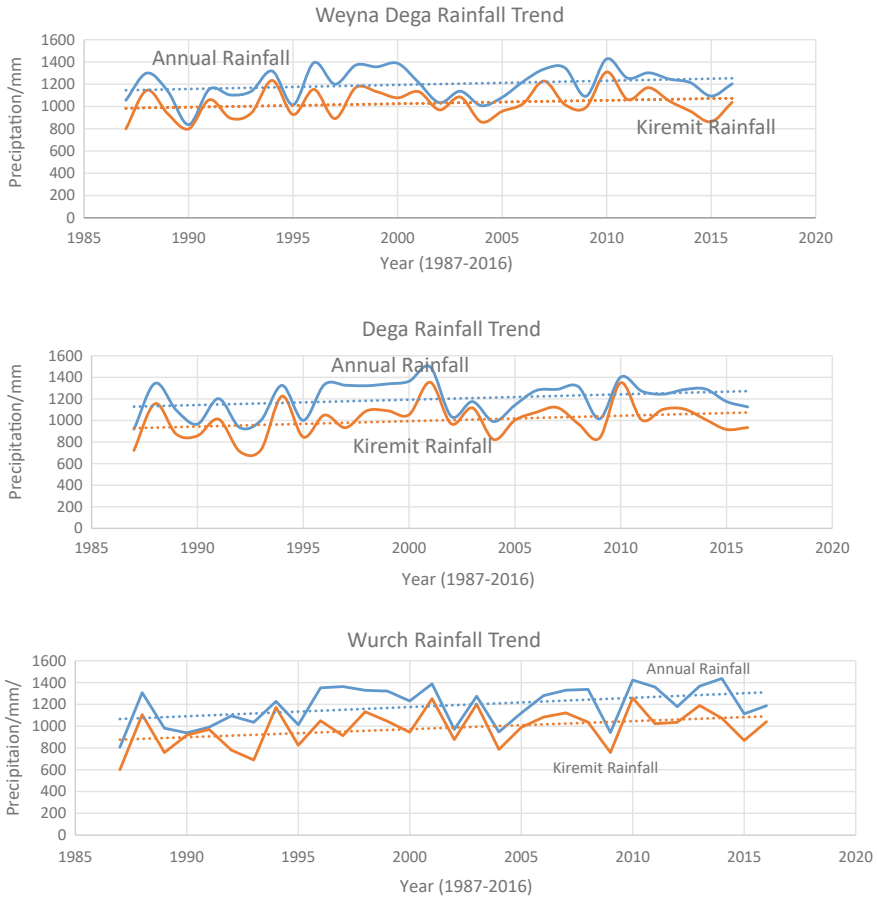

Fig. 10.3 Annual and main rainy season rainfall trendline in the agroecological zones

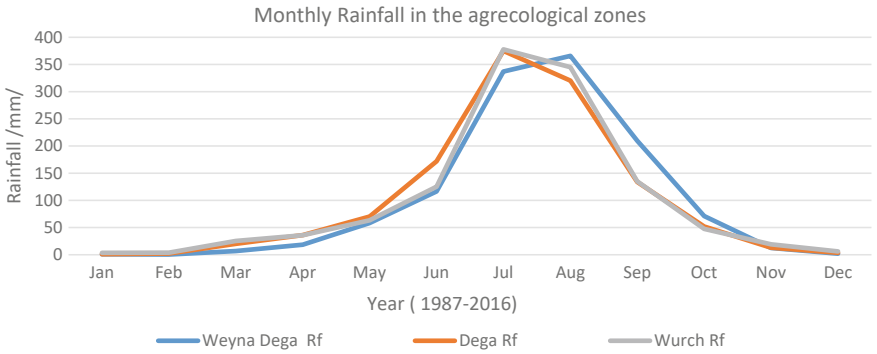

Fig. 10.4 Monthly rainfall distributions in the agroecological zones

In addition, there were a mixture of agreed-upon and disagreed-upon reports provided by previous investigations with our analysis; for example, the National Meteorological Service Agency report indicated that a declining trend has been observed over the northern half of the country and an increasing trend in annual rainfall in central Ethiopia (NMSA 2001). On the other hand, Admassu and Seid (2006) reported that there was a significant decreasing trend in Kiremit rainfall at some stations across the country (for example, Gore and Jijiga).

Abrha (2015) confirmed that the change varies by agroecology, which is consistent with our analysis, but in contrast, the Kiremit (summer) rainfall in lowlands increased significantly, whereas in a similar manner to our result, the highland area experienced a nonsignificant increasing trend. Wagesho and his friends reported results opposite to our findings indicating that there were decreasing trends in Kiremit and annual rainfall in northern and northwestern (which is our study area) parts of the country (Wagesho et al. 2013). Similarly, Admassu et al. (2006) reported that the Kiremit (main rain season) rainfall had a significantly decreasing trend in Ethiopia. Tabari et al. (2015) studied the upper Blue Nile Basin and conclude that there were insignificant decreasing trends in annual precipitation at most of the stations. The possible reason for this change may be the local effect.

The rainfall trend reported by Bekele et al. (2016) was also the one that fit our study. The results indicated that Kiremit (main rain season) rainfall showed insignificant increasing trends at five stations out of 12 stations. A study by Kiros et al. (2016) in northern Ethiopia indicated a mix of nonsignificant positive trends in annual rainfall. Another study in the central highlands of Ethiopia by Alemayehu and Bewket (2017) reported that the annual and Kiremit (June–September) rainfall exhibited statistically insignificant increasing trends which aligned with our results in all agroecological zones except the Wurch zone, where the annual rainfall showed a significant increasing trend.

Additionally, Gedefaw et al. (2018) investigated the trend of annual and seasonal rainfall variability in the Amhara regional state, and the results showed that the annual rainfall was increasing at most of the stations. The Lake Tana Basin Analysis

of Rainfall Trends by Weldegerima et al. (2018) showed that, except for one station, all other stations revealed an increasing trend of annual and Kiremit rainfall.

The Annual and Main Rain Seasonal/Kiremit/Rainfall Variability Coefficient

Table 10.8 presents the annual and Kiremit/main rain season/rainfall variability. Thus, the Weyna Dega zone annual and Kiremit variability coefficients were analyzed as 12% and 13% respectively. The Dega agroecological zone was also 13% and 16% in annual and Kiremit, respectively. However, the Wurch zone rainfall variability coefficient indicates 15% and 17% of annual and Kiremit, respectively. The variability in rainfall in general is not a specific determinable condition within the agroecological zone gridded points across elevations, similar to the trend results. However, based on the mean results, the percentage of variability increased from the lower elevation to the upper elevation across the agroecological zones of the watershed.

The degree of variability of rainfall events was classified based on the (Hare, 2003) as less (CV < 20%), moderate (20 < CV < 30%) and high (CV > 30%) variability. The results revealed that the annual and Kiremit rainfall was less variable in all agroecological zones.

Previous studies aligned with our results are as follows: Birara reported 80% of the stations annual, and Kiremit rainfall variability was revealed to be less variable in the Tana basin of Ethiopia (Birara et al. 2018). Another report by Bekele et al. (2016) stated that 8 stations are less variable out of 12 stations in the annual and Kiremit rainfall in the Awash River basin. Similar results were found in our studies in the Lake Tana Basin by Weldegerima et al. (2018), who showed less variability of 9% of annual and 11% of Kiremit (Fig. 10.5).

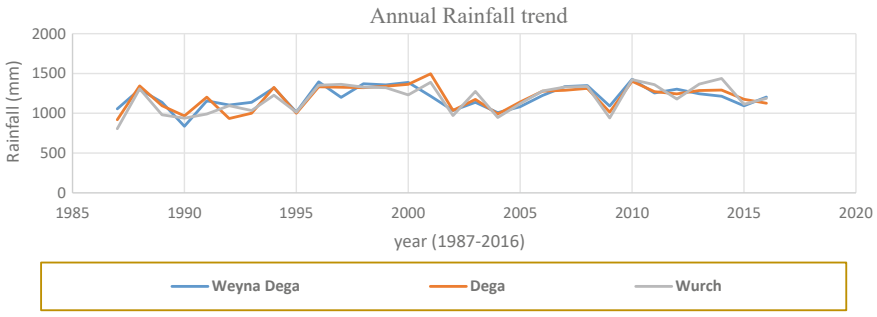

Fig. 10.5 The annual rainfall trendline in the agroecological zones

The Annual and Kiremit Temperature Trends in the AEZs

Regardless of the agroecological zones, the annual temperature trends in the watershed result in Table 10.7 indicate a statistically significant increase in all temperature variables. In the whole period (1987–2016), the recorded increasing value of increment was 1.2 °C with 0.4 °C decadal rate and a 0.04 °C yearly rate of minimum and maximum temperatures, respectively. The mean temperature was recorded in 1.5 °C increments in the last 30 years with 0.5 °C decadal and 0.05 °C yearly rates of increment. However, the rate of increase differed in the agroecological zones.

Table 10.9 also indicates the annual temperature value in the agroecological zones, indicating statistically significant increasing trends in all temperature variables in the watershed agroecological zones.

Maximum Temperature

In the same period (1987–2016) of 30 years, both the annual and the Kiremit maximum temperature increment at all zones were also revealed to be similar at 0.3, 0.4 and 0.5 °C per decade, with 0.03, 0.04 and 0.05 °C yearly increasing rates in the Weyna Dega, Dega, and Wurch zones, respectively. The maximum temperature rate of increase in the zones indicates an increase in elevation.

Minimum Temperature

The annual minimum temperature result indicates that 0.8 °C at Weyna Dega and 0.3 °C at both Dega and Wurch zones increase per decade with 0.08 °C and 0.03 °C yearly increments, respectively. The Kiremit minimum temperature was also 0.07°c at Weyna Dega and 0.04 °C in the Wurch zone of yearly increments in the period of 1987–2016 with 0.08 °C and 0.03 °C rates per year. A higher value of increasing trends of the annual minimum temperature was recorded at Weyna Dega. The minimum values were recorded with a similar value of 0.3 °C per decade with 0.03 yearly rates in the Wurch zones. There is no sign of change in either increasing or decreasing trends in minimum temperature in the Dega zone with a higher p-value and '0%' slope.

Table 10.9 Annual and seasonal rainfall Coefficients of Variability (CV) in the AEZs

Determinants	Weyna Dega		Dega		Wurch	
	Annual	Kiremit	Annual	Kiremit	Annual	Kiremit
Mean	1200	1029	1200	1001	1188	983
Std	140	131	157	163	178	170
CV	0.12	0.13	0.13	0.16	0.15	0.17

Mean Temperature

The mean annual temperature rate of decadal increments is 0.6 °C at Weyna Dega and 0.4 °C at both Dega and Wurch zones, with rates of 0.06 and 0.04 °C per year, respectively. However, the Kiremit mean temperature trend was 0.6, 0.2 and 0.5 °C in a decade and 0.06, 0.02, and 0.05 °C per year increment in the 1987–2016 period (Table 10.10).

In our analysis, the increasing trend of the temperature variables aligned with other studies, such as (Asfaw et al. 2018; Mengistu et al., 2014; Jury and Funk 2013; Behailu 2018; IPCC 2018). Temperatures are increasing in Ethiopia (Azage et al. 2017). In the decadal bases from 2006 to 2015, the observed global mean temperature was 0.87 °C on average between 0.75 and 0.99 °C fluctuations, which is higher than the average of the 1850–1900 period (IPCC 2018).

Most specifically, Regassa et al. (2010) reported that the annual minimum temperature in Ethiopia increased by approximately 0.37 °C every decade and between 1960 and 2006, the mean annual temperature increased by 1.3 °C, at an average rate of 0.28 °C per decade between 1951 and 2006. Another finding investigated by Mengistu et al. (2014) indicated an increased annual average minimum temperature and average maximum temperature (0.8 and 1.4 °C per decade, respectively). These results are mostly close to our findings.

On the other hand, Kassie et al. (2014) reported that, the mean annual temperature significantly increased by 0.12–0.54 °C per decade during 1977–2007 in Ethiopia. The rate of temperature increments aligned with our findings; the Poudel and Shaw (2016) analysis of the climate variability studies in Nepal showed an increase in maximum and minimum temperatures of approximately 0.02–0.07 °C per year, respectively.

Other studies conducted by Jury and Funk (2013) stated that upward trends in air temperature of 0.0 °C per year were observed over Ethiopia's southwestern region in the period 1948–2006. The National Meteorological Agency (NMSA 2007)

Table 10.10 Annual and Kiremit temperature trends in the AEZs (0.05 significance level)

Season	Temp	Agroecological zones								
		Weyna Dega/Midland/			Dega/High land			Wurch/Upper High land		
		MK (Z)	p-value	Sen's slope: (δ)	MK (Z)	p-value	Sen's slope: (δ)	MK (Z)	p-value	Sen's slope: (δ)
Annual	Min	0.57	< 0.0001	0.08	0.37	0.00	0.03	0.37	0.003	0.03
	Max	0.34	0.008	0.03	0.44	0.00	0.04	0.52	< 0.0001	0.05
	Mean	0.60	< 0.0001	0.06	0.55	< 0.0001	0.04	0.61	< 0.0001	0.04
Kiremit	Min	0.55	< 0.0001	0.07	0.00	1.00	0.00	0.42	0.00	0.04
	Max	0.35	0.01	0.03	0.44	0.00	0.04	0.47	0.00	0.05
	Mean	0.60	< 0.0001	0.06	0.31	0.01	0.02	0.60	< 0.0001	0.05

where MK = (Z) = Mann Kendall test and Δ = Sen slope

also reported an increasing trend of 0.37 °C per decade in the annual minimum temperature from 1951 to 2005 in Ethiopia.

Birara et al. (2018) provided an increased result of annual maximum temperature of 1.08 °C from 1980 to 2015, with an average rate of 0.2 °C per decade, and the minimum temperature also increased by 0.29 °C per decade in the Tana basin region (Birara et al. 2018), in which our study area was located. The hotter maximum temperatures during Kiremit (June–September) (+0.4–0.6 °C/decade) were reported in the period of 1981–2014 in Ethiopia by Conway and Schipper (2011). It fits with the Weyna Dega zone of our analysis.

Following the temperature increments, the Intergovernmental Panel for Climate Change (IPCC) reported some related points; warming more than 3°C would have negative effects on crop productivity globally. However, there is a marked difference regionally with regard to the threshold level. For instance, the local mean temperature increases up to 1–3 °C the potential for crop productivity is likely to increase slightly at mid to high latitudes. In contrast, low latitudes will experience losses in crop productivity for even small local temperature increases of 1–2 °C (Parry et al. 2007).

Length of Growing Period of the Agroecological Zones

The annual minimum LGP results (Table 10.11) indicate 122 days at Weyna Dega and 92 days at Wurch zone. However, the Kiremit minimum LGP was recorded as 92 days in the Weyna Dega and Wurch zones and 122 days in the Dega zone. The annual maximum LGP at a zone also accounted for 214, 245, and 275 days at Weyna Dega, Dega, and Wurch zones, respectively. The Kiremit maximum LGP was also analyzed as 122 days in all agroecological zones. We learned from the Kiremit minimum and maximum recorded LGP result differences, as there may be effects on crop diversity in the decadal bases. As we confirmed from the contribution of LGP, Kiremit rainfall was the main rain and crop growing season. Thus, it had a great share of the annual recorded value, contributing 68.5% and above in the agroecological zones.

Spatial and Temporal LGP Conditions

Table 10.12 depicts the decadal values of LGP. The results also indicate that during the three decades in the period of 1987–2016, there were 150 days in the first period and 156 days in the second and third periods in the Weyna Dega zone. The Dega zone also accounted for 190, 165, and 180 days. However, the Wurch zones showed 168, 165, and 180 days of recorded LGP values. Based on the decadal data mean of 154, 178, and 171 days in the Weyna Dega, Dega, and Wurch zones, we found that there was no significant difference in LGP between agroecological zones.

Thus, based on the FAO 1989 classification system in the LGP, we could not define and categorize the agroecological zones differently within the watershed. Among the whole periods, the recent period (2007–2016) Weyna Dega and Wurch

Table 10.11 The trend and variability of LGP in the agroecological zones

Determinants	Weyna Dega LGP		Dega		Wurch	
	Annual	Kiremit	Annual	Kiremit	Annual	Kiremit
Min LGP	122	92	122	122	92	92
Max LGP	214	122	245	122	275	122
Mean LGP	**154**	**121**	**178**	**122**	**171**	**118**
Contribution (%)	100	78.6	100	68.5	100	69.0
Trend						
MK(Z)	0.09	-0.13	-0.07	(0) No trend	0.05	0.24
p-value	0.54	0.42	0.62		0.73	0.12
δ	0.00	0.00	0.00		0.00	0.00
Variability						
Std	24.9	5.5	36.0	(0) No variability	44.4	10.4
CV	0.16 (16%)	0.05 (5%)	0.20 (20%)		0.26 (26%)	0.09 (9%)
LGP > 50%	**153**		153		153	
LGP > 75%	**122**		153		122	

Table 10.12 The decadal LGP in the AEZs

Periods	Weyna Dega Zone		Dega Zone		Wurch Zone	
	Annual	Kiremit	Annual	Kiremit	Annual	Kiremit
1987–1996	150	122	190	122	168	123
1997–2006	156	122	165	122	165	122
2007–2016	156	119	180	122	180	119
Mean/1987–2016/	154	121	178	122	171	118

zones recorded the smallest number of Kiremit LGP compared to the Dega zone and the other periods. The Wurch zone Kiremit LGP also decreased from 123 to 122 and 119 days.

Trends and Coefficient of Variability of LGP in the AEZs

The annual trend of LGP in Table 10.10 indicates no trend with Z values of 0.09 and 0.05 at Weyna Dega and Wurch, respectively, at 5% significance level. The DZ also showed nonsignificant decreasing trends ($Z = -0.07$) at the same significance level. However, there was no distinct slope (magnitudes) in all zones. The Sen Slops estimator indicates zero means; there were no either increasing or decreasing signs in the zones. In the same table, the coefficient of variability result indicates 5% and

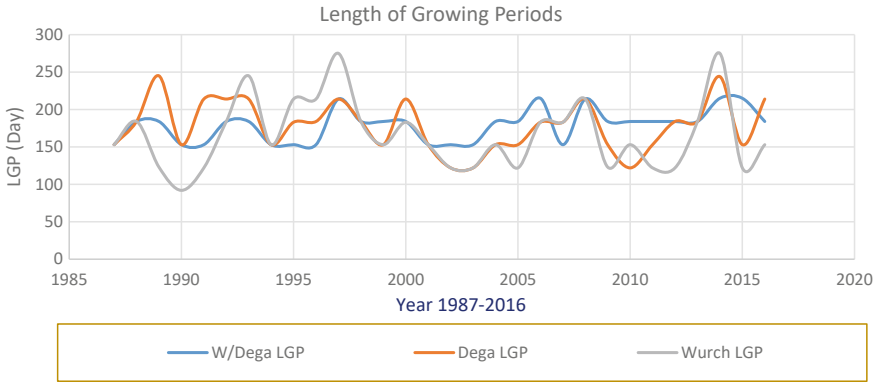

Fig. 10.6 The mean annual length of growing period trendlines in the AEZs

9% of the Kiremit LGP variability and 16%, 20%, and 26% of the annual LGP variabilities in the watershed agroecological zones.

Bekele and his friends investigated the trends in the length of growing periods in the Awash River basin, Ethiopia, and they reported that, except for the Koka station which had a significant increasing trend in the Kiremit LGP, other stations showed insignificant (Bekele et al. 2016) as the Weyna Dega and Wurch zones in our study results (Fig. 10.6).

The LGP coefficient of variability results in the Mieso, Melkassa, and Adami Tulu areas of Ethiopia were 44.5, 25.6, and 37.5%, respectively, as reported by Edao et al. (2018).

Decadal Crop Diversity Dynamics

Decadal Crop Diversity Dynamics in LGP Variability

As depicted in Table 10.13, out of the seven selected indigenous crops, all 7 at Weyna Dega, 6 (except Maize) at Dega and 2 (Niger Seed and Finger Millet) at Wurch zones were safely growing with their moisture requirement ranges. Based on the FAO (1989) crop-moisture availability ranges, the length of the growing period was a limiting factor at Dega for maize crops and all except Niger seed and finger millet crops in the Wurch zones. To support the occurrence of crops in these zones, LGPs must satisfy their moisture needs. Indeed, all crops that exist suitably in the Weyna Dega zone may grow in the Dega and Wurch zones in time. These zones satisfy the crop-moisture availability conditions required at the lower elevation (Weyna Dega) zone of the watershed. However, the length of moisture availability days is not met at these elevational ranges, as FAO specified.

Table 10.13 The decadal and crop-moisture suitability ranges in the AEZs

Crops types	Expected Crop-Moisture Requirement Ranges/Days/in zones mean elevation			Based on calculated decadal LGP, total crops suitably growing in the AEZs								
				Weyna Dega			Dega			Wurch		
	Weyna Dega (2000 m.a.s.l)	Dega (2500 m.a.s.l)	Wurch/ upper Dega/ (3000 m.a.s.l)	P1 (1987–1996)	P2 (1997–2006)	P3 (2007–2016)	P1 (1987–1996)	P2 (1997–2006)	P3 (2007–2016)	P1 (1987–1996)	P2 (1997–2006)	P3 (2007–2016)
S1												
Maize	140–255	245–360	> 285	S↕	S↕	S↕	NS↓	NS↓	NS↓	NS↓	NS↓	NS↓
Tef	95–230	145–280	180–315	S↕	S↕	S↕	**S↕**	**S↕**	**S↕**	NS↓	NS↓	NS↓
Barley	105–240	155–290	190–325	S↕	S↕	S↕	S↕	S↕	S↕	NS↓	NS↓	NS↓
Wheat	115–240	165–290	200–325	S↕	S↕	S↕	S↕	S↕	S↕	NS↓	NS↓	NS↓
Niger Seed	120–155	120–155	120–155	S↕	S↕	S↕	S↕	S↕	S↕	S↕	S↕	S↕
Linseed	130–240	160–270	180–290	S↕	S↕	S↕	S↕	S↕	S↕	NS↓	NS↓	NS↓
Finger Millet	90–120	160–280	NS	S↕	S↕	S↕	S↕	S↕	S↕	S↕	S↕	S↕
Total crops in AEZs				7	7	7	6	6	6	2	2	2

where P1 = period 1, P2 = period 2, P3 = period 3

The possible reason for this failure of LGP to satisfy crop needs in the elevational range in the Dega and Wurch zones may be the statistically significant increasing temperature effect on the insignificantly increasing rainfall during the main/Kiremit/rain season. In addition, the rainfall distribution is lower at the higher elevation/Wurch/zone. Abrha (2015) reported that the Kiremit rainfall (main rainy season) in highlands experienced a nonsignificant change.

However, since the LGP results are calculated from the interaction between temperature variables and rainfall, the higher temperature lagged the number of moisture availability days through higher evapotranspiration. The significantly increasing temperature shortened the expected moisture availability days at the higher elevations and in time (decadal periods from earlier to the recent). Thus, the effects shifted the crop suitability range from the first suitability range (S1) to the second suitability range (S2) of the area. Finally, the crop may shift from its original place to higher elevations.

All previous literature concerned with climate, agroecology, and crop distribution agreed, as recent global warming may have a positive effect, which makes it comfortable for cultivation and for the existence of new crops in highland areas and negatively in lower elevation areas. In turn, in their continuous effects, have resulted in species extinctions (Rinawati et al. 2013; Pearson 2014). Temperature may support crop-temperature requirements as a growing factor that affects the existence of crops in a specific area and helps to move to higher elevations. However, the inconsistent and erratic nature of the rainfall in the study area agroecological zones may not support the longtime existence of crops in the area across their shifts.

However, similar to the results reported by Abrha (2015), a small amount and insignificant increment of Kiremit rainfall were recorded in the highland area/Wurch zone/of our study area/watershed. This case may exacerbate the failure of moisture availability in the zones. Thus, the existence of crops in the highland/temperate/areas may no longer stay in the middle and lower elevation areas. Rainfall has an insignificant increasing trend with the linear increase in all the temperature variables unless the moisture availability condition of the area should be improved or actions should be incorporated.

where **NS↑** = Not suitable due to higher moisture availability (above crop needs), in this case intercropping or growing more than one crop may be possible (FAO 1989). NS↓ = Not suitable due to/the shortage/lower moisture availability for crop growth. S↕ = In a suitable range and NS = out of the range (crop has not existed at all).

Crop-Temperature-Related Diversity Dynamics

The number of suitably growing crops in the agroecological zones differed over time. The difference was not only between the agroecological zones but also within the agroecological zone parts. Crop diversity dynamics are the interplay changes in the number of crops due to the varied temperature variables in an agroecological zone in decadal periods. Crop migration is the movement of crops from one AEZ to another in decadal periods.

The effects of mean temperature were not the sole variable that changed the crop suitability conditions. However, the maximum and minimum temperatures may exert their own effects on the crop diversity situation in agroecological zones. The maximum temperature (daytime temperature) accelerates crop maturity, resulting in reduced grain filling, while higher minimum/nighttime/temperatures increase respiration losses (Niang et al. 2017). Following the effects, farmers in different AEZs employ different crop species selections that fit that AEZ (Seo, 2011).

Crop-Temperature Diversity Dynamics in the Weyna Dega Zone

In the mean temperature at Weyna Dega zone parts, all selected indigenous crops were suitably grown in all decadal periods from 1987 to 2016. This means that the mean temperature had no visible spatial and temporal negative effects on crop diversity/changes in the number of selected crops to create dynamics within the zone. (Table 27.13). Thus, fortunately, we used this zone as an initial crop saturated zone. However, the minimum and maximum temperature requirements of the crop in each part and period do not equally meet the crop requirements.

In a decade, the maximum temperature affects the suitability of most crops ranging from first suitability to second suitability ranges and from the first to the recent period. In the first/1987–1996/period, except for the Tef and Niger sees crops, the zone had 5 suitably grown crops. However, in the second (1997–2006) and third (2007–2016) periods, only 2 crops (maize and Finger Millet) were supported to suitably grow in the zone. Thus, the maximum temperature at the lower elevation caused most crop diversity dynamics to increase the above crop suitability ranges in decadal periods and reduced the number of crops from 5 to 2 in the whole 1987–2016 period in a zone. Tef and Niger seed crops are more affected crops in Weyna Dega than other crops in both maximum and minimum temperature variables. The maximum temperature increment plays an important role in restricting the Tef existence under lower elevations and shifting to higher elevations under warming conditions. The suitability conditions of the area for these selected crops also decreased in recent years.

At minimum temperatures, the first and second periods were not satisfactory for the maize and Niger seed crops in the Weyna Dega Zone. It was suitable for barley crops only in this zone. Opposed to the maximum temperature, the suitability condition of the area in minimum temperature was improved from time to time; for example, the suitability condition for wheat crops was shifted from S3 to S2 and S4 to S3 for Tef and linseed crops (Table 10.14). Crops existed and grew in a zone due to maximum temperature supports as the mean temperature value, but they may suffer from grain filling losses. Since the minimum temperature did not support the existence of crops, they were simply considered crops growing for mere vegetative parts.

Table 10.14 The spatial and temporal crop-temperature suitability analysis in Weyna Dega

Crop type	Maximum Temperature			Mean 1987–2016	Minimum Temperature			Mean 1987–2016	Mean Temperature			Mean 1987–2016
	Decadal period				Decadal period				Decadal periods			
	1987–1996	1997–2006	2007–2016		1987–1996	1997–2006	2007–2016		1987–1996	1997–2006	2007–2016	
Maize	S1	S1	S1	S1	NS	NS	S4	NS	**S**	**S**	**S**	**S**
Tef	S4	S4	S4	S4	S4	S4	S3	S4	**S**	**S**	**S**	**S**
Barley	S1	S2	S2	S2	S1	S1	S1	S1	**S**	**S**	**S**	**S**
Wheat	S1	S2	S2	S2	S3	S3	S2	S3	**S**	**S**	**S**	**S**
Nigger Seed	S2	S3	S3	S3	NS	NS	NS	NS	**S**	**S**	**S**	**S**
Linseed	S1	S2	S2	S2	S4	S4	S3	S4	**S**	**S**	**S**	**S**
Finger Millet	S1	S1	S1	S1	NS	NS	NS	NS	**S**	**S**	**S**	**S**
Number of crops	S1 = 5 S2 = 1 S4 = 1	S1 = 2 S2 = 3 S3 = 1 S4 = 1	S1 = 2 S2 = 3 S3 = 1 S4 = 1	S1 = 2 S2 = 3 S3 = 1 S4 = 1	S1 = 1 S3 = 1 S4 = 2 NS = 3	S1 = 1 S3 = 1 S4 = 2 NS = 3	S1 = 1 S2 = 1 S3 = 2 S4 = 1 NS = 2	S1 = 1 S3 = 1 S4 = 2 NS = 3	S = 7	S = 7	S = 7	S = 7

Crop-Temperature Diversity Dynamics in the Dega Zone

In mean temperature at the Dega zone, due to the significantly increasing mean Kiremit temperature by 0.2 °C per decade, the suitability condition in the three periods indicates that three (Tef, Barley, and Wheat) out of seven crops are growing in a suitable condition in all periods (1987–2016). However, the area for other crops was not suitable. However, the number of crops in a decadal base differed as 3 crops in the first and second periods as well as 4 crops in the recent period by one crop increasing (Linseed). This implies that the recent mean temperature increase supports linseed crop growth and increase the crop diversity in the DZ.

The decadal crop-maximum temperature associations in Dega zone implied that in the first period, seven crops were grown under the best suitability conditions. However, during the second and third periods, the area suitability condition for the Tef crop was shifted to the second suitability range. The recent significantly increased maximum temperature in the Dega zone also exerted a negative effect on the Tef crop in the Weyna Dega zone. However, the level of effects on the selected crops differed in the two zones. For example, in the Weyna Dega zone, the maximum temperature increase affected the suitability conditions of 2 crops (Tef and Niger Seed) in the first period and five crops (except the Maize and Finger Millet) in the second and third/recent/decadal periods. In the Dega zone, the Tef crop was affected starting from the second and recent period suitability. Thus, toward the higher elevation, the maximum temperature increment effect was reduced and made comforts for crops shift to the high land area (Table 10.14).

In minimum temperature, because of its insignificant increasing trends, there are no crops that exist in a suitable/S1/condition from the beginning to the recent periods. Barley is growing in a second (S2) suitability condition followed by Wheat and Linseed crops of their not suitable (NS) to the last suitability (S4) condition shifts in a recent time. With the inverse relationship, minimum temperature is the most limiting factor under crop suitability conditions for the growing of crops in the Dega zone compared to maximum temperature, unlike in the Weyna Dega zone (Table 10.15).

Crop Diversity Dynamics in the Wurch Zone

As we can see in Table 10.16, the statistically significant increasing mean Kiremit temperature in 0.5 °C per decade, the Wurch zone affords the existence of three (Tef, Barley, and Wheat) crops in a suitable condition as the Dega zone from the total mean periods of 1987–2016. However, the existence was not permanent in the decadal periods as in the Weyna Dega zone. This means that the Weyna Dega zone period has a similar number of crops to the area mean temperature. In the Wurch zone, the suitably growing number of crops increased in time from the first period of 2 crops (Barley and wheat) to 3 crops (Barley, Wheat and Tef) in the second and third/recent periods.

Table 10.15 Decadal crop-temperature suitability analysis in parts of the Dega Zone

Crop types	T_{Max}			Mean 1987–2016	T_{min}			Mean1987–2016	T_{mean}			Mean
	1987–1996	1997–2006	2007–2016		1987–1996	1997–2006	2007–2016		1987–1996	1997–2006	2007–2016	1987–2016
Maize	S1	S1	S1	S1	NS	NS	NS	NS	NS	NS	NS	NS
Tef	S1	S2	S2	S2	NS	NS	NS	NS	S	S	S	S
Barley	S1	S1	S1	S1	S2	S2	S2	S2	S	S	S	S
Wheat	S1	S1	S1	S1	NS	NS	S4	S4	S	S	S	S
Nigger Seed	S1	S1	S1	S1	NS	NS	NS	NS	NS	NS	NS	NS
Linseed	S1	S1	S1	S1	NS	NS	S4	S4	NS	NS	S	NS
Finger millet	S1	S1	S1	S2	NS	NS	NS	NS	NS	NS	NS	NS
Number of crops	S1 = 7	S1 = 6 S2 = 1	S1 = 6 S2 = 1	S1 = 5 S2 = 2	S2 = 1	S2 = 1	S2 = 1	S2 = 1	S = 3	S = 3	S = 4	S = 3

Table 10.16 Decadal Crop-Temperature suitability analysis at the Wurch Zone

Wurch AEZ	Maximum Temperature			Max-Mean 1987–2016	Minimum Temperature			Min-Mean	Mean Temperature			Mean-Mean 1987–2016
	1987–1996	1997–2006	2007–2016		1987–1996	1997–2006	2007–2016	1987–2016	1987–1996	1997–2006	2007–2016	
Maize	S1	S1	S1	S1	NS	NS	NS	NS	NS	NS	NS	NS
Tef	S1	S1	S2	S1	NS	NS	NS	NS	NS	S	S	S
Barley	S1	S1	S1	S1	S3	S2	S2	S2	S	S	S	S
Wheat	S1	S1	S1	S1	NS	NS	NS	NS	S	S	S	S
Nigger Seed	S1	S1	S1	S1	NS	NS	NS	NS	NS	NS	NS	NS
Linseed	S1	S1	S1	S1	NS	NS	NS	NS	NS	NS	NS	NS
Finger Millet	S1	S1	S1	S1	NS	NS	NS	NS	NS	NS	NS	NS
Number of crops	S1 = 7	S1 = 7	S1 = 6 S2 = 1	S1 = 7	S3 = 1 NS = 6	S2 = 1 NS = 6	S2 = 1 NS = 6	S2 = 1 NS = 6	S = 2 NS = 5	S = 3 NS = 4	S = 3 NS = 4	S = 3 NS = 4

The maximum temperature had positive responses for all crops in the whole period (1987–2016) in the zone. It has been noted that higher temperature makes favorable conditions for the existence and expansion of maize and wheat crops in wet mountain areas (Hussain and Bangash 2017). Additionally, the increase in maximum temperature in such areas may have some positive influences on the occurrence of midland crops by limiting extreme cold conditions and shortening their maturity days in the region. However, some short-range crops may also be affected by the increased maximum temperature even in higher elevation areas. For example, in the recent period (2007–2016) temperature negatively affected the Tef crop by shifting the area suitability conditions from S1 to S2.

Except for the barley suitability condition shifting from suitable three/S3/in the first period to a second suitable condition/S2/in the second and third periods, the existence of all other crops is not supported by minimum temperature. In general, minimum temperature was a limiting factor for almost all crops in the Wurch and Dega zones as well as for most Weyna Dega crops. Previous research reports in line with our analysis proved that any changes in the recommended crop-minimum temperature requirement below the threshold level in wet mountain areas may adversely affect the growth of crops (Hussain and Bangash 2017).

The effects of climate variability on crop growth and distribution across agroecological zones are not uniform. The results show that the effect of average temperature is positive on all selected major indigenous crops across the three agroecological zones. This is in line with Hussain and Bangash (2017) reports.

As concluded by Evangelista et al (2013), the change in temperature in Ethiopia directly affects the distribution of the Tef crop (Evangelista et al. 2013). On the other hand, in the elevational bases, Yumbya and colleagues discussed that the Tef crop had quickly shifted from the lower elevation to higher elevation (Yumbya et al. 2014). Following its short range of climate suitability conditions in our analysis, Tef is highly vulnerable to climate variability, especially due to the significantly increasing state of temperature. Previous studies have additionally discussed that the suitable areas at lower elevations are affected early and will be concentrated between 1200 and 2500 m.a.s.l. as predicted. Additionally, they provided detailed information on the loss of 24% of the climatic suitable area of land for the Tef crop in 2050. It will be concentrated in the area where the temperature is between 27 °C and a low of 15 °C in 2050. That is why in our analysis, the Tef crop is shifting and moving fast to the higher elevation (Dega and Wurch zones) than other selected cops.

Other studies in the growing season of crop-temperature relationship analysis by Hussain and Bangash (2017) reported that any changes in temperature beyond and below the optimum level make it disastrous for crop growth. In our analysis, we proved that the lower state of minimum temperature related to crops in the higher elevation was the limiting factor for the occurrences of all selected indigenous crops except Tef, Barley, and Wheat. The significant increase in minimum temperature supported the growth of all crops by staying below their requirements, lagging the maximum temperature effects on crops and supporting them by mean temperature. However, both the maximum and minimum temperatures contributed their own positive and negative effects on selected crops in the whole period on an area.

On the other hand, they discussed that increases in maximum temperature during the growing period did not negatively affect wheat and maize crop growth. Although our results indicate that the maximum temperature at lower elevations negatively affects most crops from earlier to more recent times, they also support crop growth at higher elevations.

Furthermore, the average temperature increases were positively related to wheat and maize crop production. In our case, production is the function of diversity. A reduction in yield is a reduction in diversity due to the low producer choices in their farmlands. As the average temperature increases, the yield of these two crops also increases (Hussain and Bangash 2017). The mean temperature was the reason for the dominant growth of all selected crops at the lower elevation (Weyna Dega) to the higher elevation (Dega and Wurch) zones accordingly.

Maize dominantly grows in the lower part of our study area. Barley is dominant and grows in all agroecological zones and considered a wide range crop. Tef was the fastest moving crop across the watershed agroecological zones toward higher elevations and suffered in the lower part of the study area.

Summary

The paper aims to analyze the quantitative data at the watershed and, most specifically, at the agroecological zone levels. The trend of climate variables in Gumara watersheds' agroecological zones was evaluated by Mann–Kendal and Sen Slope's estimator. The coefficient of variability (CV) was used to analyze climate variables. In addition, the decadal climate trend was analyzed. Based on the FAO crop-climate specification, the crop-climate requirement and the decadal crop diversity dynamics were analyzed.

The historical annual rainfall data trend result indicates insignificantly increasing trends, whereas the length of the growing period in the watershed also showed nonsignificant trend with no slope magnitude. The annual and Kiremit rainfall coefficients of variability between the agroecological zones increased in variability with elevation (i.e., Weyna Dega to Dega to Wurch zones). However, the result is in a similar category of less/slightly variable. The temperature variable trends also show statistically significant increasing trends. However, based on the gridded point data analysis, there was a result variation of these climate variables between agroecological zones and even within the agroecological zone parts itself across the watershed. The trend of rainfall in the gridded points of the agroecological zones of the watershed could not be in a concludable manner in terms of place and time. It fluctuates up and down within the study period. As with the temperature results, the patterns and distribution of rainfall are not governed by elevation. The calculated LGP has no significant difference in elevation within the watershed, so that it is impossible to categorize the watershed into agroecological zones in terms of moisture availability

within the watershed. Thus, based on the moisture availability, we could summarize the watershed into one moisture availability condition called the cool and humid zone.

Although the LGP decadal variability does not affect crop dynamics in the analysis period, temperature does in the Weyna Dega zone in the second and third periods. The effect of temperature lagged behind the upper zones LGP in the watershed and helped to accept and grow some locally new indigenous crops from the lower zones. The Weyna Dega zone mean temperature supports growth of all selected indigenous crops in all periods. However, due to the significantly increased maximum temperature, some crops suffered from earlier to recent periods. The maximum temperature increment at higher elevations permits crops to exist in suitable conditions, whereas the minimum temperature causes oppressed crops to suffer below their needs. Similar reports were reported by Hussain and Bangash (2017), as the maximum temperature increment at higher elevations and the state of minimum temperature at lower elevations support the existence of crops accordingly. Indeed, when we move toward the elevation within the watershed zones, we find that the number of selected crops existed within their better suitability ranges (S1) in maximum temperature. Almost all selected indigenous crops in the Weyna Dega zone received their optimum rate of mean temperature requirement. These crops may start to lose their best suitability condition (S1/and start to grow in other suitability condition (S2, S3…) in the near future in the mean temperature, if all temperature variables increment will be continued as recent rate. Further away, Tef suffered more from the maximum temperature in the Weyna Dega zone, followed by the Nigger Seed crop. On the other hand, the minimum temperature in this zone was the limiting factor for the distribution and growth of some crops increasing to higher elevations. However, inversely to the maximum temperature, the recent decade temperature made better opportunities for crops growing in the zone in terms of mean temperature.

In the Dega zone, the mean temperature affects the dynamics of the crops in a decadal period in all parts. The number of crops growing in the zone and its parts increased from the earlier decade to the second and third/recent decades. For example, the lower part of the Dega zone accepts three crops/Tef, Barley, and Wheat/from the upper part of Weyna Dega in the first decade and the area increased its number of growing crops to five by making comfort for Maize and Linseed crops. Likewise, in the Weyna Dega zone, the recent maximum temperature has negatively affected some of the aforementioned crops in the lower part of the Dega zone.

References

Abrha MG (2015) Local climate trends and farmers' perceptions in Southern Tigray, Northern Ethiopia. Int J Environ

Admassu S, Seid IAH (2006) Analysis of rainfall trend in Ethiopia. Ethiopian J Sci Technol 3:15–30

Agbossou E, Toukon C, Akponikpè P, Afouda A (2012) Climate variability and implications for Maize production in Benin: a stochastic rainfall analysis. Afr Crop Sci J 20:493–503

Alemayehu A, Bewket W (2017) Local spatiotemporal variability and trends in rainfall and temperature in the central highlands of Ethiopia. Phys Geogr 99**:**85–101
Alemayehu AAB, Woldeamlak (2016) Local climate variability and crop production in the central highlands of Ethiopia. Environ Dev 19:36–48
Araya A, Stroosnijder LJA, Meteorology F (2011) Assessing drought risk and irrigation need in Northern Ethiopia. Agri Forest Meteorol 151:425–436
Asai K (2017) Questionnaire survey on farming adaptation for climate variability in Serang Municipality, Indonesia. Memoirs Faculty Eng 67**:**99–106
Asfaw A, Simane B, Hassen A, Bantider AJW, Extremes C (2018) Variability and time series trend analysis of rainfall and temperature in Northcentral Ethiopia: a case study in Woleka Sub-Basin. Weather Climate Extremes 19:29–41
Azage M, Kumie A, Worku A, Bagtzoglou AC, Anagnostou EJPO (2017) Effect of climatic variability on childhood diarrhea and its high risk periods in Northwestern Parts of Ethiopia. PloS one 12:e0186933
Bayissa Y, Tadesse T, Demisse G, Shiferaw AJRS (2017) Evaluation of satellite-based rainfall estimates and application to monitor meteorological drought for the Upper Blue Nile Basin, Ethiopia. Remote Sensing 9:669
Behailu G (2018) Climate change and variability: farmers' perceptions in Sekota Woreda, Northeastern Ethiopia. Addis Ababa University
Bekele D, Alamirew T, Kebede A, Zeleke G, Melese AM (2016) Analysis of rainfall trend and variability for agricultural water management in Awash River Basin, Ethiopia. J Water Climate Change 8**:**127–141
Benin S, Ehui S, Pender J (2003) Policies for livestock development in the Ethiopian highlands. Environ Dev Sustain 5**:**491–510
Birara H, Pandey R, Mishra SK (2018) Trend and variability analysis of rainfall and temperature in the Tana basin region, Ethiopia. J Water Climate Change 9**:**555–569
Chakilu G, Moges MJHCR (2017) Assessing the land use/cover dynamics and its impact on the low flow of Gumara Watershed, Upper Blue Nile Basin, Ethiopia. Hydrol Curr Res 7:2
Conway D, Schipper, ELF (2011) Adaptation to climate change in Africa: challenges and opportunities identified from Ethiopia. Global Environ Change 21**:**227–237
Degefu MA, Bewket WJREC (2014) Variability and trends in rainfall amount and extreme event indices in the Omo-Ghibe River Basin, Ethiopia. Reg Environ Change 14:799–810
di Falco S, Bezabih M, Yesuf MJEE (2010) Seeds for livelihood: crop biodiversity and food production in Ethiopia. Ecol Econ 69:1695–1702
Edao A, Kibert K, Mamo GJACST (2018) Analysis of start, end and length of the growing season and number of rainy days in Semi-Arid Central Refit Valley of Oromia State, Ethiopia. Crop Sci Technol 6:2
Esayas B, Simane B, Teferi E, Ongoma V, Tefera N (2018) Trends in extreme climate events over three agroecological zones of southern Ethiopia. Adv Meteorol 2018:1–17
Evangelista P, Young N, Burnett JJCC (2013) How will climate change spatially affect agriculture production in Ethiopia? Case Stud Important Cereal Crops 119:855–873
FAO (1989) Reconnaissance physical land evaluation in Ethiopia. The Peoples of Democratic Republic of Ethiopia Ministry of Agriculture, Land use Planning and Regulatory Department, Addis Ababa Ethiopia. Food & Agriculture Organization of the UN (FAO)
FAO (1996) Agro-ecological zoning: guidelines. Agriculture Organization of the United Nations. Soil Resources Conservation Service
Food & Agriculture Org. FAO (1998) Crop evapotranspiration: guidelines for computing crop water requirements. FAO irrigation and drainage paper 56. Rome, Italy
Ganaie SA, Bhat MS, Kuchay NA, Parry J (2014) Delineation of micro agro-climatic zones of Jammu and Kashmir. Int J Agri Stat Sci 10:219–225
Gebrechorkos S, Hülsmann S, Bernhofer C (2018) Evaluation of multiple climate data sources for managing environmental resources in East Africa. Hydrol Earth Syst Sci 22:4547–4564

Gebremicael TG, Mohamed YA, van der Zaag P, Berhe A, Haile GG, Hagos EY, Hagos MK (2017) Comparison and validation of eight satellite rainfall products over the rugged topography of Tekeze-Atbara Basin at different spatial and temporal scales. Hydrol Earth Syst Sci Discussions 2017:1–31

Gedefaw M, Yan D, Wang H, Qin T, Girma A, Abiyu A, Batsuren DJA (2018) Innovative trend analysis of annual and seasonal rainfall variability in Amhara regional state, Ethiopia. Atmosphere 9:326

Gorfu D, Ahmed E (2012) Crops and agro-ecological zones of Ethiopia. Ethiopian Inst Agri Res

Hare W (2003) Assessment of knowledge on impacts of climate change-contribution to the specification of art. 2 of the UNFCCC: Impacts on ecosystems, food production, water and socio-economic systems

Hurni H (1998) Agroecological belts of Ethiopia. Explanatory notes on three maps, 1

Hussain A, Bangash RAJP (2017) Impact of climate change on crops' productivity across selected agro-ecological zones in Pakistan. Pakistan Dev Rev 56:163–187

IPCC (1990) Scientific assessment of climate change: the policymakers' summary of the report of Working Group I to the Intergovernmental Panel on Climate Change, World Meteorological Organization/United Nations Environment Programme

IPCC (2018) Global warming of 1.5° C: an IPCC special report on the impacts of global warming of 1.5° C above pre-industrial levels and related global greenhouse gas emission pathways. In: the context of strengthening the global response to the threat of climate change, sustainable development, and efforts to eradicate poverty, Intergovernmental Panel on Climate Change

Jury MR, Funk CJIJOC (2013) Climatic trends over Ethiopia: regional signals and drivers. Int J Climatol 33:1924–1935

Kassie B, Rötter R, Hengsdijk H, Asseng S, van Ittersum M, Kahiluoto H, van Keulen HJTJOAS (2014) Climate variability and change in the Central Rift Valley of Ethiopia: challenges for rainfed crop production. J Agri Sci 152:58–74

Kiros G, Shetty A, Nandagiri LJAJOG (2016) Analysis of variability and trends in rainfall over Northern Ethiopia. Arab J Geosci 9:451

Koudahe K, Koffi D, Kayode J, Awokola S, Adebola A (2018) Impact of Climate variability on crop yields in Southern Togo. Environ Pollut Clim Chang 2:1–9

Lane A, Jarvis A (2007) Changes in climate will modify the geography of crop suitability: agricultural biodiversity can help with adaptation

Longobardi A, Villani PJIJOC (2010) Trend analysis of annual and seasonal rainfall time series in the Mediterranean Area. Int J Climatol 30:1538–1546

Melke A (2015) Impact of climate change on hydrological responses of Gumara catchment, in the Lake Tana Basin-Upper Blue Nile Basin of Ethiopia. Addis Ababa University

Mengistu D, Bewket W, Lal RJIJOC (2014) Recent spatiotemporal temperature and rainfall variability and trends over the Upper Blue Nile River Basin, Ethiopai. Int J Climatol 34:2278–2292

Ngongondo C, Xu C-Y, Gottschalk L, Alemaw BJT, Climatology A (2011) Evaluation of spatial and temporal characteristics of rainfall in Malawi: a case of data Scarce Region. Theor Appl Climatol 106:79–93

Niang I, Ruppel O, Abdrabo M, Essel A, Lennard C, Padgham J, Urquhart P (2017) Climate change 2014: impacts, adaptation, and vulnerability. Part B: regional aspects

NMSA (2007) Climate change national adaptation programme of action (Napa) of Ethiopia. National Meteorological Services Agency, Federal Democratic Republic of Ethiopia, Addis Ababa

Pachauri RK, Allen MR, Barros VR, Broome J, Cramer W, Christ R, Church JA, Clarke L, Dahe Q, Dasgupta P (2014) Climate change 2014: synthesis report. Contribution of Working Groups I, II and III to the fifth assessment report of the Intergovernmental Panel on Climate Change, IPCC

Parry M, Parry ML, Canziani O, Palutikof J, van der Linden P, Hanson C (2007) Climate change 2007-impacts, adaptation and vulnerability: working group II contribution to the fourth assessment report of the IPCC. Cambridge University Press, Cambridge

Partal T, Kahya EJHPAIJ (2006) Trend analysis in Turkish precipitation data. Hydrol Process Int J 20:2011–2026

Pearson R (2014) Climate change, biodiversity and extinction risk. Academy of Science of South Africa

Pecl GT, Araújo MB, Bell JD, Blanchard J, Bonebrake TC, Chen I-C, Clark TD, Colwell RK, Danielsen F, Evengård BJS (2017) Biodiversity redistribution under climate change: Impacts on ecosystems and human well-being, 355**,** eaai9214

Poudel S, Shaw RJC (2016) The relationships between climate variability and crop yield in a mountainous environment: a case study in Lamjung District, Nepal. Climate 4:13

Regassa S, Givey C, Castillo G (2010) The rain doesn't come on time anymore: poverty, vulnerability, and climate variability in Ethiopia 6:90–134

Rinawati F, Stein K, Lindner A (2013) Climate change impacts on biodiversity—the setting of a lingering global crisis. Diversity 5:114–123

Sadoff C (2019) Managing water resources to maximize sustainable growth: a World Bank water resources assistance strategy for Ethiopia

Salmi T, Määttä A, Anttila P, Ruoho-Airola T, Amnell T (2002) Detecting trends of annual values of atmospheric pollutants by the Mann-Kendall test and Sen's slope estimates MAKESENS–The excel template application

Seleshi Y, Zanke U (2004) Recent changes in rainfall and rainy days in Ethiopia. J Climatol J R Meteorol Soc 24:973–983

Seo SN (2011) A geographically scaled analysis of adaptation to climate change with spatial models using agricultural systems in Africa. J Agri Sci 149:437–449

Surendran U, Sushanth C, Mammen G, Joseph EJAP (2015) Modelling the crop water requirement using FAO-CROPWAT and assessment of water resources for sustainable water resource management: a case study in Palakkad district of humid tropical Kerala, India. Aquatic Proc 4:1211–1219

Swiderska H, Swiderska K (2008) Biodiversity, climate change and poverty: exploring the links. An International Institute for Environment and Development (IIED) Briefing

Tabari H, Taye MT, Willems PJSER (2015) Statistical assessment of precipitation trends in the Upper Blue Nile River Basin. Stochastic Environ Res Risk Assess 29:1751–1761

Taye M, Zewdu F, Ayalew D (2013) Characterizing the climate system of Western Amhara, Ethiopia: a GIS approach. Am J Res Commun 1**:**319–355

UNDP (2011) Framework for UNDP Ethiopia's climate change, environment and disaster risk management Portfolio, Ethiopia

Wagesho N, Goel N, Jain MJHSJ (2013) Temporal and spatial variability of annual and seasonal rainfall over Ethiopia. Hydrol Sci J 58:354–373

Weldegerima TM, Zeleke TT, Birhanu BS, Zaitchik BF, Fetene ZA (2018_ Analysis of rainfall trends and its relationship with SST signals in the Lake Tana Basin, Ethiopia. Adv Meteorol 2018:1–10

Woldeamlak B (2007) Rainfall variability and agricultural vulnerability in the Amhara region, Ethiopia. Ethiopian J Dev Res 29**:**1–34

Woldeamlak B (2009) Rainfall variability and crop production in Ethiopia: case study in the Amhara region. In: Proceedings of the 16th international conference of Ethiopian Studies. Norwegian University of Science and Technology Trondheim, Norway, pp 823–836

Wubie MA, Assen M, Nicolau MDJESR (2016) Patterns, causes and consequences of land use/cover dynamics in the Gumara watershed of lake Tana basin Northwestern Ethiopia. Environ Syst Res 5:8

Yue S, Pilon P, Cavadias GJJOH (2002) Power of the Mann-Kendall and Spearman's Rho tests for detecting monotonic trends in hydrological series. J Hydrol 259:254–271

Yumbya J, de Vaate MB, Kiambi D, Kebebew F, Rao KJACSJ (2014) Geographic information systems for assessment of climate change effects on Teff in Ethiopia. Afr Crop Sci J 22:847–858

Chapter 11
Wind as a Promising Alternative Energy Source in Ethiopia: Feasibility Analysis for Wind Farm Establishment and Investigation of Wind Energy Potential in the Upper Blue Nile River Basin

Yewubdar Berhanu Alemu and Eyale Bayable Tegegne

Abstract Ethiopia has an abundance of renewable energy resources, such as hydro, wind, geothermal, solar, and biomass. Access to sustainable energy services, on the other hand, is a major challenge for its people. The country is one of the 20 most impoverished countries in terms of clean energy access, with approximately 46% of the population without electricity. Ethiopia's government is focused on utilizing the country's renewable energy resources. Hydropower is the primary renewable energy source that has been identified for this purpose. The Upper Blue Nile Basin (UBNB) is one of Ethiopia's 12 river basins with massive hydropower potential. It accounts for a significant portion of the country's current electricity consumption. As hydropower is rainfall dependent, its long-term viability, under climate change, is highly uncertain in the future. Hence, there is a need to focus on diversifying renewable energy sources in addition to hydropower in the UBNB. The goal of this study is to investigate the suitability of wind farms in the UBNB using a multicriteria decision method as well as geographic information system and to determine the energy potential of suitable areas. Wind speed, slope, land use/land cover, distances from grids, roads, urban and protected areas were considered when determining suitable wind farms. Of the total area of the basin, only 1,498.69 km^2 (approximately 1% of the basin) was found to be highly suitable. Wind speed data from ten automatic weather station (AWS) sites at 15-min intervals were obtained from the National Meteorology Institute of Ethiopia (NMIE) for the purpose of estimating wind power potential over a four-year period (2017–2020). After performing vigorous quality control checks for internal consistency and technical wind sensor problems, the AWS

Y. B. Alemu
Space Science and Geospatial Institute (SSGI), Addis Ababa, Ethiopia

Y. B. Alemu · E. B. Tegegne (✉)
College of Natural and Computational Sciences, Center for Environmental Science, Addis Ababa University, Addis Ababa, Ethiopia
e-mail: eyale.bayable@aau.edu.et

A. M. Melesse et al. (eds.), *Land and Water Degradation in Ethiopia*, Springer Geography, https://doi.org/10.1007/978-3-031-60251-1_11

wind speed data were analyzed using Microsoft Excel and MATLAB software. The highest wind power density was recorded at Wogeltena and Gatira, with wind power densities of 227.56 and 216.50 W/m^2, respectively, at a turbine height of 50 m. There is a noticeable seasonal difference in wind power density production. Power densities were higher during the dry and short rainy seasons than during the wet season. As a result, it is reasonable to consider wind as a viable supplement to hydropower in the UBNB. The most promising sites are in the northeastern parts of the study area. As a result, these areas may be considered viable for grid-connected and stand-alone wind energy applications. However, most of the wind speed data in this study had short durations and were insufficient for estimating wind energy potential at large scales. Furthermore, the meteorological stations were primarily installed for weather forecasting purposes, and their location might not be optimal for wind energy purposes. Therefore, future research should concentrate on identifying optimal wind energy-producing areas in the region. Furthermore, different wind speed measuring tools, such as taller wind masts than the AWS wind speeds, are recommended for further wind energy potential investigations.

Keywords Wind farm · GIS · Suitability analysis · Weibull parameters · Wind power potential · Upper Blue Nile

Introduction

Energy plays an important role in a country's economic and social development. The world obtains its energy from a variety of renewable and nonrenewable sources. Most of the world's energy supply is currently derived from fossil fuels, which have a significant impact on the environment and human health due to greenhouse gas emissions (Uyan 2013). Furthermore, following the mid-1970s oil crisis, energy production from fossil fuels alone has proven unsustainable. Subsequently, countries are seeking alternative energy sources to reduce their reliance on fossil fuels. International organizations and recent multilateral environmental agreements have emphasized the importance of clean and sustainable sources of energy. Thus, developing renewable energy sources can help alleviate global issues such as climate change and energy supply shortages (Tekle 2014).

Renewable energy sources include the sun, wind, water, heat, and biomass, which are constantly replenished by nature; they are not depleted, spread across a large geographical area, and are available all year (Alrikabi 2014). Renewable energy has three end uses: electricity, heat, and transportation (IEA 2019). Inovations in renewable energy have made significant progress in decarbonizing the energy sector. Renewable energy use for electricity is increasing, owing to the rapid expansion of alternative energy technology sources such as hydro, wind and solar. Many countries have recently started producing energy from these energy sources. However, the production of energy from hydropower varies throughout the year due to weather

variability and local conditions. Hence, it should be supplemented by energy production from other clean sources. Wind energy is one such source that can supplement hydropower, reduce reliance on fossil fuels, reduce CO_2 emissions and protect the environment (Caralis et al. 2008).

Ethiopia is endowed with abundant renewable energy resources such as hydro, wind, geothermal, solar and biomass. However, access to sustainable energy services is a major challenge for its people. The country is one of the 20 countries with the largest electricity access deficit, with approximately 46% of the population living without electricity (SDG 2021). Wind energy has the potential to play a major role in Ethiopia's energy future, contributing to energy security, economic development, and environmental sustainability. While current utilization is low (less than 1%), strategic investments and supportive policies can unlock the country's vast wind energy resources, helping Ethiopia to meet its growing energy demands and environmental goals (Wagle and Gowda 2019).

Ethiopia has a gross wind energy reserve of 3030 GW, with 1350 GW potentially exploitable (Hailu and Kumsa 2021). Investment in wind energy helps to meet the community's energy needs in both rural and urban areas, reduces the depletion of forest resources, has a positive impact on the environment and human health, and reduces the workload on women and children. Furthermore, local wind energy production will boost the country's economy at large by lowering the cost of importing fossil fuels from other countries. Although there are numerous advantages to investing in wind farms, the process of realizing wind energy projects is extremely difficult. Environmental factors are among the important barriers to realizing wind energy (Rathore et al. 2021). The difficulty usually begins with selecting appropriate wind farm sites based on both environmental factors and future energy production potential. Good sites are often located in remote locations, far from cities where electricity is needed. This chapter investigates the suitability of wind farms and wind energy potential in the Upper Blue Nile Basin (UBNB) by analyzing different datasets in a GIS environment. This is especially relevant in this basin, where the availability of large hydropower potential has received primary attention, casting a shadow on the assessment of other renewable energy potentials in the basin.

Wind Energy

Wind is the flow of air caused by a pressure gradient in the atmosphere. Wind blows from areas of higher pressure to areas of lower pressure (Belay 2009; Mathew 2006). The greater the air pressure gradient is, the greater the wind speed, and the greater the wind energy that can be produced. Solar heating (uneven heating of the atmosphere by the sun), the Coriolis effect due to the Earth's self-rotation, and local geographical conditions (irregularities of the Earth's surface) all influence wind generation and movement (Bulut and Büyükalaca 2007; Mathew 2006; Tong 2010). Similarly, the earth's terrain, bodies of water, and vegetation cover influence wind flow patterns (Bulut and Büyükalaca 2007).

Wind energy is an environmentally friendly source of renewable energy. It is available, with significant variations, anywhere on the planet. Wind harvesting for electricity generation is a simple and mature technology. It is, after hydropower, the fastest growing renewable energy source. Since 2000, it has grown at a compound annual growth rate of more than 21% on average (IRENA 2019a; Prakash et al. 2019). The global cumulative installed capacity of onshore wind power alone reached 542 GW by the end of 2018 (IRENA 2019b). Thus, wind energy resources have received special attention as alternative substitutes for fossil fuels and supplements for hydropower. Wind conditions such as speed, direction, and probability of blowing are important when developing a wind farm and projecting the degree of power production as well as its economic viability (Kumar et al. 2015). However, there are geographical and temporal limitations to wind forecasting. As a result, a clear assessment of wind characteristics is required for the effective planning and installation of wind power generation units. Accurate data on wind characteristics are critical for designing wind turbines, developing wind measurement techniques, and selecting wind farm sites (Mathew 2006).

Wind Energy Status in Ethiopia

Uninterrupted access to energy at affordable prices is necessary to ensure sustainable development, especially in developing countries. Ethiopia is a developing country that has been working hard to meet the energy needs of its people. However, in meeting rising energy demand, Ethiopia's energy sector faces two challenges: limited access to modern energy and a heavy reliance on traditional biomass energy sources (Hailu and Kumsa 2021). According to the Ethiopian Ministry of Water, Irrigation, and Energy, 56% of Ethiopians have access to the electric grid, while only 25% have household connectivity (Mondal et al. 2018). In 2014, the country's expected per capita electricity consumption was 70 KWh, rising to nearly 100 KWh by 2017. Nonetheless, this figure is much lower than the global per capita energy consumption average (Hailu and Kumsa 2021). Maintaining the country's rapid economic growth in the future will require a significant increase in energy supply. Ethiopia's electricity is primarily dependent on hydropower production, which is severely impacted during prolonged dry periods, resulting in potentially significant variations in power availability.

The water flow in the UBN River is characterized by seasonal variation, with 82% of the annual flow occurring between July and October (Engida and Esteves 2011). Hydropower production is susceptible to fluctuating water levels because the head and flow of water are important factors in the energy production processes. Reservoirs help to regulate these variations, but even with the construction of large-scale hydropower dams, the problem of fluctuating water levels will not be completely solved (Abdella 2015). During severe drought events, water levels at some large dams, including China's Three Gorge Dam, have been observed to fall below the level required for full power generation (Qiu 2011). To reduce reliance on hydropower, the

Government of Ethiopia (GOE) plans to diversify energy sources in the country. Wind energy development plans are one of the diversifying mechanisms. Naturally, both hydroelectric and wind generation follow seasonal patterns. Hydroelectric generation in Ethiopia is typically greatest when there is sufficient precipitation during the 'Kiremt' (June–September) season, and the generating capacity is prone to disruption during very dry seasons locally named 'Bega' (October-February) and 'Beleg' (March to May) (Hailu and Kumsa 2021; Sadoff 2008). On the other hand, wind generation is usually greatest in the dry seasons and smallest during wet seasons in the country. This makes wind a vital backup energy source for hydropower in the dry season when hydropower reservoirs are low in water. Moreover, the expected negative impacts of climate change on wind are lower than those of precipitation, runoff, and water resource availability (Mekonnen et al. 2022). All these factors make the synergy between hydropower and wind energy complementary and a profitable combination (Hailu and Kumsa 2021; MOWE 2019). Several wind power projects have been planned, and some are already operational in various parts of the country. Short-term, medium-term, and long-term wind farm projects with goals of producing 970 MW, 1750 MW and 4000 MW, respectively, were proposed (Benti and Asfaw 2017; Tiruye et al. 2021). To date, the country has produced 324 MW of wind power from three wind farms: Adama I (51 MW), Ashegoda (120 MW), and Adama II (153 MW). Feasibility studies for wind farms in areas that rely on hydropower should be evaluated to ensure accessibility of energy during dry periods. Aside from assessing wind energy potential, identifying suitable locations for establishing a wind farm using appropriate geospatial techniques such as GIS tools is important for long-term energy security.

GIS for Wind Farm Site Selection

A geographic information system (GIS) is a computerized system that facilitates data entry, processing, and presentation, particularly when dealing with georeferenced data (Rolf and de By 2001). GIS also provides powerful tools and services to collect, organize, manipulate, interpret, and display geographic data. Because of its adaptability, GIS is useful as a planning and decision support tool. It is capable of processing and analyzing large amounts of complex multidisciplinary data, creating and running management scenarios for evaluating the impact of various planning policies, modeling the consequences, and recommending changes to reduce negative impacts. Decision-makers would also be able to assign different levels of significance to recommendations using GIS (Baban and Parry 2001; Endalkachew 2018). GIS has been identified as an effective tool for land use planning and suitability mapping (Malczewski, 2004). This chapter primarily used GIS for suitability analysis for wind farm development. Suitability analysis refers to the process used to determine a system's appropriateness in relation to stakeholder needs (Parry et al. 2018). Site suitability, according to Jain and Subbaiah (2007), is a process for assessing the condition of an existing site and defining factors that will determine the location of

a specific operation. A specific set of criteria is used to select suitable sites (Jain and Subbaiah 2007). The selection of suitability criteria depends on the purpose and location of the study area (Belay 2009). Selection variables differ for each development plan, and because the parameters are spatially distributed unevenly, the variables used to select wind farm sites are not standardized globally.

GIS and Multicriteria Decision-Making

Multicriteria decision-making (MCDM) is a decision-making tool that uses multiple criteria for the evaluation of complex, multidimensional trade-offs between various options, such as locations or the suitability of a region (Grima et al. 2018; Malczewski 2006; Meng et al. 2011). In conjunction with GIS, the MCDM method enables categorizing, examining, and properly organizing the available information on spatial planning options. MCDM results can be mapped to show the spatial extent of suitable areas or the ranking of land suitability. The use of GIS-based MCDM analysis for wind farm planning gained popularity in the early 2000s and has since been used in many countries. It aids in achieving the desired result in less time and at a lower cost while maintaining or improving quality (Baseer et al. 2017).

The analytic hierarchy process (AHP) is a decision-making technique that helps with decisions that have multiple conflicting and subjective parameters (Meng et al. 2011). It uses hierarchical structures to represent a problem and develops priorities for alternative solutions based on the user's judgment (Saaty 2008). AHP is an effective method of acquiring both subjective and objective elements of a decision because it reduces complex decisions to a series of pairwise comparisons and then analyzes the results. Furthermore, the AHP includes a useful method for verifying the consistency of the decision-maker's evaluations, thereby eliminating decision-making bias. The decision-maker can assess the balance of goals by incorporating all relevant decision criteria and comparing them pairwise. Such multicriteria decision problems are common in the selection of suitable sites for various developments. As a result, in a hierarchical framework, AHP assists decision-makers in visualizing the relationship between the goal, aims, specifications, and alternatives.

AHP and GIS are integrated techniques used in this study to assess suitable sites for wind farm development in the UBNB. In a pairwise comparison matrix, each criterion was compared to the other criteria in terms of its importance on a scale of one to nine (Saaty 2008). A value of '1' is assigned to factors of equal importance, while a value of '9' is assigned to factors of extreme importance over another factor, and so on. Each assessment criterion's importance in influencing the selection of potential wind farm locations is not equal. As a result, the AHP approach is used to assign appropriate weights to the criterion based on their relative importance. Some criterion pairs, however, may not be completely consistent during comparison. As a result, the consistency ratio (CR) is employed to determine the accuracy of the criteria comparison. If the CR is less than 0.1, the ratio is consistent in pairwise comparisons (Okechukwu 2019). If the CR is much greater than 0.1, the decisions

are unreliable because they are too close to chance, and the exercise is either useless or must be repeated. A CR of 0.1 is acceptable in general (Saaty 1994).

Criteria Used for Wind Farm Site Selection

The primary concern for wind energy planners in wind farm design and development is appropriate site selection. Baseer (2017) proposed that wind energy sites should address several environmental and socioeconomic criteria in addition to meeting wind energy needs. Locating wind farms successfully will require a scientific approach that takes into account relevant factors. Nonetheless, the lack of information could make developing a scientific methodology for locating wind farms difficult (Baban et al. 2004).

Many technical variables, including wind speed, wind potential, topography, geology, grid structure, existing infrastructures, distance and turbine size, influence the decision-making on site selection for wind farm development (Conover 2001; Talinli et al. 2011a). Therefore, before securing land for new wind development, it is critical to research local infrastructures such as current transmission system operation, long-term plans, and proposed system upgrades for the chosen area. Furthermore, restricted areas such as national parks, as well as visual impacts on areas of outstanding beauty, must be considered (Conover 2001). Different researchers have used various criteria, and the most common factors for suitability analysis are listed below. Figure 11.1 summarizes the overall tasks and methods used to conduct a wind farm suitability analysis and wind energy investigation.

Wind Speed

Wind speed is an excellent predictor of an area's potential for energy production. In general, the higher the wind speed is, the more power can be generated at the chosen location. Wind speed data for all automatic weather stations (AWS) in the UBNB were obtained from the National Meteorology Institute of Ethiopia (NMIE). After vigorous quality control checks for internal consistency and technical issues with wind sensor, ten AWS wind speed data points were selected for this work. A 15-min interval wind speed data of AWS gathered by the NMI over the study area was used as the main input dataset in this study (Fig. 11.2).

In the absence of directly observed data, a spatial interpolation method was used to predict wind speed between meteorological stations. The inverse distance weighted (IDW) method was used to convert the point data to a surface raster data format. Since the IDW method has a root mean square error (RMSE) value of 0.062, which is lower than that of other interpolation methods, it is more accurate than other geospatial interpolation techniques.

As a rule of thumb, a wind speed greater than 3.5 m per second (m/s) was considered highly suitable (Okechukwu 2019). According to the findings of our research,

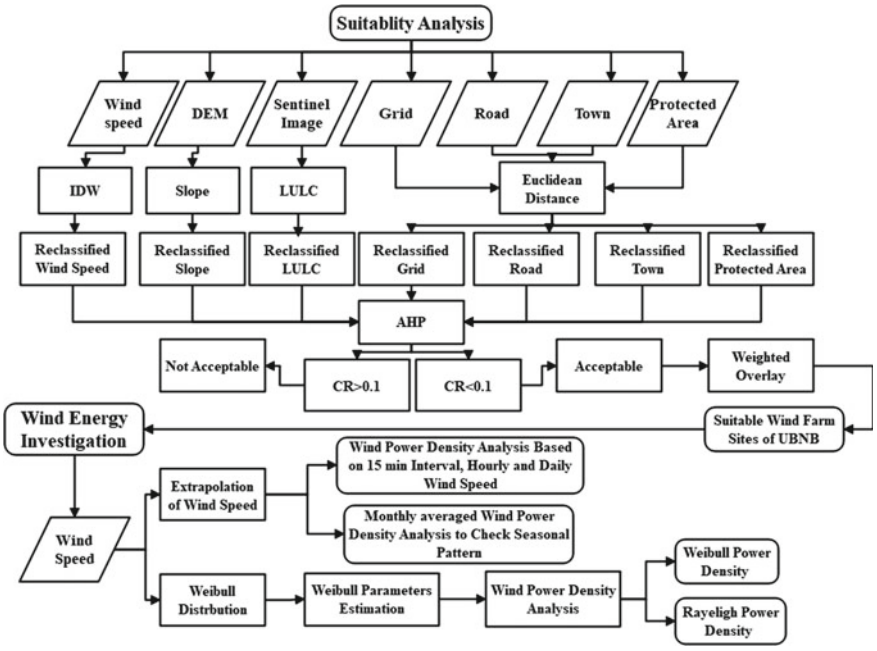

Fig. 11.1 Overall methodology used for suitability analysis for wind energy investigation in the UBNB

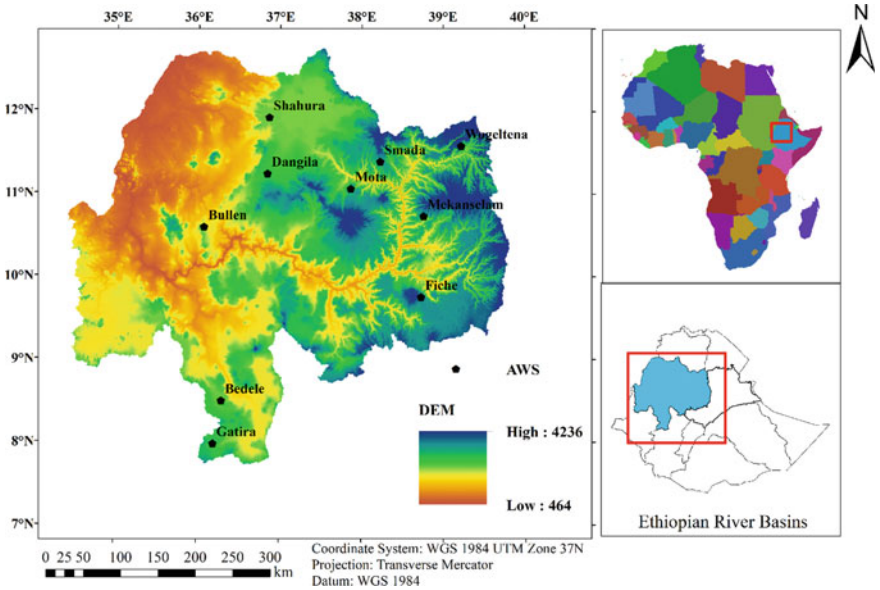

Fig. 11.2 Location map of the study area showing the elevation (m) and selected automatic weather stations (AWS) in the UBNB

Table 11.1 Wind speed suitability classes and area coverage in the UBNB

Wind speed class (m/s)	Suitability class	Suitability level	Area coverage (%)
< 2.16	1	Unsuitable	3.76
2.16–2.66	2	Less suitable	33.25
2.66–3.17	3	Moderately suitable	26.95
3.17–3.5	4	Suitable	20.95
> 3.5	5	Highly suitable	15.09

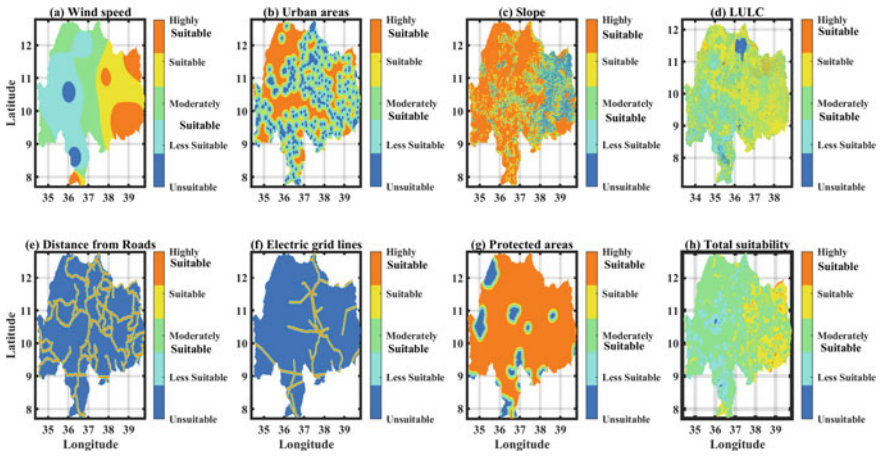

Fig. 11.3 Wind farm suitability in terms of reclassified **(a)** wind speed, **(b)** urban areas, **(c)** slope, **(d)** LULC, **(e)** distance from roads, **(f)** electric transmission lines, **(g)** protected area, and **(h)** final site suitability map of the UBNB

more than 60% of the land is moderately suitable, suitable, or highly suitable for wind farms, as given in Table 11.1. Figure 11.3 depicts the overall spatial coverage of wind energy suitability. In terms of wind speed, the northeastern, southeastern, and southern regions of the study area are more suitable for wind farm development (Fig. 11.3(a)).

Distance from Urban Areas

Wind farm construction near towns results in sound pollution from turbine noise, and residents may experience sleep disruption, headaches, and minor blurring (Horner et al. 2011; Sadeghi and Karimi 2017). Wind farms should be built at a certain distance from urban areas to reduce visual and acoustic pollution (Baseer 2017; Belay 2009; Mentis 2013; Talinli et al. 2011b; Tesfaye 2016). Some researchers recommend a distance of at least 2000 m (Al-Yahyai et al. 2012; Baban and Parry 2001; Belay

Table 11.2 Urban area suitability classes and area coverage in the UBNB

Distance from the nearby town	Suitability class	Suitability level	Area coverage (%)
< 2.5	1	Unsuitable	5.76
2.5–5	2	Less suitable	9.88
5–7.5	3	Moderately suitable	8.31
7.5–10	4	Suitable	15.34
> 10	5	Highly suitable	60.71

2009). Others advise avoiding distances of less than 2500 m (Bennui et al. 2007; Endalkachew 2018; Höfer et al. 2016; Moradi et al. 2020; Okechukwu 2019).

For this study, regional capitals (such as Asosa and Bahirdar), zonal, and woreda administration capitals were all designated as urban areas. As given in Table 11.2 and Fig. 11.3(b), more than half of the study area is located at a distance greater than 10 km from towns, making it ideal for the establishment of wind farms. This is because the study area does not have many urban settlements.

Distance to Existing Roads

As building new roads takes time and money, wind farm modeling requires the availability of road networks for both technical and commercial reasons. According to Ethiopian Road Authority (ERA) data, the most common road types in the UBNB are asphalt concrete and gravel roads. To transport wind turbines, (Van Haaren and Fthenakis 2011) recommended that roads should be paved with solid materials. In most wind farm site evaluations, areas farther away from roads are deemed less suitable than those closer to roads (Baseer et al. 2017; Höfer et al. 2016). In this study, areas less than 5 km from existing roads were deemed very appropriate (Belay 2009; Mentis 2013; Okechukwu 2019). As given in Table 11.3, only 8.44% of the total study area was highly suitable for wind farms in terms of road proximity, while 71.07% was unsuitable due to their distance from roads. The majority of the UBNB, as shown in Fig. 11.3(e), is unsuitable for the establishment of wind energy farms, which could be attributed to the study area's low road density.

Table 11.3 Road suitability classes and area coverage in the UBNB

Distance to nearby road (Jacob et al. 2016)	Suitability class	Suitability level	Area coverage (%)
< 1.25	5	Highly suitable	8.44
1.25–2.5	4	Suitable	6.42
2.5–3.75	3	Moderately suitable	7.37
3.75–5	2	Less suitable	6.70
> 5	1	Unsuitable	71.07

Table 11.4 Transmission line/grid suitability classes and area coverage in the UBNB

Distance to nearby electric grid (Jacob et al. 2016)	Suitability class	Suitability level	Area coverage (%)
< 1.25	5	Highly suitable	3.71
1.25–2.5	4	Suitable	2.89
2.5–3.75	3	Moderately suitable	3.48
3.75–5	2	Less suitable	3.11
> 5	1	Unsuitable	86.81

Distance to Transmission Lines/grids

Electric gridlines are important factors to be considered when locating a wind farm because they have a direct impact on production costs. Building a wind farm as close to an existing grid line as possible reduces the cost of construction and long-distance transmission. Hence, areas near the transmission line are considered highly suitable, while areas far from the transmission line are considered unsuitable. As given in Table 11.4 and Fig. 11.3(f), highly suitable areas are defined as being less than 1.25 km from gridlines.

Slope

Slope is an important consideration in the site selection for wind farm projects. This is because the slope of the terrain greatly influences the approachability of wind turbines for installation and maintenance. As wind turbines are more difficult to build and maintain on a steep slope than on a gentle slope, the steeper the slope of the installation area is, the higher the construction cost (Höfer et al. 2016; Kabu 2016). Furthermore, transporting turbines and cranes to the site is challenging in areas with steep slopes. A steep slope was deemed inappropriate, whereas a gentle slope was deemed ideal (Belay 2009; Endalkachew 2018). In general, a slope map (Fig. 11.3(c)) was generated in the GIS environment from 30-m resolution Shuttle Radar Topography Mission (SRTM) digital elevation model (DEM) data. Next, the slope raster was reclassified into five classes based on slope degrees. For wind farm suitability analysis, a slope of less than ten degrees was considered ideal (Belay 2009; Mentis 2013; Van Haaren and Fthenakis 2011). The region's topography was dominated by a slope of 0°–2.5°, accounting for 54.94% of the total area, as given in Table 11.5 and Fig. 11.3(c), while 8.54% of the study area had a slope greater than 10°.

Table 11.5 Slope suitability classes and area coverage in the UBNB

Slope class (degree)	Suitability class	Suitability level	Area coverage (%)
< 2.5	5	Highly suitable	54.94
2.5–5	4	Suitable	19.84
5–7.5	3	Moderately suitable	10.18
7.5–10	2	Less suitable	6.50
> 10	1	Unsuitable	8.54

Land Use Land Cover (LULC)

The available land cover types also impact the feasibility of wind turbine installation sites. Bare land is mostly preferred for wind farm development due to its low surface roughness. Areas covered by short vegetation are widely acknowledged in the literature to be preferable to tall vegetation covers because such short vegetation covers have lower surface roughness than tall vegetated areas (Endalkachew 2018). Agricultural, grass, and shrub lands are also more suitable for wind farm development than other land use/land cover types in addition to bare land (Gorsevski et al., 2013).

Forests, wetlands, archaeological sites, aviation, and military zones, on the other hand, are not suitable for wind farm development. Due to its higher spatial resolution, the sentinel image was selected for LULC in this study. ENVI 5.2 was used to preprocess the 2020 sentinel image, which was then exported to ArcMap for further analysis. To examine and validate the current LULC situations in the study area, a supervised classification (maximum likelihood classification) was performed. Grassland, forest, and wetland/settlement/waterbodies are moderately suitable, less suitable, and unsuitable, respectively, as shown in Table 11.6 and Fig. 11.3(d). Bare land accounted for approximately 2.09% of the total area, while cropland accounted for 46.71%.

Table 11.6 LULC suitability classes and area coverage in the UBNB

LULC class	Suitability class	Suitability level	Area coverage (%)
Bare land	5	Highly suitable	2.09
Cropland	4	Suitable	46.71
Grassland	3	Moderately suitable	26.34
Forest	2	Less suitable	22.25
Wetland/settlement/waterbody	1	Unsuitable	2.61

Table 11.7 Protected area suitability classes and area coverage in the UBNB

Distance from the nearby national parks (Jacob et al. 2016)	Suitability class	Suitability level	Area coverage (%)
< 1	1	Unsuitable	4.04
1–4	2	Less suitable	1.96
4–8	3	Moderately suitable	2.85
8–10	4	Suitable	1.55
> 10	5	Highly suitable	89.60

Distance from Protected Areas

Protected areas are defined as areas that are safeguarded, managed, and maintained to achieve specific conservation goals. As a result, any development should consider and set the necessary distance to protect and preserve these areas for current and future generations. Previous studies deemed a distance greater than 10 km from a protected area to be highly suitable for wind farm development, while a distance less than 0.5 km was deemed unsuitable (Abdelrazek 2017). Furthermore, distances greater than 1 km were deemed appropriate for the establishment of wind farms in other studies (Baban and Parry 2001; Effat 2014). Wind turbines should, therefore, be located safely away from sensitive areas. National parks in the study area have been classified into five classes and assigned a suitability score based on their feasibility for wind farm development (Baban and Parry 2001; Dudley 2008; Effat 2014). More than half of the study area is greater than 10 km away from protected areas (Table 11.7 and Fig. 11.3(g)), making it ideal for wind farming.

The overall wind farm suitability analysis results are shown in Fig. 11.3(a)–(g) and are based on the values given in Table 11.7 for each criterion.

Determining Factor Weights and Overall Suitability Analysis

All the factors that influence wind farm suitability in the study area are discussed in detail in the sections above. In this section, the relative weights of these factors were calculated and overlaid using the principle of pairwise comparison in the context of AHP. All factors were evaluated using a pairwise comparison matrix, which is a metric for expressing relative preference among factors. Each factor was weighted, indicating a preference or assessment of the relative value of one factor over another.

Among the seven factors, wind speed has the greatest influence (37.23%), while protected area (2.88% weight) has the least influence on wind farm development. The final suitability map for wind farm development in the UBNB was created using a weighted overlay in ArcMap based on the weights for each factor listed in Table 11.8. Only a small portion of the study area (approximately 1% of the total area or 1499 km^2) is rated as highly suitable for wind farm production, as given in Table 11.9.

Table 11.8 Weight of criteria based on AHP

Criteria	AHP weight (%)
Reclassified wind speed	37.227
Reclassified town	24.403
Reclassified road	17.679
Reclassified grid/transmission line	7.247
Reclassified LULC	3.796
Reclassified slope	6.771
Reclassified protected area	2.877
Total	100.00

Table 11.9 Final overall wind farm suitability value and area coverage

Suitability level	Suitability class	Area (km^2)	Area coverage (%)
Unsuitable	1	294.80	0.15
Less suitable	2	21,097.37	10.58
Moderately suitable	3	132,496.99	66.46
Suitable	4	43,965.85	22.05
Highly suitable	5	1498.69	0.76
Total		199,353.70	100.00

A total area of 43,965.85 km^2 (nearly 22% of the land) is suitable. Approximately 66.5% (132,496.99 km^2) of the land is classified as moderately suitable. A total of 10.58% of the total area (21,097.37 km^2) is less suitable for wind turbines, and the remaining 0.15% (294.80 km^2) is designated unsuitable. According to Fig. 11.3 and Table 11.9, the majority of the UBNB area (66.46%) is moderately suitable.

Factors Affecting Wind Energy Potential

Wind Direction

Wind direction and its value over time are very important in wind farm site selection as well as wind turbine layout in the wind farm (Tong 2010). Determining proper wind directions reduces system malfunction times, increases wind power harvesting efficiency, ensures wind turbine operational security, and extends turbine life (Dar et al. 2016; Shen et al. 2018). Hence, determining wind direction is a critical activity for installing wind energy conversion systems. If a specific direction provides most of the available wind energy, the turbine should be exposed in that direction, and obstructions to the wind flow should be avoided from that direction. As a result, wind rose (WRPLOT) software was used to analyze the wind direction of each

selected automatic weather station. The wind at any given location, however, is greatly influenced by local terrain as well as man-made structures. Although the wind direction in the study area is generally seasonal and either northeast or southwest trade winds, there is a significant difference in the directions of the prevailing wind among the stations, as shown in Fig. 11.4(a)–(j). These significant differences in wind direction could be attributed to mesoscale phenomena (for example, mountain valley breezes) caused by the area's rugged topography. It could also be influenced by man-made structures, as most weather stations are located in or near towns.

Wind Speed Estimation at Hub Height

Wind blowing across the Earth's surface encounters friction from turbulent flows as it passes over and around forests, mountains, hills, trees, buildings, and other objects in its path (Jha 2011). Thus, increasing the turbine hub height reduces the obstacles that affect wind speed; taller towers provide higher wind speeds and allow for the use of larger turbine blades, resulting in significant annual output power performance. Three of the ten selected AWS stations were measured at 10 m, while the remaining seven were measured at 2 m. As wind speed at 10 m above ground is considered the standard instrument height, all wind speeds at 2 m above ground were extrapolated to 10 m height. Finally, the wind speed data from all stations were made uniform in height by extrapolating to more applicable heights (50, 80, and 100 m) using the power law formula (Eq. 11.1). Following a review of previous studies and the wind power classification guidelines, the hub heights were determined (Tong 2010). During the study period, the average 15-min wind speed at the required hub heights for the selected stations is calculated using Eq. 11.1, and extrapolated values are given in Table 11.10.

$$\frac{v}{v_o} = \left[\frac{H}{H_o}\right]^{\alpha}, \tag{11.1}$$

where v is the wind speed at the required height H, v_o is the wind speed at the reference height H_o, and α is the ground surface friction coefficient, which lies in the range of 0.05–0.5. Because all of the stations were in or near towns with some trees and shrubs in the surrounding areas, the friction coefficient (α) was set to 0.3 (Patel and Beik 2021).

Wind Speed Frequency Distribution

To identify statistical distributions suitable for representing wind regimes, several probability functions were fitted to the AWS wind speed data. Weibull and Rayleigh distributions have been found to accurately describe wind variations in a regime and

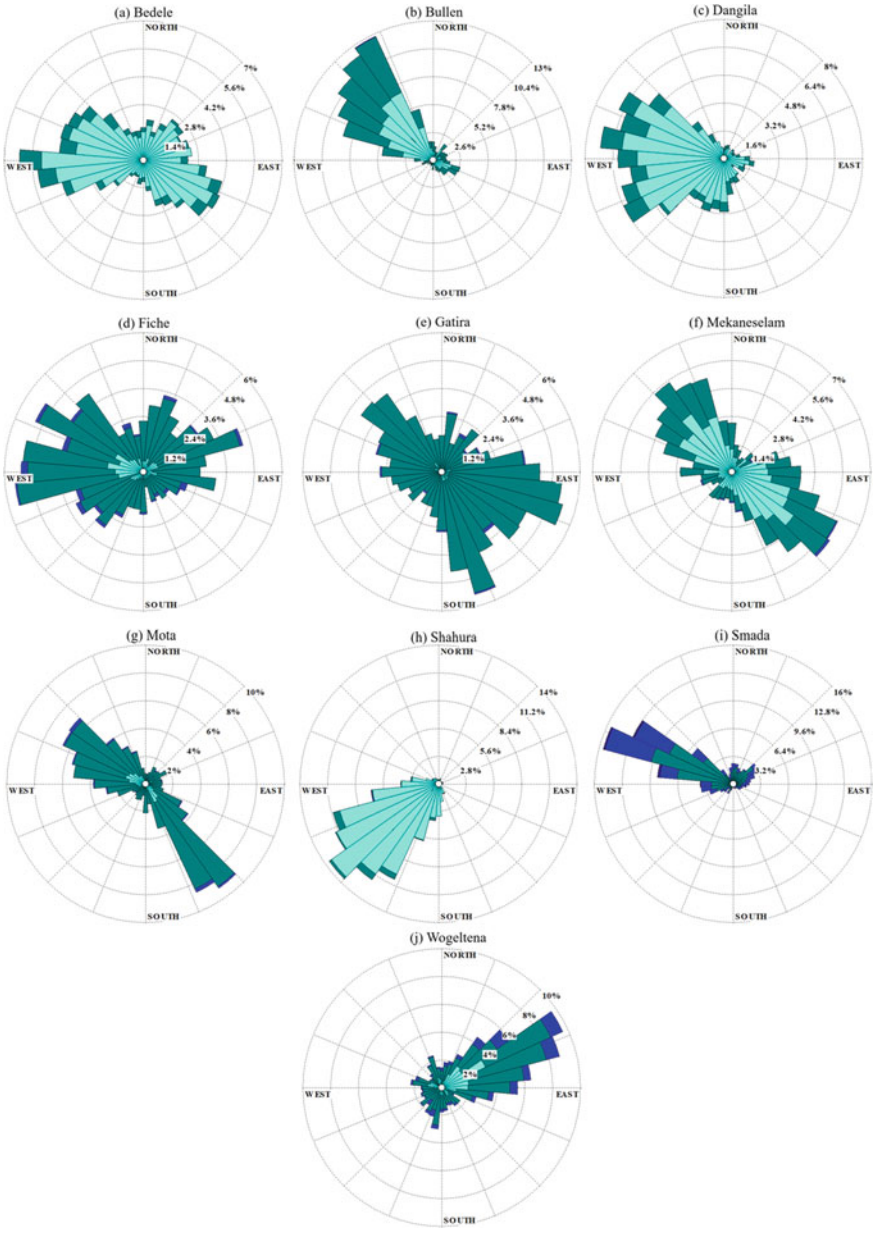

Fig. 11.4 Wind rose map of **(a)** Bedele, **(b)** Bullen, **(c)** Dangila, **(d)** Fiche, **(e)** Gatira, **(f)** Mekaneselam, **(g)** Mota, **(h)** Shahura, **(i)** Smada, and **(j)** Wogeltena

Table 11.10 Average 15-min wind speed at different hub heights

Station name	Average wind speed (m/s)			
	10 m	50 m	80 m	100 m
Bedele	1.65	2.67	3.07	3.28
Bullen	1.99	3.22	3.71	3.95
Dangila	2.83	4.58	5.28	5.65
Fiche	3.90	6.32	7.28	7.79
Gatira	4.19	6.78	7.82	8.36
M/selam	3.29	5.36	6.18	6.61
Mota	3.69	6.20	7.14	7.64
Shahura	2.48	4.02	4.64	4.96
Smada	3.27	5.31	6.11	6.52
Wogeltena	3.99	6.46	7.45	7.97

are widely used in wind energy analysis (Mathew 2006; Mengesha 2015). These models are used to calculate the probability density function and cumulative distribution function of wind speed, as well as to plot the corresponding graphs. The parameters used by the two distributions, however, differ. The average wind speed is the only parameter in the Rayleigh distribution, whereas the Weibull distribution has two parameters (i.e., shape parameter and scale parameter).

The Weibull distribution is commonly used reliably to understand an object's lifetime properties, and it displays the frequency of each mean wind speed during a wind turbine's design lifetime (McCool 2012). It has been found to fit a wide range of recorded and documented wind data, and it is used to characterize wind variation at a typical location (Wagner 2020). It appeared to better represent the actual data than the Rayleigh distribution (Mathew 2006). The probability density function ($f(v)$) expresses the fraction of time (or probability) that the wind is moving at a given velocity v as follows:

$$f(v) = kc * \text{vck} - 1 * \exp - \text{vck}, \tag{11.2}$$

where $f(v)$ is the probability of observing wind speed v, k is the shape parameter that describes how peaked the wind distribution is, and c is a scale parameter that designates how windy a wind location is.

Weibull Parameter Estimation Method

In all cases, the Weibull parameters (k and c) could be calculated using various methods for analyzing a wind system (Abdella 2015; Yissa Dawde 2013; Sadeghi and Karimi 2017). However, this chapter only looked at the three most common

methods: the empirical method, the moment method, and the energy pattern factor method.

Empirical Method (EM): Weibull parameters can be calculated using the average wind speed and standard deviation. These parameters are calculated using the formula below adapted from other researchers (Benti and Asfaw 2017; Kumar and Gaddada 2015a).

$$k = \left(\frac{\mathrm{SD}}{v_{\mathrm{m}}}\right)^{-1.086}, \tag{11.3}$$

$$c = \frac{v_{\mathrm{m}}}{\Gamma\left(1+\frac{1}{k}\right)}, \tag{11.4}$$

where Γ is a gamma function and is given by (Kumar and Gaddada 2015b; Mentis 2013).

$$\Gamma = \int_0^{\infty} e^{-t} * t^{x-1} \mathrm{d}t. \tag{11.5}$$

Energy Pattern Factor Method (EPFM): This method is commonly known as the power density method, and it is straightforward and easy to use. The method employs an average of the cubed wind speed as well as a sum of the cubed wind speed. The energy pattern factor directly determines the shape factor (Benti and Asfaw 2017; Kumar and Gaddada 2015a). As a result, the energy pattern factor equation is as follows:

$$\mathrm{Epf} = \frac{\frac{1}{n}\sum_{i=1}^{n} vi^3}{[\sum_{i=1}^{n} vi]^3}. \tag{11.6}$$

Following the calculation of the energy pattern factor, the shape and scale factors were determined using the formula below.

$$k = 1 + \frac{3.69}{\mathrm{Epf}^2}, \tag{11.7}$$

$$c = \frac{v_{\mathrm{m}}}{\Gamma\left(1+\frac{1}{k}\right)}, \tag{11.8}$$

where v_{m} is the mean wind speed (m/s), epf is the energy pattern factor, and k and c are the Weibull function shape and scale parameter, respectively.

Methods of Moments (MoM): The method of moments is one of the most commonly used techniques in the estimation of Weibull parameters. It is based on the works of (Benti and Asfaw 2017; Kumar and Gaddada 2015a; Woldegiyorgis and Terefe 2020).

$$k = \left(\frac{0.9874}{\frac{\mathrm{SD}}{v_{\mathrm{m}}}}\right)^{1.0983}, \tag{11.9}$$

$$c = \frac{v_{\mathrm{m}}}{\Gamma\left(1 + \frac{1}{k}\right)}. \tag{11.10}$$

Statistical Test

To evaluate the effectiveness of the three methods for calculating the Weibull parameters, the accuracy assessment methods mean bias error (Uwiragiye et al. 2023), root mean square error (RMSE), and mean percentage error (MPE) were used, as given in Table 11.11.

where n is the number of wind speed observations, y_{i} is the measured value, and x_i is the value estimated by the Weibull distribution.

The values of the shape and scale parameters in Figs. 11.5, 11.6, and 11.7 show that there is a significant difference in the nature of the wind speed distribution among the stations. Since the study area experiences the same types of synoptic or planetary winds, variations in wind speed distribution can be attributed to local environmental factors. Bedele ($k = 2.00$), Bullen ($k = 2.09$), Gatira ($k = 2.89$), Mekaneselam ($k = 2.23$), and Shahura ($k = 2.04$) are among the stations with shape parameters between two and three. As a result, the distributions of wind speeds at these stations are skewed towards higher wind speeds (Wagner 2020).

A higher k value also indicates that the wind speed is uniform and spreads more widely (Mathew 2006). For Dangila, Fiche, Mota, Smada, and Wogeltena stations, the shape parameter was between one and two, with values of 1.50, 1.89, 1.87, 1.90, and 1.68, respectively. This shows that the distribution of wind speeds is skewed toward lower speeds. Slower speeds are more likely at these stations (Wagner 2020). The energy pattern factor method was used to fit the distribution and calculate the Weibull shape and scale parameters for Bedele, Bullen, Dangila, and Fiche (Fig. 11.6(a)–(d)). In calculating the Weibull parameters, the empirical method outperformed the

Table 11.11 Summary of statistical parameters for the evaluation of the model performance

Statistical tools	Mathematical expression in terms of measured and calculated results	Preferable Value
Root mean square error (RMSE)	$\mathrm{RMSE} = \left(\frac{1}{n}\sum_{1}^{n}[y_i - x_i]^2\right)^{1/2}$	Close to zero
Mean bias error (Uwiragiye et al.)	$\mathrm{MBE} = \frac{1}{n}\sum_{1}^{n}[x_i - y_i]$	Close to zero
Mean percentage error (MPE)	$\mathrm{MPE}(\%) = \frac{1}{n}\sum_{1}^{n}\left(\frac{[x_i - y_i]}{y_i}\right) * 100$	Between − 10% and + 10%

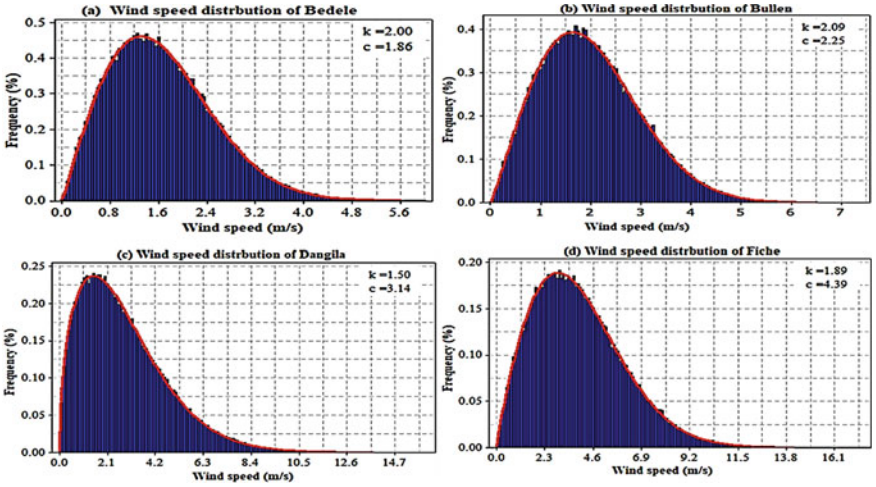

Fig. 11.5 Wind speed distribution and the values of k & c for **(a)** Bedele, **(b)** Bullen, **(c)** Dangila and **(d)** Fiche

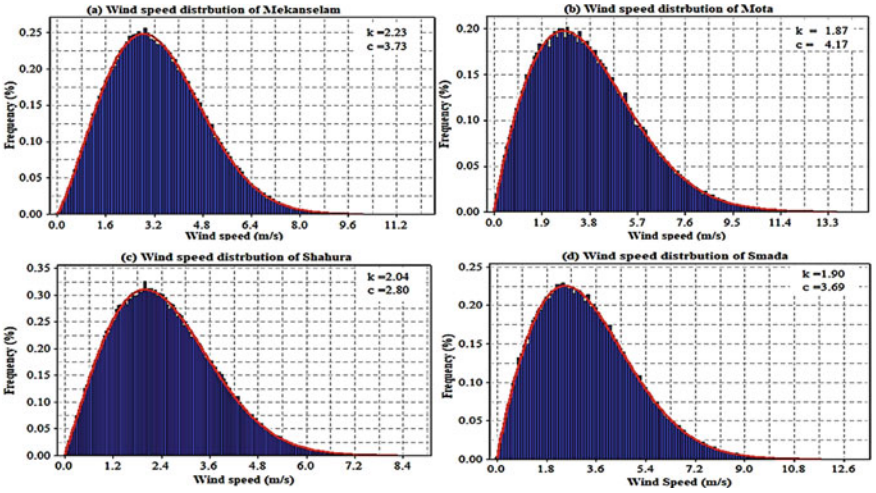

Fig. 11.6 Wind speed distribution and value of *k* and *c* for **(a)** Mekaneselam, **(b)** Mota, **(c)** Shahura and **(d)** Smada

maximum likelihood, energy pattern factor, and methods of moment methods for Mekaneselam, Mota, Shahura and Smada, as shown in Fig. 11.6(a)–(d).

The method of moment was used to estimate the Weibull shape and scale parameters and to fit the wind speed distribution at the Gatira and Wogeltena stations, as shown in Figs. 11.7(a) and 11.7(b), respectively.

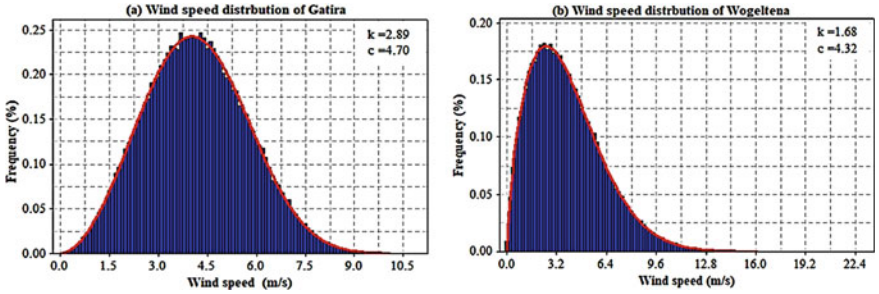

Fig. 11.7 Wind speed distribution and the values of k and c for **a** Gatira and **b** Wogeltena

Wind Power Potential Calculations

Wind power is the conversion of wind energy into usable forms of energy, such as using wind turbines to generate electricity, windmills to provide mechanical power, and wind pumps to pump or drain water (Mathew 2006). The amount of kinetic energy of wind can be expressed as a function of air mass and speed. The kinetic potential of wind energy (also known as wind power density) is a good way to assess wind resources available at a potential site and can be calculated using the formula below (Mathew 2006; Mentis 2013).

$$\frac{P}{A} = \frac{1}{2}\rho v^3, \tag{11.11}$$

where P is the theoretical power (Watts), ρ is the air density (1.225 kg/m^3), v is the wind speed (m/s), and A is the cross-sectional area of the wind turbine (m^2).

Wind power density is proportional to air density; as air density decreases with height, so does wind power density (Mathew 2006). The air density can be calculated using the formula below, which takes the elevation above sea level in meters into account (Mentis 2013).

$$\rho = 1.225e^{\frac{-z}{Hp}}, \tag{11.12}$$

where z is the elevation above sea level in metres and H_p is the scale height, which is equal to 8.5 km. The wind power density was calculated based on the density of each station obtained using Eq. 11.12, as given in Table 11.12.

The wind power density was calculated over a four-year period (2017–2020) using Eq. 11.11. The wind speed was initially measured at 15-min intervals. It was later converted to hourly, daily, and monthly time scales. The air density was calculated using Table 11.12. Furthermore, as given in Table 11.13, the wind class was assigned to each station based on the standard wind density and wind speed classification set for 10 m and 50 m hub heights.

Table 11.12 Density value based on the elevation of ten selected stations

Stations	Bedele	Bullen	Dangila	Fiche	Gatira	M/ Selam	Mota	Shahura	Smada	Wogeltena
Elevation (m)	1943	1673	2122	2819	2230	2559	2431	2219	2584	2956
Density (kg/m^3)	0.976	1.001	0.956	0.881	0.944	0.908	0.922	0.945	0.905	0.867

Table 11.13 Wind power classes at heights of 10 m and 50 m

		10 m height		50 m height	
Class	Resource potential	Wind powerdensity (W/m^2)	Wind Speed (m/s)	Wind power density (W/m^2)	Wind Speed (m/s)
1	Poor	< 100	< 4.4	< 200	< 5.6
2	Marginal	100–150	4.4–5.1	200–300	5.6–6.4
3	Moderate	150–200	5.1–5.6	300–400	6.4–7.0
4	Good	200–250	5.6–6.0	400–500	7.0–7.5
5	Excellent	250–300	6.0–6.4	500–600	7.5–8.0
6	Excellent	300–350	6.4–7.0	600–800	8.0–8.8
7	Excellent	400–1000	7.0–9.4	> 800	> 8.8

The wind power density calculated at various temporal scales is summarized in Table 11.14. As the wind speed varies over different time periods, the wind power density also varies. The wind power density was highest at 15-min intervals when compared to the hourly and daily values. Gatira and Wogeltena were classified as 'Class 2' at 50 m for a 15-min interval and hourly analysis, with wind power densities of 216.52 and 227.56 W/m^2, respectively (Table 11.14). Nonetheless, the power density decreased when the wind speeds were adjusted on a daily basis. As a result, for the daily wind power density at 50 m, Gatira (154.5 W/m^2) and Wogeltena (156.35 W/m^2) were classified as 'Poor.' Furthermore, the wind power density for Fiche (204.30 W/m^2) was 'Class 2' (i.e., 'Marginal') for 15-min-based wind power density at 50 m, whereas it was 'Class 1' (i.e., 'Poor') for wind power density analysis based on hourly and daily wind speed, as given in Table 11.14. Most of the stations were classified as class one (i.e., "Poor") at 10 m, and the wind power density, calculated by wind speed at 15-min intervals, was higher for each station. Nevertheless, when the wind speeds were adjusted on a daily basis, the power density decreased. As a result, Gatira (154.5 W/m^2) and Wogeltena (156.35 W/m^2) were classified as 'Poor' for daily wind power density at 50 m.

Furthermore, when considering the frequency distribution of wind speed, air density, and the cube of wind velocity, wind power density is thought to be a good predictor of wind resources (Ayodele et al. 2016; Woldegiyorgis and Terefe 2020). In this paper, the actual wind power density obtained using Eq. 11.11 was compared to the Weibull and Rayleigh wind power densities obtained using Eqs. 11.13 and

Table 11.14 Wind power density based on a 15-min interval, hourly and daily wind speeds of stations at 10, 50, 80, and 100 m hub heights for 2017 to 2020

Hub heights	Bedele	Bullen	Dangila	Fiche	Gatira	M/Selam	Mota	Shahura	Smada	Wogeltena
	15-min interval wind power density (W/m^2)									
10 m	4.22	7.31	29.46	49.87	53.07	28.48	47.14	15.02	31.1	53.79
50 m	17.96	30.15	124.63	204.3	216.5	117.59	199.4	61.59	129.2	227.56
80 m	27.44	46.08	190.88	312.88	331.6	180.08	305.4	94.33	202.1	348.51
100 m	33.29	55.89	233.53	382.79	405.7	220.32	373.6	115.41	245.1	426.38
	Hourly wind power density (W/m^2)									
10 m	3.87	6.86	27.92	46.81	49.73	26.62	45	13.99	28.99	53.52
50 m	16.47	29.15	118.11	198.02	210.4	112.59	190.4	59.17	123.2	226.4
80 m	25.17	44.55	180.89	303.27	322.2	172.44	291.6	90.61	188.3	346.73
100 m	30.53	54.03	221.31	371.04	394.2	210.97	356.7	110.86	228.4	424.2
	Daily wind power density (W/m^2)									
10 m	2.49	4.68	12.41	29.41	36.53	18.33	29.45	7.95	18.29	36.96
50 m	10.59	19.88	52.49	124.42	154.5	77.48	124.6	33.61	77.79	156.35
80 m	16.19	30.38	80.39	190.55	236.7	118.63	190.8	51.48	118.9	239.44
100 m	19.64	36.85	98.35	233.13	289.6	145.14	233.4	62.98	144.2	292.95

11.14, respectively. To determine how well a theoretical probability density function matches the actual wind power density, RMSE, MPE, and MBE were used to select the appropriate density function (Table 11.11). The following equations define the Weibull and Rayleigh density functions (Ayodele et al. 2016; Woldegiyorgis and Terefe 2020).

$$\mathrm{WPD} = \frac{1}{2}\rho c^3 \Gamma\left(1 + \frac{3}{k}\right), \tag{11.13}$$

$$\mathrm{RPD} = \frac{3}{\pi}\rho c^3 \left(\frac{\pi}{4}\right)^{\frac{3}{2}}, \tag{11.14}$$

where WPD is the Weibull power density function and RPD is the Rayleigh power density function.

However, for the calculation of Rayleigh power density, a shape factor of 2 was used as the default value (Mathew 2006). Table 11.15 illustrates how increasing the frequency distribution improves wind power density.

The wind power densities predicted by the Weibull density function for Fiche, Mota, Smada, and Wogeltena were statistically closer to each other than those predicted by the Rayleigh function. For Gatira and Mekaneselam, however, the Rayleigh wind power density was preferable to the Weibull power density. Based on wind power classification (i.e., Table 11.13), Fiche, Gatira, Mota, and Wogeltena were classified as wind 'Class 2' (i.e., 'Marginal') at 50 m, with average wind power densities of 215.47, 242.07, 205.49, and 246.81 W/m^2, respectively. In general, the findings show that wind power density is a better indicator because it takes into account the frequency distribution function, which agrees with the findings of the

Table 11.15 Summary of the actual, Weibull and Rayleigh wind power densities at 10 and 50 m

Height	Parameters	Fiche	Gatira	M/selam	Mota	Smada	Wogeltena
10 m	v_m (m/s)	3.90	4.19	3.30	3.70	3.27	3.86
	k	1.89	2.89	2.23	1.87	1.90	1.68
	c	4.39	4.70	3.73	4.17	3.69	4.32
	APD (W/m^2)	49.87	53.07	30.48	47.14	31.1	53.19
	WPD (W/m^2)	52.72	49.61	28.01	47.84	32.17	57.43
	RPD (W/m^2)	49.49	64.87	31.05	44.34	30.39	46.09
50 m	v_m (m/s)	6.32	6.78	5.36	6.20	5.31	6.46
	k	1.97	2.91	2.23	2.04	1.99	1.81
	c	7.13	7.29	6.05	7.00	5.99	7.27
	APD (W/m^2)	204.3	216.52	117.59	199.4	129.24	227.56
	WPD (W/m^2)	215.47	184.54	119.53	205.49	130.69	246.81
	RPD (W/m^2)	212.02	242.07	132.48	209.76	130.00	219.65

studies conducted in Wereilu and Debre Birhan (Ayodele et al. 2016; Woldegiyorgis and Terefe 2020).

Monthly Average Wind Power Density

To characterize seasonal changes at each station, the monthly average wind power per unit cross-sectional area of a turbine was calculated (Eq. 11.15). This entity was estimated for wind power extracted at various heights: 10, 50, 80, and 100 m.

$$\frac{P}{A} = \frac{1}{2}\rho\frac{1}{n}\sum v_i{}^3, \tag{11.15}$$

where P is the theoretical power, ρ is the air density of each station, v is the wind speed, A is the cross-sectional area, and n is the number of days in the month.

Bullen and Mekaneselam had the highest wind power density in March, as shown in Fig. 11.8(a)–(d). In April, the wind power density was highest in Bedele, Dangila, Gatira, Mota, and Smada. For Smada and Wogeltena, the month of May has the highest wind power density. Similarly, Shahura and Fiche have the highest wind power densities in January and October, respectively. For the months of January, February, October, and November, the average wind speed at 50 m in Fiche is 6.87 m/s. Gatira's average wind speed is 6.99 m/s from January to June and in October. Similarly, Mota experienced average wind speeds of 6.75 m/s from March to June. Thus, Fiche, Gatira, and Mota were classified as 'Class 3' or 'Moderate' based on the average wind speed. Instead, Wogeltena, with an average wind speed of 7.79 m/s and a power density greater than 200 W/m^2, was classified as 'Class 4' (i.e., 'Good') and 'Class 2' (i.e., 'Marginal') at 50 m, as shown in Fig. 11.8(b).

When compared to previous research, our findings show that Bedele and Bullen have lower average wind power densities than Debre Birhan, Mekele, and Wereilu (Gaddada and Kodicherla 2016; Woldegiyorgis and Terefe 2020). In contrast to Bedele and Bullen, Dangila had a higher wind power density. Fiche, Mekaneselam, and Mota have higher wind power densities at 10 and 50 m (Woldegiyorgis and Terefe 2020), which could be attributed to Fiche, Mekaneselam, and Mota's higher wind speeds. Wogeltena and Gatira, on the other hand, had lower wind power densities than previous studies in Adama II (Tadesse 2014), Ayesha (Mengesha 2015), and Mosobo-Harena (Abdella 2015). This could be because the wind speeds in Adama, Ayesha, and Mosobo-Harena were measured using a separate wind measurement tower, which improved the measurement quality. The Wogeltena station has the highest mean wind power density at 10, 50, 80, and 100 m, followed by the Gatira station. According to the findings of this study, the Bedele station had the lowest average wind power density.

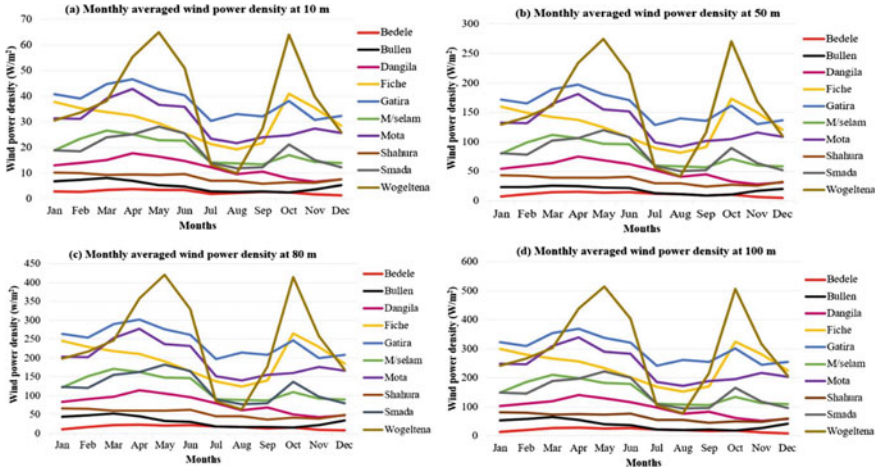

Fig. 11.8 Average monthly wind power density for each station at **(a)** 10 m, **(b)** 50 m, **(c)** 80 m, and **(d)** 100 m

Conclusion and Recommendations

In this study, seven criteria (wind speed, slope, LULC, distance from electric grids, roads, urban areas, and protected areas) were identified for wind farm suitability analysis. These criteria were then processed in the GIS environment. The processed results revealed that wind speed is the most important factor influencing wind farm development. Because of the uneven spatial distribution of weather stations in the study area, extensive wind farm suitability analysis at fine spatial resolution has rarely been implemented, and suitability analysis has been performed at only a few sites. However, at some of the study sites, we were able to identify promising wind energy potentials. An area of 1499 km^2 in the northeastern section of the study area, which is characterized by elevated and flat areas surrounded by the valleys of the Abay, Tekeze, and Awash River basins, was very suitable for wind farm development. Because the UBNB is mostly mountainous, future wind energy research should consider additional wind parameters such as turbulence intensity and surface roughness. Incorporating such wind parameters will improve wind power research results. Furthermore, to establish accurate wind energy data, higher-quality wind assessment equipment should be deployed in the region. When wind power density was estimated using 15-min interval wind speeds, the results were found to be greater than the hourly and daily averages at all stations. This shows how small changes in wind speed can increase or decrease wind power output. Meanwhile, when the frequency distribution was considered, the wind power density increased noticeably. The wind follows a seasonal pattern in the research area, with most stations reporting relatively high wind power density in January, March, April, May, and October. Wind energy could be a useful supplement to hydropower in these months because the water level in Ethiopia's hydropower reservoirs is typically low during the dry season.

Finally, some areas, most notably Wogeltena and Gatira, have greater wind potential than others. However, as the available meteorological stations in the region were primarily designed and installed for weather forecasting, the researchers believe that they may not be ideal for estimating wind energy potentials. As a result, various wind speed measuring tools (for example, a taller wind mast) are proposed for future wind energy potential investigations. The most promising sites discovered in this study are the northeastern corner of the study area. These areas may be considered viable for both grid-connected and stand-alone energy production. The Ethiopian government should prioritize maximizing wind energy potential in these areas. This could reduce the risks of energy spillovers from the country's highly hydropower-dependent energy system while also securing energy production, especially during the dry season when water storage in hydroelectric dams is limited and areas become extremely windy.

Acknowledgements We would like to thank the National Meteorology Institute (NMI) of Ethiopia for providing automatic weather station data free of charge. The first researcher was funded by the female student scholarship office of Addis Ababa University. This research was also partly supported by the 9th round of the Addis Ababa University thematic research project fund (TR/022/2021). The researchers would like to acknowledge both the female student scholarship and thematic research offices.

References

Abdella M (2015) Wind resource data analysis for Mosobo-Harena wind farm. Addis Ababa University, 87 pp

Abdelrazek M (2017) GIS approach to find suitable locations for installing renewable energy production units in Sinai Peninsula. Egypt, M. Sc. Geoinformatics, University of Salzburg, Austria, pp 1–84

Al-Yahyai S, Charabi Y, Gastli A, Al-Badi A (2012) Wind farm land suitability indexing using multicriteria analysis. Renew Energy 44:80–87

Alrikabi N (2014) Renewable energy types. J Clean Energy Technol 2(1):61–64

Ayodele T, Ogunjuyigbe A, Amusan T (2016) Wind power utilization assessment and economic analysis of wind turbines across fifteen locations in the six geographical zones of Nigeria. J Clean Prod 129:341–349

Baban S, Ramlal B, Al-Tahir R (2004) Issues in information poverty and decision-making in the Caribbean—a way forward. West Indian J Eng 27(1):28–37

Baban SM, Parry T (2001) Developing and applying a GIS-assisted approach to locating wind farms in the UK. Renew Energy 24(1):59–71

Baseer M, Rehman S, Meyer JP, Alam MM (2017) GIS-based site suitability analysis for wind farm development in Saudi Arabia. Energy 141:1166–1176

Baseer MA (2017) Wind resource assessment and gis-based site selection methodology for efficient wind power deployment. University of Pretoria

Belay E (2009) Modeling site suitability for wind farm using remote sensing and GIS: the case of adama woreda. Addis Ababa University

Bennui A, Rattanamanee P, Puetpaiboon U, Phukpattaranont P, Chetpattananondh K (2007) Site selection for large wind turbine using GIS. In: PSU-UNS international conference on engineering and environment, pp 561–566

Benti N, Asfaw A (2017) Evaluations of wind speed distribution and wind power potential over Ethiopia (a case of Ambo). J Phys Chem Sci 5(4):2348–3327
Bulut H, Büyükalaca O (2007) Simple model for the generation of daily global solar-radiation data in Turkey. Appl Energy 84(5):477–491
Caralis G, Perivolaris Y, Rados K, Zervos A (2008) On the effect of spatial dispersion of wind power plants on the wind energy capacity credit in Greece. Environ Res Lett 3(1):015003
Conover K (2001) Philippine wind farm analysis and site selection analysis. National Renewable Energy Lab, Golden, CO (US), United States
Dar Z, Kar K, Sahni O, Chow JH (2016) Windfarm power optimization using yaw angle control. IEEE Trans Sustain Energy 8(1):104–116
Dudley N (2008) Guidelines for applying protected area management categories. Iucn
Effat HA (2014) Spatial modeling of optimum zones for wind farms using remote sensing and geographic information system, application in the Red Sea, Egypt. J Geographic Inf Syst
Endalkachew S (2018) Wind farm site suitability analysis using GIS and remote sensing: the case of Bahir Dar City and Bahir Dar Zuriya District. Bahir Dar University, 101 pp
Engida AN, Esteves M (2011) Characterization and disaggregation of daily rainfall in the Upper Blue Nile Basin in Ethiopia. J Hydrol 399(3–4):226–234
Gaddada S, Kodicherla SPK (2016) Wind energy potential and cost estimation of wind energy conversion systems (WECSs) for electricity generation in the eight selected locations of Tigray region (Ethiopia). Renew Wind Water Solar 3(1):1–13
Gorsevski PV, Cathcart SC, Mirzaei G, Jamali MM, Ye X, Gomezdelcampo E (2013) A group-based spatial decision support system for wind farm site selection in Northwest Ohio. Energy Policy 55:374–385
Grima N, Singh SJ, Smetschka B (2018) Improving payments for ecosystem services (PES) outcomes through the use of Multi-Criteria Evaluation (MCE) and the software OPTamos. Ecosyst Serv 29:47–55
Hailu AD, Kumsa DK (2021) Ethiopia renewable energy potentials and current state. Aims Energy 9(1):1–14
Höfer T, Sunak Y, Siddique H, Madlener R (2016) Wind farm siting using a spatial analytic hierarchy process approach: a case study of the Städteregion Aachen. Appl Energy 163:222–243
Horner B, Jeffery RD, Krogh CM (2011) Literature reviews on wind turbines and health: are they enough? Bull Sci Technol Soc 31(5):399–413
IEA (2019) Tracking SDG 7: the energy progress report 2019. Washington DC
IRENA (2019a) International Renewable Energy Agency (IRENA): Abu Dhabi. In: R.C. Statistics (Editor), United Arab Emirates, p 60
IRENA (2019b) Future of wind: deployment, investment, technology, grid integration and socioeconomic aspects. Abu Dhabi
Jain K, Subbaiah YV (2007) Site suitability analysis for urban development using GIS. J Appl Sci
Jha AR (2011) Wind turbine technology. CRC Press
Kabu IK (2016) Wind farm site selection assessment in the Greater Accra, Volta and eastern regions of Ghana: a GIS spatial multicriteria assessment, NTNU
Kumar KSP, Gaddada S (2015a) Statistical scrutiny of Weibull parameters for wind energy potential appraisal in the area of northern Ethiopia. Renew Wind Water Solar 2:1–15
Kumar KSP, Gaddada S (2015b) Statistical scrutiny of Weibull parameters for wind energy potential appraisal in the area of northern Ethiopia. Renewables 2, 2(1):1–15
Kumar KSP, Kumar A, Nanduri PR (2015) Analysis of wind speed data for energy production at central Ethiopia, Adama. Int J Recent Res Sci Eng Technol 1(2)
Malczewski J (2004) GIS-based land-use suitability analysis: a critical overview. Prog Plan 62(1):3–65
Malczewski J (2006) Ordered weighted averaging with fuzzy quantifiers: GIS-based multicriteria evaluation for land-use suitability analysis. Int J Appl Earth Obs Geoinf 8(4):270–277
Mathew S (2006) Wind energy: fundamentals, resource analysis and economics, 1. Springer, Heidelberg

McCool JI (2012) Using the Weibull distribution: reliability, modeling, and inference, 950. John Wiley & Sons, Hoboken
Mekonnen TW, Teferi ST, Kebede FS, Anandarajah G (2022) Assessment of impacts of climate change on hydropower-dominated power system—the case of Ethiopia. Appl Sci 12(4):1954
Meng Y, Malczewski J, Boroushaki S (2011) A GIS-based multicriteria decision analysis approach for mapping accessibility patterns of housing development sites: a case study in Canmore, Alberta. J Geographic Inf Syst 3(01):50
Mengesha W (2015) Wind energy resource analysis: a case study of Aysha Wind Farm. Addis Ababa University
Mentis D (2013) Wind energy assessment in Africa; A GIS-based approach. In: K.R.I.o.T.i. Stockholm, p 77
Mondal MAH, Bryan E, Ringler C, Mekonnen D, Rosegrant M (2018) Ethiopian energy status and demand scenarios: prospects to improve energy efficiency and mitigate GHG emissions. Energy 149:161–172
Moradi S, Yousefi H, Noorollahi Y, Rosso D (2020) Multicriteria decision support system for wind farm site selection and sensitivity analysis: case study of Alborz Province, Iran. Energy Strategy Rev 29:100478
MOWE (2019) The Federal Democratic Republic of Ethiopia Ministry of Water Irrigation and Energy. Ethiopian Ministry of Water Irrigation and Energy
Okechukwu UC, Igbokwe JI, Ejikeme JO (2019) Site suitability analysis for locating wind energy power plant in Rivers State, Nigeria using Geospatial Technology. Int J Eng Sci Comput 9(8)
Parry JA, Ganaie SA, Bhat MS (2018) GIS based land suitability analysis using AHP model for urban services planning in Srinagar and Jammu urban centers of J&K, India. J Urban Manage 7(2):46–56
Patel MR, Beik O (2021) Wind and solar power systems: design, analysis, and operation. CRC Press
Prakash G, Anuta H, Wagner N, Gallina G (2019) Future of wind-deployment, investment, technology, grid integration and socioeconomic aspects. International Renewable Energy Agency (IRENA)
Qiu J (2011) China admits problems with Three Gorges Dam. Nature News, 25
Rathore N, Yettou F, Gama A (2021) Improvement in wind energy sector using nanotechnology. In: 2020 6th international symposium on New and Renewable Energy (SIENR). IEEE, pp 1–5
Rolf A, de By R (2001) Principles of geographic information systems. The International Institute for Aerospace Survey and Earth Sciences (ITC), Hengelosestraat, p 99
Saaty TL (1994) Fundamentals of decision making and priority theory with the analytic hierarchy process. RWS Publications
Saaty TL (2008) Decision making with the analytic hierarchy process. Int J Services Sci 1(1):83–98
Sadeghi M, Karimi M (2017) GIS-based solar and wind turbine site selection using multicriteria analysis: case study Tehran, Iran. Int Arch Photogramm Remote Sens Spat Inf Sci 42:469–476
Sadoff C (2008) Managing water resources to maximize sustainable growth: a World Bank water resources assistance strategy for Ethiopia
SDG (2021) The energy progress report. IEA, Paris, France
Shen X, Zhou C, Li G, Fu X, Lie TT (2018) Overview of wind parameters sensing methods and framework of a novel MCSPV recombination sensing method for wind turbines. Energies 11(7):1747
Talinli I, Topuz E, Aydin E, Kabakcı SB (2011a) A holistic approach for wind farm site selection by FAHP. In: Suvire GO (ed) Wind farm: technical regulations, potential estimation and siting assessment. InTech, Croatia, pp 213–234
Talinli I, Topuz E, Aydin E, Kabakcı SB (2011b) A holistic approach for wind farm site selection by FAHP. Wind farm: technical regulations, potential estimation and siting assessment. InTech, Croatia, vol 3, issue 1, pp 213–234

Tekle FT (2014) Assessment of solar energy resources in Ethiopia: modeling solar radiation and GIS-based multicriteria analysis. Norwegian University of Science and Technology, NTNU, 73 pp

Tesfaye E (2016) A fuzzy approach for modeling potential wind farm areas: a case of Hitosa Woreda, Ethiopia. Addis Ababa University, Oromia Region

Tiruye GA, Besha AT, Mekonnen YS, Benti NE, Gebreslase GA, Tufa RA (2021) Opportunities and challenges of renewable energy production in Ethiopia. Sustainability 13(18):10381

Tong W (2010) Fundamentals of wind energy, 44. WIT Press, Southampton

Uwiragiye Y, Ngaba MJY, Yang M, Elrys AS, Chen Z, Zhou J (2023) Spatially explicit soil acidification under optimized fertilizer use in Sub-Saharan Africa. Agronomy 13(3):632

Uwiragiye Y, Ngaba MJY, Zhao M, Elrys AS, Heuvelink GB, Zhou J (2022) Modeling and mapping soil nutrient depletion in humid highlands of East Africa using ensemble machine learning: a case study from Rwanda. CATENA 217:106499

Uyan M (2013) GIS-based solar farms site selection using analytic hierarchy process (AHP) in Karapinar region, Konya/Turkey. Renew Sustain Energy Rev 28:11–17

Van Haaren R, Fthenakis V (2011) GIS-based wind farm site selection using spatial multicriteria analysis (SMCA): evaluating the case for New York State. Renew Sustain Energy Rev 15(7):3332–3340

Wagle P, Gowda PH (2019) Editorial for the Special Issue "Remote Sensing of Evapotranspiration (ET)". MDPI, pp 2146

Wagner H-J (2020) Introduction to wind energy systems, EPJ Web of Conferences. EDP Sciences, p 00004

Woldegiyorgis TA, Terefe EA (2020) Wind energy potential estimation using Weibull and Rayleigh distribution models and surface measured data at Debre Birehan, Ethiopia. Appl J Environ Eng Sci 6(3):6–3, 244–262

Yissa Dawde O (2013) Wind resource data analysis: the case of MYDERHU project site, Tigray regional state, Ethiopia

Chapter 12
Analysis of Climate Variability and Agricultural Drought and their Implications for Rainfed Agriculture at Selected Stations in the Hadiya Zone, Ethiopia

Dame Yadeta, Assefa M. Melesse, and Melkamu Abate

Abstract Rainfed agriculture is the mainstay of the majority of livelihoods in Ethiopia. However, the rainfall resources on which agriculture depends vary greatly in space and time, affecting cropping patterns and productivity. Agricultural drought during the crop-growing season is the leading challenge to agricultural production in Ethiopia. As a result, this study examines the climate, specifically rainfall and agricultural droughts associated with the wheat-growing season, in Ethiopia's southern region, with a focus on the Hadiya zone. Hence, from the perspective of an agriculturalist, reliable start and end dates of the rainy season were established, and the rainfall pattern was examined using a modified Mann–Kendall test. To characterize drought events, the Standardized Precipitation Index (SPI) was used. The Markov chain model was used to assess the dry and wet spell conditions. At Fonko, the rainy season typically begins on April 23 and ends on October 30, while at Hosanna, it begins on April 14 and ends on November 1. In the study area, wheat's crop water requirements ranged from 483.6 to 512.2 mm during the growth season, and they were unaffected by the planting date. The chance of a dry period increases throughout the short rainy season. For both stations, there was a higher frequency of moderate drought episodes throughout both wet seasons, followed by severe drought. Supplemental irrigation is essential in the area, especially during the most precarious periods of crop growth. Mulching and other in situ and ex situ moisture conservation methods must be used as part of any moisture management strategy.

D. Yadeta (✉)
Semara University, Semera, Ethiopia
e-mail: dameyadeta@gmail.com

A. M. Melesse
Department of Earth and Environment, Florida International University, Miami, USA
e-mail: melessea@fiu.edu

M. Abate
Water, Mine and Energy Office, Ameka, Hadiya, Ethiopia

A. M. Melesse et al. (eds.), *Land and Water Degradation in Ethiopia*, Springer Geography, https://doi.org/10.1007/978-3-031-60251-1_12

Keywords Climate variability · Rainy season · Dry/wet spell · Drought · Wheat · Hadiya

Introduction

Rainfed agriculture, which is the basis of national subsistence, is the backbone of the Ethiopian economy. Agriculture generates more than 50% of Ethiopia's GDP and almost 60% of the country's foreign wage income (Deressa et al. 2011). Climate change has the greatest impact on agriculture (Singh 2015). Every minor change in the climate, especially in the amount of rainfall, had a significant impact on agricultural production and productivity (Asha et al. 2012). An uneven climate has a severe impact on manufacturing and the entire country's economy year over year (Ngetich et al. 2014). The obligatory use of crop-specific climate data in crop management choices reduces the sensitivity of crops to weather-induced effects. Such knowledge would enable cultivators to make wise judgments regarding the kind of crops to be sown, where to plant them, and when to do so (Wood et al. 2014).

In Ethiopia, the recurrent dry season results in a substantially harmed economy, interruptions to the growth of GDP, crop losses, and livestock harm. As a result, it is important to be ready for weather change when it happens and to adjust to it so that the impact on agriculture is reduced. The country's fluctuation in rainfall, particularly its spatial variability, is caused by moisture flows brought on by changes in pressure systems. Processes such as the subtropical jet, intertropical convergence zone, Red Sea convergence zone, tropical easterly jet, and Somalia jet are responsible for the rain that falls over Ethiopia (Meresa 2010). Moreover, geography has led to numerous sudden changes in the Rift Valley basin where this study was undertaken (Meresa 2010).

In developing countries such as Ethiopia, rainfall variability is among the frequently mentioned factors posing food insecurity (Granados et al. 2017). When compared to irrigated agriculture, yields from rainfed agriculture are consistently declining because of the frequent crop failure caused by anomalies in rain start, end, and distribution during the growing season (Bruijnzeel 2004).

The majority of Africa's agricultural activities depend on rainfall timing; therefore, accurate predictions of the start and end of the rainy season are crucial for crop production, especially for smallholder farmers (Asfaw et al. 2018). Analysis of spatiotemporal climatic variables is crucial to evaluating weather-related consequences and suggesting potential solutions (Abbas et al. 2018). Bega (dry season), which lasts from October to January, Belg (short rainy season), which lasts from February to May, and Kiremt (long rainy season), which lasts from June to September, are the three seasons that exist in Ethiopia. Whereas Kiremt is caused by the convergence of low-pressure systems and the Intertropical Zone, Belg is caused by the moist easterly and southeasterly winds of the Indian Ocean (Tabari et al. 2015).

The main dangers associated with climate change for crop failure are drought, water logging, and unpredictable rainfall. Additionally, trends in how much of a

country's GDP is attributable to agriculture clearly show that there is a strong relationship between weather and agricultural industries (World Bank 2006). Climate fluctuation affects the agro-ecological requirements for growing wheat in a number of locations (Valizadeh et al. 2013). More than 35% of the world's population depends on wheat (Triticum aestivum L.), which is produced at a rate of 772.6 million tons annually (Statista 2021). Worldwide, China, India, and Russia are the top producers of wheat, whereas in Sub-Saharan Africa, the top producers are Ethiopia and South Africa (USDA 2019).

Wheat is grown in Ethiopia from 1500 to 3200 m.a.s.l. (MoA 2010). Its ideal altitude range is between 1900 and 2700 m above sea level (CSA 2021). Ethiopia produces approximately 5.8 million tons per year on average at 3 tons per hectare (CSA 2021), which is less than the crop's potential yield (Zegeye et al. 2020). It accounts for 17% of all grain output, placing it third in terms of importance behind teff (Eragrostis tef (Zucc.) Trotter) and maize (Zea mays L.) (CSA 2021).

Global demand for wheat is rising as a result of the rising human population, urbanization, and livelihood changes (Minot et al. 2015). Between 2000 and 2009, the overall per capita demand for wheat in SSA increased by 0.35 kg/person/year (Sununtnasuk 2013). Its use in Ethiopia was approximately 29.6 kg per person per year in 2004–2005 and is anticipated to increase in the near future (Berhane et al. 2011). Some of the culinary recipes include industrially produced pasta, Ethiopian bread, boiled grains, roasted grains, loosely crushed kernels cooked with milk or water, and blended with spiced butter. Due to a lack of rain and the unpredictable nature of rainfall, agricultural planning in Ethiopia is unreliable during the short rainy season (Bekele et al. 2017a, b; Yadeta et al. 2020a).

Rainfall variability has been analyzed by various studies (Bekele et al. 2017a, b). Variations in rainfall in Ethiopia lead to a 4.4% loss in food production, a 20% decline in productivity, and a 25% increase in poverty rates. Generally, food shortages and hunger have been mostly caused by rainfall-related drought (Bekele 2017a). Therefore, the current study investigated the intraseasonal and annual variations in rainfall and agricultural drought and their implications for a wheat crop in the Hadiya zone, Ethiopia.

Research Methodology

Description of the Study Area

The research was conducted in Ethiopia's Hadiya Zone (Fig. 12.1). It is situated between latitudes 7°3′19″ and 7°56′1″ north and 38°52′13″ and 37°23′14″ east. The annual rainfall is unimodal, ranging from 600 to 2011 mm. June through August is the primary wet season. It has dega (the cool zone), woina dega (the temperate zone), and kola in terms of agro-ecology (low land sub humid). The Weina dega has a daily temperature range of 11–30 °C and is located between 1500 and 2400 masl (USLC

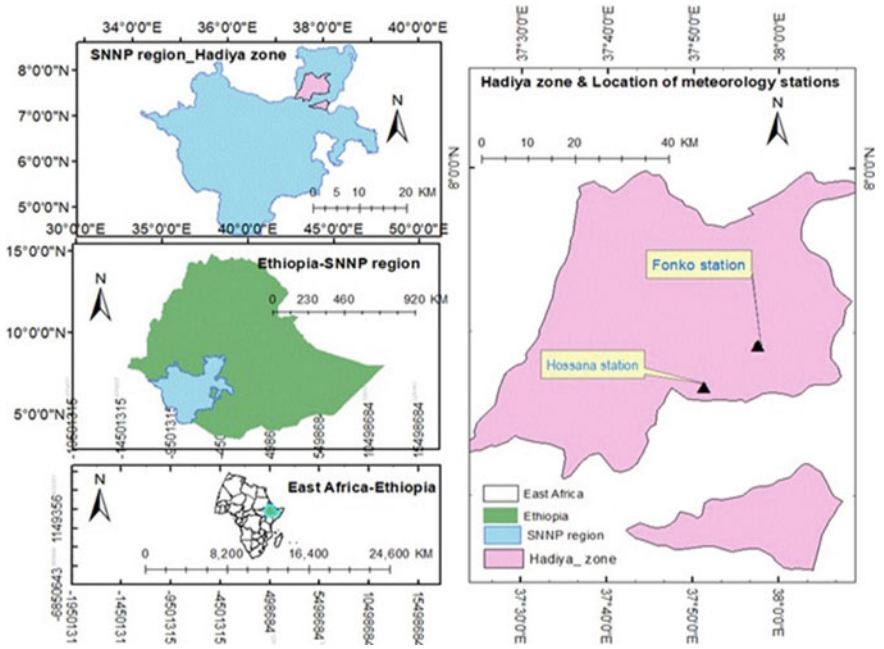

Fig. 12.1 Location of metrology stations and map of the study area

2005). It contains clay soil varieties such as Nitosoil and Chronic Luvisoil. Wheat, teff, maize, and sorghum are the four main cereal crops cultivated.

Data Collection

Meteorological Data

The Ethiopian National Meteorological Agency provided climate information for 1987–2016 for Hossana, which is located at an altitude of 2307 m, and Fonko, which is located at an altitude of 2246 m.

Preprocessing of Metrological Data

To fill in missing rainfall data, the arithmetic mean method was used because both the *Hosanna* and *Fonko* stations had a percentage difference of less than 10 mm from their normal rainfall. The percentage of missing data was 8.7% at the Hosanna station and 8.25% at the Fonko station.

$$\text{Arithmetic Mean} \quad P_x = \frac{P_1 + P_2 + \ldots p_m}{N}, \tag{12.1}$$

where P_X = missed rainfall, mm, and P_1, P_2, P_m = precipitation from base stations (1, 2…, m). The double mass-curve approach was used to verify the consistency of the data. The standard normal homogeneity test was used to assess the homogeneity of the data.

Start, End, and Length of Growing Period (LGP)

To estimate the start, cessation, and LGP, Stern et al.'s (2006) explanation was used. According to this justification, the commencement date was a day with a cumulative rainfall depth of 20 mm over three consecutive days that was not followed by a dry spell lasting more than nine days within 30 days of the planting day. The amount of water that remains in the soil and is available to the crop after the rain stops is used to estimate when the growth season ends.

Assuming a mean evapotranspiration of 5 mm/day and a soil water retention capacity of 100 mm/meter, the end of the rainy season was defined in this study as the day when the soil water reached zero. The difference between the end and onset dates was taken as the LGP. By adapting the water balance equation to the wheat water needs, the start, finish, and LGP characteristics of growing phases for rainfed wheat crops were assessed (FAO 1978). Using the crop coefficient (Crc) and reference evapotranspiration values at the appropriate stages and computed with the available rainfall in the chosen decade, the beginning and end of the rainy period that satisfies the water need of the wheat crop at a 10-day period were determined.

Variability and Stability of Start, Cessation, and LGP

Based on the criteria outlined in Reddy (1990), the variability of the onset, offset, and LGP determined by the coefficient of variation (Cof. Var) and standard deviation (Std), as well as the stability of the onset and offset of the rainy season, was calculated. Rainy season onset and offset stability were classified by Reddy (1990) as Std in decades of 1 as extremely high, 1–2 as high, 2–4 as moderate, and > 4 as low.

$$\text{Cof.Var} = \frac{\text{Std}}{\overline{x}} \times 100, \tag{12.2}$$

$$\text{Std} = \sqrt{\sum_{n=1}^{\infty}\left(\frac{(x - \overline{x})}{n}\right)^2}. \tag{12.3}$$

Estimation of Crop Evapotranspiration

Before estimating crop evapotranspiration (Etc), it was mandatory to estimate reference evapotranspiration (ETO). Thus, ETO was estimated by the Penman–Monteith FAO 56 (PMF 56) using ***CROPWAT*** software.

$$\text{PET} = \frac{0.408\Delta(\text{Rad}_\text{n} - G) + \gamma \frac{900}{T+273} U_2(e_\text{s} - e_\text{a})}{\Delta + \gamma(1 + 0.34U_2)}, \tag{12.4}$$

$$\text{CU} = \text{Crc} * \text{PET}, \tag{12.5}$$

where

CU	Crop water consumptive use (mm day^{-1});
PET	Potential evapotranspiration (mm/day);
Crc	Crop growth water use factor;
Δ	Slope of the saturated vapor pressure curve (kPa °C^{-1});
Rad_n	Net radiation (MJ m^{-2} day^{-1});
G	Soil heat change density (MJ m^{-2} day^{-1});
T_m	Average temperature (°C).
U_2	Mean wind speed at 2.0 m height (m s^{-1});
e_s	Saturation vapor pressure (kPa) at Tm;
e_a	Actual vapor pressure (kPa); ($e_\text{s} - e_\text{a}$) is the vapor pressure deficit (kPa);
γ	Psychrometric constant (kPa °C^{-1}).

Dry and Wet Spell Patterns

The pattern of dry and wet spell conditions during the rainy season is crucial for rainfed agriculture because it helps farmers decide when to plant crops, when dry spells are likely to occur during the crops' acute growth stages, and when to plan supplemental irrigation and other agricultural operations. Dry and wet periods were examined using Standard Meteorological Decades (SMDs). SMDs were created by splitting a month into three decades (10-day periods), with the first and second decades being the first and second ten days, respectively. The third decade was created by adding the remaining days of the month. The following are the Markov chain model formulas that were used to analyze the dry and wet spell patterns (Reddy 1990).

Primary probabilities

$$\text{Prob.dr} = \frac{\text{Freq.dr}}{n}, \tag{12.6}$$

$$\text{Prob.wt} = \frac{\text{Freq.Wt}}{n}. \tag{12.7}$$

Situational probabilities

$$\text{Prob.wt.wt.} = \frac{\text{Freq.wt.wt.}}{\text{Freq.wt}}, \tag{12.8}$$

$$\text{Prob.dr.dr} = \frac{\text{Freq.dr.dr.}}{\text{Freq.dr}}, \tag{12.9}$$

$$\text{Prob.wt.dr.} = 1 - \text{Prob.dr.dr}, \tag{12.10}$$

$$\text{Prob.dr.wt.} = 1 - \text{Prob.wt.wt}, \tag{12.11}$$

where

Freq.dr	Is the number of dry decades;
Freq.wr	Is the frequency of wet decades;
Freq.dr.dr	Frequency of dry decades followed by dry decade;
Freq.wt.wt.	Frequency of wet decades followed by wet decades;
Prob. dr.	Is the chance of a decade being dry;
Prob.wt.	Is the chance of a decade being wet;
Prob. wt.wt.	Is the chance of a wet decade headed by wet decade;
Prob.dr.dr.	Is the chance of a dry decade headed by dry decade;
Prob.wt.dr	Is the chance of a wet decade headed by dry decade;
Prob.dr.wt	Is the chance of a dry decade headed by a wet decade.

Drought Analysis

Standardized Precipitation Index (*Z*)

The standardized precipitation index (Z) was used to analyze the drought conditions, and the severity of the drought was determined as follows: Extremely wet was defined as 2 or more, wet as 1.5 to 1.99, moderately wet as 1.0 to 1.49, near normal as − 0.99 to 0.99, severely dry as − 1 to − 1.49, and extremely dry as − 2 and less (McKee et al. 1993).

$$Z = \frac{(x - \mu)}{\delta}, \tag{12.12}$$

where Z is the standardized precipitation index, x is the total amount of annual and seasonal precipitation for a specific year, μ is the average yearly and seasonal precipitation for the investigated years, and δ is the Std of annual and seasonal precipitation for the considered years.

Drought Frequency Analysis

According to the occurrence of each drought class (moderate, severe, and extreme) for each station with respect to the past 30 years over each station, drought frequency in the stations was estimated for the duration of 1–3–6 months. To determine which stations were most susceptible to drought on each time scale, drought frequency analysis was used.

Variability and Trend Analysis of Rainfall

A nonparametric Mann–Kendall rank test was used to analyze the trend in the rainfall data. The alternative hypothesis H1, which assumes that there is a trend, is evaluated against the null hypothesis H0, which presupposes that there is no trend (the data are independent and randomly ordered) (Abrha 2015). The Mann–Kendall test examines a trend over time without defining whether the trend is linear, making it less sensitive to outliers (Partal and Kahya 2006). The statistics' variance, $V(s)$, is calculated by:

$$\mathrm{Var}(s) = \frac{n(n-1)(2n+5)}{18}, \tag{12.13}$$

where xi $(i = 1–n)$ is the number of independent observations, and n is the total number of observations. The parameters, Kendall, S, tau test, and p values for the rainfall trend were computed by XLSTAT. As stated in Hare (2003), rainfall variability is lower (Cof. Var < 20), moderate (20 < Cof. Var < 30), and higher (Cof. Var > 30).

Results and Discussions

Seasonal Rainfall (March—October) and Annual Rainfall Trend

The average, standard deviation, and coefficients of variation of rainfall from March to October were 330 mm, 157 mm, and 47.6%, respectively, for the Hosanna station and 178.5 mm, 74 mm, and 41.9%, respectively, for the Fonko station. Conversely, the wheat CU is 483.6 mm at Hossana and 512.17 mm at the Fonko area. This means that there must be supplementary irrigation of 153.6 mm at Hossana and 333.67 mm at the *Fonko* area. On the other hand, the annual rainfall shows no significant trend at either station (Fig. 12.2). However, this could not be an indication of no changes in rainfall patterns because the annual rainfall Cof. Var shows temporal variability. The Cof. Var of mean annual rainfall is 14.13% at *Hosanna* and 26.77% at *Fonko*,

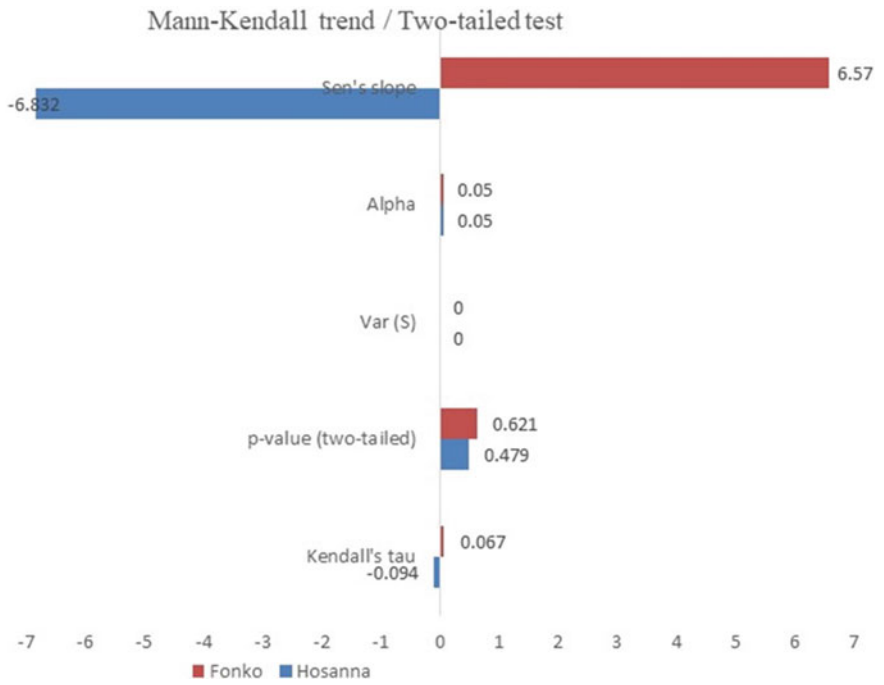

Fig. 12.2 Mann–Kendall trend/two-tailed test

respectively. Thus, the rainfall variability at *Fonko is* more moderate than that at *Hosanna.*

The seasonal rainfall at both stations is low in meeting the seasonal water requirements for a crop such as wheat, which requires approximately 450–650 mm, as recommended by the FAO. However, it can be sufficient for crops such as millet and sorghum, which are relatively tolerant to water stress. Therefore, supplementary irrigation is a suggested strategy to satisfy the shortfall water amount. July is the month with peak rainfall at both stations (Fig. 12.3).

Mesfin et al. (2018) recorded a mean annual rainfall of 1136.8 mm with a minimum of 546.5 mm to a maximum of 1556.4 mm over the previous 20 years in the Hadiya zone of Soro Woreda, which is similar to the current study under consideration. Similar findings were published by Getachew et al. (2014), who similarly recommended supplemental irrigation in the Hadiya zone. According to the NMA report, the Shashogo district in the Hadiya zone received 982.9 mm of rain annually on average with a standard deviation of 156.2 mm during the course of the previous 25 years.

According to NMSA (1996), the Cof. Var of seasonal rainfall in the area varies from 10 to 70% in most locations in Ethiopia and even more than 70% in the areas with lower rainfall in the north, northeastern, and southeastern regions, which

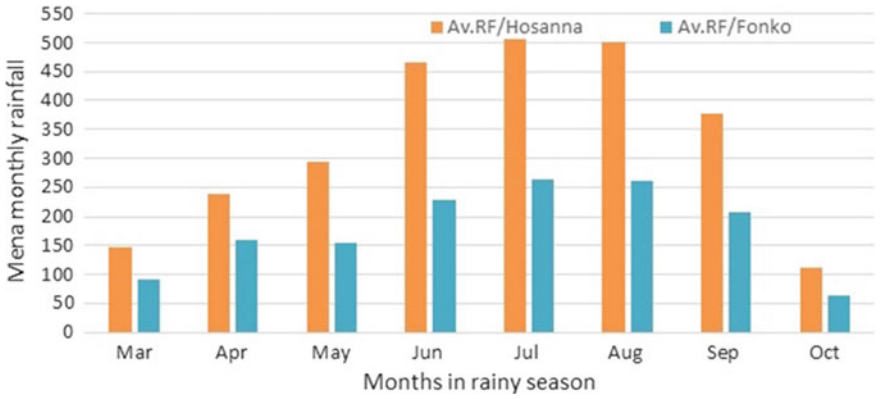

Fig. 12.3 Monthly rainfall at both stations (March–October)

include the Hadiya zone. Similarly, NMA (2007) said that Ethiopia's seasonal rainfall demonstrated significant fluctuation.

There are no common findings in the region regarding the rainfall pattern. For instance, the northern, southeastern, and southwest regions of Ethiopia experienced a significant decline in rainfall from March to September, according to (Regassa et al. 2010). According to Gebrehiwot and Simhadri (2015), the Kiremt precipitation in Ethiopia's lowlands has increased significantly by 106 mm/decade with substantial variability, whereas there has been no discernible change in the country's highlands. In southern Ethiopia, including Alaba, Angacha, Butajira, Durame, Fonko, Hossana, and Wulberag, Wagesho and Yohannes (2016) recorded an increase in seasonal Kiremt rainfall. Three stations (Alaba, Fonko, and Wolkite) exhibited a growing tendency throughout the Belg season, whereas six stations revealed a falling trend. They stated that the discrepancies in rainfall trends, with a very decreasing trend at Chida station (− 16.08 mm/year) and a very increasing trend at Butajira station (6.26 mm/year), are indicative of the increased variability in annual rainfall in the southern part of Ethiopia.

According to Abiy et al. (2014), the yearly rainfall at the Indibir station in southern Ethiopia from 1982 to 2012 exhibited substantial variability and a rising trend of 3.93 mm/year.

*Onset, Offset, Length of the Main Rainy Season (***Kiremt***), and Stability*

The results in Table 12.1 revealed that the *Kiremt* season started in the first meteorological decade of June (decade 16) for both stations, with a standard deviation of 0.75 decades (8 days) and a Cof. Var of 4.75%, indicating very high stability of the onset of *Kiremt* in both the *Hosanna* and *Fonko* areas. Similarly, the cessation of the

rainy season occurred in the last meteorological decade of October (decade 30) at both the *Hosanna* and *Fonko* stations.

At *Hossana*, except for the three minimum lengths of the Kiremt season, which were 142, 151, and 152 days in 2008, 2005, and 1987, respectively, the Kiremt season was in the range of 161–205 days in all years, with a mean length of 177 days, Std of 17 days, and Cof. Var of 9.6% (Table 12.2). Similarly, at *Fonko*, the minimum lengths of the Kiremt season are 141, 150, and 152 days in 2008, 2005, and 1987, respectively. Except for the three minimum lengths of the Kiremt season, the Kiremt season ranged from 160 to 203 days in all years, with a mean Kiremt season of 176 days, Std of 16 days, and Cof. Var of 9% (Table 12.2).

Stewart (1991) asserts that the beginning of the rainy season is a key factor to which all other seasonal rainfall qualities are connected. It establishes the expected behavior of the season's rainfall. The dependable start and end dates of the rainy season are crucial for rainfed agriculture.

At both metrological stations, the stability of the Kiremt season offset was low. This has ramifications for how the beginning, end, and length of the growing season vary from year to year. For traditional farmers, who always rely on their past experiences to schedule agricultural activities such as planting and harvesting dates, such variation is bewildering. This study is almost in agreement with a study by Yadeta et al. (2020a), which stated that in central Ethiopia, the mean Kiremt onset occurred during the second meteorological decade of June (decade 17), and the mean Kiremt end date occurred during the second meteorological decade of September (decade 26).

The NMA report states that in the Hadiya zone, the average annual rainfall decreased by 4.98 mm/year with an interannual change of $R^2 = 0.055$. The amount of rainfall varies between years, which has a large impact on LPGs. Araya and Stroosnijder (2011) confirmed that early offset, shortening of the rainy season, late commencement, and variability are the main causes of crop failure during the rainy season. As a result, the area's sporadic crop failures are most likely caused by variations in rainfall throughout the rainy season.

Table 12.1 Onset decades (A) and offset decades (B) and their stability in the Kiremt season

(A) Station	Onset (decade)	Std (decade)	Cof. Var (%)	Stability of the onset
Hosanna	16	0.75	4.75	Very high
Fonko	16	0.75	4.75	Very high
(B) Station	Offset (decade)	Std (decade)	Cof. Var (%)	Stability of the cessation
Hosanna	30	12.9	4.25	Low
Fonko	30	12.9	4.25	Low

Table 12.2 Length of Kiremt season at Hosanna and Fonko

A-Hosanna				B-Fonko		
Year	Onset (decade)	Cessation (decade)	LGP (DOY)	Onset (decade)	Cessation (decade)	LGP (DOY)
1987	16	28	152	16	28	152
1988	16	30	173	16	30	172
1989	16	30	173	16	30	172
1990	15	31	194	15	31	193
1991	16	31	183	16	31	183
1992	16	31	185	16	31	183
1993	16	30	174	16	30	172
1994	16	30	173	16	30	172
1995	16	31	183	16	31	182
1996	15	32	204	15	32	203
1997	16	29	163	16	29	162
1998	17	30	163	17	30	161
1999	16	30	175	16	30	173
2000	16	33	204	16	33	202
2001	15	32	205	15	32	203
2002	15	32	203	15	32	201
2003	16	32	192	16	32	191
2004	15	28	162	15	28	161
2005	16	28	151	16	28	150
2006	16	29	161	16	29	160
2007	16	31	181	16	31	181

(continued)

Table 12.2 (continued)

A-Hosanna				B-Fonko		
Year	Onset (decade)	Cessation (decade)	LGP (DOY)	Onset (decade)	Cessation (decade)	LGP (DOY)
2008	19	30	142	19	30	141
2009	15	31	192	15	31	191
2010	15	30	182	15	30	182
2011	15	29	171	15	29	171
2012	18	32	172	18	32	171
2013	16	30	175	16	30	174
2014	15	29	172	15	29	175
2015	16	29	162	16	29	165
2016	16	31	184	16	31	186
Mean	16	30	177	16	30	176
		Std = 17		Mean = 176	Std = 16	

*Onset and Cessation of the Small Rainy Season (*Belg*)*

The start of the *Belg* is during the last decade of April (decade 12) at both the *Hosanna* and *Fonko* stations, with standard deviations of three decades, which is on average 30 days for both. The stability of *Belg* onset is less reliable at both stations (Fig. 12.4). The offset of the Belg season is not determinable because the area has a unimodal rainfall distribution. Due to this, even the existence of the *Belg* season is less likely in the study area.

Although it is not a potential production season, *Belg* rainfall has great significance for rainfed agriculture to operate different agricultural activities. In the area, *Belg* rainfall is used mostly for land preparation and rarely for early maturing crops. Many studies have produced differing results regarding the Belg season's circumstances in Hadiya in particular and various regions of Ethiopia in general. In the Shashogo district of the Hadiya zone, Ludago and Amanuel (2018) discovered that the Belg season, which lasts from February to May, decreased by 7.06 mm/year and was extremely unpredictable. This research is similar to that of (Abiy et al. 2014; Daniel et al. 2018), who reported an unusual pattern of rainfall in Belgium. The sporadic character of Belg rainfall was documented by Yadeta et al. (2020a), who also advised presowing ground preparation. Furthermore, according to NMA (2012), the Hadiya zone and other Rift Valley areas often have shorter growing seasons with late start dates and early offset dates, especially during the short wet season.

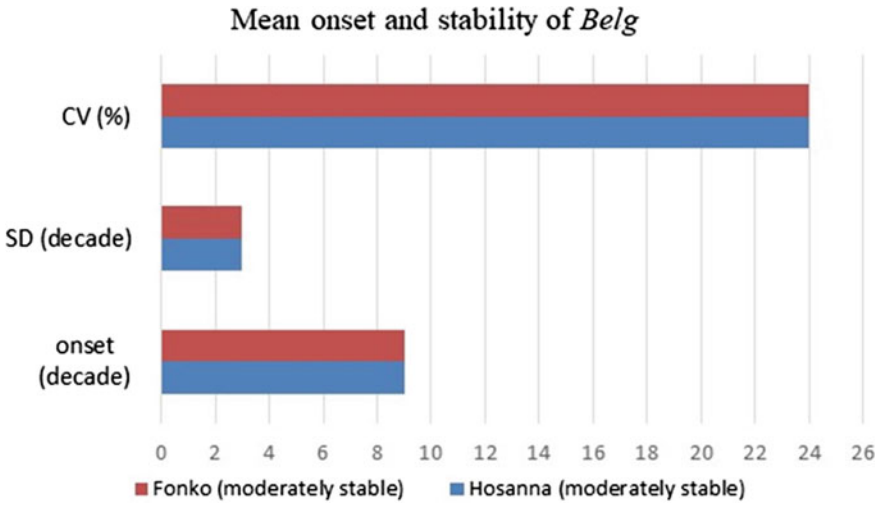

Fig. 12.4 Mean onset and stability of the small rainy season (March—May)

Dry and Wet Spell Conditions During Both Rainy Seasons (March–October)

According to Hosanna station's analysis of dry and wet decades, the 16th–27th decades had the highest probability of having a wet (Prob.wt) of more than 50%. Between the seventh and fifteenth decades, the highest risk of dry decades (Prob.dr.dr) was predicted to be greater than 50%. During every decade between the 7th and the 27th decades, it was found that the conditional probability of a wet decade followed by a wet decade (Prob.wt.wt) was larger than 50% (61–92%). Additionally, it was determined that the odds of a dry decade followed by a wet decade or vice versa (Prob.wt.dr. or Prob.dr.wt) were 3–57% and 5–39%, respectively (Table 12.3).

The 16th–27th decades at Fonko station had a probability of wetness (Prob.wt) occurring with a frequency higher than 50%. The likelihood of a dry decade (Prob.dr) with a probability greater than 50%, however, was shown to be highest between the seventh and fifteenth decades. For every decade between the 7th and 27th decades, the conditional probability of a wet decade introduced by a wet decade (Prob.wt.wt) was higher than 50% (61–91%). Similarly, it was found that the odds of a dry decade coming before a wet decade or vice versa (Prob.wt.dr or Prob.dr.wt) were 6–57% and 9–39%, respectively (Table 12.3).

Making decisions during a crop-growing season must take into account the greatest possible likelihood of receiving a specific amount of rainfall during a specific week. A reservoir's and a water harvesting dam's design must take into account the possibility of dry and rainy weather conditions during these months. A wet decade means that stored water has to stay in the reservoir, while a dry decade means that the stored water has to be released for the required purposes. This finding is similar to that of Yadeta et al. (2020a); the reported probability of having a wet decade after wetting is higher in *Kiremt* than in *Belgium,* and the probability of having a dry decade after drying is higher in *Belgium.* Konjit et al. (2016) also found that the probability of having a wet decade after a dry decade is higher in *Kiremt* than *in Belgium* and that having a dry decade after a wet decade is higher in *Belgium.*

Relative Frequency of Drought During the Kiremt and Belg Seasons

Drought frequencies revealed that on a 1-month time scale, a moderate drought occurred most frequently at *Hosanna* station (57.89%) during the period of study (1990, 1997, 2004, 2006, 2012, and 2013) and at *Fonko station* (47.05%). On a 3-month time scale, the most frequent moderate drought (33.33%) was observed at *Hosanna* (2016) *and Fonko (40%)* during the study period (1988 and 2011). Moreover, with the exception of *Hosanna* on the 1-month time scale and on the 6-month time scale, severe droughts occurred more frequently than extreme droughts (Table 12.4A).

Table 12.3 Initial and conditional probabilities of dry and wet spells during both rainy seasons at both stations

Hossana							Fonko					
SMD	Prob.dr	Prob.wt	Prob.dr.dr	Prob.dr.wt	Prob.wt.dr	Prob.wt.wt	Prob.dr	Prob.wt	Prob.dr.dr	Prob.dr.wt	Prob.wt.dr	Prob.wt.wt
D7	84	16	97	39	3	61	84	16	93	39	7	61
D8	84	16	97	31	3	69	84	16	94	33	6	67
D9	86	14	96	32	4	68	86	14	92	32	8	68
D10	67	33	92	29	8	71	67	33	87	29	13	71
D11	61	39	94	24	6	76	61	39	88	24	12	76
D12	53	47	86	18	14	82	53	47	80	19	20	81
D13	61	39	90	22	10	78	61	39	87	25	13	75
D14	60	40	82	17	18	83	60	40	82	26	18	74
D15	59	41	75	13	25	87	59	41	88	18	12	82
D16	37	63	76	16	24	84	37	63	75	21	25	79
D17	23	77	55	10	45	90	23	77	55	14	45	86
D18	22	78	53	8	47	92	22	78	53	12	47	88
D19	25	75	53	11	47	89	25	75	53	14	47	86
D20	26	74	45	20	55	80	26	74	43	21	57	79
D21	24	76	53	16	48	84	24	76	48	17	53	83
D22	29	71	50	17	50	83	29	71	50	21	50	79
D23	26	74	43	15	57	85	26	74	43	19	57	81
D24	23	85	55	11	45	89	23	74	55	15	45	85
D25	17	83	52	5	48	95	17	85	52	9	48	91
D26	23	77	60	12	40	88	23	83	54	13	46	88
D27	44	56	80	17	20	83	44	77	73	17	27	83

Table 12.4 (A) Drought frequency (B) Number of drought occurrences during the Kiremt season

A Station	Severity level	Drought frequencies at 1–3–6-month time scales		
		SPI-1	SPI-3	SPI-6
Hosanna	Moderate	57.89	33.33	60
	Severe	21.05	50	0
	Extreme	21.05	16.7	40
Fonko	Moderate	47.05	40	33.3
	Severe	35.29	60	66.67
	Extreme	17.64	0	0
B Station	Severity level	No. of drought events at 1–3–6-month time scales		
		SPI-1	SPI-3	SPI-6
Hosanna	Moderate	11	2	3
	Severe	4	3	0
	Extreme	4	1	2
Fonko	Moderate	8	2	1
	Severe	6	3	2
	Extreme	3	0	0

Similarly, the number of drought event occurrences in Table (12.4B) shows that the highest number of severe drought events (2) on a 6-month time scale occurred at *Fonko* but did not occur at *Hosanna.* The highest number of extreme drought events (4) was also experienced for *Hosanna* and (3) for *Fonko* at the 1-month time scale.

On a 1-month time scale, the number of drought occurrences also showed that there were between 8 and 11 moderate drought events. Fonko experienced the least moderate drought events (just 8), whereas Hosanna experienced the most (11). Moreover, the 6-month time scale showed that Hosanna had the most extreme drought episodes (2).

Fonko had the highest occurrence of moderate drought events (9) on a 1-month time scale, and *Hosanna* had the highest occurrence of moderate drought events (2) on a 3-month time scale. No extreme drought event occurred at *Fonko* at either the 3- or 6-month time scales (Table 12.5A). The relative drought frequency during the *Belg* season ranged from 46.7 to 90% on a 1-month time scale, with the highest drought frequency (90%) observed at *Fonko* and the lowest drought frequency observed at *Hosanna* (46.7%).

The highest frequency (40%) for moderate drought occurrences was found at Fonko at the 3-month time scale (Table 12.5B). In Hosanna, on a three-month time scale, severe drought occurrences occurred the most frequently (60%). On a three-month time scale, neither station experienced an extreme drought. Hosanna suffered the largest frequency (25%) of extreme drought, according to the 6-month time frame. On a six-month time period, Fonko had the highest frequency (33.3%) of severe drought episodes.

Table 12.5 (A) Drought frequency and number of drought occurrences (B) during the Belg season

A-Station	Severity level	Drought frequencies at 1–3-6–month time scales		
		SPI-1	SPI-3	SPI-6
Hosanna	Moderate	46.7	40	75
	Severe	46.7	60	0
	Extreme	6.7	0	25
Fonko	Moderate	90	0	66.7
	Severe	10	0	33.3
	Extreme	0	0	0
B-Station	Severity level	No. of drought events at 1–3–6-month time scales		
		SPI-1	SPI-3	SPI-6
Hosanna	Moderate	7	2	3
	Severe	7	3	0
	Extreme	1	0	1
Fonko	Moderate	9	0	4
	Severe	1	0	2
	Extreme	0	0	0

Generally, even though all drought events occur differently in the study area, moderate drought occurs most frequently at both stations for the three time scales. The drought frequency result is exceedingly similar to that of Yadeta et al. (2020a), who strongly argue that the more frequent drought events in the cropping season are, the greater the crop failure due to late onset, early offset, and prolonged dry weeks. In similar ways, the frequent drought incidences are implications of the problems of late onset, early offset, and prolonged dry days, particularly in the crop-growing season. Likewise, Solomon (2020) reported occurrences of extreme-to-moderate drought events in Rift Valley regions, an area similar to the current study. The study confirmed the highly spatiotemporally varying nature of long-term drought conditions in the region.

Wheat Length of Growing Period (LGP)

Minimum wheat LGPs of 141, 142, 146, 147, and 149 days were recorded at the Fonko station in 2005, 1988, 2006, 2012, 1992, and 1990, respectively (Table 12.6A). With a mean LGP of 150 days, a Std of 2.9 days, and a Cof. Var of 2%, the main growing season lasted between 150 and 152 days (Table 12.6A). However, at Hossana, minimum wheat LGPs of 144, 148, and 149 days were noted in 1988, 2008, and 2012, respectively (Table 12.6B). A mean LGP of 152 days, Std of 2.6 days, and a Cof. A Var of 2% characterize the main growth season, which lasted between 152 and 161 days (Table 12.6B).

Table 12.6 Onset, offset, and length of growing period (LGP) of wheat crop

Fonko (A)				Hosanna (B)		
Year	Onset	Offset	LGP	Onset	Offset	LGP
1987	183	335	152	183	335	152
1988	193	335	142	191	335	144
1989	183	335	152	183	335	152
1990	186	335	149	183	335	152
1991	183	335	152	183	335	152
1992	188	335	147	183	338	155
1993	183	335	152	183	335	152
1994	183	335	152	183	335	152
1995	183	335	152	183	335	152
1996	185	335	150	183	335	152
1997	183	335	152	183	335	152
1998	185	335	150	183	335	152
1999	186	335	149	183	335	152
2000	183	335	152	183	344	161
2001	184	335	151	183	335	152
2002	185	335	150	183	335	152
2003	183	335	152	183	335	152
2004	183	335	152	183	335	152
2005	194	335	141	184	335	151
2006	189	335	146	185	341	156
2007	188	335	147	183	335	152
2008	185	335	150	187	335	148
2009	186	335	149	183	335	152
2010	184	335	151	183	335	152
2011	184	335	151	183	335	152
2012	189	335	146	186	335	149
2013	183	335	152	183	335	152
2014	183	335	152	183	335	152
2015	183	335	152	183	335	152
2016	184	335	151	183	335	152
Mean	185	335	150	184	336	152
Std	2.956	0	2.956	1.69	1.99	2.59

It is understandable in the results that there is interannual variability in wheat LGP that could in turn affect the yield of the crop from year to year. It is also confusing to farmers to make decisions on agricultural operations, such as when to start presowing land preparation and appropriate sowing dates. The result is identical to that of Roba et al. (2021), who stated that in the middle Awash in Ethiopia during the main rainy season, the maize LGP ranged from 93 to 165 rainfall days. This result is consistent with that of Yadeta et al. (2020a), who reported a mean LGP of 113–118 rainfall days for several crops in the same region.

Dry and Wet Decade Conditions During Each Wheat-Growing Stage

The findings in Table 12.7A show that the wheat crop's first growth stage, or (D19–D20), experienced a rainy decade (July 1–15). As a result, the 19th and 20th decades can see a probability of wet conditions (Prob.wt) of more than 75%, while the probability of a dry decade was from 25 to 26%. The likelihood of two rainy decades occurring in the series was determined to be between 80 and 89%, while the likelihood of two dry decades occurring in the sequence was between 43 and 53%. It was shown that the likelihood of a wet decade following a dry decade or vice versa ranged from 11 to 57%. This indicates a high probability of wet conditions. Therefore, the rainfall during this growing season is sufficient to meet the wheat water need in amount and/or distribution during its initial growth stage because of the highest probability occurrence of wet spells.

According to the probability of wet and dry decades occurring during the crop's developmental stage, or (D20–D23) (July 16–August 15), wet decades were more likely to occur more than 76% of the time in the 20th–23rd decades, while dry decades were more likely to occur between 24 and 29% of the time. Two consecutive wet decades had a likelihood of occurring in the range of 83%–85%, while two consecutive dry decades had a probability of occurring in the range of 43%–53%. It was discovered that between 15 and 57% of times, a wet decade will be followed by a dry decade, and vice versa. Thus, decades in the developmental stage of wheat satisfy the crop water requirement of wheat crops without additional water (Table 12.7B).

Similarly, in the midseason growth stage of the crop, it can be noted that the probabilities of occurrence of wet and dry decades fall in the ranges above 17% and 87%, respectively, while the probabilities of two wet and two dry decades occurring consecutively are in the ranges of 43% and 95%, respectively. These results revealed that the probability occurrence of dry decades during this stage of the crop was relatively high (Table 12.7C). In a similar fashion, for the late growth stage, there is a high probability of dry decade occurrence. Among all the growing stages, the late growth stage was found to have the lowest probability occurrence of both a single wet spell and consecutive wet spell distributions of 1% and 69%, respectively, and

Table 12.7 Probability distribution of dry and wet spells in Kiremt during the initial (A), development (B), mid-growth (C), and late (D) growth stages of wheat at Hosanna station (I) and Fonko station (II)

A I-SMD	Prob.dr	Prob.wt	Prob.dr.dr	Prob.dr.wt	Prob.wt.dr	Prob.wt.wt
D19	0.25	0.75	0.53	0.11	0.47	0.89
D20	0.26	0.74	0.45	0.20	0.55	0.80
II-SMD	PD	PW	PDD	PDW	PWD	PWW
D19	0.25	0.75	0.53	0.14	0.47	0.86
D20	0.256	0.743	0.43	0.21	0.57	0.79
B I-SMD	Prob.dr	Prob.wt	Prob.dr.dr	Prob.dr.wt	Prob.wt.dr	Prob.wt.wt
D20	0.26	0.74	0.45	0.20	0.55	0.80
D21	0.24	0.76	0.53	0.16	0.48	0.84
D22	0.29	0.71	0.50	0.17	0.50	0.83
D23	0.26	0.74	0.43	0.15	0.57	0.85
II-SMD	Prob.dr	Prob.wt	Prob.dr.dr	Prob.dr.wt	Prob.wt.dr	Prob.wt.wt
D20	0.256	0.743	0.43	0.21	0.57	0.79
D21	0.242	0.757	0.48	0.17	0.53	0.83
D22	0.293	0.706	0.50	0.21	0.50	0.79
D23	0.263	0.736	0.43	0.19	0.57	0.81
C I-SMD	Prob.dr	Prob.wt	Prob.dr.dr	Prob.dr.wt	Prob.wt.dr	Prob.wt.wt
D23	0.26	0.74	0.43	0.15	0.57	0.85
D24	0.23	0.85	0.55	0.11	0.45	0.89
D25	0.17	0.83	0.52	0.05	0.48	0.95
D26	0.23	0.77	0.60	0.12	0.40	0.88
D27	0.44	0.56	0.80	0.17	0.20	0.83
D28	0.59	0.41	0.94	0.16	0.06	0.84
D29	0.77	0.23	0.93	0.23	0.07	0.77
II-SMD	Prob.dr	Prob.wt	Prob.dr.dr	Prob.dr.wt	Prob.wt.dr	Prob.wt.wt
D23	0.26	0.707	0.43	0.19	0.57	0.81
D24	0.23	0.737	0.55	0.15	0.45	0.85
D25	0.17	0.847	0.52	0.09	0.48	0.91
D26	0.23	0.833	0.54	0.13	0.46	0.88
D27	0.44	0.773	0.73	0.17	0.27	0.83
D28	0.59	0.563	0.89	0.16	0.11	0.84
D29	0.77	0.410	0.89	0.23	0.11	0.77
D I-SMD	Prob.dr	Prob.wt	Prob.dr.dr	Prob.dr.wt	Prob.wt.dr	Prob.wt.wt
D30	0.87	0.13	0.98	0.31	0.02	0.69
D31	0.94	0.06	1.00	0.61	0.00	0.39
D32	0.96	0.04	1.01	0.55	-0.01	0.45

(continued)

Table 12.7 (continued)

D33	0.99	0.01	1.03	0.33	-0.03	0.67
II-SMD	Prob.dr	Prob.wt	Prob.dr.dr	Prob.dr.wt	Prob.wt.dr	Prob.wt.wt
D30	0.87	0.13	0.94	0.31	0.06	0.69
D31	0.85	0.06	0.96	0.61	0.04	0.39
D32	0.88	0.04	0.98	0.55	0.02	0.45
D33	0.90	0.01	0.99	0.33	0.01	0.67

the highest probability occurrence of dry spells and consecutive dry spells was found to be above 87% (Table 12.7D).

Generally, the probability occurrence of wet decades was higher than the corresponding probability occurrence of dry decades during all stages of growth except the late growth stage. In the late growing stage, dry conditions are more likely because the rainy season is about to cease. Additionally, crop water needs will have a greater probability of ceasing in this stage. This determination of dry and wet conditions in each growing week of a crop is important information for multifaceted decision-making, including supplementary irrigation, fertigation, and other agronomic practices. In line with this, Konjit et al. (2016) argue that effective agricultural water management can be possible with the use of information such as dry and wet spell occurrence conditions.

Moreover, crops use water to chill, and weather conditions drive this process (Broner and Schneekloth 2003). As a result, the requirement for crop water increases when a dry decade occurs during the growing stage of the crop. According to Broner and Schneekloth (2003), environmental factors, which may occasionally include dry conditions, play a major role in how much water crops require. The prevalence of dry and wet spells during the growing season is also a good indicator of whether the season is healthy for the crop in question, according to Yadeta et al. (2020a).

Characterizing the **Kiremt** *Season in Terms of Dry and Wet Decades*

Since the farmers in the area mostly depend on rainfed agriculture for their livelihood, describing the Kiremt season in terms of dry and wet spell conditions in general provides crucial information for other crops cultivated in the study area in addition to the wheat LGP. According to the findings at Hossana (Table 12.7A), decade 25 is the wettest, while decade 9 is the driest. The weeks between decade 16 and decade 27 had the highest likelihood of rainy decades following rainy decades, suggesting a chance for greater soil water for scheduling agricultural operations during those times. In other words, at certain times, farmers face relatively less risk when making decisions about growing crops.

However, the decades outside decade 27 need to be closely watched since the crop may suffer from insufficient soil moisture. The period between decades 16 and 27 had the highest likelihood of rain and rain after rain at Fonko (Table 12.7B). The appropriate choice was reached to plant crops in decade 16; however, during the decades in October, crops may suffer from a lack of soil water since the crop may need more water as it grows. Thus, it is essential to establish suitable moisture conservation practices during the wet seasons (decades 16–27) so that these practices can be used later in the growing season.

In general, in the Kiremt season, agricultural operations adopt promising soil water conditions during the 16th–27th decades. The potential for successively wet decades creates a chance to collect extra water for use later in the crop development process, when the demand for water is relatively larger. Yadeta et al. (2020a) reported agreeable results that July and August are peak rainfall months where there is excess rainwater in the *Kiremt* season. Furthermore, farmers can use July and August as water harvesting months for supplementary irrigation. Konjit et al. (2016) also argued that rainfed agriculture in Ethiopia mainly depends on the rainfall of *the Kiremt* season, and thus, understanding the condition of dry and wet weeks during *Kiremt* helps as pillar information for agricultural decision-making.

Wheat-Growing Stages, Crop Coefficient (Crc) Adjustment, and Water Need

In the area, the appropriate wheat planting date is July 1. Therefore, counting the duration of days for each growing stage does not spontaneously exist in the same months. This makes the recommended Crc vary (Table 12.8).

Therefore, Crc was adjusted (Table 12.9A), and CU was estimated as indicated in Table 12.9B, C. The months and growth stages do not match one another, as illustrated in Table 12.8. The PET and Crc values are therefore inconsistent. The CU was therefore calculated on a monthly basis. Hence, Crc has to be fixed on a monthly basis, as shown in Table 12.9A. At Hossana, the wheat CU for the entire LGP was 483.6 mm, whereas it was 512.17 mm in the Fonko area.

To satisfy their water needs during their LPG, crops need prolonged wet conditions in the period. Conversely, prolonged dry spell conditions during the crop LGP restrict the crop from satisfying its water need. Hence, it follows that a late start shortens the time available for crop growth and the opportunity to meet the crop's water needs. The potential to satisfy crop water needs decreases with decreasing evapotranspiration and rainy season length (Yadeta et al 2020b: Roba et al. 2021). This study illustrated that the wheat crop grown in a *Hosanna* needs less water per day than the wheat crop grown in the *Fonko* area. Throughout the crop-growing season, there is higher crop water demand in *Fonko* than in the *Hossana* area; therefore, decision-makers, farmers, and other stakeholders need to consider this scientific information while producing wheat in these areas.

Table 12.8 Duration of growth stages (A) and daily ETO and adjusted Crc value for wheat crop-growing stages (B)

(A)

Crop	Total growing period (days)	Initial stage	Crop dev. stage	Mid-season stage	Late-season stage
Wheat	150	15	30	65	40

Starting and ending dates for each stage	
Planting date	July 1
Initial stage (15 days)	July 1–July 15
Crop development stage (30 days)	July 16–August 14
Mid-season stage (65 days)	August 15–October 19
Late-season stage (40 days)	October 20–November 29
Estimated last day of harvest	November 29

(B)

Month	June	July	August	September	October	November	December
ETo (mm/days): *Hosanna*	3.27	2.93	3.38	4.05	4.96	4.8	4.73
ETo (mm/days): *Fonko*	3.96	3.42	3.96	4.37	4.80	4.58	4.60

Growth stages		Initial stage	Crop dev. stage	Mid season	Late season	
Crc per.gr.stage		0.35	0.75	1.15	0.45	
Crc per.month		0.53	0.92	1.15		

Conclusion

This study investigated how rainfall and the occurrence of drought varied annually and within rainy seasons in connection to wheat harvests in the study area. The onset of the growing season is the last week of March, but the amount is small for planting; therefore, the effective start date of rain is in April and advances in July. The effective termination date is October. The third decade of June and the first decade of July are the best times to plant during the main wet season. The probability of getting repeated wet days is greater than the rest of the season; hence, water harvesting is recommended, and moisture is conserved for the later days at the end of the growing season, when planted crops would require more water. In the area, dry spell frequency is higher during the period close to the start date and toward the offset of the season. The mean start of the growing season is the last week of March for both stations where the growing season ends the last week of October in most years. Late-maturing crops raised close to the Hosanna and Fonko regions

Table 12.9 Estimated Crc for each wheat-growing month (A) and average daily, monthly, and seasonal wheat crop water requirements at Hosanna station (B) and Fonko station (C)

A-Wheat-growing months	*The monthly estimated Crc*	
July (**Crc**)	$\frac{15}{31} \times 0.35 + \frac{15}{31} \times 0.75 = 0.53$	
August (**Crc**)	$\frac{15}{31} \times 0.75 + \frac{15}{30} \times 1.15 = 0.92$	
September (**Crc**)	1.15	
October (**Crc**)	$\frac{20}{31} \times 1.15 + \frac{10}{31} \times 0.45 = 0.88$	
November (**Crc**)	0.45	
B-Hossana station months	*Average daily ETcrop*	*Average monthly ETcrop*
July (CU)	$2.93 \times 0.53 = 1.55$ mm/day	$31 \times 1.55 = 48.05$ mm/month
August (CU)	$3.38 \times 0.92 = 3.10$ mm/day	$31 \times 3.10 = 96.1$ mm/month
September (CU)	$4.05 \times 1.15 = 4.65$ mm/day	$30 \times 4.65 = 139.5$ mm/month
October (CU)	$4.96 \times 0.88 = 4.36$ mm/day	$31 \times 4.36 = 135.16$ mm/month
November (CU)	$4.8 \times 0.45 = 2.16$ mm/day	$30 \times 2.16 = 64.8$ mm/month
Whole growing period (CU)		483.6 mm
C-Fonko station months	*Average daily ETcrop*	*Average monthly ETcrop*
July (CU)	$3.42 \times 0.53 = 1.81$ mm/day	$31 \times 1.81 = 56.11$ mm/month
August (CU)	$3.96 \times 0.92 = 3.64$ mm/day	$31 \times 3.64 = 112.84$ mm/month
September (CU)	$4.37 \times 1.15 = 5.02$ mm/day	$30 \times 5.02 = 150.6$ mm/month
October (CU)	$4.80 \times 0.88 = 4.22$ mm/day	$31 \times 4.22 = 130.82$ mm/month
November (CU)	$4.58 \times 0.45 = 2.06$ mm/day	$30 \times 2.06 = 61.8$ mm/month
Whole growing period (CU)		512.17 mm

must be planted after the ends of March and April, respectively. Additionally, Crc is modified, and the amount of water needed for wheat is identified; as a result, Kc may be applied to irrigation and related research. Most notably, these results can be applied to agrometeorological operations and irrigation design scheduling tasks.

Acknowledgements The Ethiopian NMA is acknowledged by the authors for providing the weather data.

References

Abbas F, Rehman I, Adrees M, Ibrahim M, Saleem F, Ali S, Rizwan M, Salik R (2018) Prevailing trends of climatic extremes across Indus Delta of Sindh Pakistan. Theoret Appl Climatol 131(3–4):1101–1117

Abiy G, Shoeb Q, Girma M (2014) Analysis of seasonal rainfall variability for agricultural water resource management in Southern Region, Ethiopia. J Nat Sci Res 4(11):2014

Abrha MG (2015) Local climate trends and farmers' perceptions in Southern Tigray, Northern Ethiopia. Int J Environ Sustain 4(3)

Araya A, Stroosnijder L (2011) Assessing drought risk and irrigation need in northern Ethiopia. Agric Meteorol 151:425–436

Asfaw A, Simane B, Hassen A, Bantider A (2018) Variability and time series trend analysis of rainfall and temperature in north central Ethiopia: a case study in Woleka subbasin. Weather Clim Extremes 19:29–41

Asha KV, Munisamy G, Bhat AR (2012) Impact of climate change on rainfed agriculture in India: a case study of Dharwad. Int J Environ Sci Dev 3(4):368–371

Bekele B, Alamirew T, Kebede A, Zeleke G, Melesse AM (2017a) Analysis of rainfall trend and variability for agricultural water management in Awash River Basin, Ethiopia. J Water Clim Change 8(1):127–141

Bekele F, Korecha D, Negatu L (2017b) Demonstrating effect of rainfall characteristics on wheat yield: case of Sinana District, South Eastern Ethiopia. Agric Sci 8(05):371

Berhane G, Paulos Z, Tafere K, Tamiru S (2011) Food-grain consumption and calorie intake patterns in Ethiopia. ESSP II working paper23. International food policy research institute. Ethiop Strategy Support program II, Addis Ababa, Ethiopia

Broner I, Schneekloth J (2003) Seasonal water needs and opportunities for limited irrigation for colorado crops, newsletter of the extension irrigation services. Department of Civil Engineering, Colorado State University. No. 4.718. http:/www.googlesearch/waterrequirement

Bruijnzeel LA (2004) Hydrological functions of tropical forests not seeing the soil for the trees. Agric Ecosyst Environ 104(1):185–228

CSA (2021) Agricultural sample survey: report on area and production of major crops (Private peasant holdings, Meher Season). Volume I Statistical Bulletins 590, Addis Ababa, Ethiopia

Daniel B, Tena A, Asfaw K, Gete Z, Assefa MM (2018) Analysis of rainfall trend and variability for agricultural water management in Awash River Basin, Ethiopia. J Water Clim Change. IWA Publishing

Deressa TT, Hassan RM, Ringler C (2011) Perception of and adaptation to climate change by farmers in the Nile basin of Ethiopia. J Agric Sci 14(1):23–31

FAO (Food and Agriculture Organization) (1978) Report on the agro-ecological Zones Project, vol 1. Methodology and Results of Africa, Rome, p 1978

Gebrehiwot M, Simhadri S (2015) Local climate trends and farmers' perceptions in Southern Tigray, Northern Ethiopia. Am J Environ Sci 11(4):262

Gomoro G, Tekalign S, Uttama Reddy R (2014) Climate variability and its local perception and adaptation measures in Weliso Woreda, Ethiopia, East Africa. Int J Sci Res (IJSR). 3(11):1510–1515, Nov 2014

Granados R, Soria J, Cortina M (2017) Rainfall variability, rainfed agriculture and degree of human marginality in North Guanajuato, Mexico. Singap J Trop Geogr 38(2):153–166

Hare W (2003) Assessment of knowledge on impacts of climate change, contribution to the specification of Art, 2 of the UNFCCC. WBGU

Konjit S, Asfaw K, Shoeb Q, Fitsume Y (2016) Wet and dry spell analysis for decision making in agricultural water management in the eastern part of Ethiopia. West Hararghe 8(7):92–96. https://doi.org/10.5897/.IJWREE.0650

Ludago SC, Amanuel TW (2018) Socioeconomic impacts of climate change on smallholder livelihoods in Shashogo District, Hadiya Zone, Ethiopia. J Environ Earth Sci 8(2):2018

McKee TB, Doesken NJ, Kleist J (1993) The relationship of drought frequency and duration to time scales. In: Proceeding 8th conference on applied climatology. Anaheim, California, pp 179–184

Meresa HK (2010) Analysis of rainfall variability and frequencies and implications on water storage and rain fed agriculture development in Abbay River basin, Ethiopia

Mesfin A, Tekalign S, Sishaw T (2018) Climate variability, causes and consequences perceived by smallholder farmers of soro Woreda, Hadiya Zone, Southern Nations', Nationalities 'and Peoples' Region, Ethiopia. J Sci Sustain Dev (JSSD), 2018, 6(1):35–49. https://doi.org/10.20372/au.jssd.6.1.2018.081

Minot N, Warner J, Lemma S,Kassa L, Gashaw A, Rashid S (2015) The wheat supply chain in Ethiopia: patterns, trends, and policy options. International Food Policy Research Institute (IFPRI), Washington, DC

MoA (Ministry of Agriculture) (2010) Crop variety register. Issue No 13. Animal and Plant Health Regulatory Directorate. Addis Ababa, Ethiopia. P 227

National Meteorological Agency (NMA) (2007) Climate change national adaptation program of action (NAPA) of Ethiopia. Technical report, United Nations Development Program (UNDP). Addis Ababa, Ethiopia: NMA

National Meteorological Service Agency (NMSA) (1996) Climatic and agro climatic resources of Ethiopia. Vol. 1, No. 1. National Meteorology Service Agency of Ethiopia, Addis Ababa, p 137

National Metrological Agency (NMA) (2012) Climate change national adaptation programme of Ethiopia (NAPA). Addis Ababa, Ethiopia p 96

Ngetich KF, Mucheru Muna M, Mugwe JN, Shisanya CA, Diels J, Mugendi DN (2014) Length of growing season, rainfall temporal distribution, onset and cessation dates in the Kenyan highlands. Agric Meteorol 188:24–32

Partal T, Kahya E (2006) Trend analysis in Turkish precipitation data. Hydrol Process 20(9):2011–2026

Reddy SJ (1990) Methodology: agro climatic analog technique and applications as relevant to dry land agriculture. Agro Climatol Ser Eth 86/21-WMO/UNDP, NMSA, p 60

Regassa S, Christina G, Gina E (2010) The rain doesn't come on time anymore: poverty, vulnerability, and climate variability in Ethiopia. Oxfam Policy Pract Clim Change Resilience 6(1):90–134

Roba NT, Kassa AK, Geleta DY (2021) Modeling climate change impacts on crop water demand, middle Awash River basin, case study of Berehet woreda. Water Pract Technol. https://doi.org/10.2166/wpt.2021.033

Singh A (2015) A study on impact of climatic change on cropping pattern under rainfed area in Shahpura block of Jabalpur district (MP) (Doctoral dissertation, JNKVV)

Solomon AY (2020) spatiotemporal analysis of drought variability in central Ethiopia. J Water Clim Change.https://doi.org/10.2166/wcc.2020.226

Statista (2021) Top wheat-producing countries 2020/2021. Accessed in Aug 2021. https://www.statista.com/statistics/237912/global-top-wheat-producing-countries

Stern R, Rijks D, Dale I, Knock J (2006) INSTAT climate guide. University of Reading UK, Statistical Service Center

Stewart JI (1991) Managing climatic risk in agriculture. World Bank. In: Proceedings of the 10th agriculture sector symposium: risk in agriculture. Washington D.C., January 9–10, 1990. Dennis Holden, Peter Hazell and Anthony Pritchard, editions. pp 17–37

Sununtnasuk C (2013) Calculating wheat flour consumption: Sources and methods. In smarter features cost and economic benefit training workshop, vol 14, pp 1–61, December 10–14, 2013. USAID SPRING, Dares Salaam, Tanzania

Tabari H, Meron TT, Willems P (2015) Statistical assessment of precipitation trends in the upper Blue Nile River basin. Stoch Environ Res Risk Assess. https://doi.org/10.1007/s00477-015-1046-0

USDA (2019) USDA world markets and trade report. Accessed on 15 Dec 2022

USLC (United State Library of Congress) (2005) Ethiopia, Country Studies Handbook, Retrieved 17 Dec 2014, at 9:45pm from http://countrystudies.us/ethiopia/

Valizadeh J, Ziaei SM, Mazloumzadeh SM (2013) Assessing climate change impacts on wheat production (a case study). J Saudi Soc Agric Sci 13(2):107–115

Wagesho N, Yohannes E (2016) Analysis of rainfall variability and farmers' perception toward it in agrarian community of Southern Ethiopia. J Environ Earth Sci 6(4)

Wood SA, Jina AS, Jain M, Kristjanson P, Defries RS (2014) Smallholder farmer cropping decisions related to climate variability across multiple regions. Glob Environ Chang 25:163–172

World Bank (2006) Managing water resources to maximize sustainable growth: a country water resources assistance strategy. World Bank, Washington, DC

Yadeta D, Kebede A, Tessema A (2020a) Climate change posed agricultural drought and potential of rainy season for effective agricultural water management, Kesem subbasin, Awash Basin. Theor Appl Climatol. https://doi.org/10.1007/s00704-020-03113-7

Yadeta D, Kebede A, Tessema N (2020b) Potential evapotranspiration models evaluation, modeling, and projection under climate scenarios, Kesem subbasin, Awash River basin, Ethiopia. Model Earth Syst Environ 6. https://doi.org/10.1007/s40808-020-00831-9

Zegeye F, Alamirew B, Tolossa D (2020) Analysis of wheat yield gap and variability in Ethiopia. Agric Econ 5(4):89–98

Chapter 13
Developing a Multilinear Regression Water Consumption Model: A Case Study of Addis Ababa City, Ethiopia

Yonas T. Assefa, Mukand S. Babel, Janez Sušnik, and Assefa M. Melesse

Abstract Determining water consumption using an appropriate water consumption method is fundamental in ensuring future domestic water security. Many water consumption projection studies, especially in developing countries, are performed using the traditional approach of forecasting using population and per capita consumption. In this study, we developed a new water consumption projection model for Addis Ababa by considering socioeconomic and climate change factors. The model was developed using multilinear regression statistical analysis to select the most significant factors affecting domestic water consumption. The results show that socioeconomic development, specifically rapid population growth, is the most significant factor driving water consumption in Addis Ababa.

Keywords Water security · Multilinear regression model · Water consumption forecast · Water supply · Addis Ababa

Y. T. Assefa (✉)
Ethiopian Construction Design and Supervision Works Corporation, Addis Ababa, Ethiopia
e-mail: yonasabaye@gmail.com

M. S. Babel
Water Engineering and Management, School of Engineering and Technology, Asian Institute of Technology, Pathumthani 12120, Thailand

J. Sušnik
Integrated Water Systems and Governance Department, IHE Delft Institute for Water Education, 2601 DA Delft, The Netherlands

A. M. Melesse
Department of Earth and Environment, Florida International University, Modesto A. Maidique Campus, Miami, FL 33199, USA
e-mail: melessea@fiu.edu

A. M. Melesse et al. (eds.), *Land and Water Degradation in Ethiopia*, Springer Geography, https://doi.org/10.1007/978-3-031-60251-1_13

Abbreviations

AAWSA	Addis Ababa Water Supply and Sewerage Authority
AMSL	Above Mean Sea Level
AWDO	Asian Water Development Outlook
CL	Confidence Level
CSA	Central Statistical Agency (Ethiopia)
DALYs	Disability-Adjusted Life Years
DEM	Digital Elevation Model
ETB	Ethiopian Birr (currency)
GCM	Global Climate Model
GPP	Gross Provincial Product
IPCC	Intergovernmental Panel on Climate Change
MENA	Middle East and North Africa
NMA	National Meteorological Agency, Ethiopia
RCPs	Representative Concentration Pathways
RCM	Regional Climate Model
SPSS	Statistical Package for the Social Sciences
SRES	Special Report on Emissions Scenarios
WHO	World Health Organization

Introduction

Drinking water supply is a fundamental component of water security. However, meeting the required drinking water demand is becoming a major challenge across the world, particularly in developing countries due to an increase in consumption. For this reason, access to clean water and sanitation has become one of the sustainable development goals (SDG6).

Rapid population growth, urbanization, economic growth, and climate change are some of the major factors driving water consumption (Hardy et al. 2015). As such, urban areas, especially in lower income countries, face considerable water supply and security challenges in the near future (Arsiso et al. 2017). Addis Ababa, Ethiopia, is no different.

Addis Ababa, the capital city of Ethiopia, is home to 25% of the urban population of the country and is one of the fastest growing cities in Africa (World-Bank 2015). Addis Ababa is also the headquarter of the African Union (AU) and a seat for various international organizations. The city is expanding rapidly, with many industrial parks, apartments, condominiums, and hotels under construction (Arsiso et al. 2017).

Ndaruzaniye (2011) reported that the population of Addis Ababa increased from 2 to 4 million within fifteen years, but investment in the water supply and sanitation coverage did not follow suit. The city expanded from 220 to 540 km^2 in the same period, while the water supply coverage stood at 55%. Approximately half of

the population was served for less than 12 h per day, and a quarter of the population had no service at all (Ndaruzaniye 2011). Recent studies by Bayrau (2014), Arsiso et al. (2017), and Assefa et al. (2018) also state that the city still suffers from water supply problems. Thus, investigating and determining the existing and future domestic water security status of the city considering socioeconomic and climate factors will be essential. The proper design and implementation of water supply schemes and demand management practices are needed to address the water supply issues of the city. To design and implement water supply schemes, it is fundamental to have a reliable water demand/consumption projection. This will also be very useful to assess the future domestic water security of the city.

Traditionally, water consumption projection was performed by considering only the population and the per capita water consumption, which might lead to either overestimation or underestimation of demand (Assefa et al. 2018). However, it is vital to consider various socioeconomic and climate factors as well. There are many kinds of water consumption projection models that are designed for specific areas and hence are only useful for the specified areas. Developing a tailored water consumption projection model for Addis Ababa by incorporating socioeconomic and climate factors would be valuable for the enhancement and management of its water supply. Therefore, this study aims to develop a domestic water consumption model by considering socioeconomic and climate factors through multilinear regression analysis.

Water Consumption Projection Options

Long-term water consumption projections are necessary to assess the future adequacy of water resources, satisfy efficient water allocation among different water users, and ensure long-term water sustainability. To predict future water consumption, different mathematical models are used.

There are different methods that are useful in determining future water demand. Based on the study by Pradhan (2003), the following are the most widely used water demand forecasting techniques.

I. **Time extrapolation**: The basic concept of this method is that future water consumption is based on past data. In many cases, future water use is found by extrapolating current/past demand assuming linear, logistic, exponential or other functions over time.
II. **Single coefficient requirement methods**: This method considers the projected serviced population and projected per capita water consumption to forecast the future water demand.
III. **Multiple coefficient requirement models**: This approach considers different variables excluding price and other economic factors.

IV. **Multiple coefficient demand models**: This approach is similar to the above except that the price for water use and related economic factors are considered in this approach.
V. **Disaggregated water use forecasts**: This method estimates the future water use by determining the water use for each sector, season, or region separately and gives a more accurate composite forecast.

House-Peters and Chang (2011) compare methods and models that were applied in water demand forecasting over the last 3 decades. The review shows that increasingly effective models have resulted from technological advances in spatial science and innovation in statistical methods. These models provide unbiased and accurate estimates of the determinants of urban water consumption at increasingly fine spatial and temporal resolutions. Dynamic models capable of incorporating alternative future scenarios and local stochastic analysis are leading a trend away from deterministic prediction.

Donkor et al. (2012) explained different water consumption projection methods and models used in the period between 2000 and 2010. This paper shows that although a wide variety of methods and models have attracted attention, the applications of these models differ depending on the forecast variables, their periodicity, and the forecast horizon. Multiple linear regression approaches are useful for short-term and long-term projections that include different socioeconomic factors and climate data (Qi and Chang 2011). In addition, a study by Haque et al. (2013) showed that multiple linear regression models are capable of predicting water consumption more accurately. The multiple linear regression method is selected for this study because it includes different socioeconomic and climate factors that are already included in the domestic water security assessment.

Study Area

The research was carried out in Addis Ababa, which is the capital city of Ethiopia. Addis Ababa is located in the central plateau of Ethiopia. Geographically, the city is located with its center at 9°1′48″ N and 38°44′24″ E (see Fig. 13.1).

Methodology

To develop the water consumption projection model for this study, the procedures in Fig. 13.2 were applied.

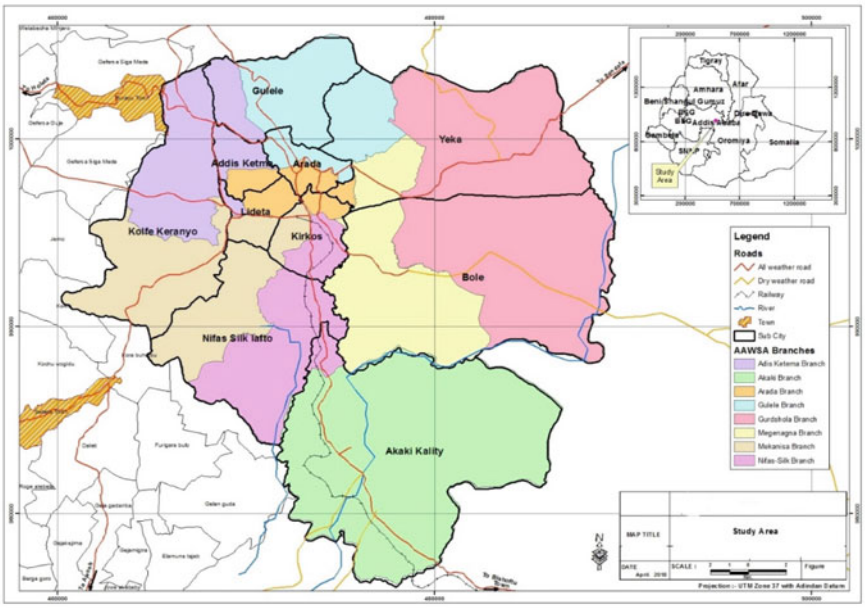

Fig. 13.1 Map of Addis Ababa extracted from Ethiopia

Data Collection and Analysis

Data Collection

The data in Table 13.1 were collected from different sources to develop the water consumption projection model for Addis Ababa.

Data Analysis

The water consumption model was prepared by choosing nine independent variables that have an impact on daily water consumption. The first step was to prepare the data for the multiple linear regression analysis for the period from 2000 to 2015. The data were collected and prepared to be suitable for SPSS.

Then, different equations were used to develop the required water consumption projection model. The models used were linear, semi-log, and log-log. Each of those equations has its own coefficients. The coefficients for each of those equations were then obtained after the multilinear regression analysis.

The multilinear regression analysis was performed for the total time period (2000–2015) as follows: First, the distribution of the collected data was checked. Then,

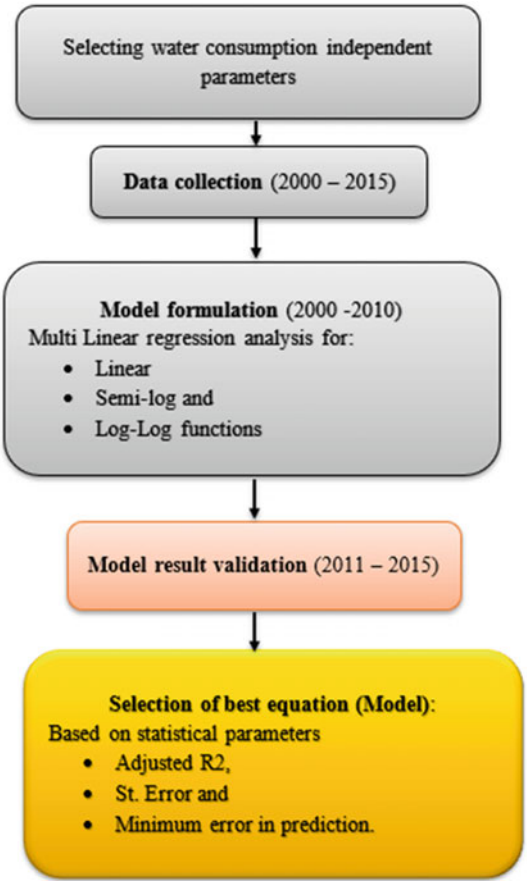

Fig. 13.2 Detailed methodological framework for water consumption projection model preparation

the relationship between the dependent and independent variables was checked to determine whether it was linear. To check linearity, the residual of each of the independent variables against the dependent variables was plotted. The next step was to check for multicollinearity of each independent variable against each other. This will help minimize misleading information regarding the significant parameters. Then, the multicollinearity variables were removed from the analysis, and one important factor was selected among them.

Next, the model was set for the 2000–2010 period from multilinear regression analysis using the selected variable in the previous step with the rest of the variables. Regression analysis was performed for confidence levels of 95% and 90% to determine how many parameters will be significant in determining water consumption at different confidence levels. Regression was performed for the three proposed model equations (linear, semi-log, and log-log). Then, the required coefficients based on the significance level were determined.

Table 13.1 Data collected for water consumption projection model preparation

Independent parameters	Independent parameters (X)	Unit	Duration	Data source	
$X1$	Maximum annual temperature				
$X2$	Minimum annual temperature	°C	30 years	National Meteorology Agency, Ethiopia (NMA)	
$X3$	Average annual temperature				
$X4$	Annual rainfall	mm			
$X5$	Population	Numbers		Central Statistics Agency (CSA)	Socioeconomic data
$X6$	Number of households	Numbers	16 years		
$X7$	Household size	Numbers			
$X8$	Residential water tariff	US$/m^3		Addis Ababa Water and Sanitation Agency (AAWSA 2011)	
$X9$	The ratio of population to the no. of university student	Numbers		Annual report of Ethiopian Ministry of Education	
$X10$	Per capita income	USD		Spaliviero and Cheru (2017)	
$X11$	Number of connections	Numbers		AAWSA (2011)	

The final step was to validate the developed equations. The models were validated for the observed data from 2011 to 2015. Finally, the best equation among those three models was chosen based on the adjusted R^2, standard error, and minimum error in predicting future water consumption.

Results and Discussion

Description of the Data for Water Consumption Projection Modeling

There are many factors that affect water consumption. It is possible to categorize the factors into two categories: socioeconomic and climate factors. Socioeconomic and demographic factors are factors related to population growth and migration,

the economic condition of the community (income), religion, tradition, educational status, etc. The climatic factors are related to the temperature and rainfall conditions of the area.

The parameters used in this study were selected based on the assumption of the relationship of socioeconomic, demographic, and climate factors with water consumption and the availability of data. This means that the increase in population, number of water supply connections, temperature, and income will increase the water demand. On the other hand, the increase in rainfall, education, and conservation policies will decrease water demand. Each of the independent variables will be discussed below in detail.

(a) **Annual Temperature ($X1$, $X2$, and $X3$)**

It is assumed that as the temperature increases, the water consumption with regard to drinking, bathing, laundry, etc., will also increase (Akuoko-Asibey et al. 1993). Thus, taking into consideration temperature as an independent factor will be significant in determining the future water demand. The average annual temperature ($X3$) was taken as an input for the analysis. This average annual temperature of Addis Ababa was obtained from the given daily minimum ($X2$) and maximum temperature ($X1$) of the city (1970–2017) from the Ethiopian National Meteorological Agency (NMA). Figure 13.3 shows the minimum, maximum, and average temperatures. We can see from the graph that the annual average temperature varies between 15.7 °C (minimum average in 1986) and 18.1 °C (maximum average in 2015).

(b) **Total Annual Rainfall ($X4$)**

The greater the annual precipitation is, the lower the water demand will be. Therefore, the yearly rainfall amount will be useful in determining the water demand of the city. The yearly rainfall data were obtained from the National Meteorological Agency of Ethiopia from 1970 to 2017. As shown in Fig. 13.4, the precipitation of Addis Ababa varies between 772.2 mm (the minimum rainfall in 2014) and 1553 mm (the

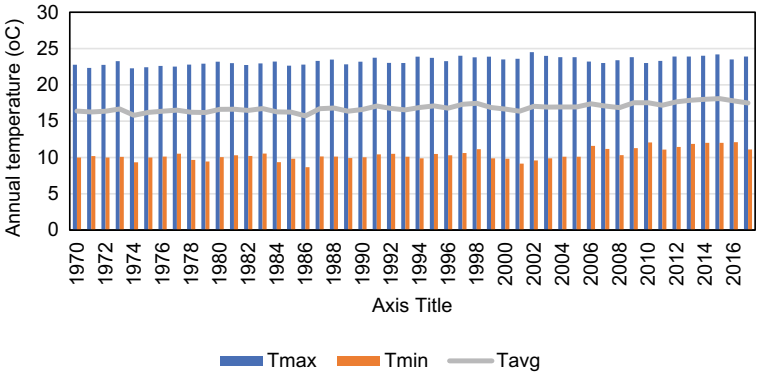

Fig. 13.3 Annual (minimum, maximum, and average) temperature of Addis Ababa

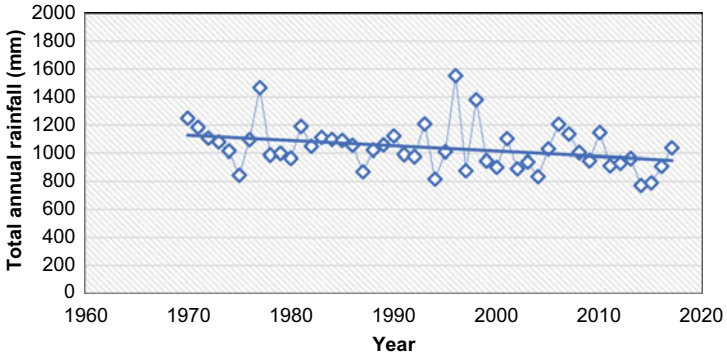

Fig. 13.4 Total annual rainfall of Addis Ababa (1970–2017)

maximum rainfall in 1996). The annual average rainfall between 1970 and 2017 was approximately 1039 mm. The linear trend in the rainfall shows a decrease during this period.

(c) **Population (*X*5)**

Population size is the main driver of water consumption. When the population size increases, the water consumption will also increase. The population projection for the period of 1995–2037 is shown in Table 13.2.

(d) **Number of Households (*X*6)**

This indicator was included by taking into consideration that if the number of households grows, the water consumption will also increase. The number of households was computed from the total population living in conventional houses and divided by average household size (see next section). The number of households in Addis Ababa is shown in Fig. 13.5. The graph shows the increase in the number of households. However, the conventional population count excludes people residing in collective quarters such as universities/colleges, hotels/hostels, monasteries, and the homeless, which is a limitation.

(e) **Household Size (*X*7)**

It is considered that an increase in household size will increase water supply consumption. The household size of Addis Ababa in Fig. 13.6 shows a decreasing trend. This might be due to the reduction in the number of children in a family due to socioeconomic conditions.

(f) **Ratio of the Number of University Students to the Total Population (*X*8)**

It is assumed that an increase in the level of education will have an impact on water consumption. The initial plan for this study was to obtain data on the number of university-educated people who live in the city. However, it was impossible to obtain

Table 13.2 Population projection of Addis Ababa (1994–2037)

Year	Population[a]	Population[b]	Population from CSA (2013)[c]
1994	2,112,737		
2000	2,354,288		
2001	2,405,816		
2002	2,458,472		
2003	2,512,280		
2004	2,567,266		
2005	2,623,456		
2006	2,680,875		
2007	2,737,769	2,739,551	2,739,551
2008	2,795,870	2,797,690	2,792,000
2009	2,855,204	2,857,063	2,851,000
2010	2,915,797	2,917,695	2,912,000
2011	2,977,676	2,979,615	2,977,000
2012	3,040,869	3,042,848	3,046,000
2013	3,105,402	3,107,424	3,119,000
2014	3,171,305	3,173,370	3,194,000
2015	3,238,607	3,240,715	3,272,000
2016	3,307,337	3,309,490	3,353,000
2017	3,377,525	3,379,724	3,435,000
2018	3,449,203	3,451,449	3,519,000
2019	3,522,402	3,524,695	3,604,000
2020	3,597,155	3,599,497	3,689,000
2021	3,669,822	3,672,211	3,774,000
2022	3,743,958	3,746,395	3,860,000
2023	3,819,591	3,822,077	3,945,000
2024	3,896,751	3,899,288	4,030,000
2025	3,975,471	3,978,059	4,114,000
2026	4,055,781	4,058,421	4,198,000
2027	4,137,713	4,140,407	4,281,000
2028	4,221,300	4,224,049	4,364,000
2029	4,306,576	4,309,380	4,447,000
2030	4,393,575	4,396,435	4,530,000
2031	4,482,331	4,485,249	4,613,000
2032	4,572,880	4,575,857	4,697,000
2033	4,665,258	4,668,296	4,781,000
2034	4,759,503	4,762,601	4,866,000
2035	4,855,651	4,858,812	4,953,000

(continued)

Table 13.2 (continued)

Year	Population[a]	Population[b]	Population from CSA (2013)[c]
2036	4,953,742	4,956,967	5,041,000
2037	5,053,814	5,057,104	5,132,000

[a] Forecasted from the 1994 census data
[b] Forecasted from 2007 census data by using an exponential equation for this study
[c] Adopted from CSA (2013) report

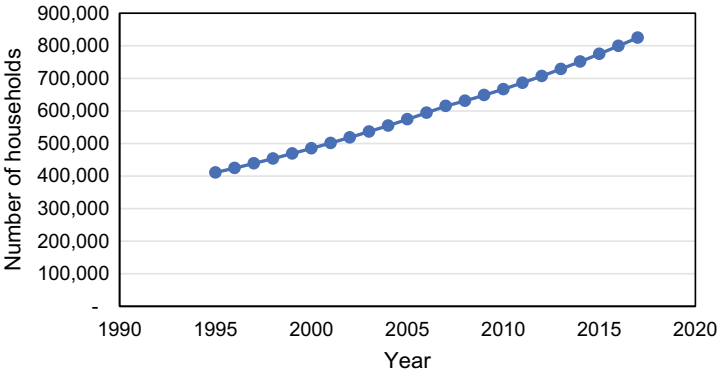

Fig. 13.5 Number of households in Addis Ababa

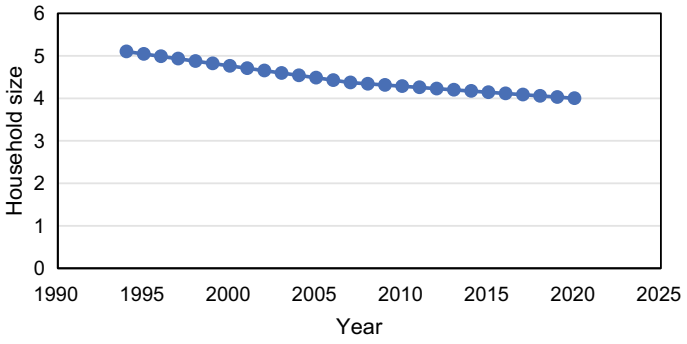

Fig. 13.6 Household size of Addis Ababa

the exact figure. Accordingly, we have changed our way of thinking to consider the impact of graduated people on water consumption. The study conducted in 2015 states that considering the ratio of the number of graduate students to the population will have an impact on the water consumption of an area. Since we already have population data as discussed above, the next task was to find the number of university-graduate students of Addis Ababa from both the governmental and private sectors.

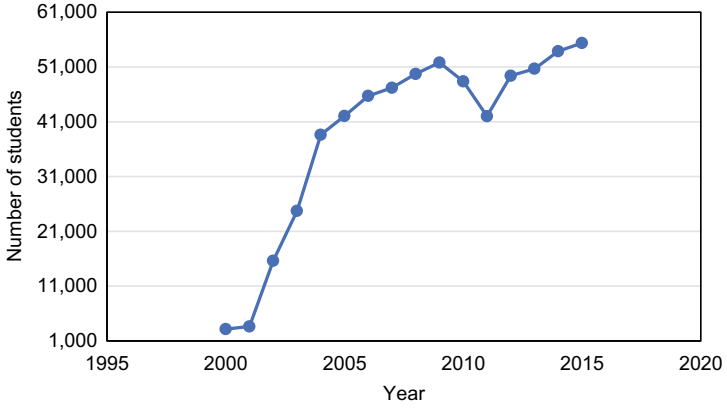

Fig. 13.7 Number of students at Addis Ababa University

Addis Ababa University is selected for consideration in this study because it is the largest university in Ethiopia and accommodates a large number of students in the city.[1]

The number of students at Addis Ababa University since 2000 is shown in Fig. 13.7. During the analysis in SPSS, the data are converted into the ratio of university-graduate students to the population.

(g) **Domestic Water Supply Tariff (*X*9)**

The tariff system for water supply uses a band system in which the domestic water supply is divided into seven bands. For this study, the domestic water supply tariff was taken according to the proportion of bands. The water tariff of the city shows a flat rate for the last ten years (Fig. 13.8). The data were obtained from 2000 to 2017. The currency exchange rate at the time of this study of 1 USD = 27.07 ETB was taken to convert the price into USD. Based on this currency exchange rate, the water tariff during this study will be approximately 0.11 USD/m^3.

(h) **Per Capita Income (*X*10)**

As income increases, water consumption will also increase. To see the impact of income on the water supply consumption of Addis Ababa city, the per capita income of Addis Ababa was taken into consideration from the Spaliviero and Cheru (2017) study. The data from 2011 to 2015 were given together with a growth rate of 10% per year. Figure 13.9 is obtained by assuming the given growth rate. For the analysis, the amount is converted into ETB (Ethiopian currency) by the same exchange rate of the tariff.

[1] http://www.aau.edu.et/aau-at-A-glance/.

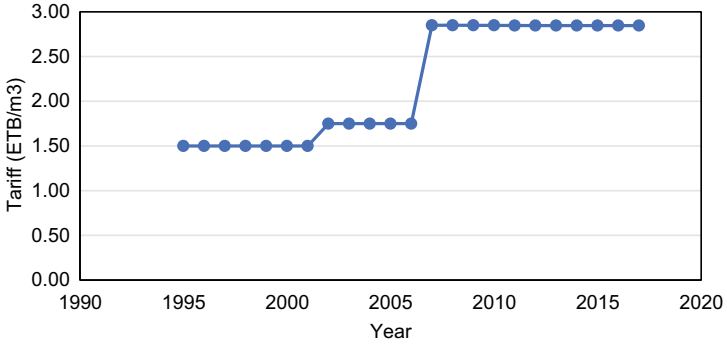

Fig. 13.8 Domestic water supply tariff of Addis Ababa

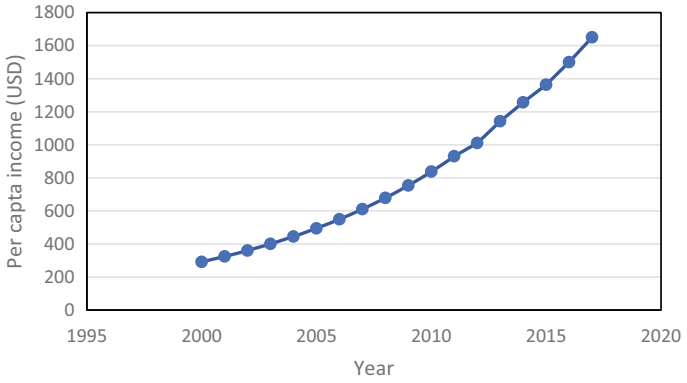

Fig. 13.9 Per capita income of Addis Ababa

(i) **Number of Connections (*X*11)**

The number of domestic water supply connections of the city is considered in this study. This is because there is a direct correlation between the number of connections and water consumption. As the number of connections grows, the water use will also increase. Figure 13.10 shows that there is an increment in the number of connections every year.

Water Consumption Projection Models

The analysis of the domestic demand projection model will be achieved based on the significance of the selected independent variables (X). Therefore, the demand (Y) is a function of different independent parameters that can be expressed as follows:

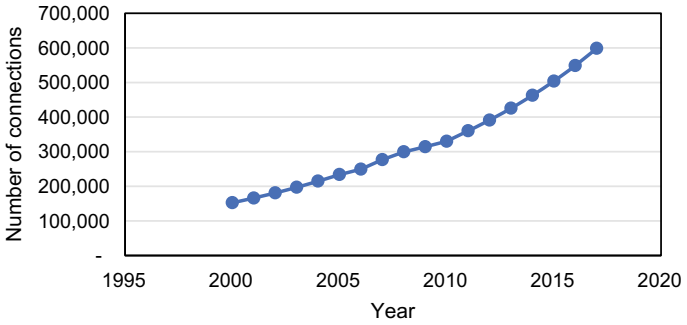

Fig. 13.10 Number of domestic water supply connections

$$Y = f(X_1, X_2, X_3, X_4, X_5, X_6, X_7, X_8, X_9, X_{10}). \tag{13.1}$$

1. Depending on the type of model used, the relationship can also be described as follows: **Linear models** are often chosen because of their ease of estimation. However, they yield constant elasticity at all points of the demand function.

$$Y = b_0 + b_1X_1 + b_2X_2 + b_3X_3 + \cdots + b_kX_k. \tag{13.2}$$

2. **Semi-log models** are often used to compare the results with linear and log-log functions.

$$\ln(Y) = b_0 + b_1X_1 + b_2X_2 + b_3X_3 + \cdots + b_kX_k. \tag{13.3}$$

3. **Log-Log model** provides direct estimates of the respective elasticity of the independent variables with respect to the dependent variable.

$$Y = b_0X_1^{b_1}X_2^{b_2}X_3^{b_3}X_4^{b_4}X_5^{b_5}X_6^{b_6}X_7^{b_7}X_8^{b_8}X_9^{b_9}X_{10}^{b_{10}} \tag{13.4}$$

or

$$\begin{aligned}\ln(Y) = b_0 &+ b_1{*}\ln(X_1) + b_2{*}\ln(X_2) + b_3 * \ln(X_3) \\ &+ b_4 * \ln(X_4) + b_5 * \ln(X_5) + b_6 * \ln(X_6) \\ &+ b_7 * \ln(X_7) + b_8 * \ln(X_8) + b_9 * \ln(X_9) \\ &+ b_{10} * \ln(X_{10}),\end{aligned} \tag{13.5}$$

where

Y	dependent variable, water use (Million Liter/day) (MLD).
X	independent parameters.
b_0	intercept.

$b_1, b_2 \ldots b_{10}$ coefficient of respective independent variables equivalent to the elasticity in the case of log-log transformation.

Note: The values of the intercept and coefficients of all three functional forms are obtained through multiple regression analysis employing the **SPSS** software package with time series data of the dependent and independent variables as inputs. After the model was developed, the best equation was selected to forecast the future water demand.

Developing the Water Consumption Projection Model

The domestic water consumption model was developed based on the following steps:

I. The distribution of data was checked to determine if it was normally distributed through a natural distribution graph.
II. Testing the relationship of each of the independent variables with the dependent variable whether it is linear or not.
III. The multicollinearity of each of the independent parameters was checked.
IV. One parameter was selected out of the multicollinearity independent factors.
V. Using the selected independent and non-multicollinearity independent variables, multilinear regression analysis was performed.
VI. Multilinear regression analysis was performed for the linear, semi-log, and log-log models.
VII. The validation of each of the model equations was checked.
VIII. The most suitable equation was selected for demand forecasting.

Note: Eleven years of data (2000–2010) in the italic emphasized part of Table 13.3 were used to develop the model (model training), and five years of data (2011–2015) were used for validation.

Correlation Matrix

The correlation matrix is used to investigate the dependence between multiple variables at the same time. The higher the value of the correlation coefficient is, the greater the significance of the independent factor to the dependent factor. The correlation matrix was performed for both dependent and independent variables and among independent variables (shown in Table 13.4). The correlation between dependent and independent variables will help us to see the correlation of the nominated independent variables to the dependent one. On the other hand, the correlation among independent variables will be useful in the investigation of multicollinearity among independent variables. Having multicollinearity within the variables might lead us to create an error in determining the significant factors.

Table 13.3 Summary of data for water consumption projection model preparation

Year	Dependent variable	Independent variable											
	Domestic water consumption ($\times 10^3$ m^3/day)	Maximum annual temperature (°C)	Minimum annual temperature (°C)	Average annual temperature (°C)	Annual rainfall (mm)	Population	Number of households	Household size	The ratio of population to the no. of university student	No. of university students	Domestic water tariff (ETB/m^3)	Per capita income (ETB)	Number of connections
	Y	*X*1	*X*2	*X*3	*X*4	*X*5	*X*6	*X*7	*X*8	*X*8#	*X*9	*X*10	*X*11
2000	*42.33*	*23.5*	*9.82*	*16.66*	*902.10*	*2,354,288*	*2,309,637*	*4.76*	*747*	*3,153*	*1.50*	*7909*	*152,279*
2001	*45.58*	*23.6*	*9.16*	*16.38*	*1,102.70*	*2,405,816*	*2,360,188*	*4.71*	*661*	*3,638*	*1.50*	*8787*	*165,922*
2002	*47.27*	*24.5*	*9.60*	*17.05*	*891.00*	*2,458,472*	*2,411,845*	*4.65*	*157*	*15,633*	*1.75*	*9764*	*180,787*
2003	*54.25*	*24.0*	*9.88*	*16.94*	*939.10*	*2,512,280*	*2,464,633*	*4.59*	*102*	*24,725*	*1.75*	*10,849*	*196,984*
2004	*59.64*	*23.8*	*10.10*	*16.95*	*835.10*	*2,567,266*	*2,518,576*	*4.54*	*66*	*38,618*	*1.75*	*12,054*	*214,632*
2005	*64.13*	*23.8*	*10.10*	*16.95*	*1,028.70*	*2,623,456*	*2,573,700*	*4.48*	*62*	*42,052*	*1.75*	*13,393*	*233,861*
2006	*67.74*	*23.2*	*11.60*	*17.40*	*1,205.90*	*2,680,875*	*2,630,030*	*4.43*	*59*	*45,708*	*1.75*	*14,882*	*249,407*
2007	*70.63*	*23.0*	*11.18*	*17.09*	*1,135.60*	*2,739,551*	*2,687,593*	*4.37*	*58*	*47,208*	*2.85*	*16,535*	*276,917*
2008	*74.48*	*23.4*	*10.32*	*16.86*	*1,004.60*	*2,792,000*	*2,739,047*	*4.34*	*56*	*49,725*	*2.85*	*18,372*	*299,476*
2009	*83.17*	*23.8*	*11.28*	*17.54*	*947.00*	*2,851,000*	*2,796,928*	*4.31*	*55*	*51,800*	*2.85*	*20,414*	*314,172*
2010	*88.82*	*23.0*	*12.06*	*17.53*	*1,146.10*	*2,912,000*	*2,856,771*	*4.28*	*60*	*48,368*	*2.85*	*22,682*	*330,006*
2011	101.00	23.3	11.08	17.19	911.70	2,977,000	2,920,539	4.26	71	42,013	2.85	25,202	360,145
2012	106.76	23.9	11.44	17.67	929.40	3,046,000	2,988,230	4.23	62	49,400	2.85	27,368	391,216
2013	112.72	23.9	11.86	17.88	960.80	3,119,000	3,059,845	4.20	62	50,673	2.85	30,941	425,294
2014	118.84	24.0	12.02	18.01	772.20	3,194,000	3,133,423	4.17	59	53,869	2.85	34,027	462,688
2015	125.21	24.2	12.02	18.11	790.20	3,272,000	3,209,944	4.14	59	55,369	2.85	36,923	503,739

Table 13.4 Correlation of all variables

Correlations												
	Y	$X1$	$X2$	$X3$	$X4$	$X5$	$X6$	$X7$	$X8$	$X9$	$X10$	$X11$
Y	1											
$X1$	0.112	1										
$X2$	**0.864****	−0.186	1									
$X3$	**0.900****	0.246	0.907**	1								
$X4$	**−0.363**	−0.701**	−0.043	−0.343	1							
$X5$	**0.995****	0.082	0.882**	0.905**	−0.322	**1**						
$X6$	**0.995****	0.082	0.882**	0.905**	−0.322	**1.000****	1					
$X7$	**−0.955****	0.047	−0.898**	−0.866**	0.185	**−0.975****	−0.975**	1				
$X8$	**−0.550***	−0.058	−0.588*	−0.605*	0.045	−0.596*	−0.596*	0.710**	1			
$X9$	**0.834****	−0.163	0.778**	0.698**	−0.156	0.865**	0.865**	−0.909**	−0.587*	1		
$X10$	**0.994****	0.150	0.853**	0.906**	−0.394	**0.991****	0.991**	−0.938**	−0.510*	0.823**	1	
$X11$	**0.994****	0.134	0.858**	0.904**	−0.375	**0.995****	**0.995****	**−0.953****	−0.547*	0.840**	**0.998****	1

** Correlation is significant at the 0.01 level (two-tailed)

* Correlation is significant at the 0.05 level (two-tailed)

As seen from Table 13.4, the nominated independent variables have a good correlation with the dependent factor except that of the $X1$ and $X4$ variables, which have small correlation values compared to the other variables. Table 13.4 also shows that some of the independent variables are strongly correlated with each other. Based on this, multicollinearity was checked for the independent variables, as shown in Table 13.5.

From Table 13.5, note that $X3$ and $X5$ were excluded by SPSS analysis due to multicollinearity. This is because SPSS excludes variables that are linearly dependent on other variables. It can also be observed from the table that the value of Variance Inflation Factor (VIF) is above the tolerable value (greater than 10) for most of the independent variables except variables $X1$, $X2$, and $X4$. This indicates that all of the variables, including $X3$ and $X5$, except $X1$, $X2$, and $X4$, are correlated with each other. However, this needs to be corrected by applying possible measures of multicollinearity minimization techniques. One of the most applied techniques is to drop some of the variables.

Therefore, from the correlation matrix (Table 13.4), we can see that $X5$ and $X11$ are highly correlated with $X6$, $X7$, and $X10$ with correlation values above 0.95. It is logical that the variables $X6$ (number of households), $X7$ (household size), and $X8$ (GDP per capita) have a direct relationship with $X5$ (number of population) and $X11$ (number of connections). Thus, it is possible to choose either $X5$ and omit $X6$, $X7$, $X10$, and $X11$ or select $X11$ and exclude $X5$, $X6$, $X7$, and $X10$. The number of populations ($X5$) is chosen for the analysis.

The population ($X5$) is preferred because water consumption has a direct relationship with the population. In addition, the population is directly proportional to the

Table 13.5 Checking for multicollinearity

Coefficients[a]								
Model		Unstandardized coefficients		Standardized coefficients	*t*	Sig.	Collinearity statistics	
		B	Std. error	Beta			Tolerance	VIF
1	(Constant)	−1063.395	596.323		−1.783	0.125		
	*X*1	−1.644	2.106	−0.026	−0.781	0.465	0.194	5.157
	*X*2	−1.117	1.223	−0.040	−0.913	0.396	0.109	9.197
	*X*4	−0.009	0.006	−0.044	−1.666	0.147	0.294	3.400
	*X*6	0.000	0.000	3.352	2.822	0.030	0.000	**6744.814**
	*X*7	97.772	76.378	0.710	1.280	0.248	0.001	**1472.063**
	*X*8	0.006	0.006	0.049	0.993	0.359	0.084	**11.882**
	*X*9	−3.423	2.264	−0.076	−1.512	0.181	0.083	**12.102**
	*X*10	−0.002	0.003	−0.644	−0.731	0.493	0.000	**3712.429**
	*X*11	0.000	0.000	−0.912	−2.468	0.049	0.002	**652.669**

[a] Dependent variable: *Y*

number of connections, household number, household size, and household income. This means that all of the variables can be excluded and replaced by the number of populations to predict water use. Therefore, the analysis was performed using a number of populations ($X5$) and $X1$, $X2$, $X3$, $X4$, $X8$, and $X9$ as independent variables. The analysis was performed at two confidence levels of 95% and 90%. The discussion is presented in the following sections.

Multilinear Regression Analysis at the 95% Confidence Level

The statistical significance (p) value of 0.05 was taken as a criterion to select the most significant parameter at the 95% confidence level. Then, the equation will be developed using the coefficients having a significance level of (p) 0.05. SPSS was used for the statistical analysis, and the procedure and results will be discussed as follows for each of the models. The stepwise method was used to obtain the most significant factor.

1. **Linear Model**

By using stepwise regression analysis, the result from Y and $X1, X2, X3, X4, X5, X8$, and $X9$ regression analysis (Table 13.6) shows that only $X5$ (number of population) is significant at the 95% confidence level with a significance level of 0.000, adjusted R^2 of 0.988, and standard error of the estimated 1.686. Therefore, based on the coefficients obtained, the linear equation will be developed as follows:

$$Y = 0.000082 * X5 - 152.957. \tag{13.6}$$

2. **Semi-log Model**

The same procedure was followed for the semi-log analysis. In this case, the independent variables are transformed into a natural logarithm. Therefore, the regression was performed using Y versus Ln$X1$, Ln$X2$, Ln$X3$, Ln$X4$, LN$X5$, LN$X8$, and Ln$X9$.

The results (Table 13.7) show that only $X5$ (population) is significant at the 95% confidence level with a significance level of 0.000, an adjusted R^2 of 0.979, and a

Table 13.6 Linear model analysis result for 95% CL

Coefficients[a]								
Model		Unstandardized coefficients		Standardized coefficients	t	Sig.	95.0% confidence interval for B	
		B	Std. error	Beta			Lower bound	Upper bound
1	Constant	−152.957	7.586		−20.163	0.000	−170.118	−135.796
	$X5$	0.000082	0.000	0.995	28.592	0.000	0.000	0.000

[a] Dependent variable: Y

standard error of the estimated 2.223. Therefore, the semi-log model equation will have the same variable as the linear model, which is the population. The obtained equation is:

$$Y = 219.750 * \mathrm{LN}X5 - 3184.049. \tag{13.7}$$

3. Log-Log Model

In this case, both the dependent and independent variables are transformed into natural logarithms, and log-log linear regression analysis is performed. The regression analysis was then performed using LnY versus Ln$X1$, Ln$X2$, Ln$X3$, LN$X4$, Ln$X5$, LN$X8$, and Ln$X9$. The results (Table 13.8) show that only $X5$ is at the required significance level. Therefore, the model is found to have the same variable as the above two models, which is the number of the population only with a p value of 0.000, an adjusted R^2 of.987, and a standard error of the estimation of 0.0278. The equation is shown as follows:

$$\mathrm{Ln}Y = 3.542 * \mathrm{LN}X5 - 48.224. \tag{13.8}$$

Note: All of the above analyses were also checked by excluding $X1$ (maximum annual temperature) and $X2$ (minimum annual temperature), and the result was the

Table 13.7 Semi-log model analysis results for 95% CL

Coefficients[a]								
Model		Unstandardized coefficients		Standardized coefficients	t	Sig.	95.0% confidence interval for B	
		B	Std. error	Beta			Lower bound	Upper bound
1	Constant	−3184.049	150.231		−21.194	0.000	−3523.895	−2844.202
	Ln$X5$	219.750	10.166	0.991	21.617	0.000	196.754	242.746

[a] Dependent variable: Y

Table 13.8 Log-log model analysis result for 95% CL

Coefficients[a]								
Model		Unstandardized coefficients		Standardized coefficients	t	Sig.	95.0% confidence interval for B	
		B	Std. error	Beta			Lower bound	Upper bound
1	(Constant)	−48.224	1.880		−25.653	0.000	−52.476	−43.971
	Ln$X5$	3.542	0.127	0.994	27.847	0.000	3.254	3.830

[a] Dependent variable: LnY

same, in which the only significant factor was found to be the population size ($X5$) in all of the models.

Multilinear Regression Analysis at the 90% Confidence Level

Theoretically, it is obvious that all of the selected independent variables are associated with water consumption, but only the population is found to be significant at the 95% confidence level. Therefore, to involve other independent variables, the analysis was redone by minimizing the confidence level to 90%, and the results are discussed below.

1. **Linear Model at the 90% Confidence Level**

The linear regression analysis using Y and $X1$, $X2$, $X3$, $X4$, $X5$, $X8$, and $X9$ indicates that only $X5$ (number of population) was found to be significant as before. However, when we exclude the maximum and minimum temperatures and continue the analysis with the average temperature and other factors, the following results are obtained:

The linear regression analysis using Y and $X3$, $X4$, $X5$, $X8$, and $X9$ indicates that all of the independent variables are significant to the dependent variable except $X3$ (average annual temperature), with a significance value of less than 0.10, an adjusted R^2 of 0.994, and a standard error of the estimated 1.139. The results are shown in Table 13.9.

Therefore, the developed linear model equation at the 90% confidence level excluding the maximum and minimum temperatures will be:

$$Y = -0.007358 * X4 + 0.000106 * X5 + 0.006762 * X8 \\ -5.017295 * X9 - 197.503. \tag{13.9}$$

Table 13.9 Results of linear model analysis for 90% CL

Coefficients[a]								
Model		Unstandardized coefficients		Standardized Coefficients	t	Sig.	90.0% confidence interval for B	
		B	Std. error	Beta			Lower bound	Upper bound
1	(Constant)	−197.503	13.224		−14.935	0.000	−223.200	−171.806
	$X5$	0.000106	0.000	1.276	16.003	0.000	0.000	0.000
	$X4$	−0.007358	0.004	−0.058	−1.983	0.095	−0.015	0.000
	$X8$	0.006762	0.002	0.113	2.880	0.028	0.002	0.011
	$X9$	−5.017295	1.515	−0.196	−3.311	0.016	−7.962	−2.073

[a] Dependent variable: Y

2. Semi-log Model at the 90% Confidence Level

In this case, all of the factors are significant at the 90% confidence level except $X4$. Thus, $X1$, $X2$, $X3$, $X5$, $X8$, and $X9$ are taken with the model adjusted R^2 of 0.998 and standard error of the estimation of 0.641 (Table 13.10).

Therefore, the equation will be:

$$\begin{aligned} Y = {} & 2180.172 * \mathrm{LN}X1 + 83.643 * \mathrm{LN}X2 - 305.161 * \mathrm{LN}X3 \\ & + 297.888 * \mathrm{LN}X5 + 2.811 * \mathrm{LN}X8 \\ & - 11.644 * \mathrm{LN}X9 - 4243.916. \end{aligned} \tag{13.10}$$

Next, another analysis was performed by excluding $X1$ and $X2$ (i.e., using Y and $X3$, $X4$, $X5$, $X8$, and $X9$). In this case, only $X5$, $X8$, and $X9$ are accepted, as shown in Table 13.11. Thus, $X5$, $X8$, and $X9$ are taken with the model adjusted R^2 of 0.990 and standard error of the estimation of 1.537 (Table 13.11).

Therefore, the equation will be:

Table 13.10 Results of semi-log model analysis for 90% CL

Coefficients[a]								
Model		Unstandardized coefficients		Standardized coefficients	t	Sig.	90.0% confidence interval for B	
		B	Std. error	Beta			Lower bound	Upper bound
1	(Constant)	−4243.916	213.943		−19.837	0.000	−4700.010	−3787.822
	LN$X1$	180.172	32.351	0.222	5.569	0.005	111.205	249.139
	LN$X2$	83.643	14.003	0.479	5.973	0.004	53.789	113.496
	LN$X3$	−305.161	52.602	−0.392	−5.801	0.004	−417.301	−193.021
	LN$X5$	297.888	13.999	1.343	21.280	0.000	268.045	327.731
	LN$X8$	2.811	0.490	0.180	5.740	0.005	1.767	3.854
	LN$X9$	−11.644	2.023	−0.209	−5.757	0.005	−15.956	−7.332

[a] Dependent variable: Y

Table 13.11 Results of semi-log model analysis for 90% CL

Coefficients[a]								
Model		Unstandardized coefficients		Standardized coefficients	t	Sig.	90% confidence interval for B	
		B	Std. error	Beta			Lower bound	Upper bound
1	(Constant)	−4302.248	363.318		−11.842	0.000	−4990.582	−3613.914
	Ln$X5$	294.823	24.516	1.329	12.026	0.000	248.375	341.271
	Ln$X8$	3.356	1.015	0.215	3.305	0.013	1.433	5.280
	Ln$X9$	−9.731	4.385	−0.174	−2.219	0.062	−18.038	−1.423

[a] Dependent variable: Y

Table 13.12 Results of log-log model analysis for 90% CL

Coefficients[a]								
Model		Unstandardized coefficients		Standardized coefficients	t	Sig	90.0% confidence interval for B	
		B	Std. error	Beta			Lower bound	Upper bound
1	(Constant)	−55.232	3.482		−15.864	0.000	−61.706	−48.758
	Ln$X5$	4.023	0.238	1.129	16.891	0.000	3.580	4.466
	Ln$X9$	−0.135	0.060	−0.151	−2.252	0.054	−0.246	−0.023

[a] Dependent variable: LnY

$$Y = 294.823 * \mathrm{LN}X5 + 3.356 * \mathrm{LN}X8 - 9.731 * \mathrm{LN}X9 - 4302.248. \quad (13.11)$$

3. **Log-Log Model at the 90% Confidence Level**

The regression result for the log-log model shows that $X5$ (number of population) and $X9$ (domestic water tariff) are significant, as shown in Table 13.12. The adjusted R^2 of the model is 0.991 with a standard error of estimation of 0.0231.

Therefore, the log-log model at 90% confidence will be:

$$\mathrm{Ln}Y = 4.023 * \mathrm{LN}X5 - 0.135 * \mathrm{LN}X9 - 55.232. \quad (13.12)$$

Note: As we can see from the above linear and semi-log models at 90% CL, the sign for all of the independent variables agrees with the assumption except for that of the ratio of population to the number of university students, which shows a positive sign in which the assumption contradicts the hypothesis given initially. The hypothesis was that increasing the number of educated people will minimize water use due to an increase in awareness of water conservation. Therefore, the next step is to determine the impact of the number of university students on water consumption.

Revising the Analysis with Number of University Students

The same procedure and data were used except that the ratio of population to the number of students ($X8$) was substituted by the number of university students ($X8^{\#}$). First, multicollinearity was checked. The results show that the independent variables have high VIFs, except $X1$, $X2$, $X3$, and $X4$ (see Table 13.13). The same technique was applied to solve the multicollinearity problem, which is selecting one variable that can govern others and dropping independent variables that have more than a 0.95 correlation with the selected variable. Therefore, by applying this technique, population is also taken in this case for the next regression analysis. As shown in Table 13.13, the correlation is the same as that with the ratio of population to the

number of students, in which $X3$ and $X9$ have a high correlation with $X4$, $X5$, and $X8$ (see Table 13.13).

1. **Linear Model**

Result: The same equation is obtained as the previous linear model of 95% CL for both 95% and 90% CL.

2. **Semi-log Model**

Result: The same equation is obtained as the previous semi-log model for the 95% CL.

However, for 90% CL analysis, different equations are obtained. In addition, in this case, we can see that the sign for the number of university students is the same as the hypothesis (negative). The equation has an adjusted R^2 of 0.998 with a standard error of 0.642. The coefficients are shown in Table 13.14.

Therefore, the new equation for a semi-log model with 90% CL with a number of students ($X8^{\#}$) will be:

$$\begin{aligned} Y = {} & 181.323 * \mathrm{LN}X1 + 84.129 * \mathrm{LN}X2 - 306.495 * \mathrm{LN}X3 \\ & + 300.942 * \mathrm{LN}X5 - 2.828 * \mathrm{LN}X8^{\#} \\ & - 11.655 * \mathrm{LN}X9 - 4248.320. \end{aligned} \tag{13.13}$$

3. **Log-Log Model**

The equation for the log-log models was the same as that for the ratio of population to university students.

Therefore, from the above models using a number of university students, only the semi-log model resulted in a different equation.

Model Validation

The final model equations from the above analysis are summarized in Table 13.15. The table shows the model equations from the above analysis at both 95% and 90% confidence levels. For the semi-log model, the 90% confidence level with the number of students in both including and excluding the maximum and minimum temperature scenarios was included.

Then, based on the model type, the water uses of 2000–2010 were predicted and checked against the observed water use. Next, to validate the model, the water consumption from 2011 to 2015 was projected, as shown in the table. Finally, the observed and predicted water use was plotted to see the trend of each model (see Fig. 13.11).

The 95% CL analysis shows that from all the independent variables for this study, the only significant factor was found to be the population in all of the models for

Table 13.13 Correlation matrix of variables using the number of university students

Correlations												
	Y	$X1$	$X2$	$X3$	$X4$	$X5$	$X6$	$X7$	$X8$	$X9$	$X10$	$X11$
Y	1											
$X1$	0.112	1										
$X2$	**0.864****	−0.186	1									
$X3$	**0.900****	0.246	0.907**	1								
$X4$	**−0.363**	−0.701**	−0.043	−0.343	1							
$X5$	**0.995****	0.082	0.882**	0.905**	−0.322	1						
$X6$	**0.995****	0.082	0.882**	0.905**	−0.322	1.000**	1					
$X7$	**−0.955****	0.047	−0.898**	−0.866**	0.185	−0.975**	−0.975**	1				
$X8$	**0.791****	−0.125	0.833**	0.768**	−0.044	0.832**	0.832**	−0.920**	1			
$X9$	**0.834****	−0.163	0.778**	0.698**	−0.156	0.865**	0.865**	−0.909**	0.801**	1		
$X10$	**0.994****	0.150	0.853**	0.906**	−0.394	0.991**	0.991**	−0.938**	0.760**	0.823**	1	
$X11$	**0.994****	0.134	0.858**	0.904**	−0.375	0.995**	0.995**	−0.953**	0.794**	0.840**	0.998**	1

** Correlation is significant at the 0.01 level (two-tailed)

Table 13.14 Results of semi-log model analysis for 90% CL by including T_{max} and T_{min}

Coefficients[a]								
Model		Unstandardized coefficients		Standardized coefficients	*t*	Sig	90.0% confidence interval for *B*	
		B	Std. error	Beta			Lower bound	Upper bound
1	(Constant)	−4248.320	214.887		−19.770	**0.000**	−4706.427	−3790.214
	LN*X*1	181.323	32.403	0.223	5.596	**0.005**	112.246	250.401
	LN*X*2	84.129	14.008	0.482	6.006	**0.004**	54.267	113.992
	LN*X*3	−306.495	52.636	−0.393	−5.823	**0.004**	−418.708	−194.283
	LN*X*5	300.942	14.382	1.356	20.926	**0.000**	270.283	331.602
	LN*X*8[#]	−2.828	0.494	−0.192	−5.730	**0.005**	−3.881	−1.776
	LN*X*9	−11.655	2.026	−0.209	−5.751	**0.005**	−15.975	−7.334

[a] Dependent variable: *Y*

all of the scenarios (scenario 1: the ratio of population to the number of university students; scenario 2: excluding ratio and substituting with the number of students; scenario 3: excluding the maximum and minimum temperatures and analysis with average temperature). This makes sense, as population growth and migration are high in Addis Ababa, and water consumption will be more dependent on the population. At the same time, the population is dependent on different socioeconomic factors, as described in the multicollinearity analysis. Therefore, in this case, we can say that socioeconomic factors play a large role in the water consumption of the study area.

The analysis using a confidence level of 90% for the scenario using the ratio of population to the number of university students includes some independent variables. For the linear model, rainfall ($X4$), population ($X5$), the ratio of total population to the number of students ($X8$), and domestic water tariff ($X9$) variables are involved. At the same time, rainfall ($X4$) was omitted for the semi-log model, while population ($X5$), ratio of population to a number of students ($X8$), and domestic water tariff ($X9$) were included in the model. Finally, the log-log remains with a population ($X5$) and domestic water tariff ($X9$). For the scenario of using a number of university students, the semi-log model includes population ($X5$), number of university students ($X8^{\#}$), and domestic water tariff ($X9$). In general, in all of the scenarios, we can observe that population was the common factor.

Figure 13.11 is established based on the observed and model outputs of Table 13.15. The figure shows that the semi-log models at the 90% CL with a ratio of population to the number of university students and the number of university students only fit with the observed consumption better than the other models. Additionally, the linear model at the confidence level of 90% (excluding T_{max} and T_{min}) gives a good fit next to that of the semi-log models. This means that the error between the observed and predicted values is very small. The difference in model prediction and the observed data from 2011 to 2015 were compared with the observed consumption

Table 13.15 Summary of water consumption models in different scenarios

Year		Model result							
		Linear		Semi-log		Semi-log model with number of students		Log-log	
	Equation at 95%	(A) $Y = 0.000082 * X5 - 152.957$		(C) $Y = 219.750 * \text{Ln}X5 - 3184.049$		(E)		(H) $\text{Ln}Y = 3.542 * \text{Ln}X5 - 48.224$	
	Equation at 90%	(B) $Y = -0.007358 * X4 + 0.000106 * X5 + 0.006762 * X8 - 5.017295 * X9 - 197.503$		(D) $Y = 294.823 * \text{Ln}X5 + 3.356 * \text{Ln}X8 - 9.731 * \text{Ln}X9 - 4302.248$		(F) $Y = 298.295 * \text{Ln}X5\text{-}3.364 * \text{Ln}X8^{\#} - 9.729 * \text{Ln}X9 - 4303.884$	(G) $Y = 181.323 * \text{LN}X1 + 84.129 * \text{LN}X2 - 306.495 * \text{LN}X3 + 300.942 * \text{LN}X5 - 2.828 * \text{LN}X8^{\#} - 11.655 * \text{LN}X9 - 4248.320$	(I) $\text{Ln}Y = 4.023 * \text{Ln}X5 - 0.135 * \text{Ln}X9 - 55.232$	
	Observed water consumption (Y) ($\times 10^3$ m^3/day)	Linear model predicted @ 95% CL	Linear model predicted @ 90% CL	Semi-log model predicted @ 95% CL	Semi-log model predicted @ 90% CL	Semi-log model with number of students @90% CL	Semi-log model with number of students from the addition of T_{max} and T_{min} @90% CL	Log-log model predicted @ 95% CL	Log-log model predicted @ 90% CL
2000	42.33	40.09	42.94	40.07	41.58	41.58	41.97	42.24	42.00
2001	45.58	44.32	46.35	44.83	47.55	47.56	48.19	45.61	45.82
2002	47.27	48.64	48.82	49.58	47.62	47.61	47.23	49.24	48.96
2003	54.25	53.05	53.80	54.34	52.53	52.53	53.12	53.16	53.42
2004	59.64	57.56	60.15	59.10	57.49	57.49	58.52	57.40	58.28
2005	64.13	62.17	64.66	63.86	63.66	63.66	64.80	61.98	63.59
2006	67.74	66.87	69.41	68.61	69.84	69.83	70.06	66.92	69.37

(continued)

Table 13.15 (continued)

Year		Model result							
		Linear		Semi-log		Semi-log model with number of students		Log-log	
	Equation at 95%	(A) $Y = 0.000082 * X5 - 152.957$		(C) $Y = 219.750 * \text{Ln}X5 - 3184.049$		(E)		(H) $\text{Ln}Y = 3.542 * \text{Ln}X5 - 48.224$	
	Equation at 90%	(B) $Y = -0.007358 * X4 + 0.000106 * X5 + 0.006762 * X8 - 5.017295 * X9 - 197.503$		(D) $Y = 294.823 * \text{Ln}X5 + 3.356 * \text{Ln}X8 - 9.731 * \text{Ln}X9 - 4302.248$		(F) $Y = 298.295 * \text{Ln}X5 - 3.364 * \text{Ln}X8^{\#} - 9.729 * \text{Ln}X9 - 4303.884$	(G) $Y = 181.323 * \text{LN}X1 + 84.129 * \text{LN}X2 - 306.495 * \text{LN}X3 + 300.942 * \text{LN}X5 - 2.828 * \text{LN}X8^{\#} - 11.655 * \text{LN}X9 - 4248.320$	(I) $\text{Ln}Y = 4.023 * \text{Ln}X5 - 0.135 * \text{Ln}X9 - 55.232$	
	Observed water consumption (Y) ($\times 10^3$ m^3/day)	Linear model predicted @ 95% CL	Linear model predicted @ 90% CL	Semi-log model predicted @ 95% CL	Semi-log model predicted @ 90% CL	Semi-log model with number of students @90% CL	Semi-log model with number of students from the addition of T_{max} and T_{min} @90% CL	Log-log model predicted @ 95% CL	Log-log model predicted @ 90% CL
2007	70.63	71.69	70.63	73.37	71.44	71.44	71.65	72.25	70.86
2008	74.48	75.99	77.14	77.54	76.92	76.92	77.75	77.27	76.48
2009	83.17	80.83	83.81	82.13	83.02	83.02	82.36	83.21	83.19

(continued)

Table 13.15 (continued)

Year		Model result							
		Linear		Semi-log		Semi-log model with number of students		Log-log	
	Equation at 95%	(A) $Y = 0.000082 * X5 - 152.957$		(C) $Y = 219.750 * \text{Ln}X5 - 3184.049$		(E)		(H) $\text{Ln}Y = 3.542 * \text{Ln}X5 - 48.224$	
	Equation at 90%	(B) $Y = -0.007358 * X4 + 0.000106 * X5 + 0.006762 * X8 - 5.017295 * X9 - 197.503$		(D) $Y = 294.823 * \text{Ln}X5 + 3.356 * \text{Ln}X8 - 9.731 * \text{Ln}X9 - 4302.248$		(F) $Y = 298.295 * \text{Ln}X5 - 3.364 * \text{Ln}X8^{\#} - 9.729 * \text{Ln}X9 - 4303.884$	(G) $Y = 181.323 * \text{LN}X1 + 84.129 * \text{LN}X2 - 306.495 * \text{LN}X3 + 300.942 * \text{LN}X5 - 2.828 * \text{LN}X8^{\#} - 11.655 * \text{LN}X9 - 4248.320$	(I) $\text{Ln}Y = 4.023 * \text{Ln}X5 - 0.135 * \text{Ln}X9 - 55.232$	
	Observed water consumption (Y) ($\times 10^3$ m^3/day)	Linear model predicted @ 95% CL	Linear model predicted @ 90% CL	Semi-log model predicted @ 95% CL	Semi-log model predicted @ 90% CL	Semi-log model with number of students @90% CL	Semi-log model with number of students from the addition of T_{max} and T_{min} @90% CL	Log-log model predicted @ 95% CL	Log-log model predicted @ 90% CL
2010	88.82	85.83	88.84	86.79	89.56	89.57	88.52	89.69	90.59
2011	101.00	91.16	97.55	91.64	96.63	96.64	96.81	96.99	99.02
2012	106.76	96.82	104.67	96.67	102.92	102.93	102.10	105.19	108.58

(continued)

Table 13.15 (continued)

Year		Model result							
		Linear		Semi-log		Semi-log model with number of students		Log-log	
	Equation at 95%	(A) $Y = 0.000082 * X5 - 152.957$		(C) $Y = 219.750 * \text{Ln}X5 - 3184.049$		(E)		(H) $\text{Ln}Y = 3.542 * \text{Ln}X5 - 48.224$	
	Equation at 90%	(B) $Y = -0.007358 * X4 + 0.000106 * X5 + 0.006762 * X8 - 5.017295 * X9 - 197.503$		(D) $Y = 294.823 * \text{Ln}X5 + 3.356 * \text{Ln}X8 - 9.731 * \text{Ln}X9 - 4302.248$		(F) $Y = 298.295 * \text{Ln}X5\text{-}3.364 * \text{Ln}X8^{\#} - 9.729 * \text{Ln}X9 - 4303.884$	(G) $Y = 181.323 * \text{LN}X1 + 84.129 * \text{LN}X2 - 306.495 * \text{LN}X3 + 300.942 * \text{LN}X5 - 2.828 * \text{LN}X8^{\#} - 11.655 * \text{LN}X9 - 4248.320$	(I) $\text{Ln}Y = 4.023 * \text{Ln}X5 - 0.135 * \text{Ln}X9 - 55.232$	
	Observed water consumption (Y) ($\times 10^3$ m^3/day)	Linear model predicted @ 95% CL	Linear model predicted @ 90% CL	Semi-log model predicted @ 95% CL	Semi-log model predicted @ 90% CL	Semi-log model with number of students @90% CL	Semi-log model with number of students from the addition of T_{max} and T_{min} @90% CL	Log-log model predicted @ 95% CL	Log-log model predicted @ 90% CL
2013	112.72	102.80	112.18	101.88	109.89	109.91	108.57	114.39	119.44
2014	118.84	108.95	121.50	107.10	116.77	116.79	115.20	124.43	131.42
2015	125.21	115.35	129.63	112.40	123.88	123.89	122.21	135.54	144.81

Where: (A) Model result from all of the water consumption factors at 95% CL, (B) model result from the linear model at 90% CL excluding Tmax and Tmin, (C) model result from all variables at 95% CL, (D) model result from the excluded scenario of T_{max} and T_{min}, (E) the same result with semi-log with ratio of population to the number of students(C), (F) semi-log model result from the number of students and excluding T_{max} and T_{min} scenario, (G) semi-log model result from the number of students and including T_{max} and T_{min} scenario,(H), (I) log-log result from all of the variables at both 95% and 90% CL

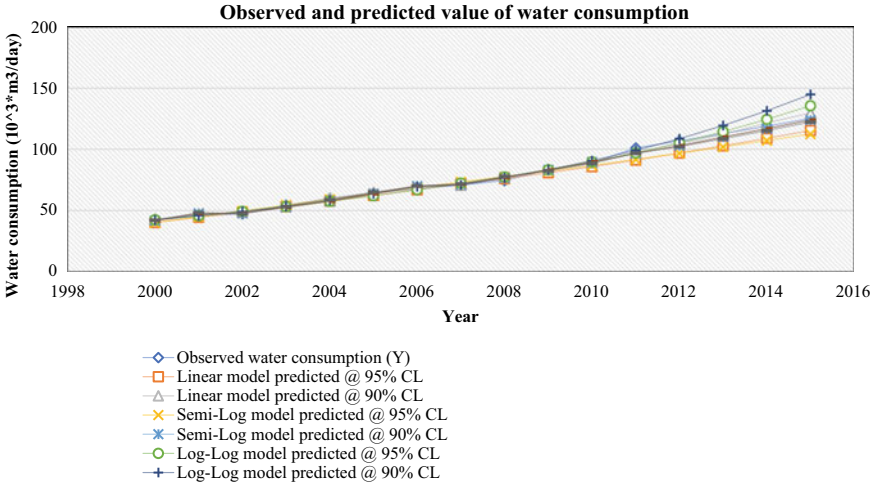

Fig. 13.11 Observed and predicted values of water consumption using the developed models

using each of the models. This is shown in Tables 13.16, 13.17, 13.18, 13.19, and 13.20.

From Tables 13.16, 13.17, 13.18, 13.19, and 13.20, we can see that the error that occurred in all of the semi-log models at 90% CL is smaller than that of the other models. The error that occurred in the linear model with a CL of 90% was also smaller and gave the second-best fit with a small error. However, the other models have a larger error.

Generally, to choose the best equation among the three models, the adjusted R^2 value of the model, the standard error, and the error due to water use prediction are considered and presented in Table 13.21.

As can be observed from Table 13.21, semi-log (both from the ratio of population to the number of students and the number of students scenarios) and linear models at the 90% confidence level are found to have smaller water use prediction errors.

Table 13.16 Checking errors from the linear model result for 95% and 90% CL

Year	Equation at 95%	$Y = 0.000082 * X5 - 152.957$			
	Equation at 90%	$Y = -0.007358 * X4 + 0.000106 * X5 + 0.006762 * X8 - 5.017295 * X9 - 197.503$			
	Observed (Y) ($\times 10^3$ m^3/day)	Linear model predicted @ 95% CL	Error	Linear model predicted @ 90% CL	Error
2011	101.00	91.16	9.84	97.55	3.45
2012	106.76	96.82	9.94	104.67	2.09
2013	112.72	102.80	9.92	112.18	0.54
2014	118.84	108.95	9.89	121.50	−2.66
2015	125.21	115.35	9.86	129.63	−4.43

The error is high for 95% CL

Table 13.17 Checking errors from the semi-log model result for 95% and 90% CL

Year	Equation at 95%	$Y = 219.750 * \text{Ln}X5 - 3184.049$			
	Equation at 90%	$Y = 294.823 * \text{Ln}X5 + 3.356 * \text{Ln}X8 - 9.731 * \text{Ln}X9 - 4302.248$			
	Observed (Y) ($\times 10^3$ m^3/day)	Semi-log model predicted @ 95% CL	Error	Semi-log model predicted @ 90% CL	Error
2011	101.00	91.64	9.36	96.63	4.37
2012	106.76	96.67	10.08	102.92	3.84
2013	112.72	101.88	10.84	109.89	2.83
2014	118.84	107.10	11.74	116.77	2.07
2015	125.21	112.40	12.80	123.88	1.33

The error is high for 95% CL

Table 13.18 Checking errors from the log-log model result for 95% and 90% CL

Year	Equation at 95%	$\text{Ln}Y = 3.542 * \text{Ln}X5 - 48.224$			
	Equation at 90%	$\text{Ln}Y = 4.023 * \text{Ln}X5 - 0.135 * \text{Ln}X9 - 55.232$			
	Observed (Y) ($\times 10^3$ m^3/day)	Log-log model predicted @ 95% CL	Error	Log-log model predicted @ 90% CL	Error
2011	101.00	96.99	4.01	99.02	1.98
2012	106.76	105.19	1.57	108.58	−1.82
2013	112.72	114.39	−1.67	119.44	−6.72
2014	118.84	124.43	−5.59	131.42	−12.57
2015	125.21	135.54	−10.33	144.81	−19.61

The errors are higher for 95% CL

Table 13.19 Checking errors from the semi-log model with the number of university students' results for 90% CL excluding the T_{max} and T_{min} scenarios (2011–2015)

Year	Equation at 95%	Same with semi-log @95% CL	
	Equation at 90%	$Y = 298.295 * \text{Ln}X5 - 3.364 * \text{Ln}X8^{\#} - 9.729 * \text{Ln}X9 - 4303.884$	
	Observed (Y) ($\times 10^3$ m^3/day)	Log-log model predicted @ 90% CL	Error
2011	101.00	96.64	4.36
2012	106.76	102.93	3.83
2013	112.72	109.91	2.81
2014	118.84	116.79	2.05
2015	125.21	123.89	1.31

The errors are almost equal for 95% and 90% CL

Table 13.20 Checking errors from the semi-log model with the number of university students' results for 90% CL excluding the T_{max} and T_{min} scenarios (2011–2015)

Year	Equation at 95%	Same with semi-log @95% CL	
	Equation at 90%	$Y = 181.323 * \text{LN}X1 + 84.129 * \text{LN}X2 - 306.495 * \text{LN}X3 + 300.942 * \text{LN}X5 - 2.828 * \text{LN}X8^{\#} - 11.655 * \text{LN}X9 - 4248.320$	
	Observed (Y) ($\times 10^3$ m^3/day)	Log-log model predicted @ 90% CL	Error
2011	101.00	96.81	4.19
2012	106.76	102.10	4.65
2013	112.72	108.57	4.15
2014	118.84	115.20	3.64
2015	125.21	122.21	3.00

However, the other four models have a large error. Therefore, the semi-log and linear models at a CL of 90% are selected for comparison.

The linear model with 90% CL is selected for this study because it has a high adjusted R^2 value of 0.994 with a lower standard error and smaller prediction error than the semi-log models. Consequently, the model contains four different independent variables, namely, population ($X5$), rainfall ($X4$), ratio of population to the number of students ($X8$), and domestic water tariff ($X9$), in which the dependent variable is predicted by those variables at approximately 99.4%.

Therefore, the following linear equation will be used to project the future water consumption of Addis Ababa:

$$Y = -0.007358 * X4 + 0.000106 * X5 + 0.006762 * X8 - 5.017295 * X9 - 197.503. \quad (13.14)$$

The above-selected linear model shows that all of the independent variables are aligned with the assumed sign except the ratio of population to the number of students ($X8$). $X8$ was taken as a water conservation parameter by assuming that as the number of students increases, the water consumption will decrease due to the increment in awareness of water conservation. This was proven from the semi-log model result using the number of university students ($X8^{\#}$) at 90% CL.

However, in this model, the concept contradicts the assumed one in which the model shows a positive sign, i.e., for a 1% increase in the ratio of population to students ($X8$), the water consumption will increase by 0.007%. This might be because the ratio of population to the number of students is large or the number of students is smaller compared to the total number of populations. On the other hand, this might be because the population of university students is not adequate in terms of education on water use. Thus, the result is acceptable for this study.

The relationship between rainfall and water consumption shows that a 1% increase in precipitation will reduce water use by 0.007%. It is logical that if there is rainfall,

Table 13.21 Comparison of models based on adjusted R^2, std. error, and error from the prediction

No.	Model type	Adjusted R^2	Std. error	Error from the water use prediction (2011–2015)					Independent variables included in the model
				2011	2012	2013	2014	2015	
1	Linear model @95% CL	0.989	1.686	9.84	9.94	9.92	9.89	9.86	*X*5
2	**Linear model @90% CL**	**0.994**	**1.139**	**3.45**	**2.09**	**0.54**	**−2.66**	**−4.43**	***X*4, *X*5, *X*8, and *X*9**
3	Semi-log model @95% CL	0.979	2.222	9.36	10.08	10.84	11.74	12.80	*X*5
4	Semi-log model @90% CL	0.990	1.537	4.37	3.84	2.83	2.07	1.33	*X*5, *X*8, and *X*9
5	Log-log model @95% CL	0.987	0.0278	4.01	1.57	−1.67	−5.59	−10.33	*X*5
6	Log-log model @90% CL	0.991	0.0237	1.98	−1.82	−6.72	−12.57	−19.61	*X*5 and *X*9
7	Semi-log model with number of university students@90% CL excluding the T_{max} and T_{min} scenarios	0.990	1.5469	4.36	3.83	2.81	2.05	1.31	*X*5, *X*8,, and *X*9
8	Semi-log model with number of university students@90% CL including the T_{max} and T_{min} scenarios	0.998	0.642	4.19	4.65	4.15	3.64	3.00	*X*1, *X*2, *X*3, *X*5, *X*8#, and *X*9

different household services, such as gardening and car washing, might be substituted by rainwater. It is also possible that during the rainy season, water consumption will be reduced.

As shown, the sign for a number of the population is positive. For a 1% increase in population size, water use is increased by 0.0001%.

The water tariff is a measure of water reduction. In this case, the water tariff sign shows that a 1% increase in the water price will reduce the water use by 5%, which is quite large compared to the other variables.

Sensitivity Analysis

Sensitivity analysis was performed to identify which factor is the most sensitive in the water consumption of Addis Ababa among the four identified factors (rainfall ($X4$), population ($X5$), number of students (education level) ($X8$), and domestic water tariff ($X9$)). The analysis was performed based on two scenarios: (i) checking for the 5% increment and (ii) checking for the 10% increment at one of the factors and keeping the others constant, and finally, determining which parameter is the most sensitive. The results are shown in Tables 13.22 and 13.23.

From Tables 13.22 and 13.23, we can observe that the population is highly sensitive to water consumption.

Table 13.22 Sensitivity analysis for water consumption modeling at 5% increments

Year	Observed (Y)	Y at 5% increment of $X4$ and keep others constant	Y at 5% increment of $X5$ and keep others constant	Y at 5% increment of $X8$ and keep others constant	Y at 5% increment of $X9$ and keep others constant
Y ($\times 10^3$ m^3/day) $= -0.007358 * X4 + 0.000106 * X5 + 0.006762 * X8 - 5.017295 * X9 - 197.503$					
2011	101.00	97.21	113.33	97.57	96.83
2012	106.76	104.33	120.81	104.69	103.95
2013	112.72	111.82	128.71	112.20	111.46
2015	118.84	121.21	138.43	121.52	120.78

Table 13.23 Sensitivity analysis for water consumption modeling at 10% increments

Year	Observed (Y)	Y at 10% increment of $X4$ and keep others constant	Y at 10% increment of $X5$ and keep others constant	Y at 10% increment of $X8$ and keep others constant	Y at 10% increment of $X9$ and keep others constant
Y ($\times 10^3$ m^3/day) $= -0.007358 * X4 + 0.000106 * X5 + 0.006762 * X8 - 5.017295 * X9 - 197.503$					
2011	101.00	96.88	129.10	97.60	96.12
2012	106.76	103.99	136.96	104.71	103.24
2013	112.72	111.47	145.24	112.22	110.75
2015	118.84	120.93	155.35	121.54	120.07

Conclusion

- Multilinear regression analysis is helpful in identifying the most significant factor that affects water consumption. Collecting reliable data for a longer period is required to minimize the error in prediction.
- Socioeconomic development is found to be more influential in the future water security status of cities than climate change impact. The most significant factor that affects the water consumption of Addis Ababa is the population. According to Spaliviero and Cheru (2017), migration is a very serious problem in cities that results in rapid population growth.

Recommendations

The following recommendations have been suggested based on the research findings:

- As we have seen from the study, population is the main driver in the water supply consumption of Addis Ababa. The fundamental causes were also discussed from the existing situation section of the report. One of the reasons for the rapid population growth of the city is migration (Spaliviero and Cheru 2017), and the root cause for this migration is that the available job opportunities in Addis Ababa are better than those in other cities of the country. In this regard, we recommend that the government look at the implementation of national policies and distribute work opportunities to other parts of the country.
- From the water consumption model, we can observe that an increase in water tariffs can reduce water consumption. Therefore, we recommend that the utility revise the water tariff and apply other water conservation mechanisms.
- Looking at alternative water supply systems might be helpful in reducing water consumption (investigation and implementation of water demand management).

Acknowledgements We would like to express our special gratitude to Ms. Mekdelawit M Deribe and Ms. Ethiopia B Zeleke (Ph.D. candidates in the Department of Earth and Environment, Florida International University, Miami, USA) for their kind support during the book chapter review and editing.

References

AAWSA (2011) City government of Addis Ababa, Addis Ababa Water and Sewerage Authority business plan 2011–2020 final report. Business plan

Akuoko-Asibey A, Nkemdirim LC, Draper DL (1993) The impacts of climatic variables on seasonal water consumption in Calgary, Alberta. Can Water Resour J/Revue canadienne des ressources hydriques 18(2):107–116.https://doi.org/10.4296/cwrj1802107

Arsiso BK, Tsidu GM, Stoffberg GH, Tadesse T (2017) Climate change and population growth impacts on surface water supply and demand of Addis Ababa, Ethiopia. Climate Risk Management

Assefa YT, Babel MS, Sušnik J, Shinde VR (2018) Development of a generic domestic water security index, and its application in Addis Ababa, Ethiopia. Water 11(1):37

Bayrau A (2014) Building a resilient city to water mediated climate change: policy and institutional options (Reserch Report 19). Retrieved from Addis Ababa, Ethiopia

CSA (2013) Population projections for Ethiopia 2007–2037. Retrieved from Addis Ababa

Donkor EA, Mazzuchi TA, Soyer R, Alan Roberson J (2012) Urban water demand forecasting: review of methods and models. J Water Resour Plan Manag 140(2):146–159

Haque MM, Rahman A, Hagare D, Kibria G (2013) A comparison of linear and nonlinear regression modeling for forecasting long term urban water demand: a case study for Blue Mountains Water Supply System in Australia. Paper presented at the Water & Environment Dynamics: Proceedings of the 6th International Conference on Water Resources and Environment Research, 3–7 June 2013, Koblenz, Germany

Hardy D, Cubillo F, Han M, Li H (2015) Alternative Water resources: a review of concepts, solutions and experiences. http://www.iwa-network.org/publications/alternative-water-resources-a-review-of-concepts-solutions-and-experiences/

House-Peters LA, Chang H (2011) Urban water demand modeling: review of concepts, methods, and organizing principles. Water Resour Res 47(5)

Ndaruzaniye V (2011) Water security in Ethiopia: risks and vulnerabilities' assessment. Global Water Institute for Africa Climate Change, Environment and Security

Pradhan (2003) Water demand forecast and management modeling: an application to Kathmandu Valley, Nepal. (Masters), Asian Institute of Technology, Bangkok, Thailand, Unpublished master's thesis

Qi C, Chang N-B (2011) System dynamics modeling for municipal water demand estimation in an urban region under uncertain economic impacts. J Environ Manage 92(6):1628–1641. https://doi.org/10.1016/j.jenvman.2011.01.020

Spaliviero M, Cheru F (2017) The state of Addis Ababa 2017: the Addis Ababa we want

World-Bank (2015) Addis Ababa—enhancing urban resilience: city strength resilient cities program (English). Retrieved from World Bank Group, Washington, D.C. https://documents.worldbank.org/curated/en/559781468196153638/Addis-Ababa-Enhancing-Urban-Resilience-city-strength-resilient-cities-program

Chapter 14
Effects of Deficit Irrigation and Mulching on the Water Footprint of Maize Production in the Koga Irrigation Scheme, Ethiopia

Ertiban Wondifraw, Tena Alamirew, Abebech Abera, Amanuel Abate, and Hanibal Lemma

Abstract In Ethiopia, it is crucial to utilize water management strategies such as mulching and deficit irrigation that use less water per unit of a product to address the water challenges that the country faces. This chapter presents findings on the effects of deficit irrigation (DI) and mulching materials on the reduction in the blue water footprint (WFb) of maize. The experiment has 12 treatments comprising four levels of water application depths (50 (DI4), 60 (DI3), 80 (DI2), and 100% (DI1) of the crop water requirement) and three types of mulching (no mulch (NM), wheat straw (SM), and white transparent polyethylene materials (PM)). The experiment was laid in a randomized complete block design with three replications in factorial arrangements. Water applied per irrigation event and soil moisture contents just before and 24 h after each irrigation event were monitored throughout the season. The data were analyzed using the *R* statistical package. The moisture monitoring results showed that lower evapotranspiration (ET) was recorded in the plastic mulch treatments and higher ET in the no-mulch treatments. The variance analysis showed that mulching and DI significantly affected the WFb and grain yield of maize; soil temperature (soil T^{o}) and hundred kernel weight (HKwt) were affected by mulch application only. However, there were no interaction effects between the two factors. The PM treatment resulted in the highest grain yield (8.17 tons ha^{-1}) and the lowest WFb

E. Wondifraw (✉) · H. Lemma
Faculty of Civil and Water Resources Engineering, Bahir Dar Institute of Technology, Bahir Dar University, Bahir Dar, Ethiopia
e-mail: ewodifraw@gmail.com

T. Alamirew
Water and Land Resources Centre (WLRC), Addis Ababa University, Addis Ababa, Ethiopia

A. Abera
Blue Nile Water Institute, Bahir Dar University Institute of Technology, Bahir Dar, Ethiopia

A. Abate
College of Agriculture and Environmental Sciences, Department of Natural Resources Management, University of Gondar, Gondar, Ethiopia

A. M. Melesse et al. (eds.), *Land and Water Degradation in Ethiopia*, Springer Geography, https://doi.org/10.1007/978-3-031-60251-1_14

(794.74 m^3 ton^{-1}). The PM treatment also gave the best HKwt of 34.0 g, which was 6.56% higher than that of the NM treatment. A significantly higher soil T^o was recorded at the application of PM because much of the heat is retained by PM. The DI treatments showed that DI4 gave the lowest WFb (720.31 m^3 ton^{-1}), which had a 38.93% water consumption reduction, followed by DI3. The results showed that there was a significant grain yield difference among DI1, DI3, and DI4. The application of DI1 produced the largest grain yields (7.74 tons ha^{-1}), while the application of DI4 had the smallest yield (6.59 tons ha^{-1}), which was 14.86% lower than that of DI1. Therefore, the application of 60% ETc DI and plastic mulch could be an important practice for blue water footprint reduction in this study area and areas with similar agroecology.

Keywords Water footprint reduction · Deficit irrigation · Mulching · Maize · NW Ethiopia

Introduction

Ethiopia's freshwater resources have been challenged by spatial and temporal variations in rainfall, dry spells, frequent droughts (Kassie 2019), and a lack of appropriate water management technologies, such as a lack of irrigation water use efficiency through proper scheduling and on-farm management (Eshete et al. 2020). Moreover, there is competition for irrigation water between water users located upstream and downstream, different crop growers, and land size owners (Amede 2015). To overcome these limitations, efficient water usage and management are currently the main priorities in the nation (Eshete et al. 2020).

According to Hoekstra et al. (2011), the water footprint (WF) implies the freshwater use (direct and indirect) of consumers or producers. The WF has three components: blue, green, and gray water footprints. The blue WF (WFb) represents the irrigation water consumed in crop production, which is an indicator of the consumptive use of fresh surface and groundwater along the value chain of the product. The term 'consumptive water use' refers to water that evaporates, water incorporated into the product, water that does not return to the same catchment area, or water that does not return in the same period. Among these components, evaporation is highly significant (Hoekstra et al. 2011); hence, in this study, the consumptive water use was equated with evaporation only.

Applying irrigation water management strategies and philosophies, such as deficit irrigation, drip and sprinkler irrigation, alternative furrow irrigation, mulching, and supplemental irrigation, can greatly reduce the WFb (Kolokytha 2014). Generally, technologies that require less water per unit of product can reduce the WF or increase water productivity (Hoekstra and Chapagain 2007). WF is the reverse of water productivity, which is the ratio of the required water to produce the crop product in a meter cube to the amount of the crop product in tons.

This study focuses on reducing the WFb of maize through local agricultural practices that combine mulching (Chala and Quraishi 2015) and deficit irrigation (Zhou et al. 2011). Based on 12 years of average CSA data (2007–2018) of cereal production in Ethiopia, maize is the largest in production and the second largest in area coverage next to Teff (Gizaw and Assegid 2021). According Mekonnen and Hoekstra (2014), the green–blue WF of maize at the > 50th percentile is greater than 754 m^3 t^{-1} for the Ethiopian case, and the global average is 1028 m^3 t^{-1}. Previous studies have shown that mulching can increase crop yield and water productivity by conserving soil moisture, reducing soil erosion, weeds and evaporation, and moderating soil temperature (Chakraborty et al. 2008; Chala and Quraishi 2015; Kader et al. 2017). Mulching helps prevent direct evaporation of water from the soil surface (Perry et al. 2009). A study in the Upper Litani Basin, Lebanon, on nine different crops, including maize, confirmed that on average, mulching has reduced the WFb by 3.6% or 6.3 million m^3 y^{-1} (Nouri et al. 2019). Another study has revealed that with the application of organic mulching, a 13% consumptive WF reduction can be achieved compared with using full irrigation in the furrow system alone (Chukalla et al. 2015).

The effects of mulching vary widely depending on the material used. The color of plastic mulch, source of organic materials, or condition of the mulch (living/dead) have distinct impacts on the hydrothermal regimes of soil and plants (Chakraborty et al. 2008; Zribi et al. 2015; Lamont 2017). Kader et al. (2017) stated that plastic mulching materials have a more significant effect than organic materials in controlling the soil environment and increasing crop yield by improving crop-water use efficiency. However, organic mulching materials are inexpensive and environmentally friendly and can also be decomposed easily into the soil and improve the chemical and physical properties of the soil (Aniekwe and Anike 2015; Kader et al. 2017).

Deficit irrigation is considered in this study as another important practice for irrigation water management. Deficit irrigation helps to reduce the WF and increase overall production by reducing the amount of crop water required throughout the growing season or at a predetermined stage in the growing season. Hence, overall high-yield production would be achieved by expanding the irrigation area with the saved water during deficit irrigation (Karrou et al. 2012). It has been argued that instead of using full irrigation, deficit irrigation can be an important strategy for crop production in water-scarce regions globally (Zhou et al. 2011). Chukalla et al. (2015) showed that WFb could be reduced by at least 1% when moving from full to deficit irrigation. A study in Kenya also indicated that the application of DI of 80% of crop evapotranspiration (ETc) to onion saved 10.7% of irrigation water without significantly affecting yield (ROP 2016).

It should be realized that the different water management strategies that reduced the WF are environmentally dependent, and one strategy that was effective somewhere might not be as effective in other places. Moreover, appropriate mulching material selection should be based on crop type, crop management practices, and climatic conditions (Kader et al. 2017). According to Kim and Kim (2019), the WF of a product is affected by weather conditions. Therefore, site-specific evaluation is needed for WF reduction strategies. Therefore, we decided to evaluate on-farm

deficit irrigation and mulching practices in the Tana Basin, Northwest Ethiopia, with the following objectives: (a) to evaluate the effects of these practices on the WFb reduction of maize and (b) to evaluate the effects of these practices on the yield of maize.

Materials and Methods

Description of the Experimental Site

The field experiment was conducted at the Koga irrigation scheme, which is one of the watersheds of the Lake Tana Sub-Basin, in the Amhara Region of Northwest Ethiopia in the growing season of 2021/22. The Koga irrigation scheme has a catchment area of 20,000 ha and is designed to irrigate 7000 ha (MacDonald 2004). The source of water for the scheme is the Koga Reservoir. Geographically, the experimental site is located at $11^0 23' 20''$ latitude, 37° 6′ 29″ longitude and an elevation of 1980 m above sea level (Fig. 14.1). The annual rainfall is approximately 1480 mm at the Merawi meteorological station. The Koga watershed falls under the subtropical climate zone, and the long-term mean annual minimum and maximum temperatures are 9 °C and 32 °C, respectively. The weather conditions during the maize growing season from the end of December 2021 to the end of May 2022 are shown in Fig. 14.2. The dominant soil type of the area is mainly paleosol with a clay texture (Abiyu and Alamirew 2014).

Experimental Design

The experimental design was laid out in a randomized complete block design (RCBD) with three replications. Each treatment was a combination of four levels of deficit irrigation and three types of mulching (Table 14.1). Factor one was four sustained deficit irrigation depths (DI1, DI2, DI3, DI4): DI1 is 0% DI, which is the amount of irrigation water applied at 100% of the ETc; DI2 is 20% DI, which is the amount of irrigation water applied at 80% of the ETc; DI3 is 40% DI, which is the amount of irrigation water applied at 60% of the ETc; and DI4 is 50% DI, which is the amount of irrigation water applied at 50% of the ETc. Here, sustained deficit irrigation implies that deficit irrigation is applied uniformly at all growing stages. Factor two was three mulching materials (transparent plastic mulch, wheat straw mulch and a control-no mulch) to give a total of twelve treatment combinations. Straw mulching was applied at a rate of 6 tons ha^{-1}, and transparent plastic mulch 25 mm thick was spread by leaving free space or a hole for the plant (Fig. 14.3). Mulching was performed one month after planting (January 17–18, 2022).

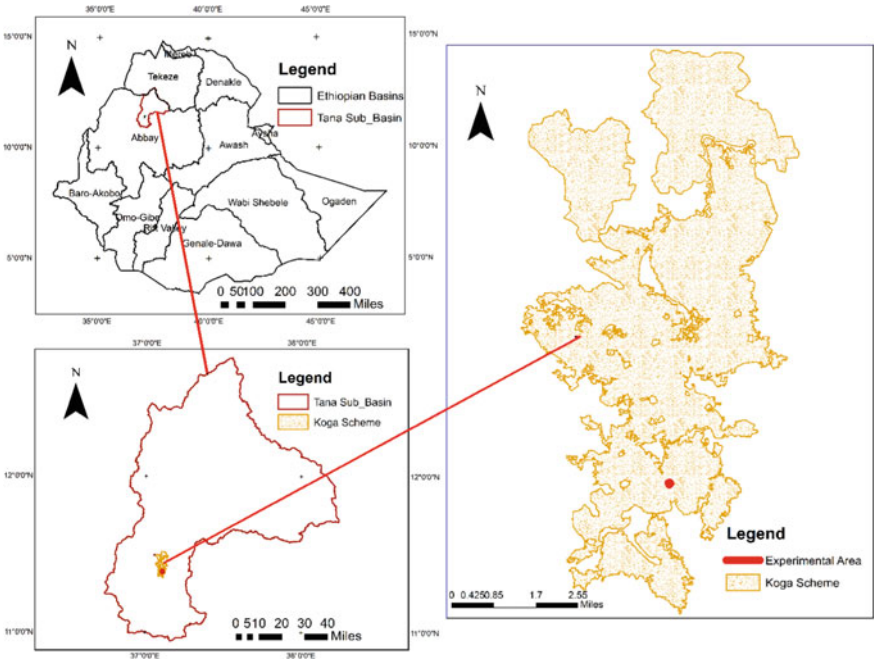

Fig. 14.1 Location of the experimental area

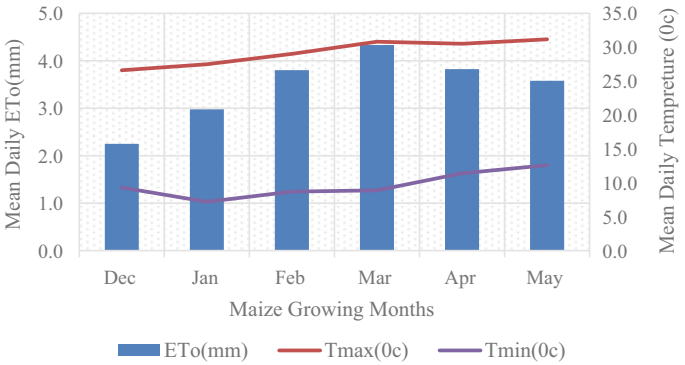

Fig. 14.2 Weather conditions during the maize growing season (*Source* Recorded data at the experimental site metrological station during the maize growing season)

The gross and net plot sizes were 33.6 m^2 (4.8 by 7 m) and 20.16 m^2 (4.2 by 4.8 m), respectively. The test crop was a maize variety called 'BH_546' that was sown using 70 cm row spacing and 30 cm plant spacing on 17 December 2021. A recommended fertilizer rate of P_2O_5 (92 kg ha^{-1}) and nitrogen fertilizer (150 kg ha^{-1}) was used. P_2O_5 was applied once during plating, while nitrogen was split into three

Table 14.1 Treatment setup of the experiment

Treatment	Factor 1: deficit irrigation (DI)	Factor 2: mulching Materials
1	DI1: Control (Zero deficit or full irrigation)	NM: No mulch (control)
2	DI2: 80% of ETc (or 20% deficit)	NM: No mulch (control)
3	DI3: 60% of ETc (or 40% deficit)	NM: No mulch (control)
4	DI4: 50% of ETc (or 50% deficit)	NM: No mulch (control)
5	DI1: Control (Zero deficit or full irrigation)	SM: Wheat straw
6	DI2: 80% of ETc (or 20% deficit)	SM: Wheat straw
7	DI3: 60% of ETc (or 40% deficit)	SM: Wheat straw
8	DI4: 50% of ETc (or 50% deficit)	SM: Wheat straw
9	DI1: Control (Zero deficit or full irrigation)	PM: Transparent polyethylene plastic
10	DI2: 80% of ETc (or 20% deficit)	PM: Transparent polyethylene plastic
11	DI3: 60% of ETc (or 40% deficit)	PM: Transparent polyethylene plastic
12	DI4: 50% of ETc (or 50% deficit)	PM: Transparent polyethylene plastic

Fig. 14.3 The experimental site with transparent polyethylene mulch

equal amounts and applied during the planting, knee height, and tasseling stages. Full applications of nitrogen fertilizer at once are less efficient than split applications due to the increased risk of nitrogen loss through leaching or denitrification (Randall et al. 2003).

Agronomic practices, including land preparation, plowing, thinning, and pest control, were applied uniformly for each plot. Weeding was performed three times (on January 13, 2022, February 16, 2022, and March 17, 2022). Weeding was performed only once in white polyethylene mulched plots because it was no longer possible to remove the mulch material, as such an attempt may destroy the plant. Disease and pest attacks were noticed in all plots, particularly in the straw-mulched plots at an early stage of the growing period, and controlled with chemical application in the initial and developmental stages.

Irrigation Requirement and Blue Water Footprint Determination

The pan evaporation method is helpful in irrigation scheduling in terms of technical facilities and easy adaptation to climatic change (Ahmet 2011); therefore, irrigation scheduling for this experiment was based on the cumulative class-A pan evaporation that was installed at the station and calculated as the sum of the daily class-A pan evaporation as follows:

$$\mathrm{ETc} = \sum_{k=0}^{n} E\mathrm{KpKc} \tag{14.1,}$$

where

- n the number of days since the last watering.
- E daily evaporation from the class-A evaporation pan located 100 m away from the experimental plots.
- Kc crop coefficient for maize, varied from 0.5 to 1.2 in relation to the phase of the crop's biological cycle for maize crop.
- Kp pan coefficient value of 0.8 (Doorenbos and Kassam 1979).

The consumptive blue crop water use (CWUb, m^3 ha^{-1}) was calculated by an accumulation of daily evapotranspiration (ET, mm day^{-1}) from irrigation over the complete growing period as follows.

$$\mathrm{CWUb} = 10 \times \sum_{t=1}^{\lg p} \frac{\mathrm{Sbt}}{\mathrm{St}} \mathrm{ETb}t \tag{14.2,}$$

where ETb is blue evapotranspiration, 10 is a factor to convert water depths in mm into water volumes per land surface (m^3 ha^{-1}), and lgp is the total length of the

growing period in days. This is the sum over the length of the growing period in days from planting to the day of harvest. There was no effective rainfall during the maize growing seasons.

To obtain the blue component of the water (WFb), the CWU of blue divided by the marketable yield obtained after maize harvest in m^3 ton^{-1} (Hoekstra et al. 2011):

$$\mathrm{WFb} = \frac{\mathrm{CWUb}}{Y} \tag{14.3,}$$

where Y is the yield of the crop in tone.

Water was applied using a furrow system with a 14-day irrigation interval, and the irrigation system efficiency was considered to be 70%. The furrows were close-ended, and all water flowing into the furrows infiltrated over the entire length without causing runoff. The depth of water entering each plot was measured using an RBC flume, and the time required to apply the required depth of water to the plot was monitored using a stopwatch. The DI application was based on the percentage stated in Table 14.1. The irrigation water application for the deficit treatments was evenly distributed throughout the season (Tsakmakis et al. 2018).

For blue water components, the reductions in yield and water savings were calculated from the following equations (Ismail 2010).

$$\text{Reduction in yield} = 100 - \left(\frac{\text{The yield of DI2 or DI3 or DI4}}{\text{Yield of DI1}} \times 100\right) \tag{14.4}$$

$$\text{Water Saving} = 100 - \left(\frac{\text{Water consumption of DI2 or DI3 or DI4}}{\text{Water consumption of DI1}} \times 100\right) \tag{14.5}$$

Soil Moisture Measurement

The volumetric soil moisture status of each plot was monitored throughout the crop growing season using an SDI-12 profile probe. A total of twelve profile probes were installed at 12 plots that represented the twelve treatments of the experiment. The measurement was performed using a moisture meter type HH2 at 10, 20, 30, 40, 60 and 100 cm depths. The volumetric water content is the volume of soil water per volume of soil and was recorded as a percentage at each soil depth. Moreover, gravimetric moisture monitoring up to 40 cm of soil depth was performed at different stages of the growth period.

Determination of Crop Water Use

The average daily evapotranspiration (ET) between successive moisture measurements was estimated using the soil water depletion method:

$$\mathrm{ET} = \frac{\sum_{i=1}^{n}(\mathrm{SMC1}i - \mathrm{SMC2}i) * Di}{t} \qquad (14.6,)$$

where ET is the average daily evapotranspiration between successive volumetric soil moisture content sampling periods (mm day^{-1}); SMC1i is the soil moisture content (mm^3/mm^3) at the time of first sampling (2 days after irrigation) in the ith soil layer; SMC2i is the soil moisture content (mm^3/mm^3) at the time of second moisture sampling (before irrigation) in the ith layer; Di is the thickness of the ith layer (mm); n is the number of soil layers sampled in the root zone depth D, and 't' is the number of days between successive soil moisture content sampling. The seasonal evapotranspiration was obtained from the summation of the weekly ET.

Data Collection

The grain yield was weighed and adjusted to 12.5% grain moisture content, and hundred kernel weight was collected by counting hundred seeds and weighed. Soil moisture at different stages was recorded with the standard oven-dry method and moisture prob. Daily meteorological data, such as RF and maximum and minimum temperature, were collected at the experimental site metrological station, and the standard class-A pan was used to record daily ETo. Soil temperature was measured at a 10 cm soil depth at 9:00 AM, 12:00 AM, 3:00 PM, and 12:00 PM at different stages of the growing season.

Data Analysis

The data were analyzed using analysis of variance (ANOVA) with the R program (R Core Team 2021). The variance among treatments was compared with Tukey's honestly significant difference test (Tukey's HSD) to test differences among sample means for significance at a 5% level of probability (Nanda et al. 2021). The expected hypothesis was that irrigation strategies such as deficit irrigation and mulching used in this experiment decrease the WFb, while the null hypothesis suggests that irrigation strategies had no effect on the WFb.

Table 14.2 Applied irrigation water depth (IWD) and evapotranspiration (ET) for the maize growing season

Treatment	ET mm	IWD (mm)
DI1NM	531.00	534.78
DI2NM	548.2	427.824
DI3NM	222.04	320.868
DI4NM	348.82	267.39
DI1SM	529.96	534.78
DI2SM	458.38	427.824
DI3SM	410.50	320.868
DI4SM	229.36	267.39
DI1PM	274.40	534.78
DI2PM	217.16	427.824
DI3PM	224.82	320.868
DI4PM	250.22	267.39

Results and Discussion

Evapotranspiration and Applied Irrigation Water Depth in the Maize Growing Season

The applied irrigation water depth in the growing season (IWD) ranges from 267.39 to 534.78 mm, while evapotranspiration in the maize growing season (ET) ranges from 217.16 to 548 mm for maize crops. The smallest ET was recorded at DI2PM (217.16 mm), and the largest ET was recorded at DI2NM (548.2 mm). As the values in Table 14.2 show, relatively lower ET was recorded in the plastic mulch treatments, and higher ET was recorded in the no-mulch treatments. This result is in line with Zribi et al. (2015) because there is low evaporation through the hole part of the plastic.

Grain Yield of Maize

Analysis of variance (ANOVA) showed that both mulching ($P = 0.0000243$) and DI ($P = 0.0368$) significantly affected the grain yield (GYLD ton ha^{-1}) of maize, and there was no interaction effect between the two factors. As presented in Table 14.3, the application of DI1 produced the largest grain yields (7.74 t ha^{-1}). The DI4 treatment had the smallest yield of 6.59 t ha^{-1}, which was a 14.86% yield reduction compared to DI1. The results showed that there was no significant difference ($P = 0.0996657$) between DI1 and DI2, but DI1 had 9.43% and 13.57% yield increments over DI2 and DI3, respectively. There was also a 6% yield reduction observed with the application of DI4 compared to DI2, but there was no significant difference between them ($P = 0.0825304$). The transparent plastic mulch gave the highest grain yield

Table 14.3 Grain yield blue water footprint and hundred kernel weight of deficit irrigation and mulching treatments

Deficit irrigation	Mean of WFb (m^3 ton^{-1})	Mean of GYLD (ton ha^{-1})	HKwt (g)
DI1	1179.52[a]	7.74[a]	32.81[a]
DI2	1035.68[a]	7.01[a,b]	33.68[a]
DI3	837.22[b]	6.69[a,b]	32.09[a]
DI4	720.31[b]	6.59[b]	32.59[a]
Mulch	Mean of WFb (m^3 ton^{-1})	Mean of GYLD (ton ha^{-1})	HKwt (g)
SM	1066.73[a]	6.14[b]	32.60[a,b]
NM	968.08[a]	6.72[b]	31.77[b]
PM	794.74[b]	8.17[a]	34.00[a]

Note
WFb blue water footprint; *GYLD* grain yield; *HKwt* hundred kernel weight; *Soil T*^{o} soil temperature. Means followed by the same letter(s) within a column are not significantly different from each other at a 5% level of significance

of 8.17 t ha^{-1}, which was 24.85% and 17.75% higher than the straw and no mulch treatments, respectively. This result agrees with (Kader et al. 2017), who stated that plastic mulching materials increase crop yield more than organic mulching. Aniekwe and Anike (2015) also indicated that plastic mulching was a better crop production technique than other mulch types. In our study, straw mulch resulted in the lowest yield of 6.14 t ha^{-1}, but there was no significant yield difference between the straw and no-mulch treatments. This is because there was pest incidence at the early growth stage of the maize crop. Although the pest incidence was treated by chemical applications, it was observed that pest incidence was higher in the plots mulched with wheat straw than in the plastic and no mulch treatments. As a consequence, plots that received wheat straw mulch produced lower yields. This study revealed that particular attention is needed at the early stage of growth when using straw mulch in crop production for pest control. Similarly, (Ramakrishna et al. (2006) indicated that disease buildup and other interactions need to be studied for the wider adoption of straw mulch.

Blue Water Footprint

The ANOVA showed that both mulching and DI significantly affected ($P = 0.0000266$ and $P = 0.0000000749$) the WFb (m^3 ton^{-1}) of maize, and there was no interaction effect between the two factors. The application of DI1 produced the largest WFb (1179.52 m^3 ton^{-1}), which indicates that since the application of DI received high irrigation water, it gave the highest WFb or low water consumption reduction. On the other hand, the DI4 treatment had the smallest WFb of 720.31 m^3 ton^{-1}, which

was a 38.93% water consumption reduction compared to DI1. There was also a significant difference between the DI1 and DI3 (837.22 m^3 ton^{-1}) treatments, and there was a 29.02% WFb reduction when using DI3 over DI1. As shown in Table 14.3, however, there was no significant difference in grain yield between DI1 and DI3, which implies that considerable amounts of consumptive water reduction can be achieved by practicing deficit irrigation with no significant reduction in yield. This result agrees with Karrou et al. (2012), who stated that a negligible yield reduction of maize and wheat occurred while applying deficit irrigation. The results also showed that there was a significant difference between the WFb of the DI2 (1035.68 m^3 ton^{-1}) and DI4 treatments, and DI4 resulted in a 30.45% WFb reduction compared with DI2. While there was no significant difference in yield between DI1 and DI2, there was a 12.19% WFb reduction in DI2 compared with DI1. Similarly, there was no significant difference between DI3 and DI4 ($P = 0.2617603$), but there was a 13.96% WFb reduction when using DI4 compared to DI3.

The transparent plastic mulch gave the lowest WFb of 794.74 m^3 ton^{-1}, which reduced the WFb by 25.50% and 17.91% compared with the straw and no mulch treatments, respectively. This is because the transparent plastic mulch reduces the consumptive water use, consequently giving the highest yield compared to the other mulch treatments. This is because all of the mulch treatments received the same amount of irrigation water either deficit or full, but the yield at plastic mulch was better than the other mulch treatments, as it reduces the consumptive water use as well. A similar finding by Chukalla et al. (2015) stated that inorganic mulching can reduce the consumption of water use more than organic mulching. According to Nouri et al. (2019), mulching reduced the blue WF by 3.6%, although the WFb reduction was small compared to our study, which confirms the positive impacts of mulching on water savings. The straw mulch gave the highest WFb of 1066.73 m^3 ton^{-1} because, as stated above, the straw mulch gave the lowest yield, resulting in an increased WFb (Table 14.3).

Hundred Kernel Weight

ANOVA showed that mulching (M) significantly affected ($P = 0.05$) the hundred kernel weight (HKwt), whereas no significant difference was shown in the deficit irrigation treatments. As stated in Table 14.3, the transparent plastic mulch gave the best HKwt of 34.00 g, which was 4.12% and 6.56% higher than the straw and no mulch treatments, respectively, whereas treatments without mulching gave the lowest HKwt (31.77 g). The results showed that there was no significant difference between the plastic and straw mulch treatments.

Soil Temperature

ANOVA showed that mulching (M) significantly affected ($P = 0.00001678$) soil temperature (soil T°C), but there was no significant difference among deficit irrigation treatments ($P = 0.8711$). As indicated in Fig. 14.4, the transparent plastic mulch resulted in a higher soil temperature of 23.79 °C, which was 2.50% higher than that in the straw and no mulch treatments. There was no significant difference between the straw and no-mulch treatments. Transparent/clear plastic mulch absorbs little solar radiation but transmits 85% to 95% of incoming solar radiation. The undersurface of transparent plastic mulch is usually covered with condensed water droplets (Fig. 14.3), and this water is transparent to incoming shortwave radiation but opaque to outgoing longwave infrared radiation; thus, much of the heat is retained by transparent plastic mulch (Lamont 2017). Thus, daytime soil temperatures under transparent plastic mulch are generally 4–8 °C higher at a 5 cm depth and 3–5 °C higher at a 10 cm depth compared to treatments without mulch (Lamont 2017). However, most of the solar energy absorbed by black plastic mulch goes to the atmosphere through radiation and forced convection. Soil temperatures at the lower surface of black plastic mulch during the daytime are generally 2.80 °C higher at 5 cm depth and 1.70 °C higher at 10 cm depth compared to that of the unmulched surface (Lamont 2017).

A study by Habtamu et al. (2015) stated that plastic mulch increases soil temperature more than organic and no mulch treatments under polyhouse conditions. Another study by (Ramakrishna et al. 2006) also confirmed that transparent polythene plastic mulching resulted in a higher soil temperature than other mulch types. However, the range of temperature differences was narrower in our study than in those studies, which may be because of weather condition differences in the study areas.

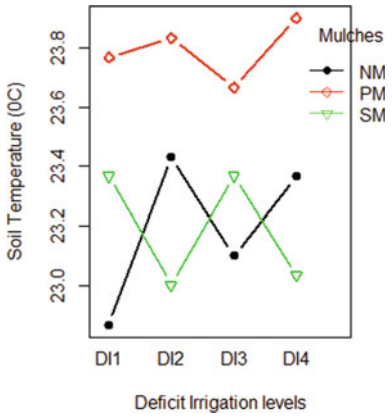

Fig. 14.4 Effects of deficit irrigation and mulching on soil temperature (NM = no mulch, SM = wheat straw mulch and PM = white plastic mulch)

Conclusion

The effects of deficit irrigation and mulching with wheat straw and white transparent polyethylene materials on the yield, soil temperature and blue water footprint of the maize crop were studied using field experiments conducted in the 2021/22 irrigation seasons in the Koga irrigation scheme, Ethiopia. The results showed that deficit irrigation combined with the application of mulch covers, particularly plastic mulch, is an appreciated strategy for maize production in NW Ethiopia. Application of full irrigation gave the largest grain yield and higher blue water footprint of the crops, whereas 50% ETc deficit irrigation produced the smallest yield and blue water footprint. The results revealed that there was no significant difference among applications of 100%, 80% and 60% ETc deficit irrigation in grain yield, and there were no blue water footprint reduction differences between 80 and 60% ETC deficit irrigation applications. On the other hand, the transparent plastic mulch gave the highest grain yield and lowest blue water footprint of maize in the study area over the straw and no mulch treatments. The seasonal evapotranspiration of the maize crop was affected by both water depth and mulching. Plastic mulch resulted in lower seasonal evapotranspiration, and straw mulch resulted in lower seasonal evapotranspiration than bare soil alone. This indicates that the potential of mulching in reducing evaporation and keeping the soil moist is high in our study area. In addition, our study revealed that plastic mulch significantly increased soil temperature in a narrower range and resulted in a higher hundred-kernel weight than straw and no-mulch treatments; however, deficit irrigation applications did not show a significant effect on soil temperature and hundred-kernel weight. In general, deficit irrigation and plastic mulching could be an important strategy to reduce the consumptive water use of maize crops. Further study would be important on pest management strategies when using straw mulch.

Acknowledgements The authors greatly appreciate the Gondar and Adet Agricultural research centers for supplying the research facilities and experimental site.

References

Abiyu A, Alamirew T (2014) Evaluation of stage-wise deficit furrow irrigation application on water advance-recession time and maize yield components at Koga Irrigation Scheme, Ethiopia. Am J Sci Indus Res

Ahmet E (2011) Importance of pan evaporation for irrigation scheduling and proper use of crop-pan coefficient (Kcp), crop coefficient (Kc) and pan coefficient (Kp). Afr J Agric Res 6(32):6706–6718

Amede T (2015) Technical and institutional attributes constraining the performance of small-scale irrigation in Ethiopia. Water Resour Rural Develop 6:78–91

Aniekwe N, Anike N (2015) Effects of different mulching materials and plant densities on the environment, growth and yield of cucumber. IOSR J Agric 8(11):64–72

Chakraborty D, Nagarajan S, Aggarwal P, Gupta VK, Tomar RK, Garg RN et al (2008) Effect of mulching on soil and plant water status, and the growth and yield of wheat (*Triticum aestivum* L.) in a semiarid environment. Agric Water Manage 95(12):1323–1334. https://doi.org/10.1016/j.agwat.2008.06.001

Chala M, Quraishi S (2015) Effect of deficit irrigation on yield and water productivity of garlic (*Allium sativum* L.) under drip irrigation and mulching at Wolaita Soddo, Ethiopia. Int J Life Sci 4(4):232–239

Chukalla AD, Krol MS, Hoekstra AY (2015) Green and blue water footprint reduction in irrigated agriculture: effect of irrigation techniques, irrigation strategies and mulching. Hydrol Earth Syst Sci 19(12):4877–4891. https://doi.org/10.5194/hess-19-4877-2015

Doorenbos J, Kassam A (1979) Yield response to water. Irrigation Drainage paper, 33, 257

Eshete DG, Sinshaw BG, Legese KG (2020) Critical review on improving irrigation water use efficiency: advances, challenges, and opportunities in the Ethiopia context. Water-Energy Nexus 3:143–154

Gizaw W, Assegid D (2021) Trend of cereal crops production area and productivity, in Ethiopia. J Cereals Oilseeds 12(1):9–17

Habtamu T, Wasu M, Yigzaw D (2015) Effects of mulching materials on soil temperature under polyhouse condition. J Biol Agric 5(17):164–168

Hoekstra AY, Chapagain AKJEE (2007) The water footprints of Morocco and the Netherlands: global water use as a result of domestic consumption of agricultural commodities. 64(1):143–151

Hoekstra AY, Chapagain AK, Aldaya MM, Mekonnen MM (2011) The Water Footprint Assessment Manual: Setting the Global Standard. Routledge, London

Ismail SM (2010) Influence of deficit irrigation on water use efficiency and bird pepper production (*Capsicum annuum* L.). 21(2):29–43. https://doi.org/10.4197/Met

Kader MA, Senge M, Mojid MA, Ito K (2017) Recent advances in mulching materials and methods for modifying soil environment. Soil Tillage Res 168:155–166. https://doi.org/10.1016/j.still.2017.01.001

Karrou M, Oweis T, El Enein RA, Sherif M (2012) Yield and water productivity of maize and wheat under deficit and raised bed irrigation practices in Egypt. Afr J Agric Res 7(11):1755–1760

Kassie AE (2019) Challenges and opportunities of irrigation practices in Ethiopia: a review. %J. J Eng Res Rep 9:1–12

Kim I, Kim K (2019) Estimation of water footprint for major agricultural and livestock products in Korea. Sustainability 11(10). https://doi.org/10.3390/su11102980

Kolokytha E (2014) Agricultural development in Lake Koronia. The role of the water footprint of major crops in combating climate change. Paper presented at the Proceedings 3rd IAHR Europe Congress, Porto

Lamont Jr WJ (2017) Plastic mulches for the production of vegetable crops. In: A guide to the manufacture, performance, and potential of plastics in agriculture. Elsevier, Amsterdam, pp 45–60

MacDonald M (2004) Koga dam and irrigation project contract KDIP 3: Koga irrigation and drainage system hydrology factual report. Ministry of Water Resources, Addis Ababa, Ethiopia

Mekonnen MM, Hoekstra AY (2014) Water footprint benchmarks for crop production: a first global assessment. Ecol Ind 46:214–223

Nanda A, Mohapatra BB, Mahapatra A, Mahapatra APKA, Mahapatra, A. (2021) Multiple comparison test by Tukey's honestly significant difference (HSD): do the confident level control type I error. IJAMS 6:59–65

Nouri H, Stokvis B, Galindo A, Blatchford M, Hoekstra AY (2019) Water scarcity alleviation through water footprint reduction in agriculture: the effect of soil mulching and drip irrigation. Sci Total Environ 653:241–252. https://doi.org/10.1016/j.scitotenv.2018.10.311

Perry C, Steduto P, Allen RG, Burt CM (2009) Increasing productivity in irrigated agriculture: agronomic constraints and hydrological realities. Agric Water Manag 96(11):1517–1524

R Core Team (2021) R: A language and environment for statistical computing. R Foundation for Statistical Computing, Vienna, Austria. URL https://www.R-project.org/

Ramakrishna A, Tam HM, Wani SP, Long TD (2006) Effect of mulch on soil temperature, moisture, weed infestation and yield of groundnut in northern Vietnam. Field Crop Res 95(2–3):115–125

Randall GW, Vetsch JA, Huffman JR (2003) Corn production on a subsurface-drained mollisol as affected by time of nitrogen application and nitrapyrin. Agron J 95(5):1213–1219

ROP, D. K (2016) Effects of deficit irrigation on yield and quality of onion crop

Tsakmakis ID, Zoidou M, Gikas GD, Sylaios GK (2018) Impact of irrigation technologies and strategies on cotton water footprint using AquaCrop and CROPWAT models. Environ Process 5(S1):181–199. https://doi.org/10.1007/s40710-018-0289-4

Zhou J-B, Wang C-Y, Zhang H, Dong F, Zheng X-F, Gale W, Li S-X (2011) Effect of water saving management practices and nitrogen fertilizer rate on crop yield and water use efficiency in a winter wheat–summer maize cropping system. Field Crop Res 122(2):157–163

Zribi W, Aragüés R, Medina E, Faci JM (2015) Efficiency of inorganic and organic mulching materials for soil evaporation control. Soil Tillage Res 148:40–45. https://doi.org/10.1016/j.still.2014.12.003

Chapter 15
Management of Transboundary Watercourse in Euphrates-Tigris and Nile River Basins

Yusuf Ali Mohammed and Yücel Acer

Abstract Despite making up two-thirds of our planet, water remains one of the most contentious resource. Transboundary watercourses, in particular, require analytical scrutiny because they involve competing interests as shared resources among riparian states. Practices of dealing with these competing interests are rarely smooth and differ across basins and time. Per international law and organizational structure, this chapter compares transboundary watercourse management practices of the Euphrates-Tigris (ET) and Nile River basins. The chapter examines whether joint institutional basin arrangements are in place in these basins and whether exemplary practices from the ET River basin could be useful in dealing with gaps observed in the Nile River basin management and vice versa. While scrutinizing these foregoing issues, the chapter explores three areas in the ET and Nile River basins management. First, it highlights the governing legal frameworks of both basins per international laws. Then it addresses their administrative structures per objective organizational models and finally explores their likeness and difference as well as their gaps and better experiences to be adopted from each river basin.

Keywords Euphrates-Tigris River · Management practice · Organizational model · Nile River · River basin · Transboundary watercourse · Watercourse law · Watercourse management

Y. A. Mohammed (✉)
Department of Public Law, Graduate School of Social Science, Anadolu University, Eskisehir 26470, Türkiye
e-mail: yusufkud@gmail.com

Y. Acer
Department of Public Law, Graduate School of Social Science, Ankara Yıldırım Beyazıt University, Ankara 06010, Türkiye
e-mail: yucelacer@hotmail.com

A. M. Melesse et al. (eds.), *Land and Water Degradation in Ethiopia*, Springer Geography, https://doi.org/10.1007/978-3-031-60251-1_15

Introduction

Although water is seemingly abundant, with two-thirds of the entire globe under water, it is still a disputed resource. In particular, transboundary watercourses that flow across several sovereign riparian states, covering '45.3% of the earth's land surface, affect[ing] 40% of the world's population, and account[ing] for 80% of global river flows,' are at the heart of water conflict (FAO 2021; UN Water 2021).

Practices of transboundary water use and management vary across time and space and precedents for smooth transboundary management are rare. How shared river basins are managed from an international watercourse law perspective is hence critical. It is imperative to extract lesson to be learned from different basins and share best practices. Such studies not only have academic relevance but also have practical significance in solving basin-wide disputes. This article considers the management of the two of the most disputed river basins in the world, the Nile and Euphrates-Tigris (ET) River basins.

The composition of riparian states in the Nile River basin and the ET River basin varies significantly. But, given their geographical location in north-eastern Africa and the Middle East, respectively, coupled with existing dispute makes them an ideal choice for comparative analysis.

Many independent studies have been conducted on the ET and Nile River basins. Several researchers have incorporated both basins along with other river basins in their case studies. Others, such as Hussen (2014) and Lencho (2014), have studied both basins in their comparative studies. However, save a mere and incidental consideration, their respective scopes of studies were majorly limited to a politico-foreign policy of basin riparian states. To the best of the authors knowledge, a critical comparative study concerning the course of international water law in both basins has not been conducted comprehensively. This chapter conducted a comparative analysis of transboundary watercourse management in both basins. The chapter limits its scope within the normative and institutional parameters of the two basins' management and employs qualitative research methodologies.

Against the above background, the chapter is organized into seven sections. The first section is an introductory section. The second and third sections deal with similarities, differences, and distinct features of the ET and Nile River basins, respectively. The fourth section comparatively scrutinizes the practices of equitable and reasonable use in both basins management. The fifth and sixth sections explore and track good experiences to be drawn from the ET and Nile River basins, respectively. The last section provides a summary of the chapter.

Similarities Between ET and Nile River Basins

The Nile River basin is considered 'one of the few regions of the earth in which extensive archaeological remains of ancient civilizations, renowned polities, kingdoms, and empires can still be found' (Arsano 2011). This river is a massive river, originating from two core founts, notably the White and Blue Nile River coupled with the Atbara River (Lie 2010; National Geographic, n.d.). These rivers confluence in Khartoum, Sudan, then cross through Egypt, and eventually flow into the Mediterranean Sea (Hamza 2006; Khartoum 2018).

Historically, the ET River is among a few popular and widely recognized river because of their attachment to the 'achievement' and 'dawn' of Mesopotamia civilization (Al-Ansari et al. 2018). These rivers arise from the South-eastern high mountains of Türkiye, run across Iran, Syria, and Iraq. After converging at Qurna city in Iraq, they form the Shat Al-Arab River and finally flow toward the Persian Gulf (Al-Ansari 2019; T.C. Ministry of Foreign Affairs 2015).

Both basins are sources of ancient civilization across their respective areas. Although the ET and Nile Rivers arise from different continents, they both eventually flow into the Middle East (Al-Ansari 2019; Okoth-Owiro 2004). In terms of contribution, Türkiye and Ethiopia contribute the lion's share of the total flow in their respective basins. The downstream most riparian countries have minimal to zero contribution in both basins. In both basins, the leading principal players are three: Ethiopia, Egypt, and Sudan in the Nile River basin, and Türkiye, Syria, and Iraq in the ET River basin (Kibaroğlu 2021; Swain 1997) (Table 15.1).

Table 15.1 Average water flow in billion cubic meters (BCM) and riparian states contribution in percentage (%)

Description	Nile River basin		ET River basin	
	Blue Nile (+Atbara) River	White Nile (+other) River	Euphrates River	Tigris River
Average flow (BCM /year)	50 (±5) + 11.4	26.6	26.6	20
	88 (±5)		46.6	
Contribution (riparian/%)	Ethiopia (69–71) Eritrea (minimal) Sudan (0) South Sudan (0) Egypt (0)	Burundi DRC Ethiopia Kenya Rwanda Tanzania Uganda (30) South Sudan (minimal) Sudan (minimal) Egypt (0)	Türkiye (89) Syria (11) Iraq (0)	Türkiye (40–65) Iraq (10–40) Iran (5–25) Syria (0)

Source Awulachew et al. 2007, Bachmann et al. 2019, Hasan et al. 2021, NBI Atlas 2016, UN-ESCWA & BGR 2013, Wheeler et al. 2020

Similar Normative Feature

Having the above introduction, this section analyzes normative practices exhibited in both basins. Starting with the river system, a major consideration is whether the respective rivers are considered as a single or divided river system. Although consensus has not been reached, there is a trend of considering the ET River as two different river systems.[1] In the ET River basin, although Türkiye considers the Euphrates and Tigris Rivers system as one, Syria and Iraq assume these rivers as two separate river system (Elvan 2012). Similarly, in the Nile River basin, there is a view of considering the Nile River as two river systems, the Blue Nile and the White Nile, through the Nile Basin Initiative's (NBI) Coordination Unit (CU)[2] and Strategic Action Plan (SAP)[3] (Johnston 2009; NBI n.d.). Although these mechanisms are designed to abate the project expenses and avoid entanglements among the basin riparian states, it '…goes against the approach of viewing the entire basin as a single unit, as is proposed within the Integrated Water Resource Management (IWRM)' (Johnston 2009; Louka 2006).

Although no enforceable basin-wide inclusive legal regimes are recorded in both basins, it is necessary to mention the existence of un-inclusive treaties. In the ET River basin, there are pre-World War II (WWII) and subsequent post-WWII treaty regimes, mostly dealing with, *inter alia*, provisional minimum river flow, flood management, and mere cooperation (Al-Ansari 2019; Kibaroğlu and Scheumann 2011; Kılıç 2018; Leb 2021.; Mazlum 1996; Sağsenç 2006; UN-ESCWA & BGR 2013; Ünver and Kibaroğlu 2000). But none of these treaties deal with basin-wide river management nor quantity apportionment or quality regulation. Similarly, the Nile River basin has colonial and postcolonial treaties (Abtew and Dessu 2019; Dellapenna 1997; Johnston 2009; Lencho 2014; Mekonnen 2010; Mtua 2017; Okoth-Owiro 2004;

[1] In the ET River basin, the down riparians, typically Iraq, argue 'that the hydraulic systems of these two rivers should be considered separate, because the two rivers irrigate different basins,' while Türkiye, asserting "the basin [as] a whole in terms of their upper water collection and lower distribution basins," considers these Rivers system as one (Elvan 2012).

[2] The NBI is composed of two CU: the Nile Equatorial Lakes SAP CU (NELSAP-CU), which 'is the executive and technical arm of the NEL-SAP," membered with ten riparian states, Burundi, DRC, Egypt, Ethiopia, Kenya, Rwanda, South Sudan, Sudan, Tanzania, and Uganda; and, the Eastern Nile Technical Regional Office (ENTRO), which "is the executive and technical arm of the Eastern Nile SAP (EN-SAP),' composed of four riparian states, Egypt, Ethiopia, South Sudan, and Sudan (NBI n.d.). In both CU, although the downstream riparian states, Egypt, Sudan (and South Sudan) are fully represented, upstream riparian states are not dully represented.

[3] In the NBI, there is a modality of dividing the SAP into two major programs: the NEL-SAP, composed of the NELSAP-CU member states; and the EN-SAP comprised of the ENTRO member states (Johnston 2009; NBI n.d.).

Teshome 2009; Ullendorff 1967). Although the UK-Egypt (1929)[4] and/or Egypt-Sudan (1959)[5] agreements deal with water apportionment, these treaties divide the Nile River flow only between the two downstream riparian countries (Egypt and Sudan). Most other treaties are mere cooperative ones, as they are neither designed to set proper basin-wide management nor put in place to settle major disputed issues among riparian states.

Aside from the above, significant similarities can be deducted from the United Nation (UN) Watercourse Convention (1997), a universal guiding legal regime governing international transboundary watercourses. Analytical scrutiny of the ET River basin uncovers the non-uniformity among basin riparian states in acceding to the Convention,[6] which entails its non-applicability in the same river basin. Similarly, in the Nile River basin, a thorough analysis shows no riparian states have hitherto acceded to the Watercourse Convention (1997),[7] due to diverse stances on the Convention between the upstream[8] and downstream riparian states.[9] Thus, the regime is in no position to regulate and serve as a guiding legal regime. The existence of the two overlapping principles, notably equitable and reasonable use[10]

[4] The UK-Egypt (1929) agreement 'was designed to recognize Egypt's acquired rights over the Nile give', in which not only—'Egypt obtained 92.3% of the utilizable flow of the Nile (48 of 52 BCM) and Sudan 7.7%,'—but also get 'the right to veto any construction projects' of upstream riparians (Johnston 2009; Mtua 2017; Okoth-Owiro 2004; Waterbury 1997).

[5] The Egypt-Sudan (1959) agreement, assumed 'to be nothing more than a continuation of the [1929] colonial' regime, dictates the full utilization of Nile water, by dividing the 'entire 84 billion cubic meters average annual flow of the Nile to be shared among the Sudan and Egypt at 18.5 and 55.5 billion cubic meters, respectively' and leaving the remaining 10 billion cubic meters for evaporation (Bulto 2008; Mtua 2017).

[6] Syria—ratified it, Iraq—acceded, and Iran—voted in favor of the UN Watercourse Convention (1997); however, Türkiye repudiated the aforesaid Convention because of its 'deep concern about the fact that certain articles of the Convention might restrain its official stance in future negotiations for the allocation and management of the [ET] river' (Kramer and Kibaroğlu 2011).

[7] Kenya and Sudan voted in favor of the UN Watercourse Convention (1997), but Burundi repudiated the Convention. While three riparians, Egypt, Ethiopia, Rwanda, and Tanzania, have abstained, the other three, DRC, Eritrea, and Uganda didn't take part in the voting process and have no record of their accession, yet (Bulto 2008; Dellapenna 1997; Salman 2014).

[8] Ethiopia and Rwanda, from upstream, openly raise their concern against the UN Watercourse Convention (1997). Ethiopia, fearing it would jeopardize its right, pointed out its vehement on the 'obligations for the notification of other riparians of planned measures and projects in their territories,' among other principles, and on the absence of a balanced approach in '[accommodat[ing] …the interest of upstream [and] developing' riparian states; while Rwanda believed it 'lacked regard for sovereignty which it considered a "sacrosanct principle" in treaty making processes' (Bulto 2008; Salman 2014; Schwabach 1998).

[9] From downstream, Egypt expressed its vehement against the UN Watercourse Convention (1997), believing it would lean toward the principle of 'equitable and reasonable [use] at the expense of the …significant harm' principle (Salman 2014).

[10] The principle of equitable and reasonable use, sourcing from limited territorial sovereignty/integrity doctrine, is a customary international law, which benefits both upper and lower riparians in letting each riparian use their shared watercourse equitably and reasonably in respective political boundaries (Mohammed 2022a).

and the no significant harm rule,[11] is one of the major issues why many riparian states hesitate to sign the UN Watercourse Convention (Mohammed 2022a). Hence, the UN Watercourse Convention (1997) is not applicable in both basins, because of riparian states conflicting stance coupled with the absence of ratification and/or accession records.

Once the application of the UN Watercourse Convention (1997) is ruled out, it is quite logical to look into both basins feature from customary international laws perspective. In terms of observing customary international watercourse law, the practices of upstream and downstream riparians of both basins are attributed to inconsistent patterns. Intending to receive most (all) of the watercourse without interruption, both basins' downstream riparians tilt toward the principle of no (significant) harm rule, whereas the upstream riparians adhere to the principle of equitable and reasonable utilization, hoping to utilize their shared watercourse equitably and reasonably (Bulto 2008; Elvan 2012; Kimenyi and Mbaku 2015; T.C. Ministry of Foreign Affairs 1996). As there is no agreement over which principle has precedence over the other, there is no basis for considering customary international watercourse laws to be the governing regime in administering both basins.

Downstream riparian states of both basins argue for what they call 'historical, established, natural, and/or acquired' right claim over their shared watercourse basins (Bulto 2008; Elvan 2012; Okoth-Owiro 2004; Salman 2014; T.C. Ministry of Foreign Affairs 1996). To prevent grounds of precedence for customary international rights claim, both basins' upstream riparian states have firmly objected to the forgoing assertions. Downstream riparian states argue the claim of historical rights is a principle to determine the equitable quantification of their common transboundary watercourses, while upstream riparian states dismiss such claims arguing that historical right is neither the only component nor a major element rather it's just a single factor considered for attaining equitable and reasonable use of shared water resources among all riparian states (Kimenyi and Mbaku 2015; McCaffrey 1989; Mohammed 2014; Stebek 2007; T.C. Ministry of Foreign Affairs 1996).

Apart from the above, external actors have had their influence over both basins, thus, examining their vital role in shaping their watercourse management is crucial. Before WWII, the active involvement of foreign powers, particularly the UK, France, Russia, Italy, Japan, Greece, Romania, and Yugoslavia can be seen in treaties at the time in the ET River basin. (Al-Ansari 2019; Lausanne Treaty of Peace 1923; Mazlum 1996; Sağsenç 2006). Similarly, in the colonial era, the direct intervention of occupying colonial powers, notably the UK, Belgium, France, and Italy in the Nile River basin can be drawn from the colonial accords (Mtua 2017; Okoth-Owiro 2004).

The abovementioned facts uncover a clear intervention of European states in both basins' management. Particularly, it is significant to underscore the influence of the

[11] The principle of no (significant) harm rule, originating from a limited territorial sovereignty/integrity doctrine, is a customary international watercourse law, which prohibits any riparian not to engage negatively against a shared watercourse while utilizing their transboundary water resource (Mohammed 2022a; User's Guide Fact Sheet Series: Number 5, n.d.).

UK in the Nile basin and France in the ET basin. In addition to other agreements, the Lausanne Treaty of Peace (1923) which prompted Türkiye into giving up its rights and coercing with the stipulation of talking with Iraq first before pursuing hydraulic projects along the ET watercourse is observable (UN-ESCWA & BGR 2013). The UK-Egypt (1929) and UK-Ethiopia (1902) concords expose similar repercussions. The 1929 treaty regime gave birth to a discourse known as 'acquired rights,' assuming the entire Nile River flow is owned by the two downstream riparians, Egypt, and Sudan. On the other hand, the 1902 accord, although widely contested by Ethiopia, was tactfully crafted to put restrictions on Ethiopia to—not block the whole flow of the watercourse—nor embark on hydraulic developments, unless the UK permits otherwise (Mtua 2017; Okoth-Owiro 2004; Paisley and Henshaw 2013; Waterbury 1997; Woldetsadik 2013, 2015).

Similar Organizational Feature

According to World Bank studies, there are three categories of institutional platforms: A River Basin Commission (Commission),[12] River Basin Authority (Authority),[13] and River Basin Coordinating Committee or Council (Committee).[14] Although the application of these organizational structural models varies based on the nature of a basin, the most common one is a Commission arrangement (Millington et al. 2006; Mohammed 2022a).

The ET River basin has an institutional structure known as the Joint Technical Committee (JTC), which can be classified as *ad-hoc*[15] and permanent.[16] The Nile River basin only has *ad-hoc* structural initiatives,[17] save the Permanent JTC of Egypt and Sudan.[18] In both basins, the institutional structures are characterized as *ad-hoc*.

[12] A Commission is a well-structured and much more formal structural arrangement, which is recommended for basin-wide transboundary watercourse management (Mohammed 2022a).

[13] Authority resembles private companies, which are designed to perform specific developmental tasks like hydropower projects (Mohammed 2022a).

[14] Committee usually comprises ministers or senior representatives, which is used during a preliminary stage of an ongoing form of basin coordination (Mohammed 2022a).

[15] The ad-hoc JTC, which was triggered by uncoordinated developmental projects, was established upon Türkiye's proposal in 1964 and, after deadlocks, came to an end in the 1970s (Kibaroğlu and Scheumann 2011; Ünver and Kibaroğlu 2000).

[16] The permanent JTC came into the picture when Türkiye embarked on South-Eastern Anatolia Projects (GAP), upon the proposal of Iraq in the 1980s. Although JTC's progress was promising, it faced deadlocks and finally halted due to domestic political turmoil in Iraq and Syria (Kankal et al. 2016; Kibaroğlu and Scheumann 2011; Ünver and Kibaroğlu 2000).

[17] The Nile River basin exhibits ad-hoc institutional initiatives, namely the Permanent JTC of Egypt and Sudan, HydroMet, '*Undugu*', TECCONILE, and NBI. (Abdo 2004; Egypt-Sudan agreement 1959; Johnston 2009; Paisley and Henshaw 2013; Mtua 2017).

[18] The Permanent JTC was established per the Egypt-Sudan (1959) agreement,—in which only Egypt and Sudan technocrats are equally represented and,—jointly aimed to 'supervise the execution of the technical provisions of such agreements' and stand against upstream riparians future share

Technical responsibilities conferred on the permanent JTC of the ET River basin and the NBI[19] of the Nile River basin are another common ground between the two basins. In the ET River basin, the permanent JTC was conferred with trading technical data on meteorological and hydrological information and hydraulic project developments among others (Ünver and Kibaroğlu 2000). Similarly, in the Nile River basin, the NBI is conferred with matters pertaining to 'environment, irrigation, watershed, flooding' (Johnston 2009; Mtua 2017; NBI n.d.).

Another similarity between both basins is that they both fall short of a positive outcome of their institutions (Johnston 2009; Leb 2021). Thus, albeit promising efforts, both basins' structural arrangements could not bear fruits and, thus, failed to achieve their ultimate respective goals.

Differing Feature Between ET and Nile River Basins

To start with a general reflection, the Nile, which is the longest river in the world at 6825 km, is considerably longer and wider than the ET River at 4700 km (Al-Ansari 2019; Arsano 2011).

In terms of basin administration, both basins descend from different historical perspectives. During Ottoman Empire, the entire ET River basin used to be governed under a single administration (Beaumont 1998). Once the Ottoman Empire collapsed, the basin got its present composition along its newly formed riparian states (Altinbilek 2004). For the Nile River basin, the mode of administration before and after the colonial period shows minimal variation. In the colonial era, the occupying powers, the UK, and Italy, have ruled almost all riparian states, save Ethiopia, the only uncolonized, independent sovereign state (Cassels 2015;'t Hart 2016). Upon declaring their independence, the Nile basin got its current composition along with its sovereign riparian states. Thus, unlike the ET River basin, the Nile River basin has never experienced a mono governance and unitary administration system.

Compositionally, although both basins have three key riparian players, considerable variation can be observed. In the ET River basin, both upstream and downstream basin have two riparian states, Türkiye and Iran, and Syria and Iraq, respectively. In the Nile River basin, there are two downstream riparian states, namely Egypt and Sudan (and South Sudan since 2011), and eight upstream riparian states, notably Burundi, DRC, Eritrea, Ethiopia, Kenya, Rwanda, Tanzania, and Uganda (NBI n.d.).

Having the above, further differences exhibited in the context of normative and organizational structure in both basins are scrutinized in the following sub-sections.

---

requests, which, however, failed to achieve its objective, was abandoned and considered inactive (Abdo 2004; Egypt-Sudan agreement 1959).

[19] The NBI is the first ever inclusive basin-wide institutional platform established in 1999 (NBI n.d.).

Differing Normative Feature

Doctrinally, quick scrutiny of both basins uncovers a considerable variation. In the ET River basin, although downstream riparian states' ideal argument tilts toward absolute territorial integrity,[20] the practices of both upstream and downstream basin riparians adhere to the doctrine of limited territorial sovereignty,[21] enabling them to use their shared river course equitably and reasonably (Elvan 2012; Sağsenç 2006; T.C. Ministry of Foreign Affairs 1996). In the Nile River basin, both upstream and downstream riparians, ideally and/or practically, lean toward irreconcilable transboundary watercourse doctrines. Claiming to use the entire Nile flow per 'historical' right, the lower riparian states, Egypt and Sudan, tilt toward the doctrines of absolute territorial integrity and the prior appropriation,[22] whereas the upper riparians follow the doctrine of limited territorial sovereignty, insisting to use the Nile River equitably and reasonably (Bulto 2008; Mohammed 2022b).

Aside from the above, the two basins differ in terms of water quantification maturity. Starting with the ET River basin, two treaty regimes govern the provisional water share among riparian states. The first one is the Türkiye-Syria (1987) protocol, a 'provisional agreement' entered during the 'Atatürk' Dam construction, in which Türkiye agreed to discharge 'not less than 500 m^3/sec' for Syria (Sağsenç 2006). According to the Syria-Iraq (1990) agreement, Syria and Iraq agreed to share this release, each getting 42% and 58% respectively (Leb 2021). Although it has not yet been resolved, various mechanisms for water allocation have been suggested by basin states in the ET River basin.[23]

Coming to the Nile River basin, a quick glance at the basin unveils a different story. The strange tale of the Nile River basin starts from the UK-Egypt (1929) and Egypt-Sudan (1959) accords, where the entire Nile watercourse is not only designated as the only property of the downstream riparian states, but also quantified between Egypt and Sudan (Bulto 2008; Waterbury 1997; Woldetsadik 2015). Upstream riparian states have been striving to change these hydro-hegemonic practices by pushing for their respective equitable shares. However, the further downstream riparian states are not willing and prepared for talks on the re/quantification of the Nile River, let alone

[20] Absolute territorial integrity is a doctrinal theory that empowers downstream riparian states 'not only – a privilege to use the total [natural] flow of the river without any interruption and due consideration to upstream riparians interest, but also—accord veto power to rule out any potential [upstream] activity that undermines' the natural water flow (McIntyre 2010; Mohammed 2022a).

[21] Limited territorial sovereignty is a legal doctrine that 'entitles all basin riparians to use their co-shared water resources in an equitable and reasonable manner within their defined sovereign territory' (McIntyre 2010; Mohammed 2022a).

[22] The prior appropriation doctrinal thought dictates any riparian state 'that puts the water to use first [can] …establish prior rights to use an amount of water depending on the date upon which that water use began,' thus, becomes the ultimate owner of the determined water amount by default (Lazerwitz 1993).

[23] Iraqi insists to quantify water as per the mathematical formula, while Türkiye proposes a three-stage plan. However, an agreement has not been reached, yet (Sümer 2015; T.C. Ministry of Foreign Affairs 1996).

discussing mechanisms of re/quantifying water shares (Arsano 2011; Mohammed 2014; Mtua 2017). Unlike the case of the ET River basin, the agenda of equitable water re/allocation in the Nile River basin is, so far, not open for discussion.

Differing Organizational Feature

Having already provided standardized organizational models, one can uncover different structural arrangements in both basins. A quick examination of the permanent organizational arrangement in the ET River basin shows the JTC is organized in conformity with a committee structural model. However, quick scrutiny of the late *ad-hoc* organizational structure in the Nile River basin uncovers the NBI is organized in line with an authority structural model. The NBI was pursued as an intermediate structure pending a comprehensive legal and institutional framework, notably the Cooperative Framework Agreement (CFA) and Nile Basin Commission (NBC), respectively, which is yet to be actualized (Abdalla 2008).

Considering the permanence of institutions in the basins, save the 1st *ad-hoc* JTC in the ET River Basin, the 2nd JTC is a far more significant and permanent institution of the river basin (Kibaroğlu and Scheumann 2011; Ünver and Kibaroğlu 2000). In contrast, a close study of institutions in the Nile River basin shows that, except the inactive permanent JTC of Egypt and Sudan, they are all *ad-hoc* by nature, although the basin intended to establish a permanent commission which could not be realized yet (Abdo 2004; Egypt-Sudan agreement 1959; Johnston 2009; Paisley and Henshaw 2013; Mtua 2017).

In relation to structural power, unlike the permanent JTC of the ET River basin which is just a committee composed of riparian experts, the NBI of the Nile River basin is comparatively a well-organized and commissioned one, with the Council of Ministers of Water Affairs of the Nile Basin (Nile-COM),[24] the Technical Advisory Committee (Nile-TAC)[25], and the Secretariat (Nile-SEC)[26] administrative arrangements (Kibaroğlu and Scheumann 2011; Leb 2021; Lencho 2014; Mtua 2017; NBI n.d.).

Looking at the operationality of institutions, the JTC for the ET River Basin stopped working in 2011, because of negotiations deadlock and the political instability of downstream riparians, Iraq and Syria (Kibaroğlu 2017). The NBI for the

[24] The Nile-COM is 'the highest political and decision-making body, [which] comprised of Ministers in charge of Water Affairs in the Member States' (NBI n.d.).

[25] The Nile-TAC is an expertize organ that 'offers technical support and advice to the Nile Council of Ministers on matters related to the management and development of the Nile waters' (NBI n.d.).

[26] The Nile-SEC, which is based in Entebbe, Uganda, is an organ responsible for 'providing administrative, financial and logistical support and services to Nile-TAC and the Nile-COM; strengthen[ing] member states' institutional and technical capacities and provides shared knowledge bases to support decision making and action at local levels; [and] the overall corporate direction' (Lencho 2014; Mtua 2017; NBI n.d.).

Nile River basin, although deemed frail, is an actively operating institution (NBI n.d.).

The Practice of Equitable and Reasonable Use in ET and Nile River Basins

According to international watercourse scholars, the precedence of equitable and reasonable use over a (significant) harm rule is, arguably, a fact per international transboundary watercourse law (McCaffrey 2001; Stebek 2007). Within this prime discourse, examining the legal regimes and institutional efforts of both river basins can be an interesting avenue.

In the ET River basin, although pending issues on mechanisms for water share quantification, there are interim treaty regimes that prescribe provisional water apportionment among upstream and downstream riparian states. Thus, there is an allocated amount of water already being used by all the basin's riparian states as per Türkiye-Syria (1987) and Syria-Iraq (1990) treaty regime.

In line with the above legal regimes, both institutions, the 1st and 2nd JTC, have played a vital role in adhering and maintaining to equitable and reasonable utilization in the ET River basin. The 1st JTC has strived to put equitable and reasonable use in place and into practice. This determination is evident from its initiatives and talks on how to favorably realize basin riparian states, inter alia, the annual water flow, irrigation needs, and projects built on the watercourse (Kibaroğlu and Scheumann 2011; Ünver and Kibaroğlu 2000). Similarly, the 2nd permanent JTC has prepared a comprehensive plan and has pursued applying the principle of equitable and reasonable use (Kibaroğlu and Scheumann 2011; Ünver and Kibaroğlu 2000).

Coming to the Nile River basin, the whole bulk of the Nile watercourse is only utilized hitherto by the two downstream riparians, Egypt, and Sudan. Although they are the source of almost all the Nile water flow and constitute most of the basin composition, none of the upstream riparian countries are currently permitted to use the resource. These facts are clearly imprinted in the UK-Ethiopia (1902), UK-Egypt (1929), and the Egypt-Sudan (1959) treaty regimes (Bulto 2008; Johnston 2009; Mtua 2017; Okoth-Owiro 2004; Paisley and Henshaw 2013; Salman 2014; Teshome 2009; Ullendorff 1967; Waterbury 1997; Woldetsadik 2013, 2015).

Although these treaty regimes were re/asserted by the UK, Egypt (and Sudan) with the sole justification of not having auxiliary water alternatives, the rising needs and demands of upstream riparian states were not appropriately accommodated. Particularly, looking at Ethiopia, the bulk tributary to the Nile River, one can see the fact that from its 123 BCM runoff water per year, a mere 3 percent remains while the rest 97% flows out of the country—into the Blue Nile and—other frontiers (Arsano 2007). These facts clearly show the dire necessity of more fresh water for Ethiopia. The concern of other upstream riparians, although relatively low due to their smaller contribution to the Nile River, is not different from Ethiopia. Sudan

and Egypt, the current recipient of the totality of the Nile water flow, however have supplementary replacements, such as desalinating salt water and aquifers. However, the willingness to consider and address the alarming need of nine upper riparian states, especially Ethiopia, is absent in the two most downstream riparian states (Arsano 2007; Mohammed 2014; Nashed et al. 2014). Thus, in the Nile River basin, compromising needs, re-quantifying, and sharing the Nile River among all riparian states equitably and reasonably is an ignored matter.

Regardless of attempts made by several institutional initiatives, such as HydroMet, *Undugu*, TECCONILE, and NBI, they were in a weak position to settle such critical issues (Arsano 2007; Brunnee and Toope 2008; Johnston 2009; Paisley and Henshaw 2013). These initiatives could not address upstream riparian states' demand to re/quantify and share the Nile watercourse among all basin riparians equitably and reasonably, since these demands are redlined by downstream riparian states (Arsano 2007; Mason 2004; Mohammed 2014). The effort of establishing NBC per the CFA (2010), which would be responsible to attain and maintain equitable and reasonable water allocation among all basin riparians, was subverted by Egypt and Sudan, as they walked away from the forgoing framework (Mekonnen 2010). In addition, save the unhelpful Declaration of Principles (2015), the dispute over the Grand Ethiopian Renaissance Dam (GERD) is also intertwined with the above-mentioned issues coupled with the downstream riparian states' intention of maintaining the *status quo* of the entire Nile water flow under any circumstances (Tekuya 2021).

Against the above facts and justifications, the practice of the ET River basin in adhering and maintaining the principle of equitable and reasonable use as well as allocating the watercourse among all/most riparians is in no way comparable to that of the Nile River basin, as the former basin management is considerably surpassing the practice of the latter basin.

Better Experience in ET River Basin

This section is devoted to scrutinizing better management practices exhibited in the ET River basin that can be potentially considered to be adopted by the Nile River basin. Bearing in mind the impact of enhancing confidence among basin riparians, the ET River basin has taken a major step that could synergize basin-wide cooperation. In 2011, the ET riparians have commenced a project plan which paved the way to construct a 'Friendship Dam' on the Türkiye and Syria frontiers (Kibaroğlu and Scheumann 2011). The significance of such joint developments in creating positive energy and trust among riparian states cannot be overstated. In contrast, in the Nile River basin, trust among upstream and downstream riparians is extremely missing. In this regard, the experience of the ET River basin can be considered and put into practice, as it can play a vital role in fruitful basin-wide cooperation.

Naturally, an international river flows through several frontiers of basin riparian states, which can potentially be overlapped with a border-related matter. The more transboundary watercourse issue is inextricably intertwined with a boundary dispute,

the harder it gets to find a breakthrough. Thus, there must be a mechanism to detach watercourse issues from that of border one. Having this aspect, it is crucial to consider the ET River basin experience, in which, per the Lausanne Treaty of Peace (1923),[27] riparian states are bound to deal with border and watercourse issues separately (UN-ESCWA & BGR 2013). However, in the Nile River basin, the transboundary watercourse dispute is inextricably intertwined with the border issue. The colonial legal regime, notably the UK-Ethiopia (1902) agreement, which was primarily crafted to address the frontiers between Sudan and Ethiopia, coincidentally incorporated one of the most disputed provision, Article III,[28] dealing with the Nile River. Although this accord was bargained more than a century ago and its legality is highly contested by Ethiopia, it is still one of the major issues that keeps dragging basin-wide cooperation into a deadlock. To come out of this stalemate, the Nile River basin should follow the ET River basin suit and disaffiliate watercourse and border issues and independently negotiate to settle their basin-wide differences.

In the Nile River basin, the GERD is under construction along the Blue Nile course (Tekuya 2021). Although comparatively huge, this dam resembles the *Atatürk* Dam which is already completed and started giving service at its full capacity (Altinbilek and Tortajada 2012). Given the disputes revolving around the first filling and operation of the GERD, the practices of the *Atatürk* Dam can be a modeled solution. Thus, a comparative study of the two dams can help pave the way to resolve the disputed critical issues relating to the ongoing first filling and operation of the GERD.

Better Experience in Nile River Basin

For the proper basin management of international watercourses, having a comprehensive basin-wide treaty has a pivotal role. In this instance, there is the CFA (2010) in the Nile River basin, a framework negotiated by all riparians for a decade. This framework, which is open for signature, is the first in its kind that deals with extensive basin-wide watercourse management in the Nile basin, although it did not come into effect[29] (NBI n.d.). In the ET River basin, despite roundtable negotiation, there is no basin-wide inclusive treaty, save post-WWII bilateral accords (Al-Ansari 2019;

[27] According to Article 109 of the Lausanne Treaty of Peace (1923), 'transboundary water should be dealt with separately' from the boundary and other cross-boundary issues (UN-ESCWA & BGR 2013).

[28] Under Article III of the UK-Ethiopia (1902) agreement, the meaning of the word 'arrest' in the *Amharic* (Ethiopian Language) and the English versions was/is a subject of dispute, as the UK 'assumed that [except for] domestic uses and local irrigational rights, the agreement had definitively deprived Ethiopia of the right to use the resource in any way whatsoever, while Ethiopia's reading [supposed] that only complete arrest of the flows of the river had been prohibited under the treaty arrangement' (Ullendorff 1967; Woldetsadik 2013).

[29] According to Article 43, for the CFA (2010) to come into force, at least six riparian states shall accede to it; thus, although six riparian countries have signed the framework accord, only four countries, notably—Ethiopia, Tanzania, Rwanda, and Uganda, have acceded (NBI n.d.).

Kibaroğlu and Scheumann 2011; Kılıç 2018; Leb 2021; Mazlum 1996; Sağsenç 2006; UN-ESCWA & BGR 2013; Ünver and Kibaroğlu 2000). The ET riparian states can consider the nature of this CFA (2010), its comprehensiveness in particular, and accordingly, adopt it in their basin.

Cooperation over basin-wide watercourse management is mostly not smooth. Following the guidance of international legal regimes, inter alia, Article 33 (2) of the UN Watercourse Convention (1997) and Article 31 (e), 34 (f), 35 (d) of the Berlin Rules (2004), continuous cooperation and negotiation through basin-wide institutionalized arrangement is so vital, as 'once international institutions are in place, they are tremendously resilient over time, even between otherwise hostile riparian nations, and even when conflict is waged over other issues' (Vollmer et al. 2009). Within this framework, in the Nile River basin, there is the NBI that is operating under its technical capacity. Although weak and lacking a positive outcome, the NBI is appreciated not only for not ceasing its operation but also applauded for—continuing, at least, to exist as an institutional platform,—serving as an umbrella in bringing riparian states under one roof, and—'help[ing] to relieve the tension within the basin' (Mtua 2017). As the only way out is to keep the conversation going and walk the talk, the ET riparian states can follow the approach of the Nile River basin, activate, and upgrade its Permanent JTC to—play its productive role in its basin-wide cooperation, and serve as a means of communication platform.

Summary

Management of international rivers shares several similar features and differences, in which ET and Nile River basins are no different. Historically, both basins are featured with wealthy history descending from ancient civilizations. Geographically, both ET and Nile River run into the Middle East. The twin basins have three principal riparian actors each as well.

In terms of a river system, upstream and downstream countries in both basins follow a similar approach, as they intend to follow the undivided and divided river system, respectively. Aiming to use almost the whole of the water flow, in both basins, the downstream riparians argue for historical rights, while the upstream riparians argue against it. Given riparian states conflicting stance over the customary international laws and UN Watercourse Convention (1997), neither govern the basins' watercourse management. External powers, primarily the UK, and France, have negatively contributed to both basins' management. Institutionally, the *ad-hoc*-ness, technical responsibilities, and failure to bear results, among others, are attributed to both basins.

Both basins are characterized by diverse attributes. In terms of distance, the ET River flows shorter than the Nile River, as the latter river is the longest river course in the world. Historically, before the twentieth century, the entire administration of the ET River basin used to be governed by the Ottoman Empire. However, the Nile River basin has never been monopolized and ruled by a single government administration

system. Although the principal players are limited to the three riparians, the total number of riparians is four in the ET and eleven in the Nile River basin, showing considerable variation. Doctrinally, both basins feature diverse practices, as almost all ET River basin riparians practically lean toward limited territorial sovereignty, but the upstream and downstream riparians of the Nile River basin adhere to contradictory legal doctrines. Downstream riparians lean to absolute territorial integrity and prior appropriation, while upstream riparians lean towards limited territorial sovereignty. In the ET River basin, per the Türkiye-Syria (1987) and Syria-Iraq (1990) treaty regimes, various mechanisms of water allocation proposals show the maturity and focus given for the basin-wide water allocation. In contrast, there is no record of positive progress in the Nile River basin, because negotiations over water allocation are redlined by the downstream riparians.

Structurally, the JTC of ET River basin is arranged following a committee model, while the NBI of Nile River basin NBI is modeled per an authority structure. In terms of organizational span, the 2nd JTC is an indefinite one, but the NBI is an interim one. The ET River basin pursues a simple committee structural format, while the NBI institutional framework, with the Nile-COM, Nile-TAC, and Nile-SEC, is structured better. Because of dead-end negotiation coupled with some riparian state's internal turmoil, the JTC failed to progress. However, despite shortcomings, the NBI is hitherto operating.

The application of the equitable and reasonable use principle in both basins exhibits major discrepancies. Although not in full agreement with mechanisms of water quantification for sustainable water utilization, there is a provisional use of the ET River course by all basin riparians conjoined and affirmed by its legal regimes and institutional efforts. However, given the usage of the entire river flow by the two downstream riparians coupled with its treaty regime and weak organizational initiatives prolonging the *status quo*, neither provisional nor sustainable water allocation mechanisms are in place in the Nile River basin. Thus, the watercourse management exhibited in the ET River basin in choosing, applying, and maintaining the principle of equitable and reasonable use is considerably better than the Nile River basin.

Last, but not least, analytically exploring better experience in both basins unveils significant results. The potential better experiences in the ET River basin are, inter alia, enhancing confidence among riparians with its Friendship dam project, disaffiliating frontier matter from transboundary water issues per the Lausanne Treaty of Peace (1923), and modelling the practices of the *Atatürk* Dam for the ongoing dispute over GERD. Similarly, among other better practices in the Nile River basin, producing the comprehensive CFA (2010) and functioning the NBI without ceasing its operation are in the first row. Therefore, each basin can consider the other basin's better management experience and adapt to its respective river basin.

Acknowledgements The corresponding author would like to acknowledge Tadesse Kebebew (Ph.D.), Hatice Kübra Ecemiş Yılmaz (Ph.D.), Çiğdem Pekar (Ph.D.), and Mahemud Tekuya (Ph.D.) for their critical guidance and positive critique, throughout the initial to the final development of this chapter. Moreover, the author's warmest gratitude also to the editors, whose critical review and constructive insight were so significant.

References

Abdalla KMEH (2008) Institutional and legal arrangements in the Nile River basin: suggestions to improve the current situation toward adaptive integrated water resources management. Water Sci Technol 58:2031–2040. https://doi.org/10.2166/wst.2008.746

Abdo M (2004) The Nile question: the accords on the water of the Nile and their implications on cooperative schemes in the Basin. PERCEPTIONS: J Int Aff 9(2), Article 2. https://dergipark.org.tr/en/pub/perception/issue/49007/625184

Abtew W, Dessu SB (2019) The grand Ethiopian renaissance dam on the Blue Nile. Springer International Publishing. https://doi.org/10.1007/978-3-319-97094-3

Agreement between Ethiopia and United Kingdom on the Frontiers between the Soudan, Ethiopia, and Eritrea, U.K.T.S. 16 6 (1902) https://www.marefa.org/images/b/bd/Treaty_of_Addis_Ababa_1902.pdf

Agreement between the Syrian Arab Republic and Iraq to Share the Euphrates Water (1990)

Agreement Between the United Arab Republic and the Republic of Sudan for the Full Utilization of the Nile Waters, 8 (1959) https://treaties.un.org/Pages/showDetails.aspx?objid=08000002801 32f7f&clang=_en

Agreement on Declaration of Principles between the Arab Republic of Egypt, the Federal Democratic Republic of Ethiopia and the Republic of the Sudan on the Grand Ethiopian Renaissance Dam Project, 5 (2015) https://www.internationalwaterlaw.org/documents/regionaldocs/Final_Nile_Agreement_23_March_2015.pdf

Agreement on the Nile River Basin Cooperative Framework, 71 (2010) https://nilebasin.org/nbi/cooperative-framework-agreement

Al-Ansari N (2019) Hydro geopolitics of the tigris and euphrates. In: Mustafa YT, Sadkhan S, Zebari S, Jacksi K (eds) Recent researches in Earth and environmental sciences. Springer International Publishing, pp 35–70. https://doi.org/10.1007/978-3-030-18641-8_4

Al-Ansari N, Adamo N, Sissakian V, Knutsson S, Laue J (2018) Water resources of the Tigris River catchment. J Earth Sci Geotechn Eng 8(3):21–42. http://urn.kb.se/resolve?urn=urn:nbn:se:ltu:diva-68443

Altinbilek D (2004) Development and management of the Euphrates-Tigris basin. Int J Water Resour Dev 20(1):15–33. https://doi.org/10.1080/07900620310001635584

Altinbilek D, Tortajada C (2012) The Atatürk Dam in the context of the Southeastern Anatolia (GAP) project. In: Tortajada C, Altinbilek D, Biswas Ak (eds) Impacts of large dams: a global assessment. Springer, Heidelberg, pp 171–199. https://doi.org/10.1007/978-3-642-23571-9_8

Arsano Y (2007) Ethiopia and the Nile: dilemmas of national and regional hydropolitics. Center for Security Studies, Swiss Federal Inst. of Technology

Arsano Y (2011) Negotiations for a Nile-cooperative framework agreement. Institute for Security Studies, Paper 222, 8. https://www.files.ethz.ch/isn/136717/PAPER222.pdf

Awulachew SB, Yilma AD, Loulseged M, Loiskandl W, Ayana M, Alamirew T (2007) Water resources and irrigation development in Ethiopia. International Water Management Institute (IWMI). https://www.iwmi.cgiar.org/publications/iwmi-working-papers/iwmi-working-paper-123/

Bachmann A, Tice V, Al-Obeidi LA, Kilıç DT (2019) Tigris-Euphrates river ecosystem: a status report. 24. https://www.savethetigris.org/wp-content/uploads/2019/03/Paper-Challenge-C-Ecosystem-FINAL-to-be-published.pdf

Beaumont P (1998) Restructuring of water usage in the Tigris-Euphrates basin: the impact of modern water management policies. Middle East Nat Environ Bull 103:168–186. https://citeseerx.ist.psu.edu/viewdoc/summary?doi=10.1.1.539.3915

Berlin Rules on Water resources, adopted International Law Association (2004) http://www.cawater-info.net/library/eng/l/berlin_rules.pdf

Brunnee J, Toope S (2008) The changing Nile Basin regime: does law matter? Harvard Int Law J 43(1):105–159. https://ssrn.com/abstract=1182962

Bulto TS (2008) Between ambivalence and necessity in the Nile Basin: occlusions on the path towards a basin-wide treaty. Mizan Law Rev 2(2), Article 2. https://doi.org/10.4314/mlr.v2i2.56149

Cassels A (2015) 15. The Anglo-Italian Colonial Entente. In: Mussolini's Early diplomacy. Princeton University Press, pp 288–314. https://doi.org/10.1515/9781400872343-019

Convention on the Law of the Non-navigational Uses of International Watercourses, 18 (1997) https://treaties.un.org/Pages/showDetails.aspx?objid=0800000280025697&clang=_en

Dellapenna J (1997) The Nile as a legal and political structure. In: Brans EHP, de Haan EJ, Nollkaemper A, Rinzema J (eds) The scarcity of water: emerging legal and policy responses. Kluwer Law International, pp 121–134. https://www.researchgate.net/publication/288014044_The_Nile_as_a_legal_and_political_structure

Elvan O (2012) Integrated water resources management work in the Euphrates and Tigris River—Basin. Sci Res Essays 7(49). https://avesis.iuc.edu.tr/yayin/2e442c0d-d9d7-46b3-8cf3-e8cd5ab3bbf8/integrated-water-resources-management-work-in-the-euphrates-and-tigris-river-basin

Exchange of Notes Between Her Majesty's Government in the United Kingdom and the Egyptian Government in Regard to the Use of the Waters of the River Nile for Irrigation Purposes, 37 (1929) http://gis.nacse.org/tfdd/tfdddocs/92ENG.pdf

FAO (2021) Land & water: transboundary water management. Food and Agriculture Organization of the United Nations. https://www.fao.org/land-water/water/water-management/transboundary-water-management/en/

Hamza W (2006) The Nile estuary. In: Wangersky PJ (ed) Estuaries. Springer, Heidelberg, pp 149–173. https://doi.org/10.1007/698_5_025

Hasan E, Tarhule A, Kirstetter P-E (2021) Twentieth and twenty-first century water storage changes in the Nile River Basin from GRACE/GRACE-FO and Modeling. Remote Sens 13(5), Article 5. https://doi.org/10.3390/rs13050953

Hussen SA (2014) Comparative study of the role of transboundary rivers in relations of Countries: the case of Nile and Euphrates. Hacettepe University

Johnston E (2009) Factors influencing a basin-wide agreement governing the Nile River [Simon Fraser University]. https://summit.sfu.ca/item/9400

Kankal M, Nacar S, Uzlu E (2016) Status of hydropower and water resources in the Southeastern Anatolia Project (GAP) of Turkey. Energy Rep 2:123–128. https://doi.org/10.1016/j.egyr.2016.05.003

Khartoum: A Tale of Two Rivers (2018) AramcoWorld. https://www.aramcoworld.com/Articles/March-2018/Khartoum-A-Tale-of-Two-Rivers

Kibaroğlu A (2017) Euphrates-Tigris River basin water management as conflict prevention. Orient - Deutsche Zeitschrift Fur Politik Und Wirtschaft Des Orients 58:18–26

Kibaroğlu A (2021) The Euphrates–Tigris River basin. In: Kibaroğlu A, Schmandt J (eds) Sustainability of engineered rivers in arid lands: challenge and response. Cambridge University Press, Cambridge, pp 94–106. https://doi.org/10.1017/9781108261142.008

Kibaroğlu A, Scheumann W (2011) Euphrates-Tigris Rivers system: political rapprochement and transboundary water cooperation. In Kramer A, Kibaroğlu A, Scheumann W (eds) Turkey's Water Policy: National Frameworks and International Cooperation. Springer, Heidelberg, pp 277–299. https://doi.org/10.1007/978-3-642-19636-2_16

Kimenyi MS, Mbaku JM (2015) International water law and the Nile River Basin. In: Governing the Nile River Basin. Brookings Institution Press, pp. 60–71. JSTOR. https://doi.org/10.7864/j.ctt130h973.9

Kılıç S (2018) Iran-Iraq transboundary water relations and Turkey, Centre for Middle Easter Studies. Centre for Middle Easter Studies, vol 79. https://www.orsam.org.tr/en/iran-iraq-transboundary-water-relations-and-turkey/

Kramer A, Kibaroğlu A (2011) Turkey's position towards international water law. In: Kramer A, Kibaroğlu A, Scheumann W (eds) Turkey's Water Policy: National Frameworks and International Cooperation. Springer, Heidelberg, pp 215–228. https://doi.org/10.1007/978-3-642-19636-2_12

Lausanne Treaty of Peace between Turkey and the 'Victorious States' [British Empire, France, Italy, Japan, Greece, Romania, and Yugoslavia] (1923) https://wwi.lib.byu.edu/index.php/Treaty_of_Lausanne

Lazerwitz DJ (1993) The flow of international water law: the International Law Commission's Law of the non-navigational uses of international watercourses. Indiana J Global Legal Stud 1(1):247–271. https://www.repository.law.indiana.edu/ijgls/vol1/iss1/12

Leb C (2021) The Tigris-Euphrates Joint Technical Committee—deadlocked. IUCN Water Programme, vol 6. Retrieved 16 July 2021, from https://www.iucn.org/sites/dev/files/import/downloads/tigris_euphrates.pdf

Lencho TR (2014) Challenges of cooperation in the Nile and Euphrates-Tigris Basins: a comparative analysis [Master Dissertation, Addis Ababa University]. http://etd.aau.edu.et/handle/123456789/4696

Lie JHS (2010) Supporting the Nile Basin initiative: a political analysis 'Beyond the River.' Norwegian Institute of International Affairs. https://www.academia.edu/2243972/Supporting_the_Nile_Basin_Initiative_A_Political_Analysis_Beyond_the_River

Louka E (2006) International environmental law: fairness, effectiveness, and world order. Cambridge University Press, Cambridge. https://doi.org/10.1017/CBO9780511618109

Mason SJA (2004) From conflict to cooperation in the Nile Basin: interaction between water availability, water management in Egypt and Sudan, and International Relations in the Eastern Nile Basin [Doctoral Thesis, ETH Zurich]. https://doi.org/10.3929/ethz-a-004773119

Mazlum İ (1996) Water in the Middle East: the scarce resource in the region [Master Dissertation, Marmara University]. https://katalog.marmara.edu.tr/veriler/yordambt/cokluortam/F/E/B/C/F/T0043183.pdf

McCaffrey S (1989) The law of international watercourses: some recent developments and unanswered questions. Denver J Int Law Policy 17(3). https://digitalcommons.du.edu/djilp/vol17/iss3/3

McCaffrey SC (2001) The law of international watercourses: non-navigational uses. Oxford University Press

McIntyre O (2010) International water law: concepts, evolution and development. In: Transboundary water management. Routledge

Mekonnen DZ (2010) The Nile Basin cooperative framework agreement negotiations and the adoption of a 'water security' paradigm: flight into obscurity or a logical Cul-de-sac? Eur J Int Law 21(2):421–440. https://doi.org/10.1093/ejil/chq027

Millington P, Olson D, McMillan S (2006) An introduction to integrated river basin management (Briefing Note No. 1; An Introduction to Integrated River Basin Management, p 20). The World Bank. https://documents1.worldbank.org/curated/en/965371468340137430/pdf/411500Intro0to1mgmt0NOTE1101PUBLIC1.pdf

Mohammed YA (2017) The "Water Security" principle under Nile Basin CFA and its Ramification (Germany: LAMBERT Academic Publishing)

Mohammed YA (2022a) The guiding legal regime and institutional arrangement of transboundary watercourse: a review. Int J Water Manage Diplomacy 1(4):75–90. https://dergipark.org.tr/en/pub/ijwmd/issue/68070/1025603

Mohammed YA (2022b) The endless controversies of the Nile River basin in the context of international transboundary watercourse doctrines. Ankara Sosyal Bilimler Üniversitesi Hukuk Fakültesi Dergisi 4(2), Article 2. https://doi.org/10.47136/asbuhfd.1050465

Mtua G (2017) Bilateral Treaties on the Nile River and their impacts on international relations [Master Dissertation, Tumaini University Makumira]. https://www.academia.edu/37288651/BILATERAL_TREATIES_ON_THE_NILE_RIVER_AND_THEIR_IMPACTS_ON_INTERNATIONAL_RELATIONS

Nashed A, Sproul AB, Leslie G (2014) Water resources and the potential of brackish groundwater extraction in Egypt: a review. J Water Supply Res Technol AQUA 63(6):399–428. https://doi.org/10.2166/aqua.2014.162

National Geographic (n.d.) Nile River. Retrieved 4 Oct 2022, from https://education.nationalgeographic.org/resource/nile-river
NBI (n.d.) Retrieved 5 Oct 2022, from https://nilebasin.org/
Nile Basin Water Resources Atlas (2016) Nile Basin initiative. https://atlas.nilebasin.org/start/
Okoth-Owiro A (2004) The Nile Treaty: state succession and international treaty commitments, a case study of the Nile Water Treaties. Konrad Adenauer Foundation
Paisley RK, Henshaw TW (2013) Transboundary governance of the Nile River Basin: past, present and future. Environ Dev 7:59–71. https://doi.org/10.1016/j.envdev.2013.05.003
Protocol between Türkiye and Syrian Arab Republic on matters pertaining to economic cooperation, signed at Damascus, 12 (1987) https://www.un-ilibrary.org/content/books/9789210596435s002-c001/read
Sağsenç İ (2006) The issue of management of the waters of the Euphrates and Tigris Basin in international context [Master Dissertation, Middle East Technical University]. https://open.metu.edu.tr/handle/11511/16168
Salman SMA (2014) Entry into force of the UN watercourses convention—where are the Nile Basin countries? International Water Law Project Blog. https://www.internationalwaterlaw.org/blog/2014/06/02/dr-salman-m-a-salman-entry-into-force-of-the-un-watercourses-convention-where-are-the-nile-basin-countries/
Schwabach A (1998) United Nations Convention on the law of non-navigational uses of international watercourses, customary international law, and the interests of developing Upper Riparians. Texas Int Law J 33:257–280. https://doi.org/10.2139/ssrn.3741091
Stebek EN (2007) Eastern Nile at crossroads: preservation and utilization concerns in focus. Mizan Law Review 1(1), Article 1. https://doi.org/10.4314/mlr.v1i1.55613
Sümer V (2015) Three decades after three-stage plan: time for a reappraisal. Center for Middle Eastern Studies. https://www.orsam.org.tr/en/three-decades-after-three-stage-plan-time-for-a-reappraisal/
Swain A (1997) Ethiopia, the Sudan, and Egypt: the Nile river dispute. J Mod Afr Stud 35(4):675–694. https://doi.org/10.1017/S0022278X97002577
't Hart MC (2016) Why was Ethiopia not colonized during the late-nineteenth century 'Scramble for Africa'? In: Baten J (ed) A history of the global economy: From 1500 to the present. Cambridge University Press, Cambridge, pp 351–352. http://www.cambridge.org/vn/academic/subjects/history/economic-history/history-global-economy-1500-present?format=PB
T.C. Ministry of Foreign Affairs (1996) Water issues between Turkey, Syria and Iraq. Department of Regional and Transboundary Waters. https://dergipark.org.tr/tr/download/article-file/817266
T.C. Ministry of Foreign Affairs. (2015). *Water: A Source of Conflict of Cooperation in the Middle East*. 10. https://www.mfa.gov.tr/data/DISPOLITIKA/WaterASourceofConflictofCoopintheMiddleEast.pdf
Tekuya M (2021) Sink or swim: alternatives for unlocking the grand Ethiopian Renaissance Dam Dispute. Columbia J Transnational Law 59(1):65–116. https://www.jtl.columbia.edu/volume-59/sink-or-swim-alternatives-for-unlocking-the-grand-ethiopian-renaissance-dam-dispute
Teshome W (2009) Colonial boundaries of Africa: the case of Ethiopia's boundary with Sudan. Ege Acad Rev 9(1), Article 1. https://dergipark.org.tr/en/pub/eab/issue/39855/472609
Ullendorff E (1967) The Anglo-Ethiopian Treaty of 1902. Bull School Oriental Afr Stud Univ Londn 30(3):641–654. https://www.jstor.org/stable/612393
UN Water (2021) Water facts: transboundary waters. UN-Water. https://www.unwater.org/water-facts/transboundary-waters
UN-ESCWA, & BGR (2013) Inventory of shared water resources in Western Asia. Water Inventory. http://waterinventory.org/surface_water/tigris-river-basin
Ünver O, Kibaroğlu A (2000) An institutional framework for facilitating cooperation in the Euphrates-Tigris River Basin. Int Negot 5(2):311–330. https://doi.org/10.1163/15718060020848785

User's Guide Fact Sheet Series, Number 5. No Significant Harm Rule (n.d.) UN Watercourses Convention. Retrieved 5 Oct 2022, from https://www.unwatercoursesconvention.org/documents/UNWC-Fact-Sheet-5-No-Significant-Harm-Rule.pdf

Vollmer R, Ardakanian R, Hare M, Leentvaar J, van de Schaaf C, Wirkus L (2009) Institutional capacity development in transboundary water management. https://www.ais.unwater.org/ais/pluginfile.php/90/course/section/126/181792e.pdf

Waterbury J (1997) Between unilateralism and comprehensive accords: modest steps toward cooperation in international River Basins. Int J Water Resour Dev 13(3):279–290. https://doi.org/10.1080/07900629749692

Wheeler KG, Jeuland M, Hall JW, Zagona E, Whittington D (2020) Understanding and managing new risks on the Nile with the Grand Ethiopian Renaissance Dam. Nat Commun 11. https://ora.ox.ac.uk/objects/uuid:95ec809c-d88f-4198-af30-d3ada9ad889f

Woldetsadik TK (2013) International watercourses law in the Nile River Basin: three states at a crossroads. Routledge. https://www.routledge.com/International-Watercourses-Law-in-the-Nile-River-Basin-Three-States-at/Woldetsadik/p/book/9781138573116

Woldetsadik TK (2015) Anglo-Ethiopian Treaty on the Nile and the Tana Dam Concessions: a script in legal history of Ethiopia's Diplomatic Confront (1900–1956). Mizan Law Rev 8(2), Article 2. https://doi.org/10.4314/mlr.v8i2.1

Chapter 16
Geospatial-Based Groundwater Potential Zone Investigation and Mapping: A Case Study of the Upper Awash Basin, Ethiopia

Gelana Daba Adugna and Berhan Gessesse Awoke

Abstract Rapid population growth and diversified activities have increased the utilization of groundwater resources for domestic and industrial processes and irrigation in the Upper Awash Basin. The objective of this study was to identify prospective groundwater zones (GWPZs) in the Upper Awash Basin by utilizing remote sensing and auxiliary data. Thematic layers of the parameters that influence groundwater occurrence and movement in the study area were produced using satellite images and other auxiliary data. Accordingly, eight thematic maps, geomorphology, geology, slope, rainfall, lineament density, land use/land cover (LULC), drainage density, and soil, were prepared and transformed into raster datasets using ArcGIS 10.7. Weights were allocated to theme layers based on their significance in the generation of groundwater potential in the study area. The AHP pairwise comparison matrix was utilized to calculate the hierarchical rank of each parameter, and the final normalized weights of each layer were estimated. The layers were then integrated using a weighted overlay technique, and a GWPZ map was produced. The study area's GWPZ map was classified into five categories: excellent (0.60%), very good (54.21%), good (32.21%), medium (12.73%), and poor (0.25%). Finally, to evaluate the validity of the results, the GWPZ map was verified using data from 201 boreholes distributed throughout the basin. The validation result confirmed that 82.3% of high-yield boreholes correspond to "very good" category of the GWPZ. Therefore, the applied method provides acceptable result that can help future planning and sustainable utilization of the groundwater resources in the Upper Awash Basin.

Keywords Upper Awash Basin · Analytical hierarchy process (AHP) · Groundwater potential zone · Land use/land cover · Remote sensing

G. D. Adugna (✉)
Department of Geology, College of Natural Sciences, Salale University, P.O. Box 245, Fiche, Oromia, Ethiopia
e-mail: gelana_dheba@slu.edu.et

G. D. Adugna · B. G. Awoke
Department of Remote Sensing Research and Development, Entoto Observatory and Research Center, Space Science and Geospatial Institute (SSGI), P.O. Box 33679, Addis Ababa, Ethiopia

A. M. Melesse et al. (eds.), *Land and Water Degradation in Ethiopia*, Springer Geography, https://doi.org/10.1007/978-3-031-60251-1_16

Introduction

Water, the essential component of all life, must be readily available in sufficient quantities and of high enough quality to fulfill the increasing demand for domestic, agricultural, and industrial processing activities (Arefayne and Abdi 2015; Fenta et al. 2014; Shanableh 2015). Urbanization, economic development, and population growth are all contributing to a rising need for freshwater globally. Approximately 0.6% of the world's total water supply comes from groundwater, which accounts for approximately 60% of all freshwater supply. Approximately 1.5 billion people depend on groundwater resources. The groundwater resources in Ethiopia are estimated at a volume of over 2.6 billion m^3 (MOWS 2002). As groundwater is present in virtually all geologic formations and is naturally protected from surface-level human activities that may contaminate it, and it is of higher quality and more accessible (Morris et al. 2003; Prasanna et al. 2011). This shows why it is important to prioritize the development of groundwater resources since surface water resources are unevenly distributed because rainfall is distributed unevenly both in time and space.

Groundwater flow and availability has been studied by various methods (Chebud and Melesse 2009, 2011; Stiefel et al. 2009). According to Arkoprovo et al. (2012), a number of factors can affect a groundwater area's potential. These parameters are geological, hydrological, biological, and physiographic elements and their interactions. Drilling, hydrogeological, geological, and geophysical approaches are expensive, time-consuming, and involve the engagement of experienced people whenever analyzing these parameters for the delineation of potential groundwater in particular areas (Arefayne and Abdi 2015; Raja Kumar et al. 2016). Nevertheless, the groundwater potential zone can be determined using the remote sensing technique, which is a quick and cost-effective means of collecting important data on geology, geomorphology, lineaments, drainage density, and slope that in turn helps to identify the groundwater potential zone (Adeyeye et al. 2019; Arulbalaji et al. 2019; Solomon 2003; Sunmin et al. 2020; Tanzeer 2020). Therefore, integrating remote sensing data with other datasets to investigate groundwater resources has become a breakthrough in groundwater research that aids in evaluating, monitoring, and preserving groundwater resources (Hussein et al. 2017).

Unwise groundwater utilization is increasingly an evident problem and a critical concern for many developing countries, including Ethiopia (Fenta et al. 2014; Hussein et al. 2017; Yitbarek et al. 2012). One of the most critical challenges is the absence of up-to-date spatial information on the quantity and distribution of groundwater resources (Hussein et al. 2017). Few studies have identified the potential of groundwater zones in particular areas in Ethiopia using remote sensing techniques (Fenta et al. 2014; Hussein et al. 2017; Meresa and Taye 2019). From the literature reviewed thus far, the application of remote sensing for evaluating the potential zones of groundwater in Ethiopia is very scant; instead, remote sensing has relied on ground-based survey methods, such as hydrogeological and geophysical methods. While remote sensing is relatively easily accessible and more uniformly distributed and is especially useful in regions with sparse measurements, it should be followed by observations.

According to the Awash Basin Authority ABA (2017), the annual water demand upstream of the Koka Dam increases due to dramatically increasing population numbers, high urbanization, and industrial activities, particularly in Addis Ababa and the surrounding area. Furthermore, the Awash Basin Authority report confirmed that areas upstream of the Koka Dam are of interest and require further groundwater assessment because surface water is insufficient for domestic, irrigation, and other uses in the area. Therefore, this research aims to identify the potential of groundwater zones using remote sensing techniques and the analytical hierarchy process method by integrating parameters that control the distribution and movement of groundwater in the area. Moreover, it aims to update the information on the spatial and temporal distribution of groundwater resources in the Upper Awash Basin.

Description of the Study Area

The study area indicated in Fig. 16.1 is the upstream portion of the Awash River Basin, which contributes a significant amount of water to the Awash River, as it originates from mountainous topography and annually receives high rainfall amounts.

Only Ethiopia's north-central plateau, the nearby escarpment, and the Great Rift Valley system are home to the Upper Awash Basin. The nearby central plateau is drained westward by the Blue Nile River drainage system and northeastward by the Awash River drainage system (Yitbarek et al. 2012). The study area's drainage system is distinguished by a dendritic and rectangular drainage pattern, as shown in Fig. 16.2. The Blue Nile Basin borders the study area in the west, and the Omo-Gibe and Rift Valley Lakes Basin borders the study area in the southwest (Henock et al. 2014). The Koka Dam, which was used as the outlet point for catchment delineation of the study area, is approximately 93 km away from Addis Ababa in the southeast direction. The study area is bounded between 8° 0′ 00″ to 9° 14′ 00″ N Latitude and 38° 30′ 30″ to 39° 80′ 00″ E Longitude. It covers a total surface area of approximately 11,645 km^2.

The study area is characterized by a high mean annual rainfall ranging from 556 to 1115 mm. The highest rainfall occurs in June, July, August, and September, with December, January, and February being the driest months. The mean monthly temperature of the study area ranges from 15.7 to 22.4 °C. The minimum and maximum temperatures vary from 8.0 to 13.5 °C and 23.1 to 31.3 °C, respectively. According to Efrem (2010), "the regional geology of the study area is divided into four successions. These are (1) prerift units, which are high-quality metamorphic rocks (biotite-gneiss), Mesozoic sedimentary rocks consisting of Adigrat sandstone, slate, marl, Antalo limestone, and Oligocene to late Miocene flood basalts (Jimma, Aiba-Alaje, Makonnen, Tarmaber-Megezez, Guraghe-Anchar, and Addis Ababa). (2) Syn Rift units, which include the Upper Miocene Quaternary products of pyroclastic Nazret rocks from welded to partially welded pyroclastic flows with rhyolite and trachytic lava domes. (3) Main rift units, which include the Quaternary-Holocene young central volcanoes of Gash Megal rhyolites and Wechecha trachyte, Chafe Donsa pyroclastic

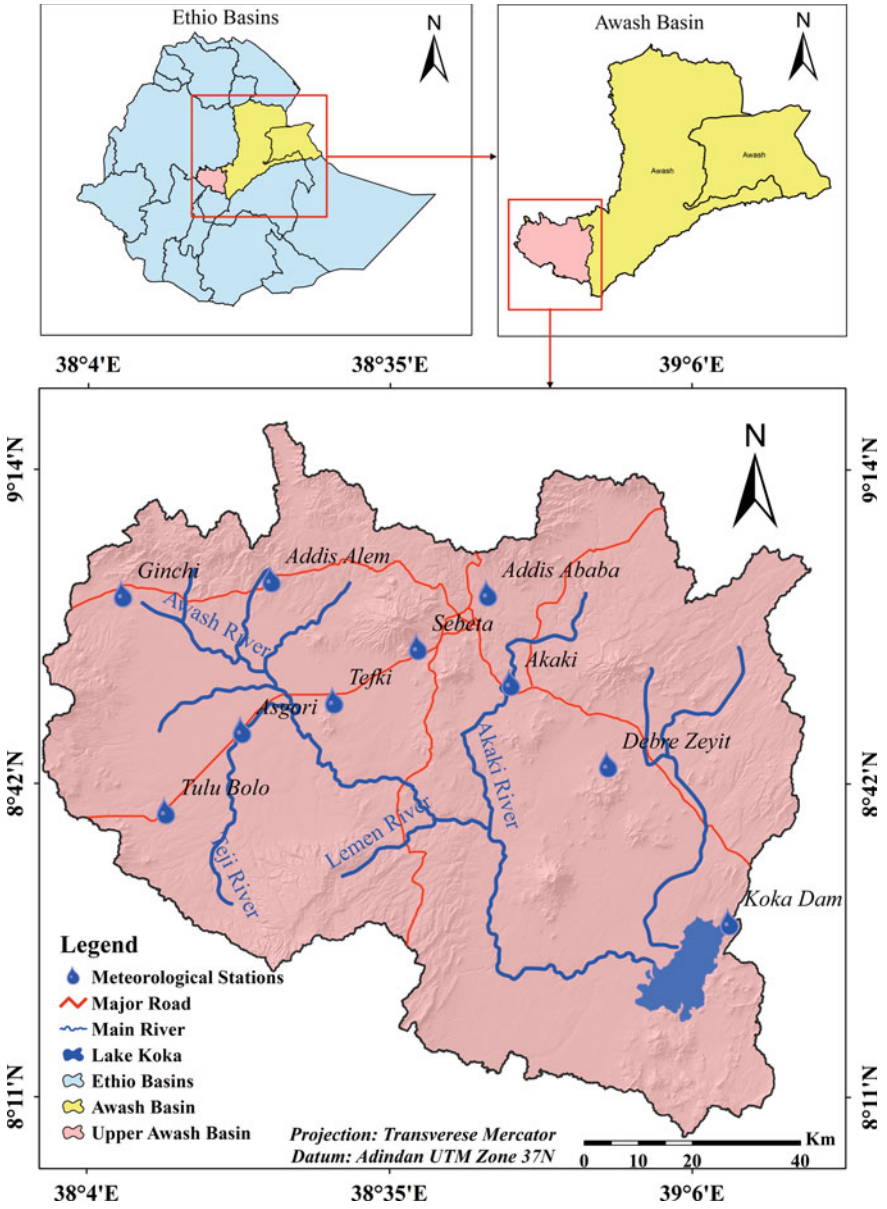

Fig. 16.1 The location map of the study area

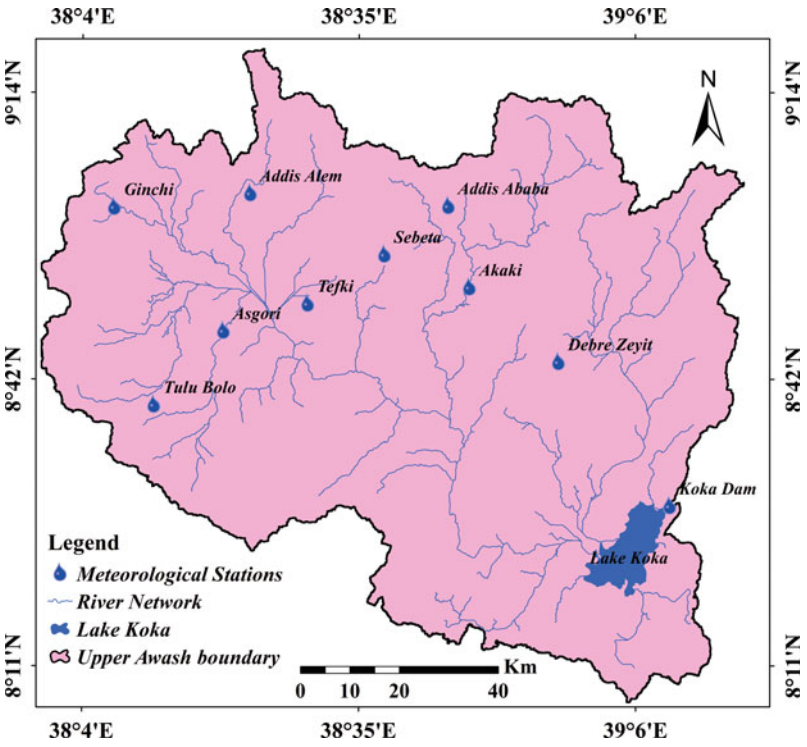

Fig. 16.2 Drainage patterns of the Upper Awash Basin

deposits, slag fallout, and phyric basalt lava flows from Akaki, zikwala lava-trachyte, fall rhyolite, Pyolithic domes deposits and from Bora-Bericha, lake sediments and phreatomagmatic, cinder cones and fallout deposits from Wonji basalts; and (4) quaternary alluvial deposits".

Similarly, Ethiopia has a diverse set of soil types; Berhanu et al. (2013) divides Ethiopia's landmasses into approximately 60 soil types, with area coverage ranging from 1.4 to 208,882 km^2. In the central Ethiopian highlands, soils develop on trap basalts and subordinately on pyroclastic rocks. There is very little spatial variability in rainfall, and as a result, soil characteristics depend mainly on topography (Billi 2015). These soils were formed due to different factors that were responsible for soil formation and development from existing geological material. The thickness of those soils in the study area varies depending on the geological setting, with a thin layer of soil on high topography and a thick layer on low topography. The soil types found in the study area are shown in Fig. 16.3.

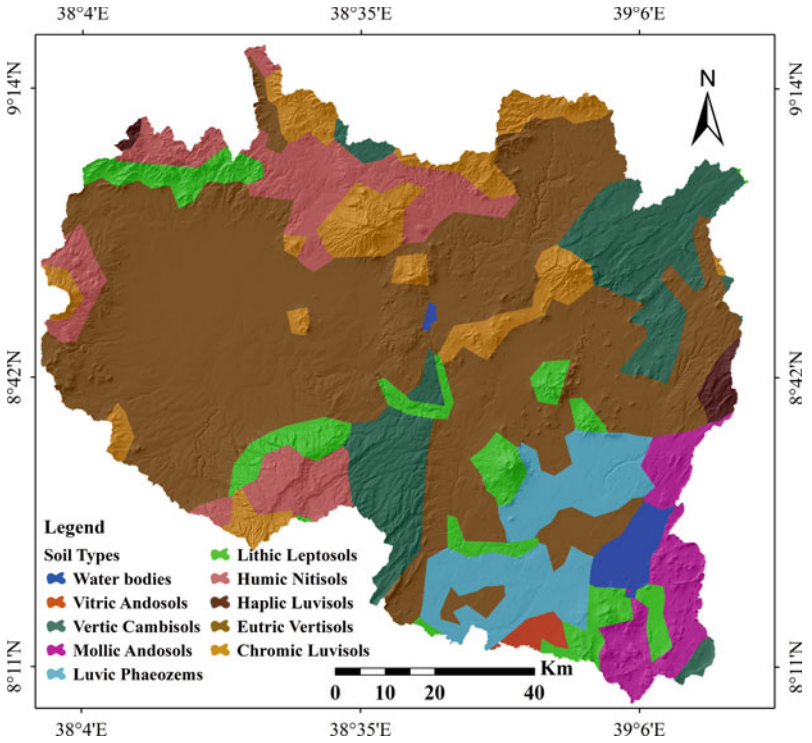

Fig. 16.3 Soil map of the study area. *Source* FAO

Datasets

In remote sensing research, the primary data collected are remote sensing images. These images serve as a foundation for the analysis, while in situ data and other ancillary information are considered secondary data, as they support and supplement the research (Bhatta 2013). Details of the data used are discussed in the following sections.

Satellite Rainfall Data

The satellite rainfall data were acquired from the Center for Hydrometeorology and Remote Sensing (CHRS) via https://chrs.web.uci.edu/, which was assessed on November 30, 2021. "The CHRS developed the first satellite precipitation estimation system, which is Precipitation Estimation from Remotely Sensed Information using Artificial Neural Network (PERSIANN). PERSIANN uses a machine learning technique known as artificial neural networks (ANNs) to determine the relationship

between remotely sensed cloud-top temperature, measured by longwave infrared (IR) sensors on geostationary satellites, and rainfall rates with bias correction from passive microwave (PMW) readings measured by low Earth-orbiting (LEO) satellites" (Hsu et al. 1997; Nguyen et al. 2018; Sorooshian et al. 2000). This satellite-based rainfall estimate data is accessible with temporal resolutions of hourly, daily, monthly, and yearly, covering a period of more than 20 years. This product's spatial resolution is 0.04° (4 km). In this study, the CHRS satellite rainfall data were processed using ArcGIS software, in which the rainfall data from year 2003 to 2020 were grouped into average annual rainfall data with the help of MS Excel.

Satellite rainfall data were preferred because the gauge stations in the study area are sparsely distributed (Fig. 16.2) and contain large amounts of missing data. Moreover, because of their long time series data availability and high spatial and temporal resolution, satellite-based datasets were used (Mengistu et al. 2019). The raster satellite rainfall data were first converted into point data, and then based on these point measurements, rainfall data at the unsampled locations of the study area were interpolated using the ordinary kriging interpolation technique in ArcGIS geostatistical analysis tools (Auchincloss et al. 2007) and computed according to Eq. 16.1.

$$Z^{\Lambda}(S_{\mathrm{o}}) = \sum_{i=1}^{N} \lambda_i Z(S_i) \tag{16.1}$$

where $Z(S_i)$ is the measured value at the ith location; λ_i is an unknown weight for the measured value at the ith location; $Z^{\Lambda}(S_{\mathrm{o}})$ is the predicted value at the location S_{o}; and N is the number of measured values.

Landsat 8 OLI Image Product

The Landsat 8 OLI image data were acquired from https://earthexplorer.usgs.gov, which was accessed on April 14, 2021. It was used to make a map of the study area's land use and land cover (LULC). The Operational Landsat Imagery (OLI) was processed with the help of the ERDAS Imagine 15 version to extract the land use and land cover map of the study area. To achieve this, the top of the atmosphere (TOA) radiance was created by converting the digital number (DN) of the satellite image reflecting bands based on the metadata file and mathematical formula given in Eq. 16.2 (USGS 2016).

$$L_{\lambda} = M_{\mathrm{L}} \times Q_{\mathrm{CAL}} + A_{\mathrm{L}} \tag{16.2}$$

where 'L_{λ}' is the TOA spectral radiance in W/m^2 sr μm, 'M_{L}' is the band-specific radiance multiplicative scaling factor, obtained from the product metafile provided with the Landsat 8 satellite image; 'A_{L}' is the band-specific radiance additive scaling factor; and 'Q_{cal}' is the quantized calibrated pixel value in DN.

Moreover, TOA planetary spectral reflectance values were created by converting the calculated TOA spectral radiance for the reflective spectral bands into TOA spectral radiance and then corrected for the elevation angle of the sun using Eq. 16.3 (USGS 2016).

$$\rho\lambda' = M_\rho Q_{\text{cal}} + A_\rho \tag{16.3}$$

where '$\rho\lambda'$' stands for TOA planetary spectral reflectance; 'M_ρ' and 'A_ρ' are the band-specific reflectance multiplicative and additive scaling factors, respectively; and 'Q_{cal}' is the quantized calibrated pixel value in digital number (DN).

In the present study, the supervised image classification technique and a parametric algorithm, which is a maximum likelihood classification method, were used. These methods are the most widely used methods for classifying medium-resolution remotely sensed data, such as Landsat 8 images (Tobiszewski et al. 2015). Furthermore, the Level I classification scheme (U.S. Geological Survey LULC Classification System) has been used (Anderson et al. 1976).

Sentinel 2 Image Products

Sentinel 2 image products were acquired from the European Space Agency (ESA) website (https://scihub.copernicus.eu), which was assessed on April 16, 2021. To produce lineament density maps, these data were employed in combination with DEM data. After digitization from the Sentinel-2 satellite image that had been displayed in the RGB band with the help of the geological map and the DEM of the study area, the lineament density was generated using the line density method in ArcGIS 10.7. The mathematical operation of the lineament density was performed using Eq. 16.4.

$$\text{LD} = \text{LL}/\text{LA} \tag{16.4}$$

where 'LD' is lineament density, 'LL' is lineament length, and 'LA' is lineament unit area. Moreover, the geomorphological map of the study area was created using a Sentinel-2 image product with the aid of ancillary data. The process included digitizing the image by overlaying it on the preexisting map.

Digital Elevation Model (DEM) Data

DEM data can be combined with digital images and vectors to create visually displayed and dramatic graphics or calculate various surface parameters such as terrain elevation, slope, drainage, and catchment of a specific area (Liu and Mason

2009). Remote sensing information fulfills its best promise when used in conjunction with other ancillary data (such as soils, elevation, and slope) often stored in a geographic information system (Jensen 2015). Accordingly, the DEM data were downloaded from the Advanced Land Observing Satellite-Phased Array type L-band Synthetic Aperture Radar (ALOS-PALSAR) of the Earth data website (https://asf.alaska.edu/), which was accessed on February 30, 2021. These data were used to delineate the catchment of the study area and prepare the slope and drainage density map of the study area.

The watershed of the study area was delineated using ArcGIS, and finally, the drainage density of the area was computed using Eq. 16.5.

$$\mathrm{DD} = \mathrm{DL}/\mathrm{DA} \tag{16.5}$$

where 'DD' is drainage density, 'DL' is drainage length, and 'DA' is the drainage unit area.

Geological Data

The digital geological map was obtained from the Geological Survey of Ethiopia (GSE) and then geo-referenced using ArcGIS software to specify the coordinate reference and project it in the desired projection and datum. Four digital geological map sheets, namely, Addis Ababa city, Akaki Baseka area, Debra Birhan area, and Nazret area at a 1:250,000 scale, were used for this study. Each geological map sheet was geo-referenced and projected, and finally, the four map sheets were mosaicked using ERDAS Imagine 15 version software. The geological map of the study was then produced by digitizing those map sheets using ArcGIS software.

Soil Data

Soil data were acquired from the Food and Agricultural Organization (FAO) website (http://www.fao.org/geonetwork/srv/en/main.home). The FAO digital soil data were used to produce the soil map for the study area, which was then downloaded and imported into ArcGIS for further reclassification.

Ground Data

The ground truth data were collected using the Global Positioning System (GPS) and Google Earth (high-resolution image) based on a systematic sampling scheme. High-resolution images were used to sample ground truth data in the area that cannot be

easily accessed by ground surveying. The ground truth data were sampled by using a systematic sampling scheme in which the sample units are chosen over the study area at defined and regular intervals (Congalton and Green 2009). The first sample is often chosen at random, and each subsequent sample is then taken at a specified interval. This type of sampling scheme was preferred because the ease of sampling was somewhat uniform over the entire study area. Ground truth data or high-resolution image data were used during digital image processing for sample training and accuracy assessment to produce a land use and land cover (LULC) map. Furthermore, well yield, spring, and hand dug well data were collected from the Ministry of Water and Energy as well as from preexisting articles (MOWS 2021; Wogari 2006; Yitbarek et al. 2012). These well yield, spring and hand dug data were used to validate the results of this study to ensure that remote sensing, which is an indirect method of obtaining information, is reliable in characterizing the groundwater potential zone of a specific area.

Methods

Analytical Hierarchy Process

The analytical hierarchy process (AHP) is a widely used method for solving complex decision-making problems. It was proposed by Saaty (1980) as a theory and methodology for making relative measurements. It is used to solve multicriteria decision-making (MCDM) problems and is particularly useful in the process of evaluating alternatives (Brunelli 2015). Saaty (1980) used the analytical hierarchy approach to establish and develop the pairwise comparison matrix (PCM) technique.

In the case of segregating multiple criteria into a series of pairwise comparisons, followed by integrating the findings, the analytical hierarchy process is the most critical method (Allafta and Opp 2021). The analytical hierarchy process is a suitable method for evaluating the potential of groundwater in the Upper Awash Basin, as it takes into account the hierarchical relationship between the factors that influence suitability. The method involves assigning weights to these factors based on their relative importance in determining suitability. Since multiple parameters characterize groundwater potential in the Upper Awash Basin, AHP is considered appropriate for producing a reliable output.

The multicriteria decision-making approach consists of three primary steps: construction of the pairwise comparison matrix, computation of criterion weights, and determination of the consistency ratio.

Development of the Pairwise Comparison Matrix

A matrix is created by comparing each input criterion to the others through pairwise comparison. The matrix values are assigned using a relative relevance scale ranging from 1 (equal priority) to 9 (extreme importance) shown in Table 16.1. To indicate inverse relationships, reciprocal values can also be used; for example, 1/9 implies that one factor is significantly less important than the other. The diagonal values are always 1, enabling identical criteria to be compared, and the values in the upper right corner of the matrix are reciprocals of those in the bottom left corner of the matrix (Liu and Mason 2009).

Based on this, the geomorphology was selected as the primary factor that influences the groundwater potential zone in the area, which is in line with the study of Waikar and Nilawar (2014), Dinesan et al. (2015) and Arulbalaji et al. (2019). Hence, the morphological setting of the area controls the movement and storage of groundwater (NRCS 2010). As a result, this parameter is placed in the first row and column of the pairwise comparison matrix, hierarchically followed by the remaining parameters (Table 16.2). The normalized pairewise matrix is indicated in Table 16.3 (Fig. 16.4).

Table 16.1 Significance estimation based on a 9-point scale (Liu and Mason 2009)

Significance	Value	Significance	Value
Extreme importance	9	Moderate to strong importance	4
Very strong to extreme importance	8	Moderate importance	3
Very strong importance	7	Equal to moderate importance	2
Strong to very strong importance	6	Equal importance	1
Strong importance	5		

Table 16.2 Pairwise comparison matrix with the analytical hierarchy process (AHP) (Klaus 2013)

	GM	GL	SL	RF	LD	LULC	DD	Soil
GM	1.00	2.00	3.00	4.00	5.00	7.00	8.00	9.00
GL	1/2	1.00	1.00	3.00	3.00	5.00	7.00	7.00
SL	1/3	1.00	1.00	3.00	3.00	5.00	5.00	7.00
RF	1/4	1/3	1/3	1.00	2.00	3.00	5.00	7.00
LD	1/5	1/3	1/3	1/2	1.00	3.00	5.00	7.00
LULC	1/7	1/5	1/5	1/3	1/3	1.00	3.00	5.00
DD	1/8	1/7	1/5	1/5	1/5	1/3	1.00	3.00
Soil	1/9	1/7	1/7	1/7	1/7	1/5	1/3	1.00
$\sum$	2.66	5.15	6.21	12.18	14.68	24.53	34.33	46.00

GM geomorphology, *GL* geology, *SL* slope, *RF* rainfall, *LD* lineament density, *LULC* land use and land cover, *DD* drainage density, and soil

Table 16.3 Normalized pairwise comparison matrix and eigenvector weight

	GM	GL	SL	RF	LD	LULC	DD	Soil	Criteria weight
GM	0.376	0.388	0.483	0.329	0.341	0.285	0.233	0.196	0.329
GL	0.188	0.194	0.161	0.246	0.204	0.204	0.204	0.152	0.194
SL	0.125	0.194	0.161	0.246	0.204	0.204	0.146	0.150	0.179
RF	0.094	0.065	0.054	0.082	0.136	0.122	0.146	0.150	0.106
LD	0.075	0.065	0.054	0.041	0.068	0.122	0.146	0.150	0.090
LULC	0.054	0.039	0.032	0.027	0.023	0.041	0.087	0.109	0.051
DD	0.047	0.028	0.032	0.016	0.014	0.014	0.029	0.065	0.031
Soil	0.042	0.028	0.023	0.012	0.010	0.008	0.010	0.022	0.019

GM geomorphology, *GL* geology, *SL* slope, *RF* rainfall, *LD* lineament density, *LULC* land use and land cover, *DD* drainage density, and soil

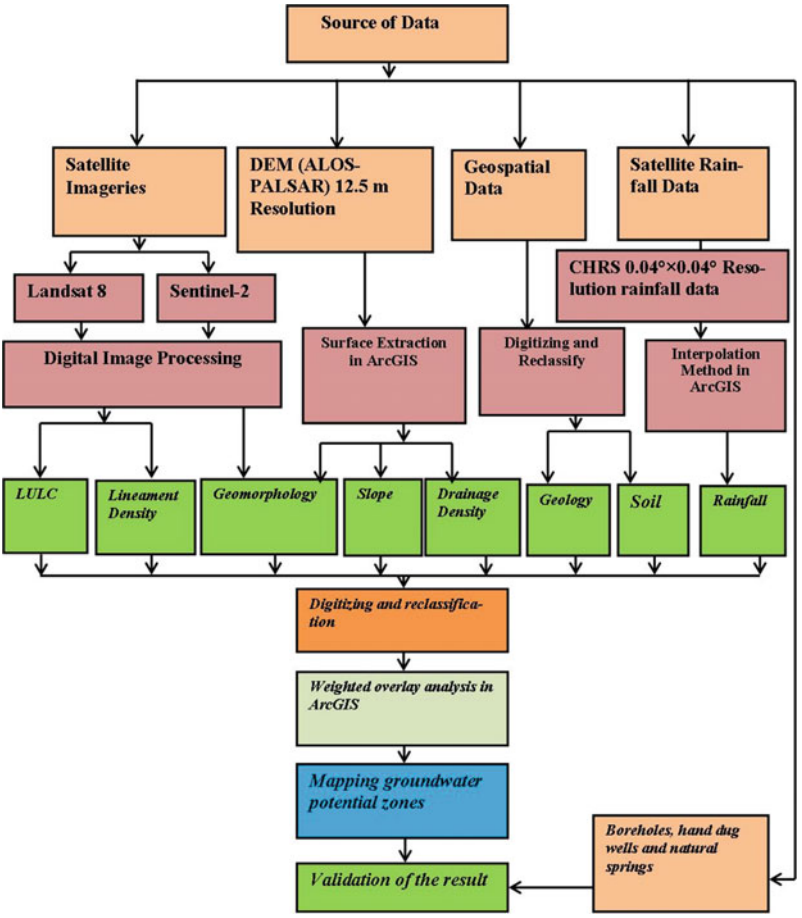

Fig. 16.4 The conceptual framework of the study

Studies including Fenta et al. (2014), Hussein et al. (2017), Andualem (2019), and Tanzeer (2020) have assigned geology as the primary parameter that controls potential groundwater zones. However, in this study, geology was selected as the second most important parameter following geomorphology for groundwater potential zone characterization. The geology of the Upper Awash Basin is known for its complex volcanic rock successions and landforms that resulted from prerift, synrift, and primary rift eruptions. As such, geomorphology has a greater influence in the area compared to geology. The identified rock units in the study area are Wechecha trachyte, Gash Megal rhyolite, Zikwala trachyte, upper basalt, Termaber Megezez formation, Bofa basalt, Pleistocene sub-recent basalt, Cheleka basalt, Entoto basalt, Quaternary basalt, Addis Ababa basalt, middle basalt, welded pyroclastic deposit, Dandi-Wenchi pyroclastic deposit, ash flow (Nazret groups), porphyritic feldspar basalt, rhyolite domes and flows, scoria fallout, lower basalt, scoria cones and fallout deposit, basaltic lava flow, and quaternary sediment deposits, as illustrated in Fig. 16.5.

These rock units have various degrees of permeability, which in turn affects how important they are for these rock units, which in turn affects how important they are for characterizing the groundwater potential zone. For instance, the trachyte rock unit and Gash Megal rhyolite are considered very low for the groundwater potential zone because they are compacted in nature and have low permeability, which implies a lower suitability for groundwater occurrence (Alemayehu 2006).

In contrast, the quaternary sediment, the upper basalts, the scoriaceous group of rock units, and the ash flow have high permeability, so they are assumed to be suitable for groundwater occurrence.

Slope is the amongst the most significant parameters that determines the groundwater potential zone of the area, as the area is characterized by both rugged and undulating landforms, as depicted in Fig. 16.5. These variations affect the rate of runoff and infiltration in the area, and as such, this parameter was selected to be the third most influential parameter that explains the spatial variability of groundwater potential in the area. Slopes ranging from 0 to 3° were categorized under ‘very high’ groundwater potential because flat topography facilitates greater infiltration. Slopes that range from 3 to 8° and 8 to 15° were categorized under ‘high’ and ‘medium’ groundwater potential zone, respectively, and slopes ranging from and 15–30° and over 30° are considered high runoff regions and are categorized as ‘low’ and ‘very low’ groundwater potential zones, respectively.

Rainfall was selected as the fourth most crucial factor in determining potential groundwater zones. The existence and occurrence of groundwater in a specific area is significantly determined by rainfall, while other factors influence its variability (Kotchoni et al. 2019). Rainfall is commonly recognized to play a critical role in regulating groundwater recharge and, consequently, the groundwater potential zone of an area. An area that receives high annual rainfall is likely to have high groundwater recharge as precipitation infiltrates into the ground and replenishes groundwater.

Lineament density, which is a measure of the frequency and density of linear features such as faults, fractures, and joints, is an important factor in determining the infiltration of water through its structure. Therefore, it has been selected as the fifth

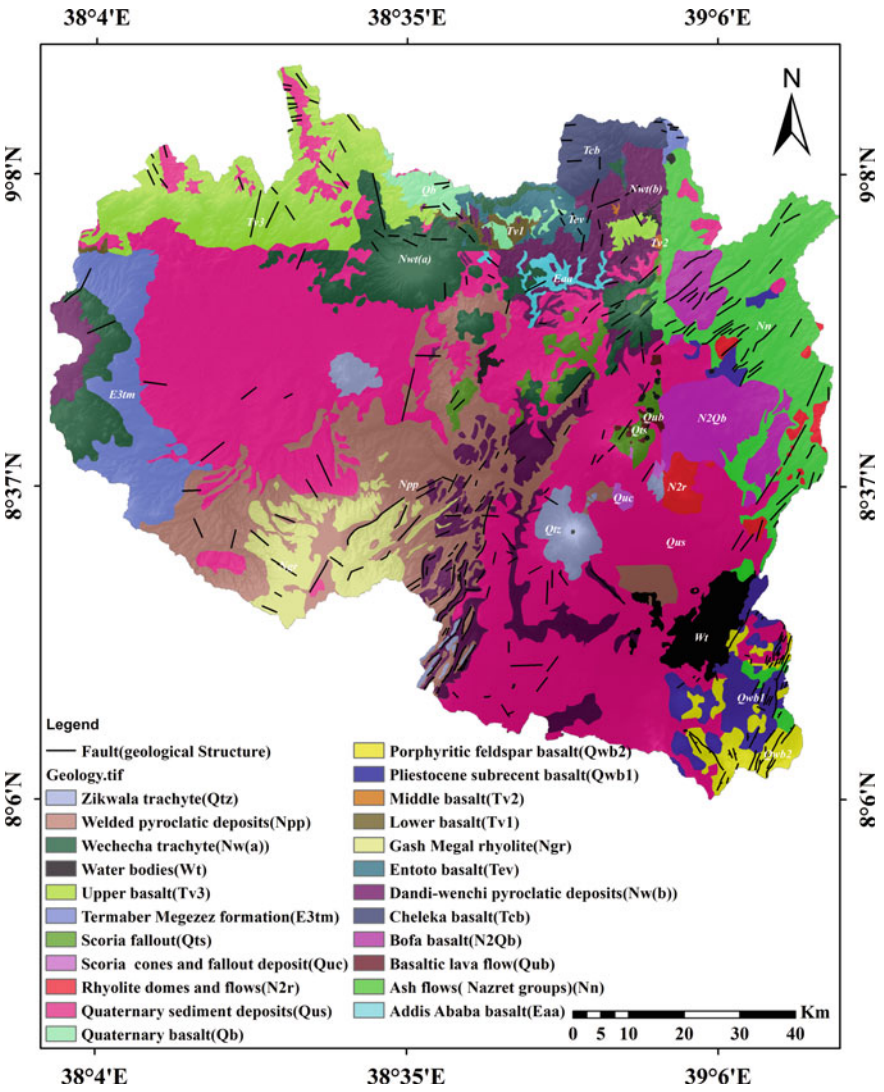

Fig. 16.5 Geology map of the Upper Awash Basin. *Source* Assiged (2007), Efrem (2010), Ilfios (2007), Meshesha et al. (2010), Kazmin and Berhe (1978); the geological map was digitized from a geological map of these sources and modified

parameter influencing groundwater potential. As there are some land use and land cover patterns such as agricultural and forests within the study area that facilitate the rate of infiltration, it has been selected as the sixth parameter. Areas within agricultural landscapes are considered to have a higher infiltration rate and better groundwater recharge (Saranya and Saravanan 2020). In addition, the soil type, which affects permeability and water flow, and drainage density, which is inversely related to

infiltration, were chosen as the seventh and eighth parameters, respectively. Because the study area has a substantial portion of clay-type soil, both drainage density and soil type have relatively little impact on groundwater recharge. Since clay soil has a low permeability rate, surface water cannot percolate into the subsurface of clay soil components. Similarly, surface runoff predominates in areas with high drainage density, resulting in a low rate of infiltration.

Derivatives of Criteria Weights

The weights are derived from the principal eigenvector of the pairwise comparison matrix (PCM) using the formulas in Eqs. 16.6 and 16.7. The values in each matrix column are summed to produce the column marginal total (Liu and Mason 2009), as shown in Table 16.2. By dividing each matrix value by its marginal total, a second matrix, normalized pairwise comparison matrix (NPCM) is generated (depicted in Eq. 16.6). These values are then averaged across the rows to obtain the weight for each criterion (Eq. 16.7). In other words, the more important a criterion is, the higher its contribution/weight (Basin et al. 2021).

$$\text{NPCM} = \frac{\text{Criteria value}}{\text{Column Total}} \tag{16.6}$$

$$\text{Weight} = \frac{\text{Sum of the total row of NPCM}}{n} \tag{16.7}$$

where 'n' is the number of criteria and 'NPCM' is the Normalized Pairwise Comparison Matrix.

Calculation of a Consistency Index Within a Matrix

It is necessary to establish a consistency ratio to ensure a logical relationships between the criteria. The consistency ratio can be checked by using a comparison technique that involves calculating a number of component parameters. It includes the following steps:

$$\text{WSV} = \sum_{i=1}^{n} wc_{\text{t}} \tag{16.8}$$

where w is the weight and c_{t} is the column value.

$$\text{CV} = \frac{\text{WSV}}{\text{Weight of each criterion}} \tag{16.9}$$

Table 16.4 Random index values for different numbers of criteria (Saaty 1980)

Random index values for $n = 1$–10										
n	1	2	3	4	5	6	7	8	9	10
RI	0	0	0.58	0.9	1.12	1.24	1.32	1.41	1.45	1.49

where 'WSV' is the weighted sum vector and 'CV' is the consistency vector.

$$\Lambda_{\max} = \frac{\text{Sum of Principal eigenvalue}}{n} \tag{16.10}$$

$$\text{Consistency Index (CI)} = \frac{\lambda_{\max} - n}{n - 1} \tag{16.11}$$

where 'n' is the number of parameters and '$\lambda_{\max}$' is the principal eigenvalue. Accordingly, the CI in this study is computed as follows, according to Eq. 16.11.

$$\text{CI} = \frac{8.635 - 8}{8 - 1} = \frac{0.635}{7} = 0.091$$

Notably, the closer the value of λ to n ($\lambda = n$ in ideal case), the more consistent the matrix is. Therefore, $\lambda - n$ represents a good measure of consistency, and CI as an estimate of the average difference gives a good judgment of consistency.

$$\text{Consistency Ratio} = \frac{\text{CI}}{\text{RI}} \tag{16.12}$$

where RI represents the random index, which is given in Table 16.4 for different n values. In this study, RI equals 1.41 for eight parameters.

Based on Eqs. 16.11 and 16.12, the computed CR is 0.064, which is less than 0.1, and as a result, it is acceptable to conduct the weighted overlay analysis to integrate the weighted parameters for mapping groundwater potential zones (Brunelli 2015; Saaty 1980).

Groundwater Potential Zone Mapping

To generate a single map output, multicriteria evaluation (MCE) integrates multiple layers of reclassified parameter maps. The groundwater potential index (GWPI) or rating index was calculated using Eq. 16.13 which was proposed by Malczewski (1999).

$$\text{GWPI} = \sum_{w=1}^{m} \sum_{j=1}^{n} \left(W_j * X_i\right) \tag{16.13}$$

where 'm' is the total number of thematic layers, 'n' is the total number of features for a particular theme, 'W_j' is the normalized weight of the 'jth' thematic layer, and 'X_i' is the normalized weight of the ith feature of the thematic layer.

Although the desirable characteristics of objectives and attributes might serve as guidelines for selecting a set of evaluation criteria, there are no techniques that are universally applicable for defining a set of criteria (Tobiszewski et al. 2015). Therefore, based on recommendations from experts, the criteria utilized for groundwater potential zone categorization have been divided into the appropriate classes, as shown in Table 16.5.

Results

Rainfall

As depicted in Fig. 16.8, the annual rainfall patterns in the study area are shaped by topography, with the northern and western highlands (Addis Ababa, Ginchi, and Tulu Bolo meteorological stations) receiving substantial annual precipitation and the lowland southern and eastern regions (Debre Zeyit and Koka Dam meteorological stations) experiencing reduced rainfall. It is well known that rainfall has a significant effect on groundwater recharge, influencing the groundwater potential of a particular area (Kabeto et al. 2022). As a result, when there is high annual rainfall, there will be high groundwater recharge. As a result, the areas that receive high annual rainfall are expected to have promising groundwater potential and vice versa. Based on the amount of annual precipitation received at each gauge station, the rainfall of the study was reclassified into five categories, namely, very low, low, moderate, high, and very high, as illustrated in Figs. 16.6 and 16.7.

Some parts of the central and eastern Upper Awash Basin are characterized by low annual rainfall. Annual average rainfall at Koka Dam meteorological station is about 614 mm and that of Ginchi mountain area is 1026 mm (location of stations indicated in Figs. 16.2 and 16.8). Moderate to high rainfall measurements were recorded in the western, southwestern, and central parts of the study area.

Reclassification of Land Use and Land Cover/LULC

In this study, the cultivated lands make up the largest proportion (Fig. 16.9 and Table 16.6), and downstream areas closer to the Koka Dam are mostly composed of bare land, shrubs, and grassland (Fig. 16.9). The aerial coverage of shrubs is minimal when compared to other land classes, which is why it was classified as bare land and grassland, as stated by Jensen (2015). Water bodies are relatively small in proportion in the study area, as depicted in Table 16.6. Each land use and land cover type has a

Table 16.5 Classification of parameters influencing the GWPZs in the Upper Awash Basin

Factors (units)	Classes	Groundwater potential	Class rank	Parameter weight
Geomorphology (Waikar and Nilawar 2014)	Escarpment	Medium	3	32.9
	Reservoirs/lakes	High	4	
	Flat undulating plains	Very high	5	
	Rift lowlands and spatter cones	Low	2	
	Volcanic mountains and spatter cones	Very low	1	
Geology	Bofa basalt	Medium	3	19.4
	Upper basalt	High	4	
	Lower basalt	Medium	3	
	Middle basalt	Medium	3	
	Entoto basalt	Medium	3	
	Scoria fallout	High	4	
	Water bodies	Medium	3	
	Cheleka basalt	Medium	3	
	Zikwala trachyte	Very low	1	
	Quaternary basalt	High	4	
	Wechecha trachyte	Very low	1	
	Basaltic lava flow	Low	3	
	Addis Ababa basalt	Medium	3	
	Gash Megal rhyolite	Very low	1	
	Ash flow (Nazret groups)	High	4	
	Porphyritic feldspar basalt	Low	2	
	Rhyolite domes and flow	Low	2	
	Welded pyroclastic deposit	Low	2	
	Pliestocene sub-recent basalt	Medium	3	
	Quaternary sediment deposit	Very high	5	
	Termaber Megezez formation	High	4	
	Scoria cones and fallout deposit	High	4	

(continued)

Table 16.5 (continued)

Factors (units)	Classes	Groundwater potential	Class rank	Parameter weight
	Dandi-Wenchi pyroclastic deposit	Low	2	
Slope (°)	0–3	Very high	5	17.9
	3–8	High	4	
	8–15	Medium	3	
	15–30	Low	2	
	30–75	Very low	1	
Rainfall (mm yr^{-1})	556–677	Very low	1	10.6
	677–753	Low	2	
	753–821	Medium	3	
	821–889	High	4	
	889–1026	Very high	5	
Lineament density (total length of lineament/km^2)	0–0.07	Very low	1	9
	0.07–0.20	Low	2	
	0.20–0.30	Medium	3	
	0.30–0.46	High	4	
	0.46–0.80	Very high	5	
Land use and land cover (Waikar and Nilawar 2014)	Water	Very high	5	5.2
	Agriculture	Very high	5	
	Forest	High	4	
	Bare land	Low	2	
	Urban	Very low	1	
Drainage density (total length of drainage lines/km^2)	0–1.23	Very high	5	3.1
	1.23–2.32	High	4	
	2.32–3.40	Medium	3	
	3.40–4.64	Low	2	
	4.64–7.40	Very low	1	
Soil (Basin et al. 2021; Tanzeer 2020)	Clay	Very low	1	1.9
	Loam	High	3	
	Sandy loam	Very high	4	

unique impact on the characterization of the groundwater potential zone and as such were reclassificed as shown in Fig. 16.10; with water and agricultural land having the highest contribution.

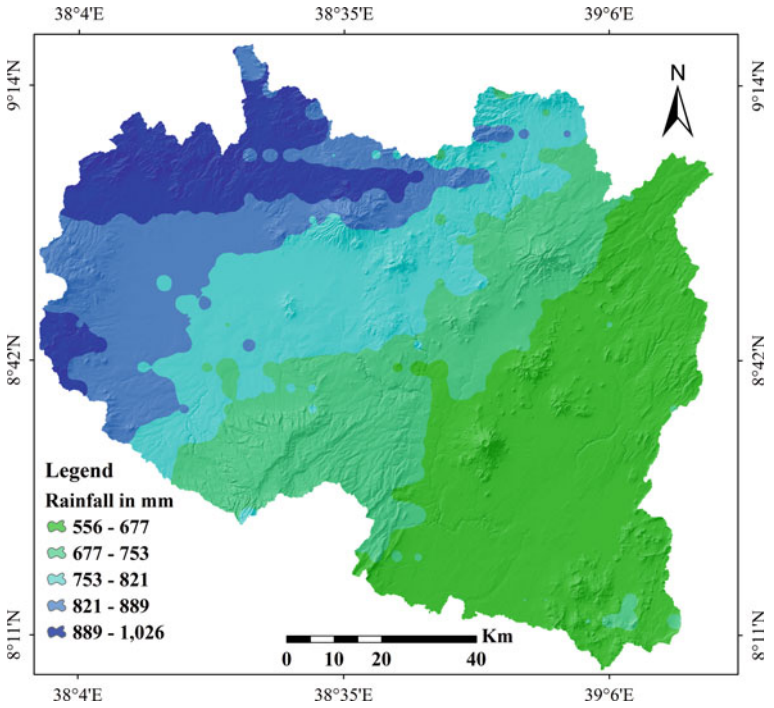

Fig. 16.6 Rainfall map of the Upper Awash Basin

Slope

The majority of the study area is characterized by flat terrain. However, the specific area where the Awash Basin begins is surrounded by mountainous terrain, which results in a rugged topography that prevents water infiltration into the subsurface and promotes runoff. As illustrated in Figs. 16.11 and 16.12, the western and northwestern parts of the study area have steep inclines with slopes ranging from 30 to 75°. Areas such as the Ginchi Mountains, the escarpment of the Entoto and Fo'ata where the Abay and Awash Basins originate, and the Zikwala and Erer Mountains are prime examples of rugged topography, characterized by steep inclines. As such, these mountainous regions have limited groundwater potential.

Conversely, the lowest slope (0–3°) is observed near Koka Lake and around most water bodies. Characterized by low to medium slopes, the Becho plains are susceptible to flooding during the rainy season due to their relatively flat topography. Such regions correspond to high infiltration rates and short retention times, leading to the water table reaching the surface during the rainy season.

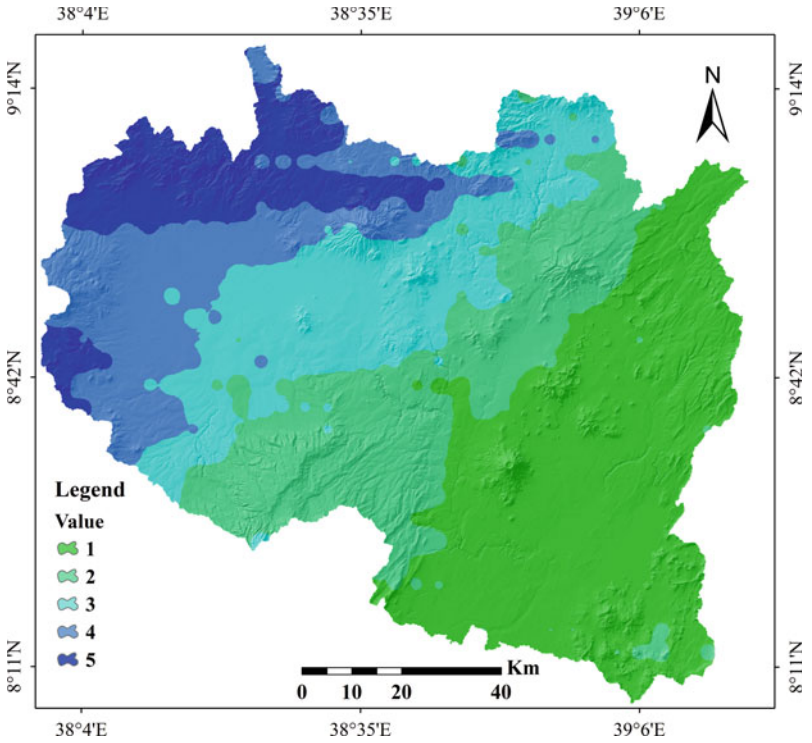

Fig. 16.7 Reclassified rainfall map of the Upper Awash Basin based on Table 16.5

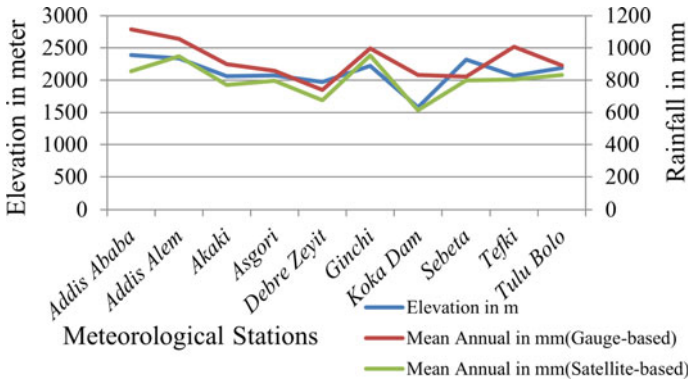

Fig. 16.8 Satellite and gauge-based mean annual rainfall in the Upper Awash Basin

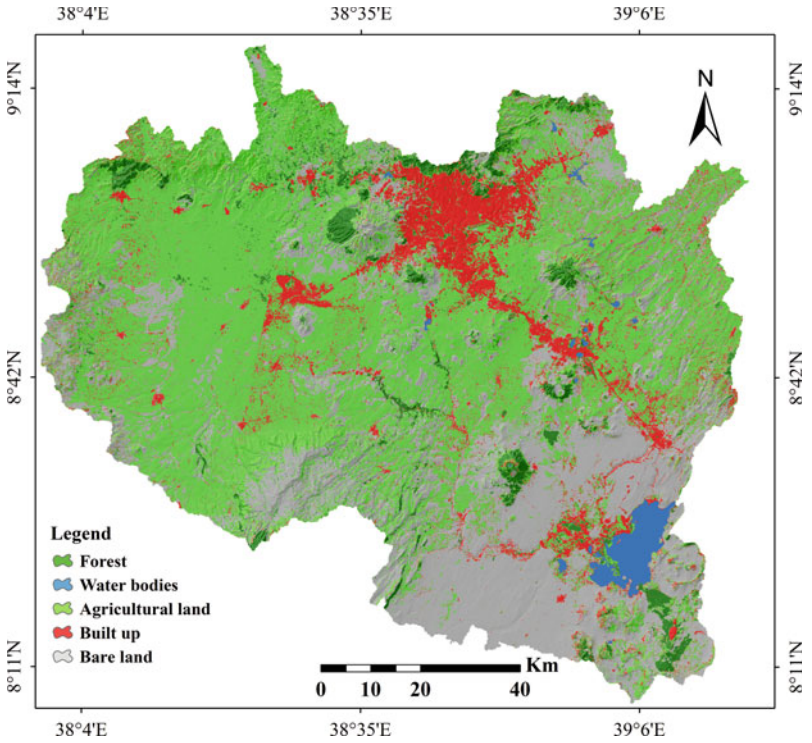

Fig. 16.9 Land use land cover map of the Upper Awash Basin

Table 16.6 Areal extent of land use/land cover and its percentage

Type of classes	Area (km^2)	Percentage (%)
Agricultural land	6217.34	53.40
Grassland	3578.07	30.72
Forest	510.46	4.38
Urban/built-up	1167.82	10.02
Water	171.31	1.47
Total sum	11,645.00	100.00

Soil

The soil map of the study area was divided into nine classes: chromic luvisols, eutric vertisols, haplic luvisols, humic nitisols, lithic leptosols, luvic phaeozems, mollic andosols, vertic cambisols, and vitric andosols. The soil types were classified based on their texture (Figs. 16.13 and 16.14) to identify their contribution to groundwater potential zone characterization.

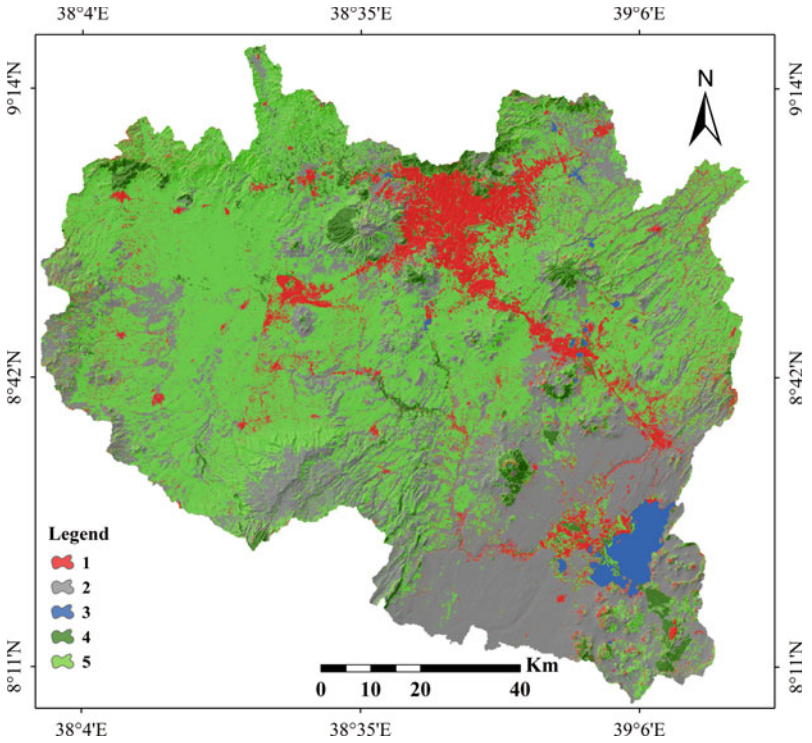

Fig. 16.10 Reclassified LULC map of the Upper Awash Basin based on Table 16.5

It is important to note that soil type alone cannot fully determine groundwater potential properties. Based on previous studies, the soil weight was assigned according to its degree of importance (Table 16.7) to groundwater occurrence and was characterized from high to low importance as water, sandy loam, loam, and clay. Sandy loam soil has higher permeability than loam and clay soil; therefore, there is a greater likelihood of that area to be categorized under high groundwater potential. In contrast, clay soil has high porosity, which prevents water from percolating into the subsurface, which implies that it is less suitable for groundwater occurrence in the area.

Geomorphology

Significant geomorphic units such as escarpments, volcanic mountains and spatter cones, rift lowlands and spatter cones, flat, undulating plains, and reservoirs were discovered and characterized as key geomorphic units in the area, as depicted in Fig. 16.15. Most of the study areas were covered with flat, undulating plains

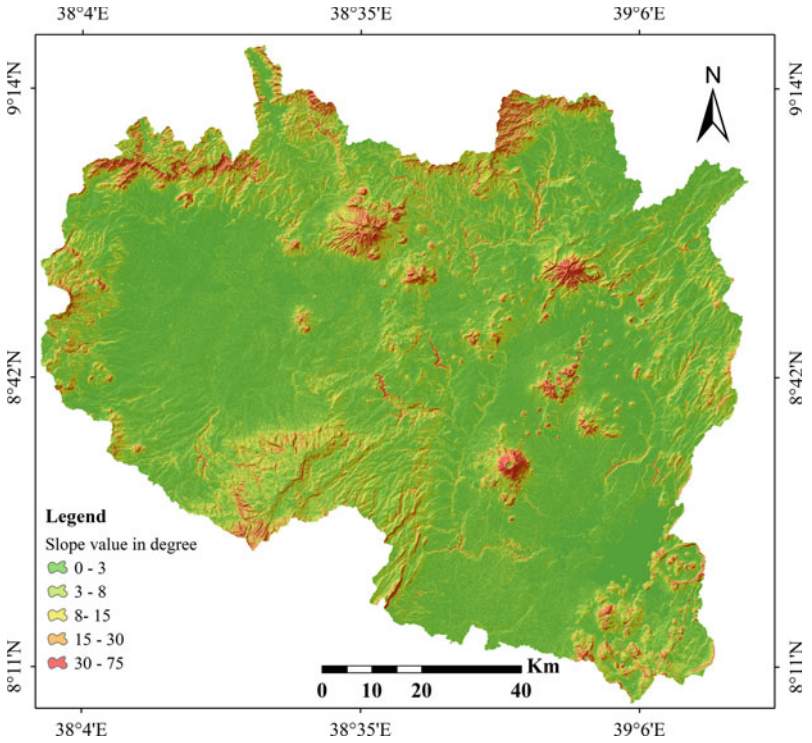

Fig. 16.11 Slope map of the Upper Awash Basin

landforms, followed by escarpments and rift lowland and spatter cones, and volcanic mountains and spatter cones covered relatively small areas, as illustrated in Table 16.8. Recent volcanic occurrences, such as volcanic ash and scoriaceous basalt, generated rift plains, and spatter cones. The escarpment landscapes were formed from the lower and upper volcanic rocks and rhyolites.

The flat and undulating landscapes are mainly composed of recent quaternary sediment deposits formed by the erosion of high mountains in the upper catchment.

These sediments accumulate during the rainy season from runoff, leading to a topography that allows for high infiltration rates as water has more time to percolate into the subsurface.

In the present study, flat, undulating plains, and lakes (water bodies) are thought to be the best groundwater recharge zones because rainfall water has a longer time to permeate into underlying materials when rain falls on such landforms. In contrast, the escarpment landform is not considered a good groundwater potential zone because it is characterized as mountainous (i.e., steep slope), which is mainly vulnerable to runoff, preventing rainfall water from percolating into subsurface formations. Consequently, the escarpment landforms have a high drainage density due to increased runoff as they receive high annual rainfall (Fig. 16.6). The rift lowland and spatter

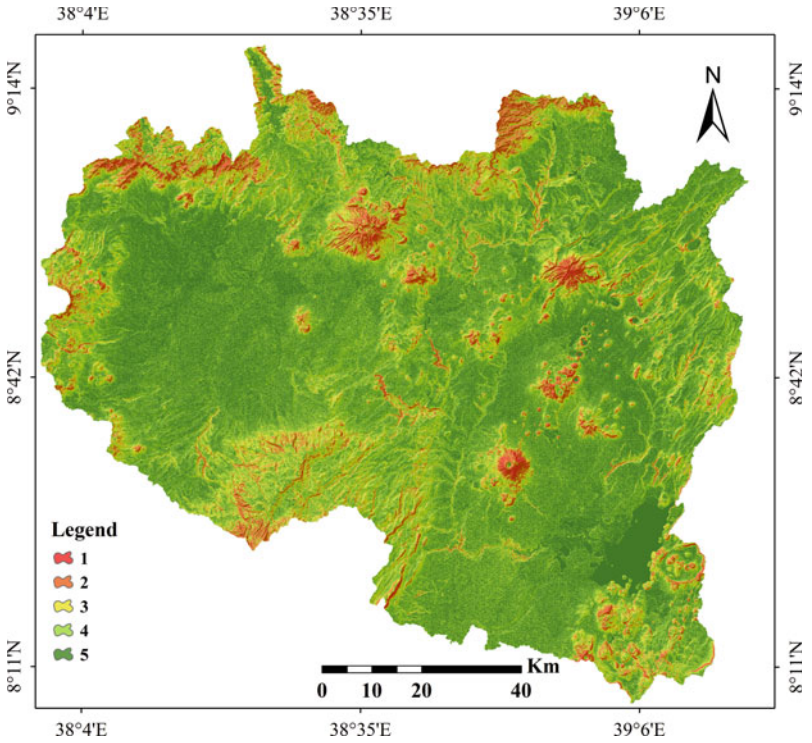

Fig. 16.12 Reclassified slope map of the Upper Awash Basin based on Table 16.5

cones can hold water as they are found in the lower part of the catchment (Fig. 16.15). These landforms receive rainfall water from the upper catchment through fractures, faults, and other geological structures. Finally, the geomorphology of the study was reclassified into five categories according to their importance to GWPZ characterization, as shown in Fig. 16.16.

Geology

There are approximately twenty-two rock units found and identified in the Upper Awash Basin. These rock units were further reclassified into five major categories based on their similarity and importance to groundwater potential zone characterization (Fig. 16.17). The trachyte rock unit and Gash Megal rhyolite are considered very low for the groundwater potential zone because they are compacted in nature and have low permeability; therefore, they are considered to have less potential for groundwater occurrence (Alemayehu 2006). Similarly, welded pyroclastic deposits,

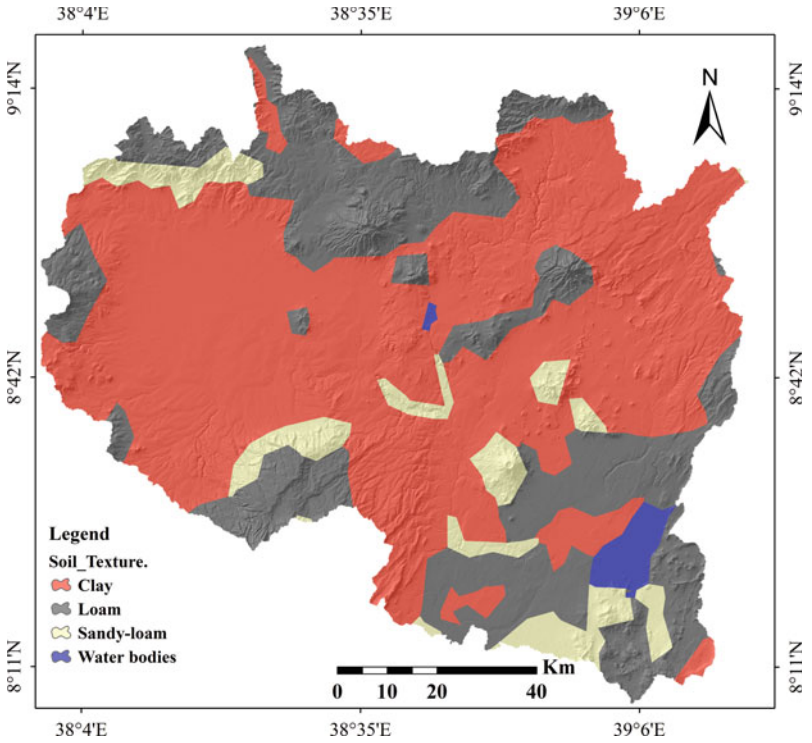

Fig. 16.13 Soil texture map of the Upper Awash Basin

basaltic lava flows, rhyolite domes, and porphyritic feldspar basalts have low to medium permeability because they are less porous.

The basalt groups of rock units have medium permeability properties because some of these rock units are susceptible to weathering. The upper basalts, scoriaceous group of rock units, and ash flow have high permeability, so they are assumed to have a higher potential for groundwater. Quaternary sediment deposits are excellent for delivering water into subsurface materials. Therefore, this rock unit is considered to have outstanding groundwater potential, as it is found below the foot of mountains in a relatively flat topography while receiving high rainfall.

Drainage Density

The drainage density is computed as the sum of all the streams and rivers in a basin divided by the overall area of the drainage basin (Eq. 16.5). The study area is bounded by many river networks, among which the main perennial rivers are the Ginchi, Berga, Holeta, Akaki, Teji, Lemen, Modjo, and Awash Rivers. The overall flow direction of

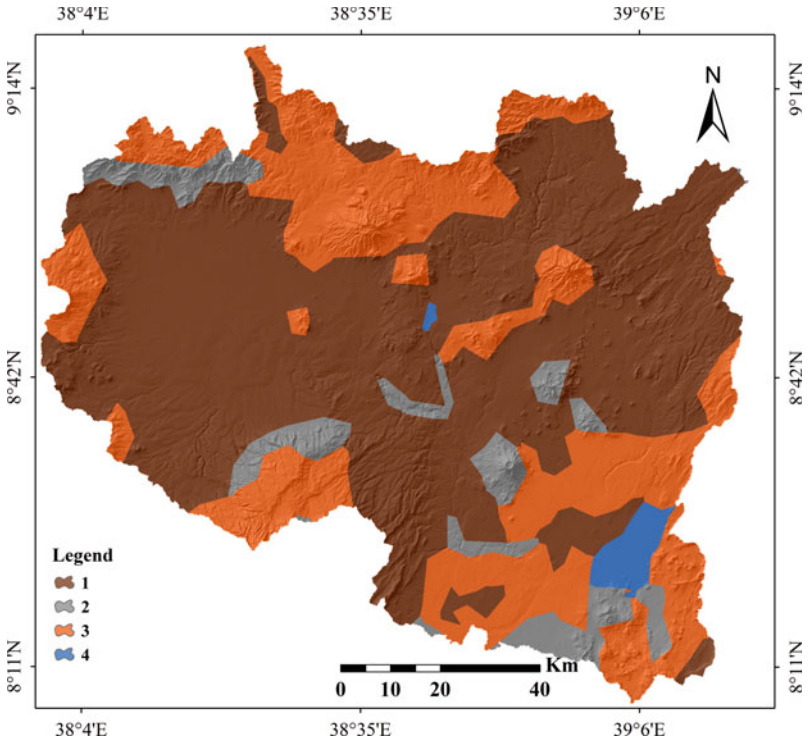

Fig. 16.14 Reclassified soil map of the Upper Awash Basin based on Table 16.5

Table 16.7 Soil texture and its importance to GWPZ

Soil texture	Area (km^2)	Percentage (%)	Importance to groundwater potential zone
Water	176.00	1.51	Very high
Sandy loam	890.00	7.64	High
Loam	3504.00	30.09	Good
Clay	7075.00	60.76	Poor
Total sum	11,645.00	100.00	

those rivers is southeast, passing through the Koka reservoir. Water infiltration into the subsurface is influenced by drainage density, which determines how much runoff will occur. High drainage density results in high runoff and low infiltration, while low drainage density indicates fewer channels for water to flow through, resulting in a high infiltration rate and higher groundwater potential.

Based on the natural break classification method in ArcGIS 10.7, the drainage density of the study area is classified into five classes, viz. very low (< 1.23 km/km^2), low (1.23–2.3 km/km^2), medium (2.32–3.40 km/km^2), high (3.40–4.46 km/km^2), and very high (> 4.46 km/km^2). Most of the study area falls in very low to

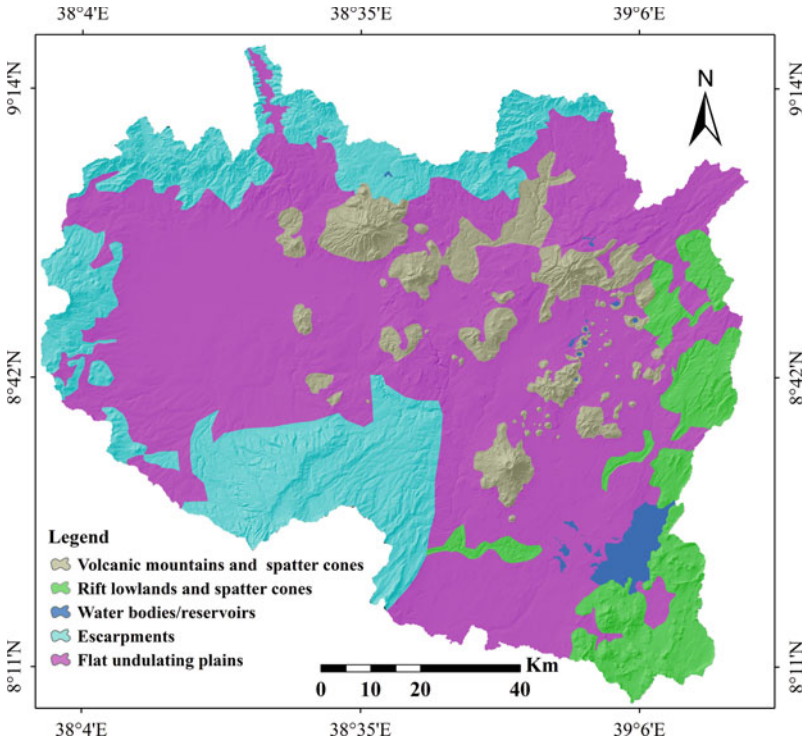

Fig. 16.15 Geomorphology map of the Upper Awash Basin

Table 16.8 Geomorphology categories in the UAB and their areal extent as percentages

Geomorphological categories	Area (km^2)	Percentage (%)
Escarpments	2560	22
Reservoirs/lakes	163	1.40
Flat, undulating plains	6765	58.09
Rift lowlands and spatter cones	1114	9.56
Volcanic mountains and spatter cones	1043	8.95
Total sum	11,645.00	100.00

low drainage density, in which the surface runoff is less; in turn, a high recharge rate would occur in the area. Accordingly, the drainage of the Upper Awash Basin has been reclassified based on its degree of contribution to groundwater potential zone characterization, as depicted in Figs. 16.18 and 16.19. Finally, the drainage density map that has been reclassified is overlaid with other parameters to develop a groundwater potential map of the area.

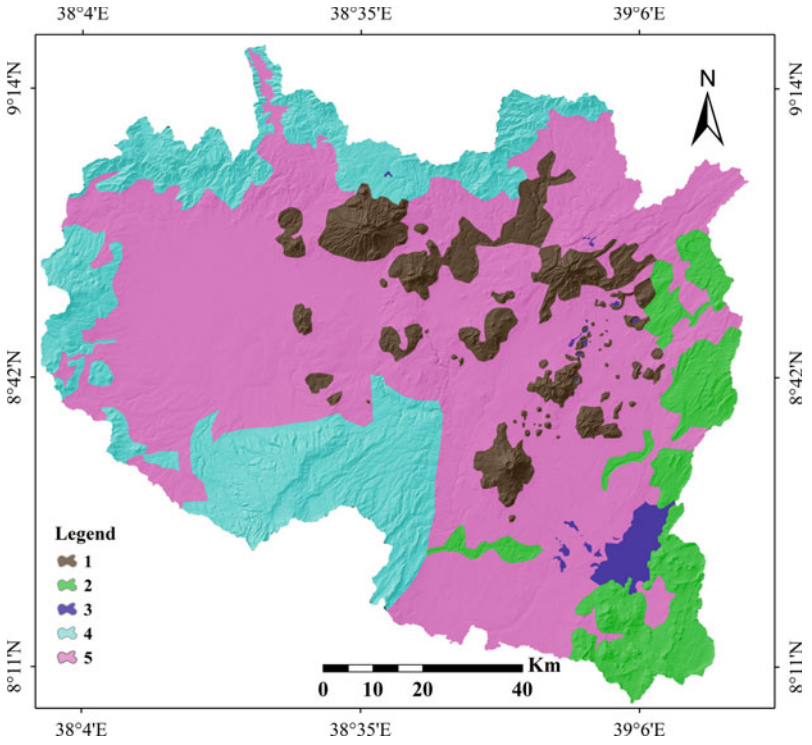

Fig. 16.16 Reclassified geomorphology map of the Upper Awash Basin based on Table 16.5

Mountainous areas with considerable vegetation cover are characterized by reduced runoff and high recharge rates, increasing the movement of water to subsurface geological materials. High drainage density areas are mainly observed in the western part of the study area, where areas are dominated by flooding during the summer season, and in the southern and southeastern parts, where an area is covered with bare land.

Lineament Density

The lineament density map of the Upper Awash Basin was created using the line density approach in ArcGIS 10.7. The lineament density of the area was classified into five categories: very low (< 0.07 km/km^2), low (0.07–0.18 km/km^2), medium (0.18–0.29 km/km^2), high (0.29–0.43 km/km^2), and very high (> 0.43 km/km^2), as depicted in Fig. 16.20, and finally, reclassified for the overlay process into five categories, as illustrated in Fig. 16.21. The lineament density extends from the northeast to the

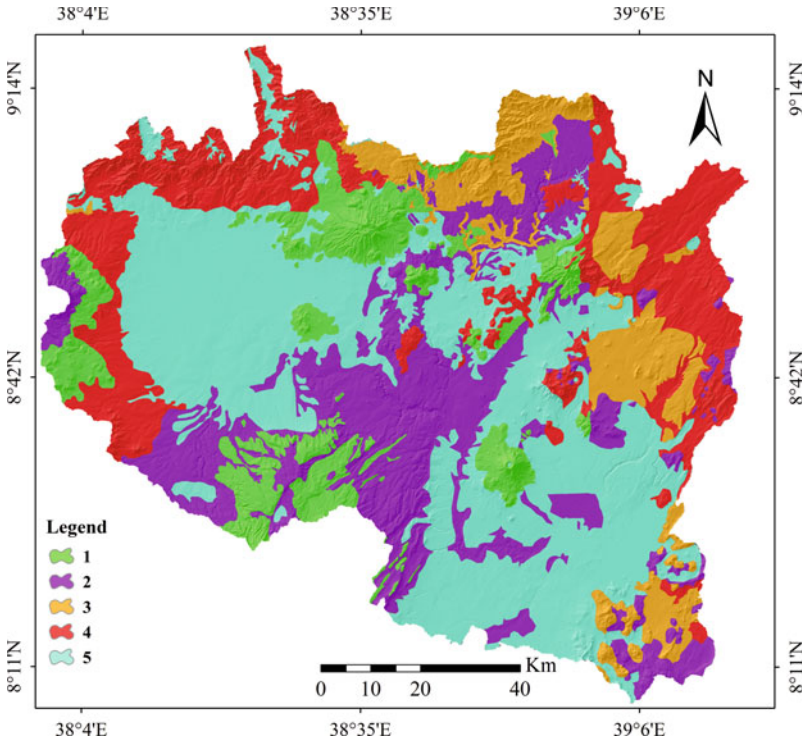

Fig. 16.17 Reclassified geology map of the Upper Awash Basin based on Table 16.5

southwest because the distribution of the lineaments is believed to be high on the escarpment and rift floor (Fig. 16.21).

The area with high lineament density is assumed to be excellent for groundwater recharge, while low lineament density is known to have low groundwater potential due to few features enabling water to percolate. Therefore, locations with low lineament density have low infiltration rates, whereas those with high lineament density have high infiltration rates (Table 16.5), making them suitable areas for groundwater occurrence. In general, highly fractured geological material facilitates groundwater replenishment through infiltration via faults, joints, and other geological structures and enhances the potential for groundwater occurrence.

Development of the Groundwater Potential Zone and Validation

By integrating all of the reclassified thematic layers using weighted overlay analysis with Eq. 16.13, the groundwater potential zone map of the Upper Awash Basin was

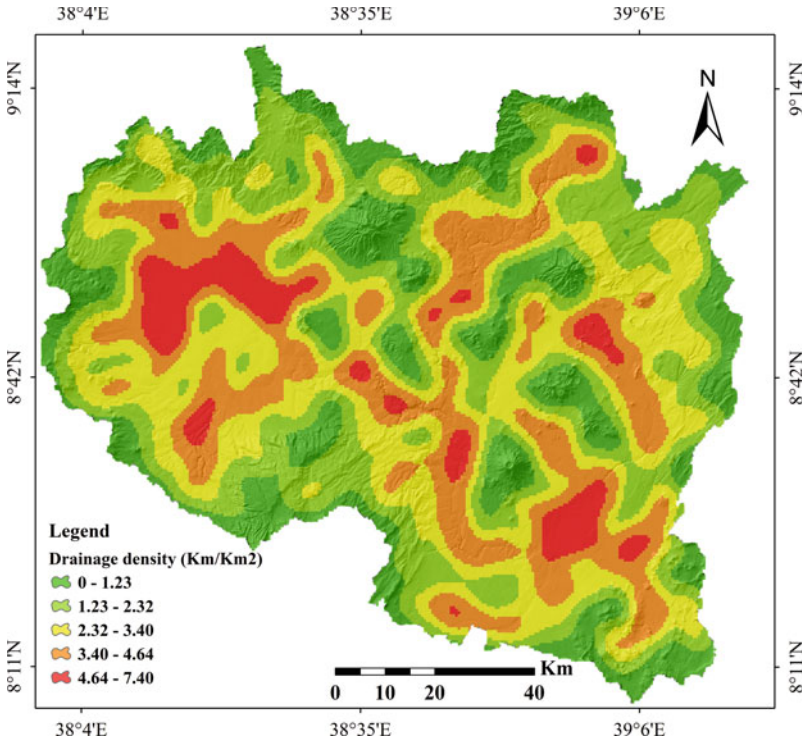

Fig. 16.18 Drainage density map of the Upper Awash Basin

generated. Consequently, the eight thematic layers were overlaid to produce a single map in ArcGIS 10.7. Based on those thematic layers, the GWPZ map of the Upper Awash Basin was classified using the natural break classification method in the GIS environment as poor, moderate, good, very good, and excellent (Andualem 2019). The study revealed that 54.21% (6312.22 km^2) of the area fell into the "very good" GWPZ category, with the remaining categories in descending order being "good", "moderate", "poor", and "excellent". The results are shown in Table 16.9.

In the mountainous area, particularly in volcanic mountains, poor, and moderate groundwater potential was noted (mainly in the marginal part of the study area). In contrast, a "good" potential groundwater zone occurs in escarpment landforms with high vegetation coverage, which facilitates infiltration. Specifically, the "very good" groundwater potential zone was primarily located in quaternary sediment and at the base of mountains (Fig. 16.22).

The methodology that was used to produce the groundwater potential map of the Upper Awash Basin highlights the importance of geomorphology, geology, and slope in the distribution of groundwater in the Upper Awash Basin. These parameters are the most significant factors in determining groundwater potential zone characterization in the area based on expert suggestions. On the other hand, the geomorphology,

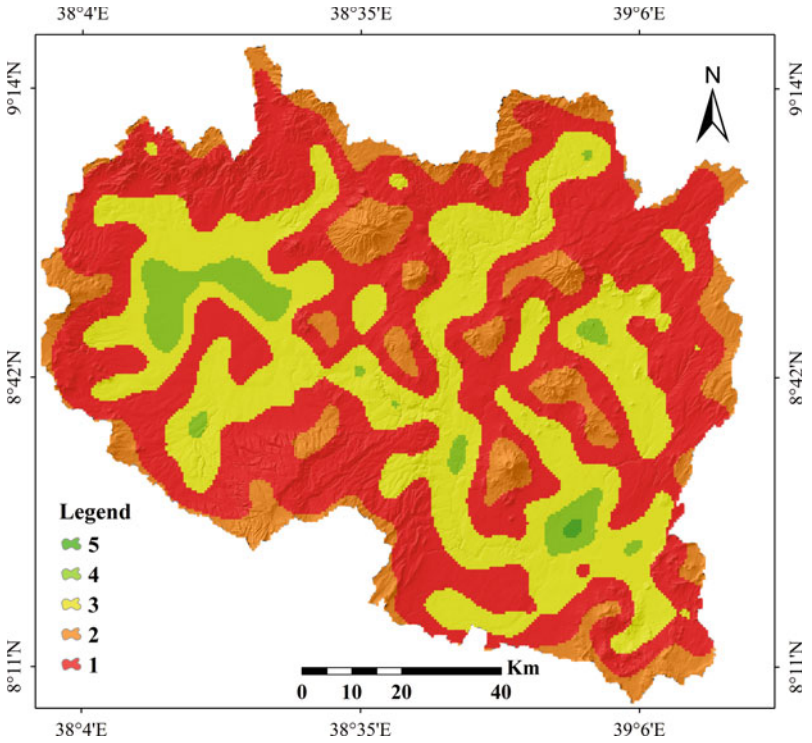

Fig. 16.19 Reclassified density map of the Upper Awash Basin

geology, and slope of the area are interconnected. For instance, undulating land forms which are also characterized by quaternary sediment and low slope were classified as zones with high groundwater potential, whereas volcanic mountains which are distinguished by trachyte and rhyolite having high slope, were classified as zones with low groundwater potential. As a result, "very good" and "good" potential groundwater zones are primarily found in flat and undulating plains, as well as medium plains. Additionally, the geological formation in the area plays a significant role in determining groundwater potential. This explains why quaternary sediment deposits and lowland volcanic units (such as scoriaceous basalt) have very high groundwater potential in the study area.

Rainfall is important for groundwater replenishment, but should be complimented by suitable landscape that promotes flow accumulation. For instance, rainfall over highlands contributes to a greater likelihood of groundwater rejuvenation and therefore occurrence groundwater in areas further downstream, where it drains to, via streams and fissures and accumulates. This results in variable contributions of rainfall over the spatial extent of the study area.

In this study, classification of groundwater potential zones using integrated GIS and remote sensing approaches closely corresponds to the available well yield data,

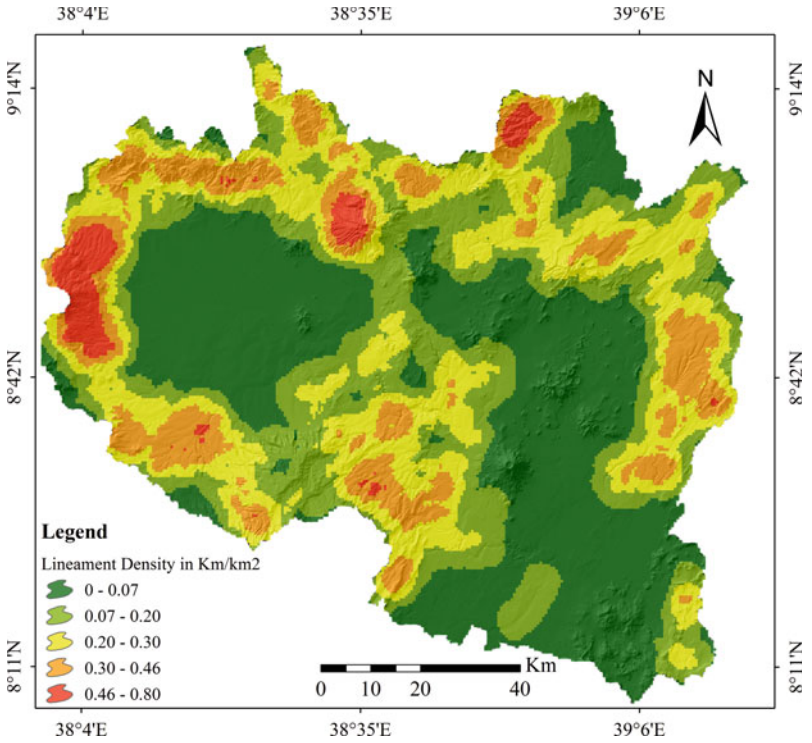

Fig. 16.20 Lineament density map of the Upper Awash Basin

as shown in Fig. 16.22 and Table 16.10. The validation results reveal that out of 96, 79 boreholes with a minimum of 0.07 l/s and maximum of 50 l/s well yields were characterized within the "very good" groundwater potential zone. Amongst the boreholes that are accurately categorized, NSPTCPW-01-17 (Nifas-silk), WPW-01-16 (Gofa mebrat-hayil), and WF01-PW18 (Akaki) had yields of 50 l/s, 40 l/s, and 38.04 l/s, respectively. However, H19PW-01-16 borehole which had a yield of 40 l/s was categorized under "good" groundwater potential. Drilling depths are considered to have contributed to these misclassifications. Wells located in a "moderate" groundwater potential zone were also misclassified. These wells have yields of 0.1, 0.3, and 0.4 l/s and were expected to be under "poor" GWPZ.

Discussion

In this study, the groundwater potential zone of the Upper Awash Basin was investigated by integrating different parameters that are known to influence the distribution and occurrence of groundwater in the area. Similar to Arulbalaji et al. (2019),

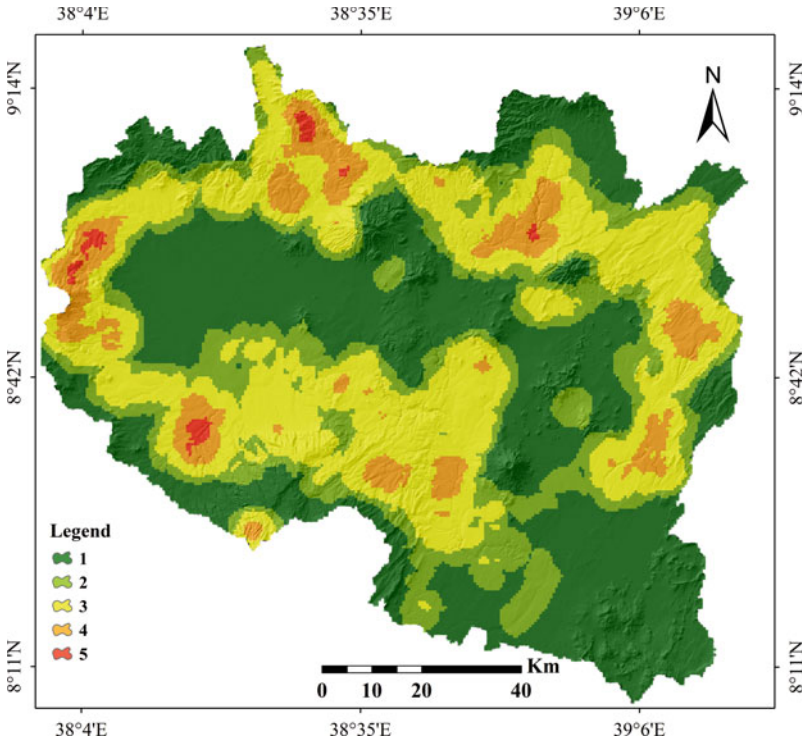

Fig. 16.21 Reclassified lineament density map of the Upper Awash Basin based on Table 16.5

Table 16.9 Groundwater potential zone aerial extent of the Upper Awash Basin

GWPZ classes	Area (km^2)	Percentage (%)
Poor	70.45	0.60
Moderate	1482.03	12.73
Good	3751.19	32.21
Very good	6312.22	54.21
Excellent	29.11	0.25
Total sum	11,645.00	100.00

landforms such as flat plains, undulating plains, rift lowlands, and spatter cones were classified as very high groundwater potential zones, whereas escarpments and volcanic mountain landforms were assigned to low groundwater potential zones. Therefore, rift lowlands serve as groundwater discharge areas, while escarpments and volcanic landforms such as basaltic plateaus and volcanic domes serve as highly suitable groundwater recharge zones due to the movement of groundwater from high- to low-elevation landforms.

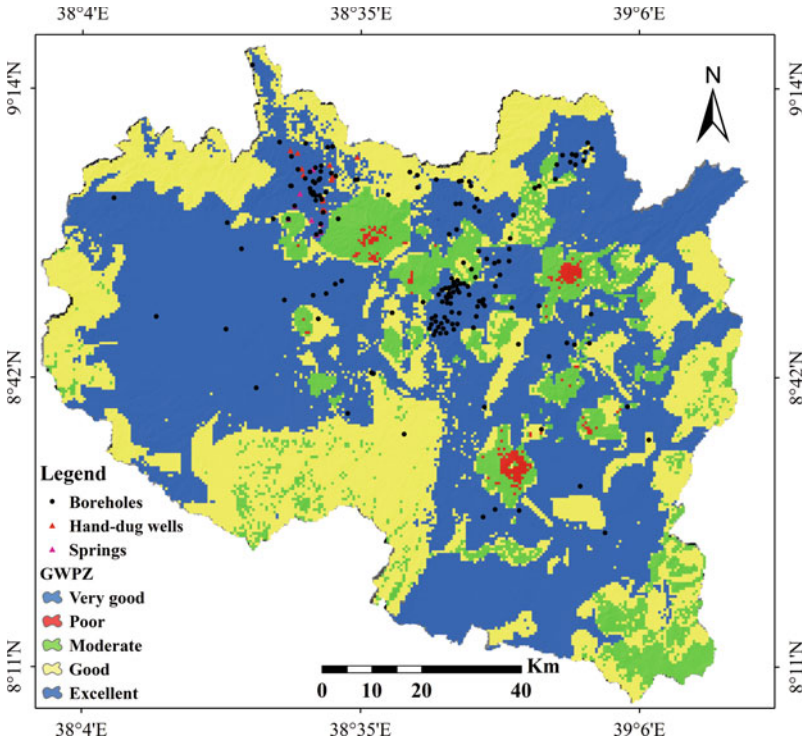

Fig. 16.22 Groundwater potential zone map of the Upper Awash Basin

Table 16.10 Description of borehole well yield corresponding to the GWPZs

GWPZ categories	No. of boreholes	Percentage of boreholes	Well yield range (l/s)
Excellent	–	0	–
Very good	79	82.30	0.07–50
Good	14	14.58	0.1–40
Moderate	3	3.13	0.1–0.4
Poor	–	0	–
Total sum	96	100	

The porosity and permeability generated during and after rock formation influence the distribution and storage of groundwater in volcanic rocks (Alemayehu 2006). Consequently, the quaternary sediment deposits, Scoria fallout, scoria cones and fallout deposits, upper basalt, Termaber Megezez Formation, quaternary basalt, and ash flow (Nazret groups), which have relatively high permeability, were given a higher weight (higher suitability for groundwater potential) (Kebede et al. 2010). On the other hand, because of their typical association with poor porosity and permeability, the pyroclastic and trachyte groups of rocks were classified as low groundwater

potential zones. In fact, the study result is in line with the expectation given to those rock units in the methodology section provided that the rock units with high permeability rates fell within high to very high groundwater potential zones.

The slope of an area has a significant effect on groundwater potential zone characterization. In this study, areas with a gentle slope and low topographic elevation have promising groundwater potential because there will be a longer residence time for surface water to percolate to the subsurface (Kumari 2017; Arulbalaji et al. 2019; Tanzeer 2020). Similarly, the groundwater potential in a particular place is directly associated with rainfall (Kotchoni et al. 2019). As a result, areas that receive high annual rainfall were recognized as having very high groundwater potential, and areas with low annual rainfall were considered to be poor groundwater potential zones.

Preeja et al. (2011) suggest that lineaments serve as the primary conduits for the movement and storage of groundwater in impermeable rocks, worldwide. Areas with a high lineament density indicate a high secondary porosity and are considered better groundwater potential zones (Silwal and Pathak 2018). Therefore, in the present study, the areas with high lineament density (Fig. 16.20), particularly those located in marginal parts of the study area, which were given a higher weight, have promising groundwater potential. In contrast, the central part of the study area was given a lower weight (Fig. 16.20). It is crucial to note that although the central region has a high groundwater potential as a result of parameters such as geomorphology, geology, rainfall, and slope, overall suitability is significantly reduced owing to smaller lineament density (Fig. 16.22).

Land use provides a better indicator of groundwater potential in a specific area since water availability is a fundamental component in determining land use patterns (Silwal and Pathak 2018). Water bodies have the highest infiltration rate, followed by forests, cropland, settlements, and industrial/quarries according to Etikala et al. (2019). As a result, water bodies have been assigned a high weight in determining the study area's groundwater potential zone, and thus, a very high groundwater potential results in this land cover class. The study area is study found that many places have agricultural land use, which encourages water penetration into subsurface materials; agricultural and forest areas were identified as groundwater potential zones with "extremely high" potential (Table 16.5). However, in defining the groundwater potential zone of the study area, built-up and bare land were given a lower weight, which is consistent with the current research results and findings of Sheikh and Rina (2017), Etikala et al. (2019) and Basin et al. (2021).

The degree of permeability that determines groundwater potential is controlled by soil properties, which in turn influence the relationship between surface runoff and infiltration rates (Gintamo 2017). As a result, sandy loam, loam, and clay were used to indicate the groundwater potential zone of the area (Fig. 16.13). Moreover, areas with low drainage density have both larger potential for groundwater and higher probability of groundwater recharge (Prasad et al. 2008). Therefore, the western part of the study area was revealed to have higher drainage density, which in turn facilitates the runoff rate in the area.

Concluding Remarks

This research demonstrates that remote sensing data combined with GIS and the AHP approach can be used to delineate the potential groundwater zones in the Upper Awash Basin. Thematic layers were created utilizing remote sensing and other auxiliary data and then weighted using the analytical hierarchy process (AHP). For mapping potential groundwater zones, the analytical hierarchical process (AHP) was useful in allocating appropriate weights to distinct thematic layers and their related classes. A total of eight thematic layers were used: geomorphology, geology, slope, rainfall, lineament density, drainage density, LULC, and soil. Groundwater potential of the Upper Awash Basin was classified into five categories according to the final overlay analysis. These include excellent (29.11 km^2), very good (6312.22 km^2), good (3751.19 km^2), moderate (1482.03 km^2), and poor (70.45 km^2).

A "very high" GWPZ was found in the middle region of the study area as a result of the interactions between slope, geology (quaternary sediment deposits), and geomorphology (flat and undulating landforms)/(flat terrain). "Good" and "moderate" GWPZs were common in volcanic mountains (lowland landscape due to volcanic mountains and spatter cones, rifts and spatter cones, hard volcanic rock units with rough surfaces and cracks, and due to the edge effect of parameters in the study area). The "poor" GWPZ, on the other hand, is found in the volcanic mountains of Erer, Zikwala, and Wechecha, which are rugged mountain rock units. The GWPZs were validated using discharge well data from boreholes, natural springs, and hand dug well data; as a result, approximately 82.3% of the well data matched a "very high" groundwater potential zone, with no borehole data in the "excellent" and "poor" GWPZ classes.

Acknowledgements We would like to acknowledge the Salale University and Space Science and Geospatial Institute for financial support to undertake this study. Similarly, we express our gratitude to the National Meteorological Agency (EMA), Geological Survey of Ethiopia (GSE), Food and Agricultural Organization (FAO), US Geological Survey (USGS), European Space Agency (ESA), Center for Hydrometeorology and Remote Sensing (CHRS), and Ministry of Water and Energy for providing us with data used in this study.

References

ABA (Awash Basin Authority) (2017) Awash Basin water allocation strategic plan

Adeyeye OA, Ikpokonte EA, Arabi SA (2019) GIS-based groundwater potential mapping within Dengi area, North Central Nigeria. Egypt J Remote Sens Space Sci 22(2):175–181. https://doi.org/10.1016/j.ejrs.2018.04.003

Alemayehu T (2006) Groundwater occurrence in Ethiopia. Addis Ababa University, p 107. http://www.eah.org.et/docs/Ethiopian-groundwater-Tamiru.pdf

Allafta H, Opp C (2021) Identification of groundwater potential zones using remote sensing and GIS techniques: a case study of the Shatt Al-Arab Basin

Anderson JR, Hardy EE, Roach JT, Witmer RE (1976) A land-use and land-cover classification system for use with remote sensor data

Andualem DTG (2019) Groundwater potential assessment using GIS and remote sensing: a case study of Guna tana landscape, upper blue Nile Basin, Ethiopia. J Hydrol Reg Stud 24:100610. https://doi.org/10.1016/j.ejrh.2019.100610

Arefayne SH, Abdi S (2015) Groundwater exploration for water well site locations using geophysical survey methods. J Waste Water Treat Anal 07(01):1–7. https://doi.org/10.4172/2157-7587.1000226

Arkoprovo B, Adarsa J, Prakash S (2012) Delineation of groundwater potential zones using satellite remote sensing and geographic information system techniques: a case study from Ganjam district, Orissa, India. Res J Recent Sci 1:59

Arulbalaji P, Padmalal D, Sreelash K (2019) GIS and AHP techniques based delineation of groundwater potential zones: a case study from Southern Western Ghats, India. Sci Rep 9(1):1–17. https://doi.org/10.1038/s41598-019-38567-x

Assiged G (2007) Geology of Addis Ababa city (NC37-10/X and Y and NC37-14/E and F)

Auchincloss AH, Diez Roux AV, Brown DG, Raghunathan TE, Erdmann CA (2007) Filling the gaps: spatial interpolation of residential survey data in the estimation of neighborhood characteristics. Epidemiology (Camb, MA) 18(4):469–478. https://doi.org/10.1097/EDE.0b013e3180646320

Basin H, Aslan V, Çelik R (2021) Integrated GIS-based multi-criteria analysis for groundwater potential mapping in the Euphrates's sub-basin, Turkey

Berhanu B, Melesse AM, Seleshi Y (2013) GIS-based hydrological zones and soil geo-database of Ethiopia. CATENA 104:21–31

Bhatta B (2013) Research methods in remote sensing. In: Springer briefs in earth science. http://www.springer.com/series/8897

Billi P (2015) Geomorphological landscapes of Ethiopia. In: Landscapes and landforms of Ethiopia. World geomorphological landscapes, pp 3–32

Brunelli M (2015) Introduction to the analytical hierarchy process. In: Springer briefs in operatonal research. https://doi.org/10.1007/978-3-319-12502-2

Chebud YA, Melesse AM (2009) Numerical modeling of the groundwater flow system of the Gumera sub-basin in Lake Tana basin, Ethiopia. Hydrol Process Spec Issue Nile Hydrol 23(26):3694–3704

Chebud YA, Melesse AM (2011) Operational prediction of groundwater fluctuation in South Florida using sequence based Markovian stochastic model. Water Resour Manage 25(9):2279–2294

Congalton RG, Green K (2009) Assessing the accuracy of remotely sensed data: principles and practices. In: Raton B (ed), 2nd edn. CRC Press

Dinesan VP, Gopinath G, Ashitha MK (2015) Application of geoinformatics for the delineation of groundwater prospects zones—a case study for Melattur Grama Panchayat in Kerala, India. Aquat Procedia 4(Icwrcoe):1389–1396. https://doi.org/10.1016/j.aqpro.2015.02.180

Efrem B (2010) Geology of the Akaki Baseka area

Etikala B, Golla V, Li P, Renati S (2019) Deciphering groundwater potential zones using MIF technique and GIS: a study from Tirupati area, Chittoor District, Andhra Pradesh, India. HydroResearch 1:1–7

Fenta A, Gebryohannes T, Gebrerufael H (2014) Spatial analysis of groundwater potential using remote sensing and GIS-based multicriteria evaluation in Raya Valley, northern Ethiopia. Hydreogeology 23:195–206. https://doi.org/10.1007/s10040-014-1198-x

Gintamo TT (2017) Ground water potential evaluation based on integrated GIS and remote sensing techniques. In: Bilate river catchment: south rift valley of Ethiopia, Dec 2015, pp 85–120

Henock B, van Essen P, Zerfu TT (2014) Integrated water resource management Upper Awash River basin, Central Ethiopia

Hsu K et al (1997) Precipitation estimation from remotely sensed information using artificial neural networks. J Appl Meteor 36:1176–1190

Hussein A-A, Govindu V, Nigusse AGM (2017) Evaluation of groundwater potential using geospatial techniques. Appl Water Sci 7(5):2447–2461. https://doi.org/10.1007/s13201-016-0433-0

Ilfios T (2007) Geology of derba (R) and fital (L) subsheets of Addis Ababa ma sheet (NC37-10)

Jensen J (2015) Introduction to digital image processing: a remote sensing perspective. University of South Carolina, Pearson Education, Inc.

Kabeto J, Adeba D, Regasa MS, Leta MK (2022) Groundwater potential assessment using GIS and remote sensing techniques: case study of West Arsi zone, Ethiopia. Water 14(12):1838. https://doi.org/10.3390/w14121838

Kazmin V, Berhe S (1978) Geology and development of the Nazret area, northern Ethiopian rift

Kebede S, Hailu A, Crane E, ÓDochartaigh BÉ, Bellwood-Howard I (2010) Africa groundwater atlas: hydrogeology of Ethiopia. Br Geol Surv. http://earthwise.bgs.ac.uk/index.php/Hydrogeology_of_Ethiopia

Klaus DG (2013) Implementing the analytic hierarchy process as a standard method for multi-criteria decision making in corporate enterprises—a new AHP Excel template with multiple inputs. In: Proceedings of the international symposium on the analytic hierarchy process. https://doi.org/10.13033/isahp.y2016.047

Kotchoni DOV, Vouillamoz JM, Lawson FMA, Adjomayi P, Boukari M, Taylor RG (2019) Relationships between rainfall and groundwater recharge in seasonally humid Benin: a comparative analysis of long-term hydrographs in sedimentary and crystalline aquifers. Hydrogeol J 27(2):447–457. https://doi.org/10.1007/s10040-018-1806-2

Kumari MAR (2017) A geospatial approach for delineation of groundwater potential zones in a part of national capital region, India. Int Res J Earth Sci 5:1–10

Liu JG, Mason PJ (2009) Essential image processing and GIS for remote sensing. Wiley-Blackwell

Malczewski J (1999) GIS and multicriteria decision analysis

Meresa E, Taye G (2019) Estimation of groundwater recharge using GIS-based WetSpass model for Birki watershed, the eastern zone of Tigray, Northern Ethiopia. Sustain Water Resour Manag 5(4):1555–1566. https://doi.org/10.1007/s40899-018-0282-0

Meshesha D, Hailemariam D, Mamo A (2010) Geology of Debre Birhan area

Morris BL, Lawrence AR, Chilton PJ, Adams B, Calow RC, Klinck BA (2003) Groundwater and its susceptibility to degradation: a global assessment of the problem and options for management. In: Early warning and assessment report series. RS, 03-3, 126

MOWS (FDRE Ministry of Water Resource) (2002) Water sector development program

MOWS (FDRE Ministry of Water Resource) (2021) Boreholes data. Department of Hydrogeology

Nguyen P, Shearer EJ, Tran H, Ombadi M, Hayatbini N, Palacios T, Huynh P, Braithwaite D, Updegraff G, Hsu K (2018) The CHRS Data Portal, an easily accessible public repository for PERSIANN global satellite precipitation data. Nature Publishing Group, pp 1–10. https://doi.org/10.1038/sdata.2018.296

NRCS (2010) Geologic and groundwater considerations, chap 7. In: Agricultural waste management field handbook

Prasad RK, Mondal NC, Banerjee P, Nandakumar M, Singh V (2008) Deciphering potential groundwater zone in hard rock through the application of GIS. Environ Geol 55:467–475

Prasanna MV, Chidambaram S, Hameed AS, Srinivasamoorthy K (2011) Hydrogeochemical analysis and evaluation of groundwater quality in the Gadilam river basin, Tamil Nadu, India. J Earth Syst Sci 1(120):85–98

Preeja KR, Joseph S, Thomas J, Vijith H (2011) Identification of groundwater potential zones of a tropical river basin (Kerala, India) using remote sensing and GIS techniques. J Indian Soc Remote Sens 39(1):83–94. https://doi.org/10.1007/s12524-011-0075-5

Raja Kumar T, Jeyavel, Dushiyanthan C (2016) Evalauation of groundwater potential zones using electrical resistivity response and lineament pattern in Uppodai sub basin, Tambaraparani river, Tirunelveli district, Tamil Nadu, India. J Geol Geophys 05(02). https://doi.org/10.4172/2381-8719.1000241

Saaty TL (1980) The analytic hierarchy process: planning, priority setting, resources allocation. McGraw-Hill

Saranya T, Saravanan S (2020) Groundwater potential zone mapping using analytical hierarchy process (AHP) and GIS for Kancheepuram district, Tamil Nadu, India. Model Earth Syst Environ 0123456789. https://doi.org/10.1007/s40808-020-00744-7

Serwait M, Gessesse B, Bedada TB, Tibebe D (2019) Evaluation of long-term satellite-based retrieved precipitation estimates and spatiotemporal rainfall variability: the case study of Awash basin, Ethiopia, chap 3. In: Assefa GS, Melesse M, Abtew W (eds) Extreme hydrology and climate variability. Elsevier, pp 23–35. https://doi.org/10.1016/B978-0-12-815998-9.00003-8

Shanableh AMT (2015) Geomatics for mapping of groundwater potential zones in the northern part of the United Arab Emiratis-Sharjah City. Sens Spat Inf Sci

Sheikh MA, Rina K (2017) A geospatial approach for delineation of groundwater potential zones in a part of national capital region, India. Int Res J Earth Sci 5(10):1–10

Silwal CB, Pathak D (2018) Review on practices and state of the art methods on delineation of ground water potential using GIS and remote sensing. Bull Dept Geol 20–21:7–20. https://doi.org/10.3126/bdg.v20i0.20717

Solomon S (2003) Remote sensing and GIS: applications for groundwater potential assessment in Eritrea. Ph.D. dissertation, Byggvetenskap

Sorooshian S et al (2000) Evaluation of PERSIANN system satellite–based estimates of tropical rainfall. Bull Am Meteor Soc 81:2035–2046

Stiefel J, Melesse A, McClain M, Price RM, Anderson AP, Chauhan NK (2009) Effects of rainwater harvesting induced artificial recharge on the groundwater of wells in Rajasthan, India. Hydrogeol J 17(8):2061–2073

Sunmin L, Hyun Y, Lee L, Lee M-J (2020) Groundwater potential mapping using remote sensing and GIS-based machine learning techniques. Remote Sens 12:1200. https://doi.org/10.3390/rs12071200

Tanzeer D (2020) Delineation of potential groundwater recharge zones using analytical hierarchy process (AHP). Geol Ecol Landsc 1–16. https://doi.org/10.1080/24749508.2020.1726562

Tobiszewski M, Tsakovski S, Simeonov V, Pena-Pereira F (2015) GIS and multicriteria decision analysis, vol 1

U.S. Geological Survey (2016) Landsat 8 data users handbook. Nasa 8:97. https://landsat.usgs.gov/documents/Landsat8DataUsersHandbook.pdf

Waikar ML, Nilawar AP (2014) Identification of groundwater potential zone using remote sensing and GIS technique. Int J Innov Res Sci Eng Technol 3(5):12163–12174

Wogari K (2006) Water resources potential evaluation of Holeta river catchment, Central Oromia. Addis Ababa University, West Shoa

Yitbarek A, Razack M, Ayenew T, Zemedagegnehu E, Azagegn T (2012) Hydrogeological and hydrochemical framework of Upper Awash River basin, Ethiopia: with special emphasis on inter-basins groundwater transfer between Blue Nile and Awash Rivers. J Afr Earth Sci 65:46–60. https://doi.org/10.1016/j.jafrearsci.2012.01.002

Chapter 17
Evaluation of the Hydraulic Performance of the Kombolcha Town Water Supply Distribution System, Ethiopia

Selamawit Workineh Tsige and Tamru Tesseme Aragaw

Abstract In this study, the hydraulic performance of the existing water supply and distribution network of Kombolcha town was analyzed by using WaterGEMS. The WaterGEMS model was used for automated calibration and analysis of the hydraulic parameters of water supply distribution systems. At selected nodes, the developed model was calibrated to reduce the difference between the measured and simulated pressures. The water supply coverage of the town was only 69.4%, which is extremely low when compared to the country's urban water supply coverage standard. The water demand was determined to be 50 L/day, which is less than the community's actual water consumption. The water balance analysis revealed that 67.1% of water production is billed quantity and 32.9% is nonrevenue water (NRW). The results from the simulation of the existing water supply distribution system revealed that during peak hour demand, 23.1% of the junctions have low pressure (15 m H_2O), and 67.4% of the junctions have high pressure (> 60 m H_2O). The hydraulic performance analysis indicated that 83.5% and 24% of the total pipes have velocities below 0.6 m/s at minimum and peak demands, respectively. The study concluded that the hydraulic performance of Kombolcha's existing water supply distribution systems is below expectations. As a result, high pressures in the distribution system should be managed with pressure-reducing valves. Furthermore, low pressure should be improved by making existing borehole rehabilitation more efficient to meet the town's peak water demand.

Keywords Hydraulic performance · Kombolcha · WaterGEMS · Water balance

S. W. Tsige (✉)
Hydraulics and Water Resource Engineering Department, College of Engineering and Technology, Bule Hora University, P.O. Box 144, Bule Hora, Ethiopia
e-mail: selikotes2009@gmail.com

T. T. Aragaw
Faculty of Water Supply and Environmental Engineering, Arba Minch Water Technology Institute, Arba Minch University, P.O. Box 21, Arba Minch, Ethiopia

A. M. Melesse et al. (eds.), *Land and Water Degradation in Ethiopia*, Springer Geography, https://doi.org/10.1007/978-3-031-60251-1_17

Introduction

An efficient water supply distribution system is a necessary service for any municipal town to provide residents with adequate amount of water. Providing safe and potable water is critical to enhancing development and for improving the health of urban communities (Brhane 2019; Massoud and Zia 2018). Although human life can survive for many days without food, even a few days without water can be fatal (Senthil and Yaashikaa 2019).

Water distribution networks are designed to meet the water needs of a variety of domestic, commercial, industrial, and firefighting applications (Mehta et al. 2017). A high-performing water distribution system should provide a safe, sufficient, and affordable water supply service with low water loss and good water quality that meets national and international standards (Agunwamba 2018). However, one-third of Africa's urban water supply systems are not continuously operational (Abebe 2020). The main causes of water distribution system performance loss were increasing population, shortage of source water, treatment plant size, reservoir and storage tank capacity, power outages to run water pumps, intermittent pumping, and high water loss (Alexandra et al. 2009; Grady et al. 2014).

The significant difference between the amount of water produced in the distribution system and the amount of water consumed in the system is another major factor affecting the hydraulic performance of urban water supply systems. A significant amount of water is lost due to leaking distribution system pipes, joints, valves, and fittings (Shao et al. 2019). The global volume of nonrevenue water (NRW) is staggering, according to USAID (2010). Every year, more than 32 billion m^3 of treated water is lost due to distribution network leakage. An additional 16 billion m^3 is delivered to customers each year but not invoiced due to theft, poor metering, or corruption.

According to Sivakumar and Prasad (2012), the first and most obvious element to address in improving water distribution systems is hydraulic performance. Evaluating system performance entails indirectly estimating the circumstances and rehabilitation requirements to ensure the continuous and reliable operation of all system components throughout their entire service life prior to failure (Chaki 2017). Hydraulically, water distribution modeling aids in predicting system performance and solving a wide range of design and operational issues (Walski 2000).

The computation of flow and pressure at nodes constitutes the analysis of water distribution network (WDN) modeling. It must be carefully designed and properly maintained to reach the consumer (Vaidya Deepali and Sandip 2019). A computer model is often useful for analyzing the hydraulic parameter behavior of an urban water distribution network (Haider et al. 2014). Developing a hydraulic model is useful in evaluating system functions (i.e., whether the system meets the standard level of service based on pressure and velocity considerations) and supports decision-making (Awe et al. 2019). There are a variety of modeling software (both free and commercially available) for design and analysis of water distribution networks (Awe et al. 2019). Examples include EPANET, Bentley Water CAD v8i, and Bentley

WaterGEMS (Mehta et al. 2017; Rai et al. 2019). WaterGEMS is software that performs extended-period simulations of hydraulic and water quality behavior in pressurized pipe networks. It tracks the flow of water in each pipe, the pressure at each junction, and the height of water in each tank. The data presentation mode of WaterGEMS is user friendly, easily interpretable and can be integrated with a GIS software. Berhane (2020) and Bhoyar and Mane (2017) demonstrated that WaterGEMS has a better performance in optimizing pipe diameters for adequate water supply that meets pressure requirements.

Kombolcha is among one of the first cities in Ethiopia to have a water distribution network since 1963 (Metaferia 2011). According to the Kombolcha town water supply and sewerage office information, rapid population growth, large volumes of unaccounted water due to pipeline breakage, and economic development have contributed to the increased water demand and water shortage. These issues have a considerable impact on the hydraulic performance of the water distribution system. However, studies that thoroughly evaluate the hydraulic performance of the system are lacking and model-based analyses are yet to be applied to the town of Kombolcha. As such, the objective of the study is to evaluate the hydraulic performance of Kombolcha town's water distribution system by estimating the hydraulic parameters at each node and pipe using WaterGEMS software and comparing the results with standards.

Material and Methods

Description of the Study Area

This research was carried out in Kombolcha town, which is located in the South Wollo Administrative Zone in the eastern part of the Amhara region at 11° 06′ latitude and 39° 45′ longitude (Fig. 17.1). The average monthly temperature in the area ranges between 16.1 and 22.1 °C, and the average annual rainfall is 1248 mm. Based on data from the Central Statistical Agency of Ethiopia (CSA), with an annual growth rate of 4% (CSA 2013), population of the town in the year 2020 was 134,599. The altitude of the town varies from 1500 to 2300 m above mean sea level.

Kombolcha town's current water source is groundwater from boreholes located in the city having a combined expected average water production capacity of 303 L per second. The current total discharge is about 155 L per second with a 16 h average pumping rate. Water distribution system components include reservoirs, tanks, pipes, and pumps. The percentage population of the town that has access to safe water (in-house or yard connection) from the total population is 69.4%; the remaining people use traditional and often unprotected sources. Figure 17.2 illustrates the layout of the study area's water distribution system.

There are seven circular-type storage reservoirs with a total capacity of 2950 m^3. All storage reservoirs are located on elevated ground surfaces to maintain sufficient

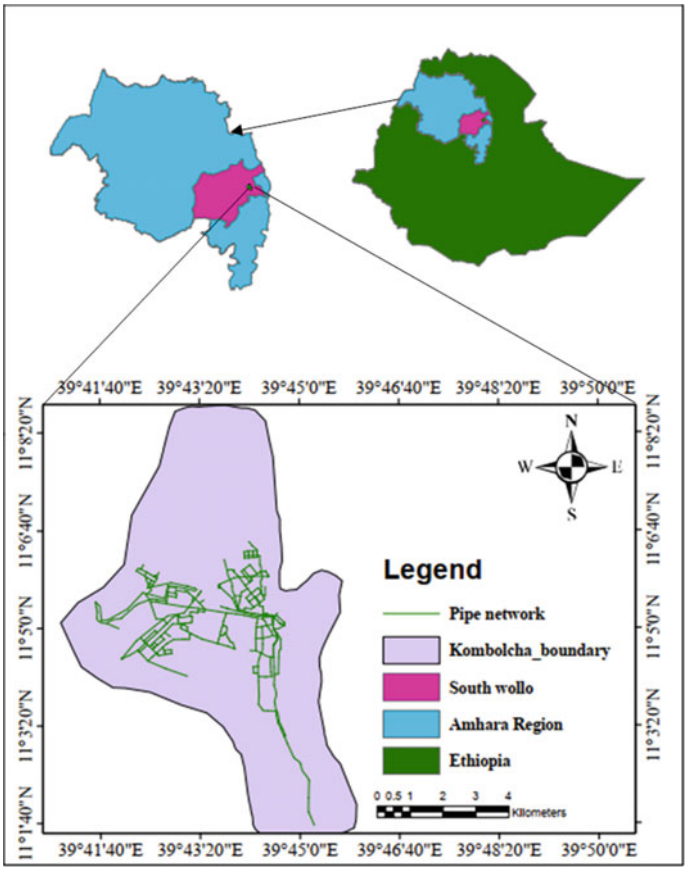

Fig. 17.1 Location of the study area

pressure in the downstream pipe network and to provide adequate flow to the area being served.

The town's water distribution system (WDS) is a combination of a branched and looped network made of a mixture of ductile iron (DCI), high-density polyethylene (HDPE), polyvinyl chloride (PVC), and galvanized iron (GI) pipe materials with sizes ranging from DN 40 mm to DN 315 mm. The total estimated length of distribution lines is approximately 67.5 km. The main pipe in Kombolcha's distribution system is HDPE, which covers approximately 54.38% of the total distribution system length. Galvanized iron, ductile iron, and polyvinyl chloride cover approximately 24.56%, 1.6%, and 19.45% of the total length of the distribution system, respectively.

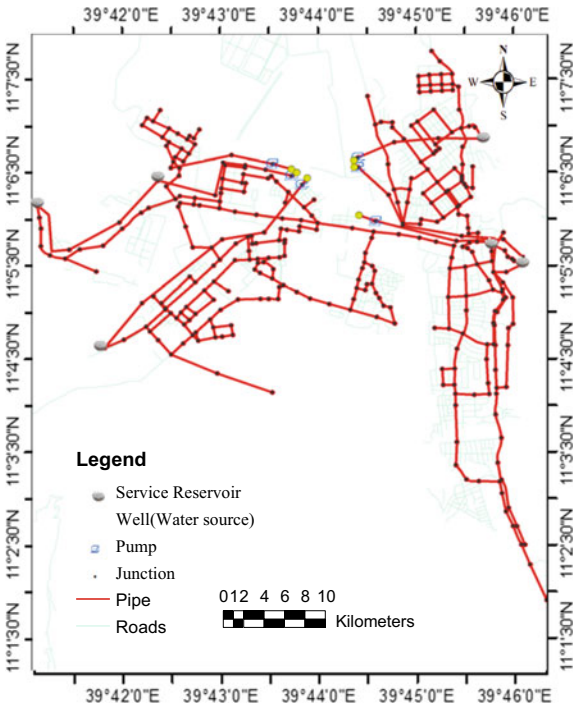

Fig. 17.2 Existing water supply and distribution systems of Kombolcha town

Materials and Tools

The aim of this study was to assess the performance of Kombolcha's existing water supply distribution system. The equipment used to achieve this goal included a pressure gauge with a size of 1/2″ or 12 mm to measure pressure at selected points. This equipment, paired with a GPS instrument, was used to collect the necessary elevation data during pressure readings to pinpoint the precise location of the sample for calibration purposes. WaterGEMS CONNECT Edition, Arc GIS version 10.4.1, Global Mapper v20, AutoCAD 2011, and Microsoft Excel 2013 were used to collect, organize, and analyze the data.

Data Collection and Sampling

The data were gathered using primary and secondary data collection methods. A field survey was used to collect primary data (including field measurements and direct observations). Elevation of nodes or boundary elements was directly measured by using a hand-held GPS, flow at end-user taps was measured by using stopwatch, water meter, and plastic jerry can of 20 L capacity, and junction pressure was measured

using a pressure gauge. On March 20 and April 20, 2021, a field visit to Kombolcha was conducted to collect additional relevant data.

Secondary data were gathered from various studies, existing Kombolcha town water supply service office documents, and Amhara Design and Supervision Work (ADSW) design reports. Major information and data gathered from secondary data sources were system map/layout of WDN, diurnal water demand curve, population data with growth rate, topographic map, cadastral map, water source/reservoir type, storage reservoir (elevations, capacity diameter and height), water production and consumption records from 2015 to 2020, and node elevation data.

Pressure was measured at end-user taps in the high- and low-pressure zones of the distribution network in April 2021. All sampling points were chosen after a reconnaissance survey of the town's water distribution network which was useful in understanding pressure variation within the area. According to AWWA (2012), five percent of nodes are sufficient for accurate calibration and validation. For this study, sixteen samples (five percent) of a total of 334 junctions were taken for calibration and validation purposes during peak (7:00–9:00 a.m.) and minimum (3:00–5:00 a.m.) hour demand (AWWA 2012; Walski 2000).

Pressure samples were taken from customer connections directly from the main line at high elevation, low elevations, and high- and low-pressure areas, according to AWWA (2012). Figure 17.3 depicts the pressure measurement sampling location in the Kombolcha town distribution system.

Data Analysis

Quantitative methods were used to analyze data collected from various sources. The quantitative methods were combined with descriptive statistical methods, percentages, and graphs to produce the desired result. The data obtained from the Kombolcha town water supply and sewerage office and the Amhara design and supervision office report were analyzed using Microsoft Excel.

Household and Per Capita Water Consumption

The average daily per capita consumption was calculated by dividing yearly water consumption by the total population of the year 2020. The total number of connections or water meters within the study area was 20,766. Based on Kombolcha town water supply system-billed data, an average family size of 4.5 was used to calculate the average number of connections per family.

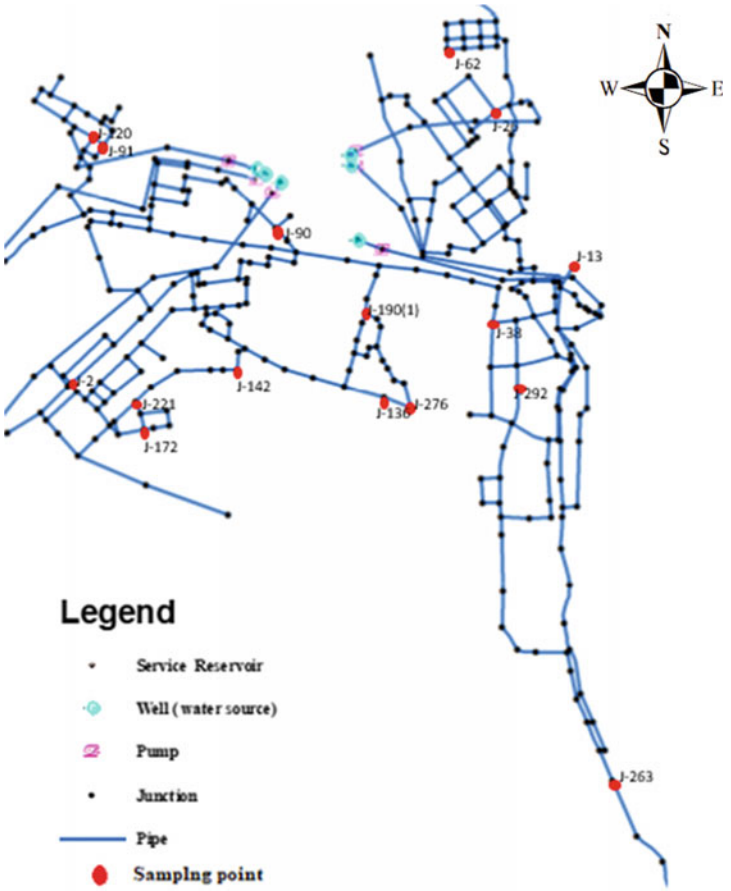

Fig. 17.3 Sample location for pressure measurement

Water Loss

The total water loss was calculated using the percentage of nonrevenue water. Percentage by input volume is recommended as a basic financial performance indicator (PI) for nonrevenue water (Farley et al. 2010). The data were obtained from the town water service office, which includes the yearly (2015–2020) and monthly water production and consumption (billed water volume). Using this information, Eq. 17.1 is used to calculate the total percentage of nonrevenue water in the system.

$$\mathrm{NRW} = \frac{W_{\text{tot. prod}} - W_{\text{tot. cons}}}{W_{\text{tot. prod}}} * 100\%, \tag{17.1}$$

where NRW is nonrevenue water (%); $W_{\text{tot. prod}}$ is total water produced (m^3/yr); and $W_{\text{tot. cons}}$ is total water consumed or used (m^3/yr).

WDS Modeling with WaterGEMS

WaterGEMS was used to calculate pressure, velocity, and head loss. The modeling process is described as follows:

1. **Model Configuration**

A main feature that WaterGEMS offers is the Model Builder. Using this tool, one can directly enter ArcGIS shape files, Excel files, and AutoCAD files at once and leverage the capabilities of these platforms to create a robust model. This enables the system map to be imported directly from other files without manually creating each component.

2. **Data Entry**

Physical parameters: Pipe characteristics (material, diameter, length, and roughness coefficient), junction (elevation and demand), pump elevation, tank and reservoir (borehole) elevation are input parameters added to the model.

Junction demand allocation: Assigning calculated base demands to the nodes in the network through the WaterGEMS model consists of several methods (i.e., point load data, area load data, and land use data). In this study, water demand was allocated using a proportional distribution by population method. This approach is considered to be the most practically applicable to the study area. Demand at each node is assigned by creating Thiessen polygons to the corresponding nodes. The steps to allocate base demand to each supply node are as follows:

- **Identify the number of houses around each node**: A Thiessen polygon was constructed to designate a service area for each node in WaterGEMS and was exported to ArcMap. The distribution network shape file was overlaid on the cadastral map in order to extract the number of houses within each polygon which is serviced by a node. Figure 17.4 shows the Thiessen polygons, the water distribution network layout, and cadastral maps used to determine the number of houses served by each node.
  - **Calculate the number of people served from each node**: The average number of people in each house (person per housing unit) was obtained from the town's revised design report. The total number of people served by each supply node was calculated by multiplying the average number of customers in each house by the total number of houses for each node.
  - **Estimating the base water demand for each node**: The town's average water demand was calculated by multiplying the per capita demand by the population. Once the system's average daily water demand (ADD) was determined,

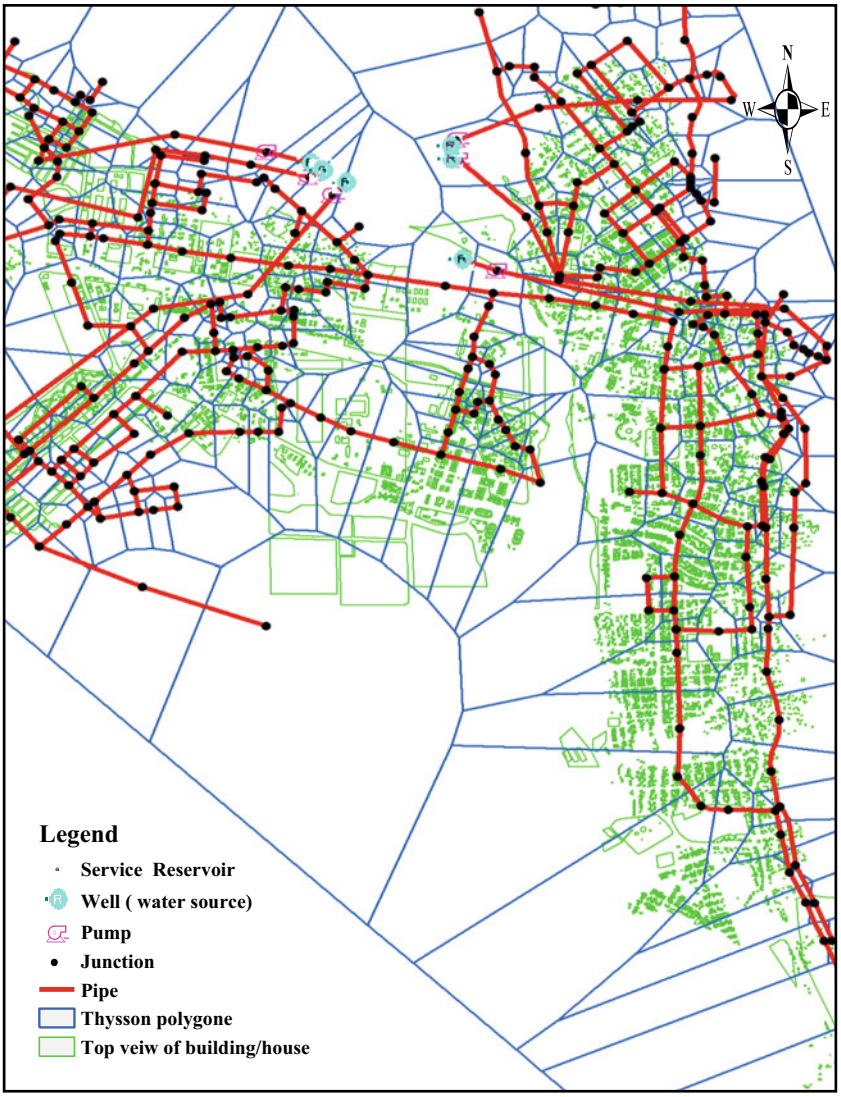

Fig. 17.4 Partial view of service area for each node together with houses

Eq. 17.2 is used to calculate the base water demand for the specific supply node (Bhadbhade 2009).

$$\text{Base water demand} = \frac{\text{population served by node}}{\text{total population}} * \text{ADD}. \tag{17.2}$$

3. **Run the Model**

The model was then run using the extended-period simulation (EPS) and steady-state simulation. The model was run in steady state for the average daily demand, which is the demand at each node that is not variable throughout the day. The system condition was computed over 24 h, beginning at 12:00 p.m. with a time increment of one hour. The software simulates dynamic state (EPS) hydraulic calculations depending on the mass and energy conservation principle. However, for the purposes of the analysis, the peak and minimum hour demands were simulated to determine the current performance of the system. The model was run from 12:00 p.m. to 5:00 a.m. for minimum hour consumption and from 6:00 to 8:00 a.m. for peak hour consumption.

4. **Model Evaluation**

Darwin calibration method: The model was calibrated using the WaterGEMS Darwin Calibrator. The Darwin Calibrator searches for an optimal solution describing the unknown calibration parameters that minimizes an objective function (e.g., error) while simultaneously satisfying constraints that describe the optimal solution (Bentley Institute 2018). The objective function in this analysis was to minimize the difference between the observed and predicted pressure values and was evaluated using the correlation coefficient and Root Mean Square Error (RMSE).

Most steady-state calibrations are sensitive to changes in pipe roughness, whereas extended-period calibrations are sensitive to changes in demand distribution (Walski 2017). Since pressure measurements were taken at the end-user tap and not on the water-main, we assumed that head loss between a sample node on the water-main and a corresponding end-use tap could be used to derive the pressure on the main line. The simulated pressure on the water-main would then be compared against the sum of observed pressure at the end-user tap and the head loss. This will be used to evaluate how much the simulated pressure deviated from the observed so that calibration parameters can be adjusted. For the steady-state simulation section of this study, the Hazen–Williams's coefficient (*C* factor) was adjusted until the pressure difference between the measured and predicted values was within acceptable limits ($\pm$ 1.5 m). After calibration, the model's consistency was evaluated by validating it against the test data obtained for an independent period (i.e., during minimum demand).

Results and Discussion

Water Supply Coverage

According to the population of the year 2020 (134,599) and water consumption data of 2,450,167 m^3 for 2020/21, the calculated per capita consumption is 50 l/c/d. This result does not satisfy the MoWIE (2006) recommended value of 70 l/c/d. This indicates that even though the per capita demand in the town is high, the consumption is low owning to inadequacy of the existing water supply system. Furthermore, the average daily demand of the town was estimated to be 11,980 m^3/d in 2020, but the

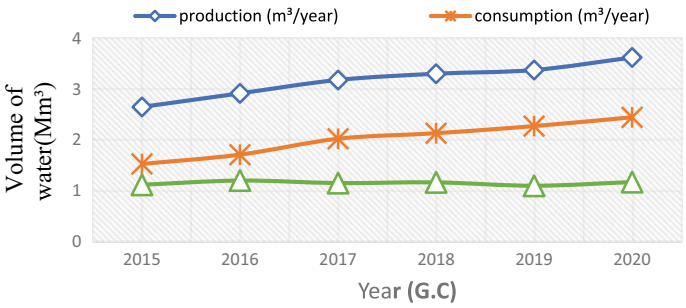

Fig. 17.5 Water production, consumption, and unaccounted for water of the town

existing water production is 10,063.4 m^3/d (116.5 L/s). This shows that an additional source is required to meet the demand.

Unaccounted for Water (NRW)

Calculating water loss and leakage requires detailed data due to its complex nature. The data are usually scarce in developing countries, and the case of Kombolcha town is no exception.

The six-year (2015–2020) actual production and consumption figures obtained from the Kombolcha town water supply and sanitation service were used to calculate water loss, as presented in Fig. 17.5, by using Eq. 17.1.

According to MoWIE (2006) classification and descriptions, water losses are considered acceptable if the loss is below 15% of water production. This indicates that the average water that is unaccounted for in 2020 for Kombolcha town (32.4%) is significantly larger than the minimum recommended value. Such a significant amount of unaccounted for water affects the financial viability of water utilities through lost revenues and increased operational costs, and effort should be made toward reducing it.

Calibration and Validation Results

Head loss between sample nodes on the water-main and end-use tap is shown in Table 17.1. The difference between simulated and measured pressures is shown in Table 17.2.

The difference between the observed and simulated pressures was greater than the minimum permissible value (± 1.5 m) according to AWWA (2012) standards for evaluation of design and operations. As shown in Table 17.2, the accuracy of the simulated pressures is relatively lower in junctions J-62, J-292, J-221, and J-276.

Table 17.1 Head loss calculation of the representative samples of a supply main node and the corresponding home faucet

No.	Junction (ID)	Elevation		Head loss between two locations		
		Node on main pipe	Node at end-user	Elevation difference (m)	Friction loss (m)	Total head loss (m)
1	J-13	1921.25	1924.36	− 3.11	0.11	− 3.00
2	J-26	1853.22	1855.25	− 2.03	0.012	− 2.02
3	J-62	1845.00	1847.07	− 2.07	0.072	− 2.00
4	J-190(1)	1830.60	1830.73	− 0.13	0.0422	− 0.09
5	J-221	1887.90	1891.38	− 3.48	0.023	− 3.46
6	J-263	1893.24	1892.23	1.01	0.13	1.14
7	J-276	1821.00	1821.79	− 0.79	0.054	− 0.74
8	J-292	1835.40	1835.07	0.34	0.065	0.40

Table 17.2 Simulated and observed pressures at the sample node

Junction (ID)	Time	*a* Simulated pressure at supply main (m H_2O)	*b* Measured pressure at customer tap	*c* Head loss between two locations (m)	*d* Observed pressure at supply main (m) ($b + c$)	Pressure difference (m) ($a - d$)
J-13	(8:00:00 a.m.) Peak demand	50.84	56	− 3.00	53	− 2.16
J-26		39.13	40	− 2.02	37.98	1.15
J-62		10.04	20	− 2.00	18	− 7.96
J-190(1)		17.49	16	− 0.09	15.91	1.58
J-221		5.05	12	− 3.46	8.54	− 3.49
J-263		45.96	46	1.14	47.14	− 1.18
J-276		20.02	27	− 0.74	26.26	− 6.24
J-292		53.78	45	0.40	45.4	− 8.38

Using the Darwin Calibrator, the roughness coefficient of the HDPE pipe was changed to 150, and those of the DI, PVC, and GI pipes were adjusted to 110, 130, and 66, respectively. This indicates that ductile and galvanized iron pipes are old pipes because the internal roughness was increased and Hazen–Williams's value was decreased due to the corrosion effect.

As shown in Fig. 17.6, RMSE and coefficient ($R^2 = 0.98$) values were within acceptable limits. According to AWWA (2012), the linear regression relationship of pressure, which showed a typical $R^2 > 0.5$ and difference error between ± 1.5 m or ± 5 m, is considered an acceptable level of model performance.

In the validation step, the calibrated model is run under different conditions from those used for calibration, and the results are compared with the measured data. If

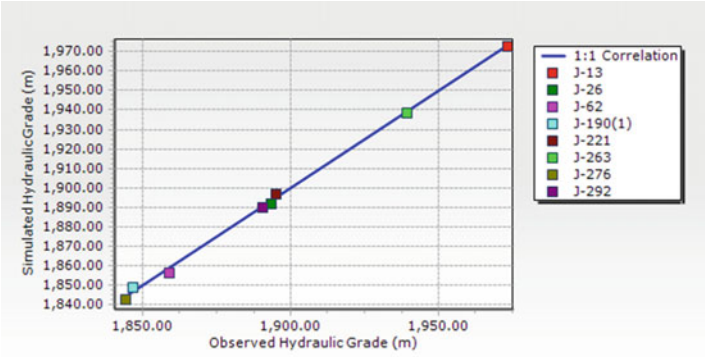

Fig. 17.6 Correlation between observed and simulated HGLs at peak demand (8:00:00 a.m.) (calibration)

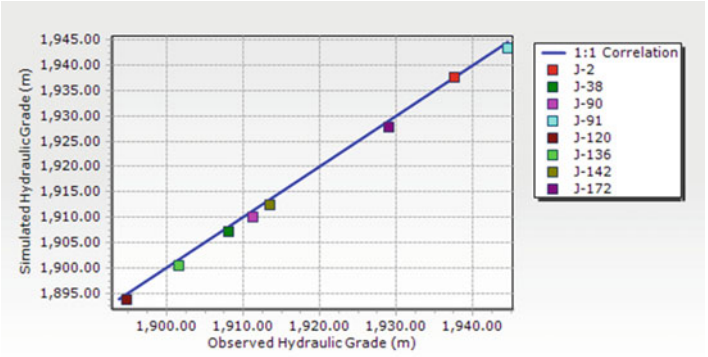

Fig. 17.7 Correlation between observed and simulated pressure parameters (validation)

the model results closely approximate the field results for an appropriate time period, the calibrated model is considered to be validated (Walski 2000). Eight samples were taken at the minimum demand scenario (at 1:00:00 p.m.) and the validation result is shown in Fig. 17.7.

As shown in Fig. 17.7, the accuracy between the simulated and measured hydraulic grades shows that the validation error is between ± 1.5 m and coefficient of determination (R^2) is 0.96 indicating that it is within acceptable limits.

Hydraulic Model Results

Hydraulic analysis was carried out to evaluate the hydraulic behaviors by considering the pressure and velocity in the existing WDS. The WDS Kombolcha town includes

Table 17.3 Pressure and velocity variation in different scenarios

No.	Percentage of the WDN corresponding to ranges of hydraulic parameters						
	Scenarios	Junction pressure (m H_2O)			Pipe velocity (m/s)		
		$P < 15$	$15 < P < 60$	$P > 60$	$V < 0.6$	$0.6 < V < 2$	$V > 2$
1	Avg. day demand (ADD)	2.4	74.6	23.1	8.2	91.3	0.5
2	Min. hourly demand (MHD)	1.5	31.1	67.4	83.5	13.5	3
3	Peak hourly demand (PHD)	23.1	64.1	12.9	43.4	46.6	10

401 pipes of different materials, 334 junctions, 6 pumps, 6 water source reservoirs, and 7 tanks, as shown in Fig. 17.2. After the model was calibrated, the current water production in the existing WDS was evaluated under consideration of the required water patterns in the study area.

The WDN of the town was classified using color coding to distinguish between pressure and velocities in the area as high, medium, or low. The result for pressure using the estimated average daily demand during peak hour consumption and minimum consumption is summarized in Table 17.3.

Pressure

The Ethiopian urban water supply guideline for the minimum and maximum operating pressure values is 15 and 60 m, respectively (MoWIE 2006).

The results showed that the pressure was low during the daytime and high during night hours when the demand was low. Figure 17.8 shows that the variation in pressure in different junctions is caused by a changing demand pattern at different hours.

i. Pressure at Minimum Hour Demand

High pressure during low demand conditions can cause leakage and a large amount of water loss through the distribution network. As per the model analysis, the maximum water pressure in the transmission main and distribution line was found downstream of the town, where the elevation in the area is low (1750–1850 msl.). As shown in Table 17.3 and Fig. 17.9, 67.4% of nodes are liable to extremely high pressure, while 31.1% of the nodes received water at an optimum pressure.

One of the main causes of high values of pressure in the system is the wide range of levels between the sources of water (service reservoirs) and the consumption nodes, as well as the absence of pressure-reducing valves. High pressure in these pipes may adversely affect the hydraulic performance of the water distribution network. Additionally, it produces high velocities, which exacerbates the deterioration and corrosion of pipes in the distribution system (Farley and Liemberger 2005).

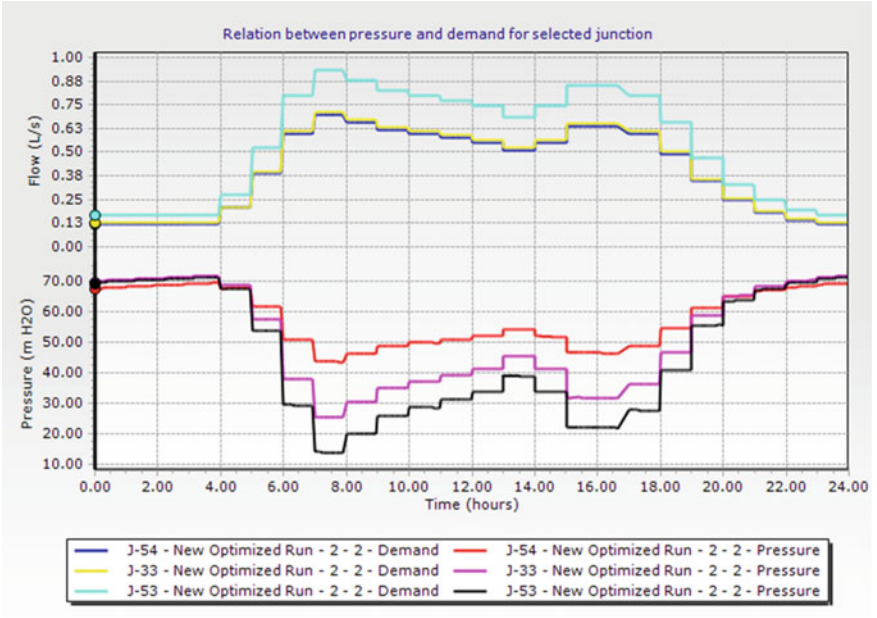

Fig. 17.8 Pressure and demand relationship for the selected junctions

ii. **Pressure at Peak Hour Demand**

As indicated in Table 17.3 during peak demand, 23.1% of nodes (located far from the source) were below the minimum acceptable pressure (15 m H_2O). About 12.9% of nodes exceeded the maximum allowable pressure of 60 m H_2, while 64.1% of nodes were within the permissible pressure range. Pressure during this peak hour is the most important for the design, improvement, and expansion of the existing system and for updating and installing new water supply distribution schemes.

Additionally, households located at higher elevations relative to the supply point and at a greater distance from the source receive water at low pressure. The effect of distance and elevation on the pressure distribution of the selected nodes is shown in Fig. 17.10 and pressure at junctions of the WDN is indicated in Fig. 17.11.

Velocity

The velocity of flow in pipes is an important indicator for evaluating the performance and efficiency of a water distribution network. The velocity ranges can also be adopted as the design criteria; low velocities do not meet the user's daily requirement, while velocities that are too high cause exceptional head loss and are not preferred.

The result of velocity and head loss of Kombolcha town is not adequate with respect to MoWIE (2006). It is summarized in Table 17.3 and Fig. 17.12a, b. The analysis shows that in systems in the minimum hour demand scenario (MHD), 83.5%

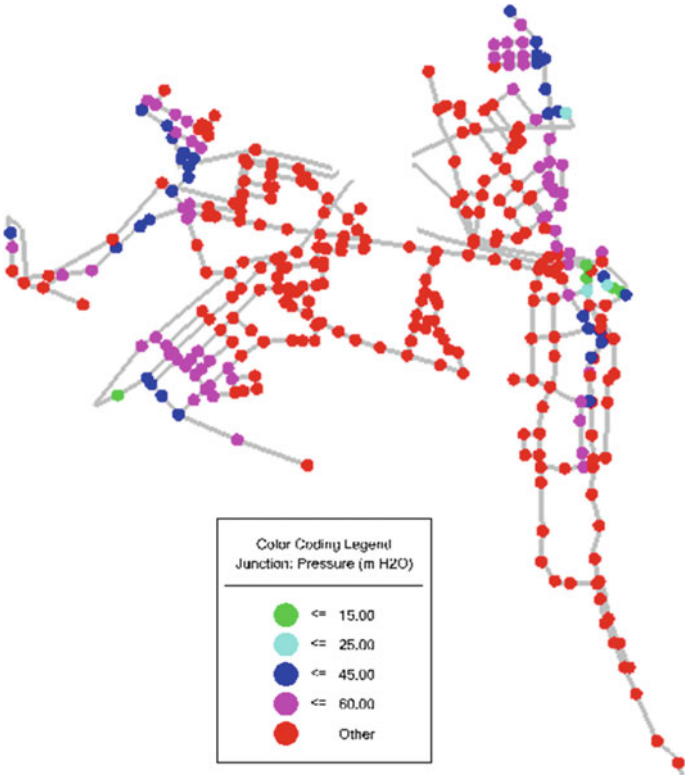

Fig. 17.9 Junction pressure map of the water distribution system at MHD

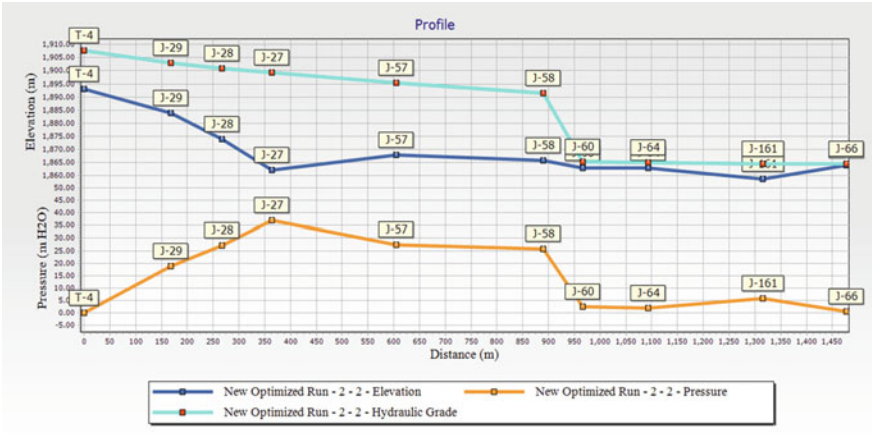

Fig. 17.10 Effects of elevation difference and distance from source (T-4) on pressure at nodes

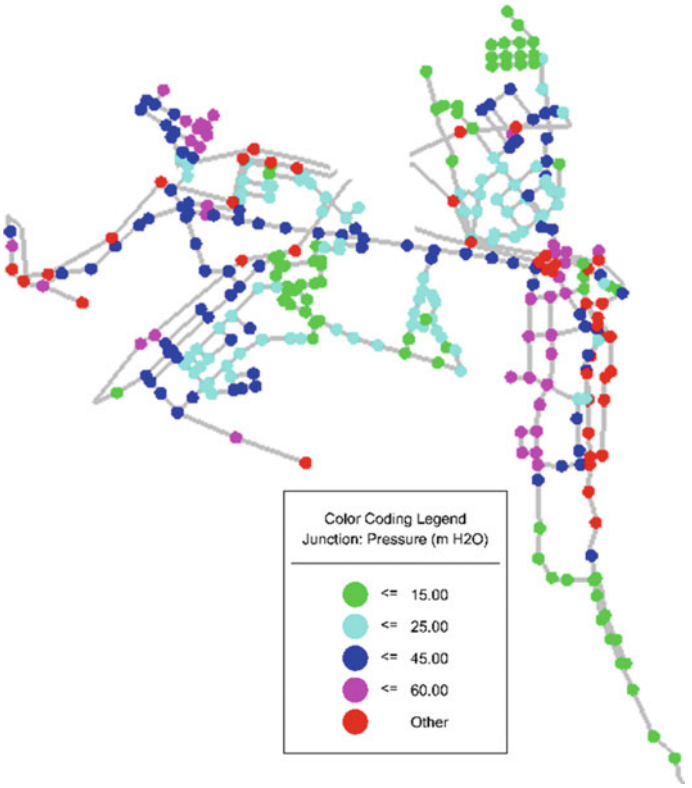

Fig. 17.11 Junction pressure of the water distribution system at the PHD

of pipes were characterized by velocities less than 0.6 m/s, and in the peak hour demand (PHD) scenario, 43.4% of pipes were in the velocity class below 0.6 m/s. The other 13.5% and 46.6% of pipes had velocities between 0.6 and 2 m/s during low and peak hour demand scenarios, respectively. These low velocities are an indication that the pipes may be oversized. Such low pressures can potentially result in deposit buildup.

Discussion

The results revealed that the designed pressure and velocity did not comply with the standard range of values in the majority of the WDNs analyzed in this study. The major problems with respect to hydraulic network modeling are undersized and oversized service pipe diameters. Low water pressure occurs in areas with high ground elevation and when there is a large distance between the water source and the end users. High pressure during low demand conditions will affect the life of pipes

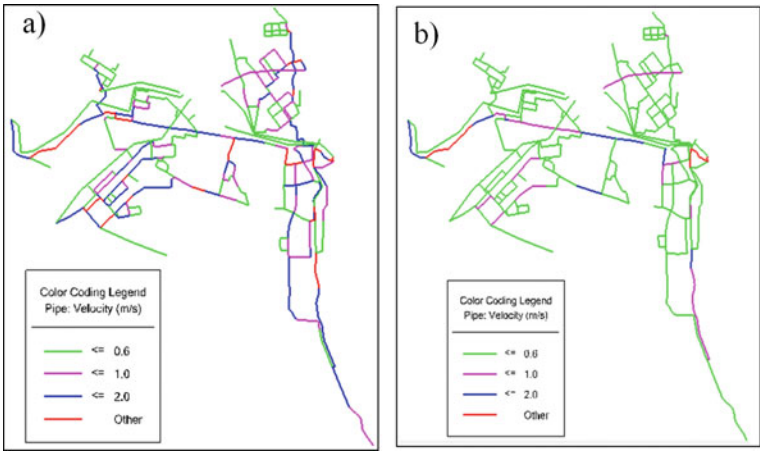

Fig. 17.12 Flow velocity **a** at PHD and **b** at MHD

and increase leakage and breakage rates while velocity can cause deposit buildup due to settling.

To improve the efficiency of a WDS, there are sets of design criteria to be considered for pressure and velocity. Some options for improvement are suggested in this study, which depend on a number of assumptions, considering future water consumption and water availability, reducing losses and maintaining velocities and pressures within acceptable limits.

a. **High-Pressure Junctions**

According to the results in Table 17.3, in the minimum demand scenario, 67.4% of junctions have pressures above the allowable limit. Therefore, the excess pressure can be reduced by installing pressure reduction valves (PRVs) at links with high pressure. This is also expected to reduce losses that cause deterioration of the pipes in the system and save the water meter of the customers from blowing up due to high pressures. The results of the model for improved systems and the location of PRVs are illustrated in Fig. 17.13.

b. **Junctions with Low Pressure and Pipes with Low Velocity**

As shown in Table 17.3, the actual velocity at the MHD and pressure at the PHD in the distribution system are less than 0.6 m/s and 15 m, respectively. This may be due to the inadequate diameter of the pipe, reduced water flow in the system, and water leakage through cracked and damaged pipes. The improvement measure for these problems is discussed in the following section.

In order to address the reduced water flow, we simulated a 51% increase in borehole yield and evaluated the hydraulic performance of the WDS while maintaining the existing pipe diameters. To fulfill the current demand of the town, the flow supplied must be greater than or equal to the flow demanded. However, for the current scenario,

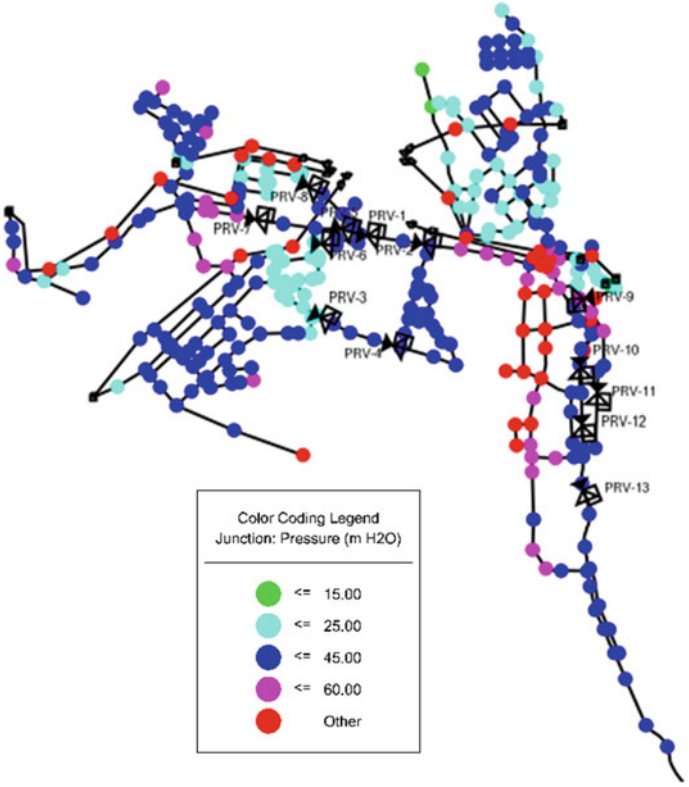

Fig. 17.13 Location of pressure-reducing valves and improved pressure values

as shown in Fig. 17.14, the current flow demand of the town is 236.18 L/s, and the flow supplied is 116 L/s. Therefore, 120.08 L/s or more is required to meet the current demand and future demand.

According to a hydrological study conducted by ADSW (Metaferia 2015), the area around Kombolcha has high ground water potential. To satisfy the current and future water demand, rehabilitation work for boreholes improves the yield capacity, and a 2000 m^3 service reservoir is required to meet the demand for users at higher elevations.

Based on the urban water supply design criteria (MoWIE 2006), one-third of the maximum daily demand is used to determine the service reservoir capacity or volume. The maximum daily demand of Kombolcha town is 14,386.8 m^3/day. Accordingly, the current required reservoir volume capacity is 4795.6 m^3. The existing 2950 m^3 reservoirs can be incorporated into the system, and an additional 2000 m^3 of new service reservoirs should be constructed to deliver adequate water in the distribution networks. This distribution reservoir (T-10) is shown in Fig. 17.15b.

When the town water demand and storage requirements are satisfied, the velocity and pressure distribution in both peak and minimum day consumptions fall within

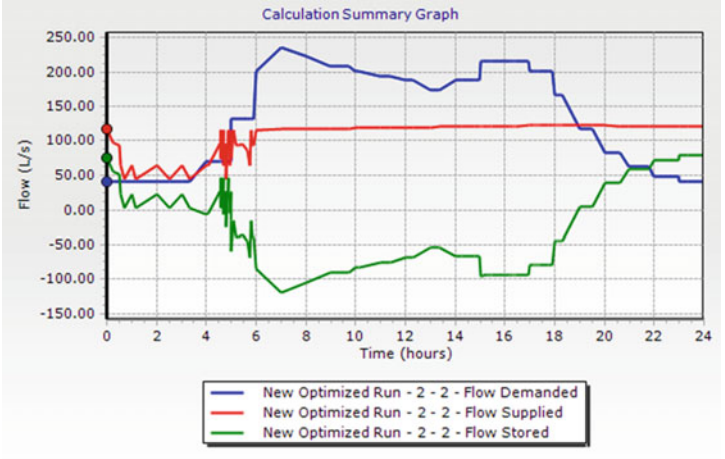

Fig. 17.14 Extended-period simulation of current flow supplied versus flow demanded

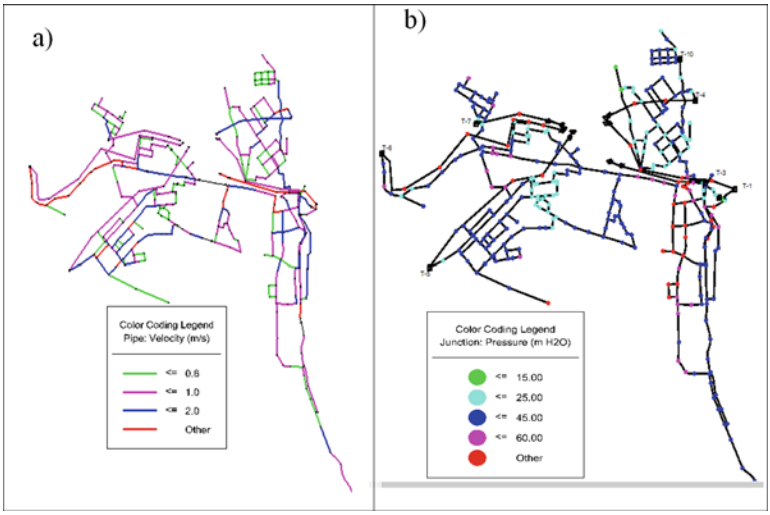

Fig. 17.15 Flow velocity (**a**) and pressure (**b**) in the current needed demand (PHD)

allowable velocity ranges. The improved velocity and pressure distribution in the model are illustrated in Fig. 17.15a, b, respectively. Figure 17.15b also contains the position of the new service reservoir.

c. Zoning and District Metering

Zoning is used to better control high water loss in the distribution system. It is used to divide the distribution network into a number of zones or District Metered Areas (DMAs), each with a defined and permanent boundary. This allows regular

monitoring of night flows into each district and allows for bursts and leakage to be easily identified and located. DMA is essential to ensure a minimum amount of NRW and to minimize the loss of precious water through system leakage.

As shown in Fig. 17.16 and Table 17.4, the boundaries of the three pressure zones proposed for the Kombolcha city water distribution system are delineated, in which WaterGEMS was particularly skillful. The network analysis identified and confirmed the preferred locations for reservoirs and pumping stations.

Fig. 17.16 Pressure zone boundaries for Kombolcha town

Table 17.4 Pressure zone results

Pressure zone	Nodes	Isolation elements	Pipes	Boundary pipes	Customer meters	Length (m)	Fluid volume (L)	Color
Pressure zone-1	174	4	201	0	0	39,255	548,683.0	Red
Pressure zone-2	100	4	112	0	0	25,487	484,906.8	Blue
Pressure zone-3	67	2	84	0	0	15,027	104,923.2	Green

Conclusion and Recommendations

In this study, the existing WDN is simulated through the construction of a model using Bentley WaterGEMS Connect edition. The system was evaluated for the existing design and operation of the water distribution network.

The results from the simulation of the existing network showed that the system failed to satisfy the desirable pressure and velocity during peak and minimum consumption hours. Due to this, it is expected that the distribution system is exposed to risks of leakage due to pipe breaks as a result of high pressures, consequently leading to the loss of a large volume of water. Generally, the model results show the existence of both design and operational problems.

Some options for improvement were suggested and modeled. The results based on these suggested modifications demonstrate how particular adjustments (such as using pressure-reducing valves and including additional service reservoirs) to the WDN were able to address issues such as low and high pressure at the junction, unmet consumer demands and low velocity in pipes. The study revealed that the system's daily water production is insufficient to meet the high water demand, necessitating regular rehabilitation of existing wells to enhance their yield. Effective leakage management requires proper pressure control, and installing pressure-reducing valves (PRVs) at low elevation points in the WDN is recommended to reduce pressure and mitigate leaks. To improve WDN management and accurately estimate water loss, dividing the network into subsystems and District Metered Areas (DMAs) is crucial, along with rehabilitating the aging pipe network to minimize water loss.

References

Abebe H (2020) Hydraulic performance of water supply distribution system in case of Aiytyef subsystem (Dessie, Ethiopia). Bahir Dar University. http://hdl.handle.net/123456789/11680

Agunwamba JC (2018) Performance evaluation of a municipal water distribution system using WaterCAD and EPANET. J Water Sanit Hyg Dev 1–9. https://doi.org/10.2166/washdev.2018.262

Alexandra D, Renwick V, Nepf HM (2009) The effects of an intermittent piped water network and storage practices on household water quality in Tamale, Ghana. Departmental Committee for Graduate Students. https://dspace.mit.edu/handle/1721.1/82721

Awe OM, Okolie STA, Fayomi OSI (2019) Review of water distribution systems modelling and performance analysis softwares. J Phys Conf Ser 1378(2). https://doi.org/10.1088/1742-6596/1378/2/022067

AWWA (2012) Hydraulic calibration manual, M32

Bentley Institute (2018) Bentley WaterCAD/GEMS, water distribution design and modeling manual

Berhane TG (2020) Optimization of water distribution system using WaterGEMS: 2013, pp 1–14. https://doi.org/10.7176/CER/12-6-01

Bhadbhade M (2009) Performance evaluation of a drinking water distribution system using hydraulic simulation software for the City of Oilton, Oklahoma. In: Aspectos Generales de la Planificación Tributaria en Venezuela, vol 2009, issue 75

Bhoyar RD, Mane SJ (2017) Modelling and optimization of water distribution system site: Nagpur, pp 210–221

Brhane T (2019) Modeling of urban water supply and water loss in distribution system of Adwa town using hydraulic simulation, Ethiopia. Civ Environ Res 11(7):1–8. https://doi.org/10.7176/cer/11-7-01

Chaki T (2017) Efficient hydraulic modelling of water distribution system for a selected district metered area of Dhaka city

CSA (2013) Federal demographic republic of population projection of Ethiopia from 2014–2017, Aug 2013, pp 1–118

Farley M, Liemberger R (2005) Developing a non-revenue water reduction strategy: planning and implementing the strategy. Water Sci Technol Water Supply 5(1):41–50. https://doi.org/10.2166/ws.2005.0006

Farley M, Wyeth G, Ghazali ZB, Istandar A, Singh S (2010) The manager's non-revenue water handbook: a guide to understanding water losses. United States Agency for International Development (USAID), pp 1–110

Grady CA, Weng S-C, Blatchley ER (2014) Global potable water: current status, critical problems, and future perspectives. In: Potable water. Springer, pp 37–59

Haider H, Sadiq R, Tesfamariam S (2014) Performance indicators for small- and medium-sized water supply systems: a review. Environ Rev 22(1):1–40

Massoud T, Zia A (2018) Dynamic management of water distribution networks based on hydraulic performance analysis of the system, Sept 2018, pp 95–102

Mehta DJ, Yadav V, Waikhom SI, Prajapati K (2017) Design of optimal water distribution systems using WaterGEMS: a case study of Surat city, p 1

Metaferia C (2011) Urban water supply sanitation and hygiene program final feasibilitiy and preliminary design of Kombolcha town. Kombolcha

Metaferia C (2015) Urban water supply sanitation and hygiene program final feasibilitiy and preliminary design of Kombolcha town. Kombolcha

MoWIE (2006) Urban water supply design criteria

Rai R, Dohare D (2019) Application of waterGEMS in hydarulic modelling and designing of water distribution network for Simhastha. Glob J Eng Sci Res 6:400–405

Senthil P, Yaashikaa P (2019) Introduction—water. In: Muthu SS (ed) Water in textiles and fashion. Woodhead Publishing, pp 1–20. https://doi.org/10.1016/B978-0-08-102633-5.00001-4

Shao Y, Yao T, Gong J, Liu J, Zhang T, Yu T (2019) Impact of main pipe flow velocity on leakage and intrusion flow: an experimental study. https://doi.org/10.3390/w11010118

Sivakumar PR, Prasad RK (2012) Analysis of water distribution network using EPANET and vertex analysis of water distribution network

USAID (2010) The manager's non-revenue water handbook for Africa (issue March)

Vaidya Deepali R, Sandip TM (2019) Pressure driven approach in water distribution network analysis: a review. Int J Anal Modal Anal XI(877)

Walski TM (2000) Advanced water distribution modeling and management: first edition, vol 114, issue 3

Walski T (2017) Procedure for hydraulic model calibration. J AWWA 55–61

Chapter 18
Assessment of Rooftop Rainwater Harvesting as an Alternative Source of Water Supply for Higher Institutes in Ethiopia: The Case of Wachemo University, Main Campus

Tamirat Abreham, Tamru Tesseme, and Eyobel Mulugeta

Abstract Rooftop rainwater harvesting has been used worldwide as an alternative source of water supply for many people. In view of this, the aim of the study is to assess the potential of rooftop rainwater harvesting as an alternative source of water supply for Wachemo University. Twenty years of rainfall data were analyzed to determine the average monthly and annual rainfall potential of the study area. The possible volume of water that could be harvested from selected rooftops at Wachemo University was quantified using the rational method. The Ripple Mass Curve method was also applied to determine the harvestable rooftop rainwater storage capacity for the study area. The water sampling points and building digitization were made using Google Earth and ArcGIS 10.3 tools. The quality of the rooftop rainwater was examined as per the standard method for the examination of water and wastewater quality. The results demonstrated that the maximum amount of water that could be harvested was 102,268 m^3 per year from a 107,587 m^2 rooftop area with an average annual rainfall of 1188.0 mm. The harvested rainfall from the rooftops could cover approximately 51% of the average annual water demand of the university. The Ripple Mass Curve analysis indicated that storage capacity of 8493.7 m^3 was required to harvest rooftop water in the study area. The water quality of the rooftop examination was found to be within the permissible limit for drinking water quality requirements, except for the bacteriological parameters. The cost analysis demonstrated that a total of 6,937,200 ETB (128,466 USD) was required to install rainwater harvesting systems for 94 buildings inside Wachemo University main campus. The study concluded that

T. Abreham (✉)
College of Engineering and Technology, Wachemo University Main Campus, Hosaina, Ethiopia
e-mail: tamirat.abreham@aau.edu.et

T. Tesseme
Arba Minch Water Technology Institute, Arba Minch University, Arba Minch, Ethiopia
e-mail: tamru.tesseme@amu.edu.et

E. Mulugeta
Emerging Technology Center, Ethiopian Biotechnology Institute, Addis Ababa, Ethiopia

A. M. Melesse et al. (eds.), *Land and Water Degradation in Ethiopia*, Springer Geography, https://doi.org/10.1007/978-3-031-60251-1_18

rooftop rainwater harvesting is a promising alternative solution to solve the water scarcity problem and ensure a continual source of non-potable water at Wachemo University.

Keywords Rooftops · ArcGIS · Water quantity and quality · Water management · Wachemo University

Introduction

Rainwater harvesting (RWH) has been used in numerous places across the world where traditional water delivery systems are incapable of meeting water demands (Lizárraga-Mendiola et al. 2015; Angrill et al. 2017). Rainwater harvesting methods are gaining popularity among municipal water managers as a way to potentially reduce potable and non-potable water usage (Lizárraga-Mendiola et al. 2015; Sanches et al. 2015; Angrill et al. 2017; Al-Houri et al. 2020). Rainwater harvesting is advocated as an efficient technique to minimize potable water usage, enabling communities to conserve their water resources, lower their water bills and operational expenses (Palla et al. 2012).

Rainwater harvesting is now widely employed as an alternate supply source for potable and non-potable applications in Ethiopia as well as in other countries such as Australia and South Africa (Andualem et al. 2019). New trends are emerging in residential areas, particularly those experiencing water scarcity, where rainwater collection is being supported through ambitious rules and incentives (Adugna et al. 2018). The amount of water removed from water sources can be lowered by using rainwater harvested from urban catchments for a range of non-potable water applications, with significant environmental, economic, and even social advantages (Rostad and Montalto 2012).

The most popular form of RWH system is rooftop runoff harvesting, which only requires a collection area, a conveyance system, a storage tank, and minimal treatment (Imteaz et al. 2013). Rainwater can replace a considerable portion of the water used in buildings (Adugna et al. 2018). However, the majority of existing buildings and other facilities, as well as new development plans, do not focus on the inclusion of rooftop rainwater collection systems in places where water delivery systems are operational. This is owing to budget constraints and lack of understanding of the potential of rooftop rainwater harvesting.

The city of Hosaena in Ethiopia, where Wachemo University is located, is one such place where water scarcity is becoming a major issue demanding more attention and action. The principal water supply issues are connected to the Hosaena Water Supply System Service (HWSSS), which has inadequate water supply capacity, no alternate water sources, insufficient budget, and limited forecasting capacity. The fast population expansion and consequent frequent interruptions in water supply make providing services in Hosaena town, notably at Wachemo University, problematic

(Ochocho 2019). These issues press water managers to promptly seek alternative options for reducing the population's water stress.

Water scarcity at Wachemo University is linked to the university's lack of alternate water supply source other than a single borehole built for the benefit of the university and the surrounding community. The borehole, approximately 8 km from the institution, was built in 2019 and has a discharge capacity of 40 L per second (l/s) (Wachemo University Water Utility, 2020). All of the university's communities rely on this one source, which operates 15 h every day. Because of this, the university is forced to limit its service hours every day due to a lack of adequate supply of water. The university pays approximately 350,000 ETB (approximately 6500 dollars) per month for the Hosaena municipal water supply service to provide water for potable and non-potable uses (Wachemo University Water Utility 2020). Still, students and the university community are confronted with the issue of not having adequate water for both drinking and other purposes. To ensure the availability of appropriate amounts of water for the rising population, alternate water sources must be considered. Rainwater harvesting has the ability to alleviate the water scarcity that the town and surrounding institutions are now experiencing. The goal of this study is to assess the potential of rooftop rainwater harvesting as an alternative source of water supply in Ethiopian higher educational institutes such as Wachemo University.

Description of the Study Area

Wachemo University (WCU) is a third-generation higher education institution in Ethiopia, founded in 2009. The location of the study area is illustrated in Fig. 18.1. It is approximately 231 km from Addis Ababa, the country's capital, and situated on 200 ha of land in the zone town of Hosaena.

Water Resource Demand and Variation in Rate of Consumption in the Community

Water demand for domestic use in urban areas depends on many factors, such as living standards, availability and suitability of supply sources, water quality, number of people, and end use of water. According to Ministry of Water Resources, Universal Access Program an average of minimum 25 L per capita per day (l/c/d) domestic water supply is considered the basic level of service (Abduro and Sreenivasu 2020). Thirty liters per capita per day was taken as an average for this case.

Only a limited amount (162 m^3/day) is discharged from Hosaena water supply services to elevated tanks and then to the community through pipelines (Wachemo University water utility 2020). This is only 29.5% of the average domestic demand of the community. A combination of other sources of water for different purposes is

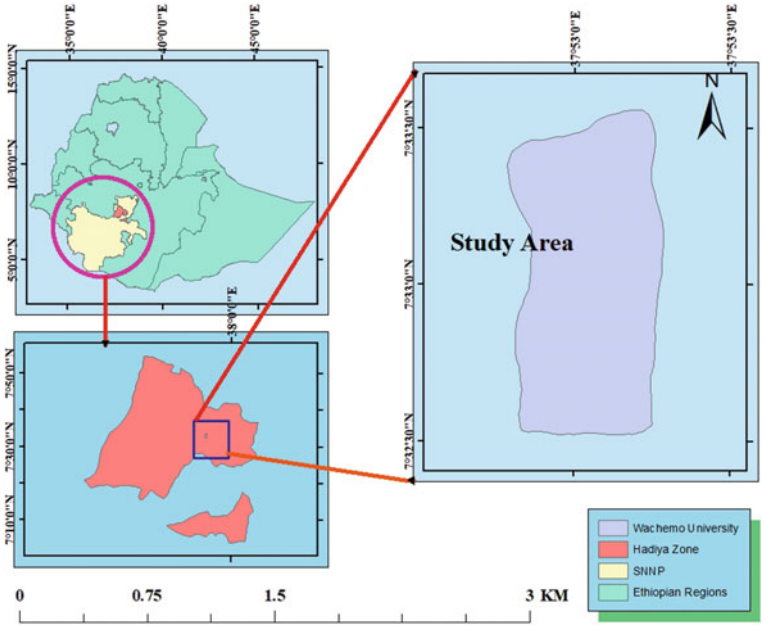

Fig. 18.1 Map of study area

used in the community because water supply is not continuous and reliable. Because of unreliable water supply, academic staff usually do not avail themselves regularly on all workdays (Wachemo University water utility 2020). The weekly water demand of the university is presented in Table 18.1.

Table 18.1 Estimated water demand in liters per week for potable and non-potable purposes in the community

S. no.	Population category	Population	Number of demand days	Demand in liter	Total demand in a week in liter
1	Regular students	15,600	7	30	3,276,000
2	Extension	2800	2	>>	168,000
3	Instructors	350	5	>>	52,500
4	Admin staffs	650	4	>>	78,000
5	Others	1500	6	>>	270,000
	Total	**20,900**		**3,844,500**	

Rain Gage Stations and Rainfall Data

The monthly and yearly average rainfall data from 2000 to 2019 were taken from four-gauge stations in the Southern Nation Nationalities and People (SNNP) meteorological stations, which are reasonably close to Wachemo University. Figure 18.2 depicts the gauge stations in the study area. The first gauge station is located in Hosanna 3 km to the south, Durame is the second gauge station located 36.9 km to the southeast, the third gauge station is located at Shone 42 km to the east, and the Fonko gauge is the fourth station, which is located 18 km to the north of Wachemo University. Details are described in detail in Table 18.2

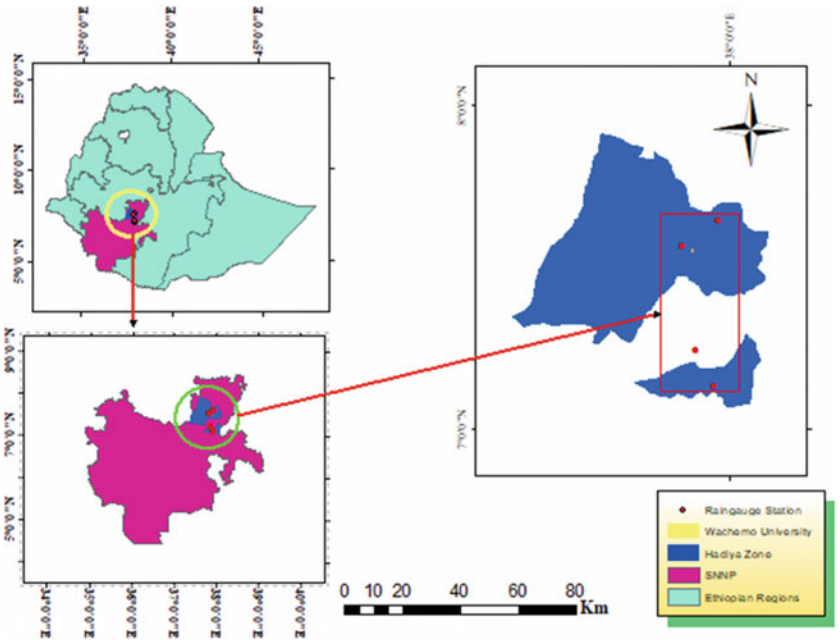

Fig. 18.2 Gauge station locations

Table 18.2 Rain gauge stations and their location details

Station name	Longitude	Latitude	Altitude
Hosaena	037° 51′ 22.1″ E	07° 34′ 04.1″ N	2306
Durame	037° 53′ 49.4″ E	07° 14′ 36.1″ N	2116
Shone	037° 57′ 16.1″ E	07° 08′ 01.4″ N	1959
Fonko	037° 58′ 08.9″ E	07° 38′ 54.0″ N	2246

Estimation of Missing Data

The quality and completeness of the data influence the results of data analysis. Among the several approaches for filling in missing rainfall data, this study used the arithmetic average method. Monthly precipitation data obtained at four different stations were used to evaluate the appropriateness of the various approaches for filling in missing data. Monthly precipitation is forecasted using complete sets.

Arithmetic Average Method

In meteorology and climatology, the arithmetic average approach is widely used to fill in missing meteorological data. Missing data can be filled in by calculating the arithmetic average of the data corresponding to the nearest gauge stations, as shown in Eq. (18.1).

$$V_0 = \sum_{i=1}^{n} V_i / N \tag{18.1}$$

where V_o is the estimated value of the missing data, V_i is the value of the same parameter at the i-th nearest weather station, and N is the number of nearest stations. The arithmetic average method is satisfactory for this study area since the gauges are uniformly distributed and their individual value does not vary greatly about the mean as stated in the studies (Canchala-Nastar et al. 2019; Ridwan et al. 2020).

From the incorporated rainfall data for the study period, the average monthly rainfall in mm was taken to evaluate the volume of rain. In addition, the main patterns of rain and drought during the studied period were identified. Intra-annual rainfall variation was obtained through the coefficient of variation of the monthly rainfall (C_{vm}) using the following Eq. (18.2):

$$C_{vm} = \frac{S_v}{V_a} \tag{18.2}$$

where C_{vm}, the coefficient of variation of the monthly rainfall; S_v, the standard deviation of the monthly rainfall in mm; and V_a, the average of the monthly rainfall in mm.

Runoff Coefficient

The runoff coefficient is the fraction of the volume of rainwater that runs off a surface to the volume of rainwater that falls on that surface. This also includes losses from spillage in the gutter system. However, for the calculation of potential harvestable rooftop rainwater the runoff coefficient is associated with the efficiency of the roof material to yield maximum runoff (Lizárraga-Mendiola et al. 2015). As

Table 18.3 Typical runoff coefficients for different types of roofing materials (Biswas and Mandal 2014)

Roof type	Runoff coefficient	Roof type	Runoff coefficient
Galvanized iron sheet	> 0.9	Brick pavement	0.5–0.6
Corrugated metal sheet	0.7–0.9	Rocky natural catchment	0.2–0.5
Tiles	0.8–0.9	Soil with slope	0.0–0.3
Concrete	0.6–0.8	Green area	0.05–0.1

the roof type in this study is corrugated metal sheet, an average runoff coefficient of 0.8 was adopted (Table 18.3).

Selected Buildings and Their Respective Rooftop Area

The roof area was calculated by summing each building roof area given by Eq. (18.3):

$$T_{\mathrm{ra}} = \sum \mathrm{ra} \tag{18.3}$$

where T_{ra}, total roof area; ra, roof area

The building rooftop area, roofing material, and corresponding runoff coefficient are presented in Table 18.4.

Digitization of Buildings

In this study, a recent satellite image (2021) that covers the areas of interest was obtained from Google Earth. The acquired satellite images were used to digitize all the buildings' rooftops. The digitizing process involves tracing building roof tops directly on top of the satellite imagery to classify the rooftops from other objects (Fig. 18.3). A satellite image from Google Earth was digitized in ArcGIS 10.3 to determine the locations of the buildings. This process resulted in digitized maps with thousands of boundaries that have been saved as several KMZ files, each representing the building roof tops, streets, tank locations, and water sample points. The KMZ files for each building are converted to shape files. The coordinate system for each

Table 18.4 Roof catchment areas of the buildings with their respective runoff coefficients

Harvesting area	No. of buildings	Total area in square meter	Roofing material	Runoff coefficient
Building's rooftop	172	107,587	Metal sheet	0.8

Source Wachemo University construction office and own field measurements

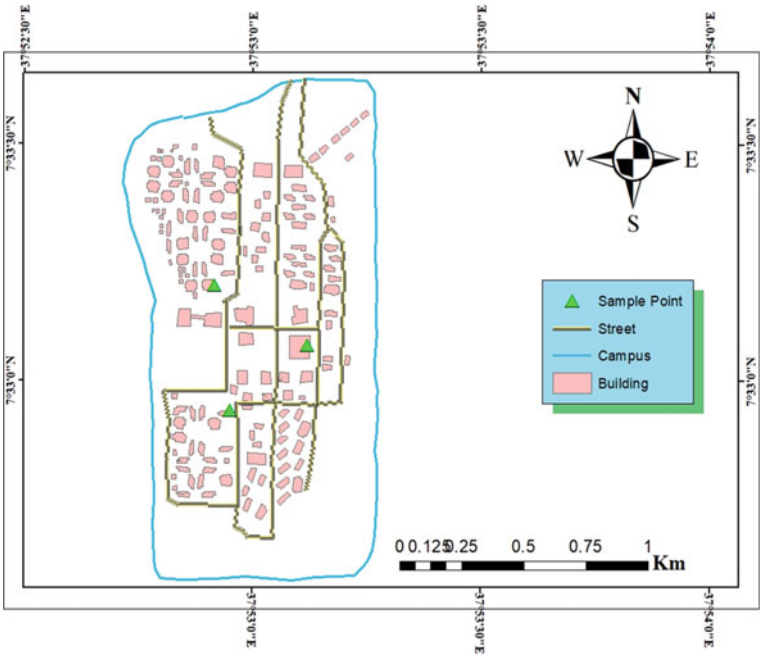

Fig. 18.3 Buildings, streets, and sample points at Wachemo University, digitized from satellite imagery

shape file was defined as WGS 1984 UTM zone 37 N to be able to compute the areas of the digitized buildings automatically by the geometry calculation tool available in the ArcGIS. Figure 18.3 shows the final digitized maps for the university.

The sum of the areas of all digitized polygons for the structures was discovered to be 141,561 square meters. The correlation factor was calculated to be 0.76 based on the ratio of real to digitized area. Similar research (Awawdeh et al. 2012) reported a correction factor over one for a small region achieved via digitalization. Although the polygon tool in ArcGIS may be used to create areas for each structure, this is not as exact as a construction office document and the accuracy is dependent on identification and tracking precision of the structures.

Quantity of Rooftop Rainwater

The quantity of rooftop rainwater obtained sequentially from the selected historical records is presented on a monthly and annual basis.

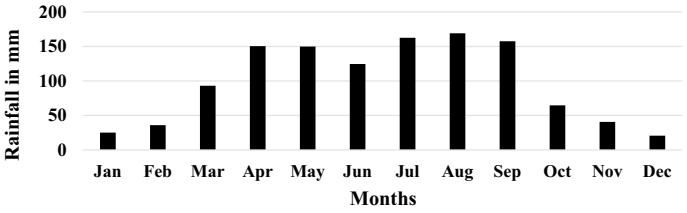

Fig. 18.4 Monthly average rainfall distribution of the study area, 2000–2019

Monthly Rainfall Potential

April, May, July, August, and September presented the highest precipitation across the two decades studied (See Fig. 18.4). The driest months of the year were January, February, and December. The institution receives an average of 99.5 mm of precipitation each month. This corresponds to the university location's climate with 1162.6–1204.9 mm of rain per year. The average monthly rainfall ranges between 20.3 mm (December) and 168.5 mm (August).

Seasonal Rainfall Potential

In terms of total rainfall variance across years, a coefficient of variation between 13 and 24% indicates a consistent rainfall pattern. Because of their climatic conditions and rainfall intensity, these high rainfall levels make rainwater a viable source at Wachemo University.

The majority of the rainfall occurs during the main rainy season between June and August, as illustrated by the graph in Fig. 18.5. The figure shows that there is a significant seasonal fluctuation in the rainfall pattern, which impacts the quantity of total rainwater that may be gathered in relation to the roof area of the structures. The annual rainfall status in the study area including the maximum rainfall amount, minimum rainfall amount, average rainfall amount, standard deviation, and coefficient of variation in the interval of 2000–2019 is shown in Fig. 18.6.

The overall monthly average rainfall became 99.01 mm, while the average annual total rainfall was 1188.0 mm. These results indicate there is considerable rainfall in the study area, providing for high roof runoff as described by (Lupia et al. 2017).

Potential of Rainwater Harvesting

The potential of monthly rainwater harvesting from the building's rooftops was calculated using the rational method given by the equation:

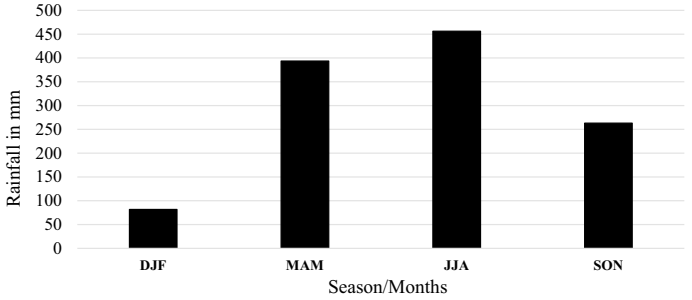

Fig. 18.5 Seasonal average rainfall distribution of the study area, 2000–2019

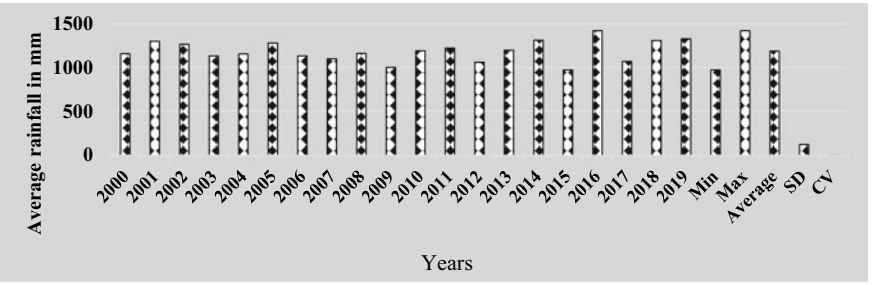

Fig. 18.6 Annual maximum rainfall, minimum rainfall, average rainfall, standard deviation, and coefficient of variation

$$\mathrm{VR} = \frac{\mathrm{R{*}Bra{*}Rc}}{1000} \tag{18.4}$$

where VR is the monthly volume of rainwater that can be harvested (m^3); *R* is the monthly rainfall depth (mm); Bra is the building roof area (m^2); and Rc is the runoff coefficient (without units) = 0.80. For the design of systems for rainwater collection and storage, the United Nations Environment Programme (UNEP) recommends considering the "first flush" by deducting the first 0.50 mm of rainfall to improve the quality of harvested rainwater (Lizárraga-Mendiola et al. 2015). Therefore, the potential water saving percentage was calculated by dividing the potential volume of harvested rainfall by the annual average water demand (potable and non-potable) by the equation:

$$\mathrm{WS} = 100\ \mathrm{V}/\mathrm{AAWD} \tag{18.5}$$

where WS is the annual rainwater potential for water savings (%), *V* is the annual volume of rainwater that could be harvested in (m^3/y), and AAWD is the average annual water demand.

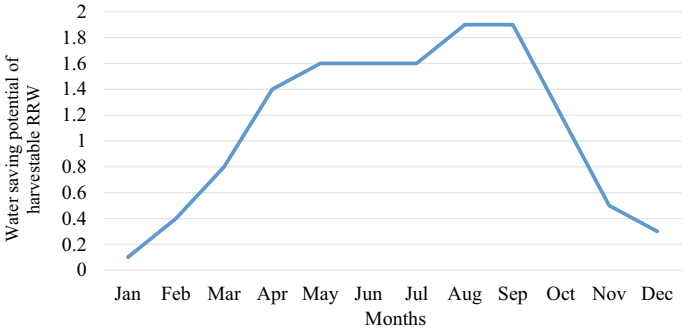

Fig. 18.7 Potential savings results based on monthly demand

Potential harvestable rooftop rainwater is evaluated based on the study area rainfall amount, total rooftop areas of the selected buildings (N), and the runoff coefficient value, which is 0.8. Therefore, the total volume of rainwater using Eq. (18.4) was 102,268 m^3/year.

By estimating the average annual rainfall, it was possible to determine that harvestable volume was sufficient to meet a large amount of water demand in general and non-potable consumption in particular throughout the year depending on the building roof area. The potential of rooftop rainwater to meet the community demand resulted in approximately 51% of the total demand of the community when evaluated on a yearly basis. If all of the rainwater harvested was to be harvested, it is possible to have a significant amount of water to supplement the current water supply. According to Biswas and Mandal (2014), rainwater harvested from rooftops in Bangladesh was able to meet approximately 90% of the demand, with the remainder supplied from an onsite bore. This large amount from previous study in Bangladesh was achieved with a large rooftop catchment area, high rainfall intensity, and low respective demand when compared with this study (Fig. 18.7).

As shown, greater water saving potential appeared in August and September on a monthly basis, while the minimum value of saving occurred in January. This is due to weather conditions of the study area and demand fluctuation across months depending on rainfall availability (Angrill et al. 2017).

Storage Capacity for Rainwater Storage Tank

The estimated average monthly non-potable water demand (60% of total demand) for the university is equivalent to 9226.8 m^3/month (Wachemo University water utility 2020). After calculating the harvestable rainwater potential on a monthly basis, storage tank capacity requirement was calculated using the mass curve method (Table 18.5).

Table 18.5 Storage tank capacity determination on a monthly basis using the mass curve method considering non-potable water consumption

Month	Rainfall (mm)	Rainfall that can be harvested (m^3)	Water demand (m^3)	Cum. harvestable rainfall (m^3)	Cum. water demand (m^3)	Difference CH–CD (m^3)
Jan	24.6	2117.3	9226.8	2117.3	9226.8	−7109.5
Feb	35.4	3046.9	9226.8	5164.2	18,453.6	−13,289
Mar	92.5	7961.4	9226.8	13,125.6	27,680.4	−14,555
Apr	150	12,910.4	9226.8	26,036	36,907.2	−10,871
May	149.4	12,858.8	9226.8	38,894.8	46,134	−7239.2
Jun	124	10,672.6	9226.8	49,567.4	55,360.8	−5793.4
Jul	162.1	13,951.9	9226.8	63,519.3	64,587.6	−1068.3
Aug	168.5	14,502.7	9226.8	78,022	73,814.4	4207.6
Sep	157	13,512.9	9226.8	91,534.9	83,041.2	**8493.7**
Oct	64.2	5525.7	9226.8	97,060.6	92,268	4792.6
Nov	40.2	3460	9226.8	100,520.6	101,494.8	−974.2
Dec	20.3	1747.2	9226.8	102,267.8	110,721.6	−8453.8

N.B:

- In January, Column 4 = Column 2;
- In February, Column 4 = Column 2 in February plus Column 4 in January
- In March, Column 4 = Column 2 in March plus Column 4 in February…, and finally, in Dec, Column 4 = Column 2 in Dec plus Column 4 in November based on Mass curve Method, and the maximum value was taken from the difference of column 4 and 5 as a storage capacity of the tank. From Table 18.5, we can see that the month of September determines the storage capacity as it has the largest difference between cumulative harvestable rain water and demand (Fig. 18.8).

The maximum interval of storage capacity exists in relation to water demand on a monthly basis, which is 8493.7 m^3. The months of August, September, and October have the potential to compensate and satisfy part of the non-potable demands such as toilet flushing, cleaning, and washing floors in those months.

Rainwater Quality Test Methods

Water quality is controlled by a collection of upper and lower limits on selected possible contaminants in water. This is evaluated by using water quality indicators, which can be physical, chemical, and biological. In each class, a number of quality variables are considered. The magnitude of these indicators can affect the

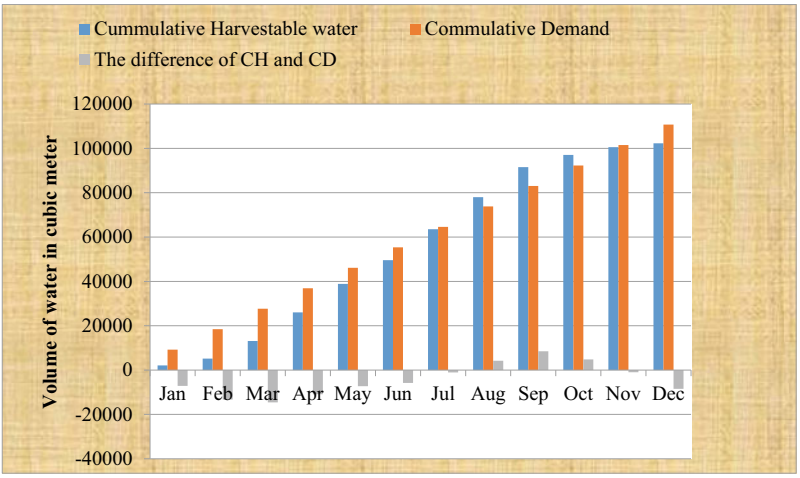

Fig. 18.8 Mass curves for calculation of required storage

acceptability of water quality for its intended use and is often governed by regulations. Acceptable quality shows the safety of drinking water in terms of its physical, chemical, and bacteriological parameters (RS2 2012).

The total number of buildings in the university was 172. For rainwater quality analysis from roof tops, 5% of the total buildings were taken as representative samples, i.e., 8 buildings. With the basic assumption that water quality varies minimally across small distance for the same roofing material (ESA 2013), samples were taken from three sampling points both from gutters and downpipe ends expecting different quality in both cases, i.e., two samples from one sampling point (from gutter and down pipe end). From each point, three water samples (total of nine samples) were taken from different roofs after the first flush diversion. Samples were taken from the gutter and pipe ends using buckets. All water samples from their source were collected using polyethylene sampling bottles, washed with distilled water to avoid contamination, and labeled to identify the sample sites.

Rainwater quality analysis was carried out in the Hosaena Town Water Supply Service (HTWSS) laboratory for the time period from April 15, 2021, to April 28, 2021. Physicochemical and microbiological parameters were performed by evaluating the test value with respect to the drinking water standard value of Ethiopia (ESA 2013) and international guidelines (RS2 2012). Color development with intensity proportional to the amount of the using YSI 9300 and 9500 Photometers, tests were performed for physicochemical parameters. A powder reagent chemical was dissolved in 10 mL of water sample in a cylindrical sample target element was measured. Each element has a unique maximum absorption wavelength at which the spectrophotometer was adjusted. Light was allowed to pass through the sample cell so that light was absorbed at the required wavelength. The results were displayed

on the LCD screen in mg/L in proportion to the amount of light absorbed at that particular wavelength.

The bacteriological quality of rainwater runoff tests was undertaken within 6 h after collection to avoid the growth or death of microorganisms in the sample (RS2 2012). Water samples were collected in presterilized plastic bags and filtered on the spot using membrane filters with a spore size of 45 μm. The filters were incubated in an ELE PAquaLab 25 field incubator in sterilized aluminum Petri dishes with a bacterial medium of m-Coli Blue24 on an absorbent pad at 37 and 40 °C for total coli forms and E. coli/fecal coli forms, respectively. The filters were examined for 24 h to assess bacterial growth, and yellow or yellow–brown colonies were counted as total coliform (TC). The results were compared with the WHO guidelines maximum permissible limit value.

Rooftop Rainwater Quality Analysis

Regarding physicochemical rooftop rainwater quality from the results in Table 18.6, rooftop rainwater can provide a relatively high-quality water source, while the bacteriological quality of rooftop rainwater usually exceeds bacteriological quality standards. The results show that there are high coliform bacteria beyond the allowable limit, indicating fecal contamination possibly due to pollution arising from the excreta of animals (birds, rodents, etc.). The study (Ahmed et al. 2011) reported that the presence of coliforms was expected because, in addition to feces, they might originate from outdoor vegetation. Other studies have also noted the poor microbiological quality of urban rooftop runoff because of high levels of bacterial contamination (Angrill et al. 2017). Therefore, this rooftop rainwater cannot be used for drinking purposes. Hence, efforts should emphasize the installation of a water treatment method that removes pathogens from rainwater, adapted to the required end use of rainwater.

Cost Calculation for Collection System Installation per Building

Construction of concrete rainwater tank storage is not feasible and cost-effective for large-scale rainwater harvesting (Farreny et al. 2011). Therefore, using locally available installation materials and plastic rainwater tanks may contribute much more to alleviating water scarcity in the study area (Table 18.7).

The cost to be invested in a installing the collection system for a single building is calculated to be **73,800** Ethiopian Birr, which includes the cost of labor, polyethylene tank, pipes, fittings, and cement base. Gutter pipes to drain rainwater from the roof into the ditches beside the buildings are already available in the buildings. If all 94

Table 18.6 Rooftop rainwater quality results for the intended parameters corresponding to the (RS2 2012) and Ethiopian standards (ESA 2013)

S. no.	Parameters	Rooftops sample (average)	(RS2 2012) Maximum value	Ethiopian standard (maximum value)
1	Temperature (°C	15.75	< 15	–
2	pH	6.7	6.5–8	6.5–8.5
3	Electrical conductivity (ECμs/cm)	15.45	800	800
4	Total dissolved solids(TDS mg/L)	8.74	< 600	1000
5	Nitrates (mg/L)	0.13	50	50
6	Sulfates (mg/L)	5	250	250
7	Turbidity (NTU)	5	5	5
8	Zinc (mg/L)	0.15	3	3
9	Total coliform Tc (CFU/mL)	46	0	0
10	Fecal coliform colony Forming unit per 100 ml (FC, CFU/100 mL)	13	0	0

similar buildings in the main campus of Wachemo University were to be equipped with this system, then the cost of installation would be **73,800** × 94 = 6,937,200 birr (128,466 USD).

The university pays approximately 350,000 ETB per month for the Hosaena municipal water supply service to provide water for potable and non-potable uses which covers only 32% of total demand. Even though the current cost for materials and labor is much higher than previous time (Awawdeh et al. 2012), the evaluated the cost of installation is much less than the cost of being paid for Hosaena town water supply service since the installations will be done once. Most importantly, this cost-effective system might save a considerable amount of money that can be invested in improving the water supply capacity on the main campus of Wachemo University.

Table 18.7 Cost of fixing such a rainwater harvesting system in a single building

Installation materials	Amount	Unit	Unit cost	Total cost (Et. Birr	Installation materials	Amount	Unit	Unit cost	Total cost (Et. Birr
Broom	1	Piece	90	90	T-valve with flush facility	1	–	470	470
Connector and fixture	1	-	400	400	Metal tap to fit in the storage tank	1	–	130	130
Sealer	1	-	190	190	Plastic bucket with jug	1	L	200	200
Metal filter piece (Mesh net)	1		350	350	PVC pipes of 5 inches 10 m	1	inch	1500	1500
Metal lock	2	-	125	300	Polyethylene plastic storage tank (20,000 L)	1	L	68,500	68,500
Sand 110 birr for 25 kg bag—for 3 bags 3 × 110 = 330 Birr	3 bag	kg	110	330	Bricks 15 cm size each	50	cm	11	550
					Cement	15	kg	10	150

Labor cost
a/Fee of labor to clean the roof before first flush = 300 Birr
b/Wages to masonry preparation and a helper = 250 + 200 = 450
c/Cost of labor for installation of the system = 270 Birr
Total sum 73,800

Conclusion

The potential rooftop rainwater harvesting has been assessed with respect to quantity and quality as an alternative supply source for Wachemo University using the current existing building roof area and 20 years of recorded monthly rainfall from the SNNPR meteorological center. The study showed great rain water potential on average recorded in September.

The maximum potential of rainwater harvesting with an annual average rainfall amount of 1188 mm and a rooftop area of 107,587 m^2 was found to be 102,268 m^3/y, which can be harvested from roofs provided that all rain falling on the roofs is collected. This is equivalent to 51% of the average water demand of the university community, and greater water saving potential appeared in August and September on a monthly basis, while the minimum value of saving occurred in May. Collecting

rainwater has been shown to be an important alternative source of water in Wachemo University.

Storage capacity needed for harvesting rooftop rainwater on a monthly basis was found to be 8493.7 m^3. The months of August, September, and October have the potential to compensate and satisfy part of the non-potable demands such as toilet flushing, cleaning, and washing floors in those months.

Rooftop rainwater can provide a relatively high-quality water source, which can be directly used for non-potable uses or with filtration and disinfection for potable uses. Using locally available installation materials and plastic rainwater tanks may contribute much more to alleviating water scarcity in the study area. The total cost of a collection system installation for 94 similar buildings was calculated to be 6,937,200 Et. Birr (128,466 USD). Therefore, by harvesting rooftop rainwater, the university can make water available for sanitation and washing and can also solve conflicts in the sharing of limited supply sources**.**

References

Abduro S, Sreenivasu G (2020) Assessments of Urban water supply situation of Adama Town, Ethiopia. J Civ Eng Res 10(1):20–28. https://doi.org/10.5923/j.jce.20201001.03

Adugna D, Jensen MB, Lemma B, Gebrie GS (2018) Assessing the potential for rooftop rainwater harvesting from large Public Institutions. Int J Environ Res Public Health 15(2):336. https://doi.org/10.3390/ijerph15020336

Ahmed W, Gardner T, Toze S (2011) Microbiological quality of roof-harvested rainwater and health risks: a review. J Environ Qual 40(1):13–21. Available at: https://doi.org/10.2134/jeq2010.0345

Al-Houri Z, Abu-Hadba O, Hamdan K (2014) The potential of roof top rain water harvesting as a water resource in Jordan: featuring two application case studies. Int J Environ Ecol Eng 8:147–153. https://doi.org/10.5281/zenodo.1096279

Andualem T, Hagos Y, Teka A (2019) Assessment of rainwater harvesting potential for non-potable use: a case study in Debre Tabor University, Ethiopia 10(2)

Angrill S, Petit-Boix A, Morales-Pinzón T, Josa A, Rieradevall J, Gabarrell X (2017) Urban rainwater runoff quantity and quality—a potential endogenous resource in cities? J Environ Manage 189:0301–4797

Awawdeh M, Al-Shraideh S, Al-Qudah K, Jaradat R (2012) Rainwater harvesting assessment for a small size urban area in Jordan. Int J Water Resources Environ Eng 4(12):415–422

Biswas BK, Mandal BH (2014) Construction and evaluation of rainwater harvesting system for domestic use in a remote and rural area of Khulna, Bangladesh. Int Scholarly Res Notices, pp 1–6. Available at: https://doi.org/10.1155/2014/751952

Canchala-Nastar T et al (2019) Estimation of missing data of monthly rainfall in southwestern Colombia using artificial neural networks. Data in Brief, 26. Available at: https://doi.org/10.1016/j.dib.2019.104517

ESA (2013) Ethiopian drinking water quality specifications. Ethiopian Standards Agency, pp 1–7

Farreny R, Morales-Pinzón T, Guisasola A, Tayà C, Rieradevall J, Gabarrell X (2011) Roof selection for rainwater harvesting: quantity and quality assessments in Spain. Water Res 45(10):3245–3254. https://doi.org/10.1016/j.watres.2011.03.036. Epub 2011 Mar 29 PMID: 21492898

Imteaz MA, Ahsan A, Shanableh A (2013) Reliability analysis of rainwater tanks using daily water balance model: variations within a large city. Resources Conserv Recycling 77:37–43. Available at: https://doi.org/10.1016/j.resconrec.2013.05.006

Lizárraga-Mendiola L, Vázquez-Rodríguez G, Blanco-Piñón A, Rangel-Martínez Y, González-Sandoval M (2015) Estimating the rainwater potential per household in an urban area: case study in Central Mexico. Water 7(9):4622–4637. https://doi.org/10.3390/w7094622. Water (Switzerland) 7(9):4622–4637. Available at: https://doi.org/10.3390/w7094622

Lupia F, Baiocchi V, Lelo K, Pulighe G (2017) Exploring rooftop rainwater harvesting potential for food production in urban areas. Agriculture 7(6):46. https://doi.org/10.3390/agriculture7060046

Ochocho A (2019) Dimensions and determinants of rural urban migration in Ethiopia: the case of Hosanna Town. Ethiopian J Environ Stud 12(5):563–574. Available at: https://ejesm.org/wp-content/uploads/2019/11/ejesm.12i5.8.pdf

Palla A, Gnecco I, Lanza LG, La Barbera P (2012) Performance analysis of domestic rainwater harvesting systems under various European climate zones. Resources Conserv Recycling 62. ISSN 0921-3449. https://doi.org/10.1016/j.resconrec.2012.02.006

Ridwan W, Sapitang M, Aziz A, Kushiar K, Najah A, El-Shafie A (2020) Rainfall forecasting model using machine learning methods: case study Terengganu, Malaysia. Ain Shams Eng J 12. https://doi.org/10.1016/j.asej.2020.09.011

Rostad N, Montalto F (2012) Rainwater harvesting: using urban roof runoff for residential toilet flushing. Metropolitan Sustain Understanding Improving Urban Environ 350–369. Available at: https://doi.org/10.1533/9780857096463.3.350

RS2 (2012) Potable water specification, 2nd edn. Rwanda Bureau of standard, Kigali

Sanches FLF, Terêncio DPS, Pacheco FAL (2015) Rainwater harvesting systems for low demanding applications. Sci Total Environ 529:91–100. Available at: https://doi.org/10.1016/j.scitotenv.2015.05.061

Wachemo University Water Utility (2020) Internal report. Unpublished

Chapter 19
Dual-Stage Solar-Powered Electrocoagulation and Electrooxidation Process for Textile Wastewater Treatment

Yemane G. Asfaha, Feleke Zewge, Teketel Yohannes, and Shimelis Kebede

Abstract The textile industry is one of the significant consumers of dyestuff, chemicals, and water. As a result, a large amount of wastewater is generated. The wastewater discharged from the textile dyeing industry is challenging to treat using conventional treatment methods as these effluents are complex, toxic to microorganisms, and recalcitrant to biodegradation. Limited studies have demonstrated that the dual-stage electrocoagulation–electrooxidation (EC–EO) process is an efficient technology for eliminating different pollutants. However, the full potential of this technology to address the challenges faced by the textile industry in developing countries like Ethiopia has yet to be realized. Additionally, the pressing global issue of energy crisis and climate change calls for the use of renewable energy sources to power this technology. Therefore, to address this problem, a dual-stage solar-powered electrocoagulation (EC) and electrooxidation (EO) process has been evaluated for its capability to remove color, total organic carbon (TOC), and chemical oxygen demand (COD). Aluminum (Al) and iridium oxide coated on titanium (IrO_2/Ti) were selected as anode/cathode for EC and EC–EO experiments, respectively. The results were evaluated based on the interaction effects of operating parameters of the treatment methods on the percentage of COD, TOC, and color removal. The dual-stage EC–EO process obtained 97% COD, TOC, and color removal efficiency. In addition, the results of the combined spectroscopy analysis confirm the complete degradation of

Y. G. Asfaha (✉)
School of Civil Engineering and Architecture, Department of Water Resources Engineering, Adama Science and Technology University, Adama, Ethiopia
e-mail: yemane.gebreselassie@aau.edu.et

F. Zewge
Africa Centre of Excellence for Water Management, College of Natural and Computational Sciences, Department of Chemistry, Addis Ababa University, Addis Ababa, Ethiopia

T. Yohannes
College of Natural and Computational Sciences, Department of Chemistry, Addis Ababa University, Addis Ababa, Ethiopia

S. Kebede
School of Chemical and Bio-Engineering, Addis Ababa Institute of Technology, Addis Ababa University, Addis Ababa, Ethiopia

A. M. Melesse et al. (eds.), *Land and Water Degradation in Ethiopia*, Springer Geography, https://doi.org/10.1007/978-3-031-60251-1_19

organic contaminants to carbon dioxide and water. In addition, the optimum operating conditions have been tested for real industrial wastewater effluents and have shown excellent performance in removing pollutants. Furthermore, the optimal working conditions were also evaluated using direct solar modules and showed comparable removal performance compared to using conventional electricity.

Keywords Textile wastewater · Solar-powered electrocoagulation · Electrooxidation · Dual-stage EC–EO · Dye degradation extent

Introduction

The textile industry is one of the largest consumers of dyestuffs, chemicals, and water used during different textile processing procedures (Afanga et al. 2020). The enormous amount of wastewater produced from textile dyeing industries has become a significant environmental concern. At the textile dyeing process stages, almost 30% of the dyestuffs remain unbound with the cotton cellulose fibers (Chavana 2004). Methods for treating wastewater effluents produced by the textile industry include biological, physicochemical, advanced oxidation process, adsorption, and nanofiltration.

Recently, there has been a growing interest in electrochemical methods such as electroflotation, electrocoagulation, and electrooxidation due to their reduced need for chemicals and their simple operation. The treatment techniques have the following advantages and drawbacks. For example, physicochemical treatments have a good removal efficiency, but their use is limited due to the high amount of chemicals required during the process and the production of bulky sludge at the end of processing (Amour et al. 2016; Dalvand et al. 2011). Biological systems are unsuitable for textile industry effluent, as wastewater effluents are toxic to microorganisms and recalcitrant to biodegradation. Thus, biological systems are less efficient in treating textile dye effluents (Dalvand et al. 2011). Likewise, adsorption and nanofiltration are not efficient in satisfying the discharge limits. The electrodeposition and electrooxidation methods require a longer treatment time.

Moreover, due to restricting environmental regulations and laws, technologies like electrochemical treatment systems seem promising and are mainly considered as clean technology (Amour et al. 2016). Among the electrochemical methods, electrocoagulation (EC), electrooxidation (EO), and the dual-stage of EC–EO processes are considered efficient methods (Isik et al. 2020).

Furthermore, while various techniques exist to treat textile industry effluents, such as dyes, it is not possible to achieve complete treatment using a single method at a reasonable cost. Recently, dual-stage processes have gained attention from researchers as a way to treat wastewater effluents from the textile industry. Many studies have been conducted on the combined EC and EO methods for treating wastewater effluents from textile industries. However, these studies have different

working conditions such as dye type, concentration, current density, pH, electrolysis time, and electrode type.

Raju et al (2008) evaluated the performance of the combined electrocoagulation (EC) and electrooxidation (EO) method in removing COD from simulated textile wastewater. They used aluminum as the anodic material for EC and compared the efficiency of graphite and $RUO_2/IrO_2/TaO_2$ anodic material for EO. The EC method was able to reduce COD concentration significantly (from 1316 to 429 mg L^{-1}). The EC effluents were further treated with electrooxidation method using anodic graphite, and $RUO_2/IrO_2/TaO_2$-coated titanium electrodes, resulting in high COD reduction. Aquino et al (2014) also conducted a study on electrooxidation treatment to remove pollutants from textile industry wastewater effluents employing Ti–Pt/β-PbO_2 and DSA® anodes. The results showed that 100% of the color and 86% of the COD concentration were removed using Ti–Pt/β-PbO_2 anodes at optimal electrolysis and current density of 180 min and 75 mA cm^{-2}, respectively.

In addition, Demir Delil and Gören (2019) investigated the performance of EC and EO processes as separate technologies for removing COD and color from textile wastewater effluent. The effect of working conditions such as electrolysis time, electrode type, pH, and electrode configuration was used to examine its performance. In the EC process at a pH of 3 and applied voltage of 6 V, Fe–Fe electrodes were found to have 89% removal efficiency for color and 93% for COD. The use of Pt-Fe electrodes in the EC process also resulted in a 93% reduction in COD at a potential of 6 V. When combined with the EO process, these treatment methods and electrode combinations were found to be effective in reducing pollutants below the allowable release level.

Regarding energy consumption, the authors found that the EO method is more cost-effective for the effective removal of COD. A recent study by Zou et al. (2017) also found that 100% COD removal from actual textile wastewater was achieved using optimal working conditions [current density 60 mA cm^{-2}, supporting electrolyte (NaCl) 3 g L^{-1}, and pH of 2] using a BDD anode within 180 min of electrolysis. However, this period of electrooxidation is considered too long and impractical.

Based on the studies conducted on integrating EC–EO processes, selecting electrode material is crucial as it influences the removal efficiency. Thus, to achieve maximum removal efficiency, the electrode material must have high electrical conductivity, resistance to corrosion, high stability, and high durability (Heffron et al. 2019; Macpherson 2015). Electrodes from a noble metal, metal alloys, metal oxide, or dimensionally stable anodes (DSAs), namely Ti/SnO_2–IrO_2, Ti/Sb–SnO_2, Ti/SnO_2–Sb_2O_5–RuO_2, Ti/Ta_2O_5–IrO_2, Ti/RuO_2–IrO_2, and Ti/TiO_2–IrO_2, boron-doped diamond (BDD), and carbon and graphite are some of the materials used in electrooxidation processes for water treatment studies.

Recently, DSA electrodes such as iridium dioxide-coated on titanium (IrO_2/Ti) mesh electrodes have been developed with a good lifetime and practical stability (Shan et al. 2015). However, no studies have been conducted on using these electrodes to treat textile wastewater.

From a review of existing literature and to the best of our knowledge, there is no prior research on the use of a dual-stage process of electrocoagulation and electrooxidation using a mesh iridium dioxide-coated onto titanium (IrO_2/Ti) electrode specifically for treating textile wastewater containing reactive dyes such as Vivizol red 3BS 150%, which is commonly used in the cotton textile industry. Additionally, many researchers have focused on determining the effectiveness of removing pollutants from water and wastewater using a one-factor-at-a-time approach (OFAT) (Ghasem et al. 2017). However, this method is an experimentation technique that involves varying a single variable while keeping the other variables fixed (Nair et al. 2014). This approach may result in inaccuracies in determining the optimum operating conditions as it does not take into account the interaction effects among the operational parameters. Moreover, to carry out OFAT, numerous experiments must be conducted, leading to high experimental costs and time-consuming processes. Furthermore, when an experiment involves more than two factors, it is more efficient and cost-effective to simultaneously vary several variables (Czitrom 1999). Therefore, considering the interaction effect of operating conditions on response is considered important in this study. To address these issues, the Design-Expert software was employed to evaluate the interaction effect of input factors on the response.

Even though several research studies have been conducted on the treatment of textile wastewater using the dual-stage EC–EO method, the dye concentration considered in these studies is not more than 100 mg L^{-1}, which is below the dye concentration emitted from textile dyeing units. In reality, of the 2 g L^{-1} dye applied during the dyeing process, nearly 30% of the dyes remain unbounded to cotton cellulose fibers that is 0.6 g L^{-1} or 600 mg L^{-1}. Therefore, this experimental study considered the same concentration as the dye industry effluent. As a result, a highly concentrated dye solution (600 mg L^{-1}) identical to the textile effluent concentration was used to test the effectiveness of the treatment method, which is also lacking in other studies.

Therefore, this experimental study aims to optimize and investigate the process efficiency of the dual-stage EC–EO method based on the interaction effect of operating conditions, to treat cotton textile industry wastewater effluents. The study also aims to investigate the removal mechanism, mineralization of the pollutants, evaluation of optimum operating conditions for real wastewater treatment, and treatment cost analysis. Moreover, combined FT-IR and ^{1}H and ^{13}C-NMR spectroscopy methods were employed to analyze the extent of dye degradation and investigate the by-products in the treated water. Box-Behnken design (BBD) was used as a design tool and for process optimization.

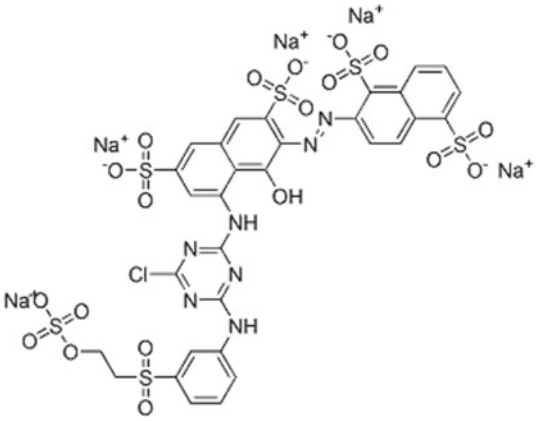

Fig. 19.1 Molecular structure of Vivizol red 3BS 150% reactive dye

Materials and Methods

Chemicals and Simulated Wastewater Preparation

Vivizol red 3BS reactive dye (VR 3BS 150%) was purchased from SM Eksoy Dyes and Chemicals PLC, Addis Ababa, Ethiopia. Concentrated simulated textile wastewater was prepared in the laboratory. This type of dye was chosen because it is widely applied in the Ethiopian cotton textile industry. A pre-laboratory experimental trial was carried out to calculate the amount of NaCl needed to achieve the desired current delivered to the system to improve the conductivity of the working solution. Accordingly, 1–2.5 g L^{-1} of NaCl was sufficient to get the required conductivity of the working solution throughout the trials. Also, 0.1 MNaOH and 0.1 MHCl solutions were prepared to adjust the pH of the simulated working solution. Cotton fabric is commonly colored using a 2 gL^{-1} shade, in which 70% of the dye is exhausted, and the remaining dye solution (30%) contributes to the effluent load (Chavana 2004). Therefore, a simulated working solution was prepared by adding 30% of 2 gL^{-1} Vivizol red 3BS 150% reactive dye to one liter of distilled water, resulting in a concentration of 600 mg L^{-1}. The molecular structure and physicochemical characteristics of Vivizol red 3BS 150% reactive dye synthetic wastewater are shown in Fig. 19.1 and Table 19.1.

Experimental Design and Procedures

Figure 19.2 depicts the experimental setup for batch studies, designed for the EC and dual-stage EC–EO processes. The EC method was performed in a 1000 mL cylindrical glass with an effective working capacity of 600 mL in all experiments.

Table 19.1 Physicochemical characteristics of synthetic wastewater of Vivizol red 3BS 150% reactive dye

Parameter	Value	RSD (%)
pH	7.8	0.27
Electrical conductivity (μS/cm)	532.0	0.19
TDS (ppm)	265.0	0.38
TOC (ppm)	121.3	0.48
COD (mg L^{-1})	397.2	0.29
Turbidity (NTU)	17.6	0.11
dye concentration (mg L^{-1})	600.0	

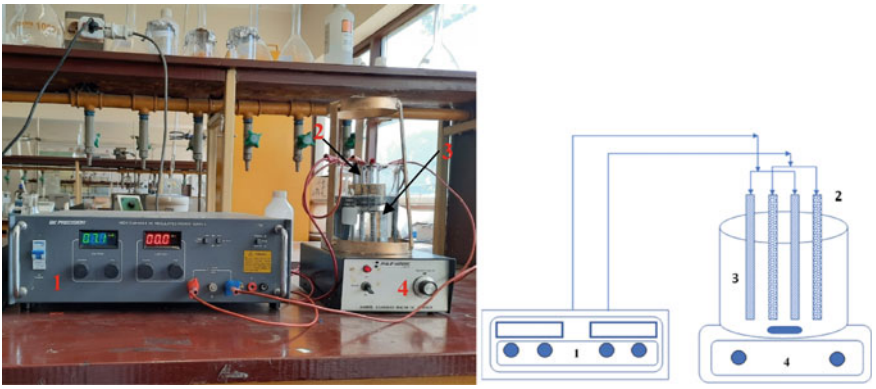

Fig. 19.2 Laboratory scale schematic diagram of experimental setup: (1) current regulator; (2) electrodes; (3) reactor; (4) magnetic stirrer

Likewise, a 500 mL reactor was considered for the EC–EO batch procedure, with an active working capacity of 400 mL.

For the EC process, four aluminum (Al) electrodes (2-anode, 2-cathode) of the same dimensions were prepared from an aluminum plate purchased from Synergy Aluminium Technics PLC, Addis Ababa, Ethiopia. The operational dimension of an Al electrode is 6.5 cm × 2.5 cm × 0.1 cm (height x width x thickness) with an effective total surface area of 65 cm^2. Likewise, two anode IrO_2/Ti electrodes provided by Sungwon Forming Company (Korea) and two Al cathode electrodes were used for the EO process. The dimension of IrO_2/Ti electrodes is 6 cm × 2 cm × 0.1 cm (height x width x thickness) with the effective surface area of 48 cm^2. Before experimentation, the weight of the two anodic electrodes, Al and IrO_2/Ti, was 18.874 and 10.673 g, respectively. The electrodes were connected to the DC power supply's negative and positive output terminal in a mono-polar connection. The applied current and voltage were controlled using a high current DC regulator power supply (BK precision 1796, 0–16 V; 0–50 A). The DC power source provided 1, 2, and 3 A, corresponding to current densities of 15.4, 30.8, 46.2 mA cm^{-2} for EC and 20.8, 41.7, 62.5 mA cm^{-2} for EO, respectively. To ensure the effective addition

of the coagulant and formation of oxidants in all EC and EO processes, respectively, the applied current was stable. In addition, the chosen level of current densities is based on literature (Yoon et al. 2015) and the pre-laboratory experimental trials.

The only difference between EC and EO experimental setup is the effective volume of the reactor (600 ml for EC and 400 ml for EO) and the anode material (Al for EC and IrO_2/Ti for EO), while the other setup parameters remain the same (Fig. 19.2).

Before each experiment, the electrodes were thoroughly cleaned with an acetone solution to clean any surface grease that might have accumulated during the cutting process. After each experiment, the electrode materials were soaked in a 2 M HCl acid solution for 3 min to remove any solid particles adhered to the surface and then rinsed multiple times with distilled water before being dried in an oven at 105 °C. All experiments were conducted in duplicate. Meanwhile, the reactor/cell was washed with a 2% HCl acid solution and water and then dried with a small towel before the next experiment.

The working solution was constantly stirred with a magnetic stirrer at 150 r.p.m. for all experimental runs. After each trial, the EC-treated water was allowed to settle for 25 min. The supernatant was then filtered with grade 42 Whatman filter paper to separate the unsettled particles. The EC effluent was used as an influent for the EC–EO process and additional water quality evaluation. The optimum working conditions/parameters of EC were first found and then combined as a single technique to determine the performance of the dual-stage EC–EO process on color and COD elimination. In addition, the model's ability to predict the interaction effects of factors (dependent) on the response (independent variable) under different conditions was evaluated, and two regression models (for color and COD) were generated.

Sampling and Data Analysis

The EC and dual-stage EC–EO treatment efficiency was evaluated by analyzing the percentage of COD, TOC, and color removal. The dye concentration in the solution was then measured using a Spectro double-beam UV–Vis spectrophotometer with a maximum absorbance (λ_{max}) of 600 nm (UVD-3200, Labomed, Inc., USA). Similarly, the COD was determined by standard methods for examining water and wastewater (5220 B). The pH meter (pH and ION-meter GLP 22, CRISON Instruments, SA) was used to measure the solution pH. The TOC level was measured by the TOC laboratory analyzer (Sievers InnovOx ES). The Fourier Transform Infrared Spectrometer (FT-IR) and Nuclear Magnetic Resonance (^{1}H and ^{13}C-NMR) were selected to evaluate the final by-products of the dual-stage EC–EO treatment system. FT-IR spectra were recorded on Spectrum 65 (PerkinElmer) in the 4000–400 cm^{-1} range (resolution: 4 cm^{-1}, number of acquisitions: 4) using KBr pellets. The ^{1}H and ^{13}C-NMR data were run using the BRUKER 400 ultra-shield at 100.6 MHz. During ^{1}H NMR testing, deuterium oxide (D_2O) was used as a solvent. The solar irradiance data were recorded using an X1(Xone-one) optometer (Gigahertz Optik GmbH, Germany).

Experimental Design and Statistical Analysis

The BBD was chosen among the various experimental RSM models because it is an independent and rotatable quadratic model without embedded factorial points. Moreover, in comparing the different design approaches of the RSM tools, BBD is more efficient than CCD and the three-level complete factorial design (Asfaha et al. 2022a, b). In addition, the BBD is generally a highly efficient and cost-effective approach because it requires fewer experiments than other experimental design techniques. It can also calculate intermediate-level response functions and estimate system performance at all test points in the range studied. As a result, BBD is widely employed to optimize research on industrial wastewater treatment compared to other experimental design methods (Asfaha et al. 2022a, b).

Therefore, the interaction effects of EC working parameters such as dye concentration, (*A*), pH (*B*), current density (*C*), and electrolysis time (*D*) and EC–EO parameters current density (X_1), pH (X_2), and electrolysis time (X_3) on the efficiency of dual-stage EC–EO process was examined by three levels according to Box-Behnken design (BBD) experimental design under RSM (Tables 19.2 and 19.3).

The applied current is the same for both processes, but the difference in current density is due to the difference in electrode size. Likewise, the variation in reactor volume for the two systems is due to the fact that the electrode size is different. Furthermore, the difference in electrolysis and pH between the two experimental configurations is based on the best performance of pre-laboratory tests and literature.

Under this condition, the BBD involved 29 and 17 experimental runs (Eq. 19.1) of EC and EC–EO, respectively, including five replicates and center points. Color (Y_1) and COD (Y_2) removals percentages were considered as response variables (Eqs. 19.2 and 19.3).

Table 19.2 Levels and ranges of variables in BBD for the EC process

Working parameters	Units	Range and levels		
		Lower (1)	Medium (0)	Upper (+1)
A: Dye concentration	mg L^{-1}	433	600	767
B: pH		3	7	11
C: Current density	mA cm^{-2}	15	31	46
D: Electrolysis time	min	5	20	35

Table 19.3 Levels and ranges of variables in BBD for the dual-stage EC–EO process

Working parameters	Units	Range and Levels		
		Lower (1)	Medium (0)	Upper (+1)
X_1: Current density	mA cm^{-2}	20	41	62
X_2: pH		2	4	6
X_3: Electrolysis time	min	20	40	60

$$\text{Run} = 2k(k-1) + C_0, \tag{19.1}$$

where k and C_0 are the number of input factors and center points, respectively

To evaluate the color removal efficiency (Eq. 19.2), five known different initial concentrations of Vivizol red 3BS dye solution were prepared, of which 600 mg L^{-1} was used as a stock solution. An absorbance-to-dye concentration calibration curve was then developed. The concentration of VR 3BS 150% for each treatment time was determined using the mathematical formula generated from the calibration graph.

$$Y_1(\%) = \frac{C_i - C_t}{C_i} \times 100, \tag{19.2}$$

where C_i and C_t are the initial and the treated effluent concentration (mg L^{-1}), respectively

Similarly, the COD reduction efficiency of all samples was calculated (Eq. 19.3):

$$Y_2(\%) = \frac{COD_i - COD_t}{COD_i} \times 100, \tag{19.3}$$

where COD_i and COD_t are the COD concentration before and after the treatment at a time t in mg L^{-1}, respectively.

ANOVA and RSM were considered to examine the interaction effects between the input factors and responses and establish the best-operating conditions. In this design, to evaluate the interactive effects of different independent variables with the dependent variables (responses), a second-order polynomial model (regression equation) was employed with the following relationship (Eq. 19.4):

$$Y = \beta_0 + \sum_{i=1}^{k} \beta_i X_i + \sum_{i=1}^{k} \beta_{ii} X_i^2 + \sum_{i=1}^{k} \sum_{j=1}^{k} \beta_{ij} X_i X_j + \varepsilon, \tag{19.4}$$

where Y is the response (percentage color or COD removal); β_0, β_i ($i = 1, 2, 3$) and β_{ij} ($i = 1, 2, 3; j = 1, 2, 3$) are model coefficients for intercept, linear, quadratic, and interaction, respectively; X_i, X_j are the coded input factors; and ε is the residuals.

This mathematical correlation between removal efficiency (predicted, %) of color and COD and the selected input variables can be used as a model equation to predict the optimum values.

Solar Photovoltaic (PV) Module

The solar cell and accessories were purchased from Universal solar PLC (Addis Ababa, Ethiopia). A mono-crystalline silicon PV panel with a maximum power of 150 W was used to supply energy to the electrocoagulation and electrooxidation

system. The dimension of the panel and other solar PV module characteristics are described in Table 19.4.

The diagram representation of the experimental system used in the solar-based experimental study is shown in Fig. 19.3. The experiments with PV panel were carried out at Addis Ababa University at the Department of Chemistry (Latitude 9.04° North, Longitude 38.77° East, Altitude 2447 m above the sea level, 20° inclination, and North orientation).

First, the experiments were conducted using conventional DC electricity to optimize the working conditions for electrocoagulation and electrooxidation processes. And then, the efficiency of removing pollutants using the optimum working conditions by electrocoagulation and electrooxidation method was carried out using solar energy and compared with the conventional DC electrical power supply.

Table 19.4 Solar PV module characteristics

Mode	Value
Material	Mono-crystalline silicon
Maximum power (Pmax)	150W
Maximum current (Imax)	8.42 A
Maximum voltage (Vmax)	17.90 V
Short circuit current (Isc)	9.01 A
Open circuit voltage (Voc)	22.7 V
Maximum system voltage	1000 V
Dimension (mm)	1485 × 668 × 30
Solar module efficiency (collection losses are 15%)	85%
Weight (kg)	10.8
Cell array (connected in series)	36 pieces in a 4*9 matrixes

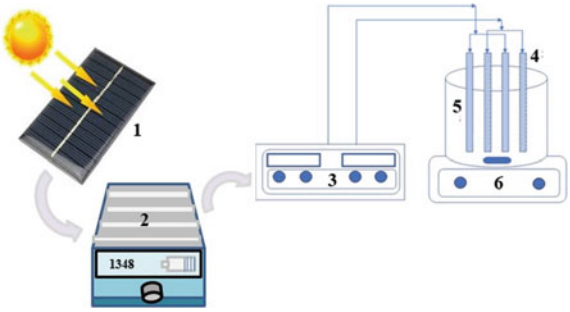

Fig. 19.3 Experimental setup of PV-dual-stage EC–EO treatment unit (1: PV solar panel; 2: charge controller 3: current regulator; 4: electrodes; 5: reactor; 6: magnetic stirrer)

Operating Cost Analysis

The cost of operating the treatment method was determined using the following equations (Eqs. 19.15–19.17), and then it was compared to other studies.

$$\text{Operating cos (US\$/m}^3) = aC_{\text{energy}} + bC_{\text{electrode}} + cCC + S.D, \tag{19.5}$$

where C_{energy} represents the electrical energy consumption (kWh/m^3), $C_{\text{electrode}}$ represents the consumption of Al and IrO_2/Ti electrodes (kg/m^3), *CC* represents the consumable chemical cost at 2021 price, and SD is for sludge disposal cost. The letters a, b, and c represent the unit price for electricity, electrodes (Al and IrO_2/Ti), and chemical cost in the Ethiopian market of January 2022. The total operating cost was determined in terms of US$ per cubic meter of treated water (US$/m^3).

Electrode Consumption

The electrode consumption during the process will be calculated as follows:

$$\text{Electrode consumption, } C_{\text{electrode}}(\text{kg/m}^3) = \frac{I \times t \times M}{n \times F \times V}, \tag{19.6}$$

where I is the current density (A), M is the molecular mass of the electrodes material (g mol^{-1}), t is the electrolysis time (s), F is Faraday's constant (96, 485 C mol^{-1}), V is the volume of the net wastewater volume (m^3), and n is the number of transferred electrons.

Electrical Energy Consumption

The value of the electrical energy consumption of the dual-stage EC–EO unit for treating the wastewater is calculated in kWh/m^3):

$$\text{Electrical energy consumption, } C_{\text{energy}}\ (\text{kWh/m}^3) = \frac{U \times I \times t}{V}, \tag{19.7}$$

where U is the cell potential (V) at desired current I (A), t is the electrolysis time (h), and V is the volume of the sample treated (m^3).

Results and Discussion

Electrocoagulation Process

Effect of Initial Dye Concentration on Color and COD Removal

As can be seen in Fig. 19.4(a), when dye concentration rises from 433 to 767 mg L^{-1}, the color and COD removals efficiencies decrease almost linearly from 76.82% to 71.21% and 70% to 59% of color and COD, respectively. Compared to color removal, the smaller COD reduction could be due to the low decomposition of dye molecules by electrocoagulation (Dalvand et al. 2011). The process of color reduction efficiency by EC is considered to be the adsorption of dye molecules by flocs. As a result, the initial concentration of dye increases at a constant current density. The available sites on the flocs for dye adsorption are limited, leading to a decreasing color and COD removal trend. Faraday's law of electrolysis also supports this result. Based on Faraday's law of electrolysis, the amount of Al^{3+} dissolved from the sacrificial electrode to the solution is constant at the same applied voltage, current, and electrolysis time (Asfaha et al. 2021). Thus, the adsorption capacity of metal hydroxide flocs formed is very restricted. The specific amount of dye molecules is absorbed by a particular amount of flocs (Dalvand et al. 2011).

Effect of Initial pH on Color and COD Removal

The initial pH of the wastewater directly influences the efficiency of the EC process, mainly the coagulation mechanism and the conductivity of the aqueous solution, zeta potential of colloidal particles, and electrode dissolution (Özyurt and Camcıoğlu 2018). The removal efficiency of both color and COD from the simulated textile wastewater at different initial pH values are plotted in Fig. 19.4a. It was obtained that the variation in pH levels has less effect on the percentage of color and COD removal of Vivizol red 3BS reactive dye (water solubility at pH 3.5) solution. Similar results were obtained by (Can et al. 2003), and variation in pH was found to have no effect on color removal capacity.

The result indicates that the maximum color and COD removal efficiency was observed at a pH of around 3. The acidic media was the most favorable for EC processes' color and COD removal efficiency. During the EC process and at different pH levels, the major interaction mechanisms are (i) charge neutralization (lower pH) and (ii) adsorption, and sweep flocculation (pH 5.0–8.0) is the most dominant removal mechanism (Eqs. 19.8–19.11). In contrast, flocculation occurs at a lower pH, with adsorption reported at a higher pH. This is because, at lower pH, charge neutralization is dominant and attained with mono Al^{+3} species generated from anodes. The positively charged metal ions neutralize the negatively charged organic molecules in the wastewater. This charge neutralization prevents solubility in the solution, facilitating the coagulation process (Shah et al. 2017). In addition to this, according to

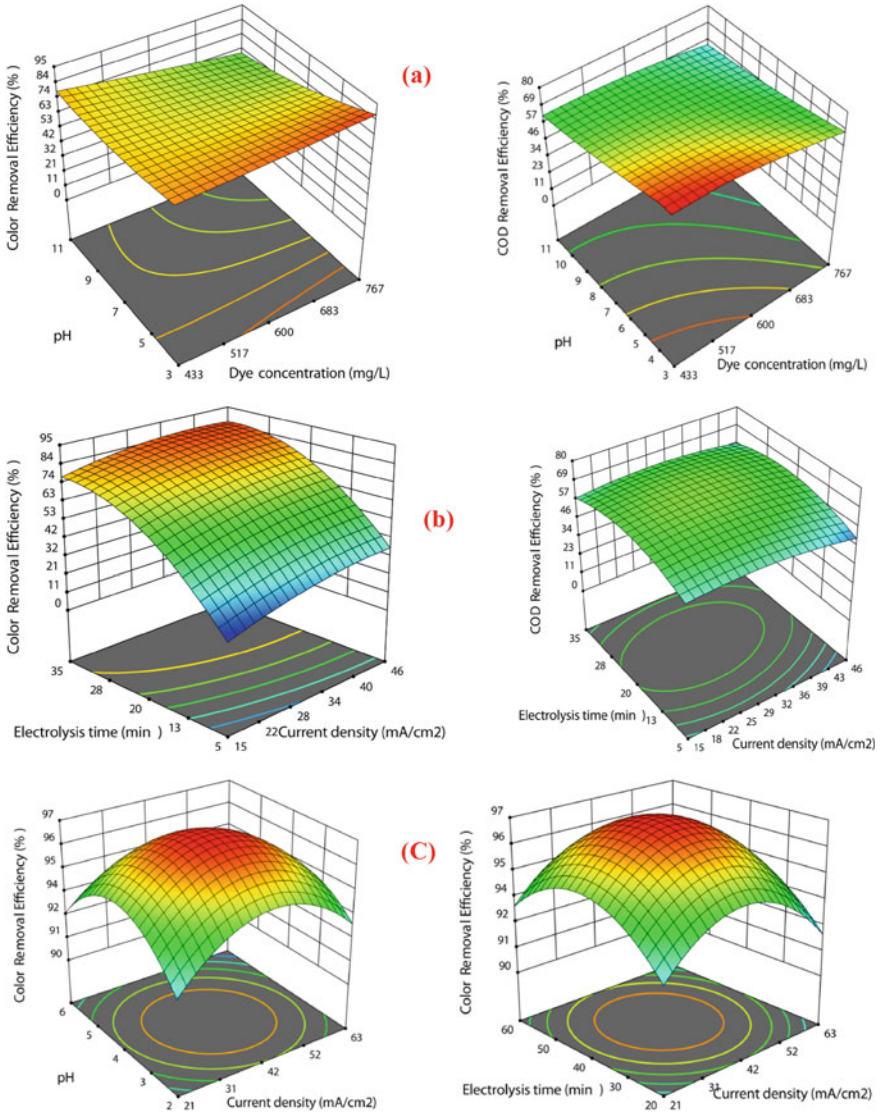

Fig. 19.4 Interaction plots for percentage color removal **a** using EC process; **c** using dual-stage EC–EO processes; and b) for COD removal using EC processes

the electrocoagulation mechanism (Eqs. 19.8 and 19.9)**,** the formation of aluminum hydroxide flocs is retarded at a low pH. The hydroxypolymeric species formation is increased, which results in efficient precipitation of dye molecules (Can et al. 2003).

Precipitation (lower pH) :

$$\text{Dye} + \text{monomeric Al} \rightarrow \left[\text{dye monomeric Al}\right]_{(S)} \text{ pH 4 to 5}, \tag{19.8}$$

$$\text{Dye} + \text{Plolymeric Al} \rightarrow \left[\text{dye ploymeric Al}\right]_{(S)} \text{ pH 5 to 6.} \tag{19.9}$$

Adsorption (pH > 6.5):

$$\text{Dye} + \text{Al(OH)}_3\text{(s)} \rightarrow \text{sludge,} \tag{19.10}$$

$$\left[\text{Dye Plolymeric Al}\right]\text{(s)} + \text{Al(OH)}_3(s) \rightarrow \text{sludge.} \tag{19.11}$$

It is a fact that the $Al^{3+}{}_{(aq)}$ and OH^- ion produced at the anode and cathode reacts and forms different monomeric species, namely $Al(OH)^{2+}$, $Al(OH)_2{}^+$, $Al_2(OH)_2{}^{4+}$, $Al(OH)_4{}^-$, and polymeric species, namely $Al_6(OH)_{15}{}^{3+}$, $Al_7(OH)_{17}{}^{4+}$, $Al_8(OH)_{20}{}^{4+}$, $Al_{13}O_4(OH)_{24}{}^{7+}$ and finally transform to $(Al(OH)_3$ through various precipitation kinetics (Kobya et al. 2003). The rate of interaction mechanism and formations of these species with dye molecules mainly depends on the pH and type of ions present in the solution.

At initial pH 3 and higher, the final pH of the solution increases during the electrolysis time. However, at alkaline pH > 9, pH of the solution declines due to the formation of $Al(OH)_4{}^-$ which consumes the hydronium ion (Eq. 19.12).

Figure 19.4a depicts the initial pH of Vivizol red 3BS dye solution increased from 3 to 11. The removal rate decreased from 84.52 to 69.25% and 77 to 60% of color and COD, respectively. (Ayhan Şengil and Özdemir 2012) conducted simultaneous color removal by EC from basic yellow 28 and dispersed blue 56 dye solution and found maximum removal of 94.7% of both dyes at pH between 2 and 4. Another study conducted by (Demir Delil and Gören 2019) achieved 92% color and 89% COD removal at pH 3.

Furthermore, it has been observed that (Fig. 19.5) when the initial pH increased from 3 to 11, the final pH also increases from 8.34 to 8.96 and then remains constant due to the buffering capacity of the system $Al(OH)_3/Al(OH)_4{}^-$ which reduces the final pH to 9.16 by consuming hydroxide ion (Eq. 19.12).

$$\text{Al(OH)}_3 + \text{OH}^- \Leftrightarrow \text{Al(OH)}_4^-. \tag{19.12}$$

Current Density Effect on Color and COD Removal

In the EC process, the formation of coagulant species occurs in situ through the electrical dissolution of the sacrificial anode. The metal anode is oxidized into cations as the applied current density flows through the electrode **(Eq. 19.13).**

$$\text{Al}_{(s)} \rightarrow \text{Al}^{3+}_{(aq)} + 3\text{e}^-. \tag{19.13}$$

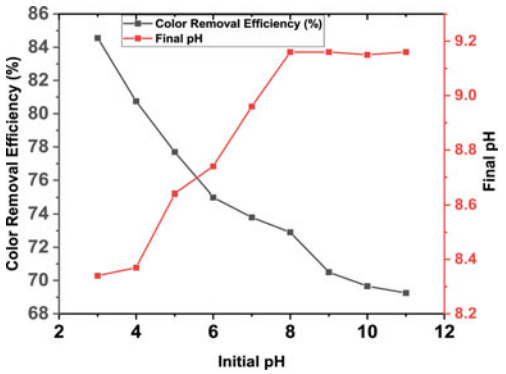

Fig. 19.5 Effect of initial pH on color removal of EC process (NaCl: 2 g L^{-1}, electrolysis time 25 min, and current density: 32.95 mA cm^{-2})

The EC process involves the release of metal cations (Al^{3+}) from the anode, which then react with hydroxide ions (OH^-) generated at the cathode. This reaction leads to the formation of non-soluble, easily precipitable metal hydroxide ($Al(OH)_{3(s)}$) sweep flocs. These flocs, having large surface areas, are highly effective in rapidly adsorbing soluble organic pollutants and trapping colloidal particles (Eq. 19.14).

$$Al^{3+}_{(aq)} + 3H_2O \rightarrow Al(OH)_{3(s)} + 3H^{+}_{(aq)}. \tag{19.14}$$

Besides, water electrolysis occurs at the cathode (cathodic reaction) as shown in Eqs. 19.15–19.17.

$$3H_2O + 3e^- \rightarrow \frac{3}{2}H_{2(g)} + 3OH^-_{(aq)} \quad \text{(at alkali solution)}, \tag{19.15}$$

$$2H_3O^+ + 2e^- \rightarrow H_{2(g)} + 2H_2O \quad \text{(at acidic solution)}, \tag{19.16}$$

$$Al_{(s)} + 4OH^- \rightarrow \left[Al(OH)_4\right]^- + 3e^- \quad \text{(at alkali solution)}. \tag{19.17}$$

Therefore, current density determines the amount of coagulant, development of flocs, bubble formation, and size of bubbles. This, in turn, affects the formation and growth of flocs. Based on Faraday's law, the dosage of metal ions dissociated from the electrode is directly proportional to charge load. Therefore, the current density applied to the EC process determines the dosage of Al^{3+} ions released.

Figure 19.4b depicts that as the current density increases from 15 to 32 mA cm^{-2} the color removal efficiency improves from 63 to 75.9%. This is likely due to the fact that as the current density increases, the number of hydroxyl polymers also increases leading to more efficient removal of the dye molecules. However, increasing current density beyond 32 mA cm^{-2} has no significant change in color removal. Increasing the current load leads to a higher production of coagulant at the electrode-solution interface, which restricts free movement of particles and results in an increased overpotential in the solution caused by Ohmic drop (Nasrullah et al. 2012). Consequently,

it prevents further adsorption of dyestuff. Therefore, limiting the applied current load at the optimal value is crucial to avoid excessive heat generation and oxygen evolution in the reactor. Similarly, when increasing the current density from 15 to 32 mA cm^{-2}, the COD removal rate increases from 65 to 67% (Fig. 19.4b). However, a decrease in COD removal is observed when the current density is further increased from 32 to 46 mA cm^{-2}. This indicates that surpassing the optimal current load can negatively impact the efficiency of the EC process.

The applied current density controls the coagulant dosing with the anode and the hydrogen gas (H_2) formation with the cathode in all electrochemical processes. Under Faraday's law, application of high current density during EC can result in a higher production of metal and hydroxide ions, leading to an increase in floc production. However, applying excessively high current density can have an adverse effect on the performance of the electrocoagulation treatment. An excessive amount of coagulant produced by high current density can lead to a secondary reaction causing a reversal in the charge of colloids and redispersing them, ultimately reducing the effectiveness of the coagulant and the durability of the electrode (Hakizimana et al. 2017).

The result obtained indicates that the variation in current density does not significantly improve the efficiency of the treatment method. This is because the minimum current density applied might be enough to dissociate the metallic ion required for electrocoagulation from the anodic material, which is in line with Faraday's law.

Effect of Electrolysis Time on Color and COD Removal

As can be seen in Fig. 19.4b, as the electrolysis time increases, a similar trend is observed in the removal efficiency of both color and COD. The electrolysis time indeed affects the treatment efficiency of the system because it determines the production rate of Al^{3+} and hydroxide ions. As shown in Fig. 19.4b, the color removal increases from 32 to 85.5% as the electrolysis time increases from 5 to 25 min. After 25 min of electrolysis time, the color removal approached maximum. Other studies reported similar results for the color removal of reactive dye wastewater by electrocoagulation (Can et al. 2003).

On the other hand, as the electrolysis time increases from 5 to 25 min, the efficiency of COD removal increases from 57 to 67%. However, after 25 min of electrolysis, the percentage of COD removal decreases to 61%. Therefore, increasing electrolysis time beyond 25 min results in a decline in the removal efficiency of COD. In addition, from the results shown in Fig. 19.4(b), it can be concluded that the maximum removal rate of both color and COD was achieved at the optimum electrolysis time of 25 min. The decline in removal rate of COD after 25 min could be due to the cathodic passivation and production of monomeric electro-coagulant species such as $Al(OH)_2^+$, $Al(OH)_2^+$, and $Al_2(OH)_2^{4+}$ (Bhagawan et al. 2016). Furthermore, the results indicate that though the electrolysis time keeps increasing, the remaining dissolved contaminants are either difficult to remove or take a longer time to remove by the EC process alone (Gürses et al. 2002).

Dual-Stage Electrocoagulation and Electrooxidation (EC–EO) Process

The optimum working conditions of the EC and EO were first determined, and then the dual-stage process was applied. Since the working solution of this process is from the effluent of EC (which finally has the same dye concentration), the initial dye concentration for the dual-stage EC–EO process was not considered as an input factor in the design of this process. Therefore, only three operating conditions: pH, current density, and electrolysis time, were taken into account to evaluate the performance of the EC–EO treatment process on color removal. The performance of the EC–EO process on COD reduction was also evaluated using the optimum working conditions determined.

Current Density and Electrolysis Time Effect on Color Removal

The interaction effect of current density and electrolysis time on color removal rate was examined by varying the values from 20 to 60 mA cm^{-2} and 20 to 60 min, respectively. The results are plotted in Fig. 19.4c. These results show that the color removal rate increased with an increasing applied current density and electrolysis time. This is because increasing the applied current density increases the production rate of hypochlorite or chlorine and hydroxyl radicals. The result shows that the color removal rises to a maximum electrolysis time and current density of 42 min and 42 mA cm^{-2}, respectively. Under these optimal conditions, 97% color removal efficiency was attained. When both electrolysis time and current density are increased beyond the optimal value, the removal efficiency of color decreases. A study by (Sánchez-Sánchez et al. 2018) also confirmed almost similar results. However, the decline in removal efficiency after the optimum working conditions could be due to less dye concentration remaining in the working solution. Thus, 42 mA cm^{-2} was selected as an optimum current density. An almost similar color removal efficiency was obtained when the electrolysis time was increased from 42 to 60 min.

Effect of Initial pH on Color Removal

The initial pH of a solution plays a crucial role in the dual-stage EC–EO process as it affects the production of strong oxidizing agents such as hypochlorite, free chlorides, chlorates, and other oxidant species. The effect of different initial pH levels (2–6) on the dye degradation process was evaluated. As depicted in Fig. 19.4c, the removal efficiency increases linearly as the initial pH increases from 2 to 4. This is because acidic conditions promote the production of hydroxyl radicals and free chlorides (dominant oxidizing agent), which enhance the oxidation of organic compounds (Yılmaz Nayır and Kara 2018). Also, working under a robust acidic condition favors the chlorine evolution, a strong oxidant (Asfaha et al. 2021). This

experimental study achieved the highest color removal efficiency of 97% at pH of 4, consistent with previous research (Oukili and Loukili 2019) that found 97.51% color removal from azo dye solution at an optimal pH of 4.

Evaluation of Optimum Operating Conditions for Real Wastewater Treatment

Compared to the simulated wastewater, the real textile industry wastewater effluent is more complex in composition. It contains various inorganic and organic materials such as active substances, surfactants, dyeing stuff, inhibitor compounds, chloride, sulfates, and total phosphates. Thus, it is essential to test and verify the optimal operating conditions of electrocoagulation (pH 3, current density 32.95 mA cm^{-2}, electrolysis time 25 min, and initial dye concentration of 600 mg L^{-1}) and dual-stage EC–EO (42 mA cm^{-2} of current density pH 4, 42 min of electrolysis) on the treatment of wastewater of the cotton-textile industry in order to ensure its effectiveness. The physicochemical characteristic of real cotton-textile industry wastewater effluent is described in Table 19.5.

As a result, at the optimum operating conditions, 86.5% and 99.9% of color were removed by EC and dual-stage EC–EO, respectively. Similarly, 75% of COD removal by EC and 96% of COD by dual-stage EC–EO have been achieved. The significance test using a simple statistical difference test (Pocock 2006) shows that the difference between the two sample tests (synthetic wastewater and actual wastewater)

Table 19.5 Physicochemical characteristics of real wastewater from the cotton textile industry

Parameters	Value
pH	12.44
COD (mg O_2 L^{-1})	6885
BOD5 (mg O_2 L^{-1})	1377
dye concentration (mg L^{-1})	1682.95
Turbidity (NTU)	34.4
Conductivity (mS cm^{-1})	48.4
TDS (mg L^{-1})	28,600
TOC (ppm)	319
Total alkalinity (mg L^{-1})	4400
Chloride concentration (mg L^{-1})	18,465
(Total hardness as CaCO3 (mg L^{-1})	440
NO_3–N (mg L^{-1})	50
SO42- (mg L^{-1})	600
PO43-(mg L^{-1})	2
NH3-N (mg L^{-1})	28.5

is insignificant ($P < 0.05$). Therefore, the treatment method tested can be efficiently implemented for the treatment of real textile wastewater.

Faradaic Efficiency

The performance of the treatment methods was evaluated using Faradaic efficiency. The Faradaic efficiency is computed using the experimentally recorded coagulant mass ratio on the theoretical mass estimated by Faraday's law (Eq. 19.18).

$$\mathrm{FE}(\%) = \frac{\text{Observed coagulant}}{\text{Theoretical Coagulant}} = \frac{\mathrm{zFm}}{\mathrm{ItM}} \times 100. \tag{19.18}$$

In which,

$$\text{Theoretical coagulant} = \frac{MIt}{zF}, \tag{19.19}$$

where z is the number of transferred electrons of the anode material, F is Faraday's constant (96,485 C mol^{-1}), m is the experimentally observed mass (g), I is the current density (A), t is the electrolysis time (s), and M is the molecular mass of the electrodes material (g mol^{-1}). At the optimum operating conditions, the experimentally observed dissolved coagulant metal was calculated based on the weight difference of the two anode electrodes before and after the treatment. The weight of Al electrode was found to have reduced from 18.874 to 18.601 g indicating a loss of 0.273 g of Al. Similarly, the weight of IrO_2/Ti electrode was found to have reduced from 10.675 to 10.673 g, indicating a loss of 0.002 g. This translates to a Faradaic efficiency of 91.24%, which is considered to be high, indicating that the theoretical amount of coagulants or oxidants used in the experiment matched well with the actual amounts observed. A 100% Faradaic efficiency is considered ideal as it means that all the current applied is being effectively utilized (Ingelsson et al. 2020).

Moreover, a simple statistical test (Pocock 2006) was performed to compare the electrode consumed experimentally with the electrode consumed theoretically and found no significant difference with a P value of 0.0025.

At the optimum operating conditions and with a fixed electrolysis time, an increase in current density results in increased electrode consumption. In the EC process, electrode consumption at a lower pH was calculated to be between 0.07 and 0.4987 kg m^{-3} while in the dual-stage EC–EO process, it is between 0.0016 and 0.0033 kg m^{-3}.

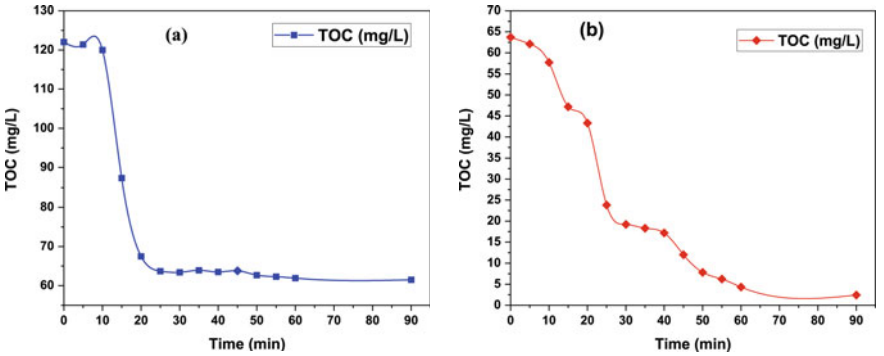

Fig. 19.6 TOC reduction as a function of electrolysis time by **a** EC process (NaCl: 2 g $L^{-}1$, pH: 3, current density: 32.95 mA cm^{-2}); **b** dual-stage EC–EO process pH: 4, current density: 42 mA cm^{-2})

Mineralization Study Through the Analysis of TOC Reduction

A comparison study was performed to assess the effectiveness of EC and dual-stage EC and EO processes in mineralizing the dye. The absence of sludge generated during the EO process (a post-treatment of EC) shows that the removal of color and COD from the textile effluent treatment is essentially due to mineralization of the pollutants. For this purpose, TOC removal analysis was made to quantify the amount of mineralization by EC and dual-stage EC and EO processes. Therefore, under the optimum operating conditions, the effect of electrolysis time on TOC reduction was investigated. Only 47% of TOC reduction was obtained during the electrocoagulation process at optimum operating conditions (Fig. 19.6a).

An extended electrolysis time did not significantly improve the TOC reduction in the EC process, with only a 2% increase observed at 90 min. However, when using the dual-stage process of EC and EO process, 97% reduction in TOC was achieved under the optimal operating conditions (Fig. 19.6b). These findings suggest that the dual-stage process is more effective in completely mineralizing organic contaminants from textile wastewater within a reasonable timeframe. Overall, the technology shows promising results and great potential for the treatment of textile wastewater.

Fourier Transform Infrared (FT-IR) and Nuclear Magnetic Resonance (NMR) Spectroscopy Measurements

The dye degradation extent and the end-products or fractions in the treated water were analyzed by combining FT-IR and ^{1}H and ^{13}C-NMR elemental analysis.

FT-IR spectroscopy detects functional groups of organic and inorganic compounds and their shifts, allowing the interference of specific organic compounds in the

sample. Under complex textile effluent conditions, multiple FT-IR spectra can overlap at high throughput, including input from various functional groups, making it difficult to describe the spectrum. On the other hand, ^{1}H and ^{13}C-NMR spectroscopy also detect the molecules' functional groups and aromatic nature. However, the ^{1}H and ^{13}C-NMR spectra of wastewater are somewhat challenging to interpret because of relatively low-resolution resonance from a complex mix of compounds (Rodríguez-Vidal et al. 2022). Thus, combining FTIR and ^{1}H and ^{13}C-NMR spectroscopy could provide a satisfactory interpretation and results to resolve the limitations mentioned above.

Because of the reduced sludge production in the dual-stage EC–EO treatment method, the solid sample for the FT-IR and ^{1}H and ^{13}C-NMR spectroscopy analysis was prepared by deep dry freezing. Figure 19.7 depicts the FT-IR spectrum of (a) raw wastewater and (b) water treated by the dual-stage EC–EO process.

Figure 19.7a depicts the FT-IR spectra of the effluent. The major peaks obtained from the untreated wastewater were 3524, 3256, 1635, and 660 cm^{-1}. The broad and strong band at 3524 cm^{-1} was due to the O–H bond of the intermolecular bonded. The spectra at 3256 cm^{-1} were due to N–H stretching. The peak at 1635 cm^{-1} suggests the presence of C=C and N=N aromatic function groups in the untreated wastewater. Figure 19.7b shows the FT-IR spectra of the treated water using the dual-stage EC–EO process. A strong and broad peak around 3400 cm^{-1} is ascribed to the stretching

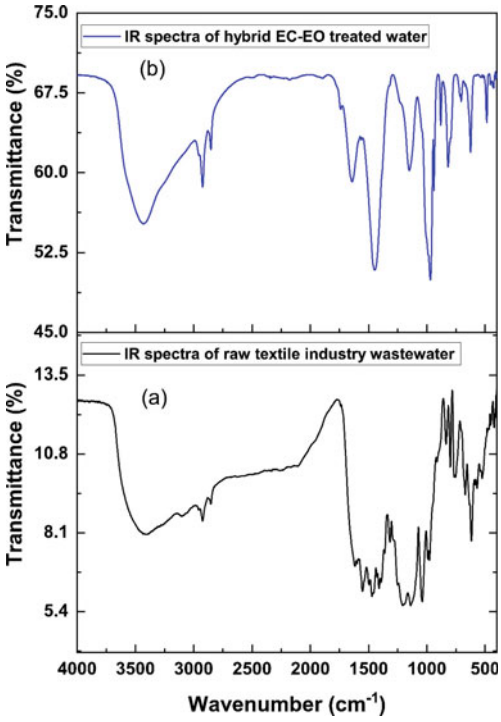

Fig. 19.7 Infrared spectra of raw textile industry wastewater (a) and treated water by dual-stage EC–EO method (b)

of the O–H bond of the hydroxyl groups. The absence of peaks at 1600 and 1635 cm^{-1} indicates the breakdown of N–H amine functions and aromatic rings, respectively. The strong peaks at 678 cm^{-1} may be due to the chlorine and hypochlorite ions in the treated water. Also, the FT-IR spectrum confirmed the presence of the nitrate anion (NO_3^-), which showed a characteristic band at 1380 cm^{-1}. In addition, the weak band at 1362 cm^{-1} can be attributed to the water (H_2O) bending vibration of interlayer water. This study shows that all the Vivizol red reactive dye bonds were utterly broken, and all the aromatic rings were mineralized during the dual-stage EC–EO treatment with IrO_2/Ti electrode. Likewise, the FT-IR analysis confirmed that the increase in transmittance of dual-stage EC–EO treated water was due to mineralization and dye decolorization.

Using standard methods (APHA 1998), an additional test was performed to investigate the oxidation of other remaining dye elements, such as nitrogen, sulfur, chlorine, and sodium. Anions like nitrate-nitrogen (NO_3^--N) and sulfate (SO_4^{2-}) were analyzed using a spectrophotometer (DR5000, HACH method). Furthermore, the concentration of chloride and sodium ions were determined using a color comparator method (with DPD free chlorine HACH reagent) and sodium chromate method, respectively. The measurements were taken three times for each sample and the results were found to be consistent with a deviation of less than 3%.

The results confirm the oxidation of nitrogen into nitrate (NO_3^-), sulfur into sulfate (SO_4^{2-}), sodium into sodium ion (Na^+), and chlorine into chloride ion (Cl^-). Similar results were achieved by (García-García et al. 2015) using an electrode of boron-doped diamond (BDD) as an anode material. Figure 19.8 represents the ^1H NMR spectra of Vivizol red 3BS reactive dye and degradation end-products. The chemical shift at 4.7 ppm represents the signal for the D_2O solvent. The ^1H and ^{13}C-NMR study of Vivizol red 3BS reactive dye confirm a complete degradation of the organic compounds from the wastewater by the dual-stage electrocoagulation-electrooxidation technique. Apart from the high oxidation ability of the generated hydroxyl radicals, active chlorine in the solution contributed a significant role in removing COD and TOC through indirect oxidation. As a result, the combined analytical techniques of the mineralization study through TOC reduction, FT-IR, and ^1H and ^{13}C-NMR analysis confirm that organic contaminants from the textile wastewater are entirely degraded into carbon dioxide (CO_2) and water (H_2O) by the dual-stage electrocoagulation and electrooxidation treatment method. Similarly, (Jain et al. 2012) completely degraded the azo-dye reactive 5R violet using indigenous SB4-acclimatized mixed bacterial cultures.

Compared to other treatment methods, the dual-stage EC–EO process shows complete degradation of the dye resulting in minimal or no sludge production. However, the activated sludge treatment system generated 40 kg of sludge per 1 m^3 of treated wastewater (García-García et al. 2015).

Depending on the efficiency and stability of the anode material, there are two different degradation behaviors of organic pollutants, namely (i) partial degradation of organic contaminants and forming of many refractory species as final end-products, (ii) the mineralization of total organic matter, conversion to CO_2, water (H_2O), and inorganic ions, and generating zero or few refractory by-products

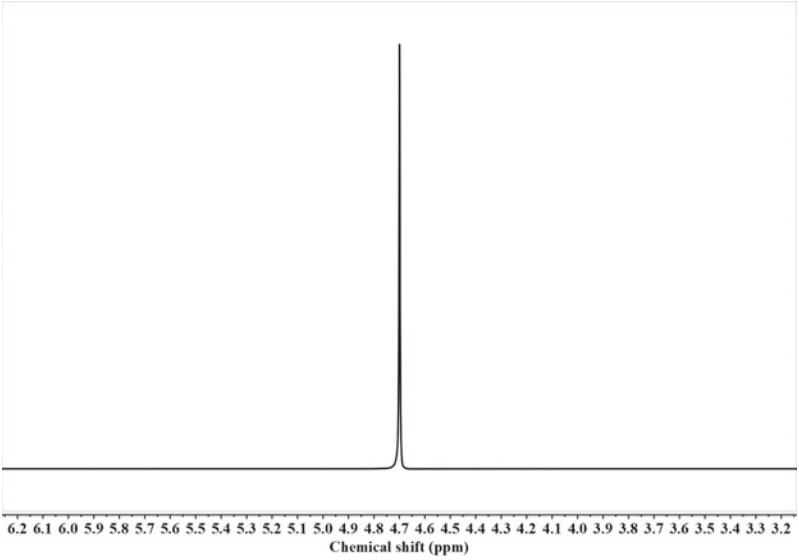

Fig. 19.8 NMR spectrum for treated water by dual-stage EC–EO process

(GilPavas et al. 2017). Therefore, the second type, which is the complete mineralization of organic contaminants and generating little or no by-products, concurs with this research findings.

Anodic and Cathodic Reactions

Two different reactions occur at the anode during the EO process, namely direct and indirect oxidation. Direct oxidation occurs at the electrode surface and is dependent on the anode material's electrocatalytic activity. Indirect oxidation, on the other hand, takes place through a surface mediator on the anode surface, allowing for continuous oxidation. Additionally, during the indirect oxidation process, salts such as sodium chloride or potassium are added to the wastewater to enhance conductivity and the formation of hypochlorite ions (Vahidhabanu and Babu 2015). Furthermore, the anodic and cathodic reactions of the electrooxidation process are discussed below.

Direct Anodic Oxidation Reaction

The following equations show the general electrooxidation of organic pollutants on IrO_2 coated Ti anodes. In this regard, Eq. 19.20 describes the dissociation of water (H_2O) and the hydroxide radical's adsorption to IrO_2. This occurs when the water is drained to the anode to produce the hydroxyl radical, which is adsorbed to the metal

surface and forms a complex $IrO_2(^{\cdot}OH)$.

$$IrO_2 + H_2O \rightarrow IrO_2(^{\cdot}OH) + H^+ + e^-. \tag{19.20}$$

When organic matters (R) are present, the active oxygen in the form of hydroxyl radicals can lead to the complete oxidation of organic pollutants (Eq. 19.21). Additionally, the active oxygen in the form of higher oxygen radicals can be used in selective oxidation process to produce specific products from organic pollutants (Eq. 19.22).

$$\frac{1}{2}R + IrO_2(^{\cdot}OH) \rightarrow \frac{1}{2}ROO + H^+ + e^- + IrO_2, \tag{19.21}$$

$$R + IrO_2(^{\cdot}O) \rightarrow RO + IrO_2. \tag{19.22}$$

When NaCl is added to enhance the electro-conductivity of the working solution, the chloride ion may also react with the active hydroxyl radical and produce a hypochlorite ion (Eq. 19.23).

$$IrO_2(^{\cdot}OH) + Cl^- \rightarrow IrO_2(^{\cdot}OCl) + H^+ + 2e^-. \tag{19.23}$$

Equations 19.24–19.26 describe the role of hydroxyl radicals in the oxidation of organic pollutants, which leads to the formation of carbon dioxide (CO_2) and water (H_2O) as the end products of this ongoing reaction. This process is further explained by Vahidhabanu and Babu (2015) in their research.

$$RH + (^{\cdot}OH) \rightarrow R^{\cdot} + H_2O, \tag{19.24}$$

$$R^{\cdot} + O_2 \rightarrow ROO^{\cdot}, \tag{19.25}$$

$$ROO^{\cdot} + R^1H \rightarrow ROOH + R^{1\cdot}. \tag{19.26}$$

Indirect Anodic Oxidation Reaction

This entails the formation of hypochlorous acid (HOCl) (Eq. 19.27) and the production and dissociation of the hypochlorite ion (OCl^-) (Eq. 19.28).

$$Cl_2 + H_2O \rightarrow H^+ + Cl^- + HOCl, \tag{19.27}$$

$$HOCl \leftrightarrow H^+ + OCl^-. \tag{19.28}$$

Cathodic Reaction

The cathodic reaction of EO process is given below (Eqs. 19.29–19.31) which shows the formation of hydrogen gas and chloride anions (Özyurt and Camcıoğlu 2018).

$$2H_3O^+ + 2e^- \rightarrow H_2 + 2H_2O \quad \text{(at acidic conditions)}, \tag{19.29}$$

$$2H_2O + 2e^- \rightarrow H_2 + 2OH^- \quad \text{(at alkaline conditions)}, \tag{19.30}$$

$$ClO^- + H_2O + 2e^- \rightarrow Cl^- + 2OH^-. \tag{19.31}$$

Furthermore, the role of hypochlorite in electrochemical treatment of dye effluent via chlorine generation is given below in Eq. 19.32.

$$\text{Dye} + OCl^- \rightarrow CO_2 + H_2O + Cl^- + \text{product}. \tag{19.32}$$

Evaluation of Optimum Operating Parameters Directly Powered by Solar Energy

Figure 19.9 shows that the highest level of solar irradiation recorded was approximately 493.7 Wm^{-2} at 1:12 p.m., and the corresponding temperature was 27 °C.

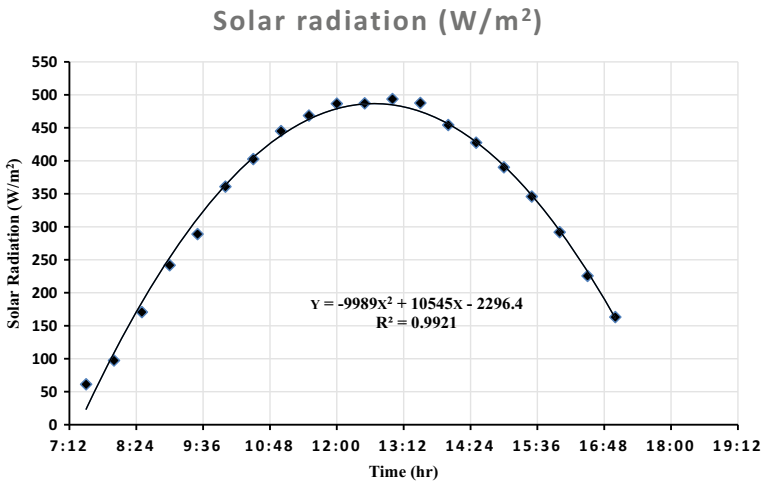

Fig. 19.9 Solar irradiation during the experimental treatment (start time at 08: 24 a.m. and finish time at 03:36 p.m.)

Table 19.6 Color removal efficiency (using solar power supply)

Parameter	Removal Efficiency (using conventional DC power source)		Removal Efficiency (using solar power source)	
	EC process (%)	Dual-stage EC–EO (%)	EC process (%)	Dual-stage EC–EO (%)
Color	89	97	85.45	96.22

The energy generated by the solar panel, as shown in (Fig. 19.9), and the energy used in the treatment system were determined to understand the available and used energy in textile wastewater treatment. The power generated by the PV panel, with a solar module efficiency of 85% (15% collection losses) for a one hour electrolysis time, reached the charge controller at 127.5 Wh. Additionally, the energy consumed by the dual-stage electrocoagulation and electrooxidation system was found to be 34.776 Wh.

To compare and evaluate the energy used by the treatment technology relative to the energy produced from the solar panel, that is, the yield of the energy received in the treatment system relative to the energy received in the PV module was calculated using Eq. 19.33.

$$\eta = \left(\frac{34.776}{127.5}\right) \times 100 = 27.28\%. \tag{19.33}$$

The results achieved with Eq. 19.33 indicate that the PV module supplied enough energy for the dual-stage electrocoagulation and electrooxidation treatment system. Thus, the surplus energy can be stored in a battery and used for other purposes.

The average color removal efficiency was 85.45% and 96.22% using the EC and dual-stage EC–EO processes, respectively (Table 19.6). The simple statistical test (Pocock 2006) shows no significant difference (with a P value of 0.036) in color removal efficiency using solar energy and conventional DC power.

Operating Cost Analysis

The analysis of operating costs is an important part of the experimental work that evaluates the feasibility of the large-scale treatment process. In this research study, the treatment cost, such as the cost of consumable chemicals (CC, NaCl), electrode cost (CE), energy consumption (En. C), and sludge disposal cost (SD), was considered to evaluate the operation costs. Accordingly, using the optimum working conditions and an applied voltage of 6 V for each process, applied current of 2.14 A for EC and 2. 016 A for dual-stage EC–EO, respectively, total Al and IrO_2/Ti electrode consumption 0.000299 and 0.0000020 kg or 0.502 kg/m^3, total cost of Al and IrO_2/Ti electrode 2.78 USD/kg (Al = 1.2 USD/kg, IrO_2/Ti = 1.58 USD/kg), the cost of 98% reagent grade of supporting electrolyte (NaCl) powder 0.06 USD/kg, and the total consumed

chemical was 2.5 g or 0.0025 kg/m^3 per each process. The current Ethiopian 2021 electricity price tariff is between 0.04 and 0.06 USD/kWh (on average, 0.05 US$/kWh). Results calculated from Eqs. 19.5–19.7 indicates that the total operating cost of the treatment method was estimated at 1.4 US$/$m^3$. The comparison of operating cost of this method is much lower than the coupled sequential EC and ozone (O_3) method, which costs 5.80 US$/$m^3$ for the treatment of textile wastewater effluent containing Black 5 reactive dye (Bilińska et al. 2019).

In addition to this, the operational cost of dual-stage EC–EO technology using IrO_2/Ti and Al electrodes is much lower than the total operating cost for dual-stage electrocoagulation and Fenton process (48.4 US$/$m^3$) (Gunawan et al. 2018).

Moreover, by utilizing the data for the dual-stage electrocoagulation and electrooxidation process and the information in Table 19.4, the overall cost for treating textile wastewater using direct energy was calculated to be 4.21 US$/$m^3$. This cost represents the initial capital cost per cubic meter of treated water. However, it is essential to note that the solar system incurs little to no energy bills and maintenance costs as compared to electricity. In contrast, Pirkarami et al. (2013) estimated that the total operating cost for the treatment of colored and actual industrial wastewater by electrocoagulation using solar energy was US$ 9.24/m^3.

Furthermore, since the volume of sludge produced from the dual-stage EC–EO process is minimal, we recommend disposing of it through incineration, which is estimated to cost 0.04 US$/kg. This is a cost-effective solution as it eliminates the need for landfilling and reduces the environmental impact of the waste.

Conclusions and Final Remarks

Strengths and Limitation

This study was performed at the laboratory scale under controlled conditions, providing a comprehensive evaluation of the performance of the dual-stage EC and EO treatment method. It aimed to provide a deeper understanding of the dual-stage electrocoagulation and electrooxidation process as a water treatment strategy, particularly in developing countries where advanced water management techniques may not be readily available. This experimental study has several strengths, including the evaluation of optimum operating conditions for real wastewater, analysis of treatment costs through detailed mechanistic studies, and the use of advanced instrumental techniques such as FT-IR and NMR spectroscopy. In light of the ongoing energy crisis and the effects of climate change, the availability of commercial energy from conventional energy sources may become uncertain. In this regard, the utilization of renewable energy sources such as photovoltaic energy in this research project is a notable strength. Despite the success of collecting and analyzing experimental data to achieve the research objective, this study met certain limitations, such as a lack of tools to characterize the surface morphology and surface area of flocs before and after

treatment. Another limitation of this study is that it was conducted under laboratory conditions in a controlled setting, which may not fully reflect the complexities and variations of real-world scenarios. Therefore, future research should focus on scaling up of the technology for field application, as well as transition from batch mode to continuous flow. The next priority of the potential study should be to investigate how the integrated EC–EO process performs at high hydraulic load rates in continuous flow mode.

Conclusions

The increasing global demand for water, driven by a rapidly growing population, is being further exacerbated by the indiscriminate release of pollutants from industries into water bodies. Among these polluting industries, the textile industry stands out as a significant contributor, consuming large quantities of dyes, hazardous chemicals, and water. Studies indicate that up to 56% of world's total synthetic dyes produced are consumed by the textile industry, leading to the release of large quantities of wastewater loaded with dyes into the environment. Conventional and biological treatment methods are often inadequate in effectively removing these synthetic dyes from wastewater, making it a pressing environmental concern that is drawing attention from researchers. Given the high demand for water and the negative impact of dye-laden wastewater on the environment, finding effective method for removing dyes from textile industry wastewater has become a crucial area of research.

Therefore, innovative and energy-efficient methods for treating dye-laden wastewater from textile industries need to be explored. Electrochemical technologies, such as electrocoagulation, electrooxidation, and the integration of both methods, have recently gained attention as a potential solution for hazardous dye-contaminated wastewater. This is due to their wide range of applications and environmentally friendly nature.

In this study, the effectiveness of the dual-stage electrocoagulation and electrooxidation (EC–EO) process in removing color, COD, and TOC from textile wastewater was successfully demonstrated. A Box-Behnken Design of the response surface methodology and second-order polynomial mathematical equations were used to determine the impact of various operating conditions on the treatment efficiency. The parameters such as initial pH, applied current density, electrolysis time, and initial dye concentration were optimized to achieve the highest removal efficiency of COD, TOC, and color from textile industry wastewater effluents.

- From the optimization results, the higher R^2 values (0.999) and the adequacy of the prediction (96%) indicate that the model predicted values are in good agreement with the actual data. This confirms that the generated second-order model equations can accurately predict the color, TOC, and COD removal by both EC and dual-stage EC–EO processes. Therefore, the developed quadratic

model can be used to optimize and evaluate different treatment methods applied to textile wastewater.

- The kinetic study of EC revealed that the second-order kinetic data is mostly in line with the experimental data. This result indicates that the chemisorption mechanism controls the removal of Vivizol red reactive dye.
- In addition, EC achieved the maximum removals efficiency (89% color and 76% COD) at 25 min electrolysis time and under optimal conditions of an initial dye concentration of 600 mg L^{-1}, a current density of 32.95 mA cm^{-2}, and an initial pH of 3. Likewise, under the optimized working conditions of a current density of 42 mA cm^{-2}, a pH of 4, and electrolysis time of 42 min, the dual-stage EC–EO processes attained 97% of both color and COD removal. The model output indicated that the interaction effect of current density with pH has little effect on the efficiency of the treatment method. The EC process resulted in a reduction of TOC from 122 mg L^{-1} to 63.7 mg L^{-1}, which is a 47% decrease in total concentration.
- However, complete mineralization was obtained by the dual-stage EC–EO treatment technology. From this, it can be concluded that the dual-stage of EC and EO can completely mineralize the pollutants from textile wastewater. The treated water can be reused for other purposes with small further water diagnostics. This is further supported by the FT-IR and ^{1}H and ^{13}C-NMR study, which shows that all organic contaminants are entirely degraded into carbon dioxide (CO_2) and water (H_2O). In addition, the results of the statistical analysis revealed that there was no significance difference in the removal efficiency of the treatment system using conventional electricity and solar power, making it a viable option for treating textile wastewater in areas where solar energy is readily available.
- Compared to other technology applied to textile wastewater effluent treatment, the operating cost of the proposed technology is less than the coupled EC and O_3 method, which costs 5.80 US$/$m^3$ for the treatment of textile wastewater effluent containing Black 5 reactive dye. In general, the results of this experimental study indicate that the dual-stage EC–EO technology using IrO_2/Ti and Al electrodes is a promising technology for the treatment of wastewater generated from the cotton textile industry.
- In general, the results of this experimental study demonstrate that the dual-stage EC–EO technology using IrO_2/Ti and Al electrodes is a promising solution for treating wastewater generated from the textile industry.

Recommendations

This study has demonstrated several findings and provided insights into the feasibility of the dual-stage EC–EO technology for textile wastewater treatment. However, some issues have emerged from this study and are the basis for the following recommendations:

- To consider all essential variables that affect the performance of the dual-stage EC–EO process in removing pollutants, future studies will need to explore a broader range of variables through multivariate analysis.
- Passivation of the electrodes to the surface of the aluminum electrodes was observed during the electrocoagulation process. Therefore, it will be beneficial to use perforated rather than metal plate electrodes to prevent the passivation of electrodes and allow free circulation of metallic ions in the electrolytic solution. Besides, frequently changing the polarity of electrodes could solve the problem of passivation.
- Future research should focus on evaluating the performance of the dual-stage EC–EO system in a continuous flow setup in order to better understand its potential for industrial application.
- This study's estimated cost for textile wastewater treatment under the optimized operating conditions of dual-stage electrocoagulation and electrooxidation appears to be high. This can be reduced by adjusting the current density and electrolysis time in the model equation, enabling a lower treatment cost to be obtained and tested in future studies.
- Solar rather than conventional electricity should be considered in this dual-stage electrocoagulation and electrooxidation process to reduce the running costs.

Acknowledgements The authors acknowledge all technical and financial support from the Africa Center of Excellence for Water Management (ACEWM), Addis Ababa University and Adama Science and Technology University. And also, for acknowledgment, Dr. Yonas Chebude for overall support and FT-IR Measurement and Dr. Mesfin Getachew for NMR measurements from the Department of Chemistry at the University of Addis Ababa.

References

Afanga H, Zazou H, Titchou FE, Rakhila Y, Akbour RA, Elmchaouri A, Ghanbaja J, Hamdani M (2020) Integrated electrochemical processes for textile industry wastewater treatment: system performances and sludge settling characteristics. Sustain Environ Res 30:1–11. https://doi.org/10.1186/s42834-019-0043-2

Amour A, Merzouk B, Leclerc JP, Lapicque F (2016) Removal of reactive textile dye from aqueous solutions by electrocoagulation in a continuous cell. Desalin Water Treat 57:22764–22773. https://doi.org/10.1080/19443994.2015.1106094

APHA (1998) Standard methods for the examination of water and wastewater, 20th edn. American Public Health Association, New York. https://doi.org/10.5860/choice.37-2792

Aquino JM, Rocha-Filho RC, Ruotolo LAM, Bocchi N, Biaggio SR (2014) Electrochemical degradation of a real textile wastewater using β-PbO2 and DSA® anodes. Chem Eng J. https://doi.org/10.1016/j.cej.2014.04.032

Asfaha YG, Tekile AK, Zewge F (2021) Hybrid process of electrocoagulation and electrooxidation system for wastewater treatment: a review. Clean Eng Technol 4:100261. https://doi.org/10.1016/j.clet.2021.100261

Asfaha YG, Zewge F, Yohannes T, Kebede S (2022a) Application of hybrid electrocoagulation and electrooxidation process for treatment of wastewater from the cotton textile industry. Chemosphere 302:134706. https://doi.org/10.1016/j.chemosphere.2022.134706

Asfaha YG, Zewge F, Yohannes T, Kebede S (2022b) Investigation of cotton textile industry wastewater treatment with electrocoagulation process: performance, mineralization, and kinetic study. Water Sci Technol 85:1549–1567. https://doi.org/10.2166/wst.2022.061

Ayhan Şengil I, Özdemir A (2012) Simultaneous decolorization of binary mixture of blue disperse and yellow basic dyes by electrocoagulation. Desalin Water Treat 46:215–226. https://doi.org/10.1080/19443994.2012.677554

Bhagawan D, Poodari S, Golla S, Himabindu V, Vidyavathi S (2016) Treatment of the petroleum refinery wastewater using combined electrochemical methods. Desalin Water Treat 57:3387–3394. https://doi.org/10.1080/19443994.2014.987175

Bilińska L, Blus K, Gmurek M, Ledakowicz S (2019) Coupling of electrocoagulation and ozone treatment for textile wastewater reuse. Chem Eng J 358:992–1001. https://doi.org/10.1016/j.cej.2018.10.093

Can OT, Bayramoglu M, Kobya M (2003) Decolorization of reactive dye solutions by electrocoagulation using aluminum electrodes. Ind Eng Chem Res 42:3391–3396. https://doi.org/10.1021/ie020951g

Chavana RB (2004) Environment-friendly dyeing processes for cotton. Indian J Fibre Text Res 26:93–100. https://doi.org/10.1533/9780857093974.2.515

Czitrom V (1999) One-factor-at-a-time versus designed experiments. Am Stat 53:126–131. https://doi.org/10.1080/00031305.1999.10474445

Dalvand A, Gholami M, Joneidi A, Mahmoodi NM (2011) Dye removal, energy consumption and operating cost of electrocoagulation of textile wastewater as a clean process. Clean: Soil, Air, Water 39:665–672. https://doi.org/10.1002/clen.201000233

Demir Delil A, Gören N (2019) Investigation of electrocoagulation and electrooxidation methods of real textile wastewater treatment. Anadolu Univ J Sci Technol Appl Sci Eng 20:80–91. https://doi.org/10.18038/aubtda.445716

García-García A, Martínez-Miranda V, Martínez-Cienfuegos IG, Almazán-Sánchez PT, Castañeda-Juárez M, Linares-Hernández I (2015) Industrial wastewater treatment by electrocoagulation-electrooxidation processes powered by solar cells. Fuel 149:46–54. https://doi.org/10.1016/j.fuel.2014.09.080

Ghasem A, Miri M, Nematollahi D (2017) Combined Electrocoagulation/electrooxidation process for the COD removal and recovery of tannery industry wastewater. Wiley Online Libr. 33:676–680. https://doi.org/10.1002/ep.12711

GilPavas E, Arbeláez-Castaño P, Medina J, Acosta DA (2017) Combined electrocoagulation and electro-oxidation of industrial textile wastewater treatment in a continuous multi-stage reactor. Water Sci Technol 76:2515–2525. https://doi.org/10.2166/wst.2017.415

Gunawan D, Kuswadi VB, Sapei L, Riadi L (2018) Yarn dyed wastewater treatment using hybrid electrocoagulation- Fenton method in a continuous system: technical and economical viewpoint. Environ. Eng. Res. 23:114–119. https://doi.org/10.4491/eer.2017.108

Gürses A, Yalçin M, Doar C (2002) Electrocoagulation of some reactive dyes: a statistical investigation of some electrochemical variables. Waste Manag 22:491–499. https://doi.org/10.1016/S0956-053X(02)00015-6

Hakizimana JN, Gourich B, Chafi M, Stiriba Y, Vial C, Drogui P, Naja J (2017) Electrocoagulation process in water treatment: a review of electrocoagulation modeling approaches. Desalination 404:1–21. https://doi.org/10.1016/j.desal.2016.10.011

Heffron J, Ryan DR, Mayer BK (2019) Sequential electrocoagulation-electrooxidation for virus mitigation in drinking water. Water Res 160:435–444. https://doi.org/10.1016/j.watres.2019.05.078

Ingelsson M, Yasri N, Roberts EPL (2020) Electrode passivation, faradaic efficiency, and performance enhancement strategies in electrocoagulation—a review. Water Res 187:116433. https://doi.org/10.1016/j.watres.2020.116433

Isik Z, Arikan EB, Ozay Y, Bouras HD, Dizge N (2020) Electrocoagulation and electrooxidation pre-treatment effect on fungal treatment of pistachio processing wastewater. Chemosphere 244:125383. https://doi.org/10.1016/j.chemosphere.2019.125383

Jain K, Shah V, Chapla D, Madamwar D (2012) Decolorization and degradation of azo dye—reactive Violet 5R by an acclimatized indigenous bacterial mixed cultures-SB4 isolated from anthropogenic dye contaminated soil. J Hazard Mater 213–214:378–386. https://doi.org/10.1016/j.jhazmat.2012.02.010

Kobya M, Can OT, Bayramoglu M (2003) Treatment of textile wastewaters by electrocoagulation using iron and aluminum electrodes. J Hazard Mater 100:163–178. https://doi.org/10.1016/S0304-3894(03)00102-X

Macpherson JV (2015) A practical guide to using boron doped diamond in electrochemical research. Phys Chem Chem Phys 17:2935–2949. https://doi.org/10.1039/c4cp04022h

Nair AT, Makwana AR, Ahammed MM (2014) The use of response surface methodology for modelling and analysis of water and wastewater treatment processes: a review. Water Sci Technol 69:464–478. https://doi.org/10.2166/wst.2013.733

Nasrullah M, Singh L, Wahid ZA (2012) Treatment of sewage by electrocoagulation and the effect of high current density. Energy Environ. Eng. J. 1:27–31

Oukili K, Loukili M (2019) Optimization of textile azo dye degradation by electrochemical oxidation using Box-Behnken design. Mediterr J Chem 8:410–419. https://doi.org/10.13171/mjc851907103ko

Özyurt B, Camcıoğlu Ş (2018) Applications of Combined electrocoagulation and electrooxidation treatment to industrial wastewaters. Wastewater Water Qual. https://doi.org/10.5772/intechopen.75460

Pirkarami A, Olya ME, Tabibian S (2013) Treatment of colored and real industrial effluents through electrocoagulation using solar energy. J Environ Sci Heal Part A Toxic Hazard Subst Environ Eng 48:1243–1252. https://doi.org/10.1080/10934529.2013.776890

Pocock SJ (2006) Statistics in practice. The simplest statistical test: How to check for a difference between treatments. Br Med J 332:1256–1258. https://doi.org/10.1136/bmj.332.7552.1256

Raju GB, Karuppiah MT, Latha SS, Parvathy S, Prabhakar S (2008) Treatment of wastewater from synthetic textile industry by electrocoagulation-electrooxidation. Chem Eng J 144:51–58. https://doi.org/10.1016/j.cej.2008.01.008

Rodríguez-Vidal FJ, Ortega-Azabache B, González-Martínez Á, Bellido-Fernández A (2022) Comprehensive characterization of industrial wastewaters using EEM fluorescence, FT-IR and 1H NMR techniques. Sci Total Environ 805. https://doi.org/10.1016/j.scitotenv.2021.150417

Sánchez-Sánchez A, Tejocote-Pérez M, Fuentes-Rivas RM, Linares-Hernández I, Martínez-Miranda V, Fonseca-Montes De Oca RMG (2018) Treatment of a textile effluent by electrochemical oxidation and coupled system electooxidation- salix babylonica. Int J Photoenergy 2018:1–12. https://doi.org/10.1155/2018/3147923

Shah AR, Tahir H, Ullah HMK, Adnan A (2017) Optimization of electrocoagulation process for the removal of binary dye mixtures using response surface methodology and estimation of operating cost. Open J Appl Sci 07:458–484. https://doi.org/10.4236/ojapps.2017.79034

Shan R, Zhang Z, Kan M, Zhang T, Zan Q, Zhao Y (2015) A novel highly active nanostructured IrO_2/Ti anode for water oxidation. Int J Hydrogen Energy 40:14279–14283. https://doi.org/10.1016/j.ijhydene.2015.04.071

Vahidhabanu S, Babu BR (2015) Degradation of C.I. reactive dyes (Yellow 17 and Blue 4) by electrooxidation. Int J Waste Resour 05. https://doi.org/10.4172/2252-5211.1000190

Yılmaz Nayır T, Kara S (2018) Container washing wastewater treatment by combined electrocoagulation–electrooxidation. Sep Sci Technol 53:1592–1603. https://doi.org/10.1080/01496395.2017.1411365

Yoon Y, Cho E, Jung Y, Kwon M, Yoon J, Kang JW (2015) Evaluation of the formation of oxidants and by-products using Pt/Ti, RuO_2/Ti, and IrO_2/Ti electrodes in the electrochemical process. Environ Technol (united Kingdom) 36:317–326. https://doi.org/10.1080/09593330.2014.946098

Zou J, Peng X, Li M, Xiong Y, Wang B, Dong F, Wang B (2017) Electrochemical oxidation of COD from real textile wastewaters: kinetic study and energy consumption. Chemosphere 171:332–338. https://doi.org/10.1016/j.chemosphere.2016.12.065

Chapter 20
Hydrochemical Suitability of High Discharge Springs for Domestic and Irrigation Purposes in the Upper Blue Nile Basin, Ethiopia

Gashaw Gebey Addis and Sileshie Mesfin Leyew

Abstract This study shows the physio-chemical suitability of high discharge springs for domestic, livestock, and irrigation use in the Upper Blue Nile Basin, Ethiopia. Temperature, electrical conductivity (EC), total dissolved solids (TDS) and pH were measured during field investigation and in laboratory analysis. The results showed that the mean concentrations of cations (Na, Ca, K and Mg) were 14.66, 20.96, 5.32 and 12.35 mg/l, respectively, while those of anions (Cl, HCO_3, SO_4 and NO_3) were 5.08, 154.67, 1.84 and 12.17 mg/l, respectively. The mean concentrations of total hardness, alkalinity, TDS, EC and pH were 140.68 mg/l, 148.33 mg/l, 291.82 mg/l, 460.45 μ and 7.15, respectively. Based on the concentration of ions, CSPG1 and CSPG2 were found to be $Ca^{2+} > Na^{+} > Mg^{2+} > K^{+}$. Birshelko, Tikurit, Lomi and AND3 springs have abundant cations $Ca^{2+} > Mg^{2+} > Na^{+} > K^{+}$, while TSS1 springs have $Mg^{2+} > Ca^{2+} > Na^{+} > K^{+}$, which are located in the Infranz and Andasa sub-basins. In the springs of TBL_SPG2, TBL_SPG3 and TBL_SPG4, which originate along the Birr sub-basin, the concentrations of cations were $Na^{+} > Ca^{2+} > K^{+} > Mg^{2+}$, while the concentrations of anions from all springs were $HCO_3 > NO_3 > Cl > SO_4$. Three major water types were identified, which are Ca–Mg–HCO_3, Mg–Ca–HCO_3 and Na–Ca–HCO_3, which label springs as fresh (shallow) groundwater, transitional (mixed) groundwater and regional (alkaline) water type. The concentration of hardness except TBL_SPG4 (Geray) spring, the rest are moderately hard to hard water type which consume more soap and scaling the pipe of water supply source. Except for CSPG1, CSPG2 and Lomi spring, the concentration of K is unsuitable for domestic purposes and is above the permissible limits of the WHO and Ethiopian Standards. CSP1, CSPG2, ASPG1 and Lomi springs show high NO_3 concentrations that desire to be protected from uncontrolled sewerage systems and agricultural activity.

Keywords Hydrochemical characteristics · High discharge springs · Upper Blue Nile · Northwestern Ethiopian

G. G. Addis (✉) · S. M. Leyew
Amhara Design and Supervision Works Enterprise (ADSWE), Bahir Dar, Ethiopia
e-mail: gashawhg219@gmail.com

A. M. Melesse et al. (eds.), *Land and Water Degradation in Ethiopia*, Springer Geography, https://doi.org/10.1007/978-3-031-60251-1_20

Introduction

Groundwater flows through geological materials as it moves along its path from recharge to discharge areas. As a result of hydrogeochemical processes such as dissolution, precipitation, and ion exchange processes that occur in such flows and the residence time along the flow path, groundwater contains a wide variety of dissolved inorganic chemical constituents.

Natural resources are degraded continuously due to rapid population explosion, global climate change, poor management and misunderstanding of the nature of resources, which results from a lack of coordination and integrated approaches. Among all, water is the prime natural resource that is basic for the healthy functioning of any ecosystem. Groundwater chemistry and its influence on groundwater quality is an important facet of hydrogeological investigations. Groundwater chemistry is controlled by hydrogeochemical processes that occur as groundwater interacts with rocks (Sawyer and McMcartly 1967; Stumm and Morgan 1996).

Groundwater, found filling interstices within geological materials (rock and soil particles) and needing permeable media for its economical exploitability, is very challenging since it is invisible. Any water resource planning and management options should start with resource quantification and suitability assessment. The physiochemical characteristics of groundwater can be affected by anthropogenic impacts (Bawoke and Anteneh 2020).

Springs vary in their yields and their water storage to meet the meet municipal, industrial, and large commercial and agricultural needs. Springs vary by their discharge, annual fluctuation of discharge, discharge regime, lithology of the recharge basin, spring water chemistry and others (Soulios 2010).

Most of the domestic water supply source in Ethiopia comes from groundwater sources. The total available groundwater in the country is not yet known with certainty. Rural communities mostly use unprotected springs and hand-dug wells. Other groundwater sources for some communities include shallow-drilled wells, deep-drilled wells, ponds, lakes, streams, and rivers. Roof water harvesting techniques are used to capture rainwater when there is rain (MoWE 2002).

The dominant water type of the Andasa area, Upper Blue Nile Basin, was found to be the Ca–HCO_3 type, which covers 59.69% of the area, resulting from incongruent dissolution and weathering of silicate minerals that can be aggravated by dissolved CO_2, and this water type is linked with groundwater recharge zones of the area (Taye et al. 2021). Good to poor water types are exposed in northern portions around waste disposal landfill sites, urban centers and irrigated areas, while very poor to unsuitable water types are spatially distributed on the northeastern tips of the area, representing highly evolved water types (Taye et al. 2021). Tikurit AND3 and TSS1 are found in the Andasa and Tull catchments south of Bahir Dar. According to the results, Tikurit spring is located in the northern parts of the Andasa catchment south of the waste disposal sites with a concentration of nitrate of 14.6 mg/l and AND3 is found in the southwest parts of the catchment at the head of the Ezana River with extensive

farmland with a NO_3 concentration of 11.5 mg/l, and TSS1 is located south of the catchment at the riverbanks of Abay with a NO_3 concentration of 12.5.

The geology of northwestern Ethiopia is dominantly covered by tertiary volcanics and shield volcanics. The groundwater in northwestern Ethiopia is controlled by geological and structural integrity. The water quality of springs, surface water bodies and groundwater is governed by the local geological nature due to ion exchange through its migration path. Shield volcanic rocks (Simen, Chokie, and Guna) are found in the study area and act as major groundwater recharge areas. The petrology, geochemistry and isotopic compositions of lavas have ages ranging from 30 to ~10 Ma, or from the peak of flood volcanism to the onset of major rifting in the northern part of the volcanic plateau (Kieffer et al. 2004).

The Northern Ethiopian Plateau (Fig. 20.1) mainly consists of tholeiitic to transitional basaltic lavas (Mohr and Zanettin 1988), which erupted at 30 Ma in a period of 1 Myr or less (Hofmann et al. 1997). The basalts cover an area of 210,000 km^2 with a lava pile up to 2000 m thick in the central-eastern part, thinning to less than 500 m toward the northern and southern boundaries.

The Cenozoic is characterized by extensive faulting accompanied by widespread volcanic activity and uplift. The outpouring of vast quantities of basaltic lava accompanied by the eruption of large amounts of ash resulted in a basaltic plateau often called trap series basalts. Several shield volcanoes, also consisting of alkali basalts and fragmental material, cover the center and the upper part of the Blue Nile basin. Over two-thirds of the Upper Blue Nile is covered by Cenozoic basalts and ashes. The mineralogical compositions of the basalts are spatially variable, but all the basalt types

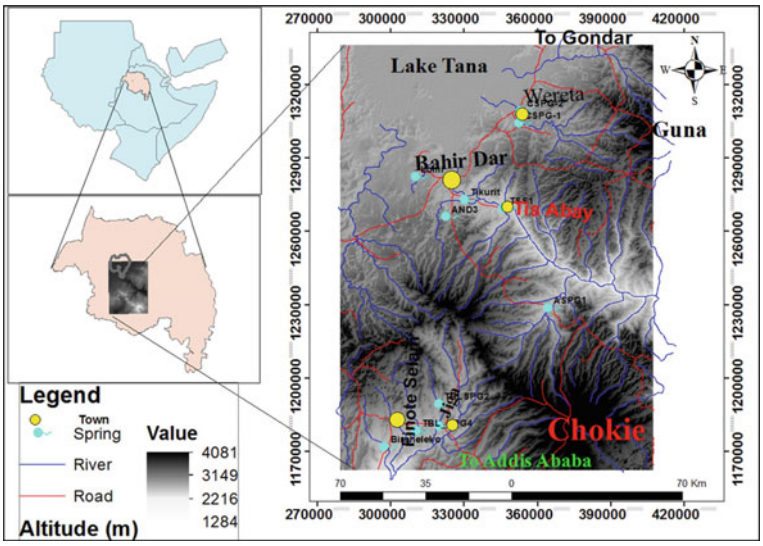

Fig. 20.1 Location map of high discharge springs in the Upper Blue Nile basin

contain dominantly olivine and clino pyroxenes with minor but variable amounts of plagioclase, K-feldspars, and brown glass (Pik et al. 1998).

General Description of the Study Area

Location and Accessibility

Location

These high discharge springs are found in northwestern Ethiopia in the Blue Nile drainage basin between 10 to 13° N Latitude and 36 to 38° E Longitude. Some of the springs are found within the Tana basin associated with Guna and Sekela Shield volcanism, while the other springs are found in the southwestern parts of the study area associated with Chokie Shield volcanism.

The geology of the area where the high discharge springs started to outflow are both tertiary and quaternary volcanics. TBL_SPG2, TBL_SPG3, Birshelko, Lomi and Tikurit are found within quaternary volcanic rocks, whereas CSPG1, CSPG2, TSS1 and AND3 are found at the contact between tertiary and quaternary volcanic rocks, and Aveya Spring is found in the lower basalt. The discharge of these springs is between 30 and 400 l/s (Kebede 2013).

All springs are found in the Upper Blue Nile basin. TBL_SPG2, TBL_SPG3, TBL_SPG4, Aveya_SPG and Birshelko springs are found in the southwestern part of the study area and emanate along the Birr sub-basin associated with the Sekela and Chokie shield volcanoes, while Lomi, Tikurit, AND3, TSS1, CSPG1 and CSPG2 springs are found in the north and northeast of the study area following the Infiranz, Gumara, Andasa and Tull drainage catchments within the Upper Blue Nile basin associated with Guna and Sekela shield volcanism. The discharge of these springs is between 30 and 150 l/s and serves as a water supply source for Bahir Dar, Kinbaba, Tis Abay, and Bebeks towns and irrigation activity by local peoples.

Accessibility

All springs are accessed through all weathered gravel and asphalt roads. TBL_SPG3, ASPG1, Tikurit, and AND3 springs are accessed through asphalt roads that run from Bahir Dar to Debere Marko through Funote Selam and Bahir Dar-Adet-Mota. The springs are located approximately 0.5–1 km from the main asphalt through all weathered gravel roads. Lomi spring is accessed through all weathered gravel roads that run from Bahir Dar Kunzila Shahura gravel road, and CSPG1 and CSPG2 springs are accessed through asphalt and all weathered gravel roads from Bahir Dar to Wereta and Wereta to the spring. The TSS1 spring is accessed through all weathered gravel roads from Bahir Dar to Tis Abay town.

Physiography and Drainage

The physiography of the area is shaped by volcanic tectonic activity on a plain escarpment and plateau. The altitude of the study area is between 1284 and 4081 m in the Abay gorge and Chokie shield volcanic massif, respectively.

The drainage type in the study area is the radial drainage type, and some trellis-type drainage radiates from Mount Guna and Chokie shield volcanism (Fig. 20.1). Based on altitude, the climate of the Upper Blue Nile is found in the warm temperate to cool climatic zone. These high discharge springs are located within an altitude range from 1604 to 1881 m.a.s.l. According to the National Atlas of Ethiopia climate classification, the upper part of the study area is situated in a temperate climatic zone.

Objective

The general objective of this study is to characterize the hydrochemical suitability of high discharge springs for domestic, livestock and irrigation purposes in the Upper Blue Nile basin.

Methodology and Material

Data Collection

To assess the hydrochemical suitability of high discharge springs in the Upper Blue Nile basin for domestic, irrigation and livestock purposes classified in data collection, measuring and sampling and analysis and interpretation of the data at the office level. Since the assessment was conducted on high discharge springs, the duration of assessment and measurements of discharge and in situ test were conducted during the dry season in April and May 2011. Collection of previous works, M.Sc. papers, Ph.D. theses and scientific journals related to these high discharge springs in the Upper Blue Nile River basin. A 1:25,000 geological map was collected from a geological survey of Ethiopia and the Amhara Water Irrigation and Energy Bureau to locate these springs. The advantage of springs was evaluated during field investigation. Collection and analysis of spring types, spring discharge and nature of appearance of those high discharge springs are analyzed during field investigation. Most springs are developed and used for domestic and irrigation purposes, so they are suitable to measure the discharge of springs by using floating and known volumes of containers. Sampling bottles, water quality test kits and handheld Garmin GPS and cameras were used during the field investigation.

Floating methods were used for springs TSS1, TBL2, CSPG1, CSPG2 and Birsheleko, while the other high discharge springs, which are Aveya, TBL_SPG3,

AND3 TBL_SPG4, Lomi and Tikurawuha, are not suitable for measuring the discharge. From previous studies, all springs are measured, and in this study, the estimated discharge is similar to that in previous studies.

Sampling and In Situ Test

Water samples were collected systematically from the high discharge springs in the area, which included in situ measurement of some parameters, such as pH, EC, *T* and TD, using a standard water quality test kit (HANNA). The test kit was calibrated by using diluted or distilled water to avoid contamination. During sampling and in situ testing, the spring types, soil type and geological formation around the spring location were characterized and used to validate the current geological map of the study area.

After in situ measurement of physical parameters, sampling of springs was conducted by using plastic bottles. Two litter samples were collected for laboratory analysis to characterize the chemical behavior or properties of the aquifer to determine the suitability of the spring water for domestic, livestock and irrigation activities.

Data Analysis and Interpretation

The major cation and anion measurements were carried out by the Amhara Design and Supervision Works Enterprise (ADSWE) laboratory. Common cations (Na^+, Ca^{2+}, K^+ and Mg^{2+}) were analyzed by using atomic absorption, and the other anions (Cl^-, HCO_3, NO_3, SO_4), total hardness, and total alkalinity were measured by using a colorimeter or photometer. The pH, EC and TDS were measured by using pH and EC meters. Those measured and analyzed samples in the laboratory were also interpreted by using Aquachem 4.0 and Microsoft Excel software to understand the water type, alkalinity, and total hardness of the samples or high discharge springs and to check the suitability for the main objective.

Sodium Absorption Ratio (SAR): SAR is a measure of groundwater suitability for use in agricultural irrigation activities (Sen 1995). The Na^+ concentration can reduce the soil permeability and soil structure (Todd 1980). The sodium adsorption ratio (SAR) is a measure of alkali/sodium hazard to crops and can be estimated by the following formula.

$$\mathrm{SAR} = \mathrm{Na}^+ / \left(\left(\mathrm{Ca}^{2+} + \mathrm{Mg}^{2+} \right) / 2 \right)^{1/2}. \tag{20.1}$$

Hydrochemical Facies

Different graphical presentations were used to infer hydrogeochemical facies from physicochemical parameters of water sample analysis. To understand the water type group or hydrochemical facies, a Piper diagram (Fig. 20.5) was used to interpret and analyze the mixing of water samples. Stiff (1951) proposed another way of presenting chemical analysis data, in which he used four parallel axes and one vertical axis to represent the chemical analysis. The Stiffs method may be useful in comparing water, especially highly mineralized zones, is simple to use and can be varied to suit the water being studied. Stiff patterns are useful in making a rapid visual comparison between water from different sources (Figs. 20.6, 20.7 and 20.8). Microsoft Excel is easily applicable software for all water-related sciences. In the current study area, this software was used to analyze the temperature, TDS and pH values of field and laboratory data to create a clear view.

Suitability of Springs

The suitability of high discharge springs for domestic, livestock and irrigation purposes was evaluated based on Ethiopian water quality standards (ES 261 2001) and World Health Organization (WHO) guidelines. Salinity, sodicity, and related parameters were considered to evaluate the suitability of the groundwater for irrigation use. Conductivity is the measure of the salinity hazard involved in the use of water for irrigation. Salinity and sodium hazards of the study area are also assessed based on the salinity classification standard of the US Department of Agriculture diagram or Wilcox plots (Wilcox 1955).

Geology and Hydrogeological Setup of Northwestern Ethiopia

The Gorge of the Nile exposes a thick section of Mesozoic sedimentary rocks that includes Lower Sandstone, Lower Limestone, Upper Limestone, and Upper Sandstone overlain by Middle Oligocene-Early Miocene and quaternary volcanic rocks (Gani et al. 2009). The Blue Nile forms a ~ 150 km semicircular loop around tertiary–quaternary shield volcanoes (Mts. Choke, Yacandach and Gish) (Gani et al. 2009) referred to this area as the Blue Nile Bend.

Lake Tana appeared Ca and Ma, marked by the deposition of lignitiferous sediments (Chorowicz et al. 1998). Fault-slip indicators are consistent with crustal subsidence centered on the present morphologic basin (Chorowicz et al. 1998).

The Choke shield volcano is a broad flat symmetrical shield made up dominantly of lava flows that extend radially out from the central conduit with dips of less than 5°

(Kieffer et al. 2004). Felsic rock trachytic and rhyolitic flows and fragmental units are limited to the upper 300–400 m of the present volcano. The northwestern traps consist of a series of Late Eocene and Oligocene fissure basalts, covered by Miocene shield volcanoes (Hofmann et al. 1997). Lavas belonging temporally to the Aden Volcanic Series cover an area of at least 3000 km^2. South of Lake Tana with a thickness of 100 m at Tis Isat fall (Mohor 1971), their centers of extrusion extend from the region of Bahar Dar to Burie, south of Enjabara. The most extensive occurrences of these more recent lavas are found along a N.N.E.–S.S.W. belt between the southern shores of Lake Tana and the Abay River west of Debra Markos. N.E. and N.W. of Burie, young lavas extruded from cones flowed southwards down tributary gorges of the Abay (Mohor 1971).

Quaternary volcanic rocks are classified as moderately to highly productive unconfined aquifers (Mamo 2015; Mamo et al. 2016; Chernet 1993; Kebede 2013). The productivity of middle basalt is relatively higher than that of the lower basalt with columnar jointed basaltic units.

The thick succession of volcanic and consolidated sediments has alternating layers of pervious and impervious layers that cause the emergence of many springs in the highlands of Ethiopia (Chernet 1993; Kebede 2013). Low-permeability tertiary volcanics outcrop in the area downstream of the major springs, which are Lomi springs and are underlying in the wetland area (Nigate et al. 2020). Regional flows from aquifers are the source of high discharge springs. Spring discharge in the quaternary basalt aquifer ranges from 1 to 108 l/s (Mamo 2015).

Most of the waters within the basic and acidic volcanic provinces are dominated by Ca–Mg and Na ions, respectively. Calcium is an essential constituent of many igneous rock minerals, especially in the silicates pyroxene, amphibole and feldspar. In the volcanics, the main sources of these ions come from the basic volcanics (Ayenew 2005).

Basalts mainly consist of plagioclase and ferromagnesian minerals rich in Ca and Mg, which weather rapidly. The release of Mg from olivine is several times faster than the release of Ca and Na from plagioclase (Singhal et al. 1999). Highly weathered and altered basalts generate Mg-rich waters.

AND3 (Kinbaba) Tikurit, TSS1 (Avrajit) and Lomi springs are located in the lowlands of the Tana depression. The water type of these high discharge springs has high concentrations of Mg and Ca, which leach from the contact of the geological units. The Bahar Dar springs are represented by two main springs (the Lomi and Areke springs) with very high yields (between 75 and 150 l/s) that are used for the Bahar Dar water supply (Figs. 20.2 and 20.3).

Fig. 20.2 **a** Birsheleko spring, **b** TBL_SPG3 (Jiga spring), **c** TBL_SPG4, **d** TSS1 springs, **e** CSPG1 and **f** AND3 springs

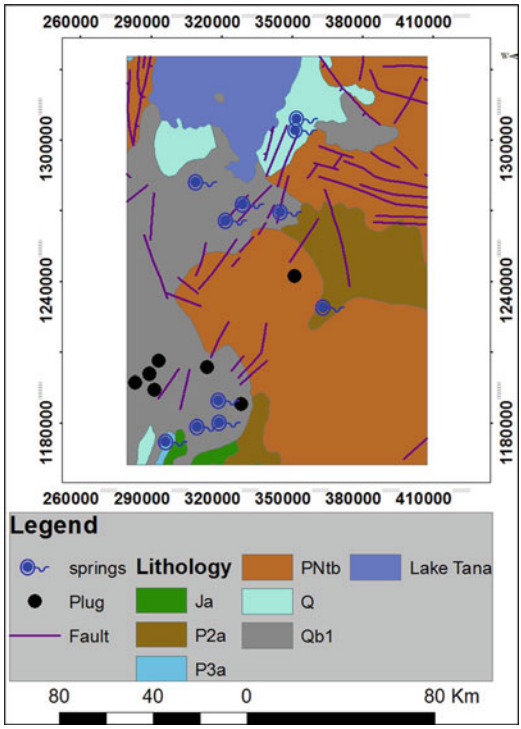

Fig. 20.3 Geological map of the study area after the Geological Survey of Ethiopia (2011)

Results and Discussion

Results

The pH value of these high discharge springs is between 6.1 and 7.8, while the temperature values are 22.9–26.70 °C. The total dissolved solids of the high discharge springs measured during the field investigation and laboratory were between 96 and 575.3 mg/l, while the electrical conductivity values were between 192 and 885 μS/cm. Both laboratory and in situ test results are described in Table 20.1. Cations and anions were analyzed by atomic absorption ratio and photometer. The results of those common ions (cations and anions) were analyzed in the laboratory, and the concentrations are shown in Table 20.2.

Correlation analysis of chemical parameters: To assess the sources of dissolved salts in the groundwater, eight chemical parameters, as shown in Table 20.3, expressed in mg/l, except pH, were used for the correlation analysis. HCO_3 has a strong positive correlation with Ca and Mg, which indicates that the groundwater is from basic groundwater. Mg has a strong positive correlation ($r = 0.82$) with Ca, which is the result of the hydrolysis of silicate minerals sourced from weathered basalt in the study area. TDS and EC have strong positive correlations with Ca, Mg, Cl and HCO_3 with abundant concentrations in groundwater or springs.

Statistics: The average cation concentrations of Na, Ca, K and Mg are 14.98, 18.93, 4.39 and 10.63 mg/l, respectively, which indicates that Ca, Na and Mg are more abundant in spring water. The minimum and maximum concentrations of chemical elements are described in Table 20.4.

Table 20.1 In situ and laboratory tests of physical parameters

ID	Sub-basin/ locality	Laboratory test			In situ test			
		TDS (mg/l)	EC (μS/cm)	pH	TDS (mg/l)	EC (μS/cm)	pH	*T* (°C)
AND3	Andasa	249.6	384	7.62	140	280	6.78	22.9
CSPG1	Gumara	136.5	210	7.8	140	280	6.4	24.9
CSPG2	Gumara	129.7	200	7.71	120	250	6.6	23.7
Birsheleko	Birr	517.5	796	7.6	250	490	7.25	25.2
Tikurit	Andasa	163.5	327	7.13	163.5	327	7.13	23.1
TSS1	Tull	575.3	885	7.47	340	650	7.45	24.5
Lomi	Infranz	96	192	6.53	96	192	6.53	26.1
TBL_SPG3	Birr	263	411	6.3	130	260	7.13	23.4
TBL_SPG4	Birr	201.5	310	6.75	90	190	7.59	23.4
TBL_SPG2	Birr	286	440	6.1	140	290	7.25	26.7
Aveya_SPG	Aveya	591.5	910	7.61	350	700	7.3	24.3

Table 20.2 Analyzed chemical ions in the laboratory

ID	Sub-basin	Na	Ca	K	Mg	Cl	HCO_3	SO_4	NO_3	F	Total hardness	Alkalinity	Data source
AND3	Andasa	7.2	17.5	7.5	9.4	2.4	121.5	2.3	11.5	0.32	**130**	**110**	This study
CSPG1	Gumara	20.32	23.4	1.1	6.8	1.7	145.72	0.3	17.9	0.16	**110.6**	**125.5**	This study
CSPG2	Gumara	18.2	18.3	1.4	4.1	1.2	110.4	0	16.3	0.2	**80.5**	**54.5**	This study
Birsheleko	Birr	6.4	31.3	3.5	21.4	6.4	205.4	3.1	7.6	0.37	**180**	**215**	This study
Tikurit	Andasa	12	23	2.2	18	4	185	5	14.6	0.16	**131.3**		MoWE (2012)
TSS1	Tull	10.8	27.5	15.3	32.5	12	248.1	3.1	12.5	0.31	**200**	**255**	This study
Lomi	Infranz	8	14	1.2	9	1	99	3.2	14.4	0.12	**71.9**	218	MoWE (2012)
TBL_SPG3	Birr	25.8	13.2	1.6	2.1	6.6	118.5	0.5	5.5	0.32	**115**	**110**	This study
TBL_SPG4	Birr	19.5	7.5	4.3	1.2	7.3	67.6	7.3	3.3	0.14	**70**	**65**	This study
TBL_SPG2	Birr	21.6	13.6	5.8	1.8	3.4	112.5	1.2	9.5	0.24	**85**	**105**	This study
Aveya_SPG	Aveya	11.4	41.3	14.6	29.5	9.9	287.6	0.3	20.8	0.41	224.2	**295**	This study

Table 20.3 Correlation coefficient of the chemical constituents

Correlation coefficient										
	Na	Ca	Mg	Cl	HCO_3	NO_3	SO_4	TDS	Cond	pH
Na	1.00	− 0.52	− 0.66	− 0.01	− 0.45	− 0.22	− 0.29	− 0.31	− 0.35	− 0.44
Ca		1.00	**0.82**	0.25	**0.91**	0.39	− 0.20	**0.59**	**0.62**	**0.68**
Mg			1.00	0.58	**0.94**	0.20	0.14	**0.72**	**0.77**	0.45
Cl				1.00	0.56	− 0.53	0.28	**0.80**	**0.81**	− 0.05
HCO_3					1.00	0.23	− 0.10	**0.74**	**0.78**	0.46
NO_3						1.00	− 0.34	− 0.35	− 0.33	0.51
SO_4							1.00	− 0.04	− 0.01	0.00
TDS								1.00	1.00	0.17
Cond									1.00	0.16
pH										1.00

Table 20.4 Statistics of high discharge springs in the study area

Statistics of chemical composition of springs							
	Min	Max	Average	St. dev.	Dev. coeff.	Var%	Sample No
Na	6.40	25.80	14.98	6.91	46.11	75	10
Ca	7.50	31.30	18.93	7.32	38.65	76	10
K	1.10	15.30	4.39	4.40	100.16	93	10
Mg	1.20	32.50	10.63	10.27	96.64	96	10
Cl	1.00	12.00	4.60	3.48	75.61	92	10
HCO_3	67.60	248.10	141.37	55.14	39.00	73	10
NO_3	3.30	17.90	11.31	4.77	42.21	82	10
SO_4	0.00	7.30	2.60	2.29	88.10	100	10
TDS	96.00	575.30	261.86	162.73	62.15	83	10
Cond	192.00	885.00	415.50	241.39	58.10	78	10
pH	6.10	7.80	6.71	6.58	98.09	22	10

The average concentrations of ions in the high discharge springs are 55.14, 4.77, 3.48 and 2.29 mg/l for HCO_3, NO_3, Cl and SO_4, respectively. HCO_3 is the highest anion in the water, and NO_3 is the second most concentrated anion in the springs.

Discussion

Temperature (*T*): The temperature of these springs is between 22.9 and 26.1 °C. From Vijverberg et al. (2009), it is possible to understand that water temperature increases with decreasing altitude. The lower limits of thermal water are 25–32 °C (Guzo 1974). The temperatures of springs located at higher elevations AND3 (1881) and CSPG2 (1838 m) are 22.9 and 24.9 m, respectively. Springs at lower elevations TSS1 (1604) and Aveya (1673 m) are 24.5 and 24.3 °C, respectively. The average temperature of these springs is 24 °C, and these springs are classified as cold springs and suitable for domestic irrigation and agricultural activities.

Total Dissolved Solids (TDS): The sum of dissolved constituents' concentrations in a water sample is known as the total dissolved solid (TDS) (Sen 1995). TDS is composed of solid residue made up mostly of inorganic elements and small amounts of organic material. It is obtained after evaporating a certain amount of groundwater volume. TDS up to 500 mg/l is the most desirable, and up to 1500 mg/l is the permissible maximum. TDS values up to 5000 mg/l are acceptable for livestock purposes (AGRI-FACTS 2007). The total dissolved solids of the springs are between 90 and 350 mg/l with an average value of 178.13 mg/l and 96–591.5 mg/l (Table 20.4) with an average of 291.8 mg/l from field measurements and laboratory results, respectively. According to the WHO and AGRI-FACTS standards, the TDS values of those springs are under the highest desirable limits for domestic and livestock purposes.

The electrical conductivity values of these springs are between 190 to 700 and 192 to 910 μS/cm from in situ and laboratory tests, respectively. These electrical conductivity values are suitable for domestic, livestock and irrigation purposes (Fig. 20.4).

Alkalinity: The alkalinity of water is a measure of its capacity to neutralize acids and is due primarily to the presence of bicarbonates. According to this study, the alkalinity values of the springs are found to be between 65 and 255 mg/l, which are under the permissible limits for domestic, irrigation and livestock purposes.

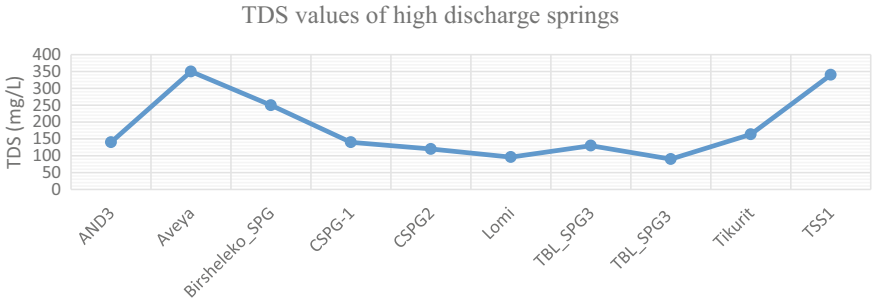

Fig. 20.4 TDS values of high discharge springs

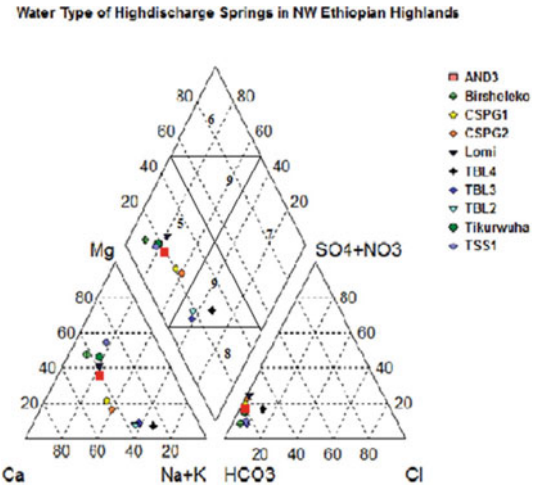

Fig. 20.5 Piper diagram of high discharge springs

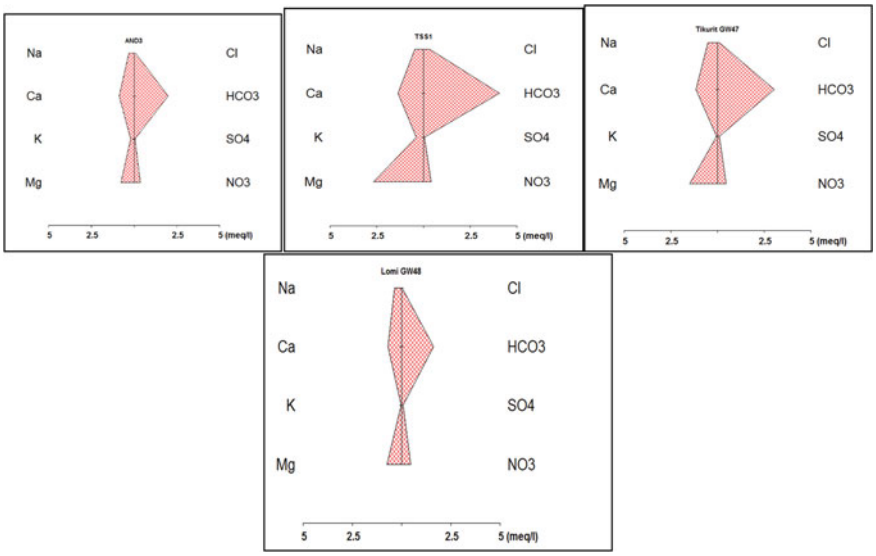

Fig. 20.6 Stiff diagram of high discharge springs in the Andasa and Infiranz sub-basins

Hardness: The concentration of total hardness is between 70 and 200 mg/l. Based on the hardness classification (Sawyer and McCarty 1967) of water TBL_SPG4 springs, Geray spring is classified as soft water with a total hardness of 70 mg/l. The remaining high discharge springs have hardness values between 75 and 150 mg/l, which are classified as moderately hard water, while the TSS1 (Avrajit) spring has a total hardness value of 200 mg/l, which is classified as hard water.

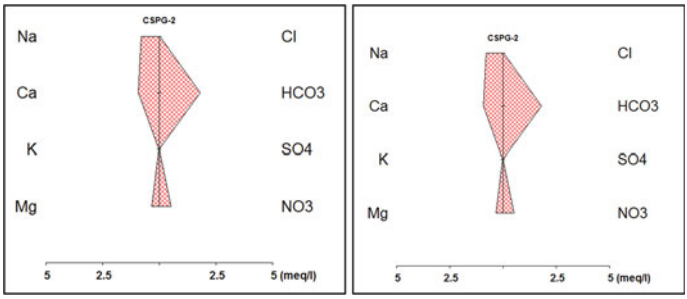

Fig. 20.7 Water type by Stiff diagram of high discharge springs in the Gumara sub-basin

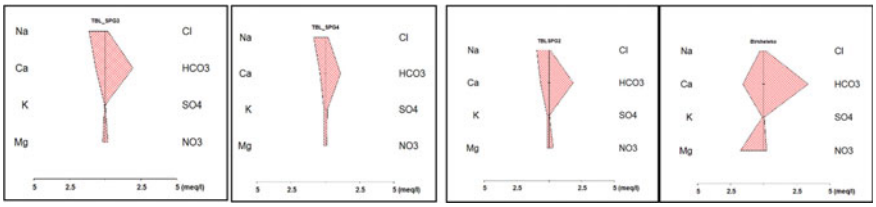

Fig. 20.8 High discharge springs in the Birr sub-basin by using a Stiff diagram

Sodium (Na^+): The source of Na in the rift waters is likely to be attributed to the dominance of acidic volcanics, mainly ignimbrite, rhyolite and pumice (Ayenew 2005).

The maximum and minimum concentrations of Na^+ in TBL_SPG2, TBL_SPG3, TBL_SPG4, TBL_Birsheleko, TSS1, AND3, Lomi, Tikurit, CSPG1, CSPG2 and Aveya were 21.6, 25.8, 19.5, 6.4, 10.8, 7.2, 8, 12, 20.32, 18.2 and 11.4, respectively.

Calcium (Ca^{2+}): The concentration of Ca^{2+} in springs is between 7.5 and 41.3 mg/l, which are under the permissible limits for domestic and livestock.

Magnesium (Mg^{2+}): Magnesium is a major constituent of ferromagnesian minerals such as olivine, pyroxene and amphiboles, which form basic rocks. The minimum and maximum concentrations of magnesium from springs are between 1.2 and 32.5 mg/l TBL_SPG4 and TSS1, respectively, with an average of 12.3 mg/l. Therefore, the concentration of magnesium is within the permissible limits for livestock and domestic purposes.

Potassium (K^+): Potassium is an essential element and is present in all animal and plant tissues. This mineral is dominantly found in rocks through dissolution and weathering of feldspars (orthoclase and microcline). Potassium is an essential element in humans and is seldom, if ever, found in drinking water at levels that could be a concern for healthy humans. The **permissible** limit of potassium (K) in groundwater or domestic water is 1.5 mg/l (MoWE 2001; WaterAid 2014). The concentration values of K^+ in these high discharge springs are between 1.1 and 15.3 mg/

l. The concentrations of K^+ in Lomi, CSPG1 (Bebeks) and CSPG2 (Tankuageberel) springs are 1.2, 1.1 and 1.4 mg/l, respectively, which are within the permissible limits of the WHO and Ethiopian standards. The other high discharge springs are TBL_SPG2, TBL_SPG3, TBL_SPG4, Tikurit and Birsheleko, AND3 (Kinbaba) and TSS1 (Avrajit), which are between 1.6 and 15.3 mg/l above the permissible limits for domestic water supply sources.

Chloride (Cl^-): Chloride is highly mobile and found in anthropogenic and natural systems, inorganic fertilizers, landfill leachates, coastal regions and other areas.

The standard chloride concentration in drinking water is 250 mg/l (MOWE 2001). High levels of chloride in drinking water cause corrosion and clogging of the pipe and water tanker. The maximum and minimum concentrations of chloride from springs are between 1 and 9.9 mg/l, with an average concentration of 5.08 mg/l. Therefore, the concentrations of chloride from these high discharge springs are under the permissible limits.

Nitrate (NO_3): Nitrate (NO_3) is one of the most common groundwater contaminants in the world, and its presence in higher concentrations poses human health and ecological risks. Studies in different parts of the USA show that agricultural fertilizers and urban septic leachates are the primary sources of large nitrate concentrations in surface and groundwater. Water supplies with high levels of nitrate have been responsible for blue baby disease in infants (infantile methemoglobinemia) and death (Singhal and Gupta 1999). This problem does not arise in adults. The maximum limit of NO_3 in natural water is 10 mg/l, while the permissible limit of nitrate in domestic water is 50 mg/l (WHO 2006; WaterAid 2014; MoWE 2001), 44 and 50 in the European Union (1998) and US EPA (2002), respectively. The WHO and the European Union have set the standard for nitrate in drinking water at 11.3 mg/l measured as nitrogen (mg N/l), which corresponds to 50 mg NO_3/l. The standard in the USA, Canada and Australia is 10 mg N/l. In this study, the maximum nitrate concentration was 17.9 mg/l, and the minimum concentration was 3.3 mg/l in CSPG1 (Bebeks) and TBL_SPG4 (Geray) springs, respectively. The nitrate concentrations of the AND3, CSPG1, CSPG2, Tikurit, TSS1 and Lomi springs are above 10 mg/l, which indicates that the concentration of nitrate is increasing due to the cultivated land supply of fertilizer and the uncontrolled sewerage system.

Fluoride (F^-): Fluorine is a common element that is widely distributed in the earth's crust and exists in the form of fluorides in several minerals, such as fluorspar and fluorapatite. Fluoride is the stable form of fluorine that combines with another element. It is abundant in the biosphere and earth's crust and can be a major source of contamination for livestock drinking ground water. Fluoride concentrations for livestock are 1–2 mg F/l, but it has also been noted that at a level of 2 mg/l, mottling of teeth may occur in the Canadian Council of Resource and Environment Ministers (CCME 1991). Fluoride affects bone development and in excess leads to dental or, in extreme form, skeletal fluorosis. Epidemiological evidence shows that concentrations above this value carry an increasing risk of dental fluorosis, and progressively higher

concentrations lead to increasing risks of skeletal fluorosis (Fawell et al. 2006). The permissible limits of florid are < 1.5 mg/l (WaterAid Ethiopia 2014; MoWE 2001).

The maximum and minimum fluoride concentrations are 0.37 and 0.12 mg/l in Birshelko and Lomi springs, respectively. The average fluoride concentration in these high discharge springs is 0.22 mg/l. Therefore, the concentrations of all springs are within the permissible limits for live stocks and domestic supply sources.

Sulfate (SO_4^{2-}): Sulfates occur naturally in numerous minerals, including barite ($BaSO_4$), epsomite ($MgSO_4 \cdot 7H_2O$) and gypsum ($CaSO_4 \cdot 2H_2O$) (Greenwood and Earnshaw 1984). Levels of sulfate in groundwater in the Netherlands were below 150 mg/l (Van Dijk-Looijaard and Fonds 1985), SO_4 up to 500 mg/l is suitable for all types of livestock, and up to 1000 mg/l is suitable for cattle sheep and horses. Sulfates of calcium and magnesium form hard scales. Large concentrations of sulfate have a laxative effect on some people and, in combination with other ions, give water a bitter taste (US EPA 1994a). The permissible limit of sulfate in drinking water is 250 mg/l (WHO 1984; ES 261 2001). Dehydration from diarrhea may be caused by high levels of sulfate in drinking water (US EPA 1999a, b). The minimum and maximum concentrations of SO_4 in these high discharge springs are between 0.0 and 5 mg/l, with an average of 1.84 mg/l. Therefore, the concentration of SO_4 in springs is suitable for domestic and livestock purposes.

Hydrochemical Facies

Hydrogeochemical facies are distinguishable genetically interrelated distinct zones that possess major cation and anion concentration classes, which aids in understanding and detecting the different water compositions in different assemblages (Ravikumar et al. 2011; Freeze and Cherry 1979). Different graphical presentations were used to infer hydrogeochemical facies from physicochemical parameters of water sample analysis. The facies reflect the response of chemical processes operating within the lithologic framework and the pattern of flow of the water.

The Piper diagram in Fig. 20.5 can also be used to classify the hydrochemical facies of the groundwater samples according to their dominant ions. Stiff patterns are useful in making a rapid visual comparison between water from different sources based on the importance of the spring water type in different locations, as shown in Figs. 20.6, 20.7 and 20.8 easily distinguishable where the source is varying.

Based on the laboratory analysis (Table 20.2), the dominant cations in the springs are $Ca^{2+} > Na^{+} > Mg^{2+} > K^{+}$ in CSPG1 (Bebeks) and CSPG2 (Tankuageberel) with Ca–Na–HCO_3–NO_3 type water, whereas Birshelko, Tikurit, Lomi and AND3 (Kinbaba) springs have abundant cations $Ca^{2+} > Mg^{2+} > Na^{+} > K^{+}$, while TSS1 spring $Mg^{2+} > Ca^{2+} > Na^{+} > K^{+}$, which are located in the Infranz and Andasa sub-basins in the Tana and Abay basins. Finally, TBL_SPG2 (Wobane), TBL_SPG3 and TBL_SPG4, which are found in the southwestern parts of the study area, emanate along the Birr sub-basin. The concentration of cations is $Na^{+} > Ca^{2+} > K^{+} > Mg^{2+}$. High

discharge springs are found around the Sekela, Chokie and Guna shield volcanoes in the study area. The concentration of anions is $HCO_3 > NO_3 > Cl > SO_4$ from all springs.

The water types of those springs were analyzed by Aquachem software (Fig. 20.5). The water type is dominantly governed by geology and residence time. is the water type being dominantly Ca–Mg–HCO_3 and Ca–Na–HCO_3–NO_3 type with dominant cations is Ca^{2+} and the second water type is Mg–Ca–HCO_3 and Mg–Ca–HCO_3–NO_3 type with dominant cations of Mg^{2+} and Ca^{2+} and the third water type is Na–Ca–HCO_3. Stiff diagram: Stiff diagrams were used to classify the groundwater according to hydrochemical facies. PCA of the major ions used to identify dominant hydrogeochemical processes controlling the evolution of groundwater chemistry and quality. Groundwater quality was assessed for domestic use suitability based on indices of total dissolved solids (TDS).

For the water type generated using the stiff diagram, the dominant ions were trace, which are Mg, Na and Ca, which are the dominant cations, and HCO_3, which is the dominant anion (Fig. 20.6). Springs emanated at the contact of quaternary and tertiary volcanic units in the Gumara River catchment, and Na and Ca from the cations and HCO_3 and NO_3 from anions are dominant (Fig. 20.7). Springs emanated in the Birr sub-basin, and the dominant ions are Na, Ca and HCO_3, which are from cations and anions, respectively (Fig. 20.8).

Ca–HCO_3-type waters were associated with the shallow systems of the plateau area (Yitbarek et al. 2012; Alemayehu 2011), representing groundwater that was recently recharged and/or contained waters at the early stages of geochemical evolution. This shallow aquifer is classified as an unconfined aquifer type that recharges these high discharge springs and contributes to pollution by fertilizers from cultivated lands.

CSPG1, CSPG2 and Lomi springs emanate quaternary volcanic rocks in the Tana Basin, specifically the Gumara and Infiranz sub-basins. These springs, CSPG1 and CSPG2, are holy springs located in the farming area in the Gumara sub-basin, whereas Lomi spring is the source of water supply for Bahir Dar town.

Uncontrolled sewerage systems from spiritual believers in and around holy springs and fertilizer from cultivated land cause an increase in the concentration of nitrate in CSPG1 and CSPG2 springs. The aquifer of the Infranz catchment is a type of unconfined aquifer that is directly recharged from surface water and direct precipitation. Fertilizer from cultivated land increases the concentration of nitrate in springs.

The Jiga cold springs (SK103), which are coded TBL_SPG2 in this study and are representative of shallow Ca–Mg–HCO_3-type groundwater, show a δ13C of −11.6%, reflecting soil CO_2 as a principal source of carbonate species in shallow groundwater (Kebede et al. 2005). In this study, not only Jiga (TBL_SPG2) springs but also Geray (TBL_SPG4) and TBL_SPG2 (Wodane) are high discharge springs that emanate in the Birr sub-basin and have a Na–Ca–HCO_3 water type, which is a transitional groundwater type.

Birshelko spring was also found downstream of the above three springs (TBL_SPG2, TBL_SPG3 and TBL_SPG4), which follow the Silala-Yisir catchment southern parts of Bure within the Birr sub-basin and have Mg–Ca–HCO_3 type.

In this study, TSS1, Lomi, AND3 and Tikurit springs are emanated at the foot of Chokie/Sekela Shield Volcano, including high TDS Andasa springs. The water types of Tikurit, Aveya_SPG and TSS1 (Avirajit) are Mg–Ca–HCO_3 type, and AND3 (Kinbaba) springs are Ca–Mg–HCO_3 type (Table 20.5).

The cations enter the groundwater system through the incongruent dissolution of feldspars and ferromagnesium minerals of the host rocks (Drever 1997). Agricultural activities, domestic wastes and marine sources also contribute Na^+, Mg^{2+} and K^+ ions to the groundwater (Rao 2014).

During the infiltration of recharge, the water adsorbs a large amount of CO_2 released from soil, which is mainly from the decay of organic matter and root respiration. In weathering reactions, it is converted to HCO_3^- salts (Berner 1992). In this study, the concentration of HCO_3 is higher than that of the rest of the anions, which is controlled by dissolution of minerals and from soil zones and silicate rocks.

The groundwater in basalts is of the Ca–Mg–HCO_3 type (Singhal and Gupta 1999). Aquifers that are carbonate rocks contain more alkaline earths and carbonate ions relative to alkalis, chlorides and sulfate with a water type of Ca–Mg–HCO_3 type (Singhal and Gupta 1999). Except for the AND3 springs, all high discharge springs are found within highly vesiculated quaternary basalt (vesicular) basalt with calcite and zeolite minerals. Therefore, the aquifer to supply these high discharge springs is from a basaltic aquifer with calcite and aragonite/zeolite precipitates and highly fractured and welded tuff radiated from the shield volcano.

The three high discharge springs (AND3, CSPG1 and CSPG2) emanate at the contact of the overlaying quaternary volcanic units and the underlying Cenozoic volcanic rocks. The top highly fractured and vesiculated quaternary volcanic rocks are replenished by incoming surface water systems, such as rivers, floods and direct perception. The water types are basic and transitional groundwater types. However, the water types of Lomi, CSPG1 and 2 springs have NO_3 concentrations, which

Table 20.5 Water type of those springs

Group	ID	*X*	*Y*	*Z*	Water type
Group 1	AND3	324,502	1,266,003	1881	Ca–Mg–HCO_3
	CSPG1	354,295	1,304,395	1838	Ca–Na–HCO_3–NO_3
	CSPG2	355,041	1,309,340	1809	Ca–Na–HCO_3–NO_3
Group 2	Birsheleko	299,309	1,171,908	1710	Mg–Ca–HCO_3
	Tikurit	332,023	1,273,035	1720	Mg–Ca–HCO_3
	TSS1	347,861	1,269,534	1604	Mg–Ca–HCO_3
	Aveya_SPG	366,206	1,228,866	1673	Mg–Ca–HCO_3
	Lomi	312,011	1,282,351	1833	Mg–Ca–HCO_3–NO_3
Group 3	TBL_SPG3	321,797	1,180,351	1820	Na–Ca–HCO_3
	TBL_SPG4	312,447	1,178,521	1794	Na–Ca–HCO_3
	TBL_SPG2	321,572	1,189,451	1920	Na–Ca–HCO_3

indicates that the local aquifer system is directly interconnected with surface activities and that they are easily prone to pollution.

CSPG1 and 2 springs are used as holy water, and the local people around spring camps use fragmented sewerage systems in the surroundings of the spring. The aquifer is open, which is an unconfined aquifer system, so it is easily polluted by anthropogenic impacts.

The high concentration of Na in the rift waters is likely to be attributed to the dominance of acidic volcanics, mainly ignimbrite, rhyolite and pumice (Ayenew 2005; Singhal and Gupta 1999). Na–Ca–HCO_3-type waters are mainly encountered in the plateau and the rift part of the study area. Na–HCO_3-type waters in the area are associated with diluted chemistry deep wells in the plateau area and wells in the southern part (rift) (Yitbarek et al. 2012). Similar to flood volcanics, shield volcanoes are bimodal and contain sequences of alternating basalts, rhyolite and trachytic lava flows, tuffs and ignimbrites, particularly near their summits (Kieffer et al. 2004).

Groundwater in basalts has more alkaline earths (Ca^{2+} and Mg^{2+}) and lower amounts of alkalis (Na^+ and K^+) (Singhal et al. 1999). The TBL_SPG2, TBL_SPG3 and TBL_SPG4, Table 20.2 show that the dominant cations are Na and Ca with the Na–Ca–HCO_3 water type, which is a transitional groundwater type leached from the Choke and Sekela Shield volcanic rocks through thick tuff and ignimbrite units and weathered olivine-bearing Cenozoic volcanic units.

The other springs have Ca and Mg concentrations that originate from hydrolyses of silicate minerals or cation exchange of weathered olivine-bearing basalts.

Irrigation: Sodium Absorption Ratio (SAR): SAR is a measure of groundwater suitability for use in agricultural irrigation activities (Sen 1995). The Na^+ concentration can reduce the soil permeability and soil structure (Todd 1980). The sodium adsorption ratio (SAR) is a measure of alkali/sodium hazard to crops and can be estimated by the following formula.

The maximum SAR value is 1.74 mg/l at TBL_SPG4 and 3, and the minimum SAR value is 0.22 meq/l, which are both less than 10 meq/l. Thus, all spring waters are suitable for irrigation activity. Currently, CSPG1 and 2, AND3, Tikurit, TBL_SPG2, 3, 4 and Birsheleko springs are used both for water supply and irrigation activity. Based on the Rechards (1954) classification method, high discharge springs are suitable for irrigation activity. All springs are found in the low sodium hazard (S1) zone. CSPG1, CSPG2 and Lomi springs are found in zones with low sodium hazards and low salinity hazards. The other springs, which are TBl_SPG2, TBL_SPG3 TBL_SPG4 and Tikurit, are located in low sodium hazards and medium salinity hazards. TSS1 and Birsheleko springs are found in low sodium hazard and high salinity hazard zones (Fig. 20.9).

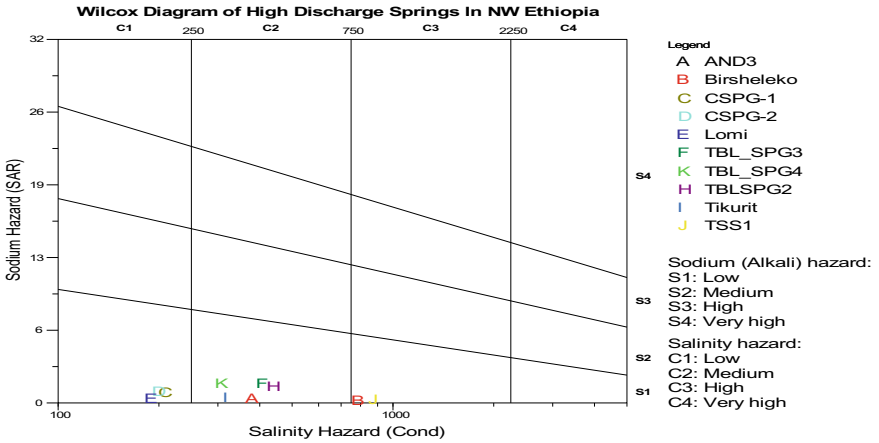

Fig. 20.9 Wilcox diagram of high discharge springs in northwestern Ethiopia

Conclusions

The hydrochemical analysis of the high discharge springs showed that TSS1, CSPG1, CSPG2 and Aveya and AND3 springs are emanated as structural spring types at lower basaltic units. The remaining TBL_SPG2, TBL_SPG3, TBL_SPG4, Birsheleko, Lomi and Tikurit springs are emanated through geological faults on quaternary volcanic units. The discharges of those springs are between 30 and 400 l/s. The maximum discharge is found in the southwestern parts of the study area near Jiga town, which is TBL_SPG3 with a discharge of 400 l/s. The water types of the spring are Ca–Na–HCO_3–NO_3, Mg–Ca–HCO_3 and Na–Ca–HCO_3, which are shallow, mixed or transitional water types.

The concentrations of K in AND3, TSS1, Tikurit, TBL_SPG2, TBL_SPG3, TBL_SPG3, Birsheleko and Aveya (ASPG1) are above the permissible limits, whereas those in CSPG1, CSPG2 and Lomi springs are below the permissible limits of the WHO standards. The concentrations of nitrate in TSS1, AND3, Aveya, Tikurit, Lomi, CSPG1 and CSPG2 spring are higher than those in the rest of the spring, which are polluted by anthropogenic sources and fertilizer from cultivated lands. Except for TBL_SPG4, all springs are grouped under moderately hard to hard water, which causes clogging of water pipes and boilers and consumes more soap during washing.

All springs are suitable for livestock and irrigation, but they need simple treatment for domestic water supply sources with higher hardness values and greater concentrations of K in the water.

Acknowledgements We would like to thank Amhara Design and Supper Vision Works Enterprise for financial support in conducting laboratory analysis.

References

AGRI-FACTS (2007) Practical information for Alberta's agricultural industry, water analysis interpretation for livestock. Agdex 400/716-2

Alemayehu T (2011) Water–rock interaction and geochemistry of groundwater in Axum area. Institute of Applied Geosciences, Graz University of Technology, Northern Ethiopia

Ayenew T (2005) Major ions composition of the groundwater and surface water systems and their geological and geochemical controls in the Ethiopian volcanic terrain. Department of Geology and Geophysics, Addis Ababa University

Bawoke GT, Anteneh ZL (2020) Spatial assessment and appraisal of groundwater suitability for drinking consumption in Andasa watershed using water quality index (WQI) and GIS techniques: Blue Nile Basin, Northwestern Ethiopia. Cogent Eng 7:1. https://doi.org/10.1080/23311916.2020.1748950

Berner RA (1992) Weathering, plants, and the long-term carbon cycle. Geochim Cosmochim Acta 56(8):3225–3231. ISSN 0016-7037. https://doi.org/10.1016/0016-7037(92)90300-8

CCME (Canadian Council of Ministers of the Environment) (1991) Appendix IX—a protocol for the derivation of water quality guidelines for the protection of aquatic life. In: Canadian water quality guidelines, Apr 1991. Canadian Council of Resource and Environment Ministers, 1987. Prepared by the task force on water quality guidelines [Reprinted in Canadian environmental quality guidelines, chap 4. Canadian Council of Ministers of the Environment, Winnipeg, 1999]

Chernet T (1993) Hydrogeology of Ethiopia and water resource development. Ministry of Mines and Energy, Geological Survey of Ethiopia

Chorowicz J, Collet B, Bonavia FF, Mohr P, Parrot JF, Korme T (1998) The Tana basin, Ethiopia: intraplateau uplift, rifting and subsidence Ethiopia. Elsevier Science. 0040-1951/98/$19.00@1998

Fawell J, Bailey K, Chilton J, Dahi E, Fewtrell L, Magara Y (2006) Fluoride in drinking-water, vol 208. World Health Organization, Geneva, Switzerland, pp 693–713

Freeze RA, Cherry JA (1979) Groundwater. Prentice-Hall International, Hemel Hempstead, xviii + 604 pp

Gani ND, Abdelsalam MG, Gera S, Gani MR (2009) Stratigraphic and structural evolution of the Blue Nile Basin, Northwestern Ethiopian Plateau. Geol J 44:30–56. https://doi.org/10.1002/gj.1127

Guzo C (1974) Hydrothermal investigation of Filwuha area. Ethiopia Memoirs of the Faculty of Education, Akita University, Addis Ababa, pp 23–25

Hofmann C, Courtillot V, Feraud G, Rochette P, Yirgu G, Ketefo E, Pik R (1997) Timing of the Ethiopian flood basalt event and implications for plume birth and global change. https://www.researchgate.net/publication/232789762

Kebede S (2013) Groundwater in Ethiopia. In: Springer hydrogeology. https://doi.org/10.1007/978-3-642-30391-3

Kebede S, Travi Y, Alemayehu T, Ayenew T (2005) Groundwater recharge, circulation and geochemical evolution in the source region of the Blue Nile River, Ethiopia. https://doi.org/10.1016/j.apgeochem.2005.04.016

Kieffer B, Arndt N, Lapierre H, Bastien F, Bosch D, Pecher A, Yirgu G, Ayalew D, Weis D, Jerram DA, Keller F, Meugniot C (2004) Flood and shield basalts from Ethiopia: magmas from the African superswell. Addis Ababa, Ethiopia. https://doi.org/10.1093/petrology/egg112

Mamo S (2015) Integrated hydrological and hydrogeological system analysis of the Lake Tana basin, Northwestern Ethiopia. Addis Ababa University, Addis Ababa, Ethiopia

Mamo S, Ayenew T, Berehanu B, Kebede S (2016) Hydrology of the Lake Tana basin, Ethiopia: implication to groundwater-surface waters interaction. J Environ Earth Sci. ISSN 2224-3216 (paper), ISSN 2225-0948

Ministry of Water and Energy (2001) Domestic water standards and guidelines ES 261-2001. Addis Ababa, Ethiopia

Mohor (1971) The geology of Ethiopia. Haile Selassie I University Press, pp 209–210

MoWE (2002) Water sector development program main report, vol 2. Ethiopia Ministry of Water Resources, p 45

Nigate F, Van Camp M, Yenehun A, Belay A, Walraevens K (2020) Recharge–discharge relations of groundwater in volcanic terrain of semi-humid tropical highlands of Ethiopia: the case of Infranz Springs, in the Upper Blue Nile. Water 12:853. https://doi.org/10.3390/w12030853

Pik R, Deniel C, Coulon C, Yirgu G, Hofmann C, Ayalew D (1998) The northwestern Ethiopian Plateau flood basalts: classification and spatial distribution of magma types. J Volcanol Geotherm Res 81:91–111

Rao N (2014) Spatial control of groundwater contamination, using principal component analysis. J Earth Syst Sci 123:715–728. https://doi.org/10.1007/s12040-014-0430-3

Ravikumar P, Somashekar RK, Angami M (2011) Hydrochemistry and evaluation of groundwater suitability for irrigation and drinking purposes in the Markandeya River basin, Belgaum District, Karnataka State, India. Environ Monit Assess 173(1):459–487

Sawyer G, McCarty DL (1967) Chemistry of sanitary engineers, 2nd edn. McGraw Hill, New York, p 56

Sen Z (1995) Applied hydrogeology for scientists and engineers, 1st edn. CRC Press. https://doi.org/10.1201/9781315137612

Singhal BBS, Gupta RP (1999) Applied hydrogeology of fractured rocks, 2nd edn. Springer, Dordrecht Heidelberg London New York, pp 267–268. https://doi.org/10.1007/978-90-481-8799-7

Soulios G (2010) Springs (classification, function, capturing). Bull Geol Soc Gr 43(1):196–215. https://doi.org/10.12681/bgsg.11174

Stiff HA (1951) Interpretation of chemical water analysis by means of pattern. J Petrol Technol 3:15–17. https://doi.org/10.2118/951376-G

Stumm W, Morgan JJ (1996) Aquatic chemistry—chemical equilibria and rates in natural waters, 3rd edn. Wiley, New York, p 214

Taye MT, Haile AT, Fekadu AG, Nakawuka P (2021) Effect of irrigation water withdrawal on the hydrology of the Lake Tana sub-basin. J Hydrol Reg Stud 38:100961. ISSN 2214-5818. https://doi.org/10.1016/j.ejrh.2021.100961

Van Dijk-Looijaard AM, Fonds AW (1985) Integrated criteria document sulfate. RIVM report no. 718612001. National Institute of Public Health and Environmental Protection, Bilthoven

WaterAid (2014) Water quality policy guideline. Addis Ababa, Ethiopia, pp 21–23

WHO (2006) Protecting groundwater for health. WHO Library Cataloging-in-Publication Data. ISBN 13: 9781843390794

Wilcox LV (1955) Classification and use of irrigation water, Circular 969. US Department of Agriculture, Washington, DC

Yitbarek A, Razack M, Ayenew T, Zemedagegnehu E, Azagegn T (2012) Hydrogeological and hydrochemical framework of Upper Awash River basin, Ethiopia: with special emphasis on inter-basins groundwater transfer between Blue Nile and Awash Rivers. J Afr Earth Sci 65:46–60. https://doi.org/10.1016/j.jafrearsci.2012.01.002

Index

A. M. Melesse et al. (eds.), *Land and Water Degradation in Ethiopia*, Springer Geography, https://doi.org/10.1007/978-3-031-60251-1